Metal-Mediated DNA G-Quadruplexes:

Spin-Labeling for Distance Measurements in Higher-Order Structures and New Ligand Functionalities for Heteroleptic Coordination Environments

This dissertation is submitted for the degree of
“Doctor rerum naturalium”

TU Dortmund
Fakultät für Chemie und Chemische Biologie

Lukas M. Stratmann

Dortmund, June 2021

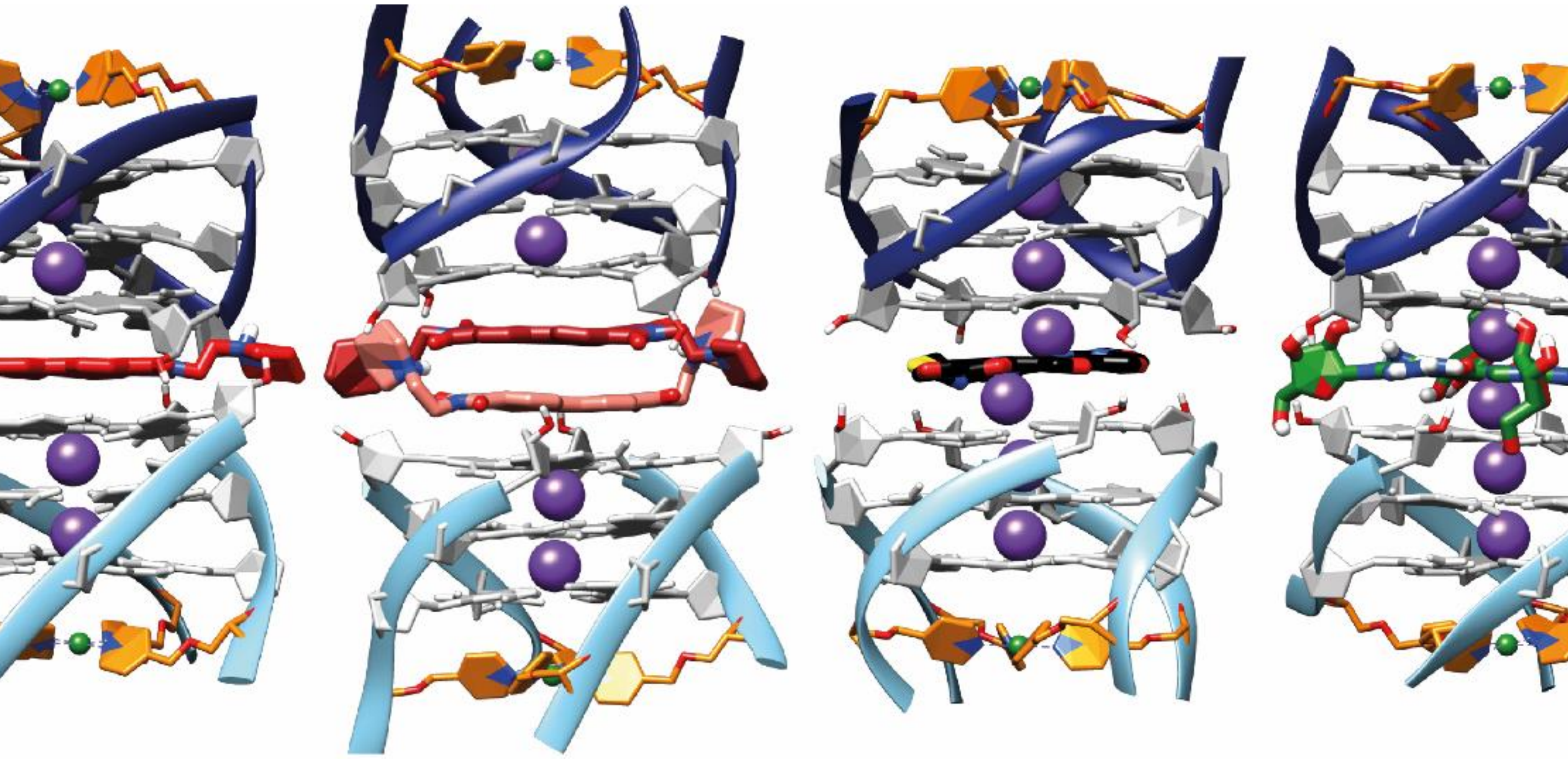

Principal advisor: **Prof. Dr. Guido H. Clever**
Faculty of Chemistry and Chemical Biology,
TU Dortmund University

Coexaminer: **JProf. Dr. Müge Kasanmascheff**
Faculty of Chemistry and Chemical Biology,
TU Dortmund University

Submission Date: 21.06.2021

Grau is‘ im Leben alle Theorie, aber entscheidend is‘ auf‘m Platz!

– Adi Preißler

… und im Labor!

Awards

2020	Poster Prize at the Twitter Poster Session of vMASC2020 (virtual RSC Macrocyclic and Supramolecular Chemistry Conference)
2019	Poster Prize at ICBIC19 (International Conference of Biological Inorganic Chemistry), Interlaken, Switzerland

Conference Contributions

Oral presentations:

May 2021	Talk at webinar series “Nucleic acid secondary structures – G4s and beyond”
Apr 2021	Talk at ACS spring, online
Mar 2021	Talk at RESOLV spring workshop, online
Mar 2021	Invited talk at RSC vMASC weekly Young Researcher Webinar
Feb 2020	Talk at Tag der Chemie, TU Dortmund, Germany
Aug 2019	Invited flash presentation at ICBIC19, Interlaken, Switzerland

Poster presentations:

Dec 2020	RSC vMASC on Twitter
Sep 2019	IMBP, Dortmund (DE)
Sep 2019	GRK-CCC, Bochum (DE)
Aug 2019	19th ICBIC, Interlaken (CH)
Aug 2018	14th EuroBIC, Birmingham (UK)
Mar 2018	9th MSCEC, Münster (DE)
Feb 2018	Tag der Chemie, Dortmund (DE)
Jun 2017	6th G4thering, Prague (CZ)

Publications

- “Precise Distance Measurements in DNA G-Quadruplex Dimers and Sandwich Complexes by Pulsed Dipolar EPR Spectroscopy” L. M. Stratmann, Y. Kutin, M. Kasanmascheff, G. H. Clever, *Angew. Chem. Int. Ed.* **2021**, *60*, 4939.

- “Heteroleptic Coordination Environments in Metal-Mediated DNA G-Quadruplexes” P. M. Punt,* L. M. Stratmann,* S. Sevim, L. Knauer, C. Strohmann, G. H. Clever, *Front. Chem.* **2020**, *8*, 26. (*: these authors have contributed equally to this work)

- “The tert-butylaminomethyl(mesityl)phosphinic acid ester and formation of its zinc dichloride complex: syntheses and characterization” M. Lutter, L. M. Stratmann, K. Jurkschat, *Main Group Met. Chem.* **2018**, *41*, 109.

- “Structure–Property Relationships in Cu^{II}-Binding Tetramolecular G-Quadruplex DNA” D. M. Engelhard, L. M. Stratmann, G. H. Clever, *Chem. Eur. J.* **2018**, *24*, 2117.

- “Syntheses, Structures, and Complexation Studies of Tris(organostannyl)methane Derivatives” A. Siakam Wendji, M. Lutter, L. M. Stratmann, K. Jurkschat, *ChemistryOpen* **2016**, *5*, 554.

Abstract

G-quadruplexes are four-stranded secondary DNA structures formed from π-stacked tetrads of Hoogsteen hydrogen-bonded guanines. Due to their important regulatory roles in several biological processes, including oncogene expression and maintenance of telomeric repeats, G-quadruplexes have been identified as potential drug targets especially in anticancer research. Many small molecules, so-called G-quadruplex binders, have been designed to selectively address and stabilize the secondary structure type thereby representing promising drug candidates. Their biological and medicinal importance calls for detailed structural information on G-quadruplexes and their adducts with binders. Due to their high topological diversity, structure elucidation of G-quadruplexes is challenging. Additionally, they tend to form higher-order structures like dimers or other motifs which are thought to influence their function *in vivo*.

In this thesis, artificial square-planar Cu(pyridine)$_4$ complexes, covalently incorporated into tetramolecular G-quadruplexes, were used as highly rigid spin labels for the detection of higher-order structures by intermolecular Cu^{2+}-Cu^{2+} distance measurements with pulsed dipolar EPR spectroscopy. Various G-quadruplex dimers of different spatial dimensions formed by tail-to-tail or head-to-head stacking were unambiguously distinguished and unprecedentedly narrow distance distributions obtained in the experiments were in full agreement with MD simulation results. Moreover, the intercalation of two drug-like G-quadruplex binders, PIPER and telomestatin, into G-quadruplex dimers resulting in sandwich complexes was investigated and previously unknown binding modes were discovered. Also, G-tetrads composed of free guanines or guanosines were revealed to intercalate into G-quadruplex dimers. The EPR-based distance measurements were also used for time-dependent monitoring of structural rearrangements of the higher-order G-quadruplex structures. The method was further applied to measure distances in more complex DNA constructs like duplex-bridged unimolecular G-quadruplexes. Since organic radicals are commonly used spin labels for distance measurements in DNA architectures, their compatibility with the Cu(pyridine)$_4$ spin label was demonstrated in a model system. The transition metal labeling approach, combined with pulsed EPR spectroscopy, opens new possibilities for examining structures of non-covalent DNA aggregates.

Furthermore, the incorporation of metal complexes into DNA structures plays an important role in DNA nanotechnology as it allows to introduce additional functionality. The covalent installation of ligand functionalities into G-quadruplex scaffolds is a promising strategy to build tailored coordination spheres within a DNA environment for transition metal complexes with fine-tuned properties. While the concept has previously been established with pyridine and imidazole ligands, the variety of ligand functionalities was expanded in this thesis. Inspired by donor groups found in amino acid side chains, hard carboxylates as well as softer thioether and thiol residues were integrated in G-quadruplexes. Therefore, new phosphoramidite building blocks had to be designed and incorporated into suitable DNA sequences. The modularity of the approach was showcased by the variation of kind, number, and positioning of donor groups in a unimolecular G-quadruplex resulting in preorganized heteroleptic coordination environments with different metal affinities. This strategy allows the simple construction of tailored transition metal complexes for future applications in DNA nanotechnology for purposes like asymmetric catalysis or redox activity mimicking functional complexes from metallo-proteins.

Zusammenfassung

G-Quadruplexe sind viersträngige DNA-Sekundärstrukturen, die aus π-gestapelten Tetraden bestehen, die sich aus Guaninen über Hoogsteen-Wasserstoffbrücken bilden. Aufgrund ihrer regulatorischen Funktionen in vielen biologischen Prozessen, wie der Onkogenexpression und der Instandhaltung der Telomerstrukturen, wurden G-Quadruplexe als potenzielle Angriffsziele für Medikamente insbesondere in der Krebsforschung identifiziert. Zahlreiche niedermolekulare Verbindungen, sogenannte G-Quadruplexbinder, wurden entworfen, die diese Sekundärstrukturen selektiv binden und stabilisieren, und dadurch vielversprechende Wirkstoffkandidaten darstellen. Ihre biologische und medizinische Bedeutung erfordert detaillierte Strukturinformationen zu G-Quadruplexen und deren Addukten mit Bindern. Die Strukturaufklärung von G-Quadruplexen ist aufgrund der hohen topologischen Vielfalt eine Herausforderung. Hinzu kommt, dass sie dazu neigen, übergeordnete Strukturen wie Dimere oder andere Motive zu bilden, die vermutlich die *in-vivo*-Funktion beeinflussen.

In dieser Arbeit wurden künstliche, quadratisch-planare Cu(Pyridin)$_4$-Komplexe kovalent in tetramolekulare G-Quadruplexe eingebaut und als hochrigide Spinmarker verwendet, um übergeordnete Strukturen durch intermolekulare Cu^{2+}-Cu^{2+}-Abstandsmessungen mit gepulster dipolarer EPR-Spektroskopie zu detektieren. Verschieden große Schwanz-zu-Schwanz- oder Kopf-zu-Kopf-gestapelte G-Quadruplex-Dimere konnten zweifelsfrei voneinander unterschieden werden und aus den Experimenten erhaltene, beispiellos schmale Abstandsverteilungen stimmten sehr gut mit Ergebnissen aus MD-Simulationen überein. Zudem wurde die Interkalation zweier wirkstoffähnlicher G-Quadruplexbinder, PIPER und Telomestatin, in G-Quadruplex-Dimere untersucht, was in Sandwichkomplexen resultiert, und bislang unbekannte Bindungsmodi wurden entdeckt. Es wurde auch aufgedeckt, dass G-Tetraden, bestehend aus freien Guaninen oder Guanosinen, in G-Quadruplex-Dimere interkalieren. Die EPR-basierten Abstandsmessungen wurden außerdem genutzt, um strukturelle Umlagerungen der übergeordneten G-Quadruplexstrukturen zeitabhängig zu verfolgen. Die Methode wurde weiter zum Messen von Abständen in komplexeren DNA-Konstrukten wie Duplex-verbrückten, unimolekularen G-Quadruplexen angewendet. Da häufig organische Radikale als Spinmarker für Abstandsmessungen in DNA-Architekturen verwendet werden, wurde deren Kompatibilität mit dem Cu(Pyridin)$_4$-Spinmarker an einem Modellsystem demonstriert. Der Ansatz der Übergangsmetall-basierten Spinarkierung in Kombination mit gepulster EPR-Spektroskopie eröffnet neue Möglichkeiten zur Strukturanalyse nicht-kovalenter DNA-Aggregate.

Des Weiteren spielt der Einbau von Metallkomplexen in DNA-Strukturen eine wichtige Rolle in der DNA-Nanotechnologie, da dadurch die Einführung zusätzlicher Funktionalität möglich ist. Die kovalente Installation von Donorfunktionalitäten in G-Quadruplex-Gerüste stellt eine vielversprechende Strategie dar, um maßgeschneiderte Koordinationsspheren innerhalb der DNA-Umgebung für Übergangskomplexe mit feinjustierten Eigenschaften zu bilden. Da das Konzept bereits mit Pyridin- und Imidazolliganden etabliert wurde, sollte die Auswahl an Liganden in dieser Arbeit erweitert werden. Inspiriert durch Donorgruppen aus Aminosäureseitenketten wurden harte Carboxylate sowie weichere Thioether- und Thiolfunktionen in G-Quadruplexe eingebaut. Dafür mussten neue Phosphoramiditbausteine entworfen und in passende DNA-Sequenzen eingebaut werden. Die Modularität des Ansatzes wurde durch die Variation von Art, Zahl und Position der Liganden in einem unimolekularen G-Quadruplex demonstriert, was zu vororganisierten, heteroleptischen Koordinationsumgebungen mit verschiedenen Metallaffinitäten führte. Die Strategie ermöglicht den einfachen Aufbau maßgeschneiderter Übergangsmetallkomplexe für zukünftige Anwendungen in der DNA-Nanotechnologie für Zwecke wie asymmetrische Katalyse oder Redoxaktivität durch Nachahmen von funktionellen Komplexen aus Metallo-Proteinen.

Table of Content

1 General Introduction

1.1 Deoxyribonucleic Acids and DNA Secondary Structures

Deoxyribonucleic acid (DNA) belongs to the most important classes of biological macromolecules. Its key function is the storage of genetic information in all living organisms. As it bears the blueprints for protein biosynthesis, its sequence is transcribed into mRNA which then serves as the template for protein production (translation). The DNA molecule is known as a linear polymer composed of monomeric building blocks called nucleotides. Each nucleotide contains a deoxyribose sugar that is bound to a phosphate group *via* the 5’ carbon atom and to one out of four nucleobases *via* the 1’ atom, either a purine (adenine, guanine) or a pyrimidine (thymine, cytosine). The connection between two nucleotides is achieved between the phosphate group and the 3’ carbon atom of the next building block forming a phosphodiester bridge (Figure 1.1a).[1]

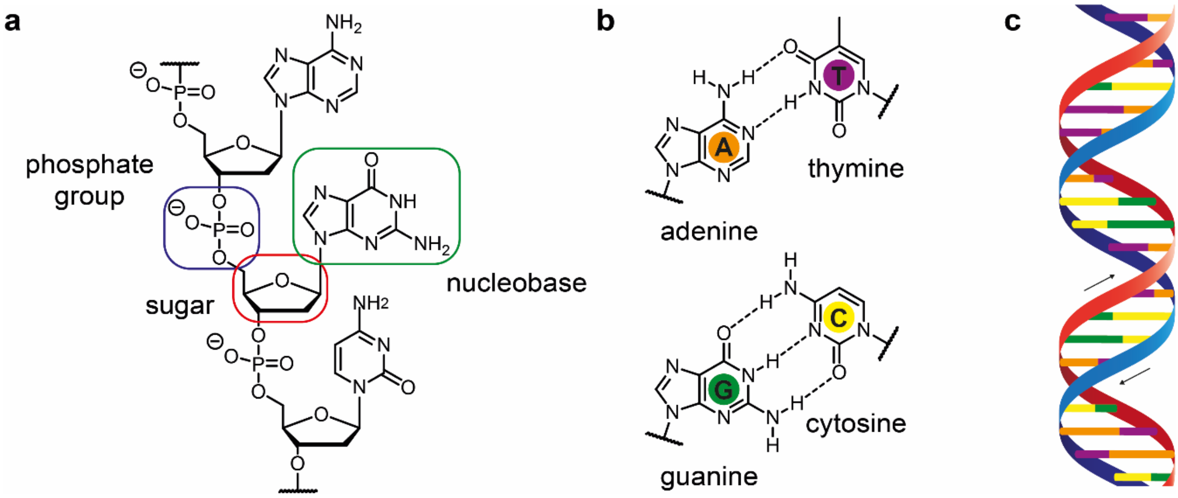

Figure 1.1: Basic DNA structure. (**a**) A DNA strand is a linear polymer of nucleotide building blocks. Each nucleotide is composed of a deoxyribose sugar (red), a phosphate group (blue) and one out of four nucleobases (green). (**b**) Canonical Watson-Crick base pairs (A-T and G-C) with specific hydrogen bonds. (**c**) Antiparallel double helix formed by two complementary DNA strands.

The main secondary structure adopted by DNA in the nuclei is the antiparallel double helix (B-DNA), where two complementary DNA strands coil around each other (Figure 1.1c) with the negatively charged sugar-phosphate backbones pointing outside. Inside the right-handed helix, highly specific interstrand hydrogen bonds form between the nucleobases (Figure 1.1b), exclusively between adenine (A) and thymidine (T) as well as between guanine (G) and cytosine (C). The plane of these π-stacking Watson-Crick base pairs is almost perfectly perpendicular to the helix axis. The correct structural model of the DNA duplex was awarded with the Nobel prize in physiology or medicine in 1962 to James Watson, Francis Crick and Maurice Wilkins.[1–3]

In addition to the B-DNA duplex, two more double helical motifs have been observed and are believed to have biological relevance. The A-DNA type is found in double-stranded RNA and DNA-RNA hybrid helices and is adopted by DNA under dehydrating conditions. Among other structural differences, the base pairs are tilted about 19° with respect to the helix axis.[1,4] A third type of double helix is the left-handed Z-DNA, which is mostly adopted by specific sequences such as alternating purine-pyrimidine sequences or can be induced with high salt concentrations.[5] Underlining its biological relevance, several proteins are known that specifically bind to Z-DNA.[6]

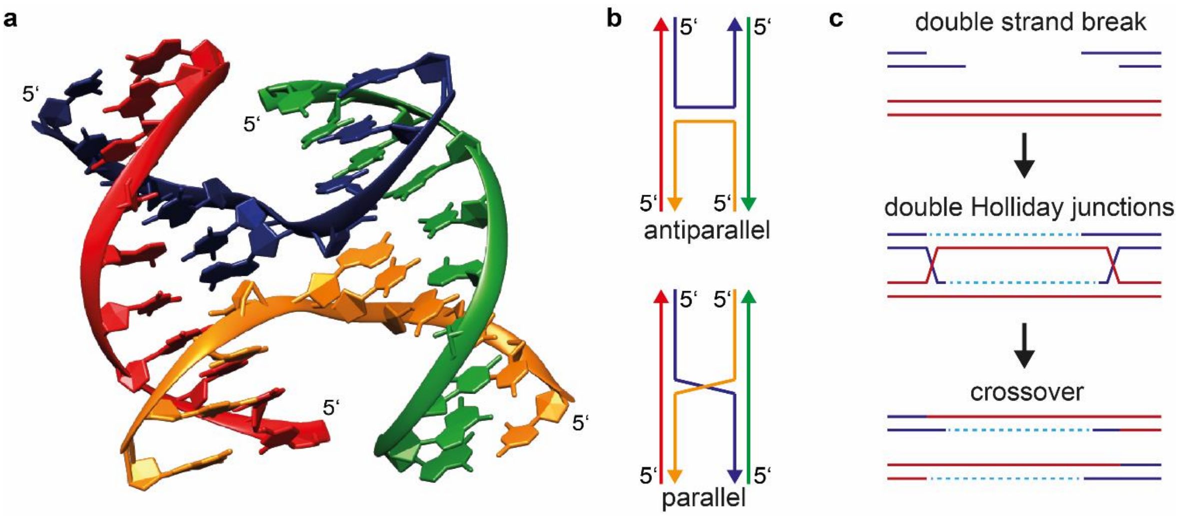

Figure 1.2: (**a**) Crystal structure of a DNA Holliday junction (PDB: 1DCW).[7] (**b**) Schematic representations of an antiparallel and a parallel oriented Holliday junction. (**c**) Structural involvement of Holliday junctions in recombination upon double strand break.[8]

Besides duplex motifs, DNA is known do adopt several other secondary structures *in vitro* which are also believed to form *in vivo* and are involved in important biological processes.[9,10] In the so called hairpin loops, cruciform DNA, three-way junctions and four-way junctions (Holliday junctions, Figure 1.2), canonical Watson-Crick base pairing is the main hydrogen bond interaction between involved DNA strands. These structural motifs play important biological roles, for example during genetic recombination or in DNA repair mechanisms.[7,8,11–13]

An additional hydrogen bond pattern between nucleobases is called Hoogsteen hydrogen bonding, which is characterized by the N7 atom of purine bases serving as hydrogen bond acceptor.[14] This motif is found in DNA triple helices, where a third nucleobase binds to a canonical Watson-Crick base pair forming a base triplet (Figure 1.3a and b).[15] Hoogsteen hydrogen bonding is also observed in so called G-quadruplex structures formed by guanine-rich sequences. Since this structural motif plays an important role in this thesis, DNA G-quadruplexes are discussed in detail in the following sections. Related to G-quadruplexes is a secondary structure type called i-motif, as it is formed by cytosine-rich sequences. It appears that complementary sequences of G-quadruplex-forming oligonucleotides are usually potential i-motif-forming DNA strands. Assembly of four-stranded i-motifs is often observed under acidic conditions, because hemiprotonated C-C$^+$ base pairs need to form (Figure 1.3c and d).[16,17]

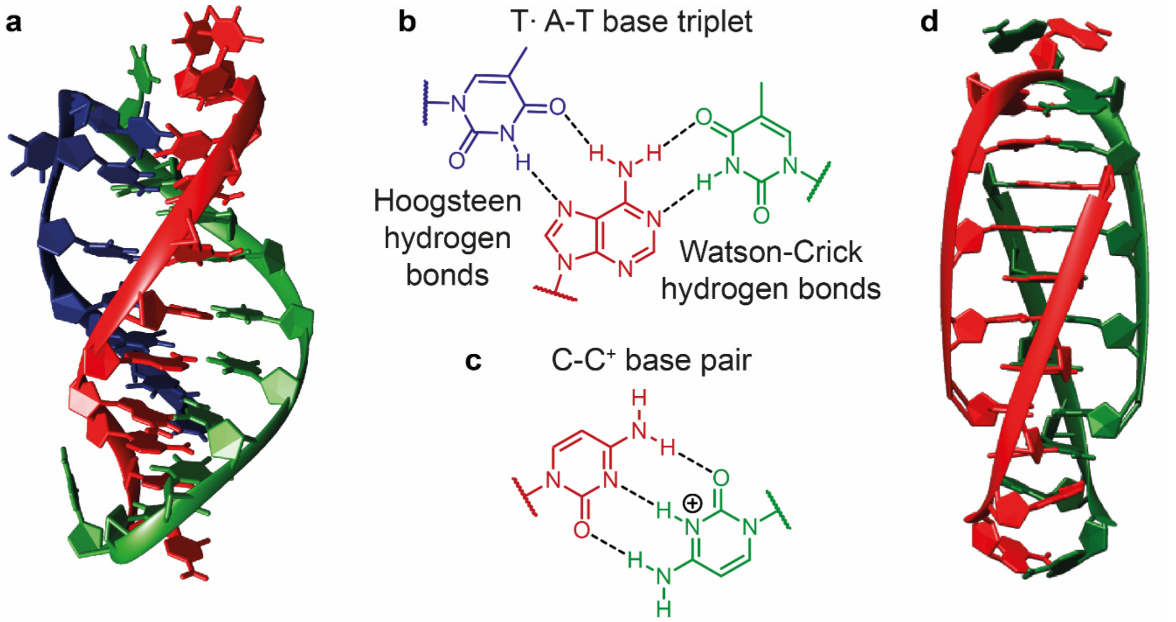

Figure 1.3: (**a**) NMR solution structure of a DNA triple helix (PDB: 1B4Y).[18] (**b**) Base triplet with Hoogsteen and Watson-Crick hydrogen bonding found in triple helices. (**c**) Hemiprotonated C-C$^+$ base pair found in i-motif structures. (**d**) NMR solution structure of an i-motif structure (PDB: 1YBL).[19]

1.2 DNA G-Quadruplexes

1.2.1 General Structure and Structural Diversity

G-quadruplexes are special DNA secondary structures adopted by guanine-rich sequences.[20,21] The basic structural motif is the planar G-tetrad (or G-quartet) assembled by four guanine nucleobases interacting *via* Hoogsteen hydrogen bonding (Figure 1.4a) proposed for the first time by Gellert, Lipsett and Davies in 1962.[22] Several planar G-quartets π-stack on top of each other forming a four-stranded right-handed helical construct called G-quadruplex. Metal ions such as K^+ or Na^+ typically reside between the stacked G-quartets to compensate the negative partial charge resulting from the inward-pointing carbonyl oxygen atoms.[23,24]

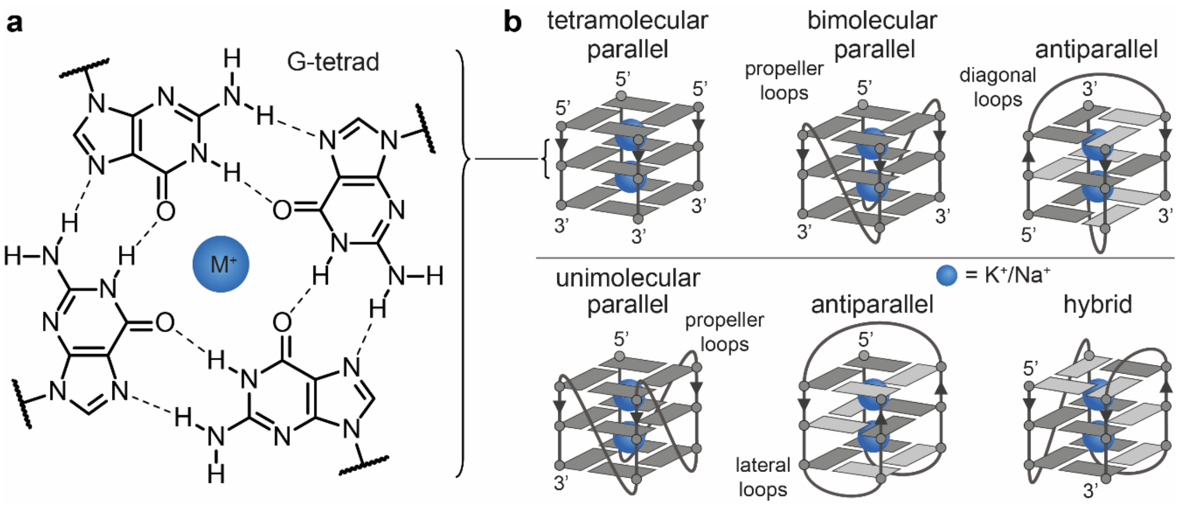

Figure 1.4: (**a**) Structure of a planar G-tetrad with Hoogsteen hydrogen bonding. (**b**) Examples for different G-quadruplex structures, including tetra-, bi-, and unimolecular constructs with parallel, antiparallel or hybrid topologies. Different loop motifs are indicated. The N-glycosidic bond conformations in the guanosines are denoted with dark grey (*anti*) or light grey (*syn*) tiles. These schematic illustrations allow a clear demonstration of different folding topologies. However, it should be kept in mind, that the structure's distinct right-handed helicity is omitted for clarity.

G-quadruplexes show a high structural diversity as a result of several variable parameters. Among these are the G-tetrad count, the stabilizing alkali metal ion and the number of involved DNA strands (i.e. uni-, bi-, tetramolecular). The folding of bi- and unimolecular G-quadruplexes results in loop regions which can differ in length, composition, and connectivity. A distinction is made between diagonal, lateral (or edgewise), and propeller-shape (or double-chain-reversal) loops (Figure 1.4b). Different loop arrangements lead to distinct directionalities of the four G-tracts in the G-quadruplex stem that can be parallel, or antiparallel with respect to each other. As a direct consequence, the N-glycosidic bonds in the guanosines must adopt either *syn* or *anti* conformations dictated by the overall structural topology. The different variables give rise to different G-quadruplex topologies, including all-parallel, antiparallel (with adjacent or opposite parallel strands), or 3+1 hybrid topologies.[25–32]

Often, a single G-rich DNA sequence can adopt several G-quadruplex topologies of similar energy which coexist next to each other. Factors like nature and concentration of electrolytes, pH, DNA concentration and molecular crowding, cosolvents or the presence of G-quadruplex-binding molecules can shift the equilibrium towards one or the other topology. As a popular example, the extensively investigated G-quadruplex-forming sequence found in the human telomeres (htel) adopts an all-parallel topology with propeller-shape loops in the solid state.[33] However, an antiparallel structure was found in Na^+-containing solution[34] and several hybrid or antiparallel topologies were observed in K^+-containing solution.[35–37] Under molecular crowding conditions mimicking a cell-like environment, again the all-parallel topology was shown to be favored.[38]

In addition to their high structural diversity, G-quadruplexes also tend to form higher-order structures like simple dimers.[33,39–47] They are usually formed by parallel G-quadruplexes with accessible terminal G-quartets interacting with each other *via* π-stacking (Figure 1.5). Also, even larger G-quadruplex assemblies are known. Examples are so called G-wires, long arrays of consecutive π-stacked G-quartets formed by short oligonucleotides.[48–50]

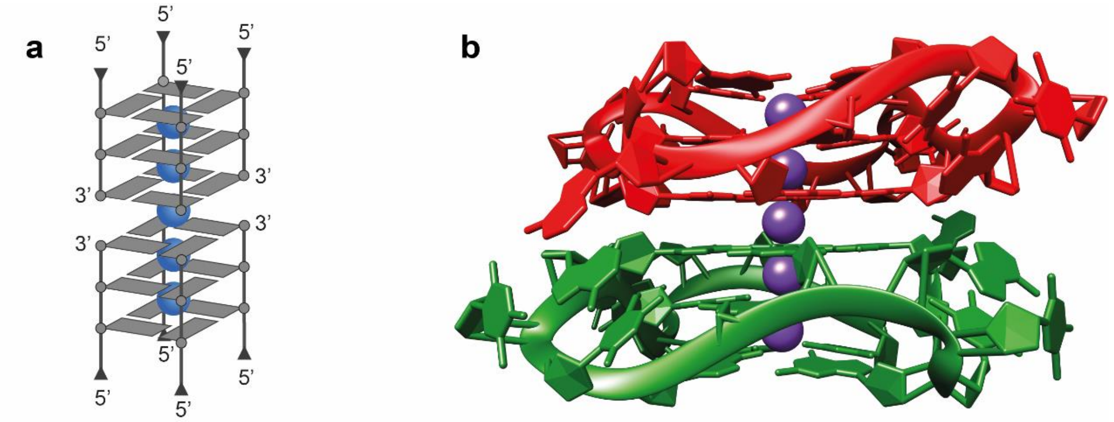

tail-to-tail stacked dimer of tertamolecular G-quadruplexes

head-to-head stacked dimer of unimolecular G-quadruplexes

Figure 1.5: Examples for G-quadruplex dimers. (**a**) Schematic illustration of a tail-to-tail (3'-3') stacked dimer of tetramolecular parallel G-quadruplexes. (**b**) Crystal structure of a head-to-head (5'-5') stacked dimer of unimolecular parallel G-quadruplexes (PDB: 1KF1).[33] The parallel topologies result in accessible terminal G-tetrads allowing dimerization *via* π-stacking.

1.2.2 Biological Relevance of G-Quadruplexes

While the formation of G-quartets has been seen as a laboratory curiosity for a long time, the potential biological significance of G-quadruplex structures became apparent in the 1980th when G-rich sequences, found for example in telomeric regions at the ends of chromosomes, were shown to adopt this type of secondary structure.[51–54] Bioinformatic approaches revealed around 375,000 putative G-quadruplex occurrences of the general sequence $G_{3\text{-}5}N_{1\text{-}7}G_{3\text{-}5}N_{1\text{-}7}G_{3\text{-}5}N_{1\text{-}7}G_{3\text{-}5}$ (N = random nucleotide) in the human genome.[55,56] Final evidence for the formation of G-quadruplex species *in vivo* was presented by Balasubramanian *et al.* in 2013 who used an engineered structure-specific antibody and amplified fluorescence to quantitatively visualize G-quadruplexes in human cells (Figure 1.6).[57,58]

Potential G-quadruplex-forming sequences are distributed non-randomly in the human genome. They are frequently found in promotor regions of genes (also oncogenes) suggesting a regulatory role in transcription involved in the up- or down-regulation of gene expression. Putative G-quadruplex-forming sequences are also frequently observed in DNA replication origins and in control regions of mRNA, indicating further involvement in the regulation of key biological processes.[27,29,31,59]

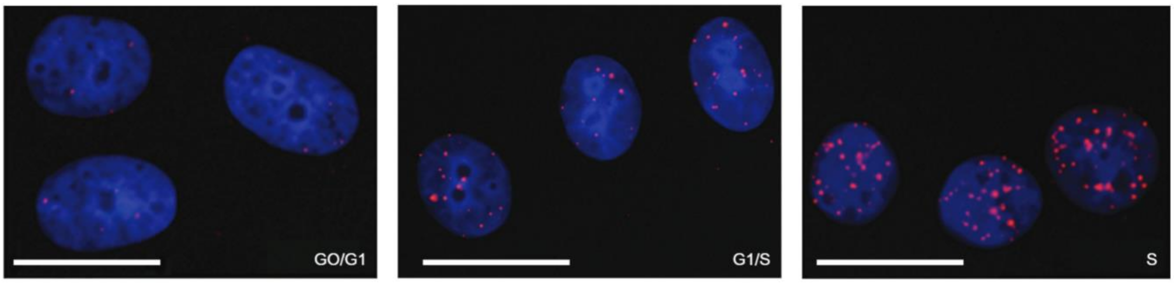

Figure 1.6: *In vivo* detection of G-quadruplex structures during different phases throughout the cell cycle using immunofluorescence. Scale bars: 20 µm. Reprinted with permission from [57]. Copyright © 2013 Nature Publishing Group.

The chromosomal regions with the highest concentration of potential G-quadruplex-forming sequences, however, are the telomeres which are nucleoprotein complexes at the ends of chromosomes. Their main function is to protect the chromosomes from degradation. The telomeric DNA consists of several kilobases of double-stranded G-rich tandem repeat units such as TTA GGG in all vertebrates or similar units, e.g. TTG GGG or TTT TGG GG in ciliates like Tetrahymena. At the 3'-end, an about 100–200 nt long single-stranded overhang is located[60] which readily forms several G-quadruplex structures. The actual structure of these region is still under debate. Especially the potential interactions of the distinct G-quadruplexes with each other are unclear and models without any inter-G-quadruplex interaction (beads-on-a-string) or with extensive π-stacking arrays have been proposed.[33,47,61–65]

G-quadruplex formation in the telomeric overhangs is known to inhibit the ribonucleoprotein telomerase. In 2009, the Nobel prize in physiology or medicine was awarded to Elizabeth Blackburn, Carol Greider and Jack Szostak for the discovery of the telomeres and the role of the telomerase.[66] This reverse-transcriptase enzyme has the function to maintain the telomeres by resynthesizing the tandem repeat units at the single-stranded 3'-overhangs which are shortened within every cell cycle. In this way it prevents aging of the cells and in popular science it was therefore named "immortality enzyme".[67–70] Although it sounds good in the first place, telomerase activity actually causes problems, since it is overexpressed in most types of cancer, which results in uncontrolled growth and proliferation.[54] Since G-quadruplex formation inhibits telomerase by preventing the hybridization of the telomeric single-stranded overhang into the active site, the initiation of G-quadruplex folding or their stabilization was identified as a promising anticancer strategy.[71]

1.2.3 G-Quadruplex-Binding Ligands as Promising Drug Candidates

Due to their inhibiting effect on telomerase, their occurrence in promotor regions of (onco-)genes, and their general regulatory roles in important biological processes (Section 1.2.2), G-quadruplexes gained attention as promising drug target. Therefore, many research groups have worked on the design and synthesis of small molecules that bind and stabilize the secondary structure type, as these so-called G-quadruplex-binding ligands represent potential drug candidates. An important challenge next to a strong binding affinity (large binding constant) is the high selectivity to G-quadruplexes compared to other DNA secondary structures, especially duplex DNA, which is present in large excess in the nuclei.[21,54,58,59,71–76] Different binding strategies have been pursued to bind to the special secondary structures addressing the nucleobases in the loop regions, the negatively charged sugar-phosphate backbone or the inner ion channel. However, the most common binding mode is the π-stacking on top of a terminal G-tetrad (Figure 1.7).[77,78] On the other hand, intercalation in between two adjacent G-quartets, resembling intercalating species between base pairs in duplex DNA, seems an unfavored binding mode, although still under debate.[79–81]

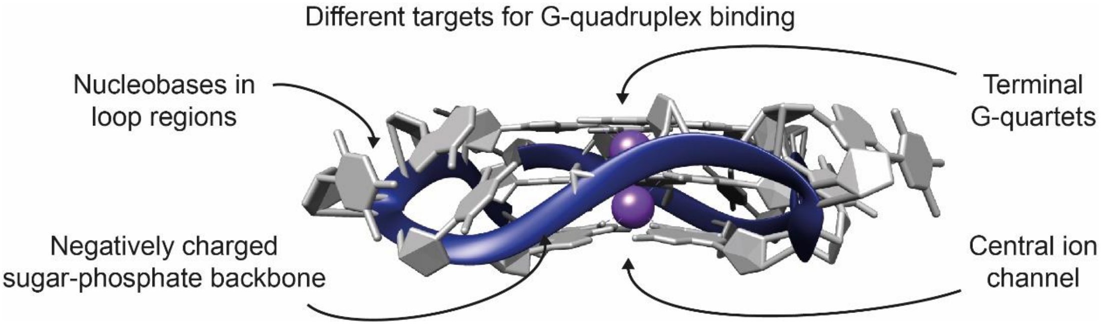

Figure 1.7: Next to the negatively charged sugar-phosphate backbone, G-quadruplexes show different unique structural sites such as terminal G-quartets, the central ion channel, and the loop regions, that can be targeted for specific G-quadruplex binding.[77]

Typical G-quadruplex-binding molecules are based on backbones with large π-surfaces such as perylene or naphthalene diimides, anthraquinone, acridines, fluorenones or porphyrins, that are substituted with cationic side chains

(Figure 1.8).[78] An example is the perylene-based G-quadruplex binder called PIPER that was shown to π-stack onto terminal G-tetrads. An early NMR-based investigation by Kerwin and Hurley *et al.* revealed that PIPER intercalates in between the two monomers of tail-to-tail stacked G-quadruplex dimers, formed by tetramolecular parallel G-quadruplexes with accessible terminal G-tetrads at the 3'-ends, resulting in a so-called sandwich complex.[82] This special sandwich binding mode has been observed for several different G-quadruplex-binding ligands and might be a relevant structural motif adopted when drug-like binders interact with G-quadruplexes in the telomeres.[83–85]

Also, metal complexes represent suitable G-quadruplex-binding ligands.[75,86,87] Especially metal porphyrins and salphen complexes have been studied, since their central metal ions resemble the alkali metal ion found in the canonical G-quadruplex structure.[77] Another famous G-quadruplex binder is the natural product telomestatin. In 2001, the macrocyclic compound was isolated and its π-stacking onto terminal G-tetrads of human telomeric G-quadruplexes was revealed, resulting in inhibition of telomerase.[88,89]

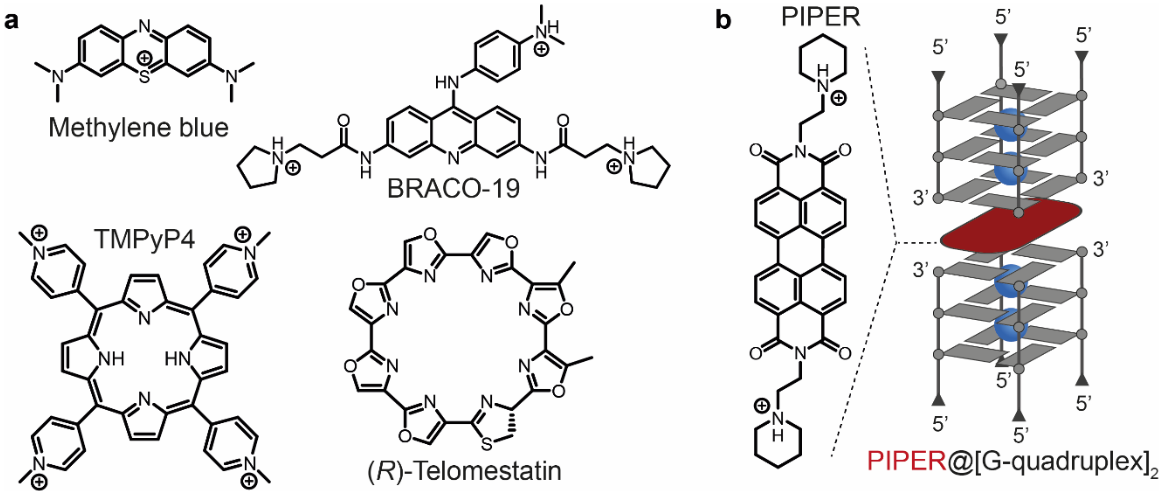

Figure 1.8: (**a**) Examples for typical reported G-quadruplex-binding ligands. (**b**) Sandwich complex with PIPER intercalating in between the two monomers of a tail-to-tail stacked dimer formed by tetramolecular parallel G-quadruplexes with accessible terminal G-tetrads.[82]

A current desirable goal is the selectivity for distinct G-quadruplex topologies (e.g. only for structures with parallel topology).[54] As up to now, no drug based on a

G-quadruplex-binding ligand has been approved for therapeutic use, future research has to continue tackling the design and *in vivo* effects of novel binders.

1.3 DNA Nanotechnology

1.3.1 G-Quadruplex Structural Motifs in DNA Nanotechnology

Beyond their biological function, nucleic acids have been extensively used in the field of nanotechnology for the self-assembly of complex 2D and 3D architectures. Pioneered by Seeman[90–95] in the 1980th and significantly influenced by Rothemund in 2006 with the development of DNA origami,[96] DNA nanotechnology has evolved into a seminal branch of research. The unprecedented properties of DNA such as its highly predictable and programmable interactions and its remarkable binding specificity are exploited for the design of nanodevices used for cargo transport or in molecular switches and machines and more.[93,95–99]

While most work is based on the typical duplex DNA structure with canonical Watson-Crick base pairing (see Section 1.1), also other secondary structure types have been applied which often show lower susceptibility to enzymatic degradation, are less flexible and show a higher sensitivity to external chemical stimuli. Examples for the latter are the strong pH-sensitivity of i-motifs and the alkali metal cation-sensitivity of G-quadruplexes.[100]

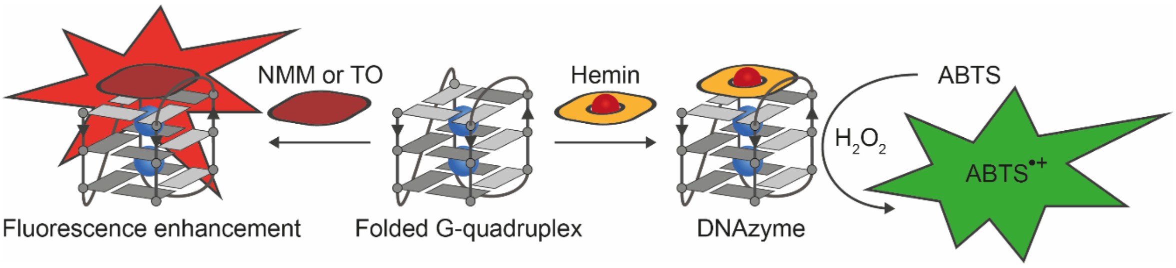

Figure 1.9: G-quadruplex-based sensors are often designed in a way that the presence of the analyte causes the formation of a folded G-quadruplex. This event can be detected by fluorescence enhancement of a G-quadruplex-binding ligand such as N-methyl mesoporphyrin IX (NMM) or thiazole orange (TO). Another approach exploits the peroxidase activity of a hemin-G-quadruplex complex that catalyzes the oxidation of an organic compound (usually 2,2'-Azino-bis(3-ethylbenzthiazoline-6-sulfonic acid)) to its strongly colored radical species.

Hence, the structural G-quadruplex motif is frequently used in nanodevices such as switches,[101–103] logic gates (Figure 1.10)[104] and motors,[105] in materials like supramolecular hydrogels[106–108] or catalytic DNA species (DNAzymes).[109–112] Several sensors have been designed based on the secondary structure which often benefit from the well-established detection of G-quadruplex formation.[113–115] One strategy applies G-quadruplex binders as fluorescent light-up probes upon binding to a folded G-quadruplex.[116–118] A second strategy exploits the DNAzyme activity of a hemin-G-quadruplex complex. The π-stacking of hemin onto an accessible G-tetrad results in a catalytic system that promotes peroxidase-like oxidation of different substrates in the presence of hydrogen peroxide.[84,119–124] The catalytic activity is exploited to generate a chromophore (the oxidation of ABTS to its strongly green radical species is commonly used) giving an easily detectable readout indicating G-quadruplex formation (Figure 1.9).

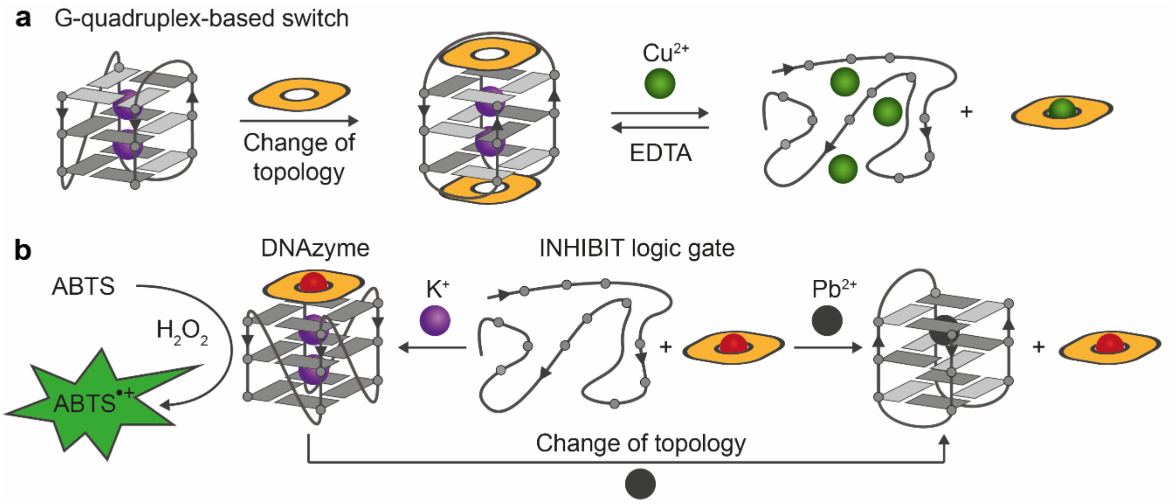

Figure 1.10: (**a**) Example for a metal-mediated, G-quadruplex-based switch. Cu^{2+} complexation of a G-quadruplex-binding ligand modulates its binding affinity to the DNA structure which can be reversed with addition of a chelate ligand such as EDTA.[125] (**b**) Example for an INHIBIT logic gate based on a hemin-G-quadruplex DNAzyme with K^+ and Pb^{2+} ions as two inputs and peroxidase activity (detected with absorption spectroscopy) as an output.[104]

1.3.2 Metal Ions in DNA Nanotechnology

Similar to nature's strategy of incorporating metal cofactors into biomolecules, e.g. in metallo-proteins, the idea to install metal complexes into artificial DNA nanostructures aims at introducing additional functionality to the otherwise passive assemblies. The approach merges the high programmability of DNA structures in the nanoscale with desired metal complex properties for the development of devices for catalysis, nanoelectronics or artificial photosynthesis.[126]

The variety of the coordination geometries of different metal complexes has been exploited to design higher-order DNA architectures. Examples are metal-DNA branch junctions with multiple DNA arms[127–130] or the construction 2D and 3D metal-DNA structures such as metal-DNA cages.[131,132]

Large contribution to the field was given with the concept of metal-mediated base pairing, where the canonical, hydrogen-bonded base pairs are replaced by metal complexes.[133,134] Addition of Hg^{2+} ions to duplexes with **TT** mismatches results in **T**-Hg^{2+}-**T** metal-mediated base pairs, initially proposed by Katz,[135] causing a strong stabilization of the duplex. Similarly, **C**-Ag^{+}-**C** metal-mediated base pair formation was observed by Ono *et al.*[136] Due to the limited binding capabilities of natural nucleobases to metal ions, artificial nucleobases with various metal-binding functionalities (ligandosides) have been developed by Schultz, Tanaka, Shionoya, Müller and others.[137] The efforts resulted in a multitude of different metal-mediated base pairs containing different metal ions such as Hg^{2+}, Ag^{+}, Cu^{2+}, Cu^{+}, Zn^{2+} and others including dinuclear representatives.[133,134,137–143] The concept was also transferred to DNA analogues such as GNA (glycol nucleic acid) duplexes (Figure 1.11b) by Meggers and coworkers.[144] Consecutive stacks of metal-mediated base pairs in duplex DNA have been reported resulting in discrete, self-assembled metal arrays with potential application as molecular wires in nanoelectronics (Figure 1.11a and c).[145–149] Other applications include sensing of (transition) metal ions or their redox states or the controlled generation of noble metal nanoclusters.[142,150–152]

A special metal-mediated base pair, introduced by Clever and Carell *et al.*, was based on a Cu^{2+}-salen complex that provided an additional interstrand crosslink composed of dynamic covalent imine bonds (Figure 1.11d).[153,154] This orthogonal base pair was proposed for the expansion of the genetic code, and replication as well as PCR amplification were successfully demonstrated.[155]

The concept of metal-mediated base pairing was additionally transferred to other DNA secondary structures.[156] An example of a metal-mediated base triplet in DNA triple helices revealed that the proton of the protonated cytidine involved in Hoogsteen hydrogen bonding in a **C**$^{+}$·**G**-**C** triplet can be substituted by a Ag^{+}

ion.[157] Further examples have been reported deploying artificial nucleobases including an organometallic variant.[158–160]

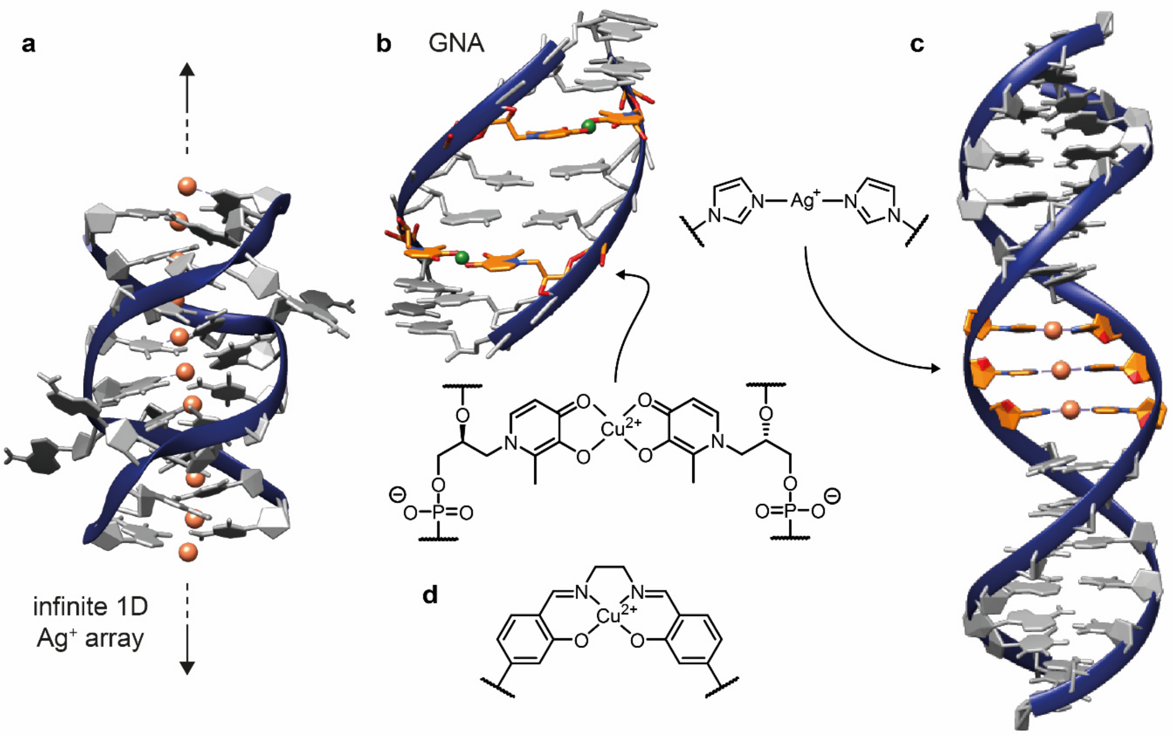

Figure 1.11: Examples for metal-mediated base pairs in duplex DNA. (**a**) X-ray structure of duplex DNA containing canonical nucleobases forming solely metal-mediated base pairs (**G**-Ag$^+$-**G**, **G**-Ag$^+$-**C**, **C**-Ag$^+$-**C**, **T**-Ag$^+$-**T**). Formation of a coordination polymer in the crystal structure results in a metallo-DNA nanowire with an uninterrupted 1D Ag$^+$ array (PDB: 5IX7).[149] (**b**) Crystal structure of a GNA duplex with two artificial **H**-Cu^{2+}-**H** base pairs (**H**: hydroxypyridone, PDB: 2JJA).[144] (**c**) NMR solution structure of a DNA duplex containing three consecutive **Im**-Ag$^+$-**Im** base pairs (**Im**: imidazole) with nearly perfect B-DNA shape (PDB: 2M54).[147] (**d**) A Cu^{2+}-salen base pair with the dynamic covalent imine bridge as interstrand crosslink.[153]

The metal-mediated stabilization of a three-way junction was achieved by Shionoya and coworkers who attached 2,2'-bipyridine groups to the nucleosides in the center of such a junction. Addition of Ni^{2+}, Fe^{2+} or Zn^{2+} ions resulted in octahedral metal complexes.[161] This design was used to build a metal-triggered reversible switch between three duplexes and two three-way junctions (Figure 1.12c).[162]

Recently, an i-motif with metal-mediated **C**-Cu$^+$-**C** base pairs was reported allowing to modulate the stability of the overall structure by the redox state of the copper ion.[163] Moreover, Gabelica and Mergny *et al.* used the **T**-Hg^{2+}-**T** base pair, known from duplex structures, to crosslink two thymidines in adjacent lateral loops in unimolecular G-quadruplexes resulting in a structural stabilization and reduced conformational polymorphism (Figure 1.12a).[164] In a different approach, Sugimoto and coworkers incorporated a 2,2'-bipyridine group into the loop region of a G-rich oligonucleotide that formed discrete antiparallel bimolecular G-quadruplexes. Addition of Ni^{2+} ions triggered a topology change yielding a G-wire structure with all-parallel strand orientations due to Ni^{2+}-bipyridine complex formation (Figure 1.12b). The assembly of long G-wires was confirmed by gel electrophoresis and visualized by atomic force microscopy (AFM). In the Clever Lab, the successful attempt to design a metal-mediated base tetrad that formally replaces a full G-tetrad in G-quadruplexes was accomplished. Since the whole thesis is based on these previous achievements, they are discussed in more detail in the next section.

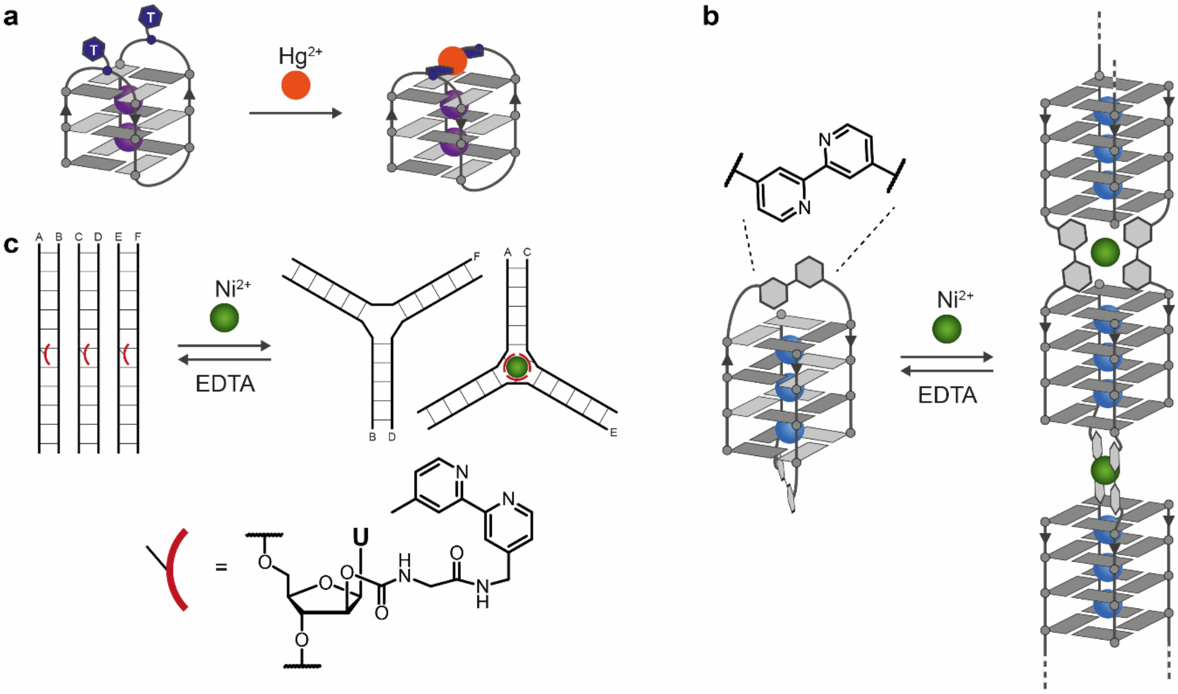

Figure 1.12: Examples for the expansion of the concept of metal-mediated base pairs to different secondary DNA structures. (**a**) A metal-mediated **T**-Hg^{2+}-**T** base pair crosslinks two adjacent lateral loops in a unimolecular G-quadruplex resulting in a stabilized structure and reduced conformational polymorphism.[164] (**b**) Metal-triggered reversible switch between discrete bimolecular G-quadruplexes and a G-wire (proposed structure is shown).[165] (**c**) Metal-triggered reversible switch between three DNA duplexes and two three-way junctions.[162]

1.4 Metal-Mediated G-Quadruplexes Designed in the Clever Lab

In the Clever Lab, the incorporation of transition metal complexes into DNA G-quadruplexes is an established concept to introduce additional functionality to the distinct secondary structures. In analogy to metal-mediated base pairing, the approach is based on the covalent installation of artificial ligandosides that carry a donor group instead of a canonical nucleobase. In a first attempt, pyridine or imidazole ligands were attached at the 5'-end of short G-rich oligonucleotides (5'-**L**G$_n$, n = 3–5) by solid-phase DNA synthesis. The formation of tetramolecular parallel G-quadruplexes resulted in prearranged chelating coordination environments at the 5'-face ([**L**G$_n$]$_4$) suitable for the complexation of transition metal cations such as Co^{2+}, Ni^{2+}, Cu^{2+}, or Zn^{2+} (Figure 1.13a).[166–168] Metal complex formation within the G-quadruplex structure (M^{2+}@[**L**G$_n$]$_4$), confirmed by EPR spectroscopy (for Cu^{2+}, Figure 1.13b) and native ESI mass spectrometry, caused a significant stabilization of the overall secondary structure expressed in a large increase of the thermal denaturation temperature (melting temperature, Figure 1.13c). This stabilization was shown to be highly reversible by adding a strong chelating agent such as EDTA.

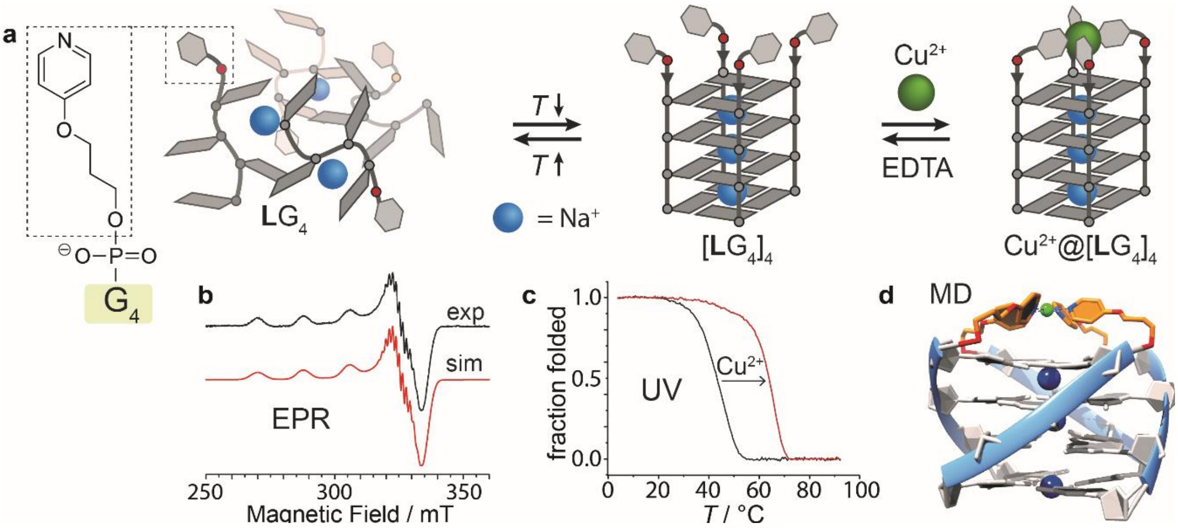

Figure 1.13: (**a**) Attachment of pyridine ligands at the 5'-end of short G-rich oligonucleotides (5'-**L**G$_n$, n = 3–5) results in tetramolecular parallel G-quadruplexes with a preorganized coordination environment ([**L**G$_n$]$_4$) suitable for transition metal complexation (M^{2+}@[**L**G$_n$]$_4$).[166,167] (**b**) EPR spectrum of Cu^{2+}@[**L**G$_n$]$_4$ and (**c**) thermal stabilization upon Cu^{2+} binding. (**d**) Structural model based on MD simulation. Adapted with permission from [166,167]. Copyright © 2013/2018 Wiley-VCH Verlag GmbH & Co. KGaA, Weinheim.

The degree of stabilization could be adjusted by the length of the linker connecting the ligand with the oligonucleotide backbone at the 5'-end (Figure 1.14a). The switchable stability allowed the use of transition metal ions as external stimuli for the reversible formation of tetramolecular G-quadruplexes. This phenomenon was exploited to design a metal-activated DNAzyme with peroxidase-like activity based on a G-quadruplex-hemin complex (Figure 1.14b).[168]

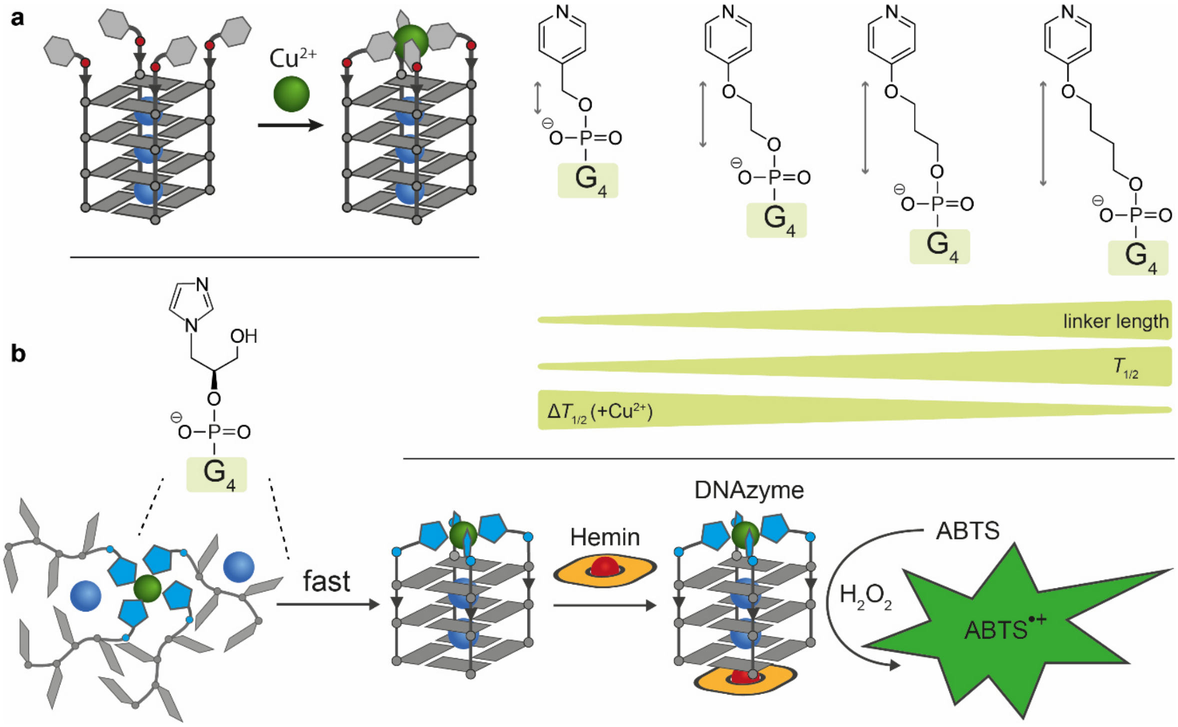

Figure 1.14: (**a**) An increased length of the linker connecting the pyridine group with the DNA backbone at the 5'-end results in a higher initial G-quadruplex stability and in a lower degree of stabilization upon Cu^{2+} addition. Adapted with permission from [167]. Copyright © 2018 Wiley-VCH Verlag GmbH & Co. KGaA, Weinheim. (**b**) A tetramolecular G-quadruplex with imidazole groups at the 5'-ends was used to design a DNAzyme that can be activated by Cu^{2+} addition.[168]

Second generation ligandosides based on a glycol backbone, again with pyridine or imidazole donor functionalities, allowed internal installation into oligonucleotide sequences. This feature enabled the incorporation of transition metal complexes into unimolecular G-quadruplexes by formally replacing one G-quartet with a metal-mediated quartet (e.g. a Cu(pyridine)$_4$ tetrad).[169,170] The right positioning of the ligandosides into the DNA sequence allowed to induce G-quadruplex topology changes upon metal addition monitored by CD spectroscopy (Figure 1.15). Also, the binding behavior of a ligand-modified G-quadruplex aptamer to the protein thrombin was controlled by absence or presence of Cu^{2+} ions as demonstrated by a fibrinogen clotting assay.[169]

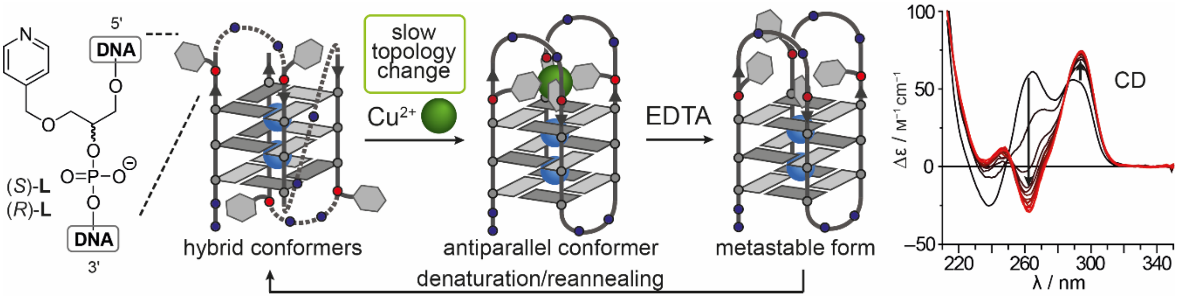

Figure 1.15: Four pyridine ligandosides were incorporated into a unimolecular G-quadruplex. Cu^{2+} addition results in a $Cu(pyridine)_4$ tetrad, which is exploited to induce a G-quadruplex topology change observed with CD spectroscopy. Adapted with permission from [169]. Copyright © 2017 Wiley-VCH Verlag GmbH & Co. KGaA, Weinheim.

Recently, the Lewis acidity of transition metal complexes incorporated into chiral G-quadruplex structures was exploited for enantioselective catalysis.[171] Key idea in the design of this special metallo-DNAzymes was to solely provide an unsaturated coordination environment for the bound Cu^{2+} ion enabling additional substrate binding. The modular approach allowed an iterative sequence modification giving rise to DNAzymes for Michael additions in water with high conversions and excellent enantioselectivities (≥ 99%). Notably, the variation of number and positions of the ligandosides in the DNA sequence allowed to control the enantioselectivity resulting in one or the other enantiomeric reaction product (Figure 1.16).

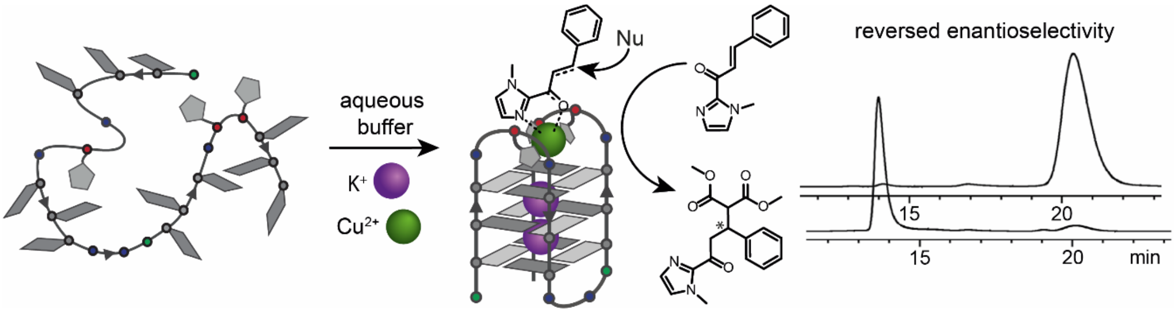

Figure 1.16: G-quadruplex-based metallo-DNAzyme for Lewis acid-catalyzed Michael additions in water. Variation of the number and positions of the ligandosides in the DNA sequence allows to control the enantioselectivity. Adapted with permission from [171]. Copyright © 2021 American Chemical Society.

1.5 References

[1] J. M. Berg, J. L. Tymoczko, G. J. Gatto jr., L. Stryer, *Biochemie*, Vol. 8, Springer, **2018**, pp. 127–162.

[2] J. D. Watson, F. H. C. Crick, *Nature* **1953**, *171*, 737–738.

[3] M. H. F. Wilkins, A. R. Stokes, H. R. Wilson, *Nature* **1953**, *171*, 738–740.

[4] R. E. Franklin, R. G. Gosling, *Acta Crystallogr.* **1953**, *6*, 673–677.

[5] A. H.-J. Wang, G. J. Quigley, F. J. Kolpak, J. L. Crawford, J. H. van Boom, G. van der Marel, A. Rich, *Nature* **1979**, *282*, 680–686.

[6] M. de Rosa, D. de Sanctis, A. L. Rosario, M. Archer, A. Rich, A. Athanasiadis, M. A. Carrondo, *Proc. Natl. Acad. Sci. U. S. A.* **2010**, *107*, 9088–9092.

[7] B. F. Eichman, J. M. Vargason, B. H. M. Mooers, P. S. Ho, *Proc. Natl. Acad. Sci. U. S. A.* **2000**, *97*, 3971–3976.

[8] Y. Liu, S. C. West, *Nat. Rev. Mol. Cell Biol.* **2004**, *5*, 937–944.

[9] J. Choi, T. Majima, *Chem. Soc. Rev.* **2011**, *40*, 5893–5909.

[10] N. Saini, Y. Zhang, K. Usdin, K. S. Lobachev, *Biochimie* **2013**, *95*, 117–123.

[11] B. F. Eichman, M. Ortiz-Lombardía, J. Aymamí, M. Coll, P. S. Ho, *J. Mol. Biol.* **2002**, *320*, 1037–1051.

[12] C. Altona, J. A. Pikkemaat, F. J. Overmars, *Curr. Opin. Struct. Biol.* **1996**, *6*, 305–316.

[13] D. R. Duckett, D. M. Lilley, *EMBO J.* **1990**, *9*, 1659–1664.

[14] K. Hoogsteen, *Acta Crystallogr.* **1963**, *16*, 907–916.

[15] P. P. Chan, P. M. Glazer, *J. Mol. Med.* **1997**, *75*, 267–282.

[16] H. A. Day, P. Pavlou, Z. A. E. Waller, *Bioorg. Med. Chem.* **2014**, *22*, 4407–4418.

[17] H. Abou Assi, M. Garavís, C. González, M. J. Damha, *Nucleic Acids Res.* **2018**, *46*, 8038–8056.

[18] M. J. P. van Dongen, J. F. Doreleijers, G. A. van der Marel, J. H. van Boom, C. W. Hilbers, S. S. Wijmenga, *Nat. Struct. Biol.* **1999**, *6*, 854–859.

[19] N. Esmaili, J. L. Leroy, *Nucleic Acids Res.* **2005**, *33*, 213–224.

[20] J. T. Davis, *Angew. Chem. Int. Ed.* **2004**, *43*, 668–698.

[21] T. M. Bryan, P. Baumann, *Mol. Biotechnol.* **2011**, *49*, 198–208.

[22] M. Gellert, M. N. Lipsett, D. R. Davies, *Proc. Natl. Acad. Sci. U. S. A.* **1962**, *48*, 2013–2018.

[23] D. Bhattacharyya, G. M. Arachchilage, S. Basu, *Front. Chem.* **2016**, *4*, 38.

[24] E. Largy, J.-L. Mergny, V. Gabelica in *Metal Ions in Life Sciences: The Alkali Metal Ions: Their Role for Life*, Vol. 16 (Eds.: A. Sigel, H. Sigel, R. K. O. Sigel), Springer, Cham, **2016**.

[25] S. Burge, G. N. Parkinson, P. Hazel, A. K. Todd, S. Neidle, *Nucleic Acids Res.* **2006**, *34*, 5402–5415.

[26] A. N. Lane, J. B. Chaires, R. D. Gray, J. O. Trent, *Nucleic Acids Res.* **2008**, *36*, 5482–5515.

[27] H. J. Lipps, D. Rhodes, *Trends Cell Biol.* **2009**, *19*, 414–422.

[28] J. L. Huppert, *FEBS J.* **2010**, *277*, 3452–3458.

[29] M. L. Bochman, K. Paeschke, V. A. Zakian, *Nat. Rev. Genet.* **2012**, *13*, 770.

[30] S. Zhang, Y. Wu, W. Zhang, *ChemMedChem* **2014**, *9*, 899–911.

[31] D. Rhodes, H. J. Lipps, *Nucleic Acids Res.* **2015**, *43*, 8627–8637.

[32] H. L. Lightfoot, T. Hagen, N. J. Tatum, J. Hall, *FEBS Lett.* **2019**, *593*, 2083–2102.

[33] G. N. Parkinson, M. P. H. Lee, S. Neidle, *Nature* **2002**, *417*, 876–880.

[34] Y. Wang, D. J. Patel, *Structure* **1993**, *1*, 263–282.

[35] K. W. Lim, S. Amrane, S. Bouaziz, W. Xu, Y. Mu, D. J. Patel, K. N. Luu, A. T. Phan, *J. Am. Chem. Soc.* **2009**, *131*, 4301–4309.

[36] A. Ambrus, D. Chen, J. Dai, T. Bialis, R. A. Jones, D. Yang, *Nucleic Acids Res.* **2006**, *34*, 2723–2735.

[37] K. N. Luu, A. T. Phan, V. Kuryavyi, L. Lacroix, D. J. Patel, *J. Am. Chem. Soc.* **2006**, *128*, 9963–9970.

[38] B. Heddi, A. T. Phan, *J. Am. Chem. Soc.* **2011**, *133*, 9824–9833.

[39] D. Sen, W. Gilbert, *Biochemistry* **1992**, *31*, 65–70.

[40] Y. Wang, D. J. Patel, *Biochemistry* **1992**, *31*, 8112–8119.

[41] Y. Krishnan-Ghosh, D. Liu, S. Balasubramanian, *J. Am. Chem. Soc.* **2004**, *126*, 11009–11016.

[42] Y. Kato, T. Ohyama, H. Mita, Y. Yamamoto, *J. Am. Chem. Soc.* **2005**, *127*, 9980–9981.

[43] V. Kuryavyi, A. T. Phan, D. J. Patel, *Nucleic Acids Res.* **2010**, *38*, 6757–6773.

[44] V. T. Mukundan, N. Q. Do, A. T. Phan, *Nucleic Acids Res.* **2011**, *39*, 8984–8991.

[45] N. Q. Do, A. T. Phan, *Chem. Eur. J.* **2012**, *18*, 14752–14759.

[46] M. Adrian, D. J. Ang, C. J. Lech, B. Heddi, A. Nicolas, A. T. Phan, *J. Am. Chem. Soc.* **2014**, *136*, 6297–6305.

[47] S. Kolesnikova, E. A. Curtis, *Molecules* **2019**, *24*, 3074.

[48] T. C. Marsh, E. Henderson, *Biochemistry* **1994**, *33*, 10718–10724.

[49] T. C. Marsh, J. Vesenka, E. Henderson, *Nucleic Acids Res.* **1995**, *23*, 696–700.

[50] K. Bose, C. J. Lech, B. Heddi, A. T. Phan, *Nat. Commun.* **2018**, *9*, 1959.

[51] E. Henderson, C. C. Hardin, S. K. Walk, I. Tinoco, E. H. Blackburn, *Cell* **1987**, *51*, 899–908.

[52] D. Sen, W. Gilbert, *Nature* **1988**, *334*, 364–366.

[53] W. I. Sundquist, A. Klug, *Nature* **1989**, *342*, 825–829.

[54] S. Neidle, *Nat. Rev. Chem.* **2017**, *1*, 0041.

[55] A. K. Todd, M. Johnston, S. Neidle, *Nucleic Acids Res.* **2005**, *33*, 2901–2907.

[56] J. L. Huppert, S. Balasubramanian, *Nucleic Acids Res.* **2005**, *33*, 2908–2916.

[57] G. Biffi, D. Tannahill, J. McCafferty, S. Balasubramanian, *Nat. Chem.* **2013**, *5*, 182–186.

[58] R. Hänsel-Hertsch, M. D. Antonio, S. Balasubramanian, *Nat. Rev. Mol. Cell Biol.* **2017**, *18*, 279–284.

[59] T. Tian, Y.-Q. Chen, S.-R. Wang, X. Zhou, *Chem* **2018**, *4*, 1314–1344.

[60] M. A. Blasco, *Nat. Rev. Genet.* **2005**, *6*, 611–622.

[61] H.-Q. Yu, D. Miyoshi, N. Sugimoto, *J. Am. Chem. Soc.* **2006**, *128*, 15461–15468.

[62] L. Petraccone, J. O. Trent, J. B. Chaires, *J. Am. Chem. Soc.* **2008**, *130*, 16530–16532.

[63] S. Haider, G. N. Parkinson, S. Neidle, *Biophys. J.* **2008**, *95*, 296–311.

[64] V. Singh, M. Azarkh, T. E. Exner, J. S. Hartig, M. Drescher, *Angew. Chem. Int. Ed.* **2009**, *48*, 9728–9730.

[65] L. Petraccone, C. Spink, J. O. Trent, N. C. Garbett, C. S. Mekmaysy, C. Giancola, J. B. Chaires, *J. Am. Chem. Soc.* **2011**, *133*, 20951–20961.

[66] E. Varela, M. A. Blasco, *Oncogene* **2010**, *29*, 1561–1565.

[67] H. Kaulen, *Das Unsterblichkeitsenzym*, Frankfurter Allgemeine Zeitung, 05.10.2009, Link: https://www.faz.net/aktuell/wissen/nobelpreise-2009/medizin-nobelpreis-2009-das-unsterblichkeitsenzym-1608682.html

[68] R. Faragher, *End of ageing and cancer? Scientists unveil structure of the 'immortality' enzyme telomerase*, The Conversation, 25.04.2018, Link: https://theconversation.com/end-of-ageing-and-cancer-scientists-unveil-structure-of-the-immortality-enzyme-telomerase-95591

[69] F. McMillan, *Researchers Have Discovered What The 'Immortality' Enzyme Looks Like*, Forbes, 28.04.2018, Link: https://www.forbes.com/sites/fionamcmillan/2018/04/28/researchers-have-discovered-what-the-immortality-enzyme-looks-like/?sh=4f806f1d2423

[70] I. Hoefer, *Unsterblichkeitsenzym?*, Spetrum.de, 01.09.1994, Link: https://www.spektrum.de/magazin/unsterblichkeitsenzym/821833

[71] H. Han, L. H. Hurley, *Trends Pharmacol. Sci.* **2000**, *21*, 136–142.

[72] S. Neidle, M. A. Read, *Biopolymers* **2001**, *56*, 195–208.

[73] L. Oganesian, T. M. Bryan, *BioEssays* **2007**, *29*, 155–165.

[74] S. Neidle, *FEBS J.* **2010**, *277*, 1118–1125.

[75] Y.-L. Jiang, Z.-P. Liu, *Mini-Rev. Med. Chem.* **2010**, *10*, 726–736.

[76] S. Neidle, *J. Med. Chem.* **2016**, *59*, 5987–6011.

[77] S. N. Georgiades, N. H. Abd Karim, K. Suntharalingam, R. Vilar, *Angew. Chem. Int. Ed.* **2010**, *49*, 4020–4034.

[78] T. V. T. Le, S. Han, J. Chae, H.-J. Park, *Curr. Pharm. Des.* **2012**, *18*, 1948–1972.

[79] X. Yao, D. Song, T. Qin, C. Yang, Z. Yu, X. Li, K. Liu, H. Su, *Sci. Rep.* **2017**, *7*, 10951.

[80] I. Haq, J. O. Trent, B. Z. Chowdhry, T. C. Jenkins, *J. Am. Chem. Soc.* **1999**, *121*, 1768–1779.

[81] I. Lubitz, N. Borovok, A. Kotlyar, *Biochemistry* **2007**, *46*, 12925–12929.

[82] O. Y. Fedoroff, M. Salazar, H. Han, V. V. Chemeris, S. M. Kerwin, L. H. Hurley, *Biochemistry* **1998**, *37*, 12367–12374.

[83] A. Funke, B. Karg, J. Dickerhoff, D. Balke, S. Müller, K. Weisz, *ChemBioChem* **2018**, *19*, 505–512.

[84] Y. Cheng, M. Cheng, J. Hao, G. Jia, D. Monchaud, C. Li, *Chem. Sci.* **2020**, *11*, 8846–8853.

[85] G. N. Parkinson, F. Cuenca, S. Neidle, *J. Mol. Biol.* **2008**, *381*, 1145–1156.

[86] Q. Cao, Y. Li, E. Freisinger, P. Z. Qin, R. K. O. Sigel, Z.-W. Mao, *Inorg. Chem. Front.* **2016**, *4*, 10–32.

[87] E. Boschi, S. Davis, S. Taylor, A. Butterworth, L. A. Chirayath, V. Purohit, L. K. Siegel, J. Buenaventura, A. H. Sheriff, R. Jin, R. Sheardy, L. A.

Yatsunyk, M. Azam, *J. Phys. Chem. B* **2016**, *120*, 12807–12819.

[88] K. Shin-ya, K. Wierzba, K. Matsuo, T. Ohtani, Y. Yamada, K. Furihata, Y. Hayakawa, H. Seto, *J. Am. Chem. Soc.* **2001**, *123*, 1262–1263.

[89] M.-Y. Kim, H. Vankayalapati, K. Shin-ya, K. Wierzba, L. H. Hurley, *J. Am. Chem. Soc.* **2002**, *124*, 2098–2099.

[90] N. R. Kallenbach, R.-I. Ma, N. C. Seeman, *Nature* **1983**, *305*, 829–831.

[91] J. E. Mueller, S. M. Du, N. C. Seeman, *J. Am. Chem. Soc.* **1991**, *113*, 6306–6308.

[92] J. Chen, N. C. Seeman, *Nature* **1991**, *350*, 631–633.

[93] C. Mao, W. Sun, N. C. Seeman, *Nature* **1997**, *386*, 137–138.

[94] E. Winfree, F. Liu, L. A. Wenzler, N. C. Seeman, *Nature* **1998**, *394*, 539–544.

[95] C. Mao, W. Sun, Z. Shen, N. C. Seeman, *Nature* **1999**, *397*, 144–146.

[96] P. W. K. Rothemund, *Nature* **2006**, *440*, 297–302.

[97] E. S. Andersen, M. Dong, M. M. Nielsen, K. Jahn, R. Subramani, W. Mamdouh, M. M. Golas, B. Sander, H. Stark, C. L. P. Oliveira, J. S. Pedersen, V. Birkedal, F. Besenbacher, K. V. Gothelf, J. Kjems, *Nature* **2009**, *459*, 73–76.

[98] C. K. McLaughlin, G. D. Hamblin, H. F. Sleiman, *Chem. Soc. Rev.* **2011**, *40*, 5647–5656.

[99] N. C. Seeman, H. F. Sleiman, *Nat. Rev. Mater.* **2017**, *3*, 17068.

[100] J.-L. Mergny, D. Sen, *Chem. Rev.* **2019**, *119*, 6290–6325.

[101] X. Wang, J. Huang, Y. Zhou, S. Yan, X. Weng, X. Wu, M. Deng, X. Zhou, *Angew. Chem. Int. Ed.* **2010**, *49*, 5305–5309.

[102] F. Wang, X. Liu, I. Willner, *Angew. Chem. Int. Ed.* **2015**, *54*, 1098–1129.

[103] C. Wang, G. Jia, Y. Li, S. Zhang, C. Li, *Chem. Commun.* **2013**, *49*, 11161–11163.

[104] T. Li, E. Wang, S. Dong, *J. Am. Chem. Soc.* **2009**, *131*, 15082–15083.

[105] Q. Y. Yeo, I. Y. Loh, S. R. Tee, Y. H. Chiang, J. Cheng, M. H. Liu, Z. S. Wang, *Nanoscale* **2017**, *9*, 12142–12149.

[106] X. Liu, J. Zhang, M. Fadeev, Z. Li, V. Wulf, H. Tian, I. Willner, *Chem. Sci.* **2018**, *10*, 1008–1016.

[107] J. S. Kahn, Y. Hu, I. Willner, *Acc. Chem. Res.* **2017**, *50*, 680–690.

[108] C.-H. Lu, X.-J. Qi, R. Orbach, H.-H. Yang, I. Mironi-Harpaz, D. Seliktar, I. Willner, *Nano Lett.* **2013**, *13*, 1298–1302.

[109] P. Travascio, Y. Li, D. Sen, *Chem. Biol.* **1998**, *5*, 505–517.

[110] I. Willner, B. Shlyahovsky, M. Zayats, B. Willner, *Chem. Soc. Rev.* **2008**, *37*, 1153–1165.

[111] T. D. Canale, D. Sen, *Biochim. Biophys. Acta Gen. Subj.* **2017**, *1861*, 1455–1462.

[112] J. H. Yum, S. Park, H. Sugiyama, *Org. Biomol. Chem.* **2019**, *17*, 9547–9561.

[113] B. Ruttkay-Nedecky, J. Kudr, L. Nejdl, D. Maskova, R. Kizek, V. Adam, *Molecules* **2013**, *18*, 14760–14779.

[114] H. Li, J. Liu, Y. Fang, Y. Qin, S. Xu, Y. Liu, E. Wang, *Biosens. Bioelectron.* **2013**, *41*, 563–568.

[115] W. Zhou, R. Saran, J. Liu, *Chem. Rev.* **2017**, *117*, 8272–8325.

[116] B. R. Vummidi, J. Alzeer, N. W. Luedtke, *ChemBioChem* **2013**, *14*, 540–558.

[117] S.-B. Chen, W.-B. Wu, M.-H. Hu, T.-M. Ou, L.-Q. Gu, J.-H. Tan, Z.-S. Huang, *Chem. Commun.* **2014**, *50*, 12173–12176.

[118] A. Laguerre, L. Stefan, M. Larrouy, D. Genest, J. Novotna, M. Pirrotta, D. Monchaud, *J. Am. Chem. Soc.* **2014**, *136*, 12406–12414.

[119] Y. Guo, J. Chen, M. Cheng, D. Monchaud, J. Zhou, H. Ju, *Angew. Chem. Int. Ed.* **2017**, *56*, 16636–16640.

[120] R. Shinomiya, Y. Katahira, H. Araki, T. Shibata, A. Momotake, S. Yanagisawa, T. Ogura, A. Suzuki, S. Neya, Y. Yamamoto, *Biochemistry* **2018**, *57*, 5930–5937.

[121] J. Kosman, B. Juskowiak, *Anal. Chim. Acta* **2011**, *707*, 7–17.

[122] D. Sen, L. C. H. Poon, *Crit. Rev. Biochem. Mol. Biol.* **2011**, *46*, 478–492.

[123] Y. Yamamoto, H. Araki, R. Shinomiya, K. Hayasaka, Y. Nakayama, K. Ochi, T. Shibata, A. Momotake, T. Ohyama, M. Hagihara, H. Hemmi, *Biochemistry* **2018**, *57*, 5938–5948.

[124] D.-M. Kong, N. Wang, X.-X. Guo, H.-X. Shen, *Analyst* **2010**, *135*, 545–549.

[125] D. Monchaud, P. Yang, L. Lacroix, M. Teulade-Fichou, J.-L. Mergny, *Angew. Chem. Int. Ed.* **2008**, *47*, 4858–4861.

[126] H. Yang, K. L. Metera, H. F. Sleiman, *Coord. Chem. Rev.* **2010**, *254*, 2403–2415.

[127] D. Mitra, N. D. Cesare, H. F. Sleiman, *Angew. Chem. Int. Ed.* **2004**, *43*, 5804–5808.

[128] I. Vargas-Baca, D. Mitra, H. J. Zulyniak, J. Banerjee, H. F. Sleiman, *Angew. Chem. Int. Ed.* **2001**, *40*, 4629–4632.

[129] K. M. Stewart, J. Rojo, L. W. McLaughlin, *Angew. Chem. Int. Ed.* **2004**, *43*, 5808–5811.

[130] K. M. Stewart, L. W. McLaughlin, *J. Am. Chem. Soc.* **2004**, *126*, 2050–2057.

[131] H. Yang, H. F. Sleiman, *Angew. Chem. Int. Ed.* **2008**, *47*, 2443–2446.

[132] H. Yang, C. K. McLaughlin, F. A. Aldaye, G. D. Hamblin, A. Z. Rys, I. Rouiller, H. F. Sleiman, *Nat. Chem.* **2009**, *1*, 390–396.

[133] E. Stulz, G. Clever, M. Shionoya, C. Mao, *Chem. Soc. Rev.* **2011**, *40*, 5633–5635.

[134] G. H. Clever, C. Kaul, T. Carell, *Angew. Chem. Int. Ed.* **2007**, *46*, 6226–6236.

[135] S. Katz, *Biochim. Biophys. Acta, Spec. Sect. Nucleic Acids Relat. Subj.* **1963**, *68*, 240–253.

[136] A. Ono, S. Cao, H. Togashi, M. Tashiro, T. Fujimoto, T. Machinami, S. Oda, Y. Miyake, I. Okamoto, Y. Tanaka, *Chem. Commun.* **2008**, 4825–4827.

[137] G. H. Clever, M. Shionoya, *Coord. Chem. Rev.* **2010**, *254*, 2391–2402.

[138] J. Müller, *Eur. J. Inorg. Chem.* **2008**, *2008*, 3749–3763.

[139] B. Jash, J. Müller, *J. Inorg. Biochem.* **2018**, *186*, 301–306.

[140] S. Mandal, M. Hebenbrock, J. Müller, *Angew. Chem. Int. Ed.* **2016**, *55*, 15520–15523.

[141] S. Mandal, J. Müller, *Curr. Opin. Chem. Biol.* **2017**, *37*, 71–79.

[142] B. Jash, J. Müller, *Angew. Chem. Int. Ed.* **2018**, *57*, 9524–9527.

[143] J. Müller, *Coord. Chem. Rev.* **2019**, *393*, 37–47.

[144] M. K. Schlegel, L.-O. Essen, E. Meggers, *J. Am. Chem. Soc.* **2008**, *130*, 8158–8159.

[145] K. Tanaka, A. Tengeiji, T. Kato, N. Toyama, M. Shionoya, *Science* **2003**, *299*, 1212–1213.

[146] K. Tanaka, G. H. Clever, Y. Takezawa, Y. Yamada, C. Kaul, M. Shionoya, T. Carell, *Nat. Nanotechnol.* **2006**, *1*, 190–194.

[147] S. Johannsen, N. Megger, D. Böhme, R. K. O. Sigel, J. Müller, *Nat. Chem.* **2010**, *2*, 229.

[148] S. Liu, G. H. Clever, Y. Takezawa, M. Kaneko, K. Tanaka, X. Guo, M. Shionoya, *Angew. Chem. Int. Ed.* **2011**, *50*, 8886–8890.

[149] J. Kondo, Y. Tada, T. Dairaku, Y. Hattori, H. Saneyoshi, A. Ono, Y. Tanaka, *Nat. Chem.* **2017**, *9*, 956–960.

[150] A. Ono, H. Togashi, *Angew. Chem. Int. Ed.* **2004**, *43*, 4300–4302.

[151] Y. Miyake, A. Ono, *Tetrahedron Lett.* **2005**, *46*, 2441–2443.

[152] J. C. Léon, D. González-Abradelo, C. A. Strassert, J. Müller, *Chem. Eur. J.* **2018**, *24*, 8320–8324.

[153] G. H. Clever, K. Polborn, T. Carell, *Angew. Chem. Int. Ed.* **2005**, *44*, 7204–7208.

[154] G. H. Clever, S. J. Reitmeier, T. Carell, O. Schiemann, *Angew. Chem. Int. Ed.* **2010**, *49*, 4927–4929.

[155] C. Kaul, M. Müller, M. Wagner, S. Schneider, T. Carell, *Nat. Chem.* **2011**, *3*, 794–800.

[156] S. Naskar, R. Guha, J. Müller, *Angew. Chem. Int. Ed.* **2020**, *59*, 1397–1406.

[157] T. Ihara, T. Ishii, N. Araki, A. W. Wilson, A. Jyo, *J. Am. Chem. Soc.* **2009**, *131*, 3826–3827.

[158] K. Tanaka, Y. Yamada, M. Shionoya, *J. Am. Chem. Soc.* **2002**, *124*, 8802–8803.

[159] D. U. Ukale, T. Lönnberg, *Angew. Chem. Int. Ed.* **2018**, *57*, 16171–16175.

[160] Y. Takezawa, W. Maeda, K. Tanaka, M. Shionoya, *Angew. Chem. Int. Ed.* **2009**, *48*, 1081–1084.

[161] J. H. A. Duprey, Y. Takezawa, M. Shionoya, *Angew. Chem. Int. Ed.* **2013**, *52*, 1212–1216.

[162] Y. Takezawa, S. Yoneda, J.-L. H. A. Duprey, T. Nakama, M. Shionoya, *Chem. Sci.* **2016**, *7*, 3006–3010.

[163] M. A. Abdelhamid, L. Fábián, C. J. MacDonald, M. R. Cheesman, A. J. Gates, Z. A. Waller, *Nucleic Acids Res.* **2018**, *46*, 5886–5893.

[164] N. M. Smith, S. Amrane, F. Rosu, V. Gabelica, J.-L. Mergny, *Chem. Commun.* **2012**, *48*, 11464–11466.

[165] D. Miyoshi, H. Karimata, Z.-M. Wang, K. Koumoto, N. Sugimoto, *J. Am. Chem. Soc.* **2007**, *129*, 5919–5925.

[166] D. M. Engelhard, R. Pievo, G. H. Clever, *Angew. Chem. Int. Ed.* **2013**, *52*, 12843–12847.

[167] D. M. Engelhard, L. M. Stratmann, G. H. Clever, *Chem. Eur. J.* **2018**, *24*, 2117–2125.

[168] P. M. Punt, G. H. Clever, *Chem. Sci.* **2019**, *10*, 2513–2518.

[169] D. M. Engelhard, J. Nowack, G. H. Clever, *Angew. Chem. Int. Ed.* **2017**, *56*, 11640–11644.

[170] P. M. Punt, G. H. Clever, *Chem. Eur. J.* **2019**, *25*, 13987–13993.

[171] P. M. Punt, M. D. Langenberg, O. Altan, G. H. Clever, *J. Am. Chem. Soc.* **2021**, *143*, 3555–3561.

2 Objectives

The aim of this thesis is to further develop the concept of incorporating transition metal complexes into DNA G-quadruplex structures. In the last years, the strategy has been well established in the Clever Lab (Section 1.4) both in tetra- and unimolecular G-quadruplexes by the covalent installation of pyridine- or imidazole-based ligandosides able to complexate Co^{2+}, Ni^{2+}, Cu^{2+} or Zn^{2+} ions.

The first applications were demonstrated based on the increased stability of the overall secondary DNA structure upon metal binding. The findings were exploited for metal-triggered G-quadruplex folding or metal-induced topology changes and the design of a metal-dependent DNAzyme with peroxidase-activity. Lewis acidic Cu^{2+} ions with unsaturated coordination environments in the chiral environment of the G-quadruplexes were further applied for enantioselective catalysis.

Another intrinsic property of Cu^{2+} complexes is their paramagnetism, a consequence of the d^9 electron configuration with a single unpaired electron. The incorporation of paramagnetic groups, so-called spin labels, into biomolecules is frequently used for their structure elucidation. With the help of pulsed dipolar electron paramagnetic resonance (PDEPR) spectroscopy methods, distances between different spin labels can be measured giving valuable structural information of proteins or DNA constructs (Section 3.1.2). In a first attempt, the $Cu(pyridine)_4$ tetrads incorporated into DNA G-quadruplexes have already been used as spin labels for intramolecular distance measurements in G-quadruplex structures in the Clever Lab (in detail described in Section 3.1.3). In Chapter 3, the application of the $Cu(pyridine)_4$ spin labels will be extended to investigate the formation of higher-order G-quadruplex structures like dimers or adducts with G-quadruplex-binding ligands and more complex DNA architectures by intermolecular Cu^{2+}-Cu^{2+} distance measurements. The Cu^{2+}-based spin label will also be tested in combination with organic spin labels commonly used in EPR-based structure elucidation of biomolecules. Furthermore, the method will be exploited for time-dependent monitoring of structural rearrangements of DNA adducts.

In the second part of the thesis (Chapter 4), the variety of ligand functionalities incorporated into G-quadruplexes will be expanded. As so far only N-heterocyclic donors (based on pyridine or imidazole) are used, additional ligandosides will be installed inspired by donor groups found in metallo-proteins. Therefore, new phosphoramidite building blocks must be designed, synthesized, and inserted into oligonucleotides by solid-phase DNA synthesis. The incorporation of hard carboxylates (benzoate and an aliphatic carboxylate) or soft sulfur-based ligands (thioether or thiol) is expected to widen the scope of transition metal ions that can be complexated by the modified G-quadruplexes. In a next step, the combination of different ligand functionalities installed, in sequences forming unimolecular G-quadruplexes, will result in preorganized heteroleptic coordination environments. The modular approach varying the kind, number, and positioning of the ligandosides within the DNA sequence will allow the design of tailored metal complexes in the G-quadruplex environment suitable for further application in catalysis or as redox agents mimicking metallo-proteins.

Within this thesis, several modified nucleotides incorporated into different oligonucleotides are discussed. To assure clarity and comprehensibility for the reader, lists containing all artificial nucleotides and synthesized oligonucleotides can be found in Figure 7.1 (page 201) and in Table 7.3 (page 226), respectively.

3 Distance Measurements in Higher-Order G-Quadruplex DNA Structures by PDEPR Spectroscopy

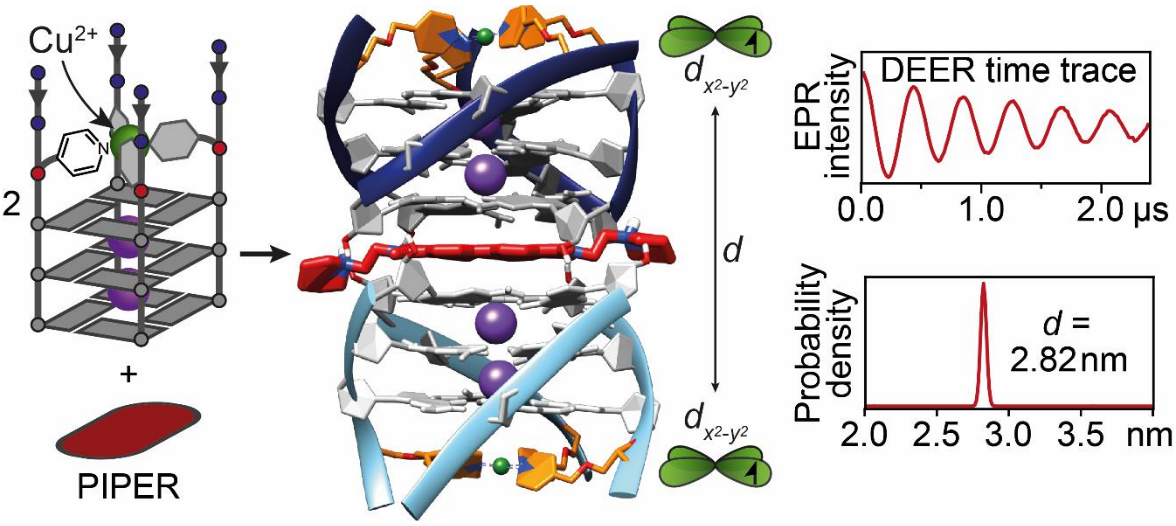

The results presented in this chapter were in part published in

L. M. Stratmann, Y. Kutin, M. Kasanmascheff, G. H. Clever, 'Precise Distance Measurements in DNA G-Quadruplex Dimers and Sandwich Complexes by Pulsed Dipolar EPR Spectroscopy', *Angew. Chem. Int. Ed.* **2021**, *60*, 4939–4947.[1]

It should be noted here that all EPR-based measurements and subsequent data processing described in this chapter were carried out by our collaboration partners Dr. Yury Kutin and JProf. Dr. Müge Kasanmascheff from Physical Chemistry Department, TU Dortmund University.

3.1 Introduction

3.1.1 Structure Elucidation of Biomolecules

An important principle in biology is that structure determines function, known as structure–function relationship. Consequently, structure elucidation of biomolecules like nucleic acids or proteins is crucial for the understanding of their function. As an evident example of how structural knowledge helps further understanding of biological processes, the discovery of the double-helical structure of DNA can be mentioned (Figure 3.1). With the help of experimental data obtained by Rosalind Franklin, the first correct DNA duplex model was developed by Watson and Crick (Nobel laureates in physiology or medicine in 1962) who state at the end of their famous publication: “It has not escaped our notice that the specific pairing [of two complementary DNA strands] we have postulated immediately suggests a possible copying mechanism for the genetic material.”[2,3]

Figure 3.1: Simplified scheme illustrating the copying mechanism for DNA containing the genetic information during replication. This mechanism (function) was directly deduced from the postulated specific pairing of two complementary DNA strands (structure) and, hence, serves as an example how biomolecular structure elucidation helps understanding biological function.

In research fields like structural and molecular biology, the molecular structure of biological macromolecules is studied. Particular interest lies also in the dynamics of biomolecules and in the question, how structural changes affect their function.

Several different techniques are available for structure elucidation of biomolecules, each with advantages and disadvantages. It is important to choose the right method for investigating a certain species in a specific environment (in particular *in vivo* studies are challenging) and the more orthogonal techniques support a structural result, the more reliable it is. Some important methods are briefly discussed hereinafter.

Circular dichroism (CD) spectroscopy is a sensitive, fast, and inexpensive method and based on the phenomenon that chiral compounds exhibit differential absorption of left- and right-handed circular polarized light. It provides information about secondary structures of peptides and proteins as well as of nucleic acids in solution. For example, α-helices and β-sheets, the two most important secondary structure types in peptides, respectively show characteristic patterns in the far-UV CD spectrum (180–250 nm).[4,5] Likewise, different DNA secondary structures can be distinguished with the help of CD spectroscopy.[6–11] In Figure 3.2, CD spectra of G-quadruplex structures with a parallel and an antiparallel folding topology are shown. The patterns are characteristic for the respective strand orientations.

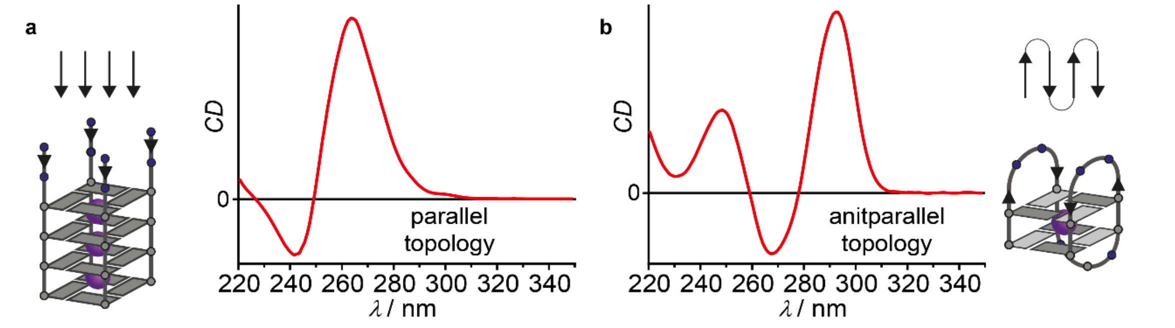

Figure 3.2: Characteristic CD patterns of G-quadruplexes with different folding topology. (**a**) Parallel G-quadruplexes show a positive Cotton effect with a minimum at ~240 nm and a maximum at ~265 nm (here: (5’-TTG GGG)$_4$ in K^+-containing solution), while (**b**) antiparallel G-quadruplexes typically show a positive Cotton effect with a minimum at ~265 nm and a maximum at ~295 nm and an additional maximum at ~245 nm (here: 5’-GGT TGG TGT GGT TGG (thrombin-binding aptamer) in K^+-containing solution).

Although extensive efforts have been made to develop algorithms that increase the information content of secondary structure prediction, CD spectroscopy usually provides merely qualitative data. Nevertheless, as a fast and simple method, CD spectroscopy has been used also in this work as a standard technique for G-quadruplex topology determination.

Single-crystal X-ray diffraction (XRD) is a technique for investigating molecular structures in the solid state. It is a powerful and widely used method and can provide atomic resolution data. It is also applied for structure determination of biomolecules. Early iconic examples are the structure determinations of the heme-containing and O_2-binding metallo-proteins myoglobin and hemoglobin by Kendrew[12] and Perutz,[13] respectively, which were awarded with the Nobel prize in chemistry in 1962 and pushed the development of a new independent research field, namely bioinorganic chemistry. The required crystallization of the species of interest is often challenging and, especially for highly flexible systems like biomolecules, sometimes impossible. Another drawback is that a solid-state structure does often not coincide with the structure in solution, which is usually of interest.

Atomic resolution data for biomolecules in solution can be obtained by nuclear magnetic resonance (NMR) spectroscopy and information about their dynamics can be provided. The method is very time consuming and fails for very large species or complicated mixtures. Also, cryo-electron microscopy (cryo-EM) gives high-resolution structures of biomolecules in solution. For this technique, the Nobel prize in chemistry in 2017 was awarded.[14] High-resolution structural data of numerous biomolecules obtained by XRD, NMR or cryo-EM can be accessed from data bases like the protein data bank.[15] Currently (June 2021), almost 180,000 structures are listed there (more than 13,000 nucleic acid-containing structures).[16]

Other frequently used tools for gaining structural information of biomolecules allow distance measurements in the nanometer range. For example, Förster resonance energy transfer (FRET) is used as a sensitive method that allows distance measurements between a FRET donor and an acceptor in a 2–10 nm range and helps monitoring conformational changes.[17,18] Site-specific labeling of biomolecules is usually required. Precise distance measurements are often not possible due to flexible linkers that attach the chromophores to biomolecules and qualitative data are obtained that allow distinguishing between a short and a long distance.

Classical examples are so-called molecular beacons that detect the presence of specific oligonucleotides in homogeneous solution. They are composed of a hairpin structure with a large loop containing the probe sequence and a fluorophore and a quencher in proximity attached to the 3'- and 5'-end, respectively. Hybridization of the probe sequence with the target strand strongly increases their distance to each other resulting in detectable fluorescence (Figure 3.3a).[19] In another iconic example, FRET was qualitatively used to confirm the closed and open states of a DNA origami box (Figure 3.3b).[20]

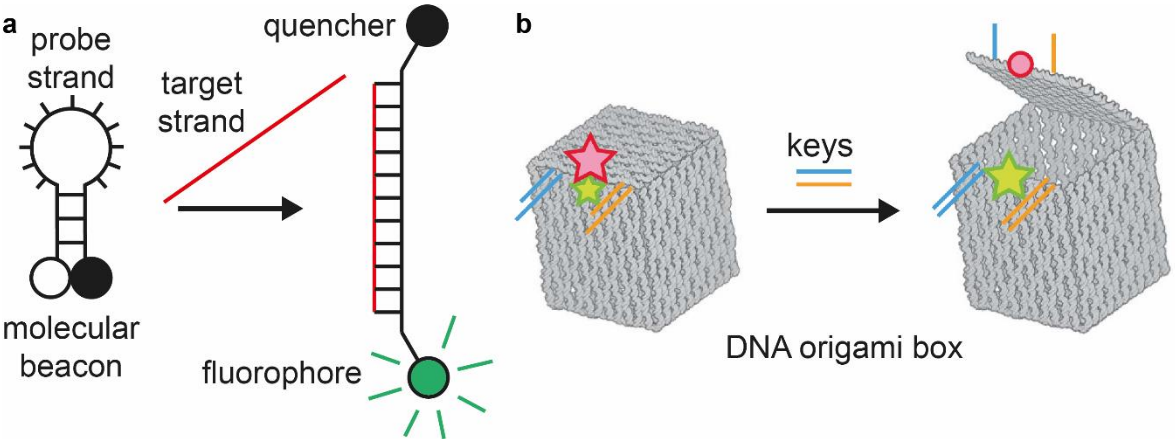

Figure 3.3: (**a**) Schematic concept of a molecular beacon. Hybridization of the target strand increases the distance between fluorophore and quencher which is detected by fluorescence spectroscopy.[19] (**b**) The distance between a FRET donor and acceptor varies in the closed and open state of a DNA origami box which allows to differentiate between the two states. Reprinted with permission from [20]. Copyright © 2009 Macmillan Publishers Limited.

In addition, pulsed dipolar electron paramagnetic resonance (PDEPR) spectroscopy can be used as an orthogonal method for distance measurements and closes gaps where other techniques are not applicable to gain structural information. Distances are measured between two paramagnetic spin labels, which are typically organic radicals or open-shell transition metal cations. Like in FRET, site-directed labeling of biomolecules is often required, and the two spin labels are used as a distance ruler in a range of 1.5–10 nm.[21] This method has been extensively used in this work and is therefore described in more detail in the following section.

3.1.2 Pulsed Dipolar EPR Spectroscopy

The EPR measurements were performed by experts in the field, our collaboration partners Dr. Yury Kutin and JProf. Dr. Müge Kasanmascheff. A very short introduction in the complex field is given to provide the basics behind the measurements and the interpretation of the results. For a detailed understanding, the reader is referred to respective literature.[22–25]

3.1.2.1 Basic Theory

Electron paramagnetic resonance (EPR) spectroscopy is based on the resonant absorption of electromagnetic radiation (usually in the microwave range) by samples containing unpaired electrons placed in an external magnetic field.[22] Electrons have an intrinsic angular momentum (electron spin) associated with a magnetic moment which is antiparallel to the spin. Quantum mechanics dictate that an electron with the spin quantum number of $S = 1/2$ can be in two states (α and β) which are degenerate in the absence of a magnetic field. In the presence of a static magnetic field, however, the two states have different energies (electron Zeeman interaction). The difference in energy is proportional to the magnetic field B_0 (magnetic flux density) and to the g-factor of the electron ($\Delta E = g|\mu_B|B_0$, where μ_B is the Bohr magneton). An electron in the lower/higher energy state can absorb/emit a photon if electromagnetic radiation with the energy ($h\nu$) matching the energy difference between α and β is applied (resonance condition). The rates of absorption and emission are proportional to the number of spins in the initial state. According to the Boltzmann distribution, the number of the spins in the lower energy state is slightly higher. Therefore, the net result represents absorption and an EPR signal can be detected. Saturation of the EPR signal due to eventual equalization of the α and β populations is prevented by energy transfer to the lattice restoring the thermal equilibrium (spin-lattice interaction).

In atoms, the orbital motion contributes to the electron angular momentum, in addition to the electron spin and both are coupled with each other (spin-orbit coupling). Although the orbital angular momentum is quenched in molecules due to their low symmetry, the spin-orbit coupling results in a deviation of the g-factor from the value for a free electron. This deviation causes a shift in the EPR spectrum and is a characteristic parameter of a molecular species which provides electronical and structural information about the paramagnetic system. The spin-orbit coupling also leads to the anisotropy of the g-factor and thus EPR spectra of crystalline powders or paramagnetic systems diluted in glassy matrices (such as shock-frozen solutions) are a superposition of the EPR signals of randomly orientated paramagnetic molecules with respect to the static magnetic field.

Also, many nuclei possess an angular momentum associated with a magnetic moment and the energy states of nuclear spins are split in the presence of a magnetic field (nuclear Zeeman interaction). The additional magnetic field created by the nuclear spin affects an electron spin in proximity and influences the resonance conditions (hyperfine interactions) resulting in a splitting of the EPR lines ($2I + 1$ lines, where I is the nuclear spin quantum number) separated by the hyperfine coupling constant (*A*). The hyperfine interaction is anisotropic as well and in EPR spectra of paramagnetic systems diluted in glassy matrices, the hyperfine separation depends on the orientation of the paramagnetic species in the magnetic field.

The traditional method to record EPR spectra is the continuous wave (CW) method, where microwave radiation with constant frequency continuously irradiates the sample. The strength of the external magnetic field is varied linearly, and absorption is detected, when the field strength matches the resonance conditions. EPR spectroscopy is a valuable method to investigate the oxidation states, spin states and coordination environments of paramagnetic metal complexes.

3.1.2.2 EPR Spectra of Tetragonal Cu^{2+} Complexes in Frozen Solution

Since Cu^{2+}-based spin labels are discussed in the following sections, a typical EPR spectrum of a shock-frozen solution containing Cu^{2+} complexes is briefly discussed. Cu^{2+} ions have a d^9 electron configuration and in the case of an octahedral crystal field, two degenerate $(e_g)^3$-configurations are possible $((d_{x2-y2})^2(d_{z2})^1$ or $((d_{x2-y2})^1(d_{z2})^2)$. Molecules with such degenerate electronic ground states are unstable and undergo a geometrical distortion removing the degeneracy (Jahn-Teller theorem). In Cu^{2+} complexes, this distortion is usually an elongation along the z-axis resulting either in a tetragonal distorted (tetragonal bipyramidal) or a square-planar coordination environment (Figure 3.4a). Also, the presence of only one axial ligand (tetragonal pyramidal geometry) is frequently found. As a result of the Jahn-Teller splitting, the d_{x2-y2} orbital is the energetically highest orbital and is occupied by the unpaired electron.[26]

Two stable Cu isotopes, ^{63}Cu and ^{65}Cu, are known with natural abundancies of around 70% and 30%. Both nuclei have a nuclear spin quantum number of $I = 3/2$ and similar gyromagnetic ratios. Consequently, their influence on an electron spin in the proximity can be treated similarly. The hyperfine interaction results in a splitting of the EPR line into four components ($2I + 1 = 4$ with $I = 3/2$, Figure 3.4b and c) separated by the hyperfine splitting constant *A*. Since the Cu^{2+} complexes in a shock-frozen solution are randomly oriented in all possible orientations with respect to the applied static magnetic field, the anisotropic character of the *g*-value and *A* is visible in a spectrum. The unpaired electron resides in the d_{x2-y2} orbital, so that the x-axis and the y-axis are equivalent. As a result, it can be written: $g_{\perp} = g_x = g_y \neq g_{\parallel} = g_z$ ($g_{\perp}$: $\theta = 90°$, $g_{\parallel}$: $\theta = 0°$) and $A_{\perp} = A_x = A_y \neq A_{\parallel} = A_z$ (θ is the angle between magnetic field and the z-axis of the Cu^{2+} complex).[27]

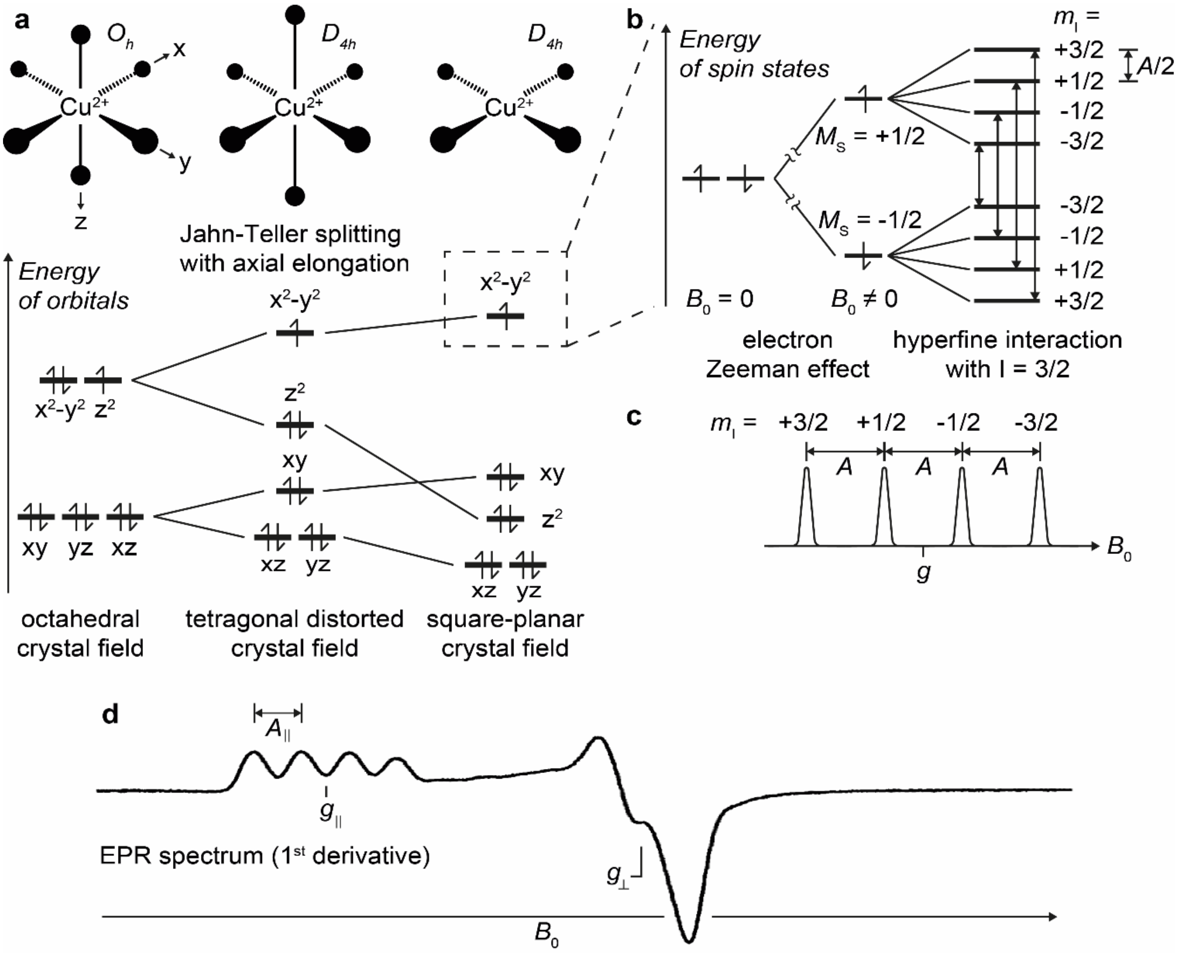

Figure 3.4: (**a**) d-orbital splitting in d^9 metal ions (such as Cu^{2+}) in an octahedral crystal field upon tetragonal distortion by elongation along the z-axis. The energy of orbitals with/without z-orientation is decreased/increased. Further distortion eventually results in a square-planar crystal field (infinite elongation). The unpaired electron resides in the $d_{x2\text{-}y2}$ orbital. (**b**) Splitting of electron spin states in the presence of a magnetic field (electron Zeeman effect, M_S = secondary electron spin quantum number). Hyperfine interaction with a nucleus with $I = 3/2$ (like Cu nuclei, m_I = secondary nuclear spin quantum number) results in further splitting and gives rise to (**c**) four components of the EPR resonance line separated by the hyperfine splitting constant A. The nuclear Zeeman interaction is omitted here since it is very small compared to the electron Zeeman interaction. (**d**) Typical EPR spectrum of a shock-frozen solution containing Jahn-Teller distorted octahedral Cu^{2+} complexes.[28]

A typical anisotropic EPR spectrum of tetragonal distorted Cu^{2+} complexes is shown in Figure 3.4d with $g_{\perp} < g_{\parallel}$ and $A_{\perp} < A_{\parallel}$.[28] The signal intensity in the perpendicular region ($\theta = 90°$) is much higher compared to the intensity in the parallel region ($\theta = 0°$), because in a statistical distribution of the spin orientations the probability of a perpendicular alignment with respect to the magnetic field is much higher. While $A_{\parallel}$ is usually easy to determine, $A_{\perp}$ is often not resolved due to large linewidths.[27]

3.1.2.3 Pulsed EPR Methods and DEER

A second, modern technique often used in addition to CW EPR is pulsed EPR. Here, short pulses of microwave radiation excite the electron spins and a signal is recorded in the absence of applied microwaves. CW spectra have a high information content about the spin system, but a lot of information is packed together, and it is often not possible to extract it. The strategy of pulsed EPR is to apply a pulse sequence that only produces a very sensitive signal for the parameter of interest.[22]

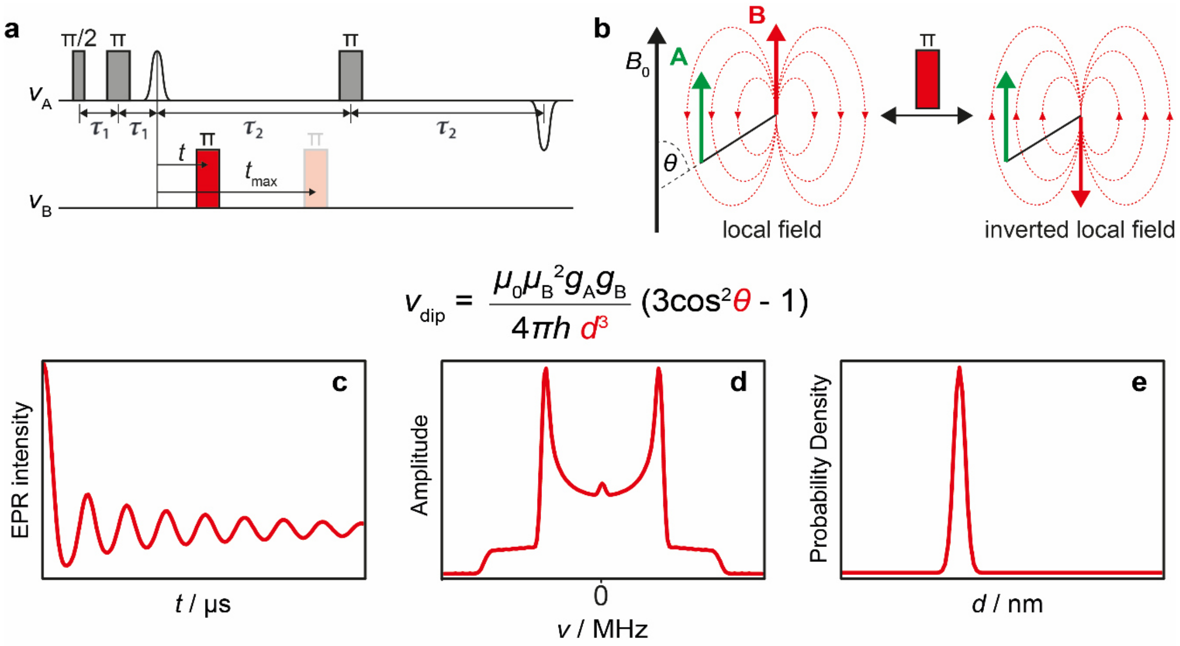

Figure 3.5: (**a**) Pulse sequence of a 4-pulse DEER experiment. (**b**) The pump pulse inverts the state of spin B (red) which results in an inverted local field experienced by spin A (green), changing its resonance frequency. The DEER experiment results in (**c**) a DEER time trace which can be converted to (**d**) a frequency spectrum. Since the dipolar frequency is proportional to the inverse cube of the distance between the two spins, the distance distribution (**e**) can be calculated.

A special pulsed EPR experiment called double electron-electron resonance (DEER) can be applied when a system contains two (or more) spins. The local field of spin B influences the resonance of spin A (magnetic dipole-dipole coupling). DEER separates these pairwise couplings between electron spins from other electron spin interactions.[21] Key of the typical DEER experiment (Figure 3.5a) is the pump pulse (at a different frequency than the detection frequency) that inverts the state of spin B and consequently inverts the local field forced by spin B on spin A (Figure 3.5b), changing its resonance frequency by the dipole-dipole coupling. Variation of the point in time when the pump pulse is applied results in the DEER time trace which can be transferred into a frequency spectrum *via* Fourier transform (Figure 3.5c and d). The dipolar frequency is then used to calculate the distance (the dipolar frequency is proportional to the inverse cube of the distance between the two electrons) between the two spins A and B (Figure 3.5e).[21,29–34]

3.1.3 EPR-based Distance Measurements in Biomolecules

Pulsed dipolar EPR spectroscopy is frequently used for the elucidation of structure and dynamics of biomolecules, especially proteins.[21,29,35] The technique requires two or more paramagnetic spin labels and the distances between them are detected. Some naturally occurring spin labels can be found in proteins including metal centers in metallo-proteins (e.g. Fe^{3+} or Cu^{2+}) or radical species (e.g. tyrosyl radicals). If no paramagnetic groups are present in the species of interest, they can be installed at suitable positions by site-directed spin labeling (SDSL). Again, paramagnetic metal complexes or organic radicals (usually nitroxides) are frequently used. Much effort has been invested to develop different SDSL strategies[36] using bioconjugation (most often to cysteines),[37–39] transition metal complexation (dHis motif)[35,40–42] or incorporation of noncanonical amino acids.[43-46]

PDEPR has been used to answer numerous structure-related questions, for example the detection of stimuli-induced conformational changes,[47–51] investigation of protein-protein interactions[52,53] or the location of native paramagnetic metal ions by trilateration (or triangulation).[32,54,55] It should be seen as a complementary technique to other methods for biomolecular structure elucidation. In contrast to XRD methods, PDEPR does not require crystalline samples and depicts the solution state of a species. Compared to NMR-based methods, it is not limited by the size of the biomolecule and can be performed in complex environments such as cells.[21] Advantages of PDEPR over FRET-based distance measurements are the possibility to measure a wide range of distances with the same labels and the smaller size of most spin labels compared to FRET labels which results in a lower structural perturbation of the labeled species. Also, distances can be measured between two identical spin labels.[36]

In addition to structural investigations on proteins, PDEPR has also been used to study nucleic acid structures.[31,56–63] A variety of spin labels has been developed mostly based on nucleobase or backbone modifications.[58,59,63–77] While mostly organic radicals like nitroxide spin labels are used, there are also examples for Cu^{2+}-based alternatives.[42,54,55,63,78–84] While most studies aimed to investigate the conformational flexibility of duplex structures, few reports describe PDEPR-based examination on other secondary nucleic acid structures. Among these, G-quadruplex topologies of human telomeric sequences were probed,[85–87] including an in-cell investigation.[88,89] Other studies explored the formation of G-quadruplex-metal complex adducts.[90,91] However, the G-quadruplex investigations resulted in very broad distance distributions which were caused either by flexible spin labels or by their installation in very flexible structural regions such as loop regions in unimolecular G-quadruplexes (Figure 3.6).

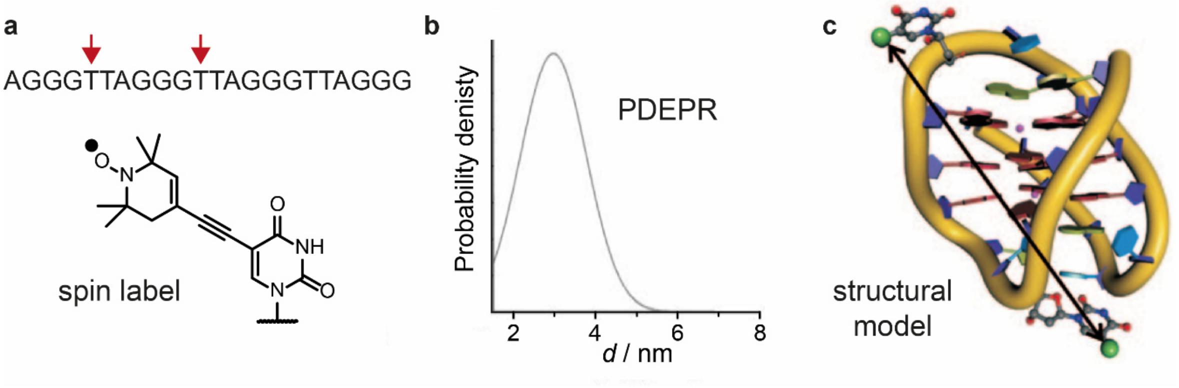

Figure 3.6: (**a**) Two nitroxide-labeled nucleotides were incorporated into a G-quadruplex-forming sequence. (**b**) PDEPR-based measurements revealed a distance that matched their separation in a folded unimolecular G-quadruplex with antiparallel topology. (**c**) The structural model was based on an NMR-based solution structure. The very broad distance distribution is caused by the installation of the spin labels in the very flexible loop regions that can adopt numerous conformations. Adapted with permission from [85]. Copyright © 2009 Wiley-VCH Verlag GmbH & Co. KGaA, Weinheim.

Recently, the intrinsic paramagnetic property of Cu(pyridine)$_4$ tetrads residing in G-quadruplexes (Section 1.4) was exploited for spin labeling by the Clever Lab. In a first attempt, metal complexes were attached at both the 5'-end and the 3'-end of tetramolecular G-quadruplexes with varying G-tetrad count ($2Cu^{2+}@[\mathbf{L^1}G_n\mathbf{L^1}T]_4$, n = 3 – 5).[92] This arrangement allowed to determine intramolecular Cu^{2+}-Cu^{2+} distances within the secondary structures with unprecedented accuracy by pulsed dipolar EPR techniques such as DEER and RIDME (Figure 3.7). The planar four-point attachment of the square-planar Cu(pyridine)$_4$ complexes resulted in a rigid and coplanar orientation of the two magnetic d_{x2-y2} orbitals separated by the stacked G-quartets. This arrangement reduced the conformational flexibility of the spin labels, enabled taking orientation selectivity into account and thus provided additional information on geometrical parameters.

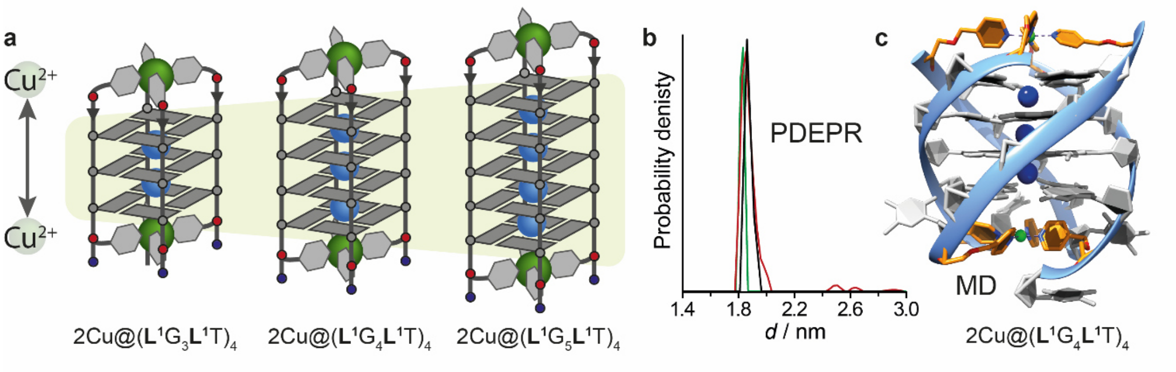

Figure 3.7: (**a**) The incorporation of Cu(pyridine)$_4$ tetrads at both ends of G-quadruplexes with various G-quartet counts allowed precise intramolecular Cu^{2+}-Cu^{2+} distance measurements by different PDEPR spectroscopy methods (**b**, shown for $2Cu^{2+}@(\mathbf{L^1}G_4\mathbf{L^1}T)_4$ in CsCl-containing solution). (**c**) Experimentally obtained distances were in good agreement with MD simulation results (shown for $2Cu^{2+}@(\mathbf{L^1}G_4\mathbf{L^1}T)_4$ in NaCl-containing solution). Reproduced from [92] with permission from The Royal Society of Chemistry.

In the work presented in this chapter, the use of the Cu(pyridine)$_4$ spin label was extended to measure intermolecular distances in higher-order G-quadruplex structures. As a simple representative of such structures, G-quadruplex dimers were investigated in the beginning which are also known to form sandwich complexes with G-quadruplex-binding ligands.

3.2 Distance Measurements in G-Quadruplex Dimers by PDEPR Spectroscopy

3.2.1 Synthesis and Standard Characterization of Spin-Labeled Tetramolecular G-Quadruplexes

The two known tandem repeat units, 5'-TTA GGG and 5'-TTG GGG, found in the telomeric regions of humans and Tetrahymena, are well-known to form tetramolecular G-quadruplexes, (5'-TTA GGG)$_4$ and (5'-TTG GGG)$_4$, in Na$^+$- or K$^+$-containing solution.[93,94] Based on these sequences, six short modified oligonucleotides, where one artificial pyridine-containing nucleotide each (**L^1**, Figure 3.8) was incorporated (oligos **A**–**F**, Table 3.1), were synthesized by solid-phase DNA synthesis. The required phosphoramidite building block (*S*)-**1** for ligandoside incorporation was synthesized according to the published procedure.[95] Only the (*S*) enantiomer of the ligandoside was used in this work.

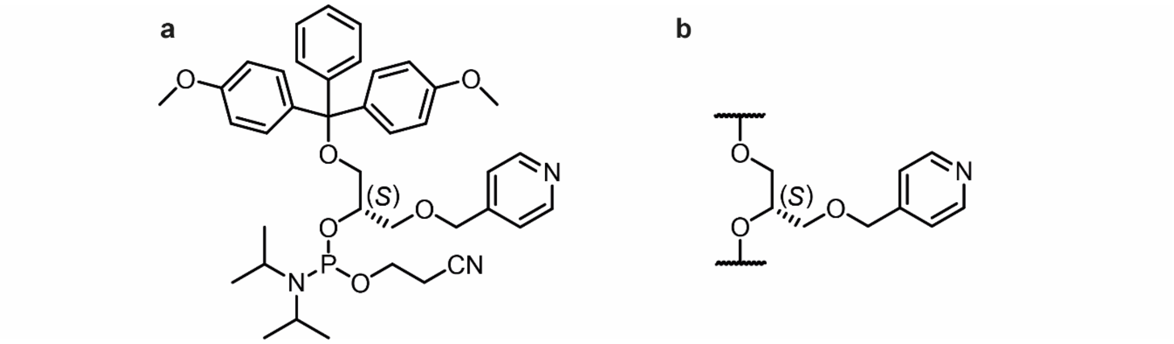

Figure 3.8: (**a**) Synthesized phosphoramidite building block (*S*)-**1** used in solid-phase DNA synthesis.[95,96] (**b**) Corresponding artificial ligandoside **L^1** (right) after incorporation into oligonucleotides.

Table 3.1: Sequences of short pyridine-modified oligonucleotides synthesized and used in this work (**L^1** signifies the pyridine-based ligandoside modification).

Name	Sequence (5' → 3')	Name	Sequence (5' → 3')
Oligo **A**	TT**L^1** GGG	Oligo **D**	GGG **L^1**TT
Oligo **B**	T**L^1**G GGG	Oligo **E**	GGG G**L^1**T
Oligo **C**	TT**L^1** GGG T	Oligo **F**	TGG G**L^1**T T

Ligand positions within the sequences were designed to place the Cu^{2+} binding site in corresponding tetramolecular G-quadruplexes at the 5'-end next to the 5'-G-tetrad, leaving the terminal 3'-G-tetrad exposed (oligos **A** and **B**) or obstructed by additional thymidines (oligo **C**). Furthermore, isomeric reverse order sequences, carrying the Cu^{2+} binding site at the 3'-end were synthesized (oligos **D**–**F**). Successful DNA synthesis and purification were verified by analytical reverse-phase HPLC and ESI mass spectrometry. Analytical data are exemplarily shown for oligo **B** in Figure 3.9.

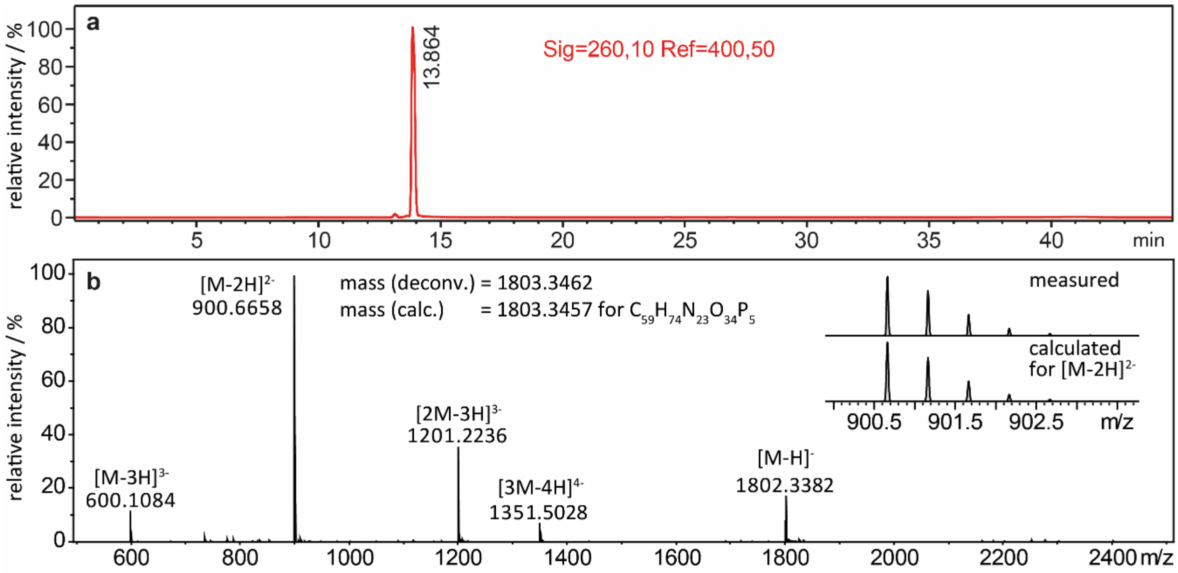

Figure 3.9: (**a**) Analytical reverse-phase HPLC trace and (**b**) ESI mass spectrum of oligo **B** after DNA synthesis and purification.

To confirm G-quadruplex formation, CD spectroscopy was applied. Samples of all six oligonucleotides with a high Na^+ or K^+ concentration at pH 7.2 were measured after annealing. The characteristic patterns in the CD spectra with minima at ~240 nm and maxima at ~260 nm indicated the formation of parallel tetramolecular G-quadruplexes for all six oligonucleotides, both in the absence and presence of Cu^{2+} ions (Figure 3.10b). Interestingly, G-quadruplexes formed from oligos **A** and **C**, respectively, showed a small dent in the CD spectra at ~265 nm in the presence of Cu^{2+} ions (Section 6.7). The observation might be explained with the TT overhang at the 5'-end that is forced into a special conformation due to $Cu(pyridine)_4$ tetrad formation.

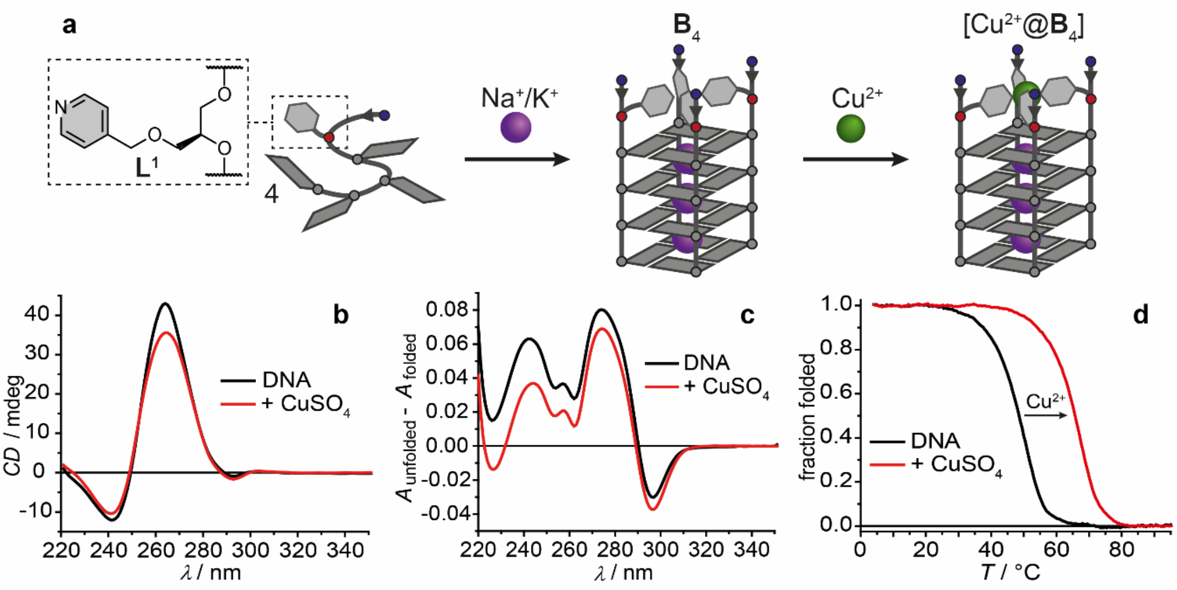

Figure 3.10: (**a**) Self-assembly of pyridine-modified G-quadruplex **B**$_4$ and its Cu^{2+} binding ([Cu^{2+}@**B**$_4$]). The structure of ligandoside **L^1** is illustrated. (**b**) CD spectra, (**c**) UV-based thermal difference spectra, and (**d**) UV-based thermal denaturation profiles of the G-quadruplex in the absence or presence of Cu^{2+} ions. Sample composition: 16 µM oligonucleotide (4 µM G-quadruplex), 4 µM $CuSO_4$ (if present), 100 mM NaCl, 10 mM lithium cacodylate buffer (pH 7.2).

In addition, characteristic patterns in UV-based thermal difference spectra of all samples confirmed G-quadruplex formation (Figure 3.10c) and UV-based thermal denaturation profiles exhibited sigmoidal curves, suggesting a simple melting process (from G-quadruplexes to single-stranded oligonucleotides, Figure 3.10d). Here, G-quadruplexes formed from oligo **D** were an exception and showed a biphasic melting curve indicating either a more complicated, stepwise melting process of a single G-quadruplex topology or the presence of a mixture of topologies (Section 6.2).

Importantly, the presence of Cu^{2+} ions resulted in a significant increase of the thermal denaturation temperatures of all G-quadruplexes, which is a valid indication for the formation of Cu(pyridine)$_4$ quartets. It was previously shown that the complex formation raises the overall stability of the folded G-quadruplex.[95–97] Thermal denaturation temperatures of the different G-quadruplex species are listed in Table 3.2.

Table 3.2: Overview of thermal denaturation temperatures and thermal stabilization upon Cu^{2+} addition for pyridine-modified G-quadruplexes.[a]

G-quadruplex	Alkali metal ions	$T_{1/2}$ / °C	$T_{1/2}$ / °C (+ Cu^{2+})	$\Delta T_{1/2}$ / °C
$\mathbf{A}_4$	K^+	37	62	+25
$\mathbf{B}_4$	K^+	>95	>95	n.d.[b]
$\mathbf{B}_4$	Na^+	49	66	+17
$\mathbf{C}_4$	K^+	45	68	+23
$\mathbf{D}_4$[c]	K^+	35 68	38 70	+3 +2
$\mathbf{E}_4$	K^+	>95	>95	n.d.[b]
$\mathbf{E}_4$	Na^+	60	62	+2
$\mathbf{F}_4$	K^+	41	49	+8

[a] Sample composition: 16 µM oligonucleotide (4 µM G-quadruplex), 4 µM $CuSO_4$ (if present), 100 mM KCl or NaCl, 10 mM lithium cacodylate buffer (pH 7.2). [b] Not determined, because denaturation temperature is out of measurable range. [c] A biphasic melting behavior with two melting temperatures was observed.

The well-known trends dictating a higher G-quadruplex stability for a higher number of G-tetrads and more stable structures in the presence of K^+ than of Na^+ ions were confirmed. In addition, G-quadruplexes with the ligand modifications residing at the 5'-end exhibited a much higher stabilization upon Cu^{2+} addition compared to their isomers with the pyridine ligands positioned at the 3'-end, as shown previously.[92]

To gain more information about the $Cu(pyridine)_4$ complex, field-sweep EPR spectroscopy was performed. A typical EPR spectrum (for [Cu^{2+}@$\mathbf{A}_4$]) with a hyperfine coupling in the parallel region and a broad signal in the perpendicular region is shown in Figure 3.11. The spin-Hamiltonian parameters ($g_{\parallel} = 2.268$, $g_{\perp} = 2.063$, $A_{\parallel} = 545$ MHz) used for the best fit were in good agreement with known parameters for Cu^{2+} ions coordinated to four nitrogen donors in the equatorial positions,[98–100] in perfect agreement with the expected $Cu(pyridine)_4$ quartet, as previously observed for a similar $Cu(pyridine)_4$ tetrad.[97]

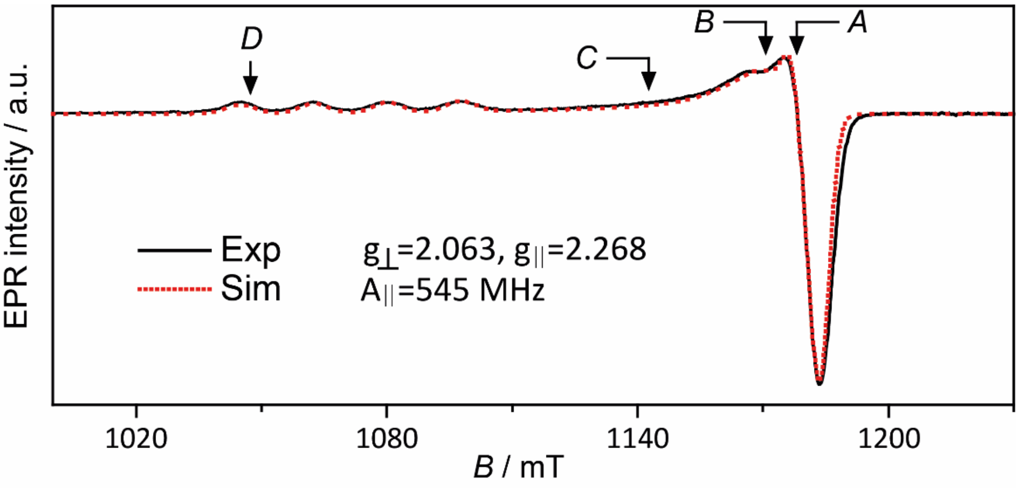

Figure 3.11: Field-sweep EPR spectrum of the Cu(pyridine)$_4$ complex in G-quadruplex [Cu^{2+}@**A**$_4$] recorded at 34 GHz and 19 K (black line) and corresponding best simulation (red dotted line) with the stated spin-Hamiltonian parameters. For *A*–*D*, see Figure 3.12. Sample composition: 500 µM oligonucleotide (125 µM G-quadruplex), 187.5 µM CuSO$_4$ (1.5 equiv. per G-quadruplex), 25 mM potassium phosphate buffer (pH 7.0) in a 1:1 (v/v) mixture of water and glycerol.

It should be mentioned here that the so far described experiments gave no hints on the potential presence of dimeric G-quadruplex species.

3.2.2 Intermolecular Cu^{2+}-Cu^{2+} Distance Measurements Reveal G-Quadruplex Dimers

In the modified G-quadruplexes, the paramagnetic Cu(pyridine)$_4$ complex with its unpaired electron served as a spin label enabling intermolecular distance measurements by PDEPR spectroscopy (Section 3.1.2). In all different investigated G-quadruplex structures, one terminal site carried the spin label, while the other end remained unmodified, which allowed dimerization *via* stacking of the terminal G-tetrads, as previously observed for unmodified G-quadruplxes.[93,94,101] Two different techniques, double electron-electron resonance (DEER or PELDOR) and relaxation induced dipolar modulation enhancement (RIDME), were applied to detect dipole-dipole interactions between the paramagnetic spin labels, which can be transferred into corresponding distances. Since almost equal results were obtained with both techniques, only the DEER data are discussed in this thesis.

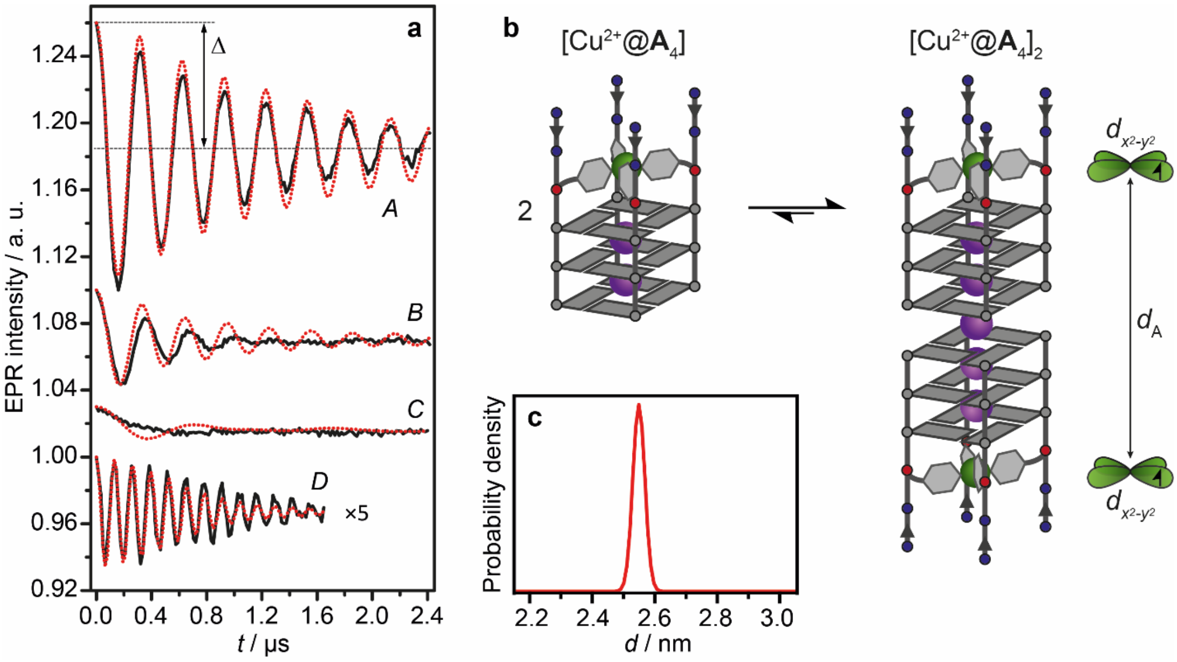

Figure 3.12: (**a**) Background-corrected orientation-selective DEER time traces measured at four different field positions (black lines) and best fit results obtained with PeldorFit (red dotted lines). Observer positions are marked in Figure 3.11 (*A*-*D*) and correspond to g_{eff} = 2.061, 2.071, 2.121, and 2.315. The modulation depth parameter *Δ* is shown (trace *A*). *Δ* of trace *D* has been increased (5-fold) for clarity. (**b**) Equilibrium between monomeric G-quadruplex [Cu^{2+}@**A**$_4$] and its dimeric species [Cu^{2+}@**A**$_4$]$_2$, formed *via* tail-to-tail stacking of the 3'-terminal G-tetrads. The distance d_A between the magnetic d_{x2-y2} orbitals of the Cu^{2+} ions containing the unpaired electrons in the dimer is indicated. (**c**) Narrow Cu^{2+}-Cu^{2+} distance distribution obtained from the DEER experiment using PeldorFit. Sample composition: 500 µM oligonucleotide (125 µM G-quadruplex, 62.5 µM G-quadruplex dimer), 187.5 µM $CuSO_4$ (1.5 equiv. per G-quadruplex), 25 mM potassium phosphate buffer (pH 7.0) in a 1:1 (v/v) mixture of water and glycerol.

Samples containing spin-labeled G-quadruplex [Cu^{2+}@**A**$_4$] revealed a single Cu^{2+}-Cu^{2+} mean distance of d_A = 2.55 nm with a very narrow distance distribution of σ = 0.02 nm (σ is the standard deviation of the distance distribution). Considering typical π-stacking distances of 0.35 nm between the G-quartets, the obtained distance matched the expected one in a G-quadruplex dimer ([Cu^{2+}@**A**$_4$]$_2$) formed through tail-to-tail stacking of the 3'-terminal G-tetrads (Figure 3.12b). Exemplarily, experimentally derived DEER data for [Cu^{2+}@**A**$_4$]$_2$ are shown in Figure 3.12. Samples containing G-quadruplex [Cu^{2+}@**B**$_4$] also revealed a dimeric structure ([Cu^{2+}@**B**$_4$]$_2$, Figure 3.13a) with a Cu^{2+}-Cu^{2+} mean distance of d_B = 3.21 nm (σ = 0.02 nm). This obtained distance was about two π-stacking distances longer compared to the one found for [Cu^{2+}@**A**$_4$]$_2$ (d_B – d_A = 0.66 nm), which was in perfect agreement with the expected distance, since each [Cu^{2+}@**B**$_4$] monomer contained one additional G-quartet.

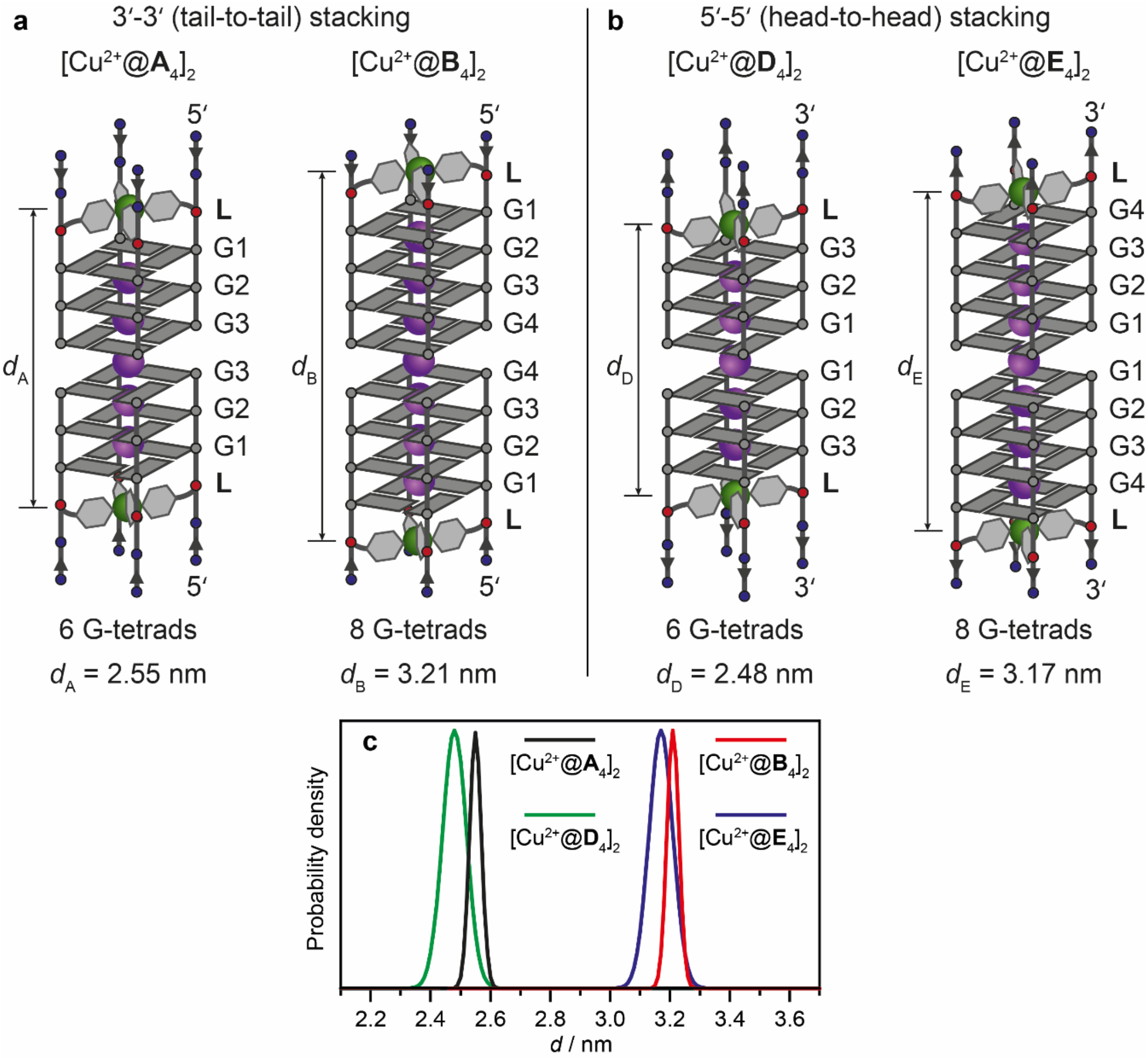

Figure 3.13: Schematic representation of investigated spin-labeled G-quadruplex dimers formed *via* tail-to-tail (**a**, [Cu^{2+}@**A**$_4$]$_2$ and [Cu^{2+}@**B**$_4$]$_2$) or head-to-head stacking (**b**, [Cu^{2+}@**D**$_4$]$_2$ and [Cu^{2+}@**E**$_4$]$_2$) of the terminal G-quartets. (**c**) Cu^{2+}-Cu^{2+} distance distributions for the different species obtained with the PDEPR experiments. For sample compositions see caption of Figure 3.12.

Moreover, isomeric G-quadruplexes [Cu^{2+}@**D**$_4$] and [Cu^{2+}@**E**$_4$] with the Cu(pyridine)$_4$ complex positioned at the 3'-end allowing dimer formation *via* stacking of the 5'-terminal G-tetrads (head-to-head stacking) were investigated. Dimeric species were evidenced detecting Cu^{2+}-Cu^{2+} mean distances of d_D = 2.48 nm (σ = 0.04 nm) for [Cu^{2+}@**D**$_4$]$_2$ and d_E = 3.17 nm (σ = 0.04 nm) for [Cu^{2+}@**E**$_4$]$_2$ (Figure 3.13b). The obtained distances were slightly shorter compared to the ones of respective isomers ($d_A - d_D = 0.07$ nm and $d_B - d_E = 0.04$ nm, Figure 3.13c), which can be explained with small structural differences of the Cu(pyridine)$_4$ tetrad located at the 5'- or 3'-end. Furthermore, the width of the distance distribution is slightly larger, indicating a higher flexibility of the spin label positioned at the 3'-end. This observation is in accordance with a less pronounced hyperfine structure in the EPR spectrum found for the Cu^{2+} spin label residing at the 3'-end (Figure 6.58). Interestingly, [Cu^{2+}@**D**$_4$]$_2$ showed a lower modulation depth (Δ) compared to the other dimers investigated (Figure 6.61). Since Δ correlates with the concentration of Cu^{2+}-Cu^{2+} pairs in the sample, the observation suggested a low dimer concentration. This finding may correlate with the aforementioned complicated denaturation behavior found in the UV-based melting profile indicating the presence of several secondary structures, where one fraction might not be able to form dimers (Section 3.2.1).

Control samples with G-quadruplexes [Cu^{2+}@**C**$_4$] and [Cu^{2+}@**F**$_4$] were inspected, both carrying additional thymidines, blocking the terminal G-tetrads. The absence of a dipolar modulation of the Cu^{2+} EPR signal in the DEER time traces indicated no dimer formation (Figure 3.14). The result corroborated that blocking thymidines inhibit dimerization of G-quadruplexes *via* tail-to-tail or head-to-head stacking in solution,[93,94,101] although dimerization has been observed in the solid state.[102]

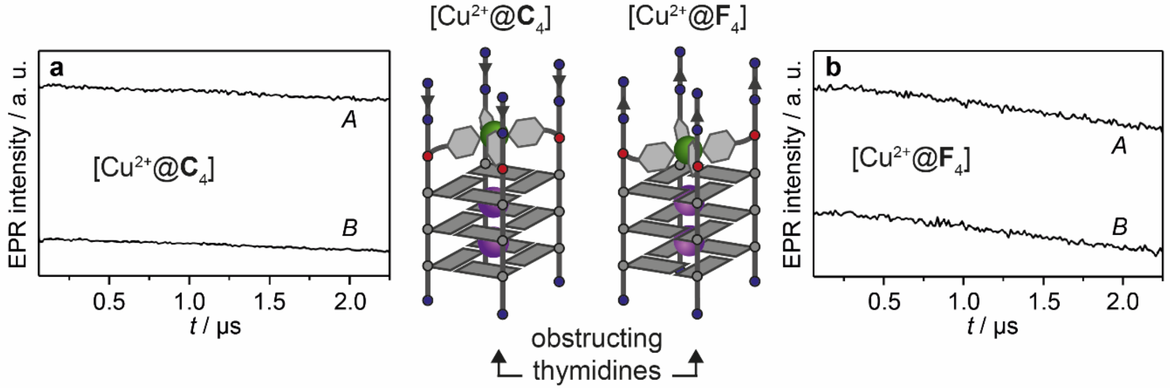

Figure 3.14: DEER time traces measured at two field positions for G-quadruplexes (**a**) [Cu^{2+}@**C**$_4$] and (**b**) [Cu^{2+}@**F**$_4$]. Observer positions are marked with *A* and *B* and correspond to $g_{eff} = 2.061$ and 2.071. The traces showed no dipolar modulation for the two modified G-quadruplexes, confirming that the additional 3'- or 5'-terminal thymidines prevent G-quadruplex dimerization in solution. For sample compositions see caption of Figure 3.12.

The Cu(pyridine)$_4$ spin label was attached to the G-quadruplex in a highly rigid fashion, where the magnetic orbital of the square-planar coordinated Cu^{2+} cation was fixed in a defined spatial orientation by decorating the four-stranded DNA species with four nitrogen donors, forming a rigid chelate environment. In the case of rigid, orientationally correlated spin pairs, orientation selectivity causes a deviation of dipolar spectra from a Pake pattern. The dipolar frequency becomes dependent on the g-tensor orientations selected in the experiment.[103] Therefore, further structural information could be obtained from the PDEPR experiments, in addition to the Cu^{2+}-Cu^{2+} mean distances. A detailed analysis revealed that the z-axes of the two Cu^{2+} spin labels within a dimeric G-quadruplex structure were aligned collinearly (Figure 3.15 and Table 3.3). These spatial orientations perfectly fit to the expected dimeric structure with two rigid coplanar Cu(pyridine)$_4$ tetrads and a tight π-stacking interface between the two monomers.

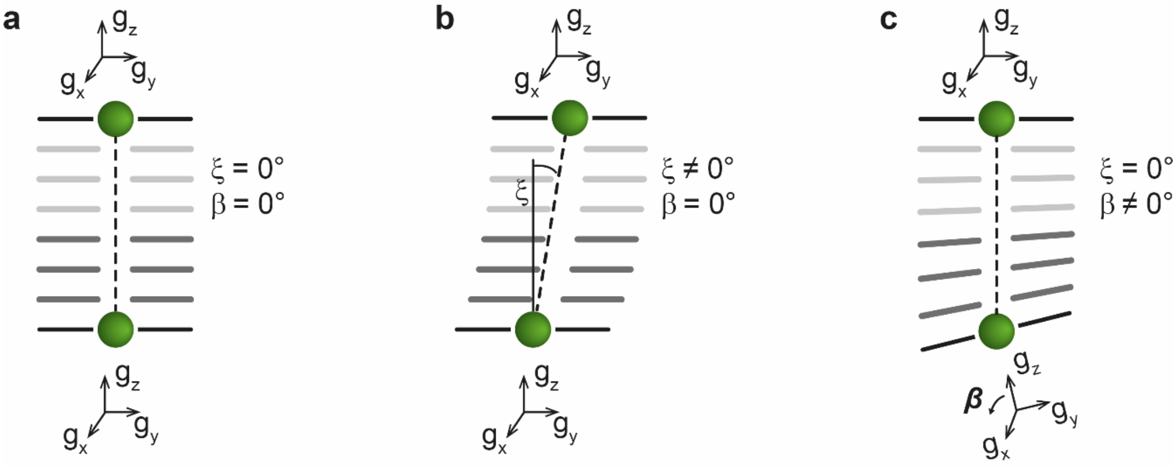

Figure 3.15: Schematic representation of a π-stacked G-quadruplex dimer showing structural details affecting the EPR-based distance measurements. Green spheres: Cu^{2+} cations; light and dark grey bars: G-quartets; black bars: Cu^{2+} coordination planes. (**a**) Coplanar G-quartet stacking. The inter-spin vector (dashed black line) is collinear with the g_z-axis of the observer spin, and the g-frames of the two Cu^{2+} ions are collinear. (**b**) Deviation from collinearity between the observer spin g_z axis and inter-spin vector. (**c**) Tilting of the plane of (at least) one Cu^{2+} complex.

Table 3.3: Cu^{2+}-Cu^{2+} distances and structural important angles obtained from DEER experiments in G-quadruplex dimers and related sandwich complexes. Cu^{2+}-Cu^{2+} distances obtained from MD simulations are listed for comparison.

G-quadruplex adduct	d / nm, DEER[a]	d / nm, MD[b]	ξ / deg[c]	β / deg[c]
$[Cu^{2+}@\mathbf{A}_4]_2$	2.55 (0.02)	2.53 (0.03)	0 (1)	0 (1)
$[Cu^{2+}@\mathbf{B}_4]_2$	3.21 (0.02)	3.23 (0.03)	8 (19)	4 (2)
$[Cu^{2+}@\mathbf{C}_4]$[d]	No dimerization	-	-	-
$[Cu^{2+}@\mathbf{D}_4]_2$	2.48 (0.04)	2.55 (0.04)	6 (6)	18 (8)
$[Cu^{2+}@\mathbf{E}_4]_2$	3.17 (0.04)	3.34 (0.04)	3 (14)	6 (11)
$[Cu^{2+}@\mathbf{F}_4]$[d]	No dimerization	-	-	-
$[Cu^{2+}@\mathbf{A}_4][Cu^{2+}@\mathbf{B}_4]$	2.88	2.92 (0.03)	-[e]	-[e]
PIPER@$[Cu^{2+}@\mathbf{A}_4]_2$	2.82 (0.03)	2.84 (0.03)	4 (8)	1 (12)
PIPER@$[Cu^{2+}@\mathbf{B}_4]_2$	3.48 (0.05)	3.46 (0.05)	6 (23)	4 (3)
2PIPER@$[Cu^{2+}@\mathbf{A}_4]_2$	3.21 (0.05)	3.18 (0.03)	3 (17)	15 (14)
telomestatin@$[Cu^{2+}@\mathbf{A}_4]_2$	2.88 (0.04)	2.88 (0.04)	4 (13)	9 (27)
guanine$_4$@$[Cu^{2+}@\mathbf{A}_4]_2$	2.88 (0.03)	-[e]	1 (0)	11 (24)
guanine$_4$@$[Cu^{2+}@\mathbf{B}_4]_2$	3.54 (0.03)	-[e]	0 (0)	14 (25)
guanosine$_4$@ $[Cu^{2+}@\mathbf{A}_4]_2$	2.88 (0.02)	2.88 (0.03)	1 (1)	6 (18)
guaniosne$_4$@ $[Cu^{2+}@\mathbf{B}_4]_2$	3.54 (0.01)	3.56 (0.03)	0 (6)	1 (10)

[a] Mean values with standard deviations in parenthesis of experimentally derived distance distributions. PeldorFit was used for data processing. [b] Mean values with standard deviations of MD-derived distance distributions. [c] ξ: polar angle of the inter-spin vector; β: tilting angle of the two equatorial planes of the complexes (see Figure 3.15). [d] Additional thymidines prevent dimerization by blocking the terminal G-tetrad. [e] Not determined.

The PDEPR experiments demonstrated that the $Cu(pyridine)_4$ spin label can be used to detect different dimeric G-quadruplex species. Experimentally derived mean Cu^{2+}-Cu^{2+} distances and corresponding distributions for all dimers, as well as structurally important angles are listed in Table 3.3. The distance distributions achieved for the different species were about 5 to 10 times narrower than those obtained for DNA and RNA structures labeled either with nitroxide-[57–59,61,85] or other, less structurally confined Cu^{2+}-based[63,91] spin labels. Such narrow distance distributions not only highlight the overall rigid and defined structure adopted by the G-quadruplex dimers investigated in this work, but also demonstrate the pronounced rigidity of our $Cu(pyridine)_4$ spin label within its G-quadruplex environment.

3.2.3 Sandwich Complexes Based on G-Quadruplex Dimers and PIPER

G-quadruplex dimers form sandwich complexes with G-quadruplex-binding ligands such as PIPER, representing a more sophisticated type of higher-order G-quadruplex structures. The study of interactions with G-quadruplex-binding ligands is of high relevance due to their role in anticancer and gene regulation strategies (Section 1.2.3). In an early NMR-based investigation, a 2:1 sandwich complex in solution had been proposed where one PIPER molecule intercalates into a tail-to-tail stacked dimer formed from two parallel tetramolecular G-quadruplexes and where PIPER interacts *via* π-stacking with the terminal G-quartets (see Figure 1.8b).[104] The ability to distinguish between different dimeric G-quadruplex species with high resolution using the rigid $Cu(pyridine)_4$ spin label as demonstrated in the previous section suggested to employ PDEPR experiments for investigating this sandwich complexes.

The PIPER dye was synthesized using a modified literature procedure[104,105] (Section 7.3) and characterized by UV-VIS spectroscopy. The dye was soluble in buffered aqueous solution at pH 6.0 due to protonation of the tertiary amino groups resulting in a distinct absorption in the visible region. At pH 7.0 and under more basic conditions, the equilibrium shifted to the unprotonated amine and PIPER precipitated (Figure 3.16).

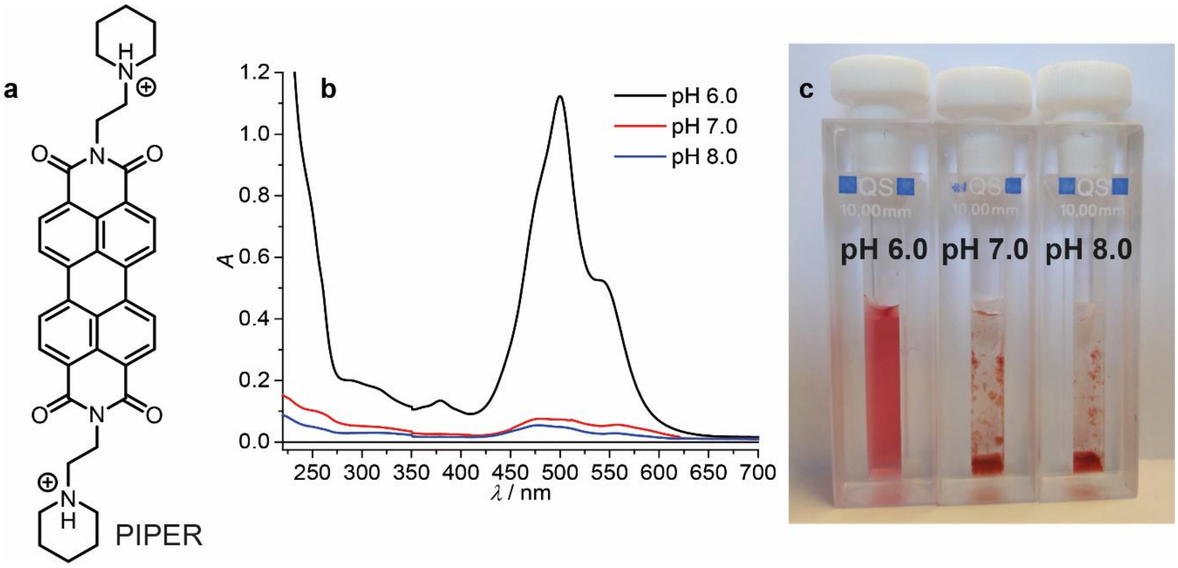

Figure 3.16: (**a**) Molecular structure of protonated PIPER. (**b**) UV-VIS spectra and (**c**) pictures of corresponding samples of 50 µM PIPER in 50 mM potassium phosphate buffer of different pH. PIPER is soluble at pH 6.0. In buffered solutions at pH 7.0 and 8.0, PIPER is not soluble and precipitates.

UV-VIS and CD spectroscopy experiments of G-quadruplexes composed of oligos **A**–**F** were repeated in the presence of 0.5 equiv. of PIPER per G-quadruplex. The formation of a parallel G-quadruplex topology was again demonstrated for all samples in the absence and presence of Cu^{2+} ions (Figure 3.17c). However, the addition of PIPER increased the thermal stability of the secondary structures (Figure 3.17d). At pH 7.2, the presence of folded G-quadruplex DNA helped red-colored PIPER to stay in solution, giving rise to a distinct absorbance signature at 450–600 nm. After thermal denaturation of the secondary DNA structure, PIPER precipitated, and the absorbance signal in the visible region vanished (Figure 3.17a and b). This observation confirmed a selective interaction of PIPER with G-quadruplex DNA as compared to single-stranded DNA.[106]

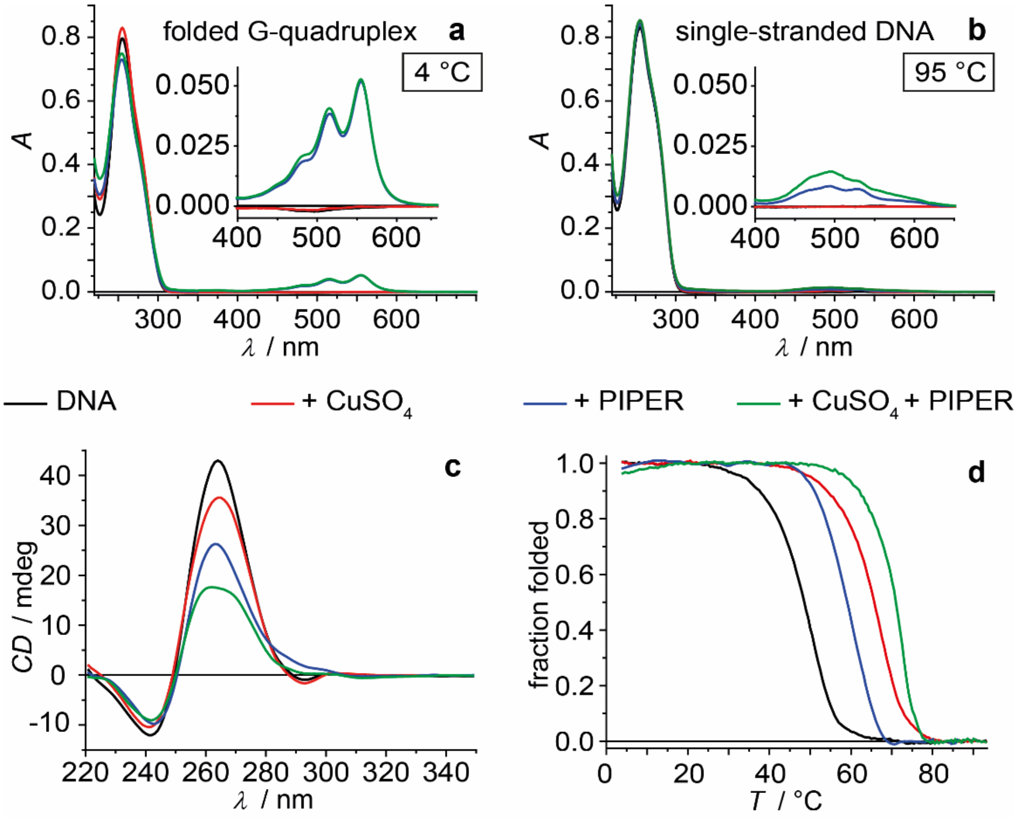

Figure 3.17: (**a**) UV-VIS spectra at 4 °C and (**b**) at 95 °C, (**c**) CD spectra, and (**d**) UV-based thermal denaturation profiles of samples composed of oligo **B** in the absence or presence of Cu^{2+} ions or/and PIPER. Sample composition: 16 µM oligonucleotide (4 µM G-quadruplex), 4 µM $CuSO_4$ (if present), 2 µM PIPER (if present), 100 mM NaCl, 10 mM lithium cacodylate buffer (pH 7.2).

Interestingly, CD bands were observed in the visible range of 400−650 nm for samples containing G-quadruplex species and PIPER (Figure 3.18). The chiral G-quadruplex DNA does not absorb light in this region, but PIPER does. The bands could be explained by induced circular dichroism (ICD)[107] due to transition dipole coupling between the chiral G-quadruplexes and achiral PIPER or due to a deformation of PIPER into a chiral conformation upon adduct formation. Different ICD bands were observed for PIPER in the presence of G-quadruplex [Cu^{2+}@**B**4], which forms dimers *via* tail-to-tail stacking of the terminal G-tetrads, and G-quadruplex [Cu^{2+}@**E**4], which forms head-to-head stacked dimers. This observation suggested a different binding mode of PIPER to the different dimeric secondary structures.

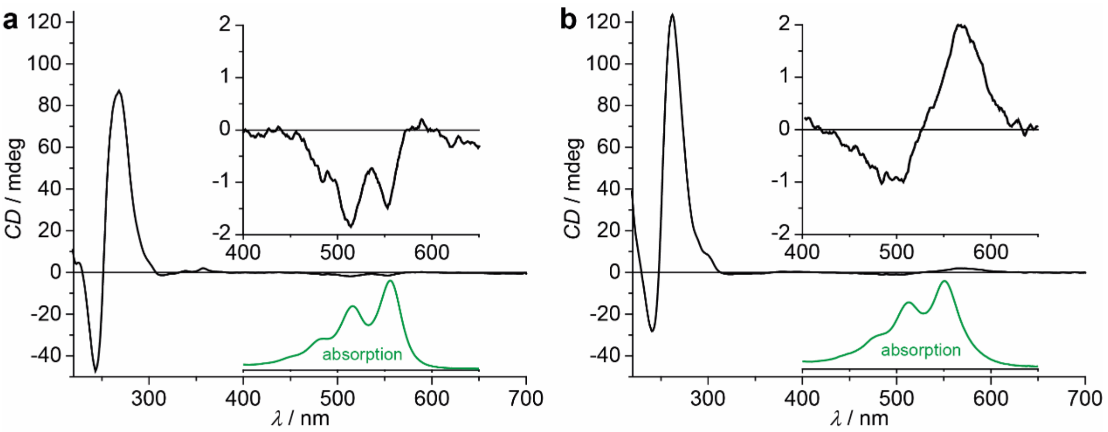

Figure 3.18: CD spectra of folded G-quadruplexes (**a**) [Cu^{2+}@**B**$_4$] and (**b**) [Cu^{2+}@**E**$_4$] in the presence of 0.5 equiv. of PIPER. The bands in the visible region are enlarged and the absorption bands of PIPER are shown for comparison (green). Sample composition: 80 µM oligonucleotide (20 µM G-quadruplex), 20 µM $CuSO_4$, 10 µM PIPER, 100 mM KCl, 10 mM lithium cacodylate buffer (pH 7.2).

PDEPR samples containing [Cu^{2+}@**A**$_4$]$_2$ dimers and a stoichiometric amount of PIPER revealed exclusively a new Cu^{2+}-Cu^{2+} distance of $d_{AP} = 2.82$ nm ($\sigma = 0.03$ nm), larger than the obtained Cu^{2+}-Cu^{2+} distance in pure [Cu^{2+}@**A**$_4$]$_2$ dimers ($d_{AP} - d_A = 0.27$ nm). A consistent result was achieved with samples containing PIPER and [Cu^{2+}@**B**$_4$]$_2$ dimers ($d_{BP} = 3.48$ nm, $\sigma = 0.05$ nm, $d_{BP} - d_B = 0.27$ nm, Figure 3.19a). The increased distances between the two Cu^{2+} ions demonstrated the formation of the sandwich complexes PIPER@[Cu^{2+}@**A**$_4$]$_2$ and PIPER@[Cu^{2+}@**B**$_4$]$_2$, in which the flat organic molecule intercalates between the 3'-terminal G-quartets of the two G-quadruplex monomers.[104]

On the other hand, addition of PIPER to both [Cu^{2+}@**D**$_4$]$_2$ and [Cu^{2+}@**E**$_4$]$_2$ dimers did not influence the detected Cu^{2+}-Cu^{2+} distances, demonstrating that PIPER did not intercalate into 5'-5'-stacked dimers (Figure 3.19b), but preferred a different binding mode, that did not affect the Cu^{2+}-Cu^{2+} distance. This result coincided with the observed differences in ICD signals of PIPER induced by the 3'- and 5'-modified G-quadruplexes that also suggested different binding modes (Figure 3.18).

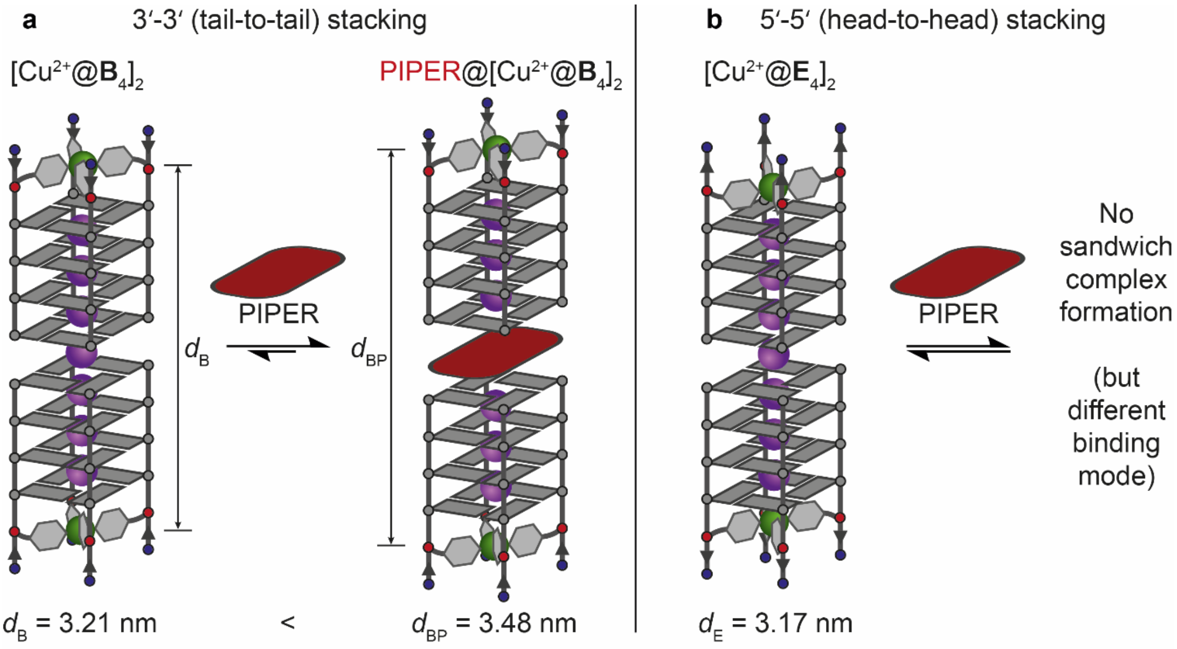

Figure 3.19: (**a**) Formation of the sandwich complex PIPER@[Cu^{2+}@**B**$_4$]$_2$, where the PIPER molecule intercalates between the two monomers of a tail-to-tail stacked G-quadruplex dimer. PIPER intercalation causes an increase in the Cu^{2+}-Cu^{2+} distance, which was detected by PDEPR spectroscopy. (**b**) PIPER does not intercalate between the two monomers of a head-to-head stacked dimer (here [Cu^{2+}@**E**$_4$]$_2$) but prefers a different binding motif, that does not affect the Cu^{2+}-Cu^{2+} distance.

To obtain additional information about the sandwich complexes, samples with varying ratios of PIPER and the [Cu^{2+}@**A**$_4$]$_2$ dimer were examined. For a PIPER:dimer ratio of 0.5:1, two peaks in the dipolar frequency spectrum were observed corresponding to the pure dimer ([Cu^{2+}@**A**$_4$]$_2$) and to the sandwich complex (PIPER@[Cu^{2+}@**A**$_4$]$_2$). Both peaks revealed equal intensity indicating an equal concentration of the two species in solution. The dipolar spectrum of a sample with a 1:1 ratio showed exclusively the peak for the sandwich complex, while the peak for the pure dimer vanished entirely (Figure 3.20). These observations displayed a large binding affinity of the PIPER dye (large binding constant) to the dimer. Furthermore, the results indicated indirectly that the equilibrium between the single G-quadruplexes and their corresponding dimeric species was located far on the side of the G-quadruplex dimers (large equilibrium constant, Figure 3.12b). Addition of 1.0 equiv. of PIPER to samples containing dimers caused no increase in modulation depth in the DEER time traces (Figure 3.20c), which is directly correlated to the concentration of dimeric species in solution. This means, that the whole G-quadruplex population was already present in the dimeric form prior to the PIPER addition, and also supports a large equilibrium constant for the dimer formation. This was further confirmed, because a 5-fold increase of the K^+ concentration in dimer-containing samples did not lead to a higher modulation depth, although higher K^+ concentrations are known to shift the equilibrium to dimeric G-quadruplex species. The conclusion of a monomer-dimer equilibrium located far on the side of the G-quadruplex dimers matched literature-known results for unmodified G-quadruplexes (5'-TTA GGG)$_4$ at high K^+ concentrations.[93]

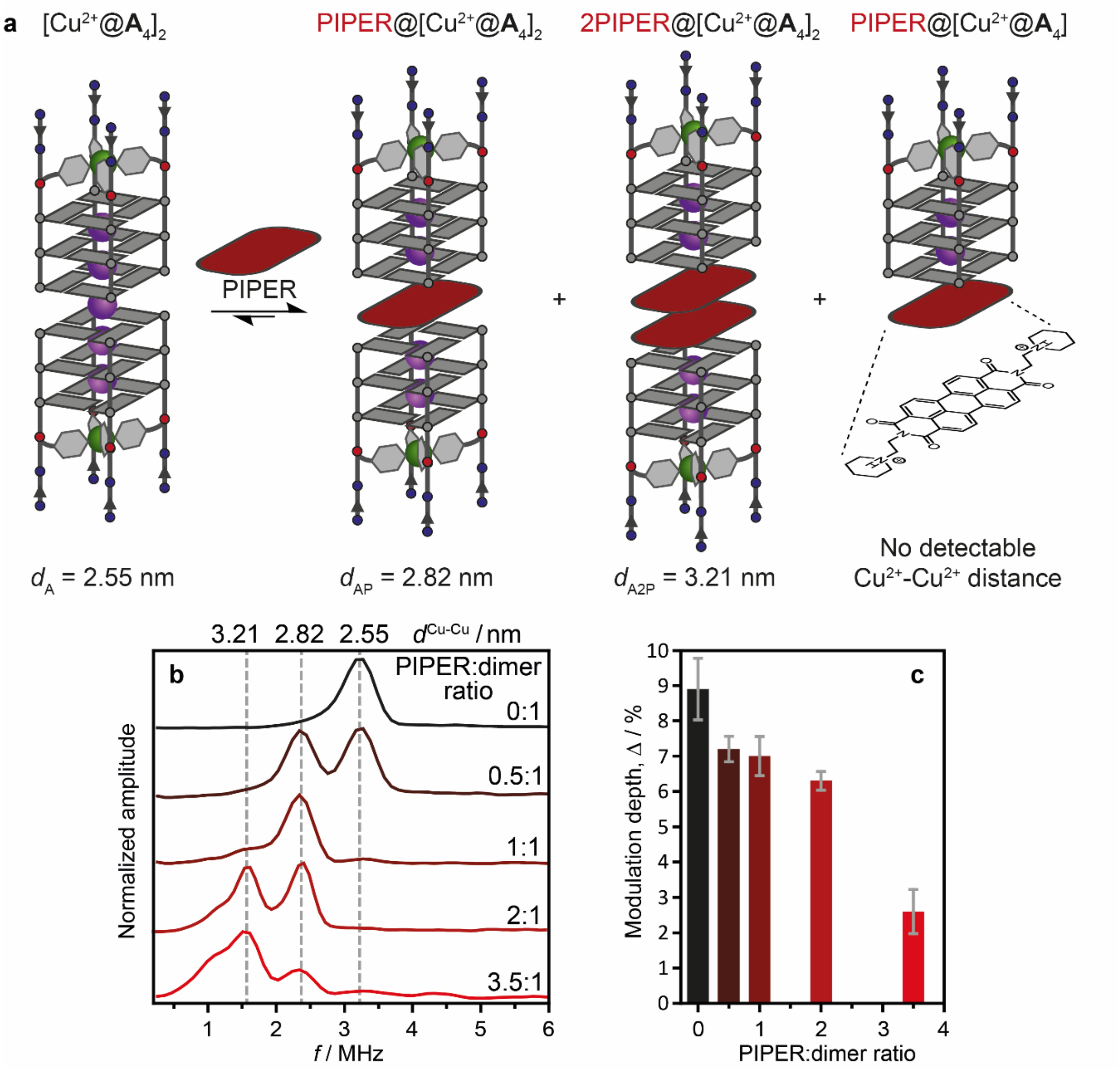

Figure 3.20: (**a**) Equilibrium between the $[Cu^{2+}@\mathbf{A}_4]_2$ dimer and different complexes with the PIPER dye ($PIPER@[Cu^{2+}@\mathbf{A}_4]_2$, $2PIPER@[Cu^{2+}@\mathbf{A}_4]_2$ and $PIPER@[Cu^{2+}@\mathbf{A}_4]$). (**b**) Dipolar spectra ($g_{eff} = 2.061$) and (**c**) modulation depths of $[Cu^{2+}@\mathbf{A}_4]$-containing samples with varying PIPER:dimer ratios. For sample compositions see caption of Figure 3.12 (plus various amounts of PIPER).

Surprisingly, further increase in the PIPER:dimer ratio to 2:1 led to the appearance of a new Cu^{2+}-Cu^{2+} distance of $d_{A2P} = 3.21$ nm ($\sigma = 0.05$ nm), about one π-stacking distance longer than that of the PIPER@[Cu^{2+}@**A**$_4$]$_2$ complex ($d_{A2P} - d_{AP} = 0.39$ nm). This distance was assigned to a species where two PIPER ligands intercalate between the two monomers of the tail-to-tail arranged G-quadruplex dimer (2PIPER@[Cu^{2+}@**A**$_4$]$_2$, Figure 3.20a). To the best of our knowledge, this double binding mode of PIPER to DNA G-quadruplexes has never been described before. It resembles a reported motif found in the solid state, where two naphthalene diimide derivatives intercalate into a head-to-head arranged dimer of unimolecular G-quadruplexes.[108] The modulation depth strongly decreased with an increase in the PIPER:dimer ratio beyond 2:1 (Figure 3.20c). This suggested a disruption of the 2PIPER@[Cu^{2+}@**A**$_4$]$_2$ complex and the formation of a monomeric species, presumably PIPER@[Cu^{2+}@**A**$_4$] (Figure 3.20a), which contains only one Cu^{2+} spin label, and thus cannot be detected with PDEPR.

3.2.4 Sandwich Complexes Based on G-Quadruplex Dimers and Telomestatin

Another well-known G-quadruplex-binding ligand is the natural product telomestatin (Section 1.2.3). The macrocycle usually π-stacks on top of a terminal G-tetrad of unimolecular G-quadruplexes and shows strong inhibition of telomerase activity.[109,110] Synthesized telomestatin was kindly provided by Dr. K. Shin-ya, National Institute of Advanced Industrial Science and Technology (AIST), Tokyo, and Prof. Dr. T. Doi, Tohoku University, Sendai, Japan, to investigate its interaction with tetramolecular G-quadruplexes using the rigid Cu(pyridine)$_4$ spin label and PDEPR spectroscopy.

A sample containing the [Cu^{2+}@**A**$_4$]$_2$ dimer and equimolar amounts of telomestatin revealed two peaks in the frequency spectrum (Figure 3.21c). One of them corresponded to the known Cu^{2+}-Cu^{2+} distance of the pure dimer. The new peak was converted into a Cu^{2+}-Cu^{2+} distance of $d_{AT} = 2.88$ nm ($\sigma = 0.04$ nm), corresponding to an increase in length of one π-stacking distance ($d_{AT} - d_{A} = 0.33$ nm). It was assigned to the sandwich complex, in which telomestatin intercalates in between the two monomers of the dimer, interacting with the 3'-terminal G-tetrads *via* π-stacking (telomestatin@[Cu^{2+}@**A**$_4$]$_2$). The two peaks observed in the frequency spectrum were of equal intensity, suggesting the presence of a balanced equilibrium between the pure dimer and the sandwich complex of equal concentration (Figure 3.21a).

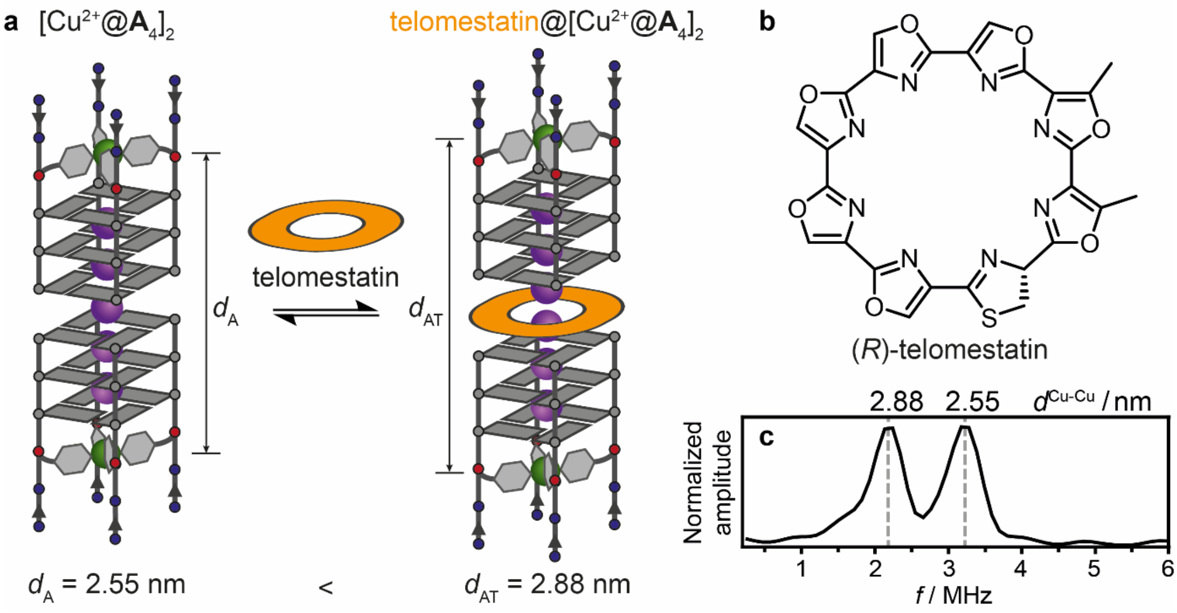

Figure 3.21: (**a**) Equilibrium between the [Cu^{2+}@**A**$_4$]$_2$ dimer and its sandwich complex with telomestatin (telomestatin@[Cu^{2+}@**A**$_4$]$_2$). (**b**) Molecular structure of the natural product (*R*)-telomestatin. (**c**) Dipolar spectrum (g_{eff} = 2.061) of [Cu^{2+}@**A**$_4$]$_2$ mixed with 1.0 equiv. of telomestatin. For sample compositions see caption of Figure 3.12 (plus 62.5 µM of telomestatin and 6.25% DMSO).

To the best of our knowledge, this was the first time that such a sandwich binding mode for telomestatin and G-quadruplexes has been observed. Human telomeric sequences are able to form parallel G-quadruplexes with exposed terminal G-tetrads and are discussed to form higher-order structures.[111–113] Consequently, the discovered binding mode might play a role in the ability of telomestatin to inhibit telomerase.

3.2.5 Intercalation of Free G-Quartets into G-Quadruplex Dimers

Furthermore, the interaction of free guanine with G-quadruplex DNA was studied exploiting the rigid Cu(pyridine)$_4$ spin label. A sample containing [Cu^{2+}@**A**$_4$]$_2$ and 4.0 equiv. of guanine revealed two peaks of similar intensity in the frequency spectrum (Figure 3.22a). One of them corresponded to the known Cu^{2+}-Cu^{2+}

distance of the pure dimer. The same observation was made for a sample containing $[\mathrm{Cu}^{2+}@\mathbf{B}_4]_2$ and 4.0 equiv. of guanine (Figure 3.22b). The new peaks were assigned to sandwich complexes, since the associated Cu^{2+}-Cu^{2+} distances of d_{AG} = 2.88 nm (σ = 0.03 nm) and d_{BG} = 3.54 nm (σ = 0.03 nm), corresponded to an increase in length of one π-stacking distance ($d_{\mathrm{AG}} - d_{\mathrm{A}} = d_{\mathrm{BG}} - d_{\mathrm{B}}$ = 0.33 nm). These observations raised the question about the nature of the intercalating species. Both the single nucleobase and a free G-quartet formed by four guanines seemed plausible intercalators.

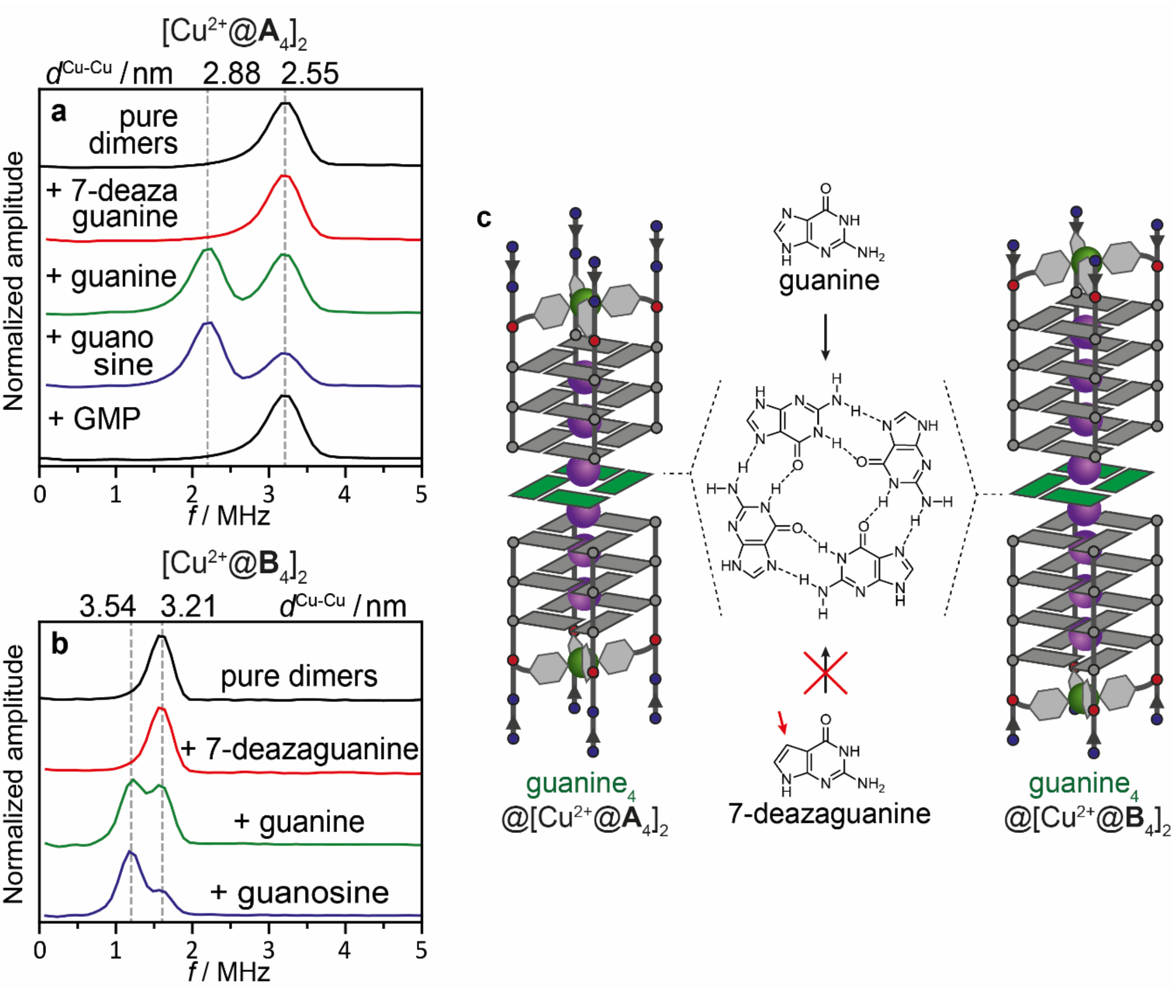

Figure 3.22: Dipolar spectra (g_{eff} = 2.061) of (**a**) $[\mathrm{Cu}^{2+}@\mathbf{A}_4]_2$ and (**b**) $[\mathrm{Cu}^{2+}@\mathbf{B}_4]_2$ in the absence or presence of 4.0 equiv. of different guanine derivatives. (**c**) Schematic representation of the sandwich complexes guanine$_4$@$[\mathrm{Cu}^{2+}@\mathbf{A}_4]_2$ and guanine$_4$@$[\mathrm{Cu}^{2+}@\mathbf{B}_4]_2$. The inability of 7-deazaguanine to form quartets is illustrated. For sample compositions see caption of Figure 3.12 (plus 250 µM of different guanine derivatives).

To address this issue, the experiments were repeated with 7-deazaguanine instead of guanine. The modified nucleobase lacks the N7 atom serving as Hoogsteen hydrogen bond acceptor and is therefore unable to form G-quartets.[114] In the presence of 7-deazaguanine, only the Cu^{2+}-Cu^{2+} distances of the pure dimers were detected and no distances corresponding to sandwich complexes were observed. These results strongly suggested that not a single nucleobase but an untethered G-tetrad intercalates into a G-quadruplex dimer forming a sandwich complex (Figure 3.22c).

Moreover, the same experiments were carried out with guanosine and guanosine monophosphate (GMP). As expected, addition of guanosine resulted in sandwich complexes (guanosine$_4$@[Cu^{2+}@$\mathbf{A}_4$]$_2$ and guanosine$_4$@[Cu^{2+}@$\mathbf{B}_4$]$_2$) with equal Cu^{2+}-Cu^{2+} distances found for guanine$_4$@[Cu^{2+}@$\mathbf{A}_4$]$_2$ and guanine$_4$@[Cu^{2+}@$\mathbf{B}_4$]$_2$, since guanosine willingly forms G-quartets. The equilibria between pure dimers and sandwich complexes were located even further on the side of the complexes, as judged by the relative peak intensities in the dipolar spectra (Figure 3.22a and b), presumably due to the higher solubility of guanosine in water compared to guanine. In contrast, only the pure dimer and no sandwich complex was observed after addition of GMP to a sample of [Cu^{2+}@$\mathbf{A}_4$]$_2$ (Figure 3.22a). The result could be explained by the high negative charge of GMP at pH 7.0, which leads to strong Coulomb repulsion in a GMP-tetrad interacting with negatively charged G-quadruplexes.

3.2.6 MD Simulation of Dimeric G-Quadruplex Structures and Sandwich Complexes

To relate the experimentally determined distances to structural models, molecular dynamics (MD) simulations were performed for each dimeric system. Starting structures were created assuming a tail-to-tail or head-to-head stacking of the terminal G-tetrads, and 50 ns MD runs in explicit TIP3P water with 100 mM KCl concentration at room temperature were conducted (for more details see Section 6.15). The dimeric structures were preserved throughout the full simulation time (Figure 3.23).

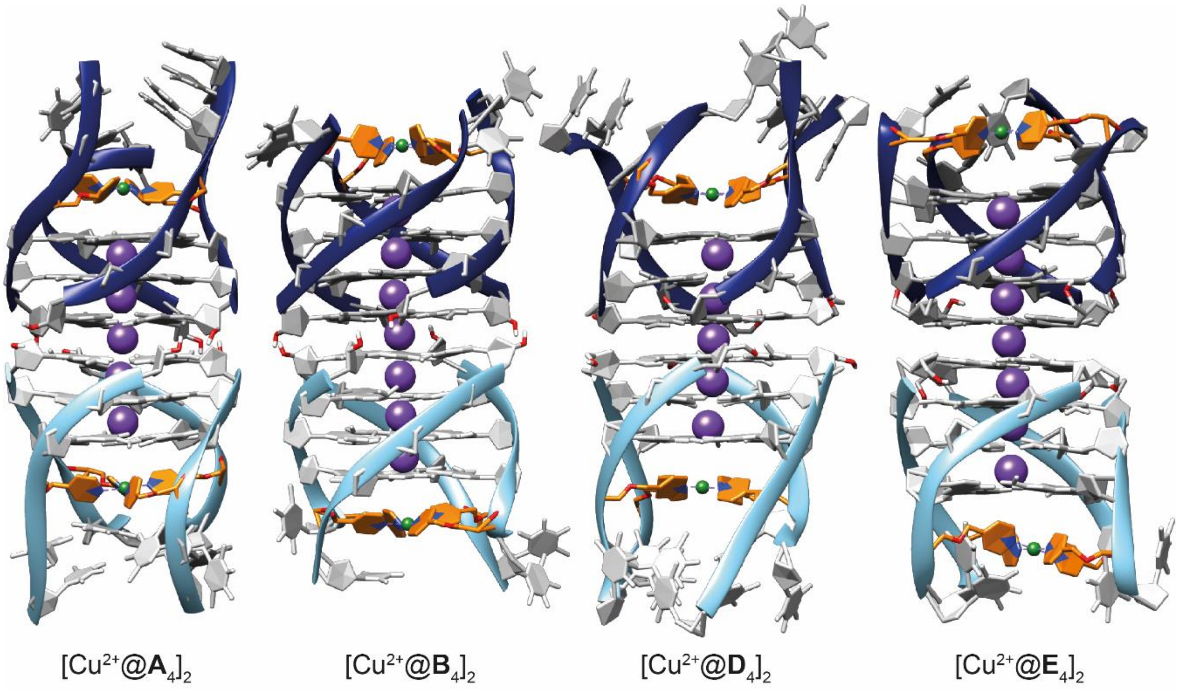

Figure 3.23: Structural models derived from MD simulations of different G-quadruplex dimers. The phosphate backbone is presented as dark and light blue ribbon, K^+ and Cu^{2+} ions as violet and green spheres, and the pyridine ligand modification in orange.

Intermolecular Cu^{2+}-Cu^{2+} distances during the simulation could be extracted and distance distributions were calculated. Obtained Cu^{2+}-Cu^{2+} mean distances and distance distributions matched well the experimentally obtained values (Table 3.3 and Figure 3.24a–f). Especially, distance distributions in tail-to-tail stacked dimers were simulated accurately, while simulated distances for head-to-head stacked dimers were slightly larger than the experimentally obtained ones.

Additionally, sandwich adducts with PIPER, telomestatin or free guanosine quartets as intercalating species were simulated. Starting structures were created with typical π-stacking distances between the respective intercalator and the G-quadruplex monomers. Again, the sandwich structures were preserved during the whole MD run, and the extracted Cu^{2+}-Cu^{2+} distance distributions matched extremely well the DEER-derived ones (Table 3.3, Figure 3.24g–l, and Figure 3.25). In the special case of adduct $2PIPER@[Cu^{2+}@\mathbf{A}_4]_2$, the simulation gave additional information on the relative orientation of the two intercalating PIPER molecules with respect to each other. Throughout the MD run, the relative rotation angle was quite flexible at around 40–60° (Figure 6.82).

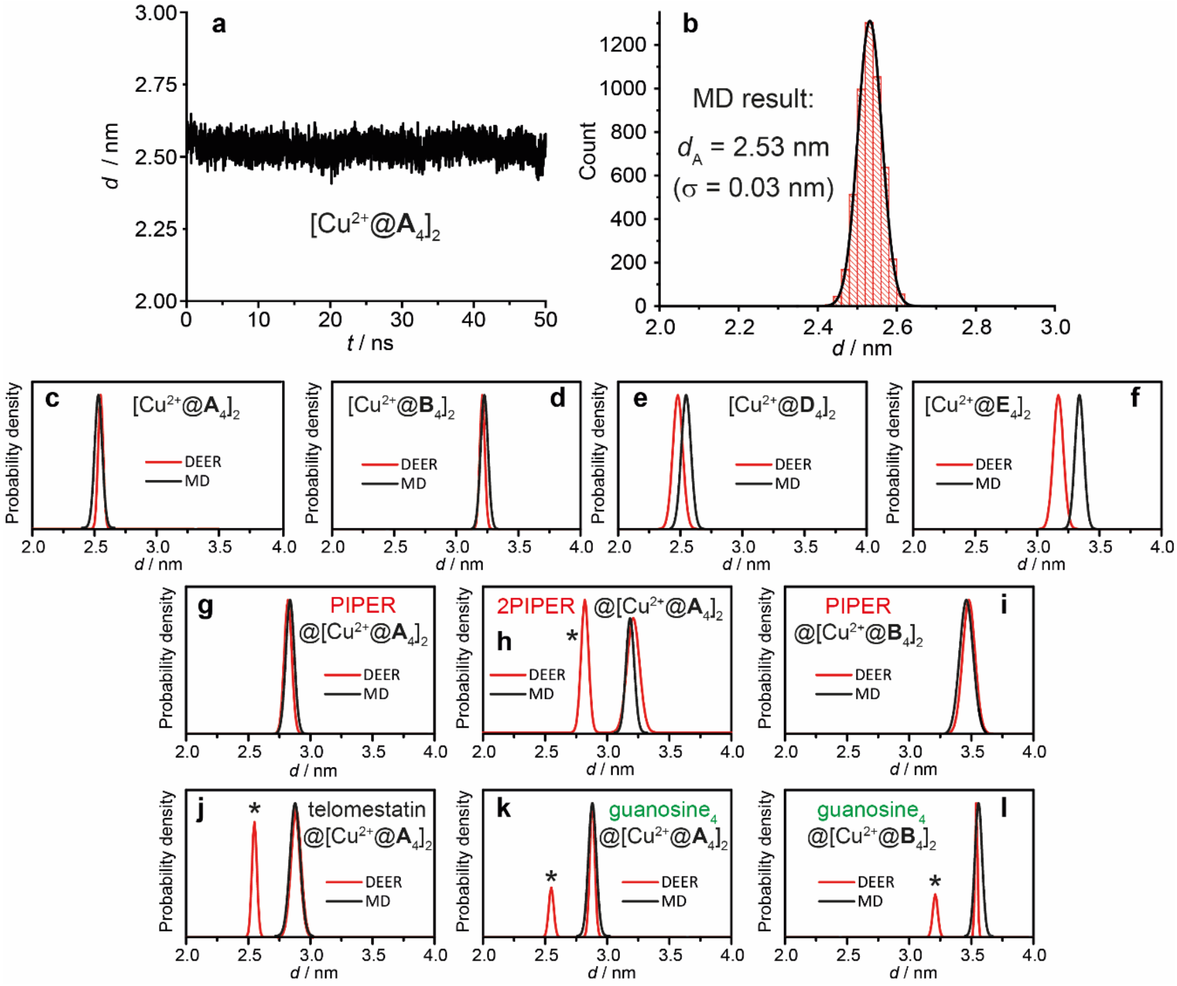

Figure 3.24: (**a**) Cu^{2+}-Cu^{2+} distance in the simulated $[Cu^{2+}@\mathbf{A}_4]_2$ dimer throughout the 50 ns MD run. (**b**) Histogram depiction of the simulated Cu^{2+}-Cu^{2+} distance (red, 0.02 nm bins) and calculated Gaussian distance distribution (black). Resulting mean distance and standard deviation are stated. (**c**-**f**) Comparison of the Cu^{2+}-Cu^{2+} distance distributions obtained by MD simulation with the experimentally, DEER-derived ones in different G-quadruplex dimers. (**g**-**h**) Comparison of the distance distributions obtained by MD simulation with the DEER-derived ones in different investigated G-quadruplex-based sandwich complexes. Peaks tagged with an asterisk correspond to the sandwich complex with only one PIPER molecule intercalated (**h**) or to the respective pure dimer (**j**-**l**).

The examples showed that the combination of PDEPR-derived distances and MD simulations allows detailed structure elucidation in solution of higher-order DNA structures and biomolecules in general.

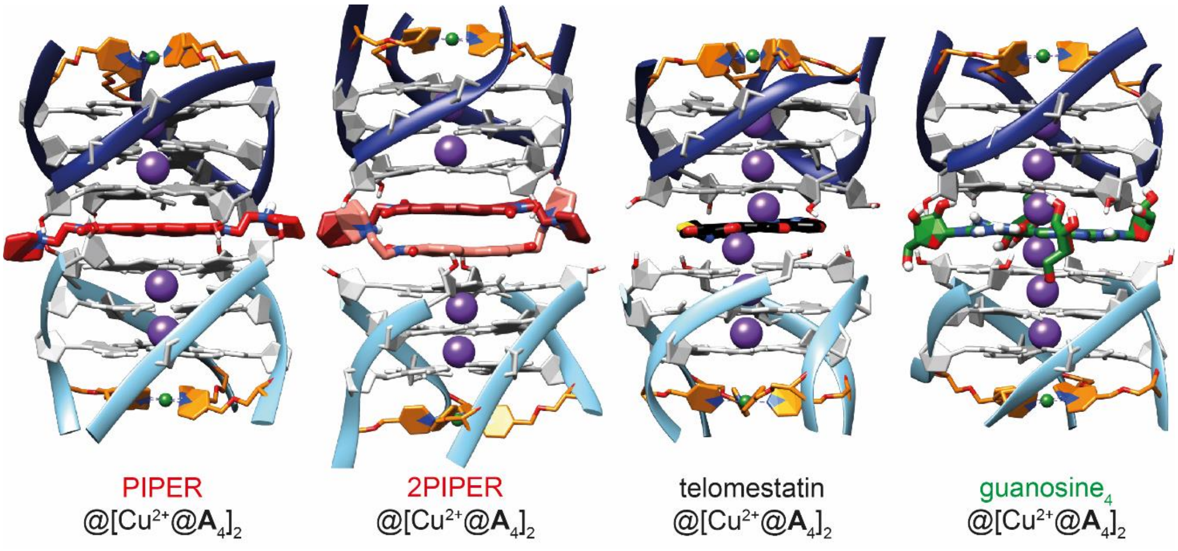

Figure 3.25: Structural models derived from MD simulations of different sandwich complexes. PIPER, telomestatin and the free guanosine quartet are highlighted in red, black, and green, respectively. Thymidine nucleotides are omitted for clarity.

3.2.7 Comparison of Intercalating Species in G-Quadruplex-Based Sandwich Complexes

Three different species, namely PIPER, telomestatin, and untethered G-tetrads (built from either guanines or guanosines), were found to π-stack in between the two monomers of tail-to-tail stacked G-quadruplex dimers, forming sandwich complexes. DEER-based distance measurements revealed small differences in the length of the resulting sandwich complexes (Table 3.4). Intercalation of telomestatin or free G-tetrads increased the Cu^{2+}-Cu^{2+} mean distance in the complexes about $\Delta d = 0.33$ nm, the typical π-stacking distance. In contrast, intercalation of PIPER caused a slightly smaller distance increase of $\Delta d = 0.27$ nm. Despite the small difference, this deviation was significant due to the highly rigid $Cu(pyridine)_4$ spin label and consequential high-resolution distance measurements. In addition, MD simulations supported the observed variations. The difference might be explained with the positive charge of PIPER at pH 7.0, which results in additional attractive Coulomb interactions between the intercalator and the negatively charged G-quadruplexes, while telomestatin and free G-tetrads are neutral species and π-stacking is the major interaction.

Table 3.4: Comparison of charge and structure of intercalating species and the increase in in Cu^{2+}-Cu^{2+} distance caused in corresponding G-quadruplex-based sandwich complexes measured with DEER spectroscopy or simulated with MD.

Intercalating species	Charge at pH 7.0	Macrocyclic structure	G-quadruplex dimer	Δd / nm (DEER)	Δd / nm (MD)
PIPER	2+	no	$[Cu^{2+}@\mathbf{A}_4]_2$	0.27	0.31
PIPER	2+	no	$[Cu^{2+}@\mathbf{B}_4]_2$	0.27	0.23
telomestatin	neutral	yes	$[Cu^{2+}@\mathbf{A}_4]_2$	0.33	0.35
guanine_4	neutral	yes	$[Cu^{2+}@\mathbf{A}_4]_2$	0.33	-[a]
guanine_4	neutral	yes	$[Cu^{2+}@\mathbf{B}_4]_2$	0.33	-[a]
guanosine_4	neutral	yes	$[Cu^{2+}@\mathbf{A}_4]_2$	0.33	0.35
guanosine_4	neutral	yes	$[Cu^{2+}@\mathbf{B}_4]_2$	0.33	0.33

[a] not determined.

A different possible explanation was based on the macrocyclic structure of both telomestatin and untethered G-tetrads, in contrast to PIPER. The macrocyclic intercalators, bearing inward-pointing donor groups, allow a continuous array of K^+ ions residing in between the π-stacking layers throughout the whole sandwich complex (Figure 3.21a and Figure 3.22c), while PIPER prevents this arrangement (Figure 3.19a). Consequently, the absence of the K^+ ions between G-quadruplex monomers and intercalator might cause the smaller distance in the PIPER-containing complexes. To approve this hypothesis, MD simulations of sandwich complexes with the macrocyclic intercalators with or without K^+ ions between G-quadruplex monomers and intercalators were performed. However, the absence or presence of the K^+ ions did not affect the extracted Cu^{2+}-Cu^{2+} distances.

3.2.8 Dynamics of Monomer Shuffling in G-Quadruplex Dimers

The possibility to measure distances between spin labels with PDEPR methods serves as a tool in structure elucidation. Moreover, structural changes and dynamics can be detected, providing further information on the investigated species such as conformational responses to various stimuli or rates of reactions.

In the present study, the shuffling of monomers between G-quadruplex dimers was examined using the spin-labeled tetramolecular G-quadruplexes.

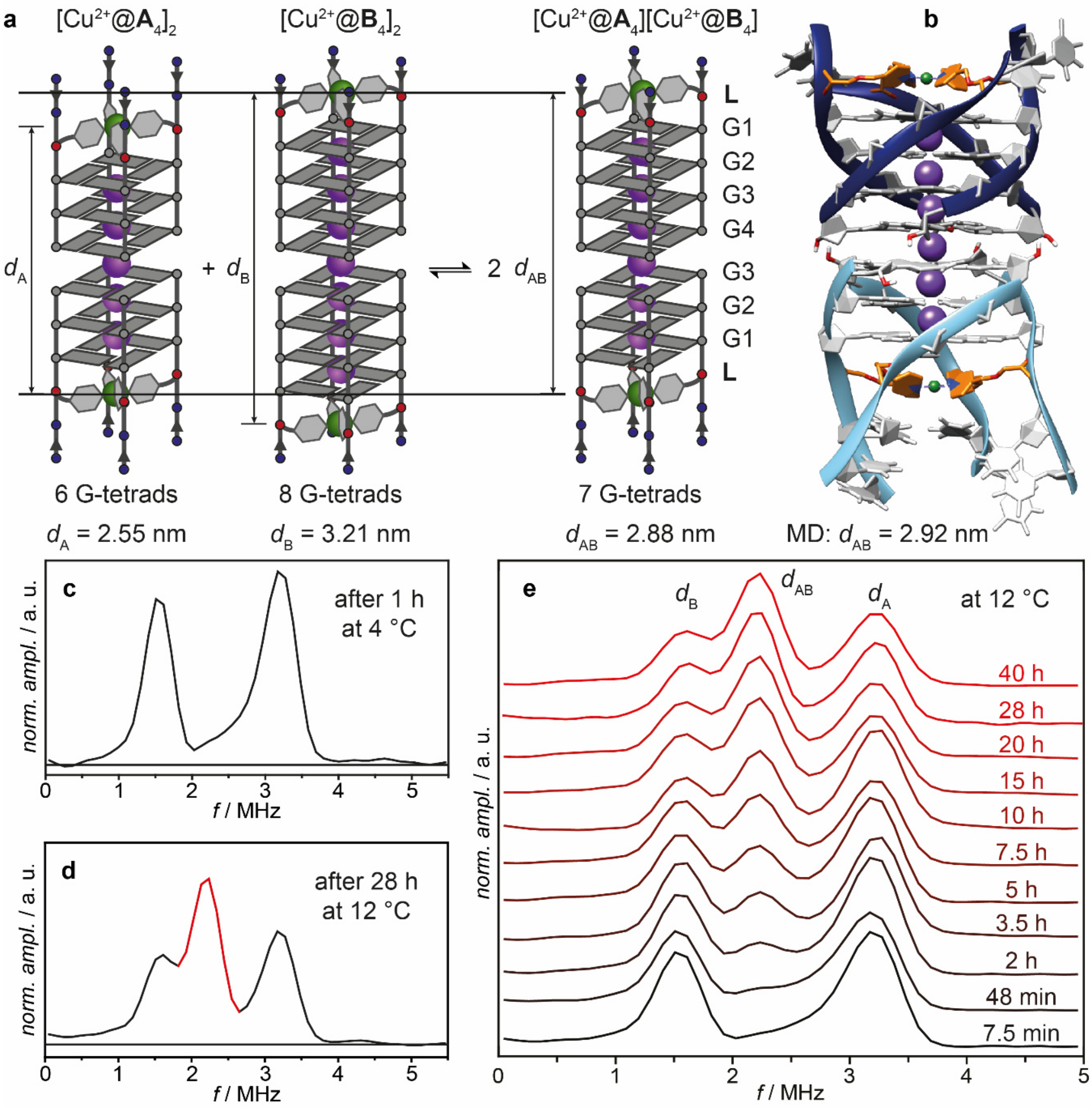

Figure 3.26: (**a**) Equilibrium between two homodimers ([Cu^{2+}@**A**$_4$]$_2$ and [Cu^{2+}@**B**$_4$]$_2$) and the respective heterodimer [Cu^{2+}@**A**$_4$][Cu^{2+}@**B**$_4$]. Different Cu^{2+}-Cu^{2+} distances are highlighted. (**b**) Structural model of the heterodimer derived from MD simulation. (**c** and **d**) Dipolar frequency spectra of samples of mixed G-quadruplex dimers after stated incubation time and temperature. (**e**) Time-dependent dipolar spectra of mixed G-quadruplex dimers. For sample compositions see caption of Figure 3.12.

In first experiments, equimolar solutions of homodimers [Cu^{2+}@**A**$_4$]$_2$ (6 G-tetrads) and [Cu^{2+}@**B**$_4$]$_2$ (8 G-tetrads) were prepared and mixed. After incubation for 1 h at 4 °C, only two peaks were detected in the dipolar spectrum corresponding to the homodimers, indicating that no shuffling of the monomers had occurred under these conditions. After 28 h, at elevated temperature (12 °C), a third peak was detected corresponding to a distance value lying exactly between the values of the two homodimers ($d_{AB} = \frac{1}{2} (d_A + d_B) = 2.88$ nm). The distance was assigned to the heterodimer [Cu^{2+}@$\mathbf{A}_4$][Cu^{2+}@$\mathbf{B}_4$] (7 G-tetrads), confirmed by an MD simulation that yielded a very similar value (Figure 3.26a-d). A ratio of the peak intensities of roughly 1:2:1 in the frequency spectrum indicated that the statistical equilibrium was reached. This equilibrium represented a complex mixture of three different species featuring very similar structural properties, for which structure elucidation is challenging (e.g. by NMR spectroscopy). On the other hand, spin-labeled homo- and heterodimers showed different Cu^{2+}-Cu^{2+} distances. Hence, DEER measurements served as an easy readout to simultaneously detect the different species.

To gain further information, aliquots of a solution containing equimolar amounts of the homodimers were taken at different points in time to perform DEER measurements. Resulting dipolar frequency spectra displayed the time-dependent formation of the heterodimer (Figure 3.26e). Detailed evaluation of these time-dependent data might allow to investigate the rate of the monomer shuffling and heterodimer formation and to determine kinetic parameters like the order of the reaction and its rate constant. In addition, investigation of the reaction at different temperatures might enable to estimate the activation energy of the process. However, these detailed kinetic studies were not part of this thesis and will be examined in future work.

In contrast to the tail-to-tail stacked dimers, which undergo monomer shuffling as shown, this phenomenon was not observed for head-to-head stacked dimers. The result emphasized the difference between 3’-3’ and 5’-5’ stacking of terminal G-quartets.[115]

3.3 Distance Measurements in Duplex-Bridged G-Quadruplex Structures by PDEPR Spectroscopy

3.3.1 Design and Standard Characterization of Duplex-Bridged Unimolecular G-Quadruplexes

In addition to their incorporation into tetramolecular G-quadruplexes, Cu(pyridine)$_4$ (and Cu(imidazole)$_4$) quartets have previously also been integrated into unimolecular G-quadruplexes and used for metal-triggered topology switches[95] or as Lewis-acidic centers in asymmetric catalysis[116,117] (Section 1.4). One goal of this work was to establish the Cu(pyridine)$_4$ quartet as a spin label for distance measurements also in DNA structures containing unimolecular G-quadruplexes.

Table 3.5: Sequences of pyridine-modified oligonucleotides that form unimolecular G-quadruplexes (**L^1** signifies the pyridine-based ligandoside modification).

Name	Sequence (5' → 3')[a]
htel22-**L**$_4$b[b]	A GG**L^1** TTA **L^1**GG TTA GG**L^1** TTA **L^1**GG
Oligo **G**	A GG**L^1** TTA **L^1**GG TTA GG**L^1** TTA **L^1**GG ATA CAG CTT AT
Oligo **H**	A GG**L^1** TTA **L^1**GG TTA GG**L^1** TTA **L^1**GG AAT AAG CTG TA

[a] Colors indicate different segments of the oligonucleotides: G-quadruplex-forming section (22 nt, green), spacer (1 nt, black), complementary single-stranded overhangs (10 nt, red and blue). [b] The sequence has previously been used in the Clever Lab[95] and is shown for comparison.

The designed system for the poof-of-principle was based on the previously used antiparallel G-quadruplex, htel22-**L**$_4$b, which is based on the htel sequence and forms a Cu(pyridine)$_4$ tetrad.[95] Two oligonucleotides (oligos **G** and **H**, 33 nt each) were synthesized by solid-phase DNA synthesis, each containing the G-quadruplex sequence (22 nt), including four pyridine ligandoside modifications (**L^1**, Figure 3.8). Additional complementary single-stranded overhangs (10 nt) were attached to the 3'-ends separated by a spacer containing one nucleotide. The design allowed linking two spin-labeled unimolecular G-quadruplexes by a duplex bridge ([2Cu^{2+}@**GH**], Figure 3.27 and Table 3.5). This DNA species contains two G-quadruplex-duplex interfaces. It might serve as a future model system to investigate the binding of G-quadruplex-binding ligands, as the G-quadruplex-duplex interface is discussed as an interesting binding target for potential drug-like DNA binders.[118–122]

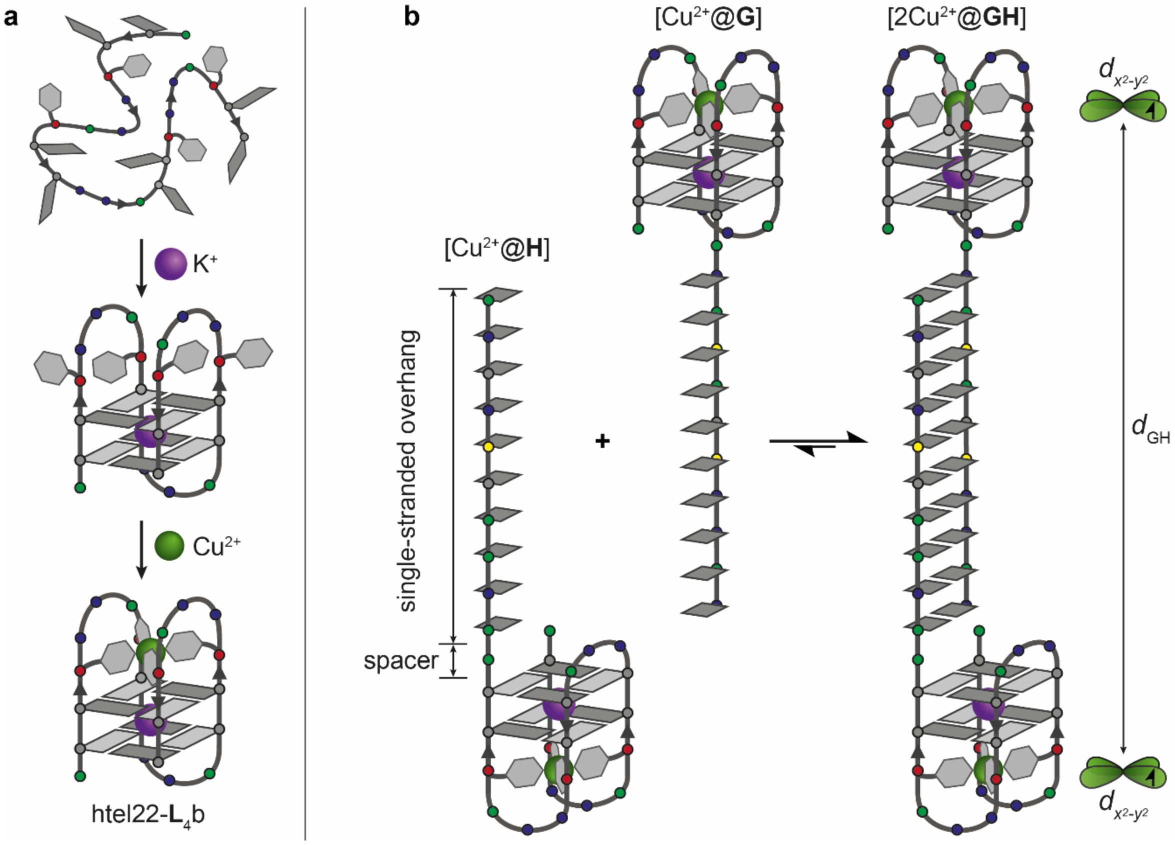

Figure 3.27: (**a**) Self-assembly of pyridine-modified unimolecular G-quadruplex htel22-$\mathbf{L}_4$b and its Cu^{2+} binding.[95] (**b**) G-quadruplexes [Cu^{2+}@**G**] and [Cu^{2+}@**H**] with marked spacer unit and single-stranded 3'-overhang, and formation of the aggregate [$2Cu^{2+}$@**GH**] with duplex-bridged G-quadruplexes. The distance d_{GH} between the magnetic $d_{x2\text{-}y2}$ orbitals of the Cu^{2+} ions containing the unpaired electrons is indicated.

Successful oligonucleotide synthesis and purification were verified by analytical reverse-phase HPLC and ESI mass spectrometry. Analytical data are exemplarily shown for oligo **G** in Figure 3.28. Samples containing equimolar amounts of oligos **G** and **H** with a high K^+ concentration at pH 7.2 were investigated after annealing with UV spectroscopy both in the absence and presence of Cu^{2+} ions (1 equiv. per oligonucleotide). Thermal denaturation and annealing profiles recorded both at 260 nm and 295 nm showed fast reversible melting processes typical for duplex DNA and unimolecular G-quadruplexes, respectively (Section 6.3).

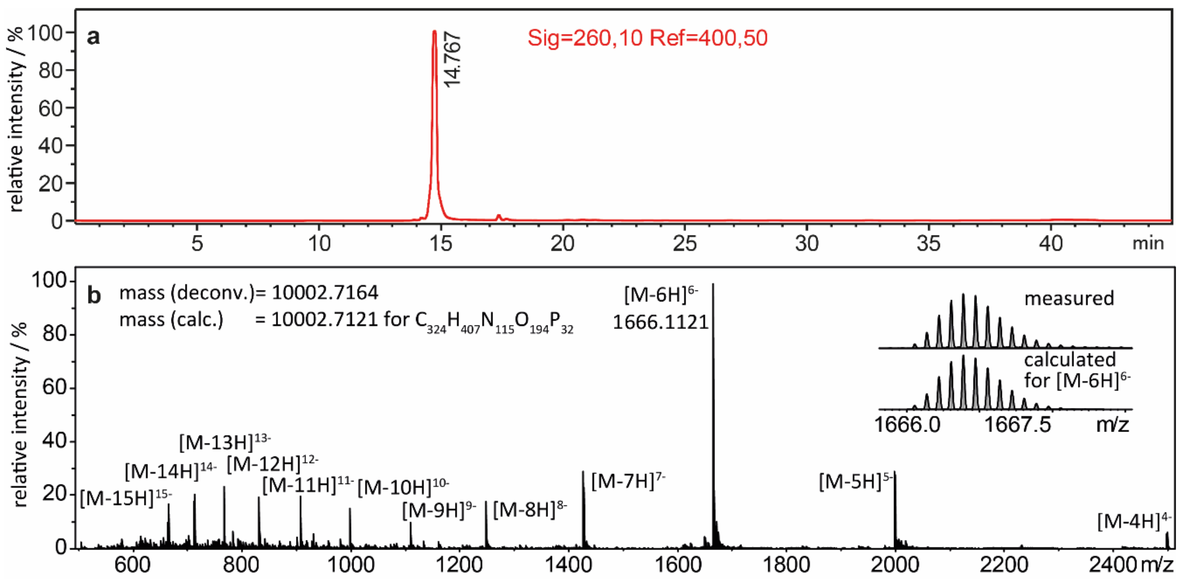

Figure 3.28: (**a**) Analytical reverse-phase HPLC trace and (**b**) ESI mass spectrum of oligo **G** after DNA synthesis and purification.

The melting curve plotted at 260 nm displayed the denaturation of the double-stranded segment. As expected, its determined melting temperature of T_m = 32 °C was not affected by the presence of Cu^{2+} ions (T_m (+Cu^{2+}) = 33 °C, ΔT_m = +1 °C, Figure 3.29a). On the other hand, the melting curve recorded at 295 nm exposed the independent denaturation of the unimolecular G-quadruplexes. The melting temperature of T_m = 10 °C was strongly affected by the presence of Cu^{2+} ions (T_m (+Cu^{2+}) = 24 °C, ΔT_m = +14 °C, Figure 3.29b). The significant increase of the thermal denaturation temperature proved the formation of $Cu(pyridine)_4$ quartets. It was previously shown that the complex formation raises the overall stability of the folded G-quadruplex.[95,97] The measurements were repeated in the absence of K^+ ions. Unsurprisingly, the thermal stability of the duplex segment was not affected (T_m (–K^+) = 31 °C, ΔT_m = –1 °C). In contrast, no G-quadruplex melting was observed at 295 nm since monovalent cations were required for the formation of this secondary structure type. The results were supported by thermal difference spectra (Figure 3.29c).

In the absence of oligo **H**, oligo **G** revealed similar G-quadruplex melting temperatures (T_m = 12 °C, T_m (+Cu^{2+}) = 25 °C, ΔT_m = +13 °C) as found in the duplex-bridged aggregate (Section 6.3). The melting temperature in the absence of Cu^{2+} ions was similar compared to the one found for G-quadruplex htel22-**L**$_4$b (T_m = 12.5 °C), which lacks the single-stranded overhang at the 3'-end.[95]

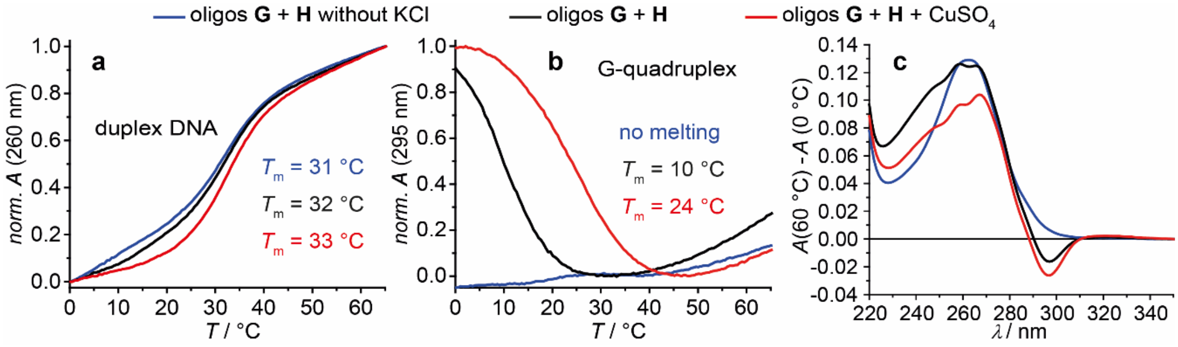

Figure 3.29: UV-based thermal denaturation curves recorded at (**a**) 260 nm and (**b**) 295 nm and (**c**) thermal difference spectra of samples containing oligos **G** and **H** in the absence or presence of KCl and $CuSO_4$. Sample composition: 1.5 µM oligo **G**, 1.5 µM oligo **H**, 3 µM $CuSO_4$ (if present), 100 mM KCl (stated, if not present), 1 mM $MgCl_2$, 10 mM lithium cacodylate buffer (pH 7.2).

Table 3.6: Overview of thermal denaturation temperatures and thermal stabilizations upon Cu^{2+} addition for G-quadruplexes with single-stranded overhangs and resulting duplex-bridged G-quadruplexes.[a]

	Melting curve at 295 nm[b]			Melting curve at 260 nm[c]		
DNA species	T_m / °C	T_m / °C (+ Cu^{2+})	ΔT_m / °C	T_m / °C	T_m / °C (+ Cu^{2+})	ΔT_m / °C
htel22-$\mathbf{L}_4$b[d]	12.5	35.5	+23	-	-	-
GH	10	24	+14	32	33	+1
G	12	25	+13	-	-	-
H[e]	24	30	+6	26	24	–2

[a] Sample composition: 1.5 µM oligo **G** and/or 1.5 µM oligo **H**, 1.0 equiv. of $CuSO_4$ per oligonucleotide (if present), 100 mM KCl, 1 mM $MgCl_2$, 10 mM lithium cacodylate buffer (pH 7.2). [b] Melting of G-quadruplex species is detected. [c] Melting of duplex fragment is detected. [d] Data were taken from literature for comparison.[95] Sample composition is slightly different. [e] Unexpected melting behaviour detected at 295 nm and 260 nm suggested formation of hairpin loops, self-dimers, or other secondary structures.

Interestingly, the Cu^{2+}-induced thermal stabilization was significantly lower ($\Delta\Delta T_m$ = –10 °C), indicating that the 3'-overhang lowers the stabilizing effect of the $Cu(pyridine)_4$ complex formation. As expected, no melting was recorded at 260 nm, since no complementary single strands were present in the sample able to form duplex DNA. In contrast to these results, in the absence of oligo **G**, oligo **H** exhibited a melting behavior recorded at 260 nm and unexpected denaturation temperatures at 295 nm (Table 3.6). These findings suggested other secondary structure types (e.g. hairpin loops, self-dimerization) being formed by oligo **H** in the absence of oligo **G**. Since only the duplex-bridged DNA aggregate [$2Cu^{2+}$@**GH**] was of interest in this work, the nature of these other secondary structures was not examined.

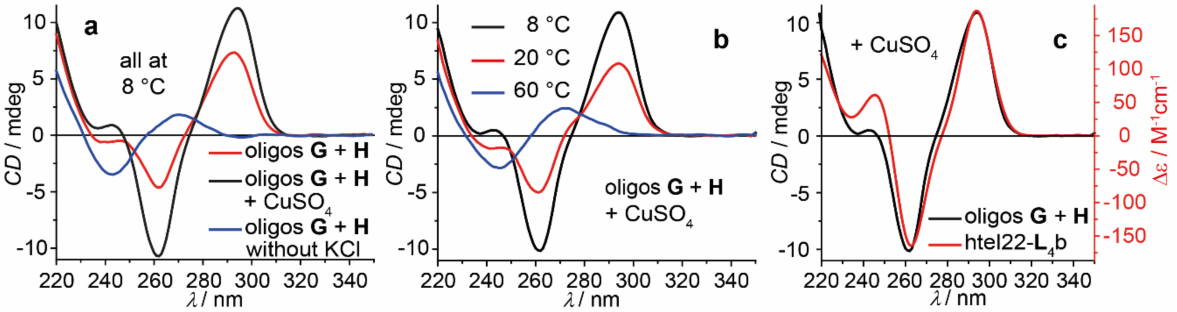

Figure 3.30: (**a**) CD spectra of a mixture of oligos **G** and **H** in the absence and presence of KCl and $CuSO_4$ at 8 °C. (**b**) Temperature-dependent CD spectra of oligos **G** and **H** in the presence of KCl and $CuSO_4$. (**c**) Comparison of CD spectra in the presence of $CuSO_4$ of duplex-bridged G-quadruplexes formed from oligos **G** and **H** and the reported G-quadruplex htel22-**L**$_4$b[95] that lacks a single-stranded 3'-overhang. For sample compositions see caption of Figure 3.29.

To obtain further structural information about the designed DNA aggregate composed of oligos **G** and **H**, CD spectroscopy was performed. Both in the absence and presence of $CuSO_4$, the CD spectra showed a typical pattern for antiparallel G-quadruplexes (Figure 3.30a). The signal intensities were lower in the absence of $CuSO_4$, since part of the G-quadruplexes was already denatured at the given measurement temperature of 8 °C (the spectrometer set up did not allow measurements at lower temperatures). In the absence of KCl, the duplex bridge could still form, but the G-quadruplex sequence segments remained single-stranded, resulting in a CD spectrum with a positive Cotton effect of low intensity with a minimum at ~245 nm and a maximum at ~270 nm. Heating the sample to 60 °C also revealed a positive Cotton effect of low intensity with a minimum at ~245 nm and a maximum at ~270 nm with minimal differences in intensity and very small shifts in minima and maxima, corresponding to the fully denatured single-stranded sample (Figure 3.30b and Section 6.8). As expected, a comparison of the CD spectra of the duplex-bridged G-quadruplexes and previously reported htel22-**L**$_4$b revealed that the spectrum of the newly designed

DNA aggregate can be interpreted as a sum of the spectrum of an antiparallel G-quadruplex structure (like htel22-**L**$_4$b) and a double-stranded DNA segment with a minimum at ~245 nm and a maximum at ~270 nm (Figure 3.30c).

Additional evidence for the duplex formation of the complementary overhangs of oligos **G** and **H** was obtained from native polyacrylamide gel electrophoresis (PAGE, Figure 3.31). With this method, DNA adducts can be separated by their size. The band of a sample containing a mixture of oligo **G** and oligo **H** migrated less far than bands of samples containing only oligo **G** or only oligo **H**. The observation confirmed the formation of an adduct containing both oligos. The absence or presence of Cu^{2+} ions did not affect the mobility of the different species. Either the change in size of the DNA species upon Cu^{2+} binding is too small to be resolved with PAGE or the Cu^{2+} ion was wrested out of the DNA adduct by the applied electric field, since the positive charged ion is pulled in opposite direction compared to the negatively charged DNA aggregate, as speculated earlier.[97]

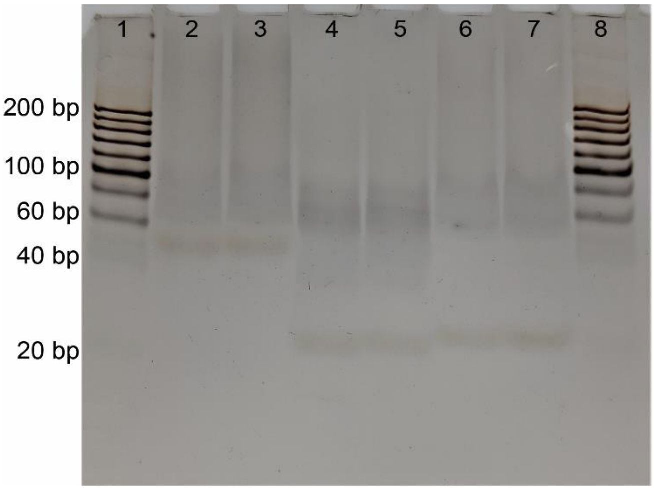

1	DNA ladder (200-20 bp)
2	Oligos **G** + **H** + 1 equiv. $CuSO_4$ per oligo
3	Oligos **G** + **H**
4	Oligos **H** + 1 equiv. $CuSO_4$ per oligo
5	Oligos **H**
6	Oligos **G** + 1 equiv. $CuSO_4$ per oligo
7	Oligos **G**
8	DNA ladder (200-20 bp)

Figure 3.31: Nondenaturing polyacrylamide gel electrophoresis of DNA adducts containing oligos **G** and/or **H** in the absence or presence of $CuSO_4$.

In native ESI mass spectrometry, the adduct formed by oligos **G** and **H** could not be detected, since the highly negatively charged oligonucleotides got separated in the gas phase, which is often observed for double-stranded DNA.[123] However, further indication for G-quadruplex stabilization upon specific Cu^{2+} binding was obtained (Figure 3.32 and Section 6.11). For species that did not contain a Cu^{2+} cation, a statistical distribution of signals corresponding to K^+ adducts of oligo **G** or **H** with roughly equal intensity were observed ([**G**–(5+n)H+nK]$^{5-}$ or [**H**–(5+n)H+nK]$^{5-}$, n = 0,1,2,3,4,…). In contrast, for species containing a Cu^{2+} cation ([**G**–(7+n)H+Cu+nK]$^{5-}$ or [**H**–(7+n)H+Cu+nK]$^{5-}$, n = 0,1,2,3,4,…), the adduct without any K^{+} ion (n = 0) is strongly disfavored. Whenever a Cu^{2+} ion was bound, at least one K^{+} ion was bound as well. One K^{+} ion is required for G-quadruplex formation and a folded G-quadruplex causes the preformation of the ligand environment suited for specific Cu^{2+} ion binding. Therefore, the results indirectly indicated the G-quadruplex formation in the gas phase, the specific binding of a Cu^{2+} ion as a Cu(pyridine)$_4$ tetrad, and its stabilizing effect on the G-quadruplex structure.

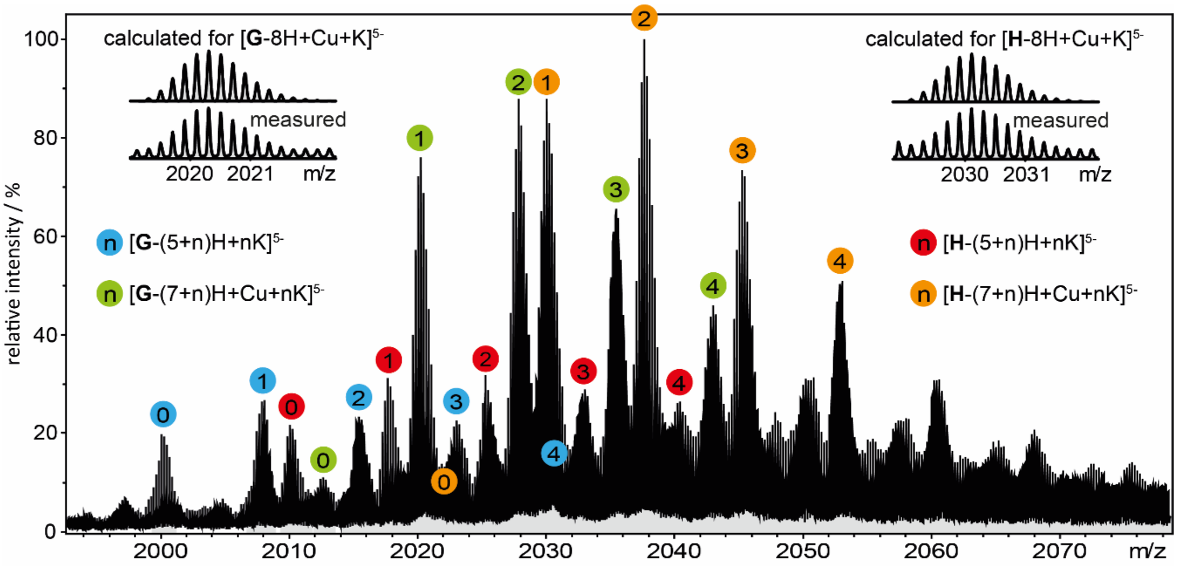

Figure 3.32: Native ESI mass spectrum of a mixture of oligos **G** and **H**. Different K^{+} adducts with or without Cu^{2+} ions are labeled. Measured and calculated isotopic patterns are shown for [**G**–8H+Cu+K]$^{5-}$ and [**H**–8H+Cu+K]$^{5-}$ in the top corners. Sample composition: 12.5 µM oligo **G**, 12.5 µM oligo **H**, 25 µM CuSO$_4$, 500 µM KCl, 50 mM trimethylammonium acetate buffer (pH 7.0) in a 1:1 (v/v) mixture of water and acetonitrile.

The combination of UV-based melting experiments, CD spectroscopy, gel electrophoresis, and ESI mass spectrometry confirmed that oligos **G** and **H** formed unimolecular antiparallel G-quadruplexes containing a Cu(pyridine)$_4$ quartet, as shown earlier for htel22-**L**$_4$b.[95] The attached complementary single-stranded overhangs at the 3'-end form a duplex and connect the two spin-labeled G-quadruplexes ([2Cu^{2+}@**GH**]). Consequently, the DNA construct was suitable for PDEPR-based Cu^{2+}-Cu^{2+} distance measurements.

3.3.2 Cu^{2+}-Cu^{2+} Distance Measurements in Duplex-Bridged G-Quadruplexes

Considering consecutive π-stacking of the base pairs in the double-stranded fragment, the nucleobase in the spacer, and the G-quartets with typical π-stacking distances of 0.35 nm, the expected Cu^{2+}-Cu^{2+} distance was around 6.0 nm. DEER measurements were conducted with samples containing the [$2Cu^{2+}$@**GH**] adduct in deuterated solvents to ensure highest signal intensity. A single peak in the distance distribution was obtained with a mean Cu^{2+}-Cu^{2+} distance of d_{GH} = 6.3 nm (σ = 0.2 nm, Figure 3.33). The much broader width of the peak was expected since the DNA adduct was much more flexible compared to the π-stacked G-quadruplex dimers investigated earlier (Section 3.2.2). Although the short duplex fragment might be quite stiff, the connection between the double-stranded part and the G-quadruplexes contained several consecutive single bonds. This feature allowed rotation or tilting of the G-quadruplexes with respect to the duplex, leading to a broader Cu^{2+}-Cu^{2+} distance distribution.

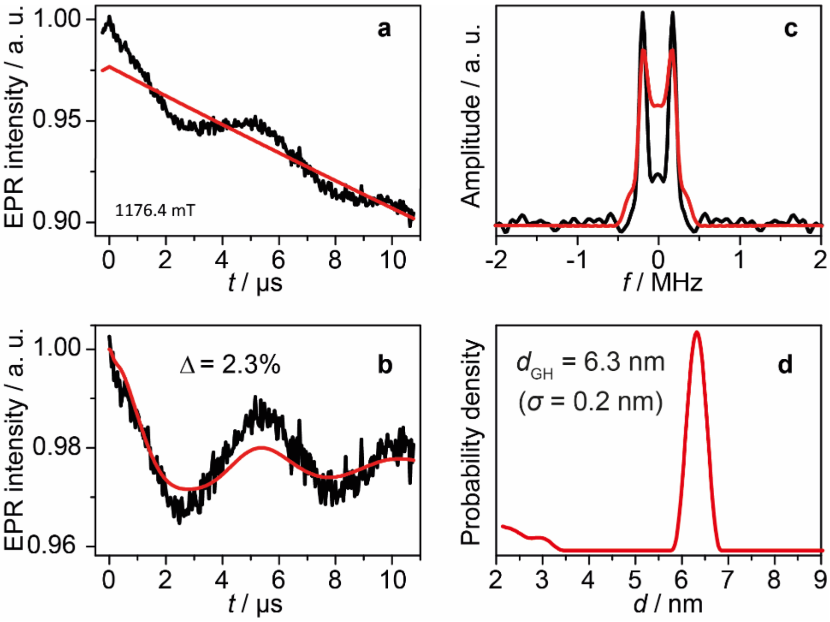

Figure 3.33: DEER-based Cu^{2+}-Cu^{2+} distance measurement between duplex-bridged G-quadruplexes [$2Cu^{2+}$@**GH**]. (**a**) Primary DEER trace (black) overlaid with the background fit (red). (**b**) Background-corrected DEER time trace (black) overlaid with the best fit result from DeerAnalysis (red). The modulation depth parameter Δ is shown. (**c**) Dipolar spectrum (black) overlaid with a Pake pattern simulated by DeerAnalysis (red). (**d**) Obtained distance distribution. Sample composition: 125 µM oligo **G**, 125 µM oligo **H**, (125 µM duplex, 250 µM G-quadruplexes), 375 µM $CuSO_4$ (1.5 equiv. per G-quadruplex), 2.5 mM $MgCl_2$, 25 mM potassium phosphate buffer (pH 7.0) in a 1:1 (v/v) mixture of D_2O and glycerol-d_8.

3.3.3 MD Simulations of Duplex-Bridged G-Quadruplexes

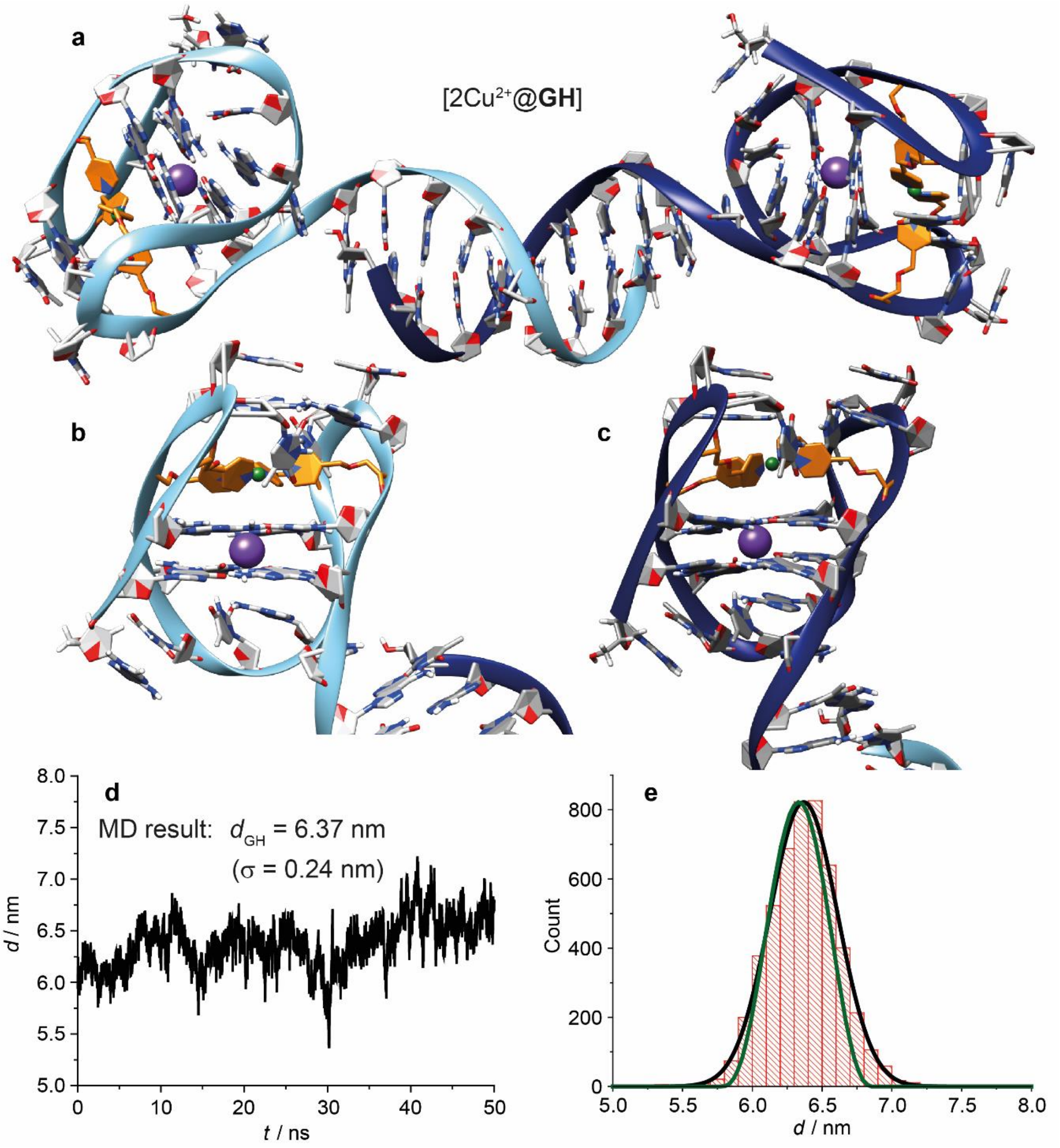

Figure 3.34: (**a**) Structural model derived from MD simulations of duplex-bridged spin-labeled G-quadruplexes [2Cu^{2+}@**GH**]. Oligos **G** and **H** are highlighted with dark and light blue ribbons, respectively. (**b** and **c**) Centered antiparallel unimolecular G-quadruplexes with clearly visible G-quartets and Cu(pyridine)$_4$ tetrads. The rotation and tilting of the G-quadruplexes with respect to the duplex segment is apparent. (**d**) Cu^{2+}-Cu^{2+} distance in the simulated [2Cu^{2+}@**GH**] adduct throughout the 50 ns MD run. Resulting mean distance and standard deviation are stated. (**e**) Histogram depiction of the simulated Cu^{2+}-Cu^{2+} distance (red, 0.1 nm bins) and calculated Gaussian distance distribution (black). The DEER-derived distance distribution is shown for comparison (green).

To relate the experimentally determined distance to structural a model, a molecular dynamics (MD) simulation was performed for the duplex-bridged G-quadruplex adduct. A starting structure was created assuming a continuous π-stacking array between the two Cu(pyridine)$_4$ quartets composed of G-tetrads, the nucleobase of the spacer nucleotide, and the base pairs of a straight duplex segment. A 50 ns MD run in explicit TIP3P water with 100 mM KCl concentration at room temperature was conducted (for more details see Section 6.15). Both the duplex segment and the G-quadruplex parts were preserved throughout the full simulation time (Figure 3.34).

The extracted mean Cu^{2+}-Cu^{2+} distance matched well the DEER-derived one. Also, the broader distance distribution obtained in the DEER experiment was accurately reproduced. The simulation revealed a stiff double-stranded segment and rigid unimolecular G-quadruplexes. However, the link between the parts was flexible. The G-quadruplexes were able to rotate and to tilt with respect to the bridging duplex, causing different conformations with different Cu^{2+}-Cu^{2+} distances.

3.4 Distance Measurements Between Cu^{2+}-Based and Organic Spin Labels in G-Quadruplexes by PDEPR Spectroscopy

3.4.1 Design, Synthesis and Standard Characterization of a G-Quadruplex Containing Both a Cu(Pyridine)$_4$ and an Organic Spin Label

For EPR-based distance measurements within DNA species or proteins, organic radicals are used as paramagnetic spin labels in most of the cases (Section 3.1). To utilize the introduced Cu(pyridine)$_4$ spin label in the broad application filed, its combination with organic spin labels must therefore be possible. This option would allow distance measurements in higher-order DNA structures or protein-DNA aggregates with differently labeled components, e.g. between a duplex carrying an organic spin label and a G-quadruplex containing the Cu(pyridine)$_4$ quartet. To test this combination, a simple species containing the Cu(pyridine)$_4$ tetrad and an additional organic spin label was designed.

Table 3.7: Synthesized sequences of modified oligonucleotides that form G-quadruplexes (**L**^{1}, **L**^{2}, and TEMPO-**L**^{2} signify the pyridine ligandoside modification, the alkyne modification and the TEMPO spin label attached *via* the linker, respectively).

Name	Sequence (5' → 3')
Oligo **I**	**L**^{2}GG GG
Oligo **J**	GGG **L**^{1}TT **L**^{1}GG GTT GGG **L**^{1}TT **L**^{1}GG G
Oligo **K**	TEMPO-**L**^{2} GGG **L**^{1}TT **L**^{1}GG GTT GGG **L**^{1}TT **L**^{1}GG G
ttel24-**L**$_4$[a]	TT GGG **L**^{1}TT **L**^{1}GG GTT GGG **L**^{1}TT **L**^{1}GG G

[a] The sequence has previously been used in the Clever Lab[95] and is shown for comparison.

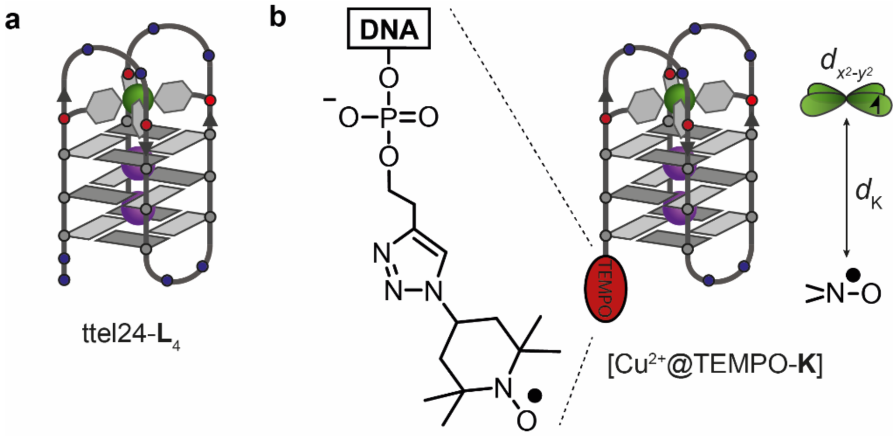

Figure 3.35: (**a**) Schematic structure of modified unimolecular G-quadruplex ttel24-**L**$_4$.[95] (**b**) Designed G-quadruplex species, [Cu^{2+}@TEMPO-**K**], containing the Cu(pyridine)$_4$ quartet at one side of the stack and an organic spin label (TEMPO) covalently attached to the 5'-end on the other side. The distance d_K between the Cu^{2+} cation and the nitroxide group is indicated.

The idea was to utilize a unimolecular G-quadruplex carrying the Cu(pyridine)$_4$ quartet at one side of the stack and to covalently attach an organic spin label to the other end. Here, the nitroxide radical 2,2,6,6-tetramethylpiperidin-1-oxyl (TEMPO) was supposed to be used, as it is frequently found as spin label in the literature.[64,66,74] The G-quadruplex htel22-**L**$_4$b used in the duplex-bridged system (Section 3.3) only contained two G-quartets and was not suited for this study, since the two spin labels must be at least 1.5 nm apart from each other for reasonable DEER measurements. At closer distances, exchange interactions between the spin labels play a larger role in addition to the dipole interactions. Previously, another modified unimolecular G-quadruplex carrying the Cu(pyridine)$_4$ quartet and bearing three G-tetrads has been established in the Clever Lab.[95] Also for this species, an antiparallel topology was revealed in the presence of Cu^{2+} ions. Consequently, the study has been based on this species (Figure 3.35).

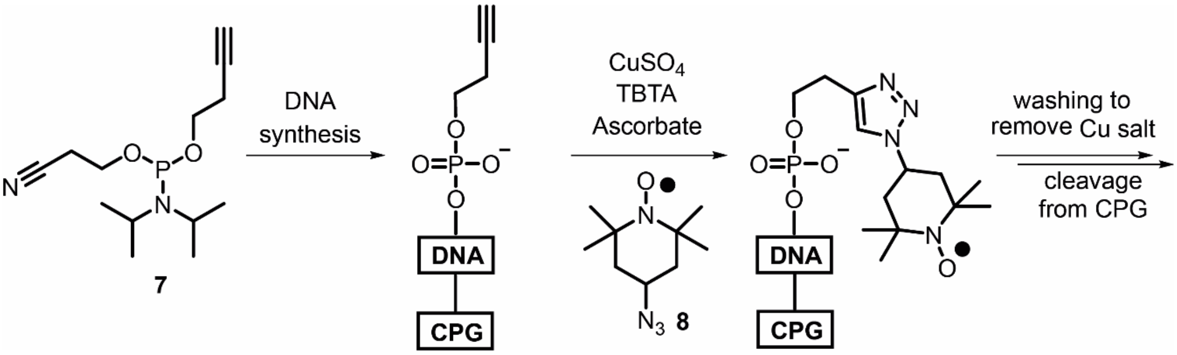

Figure 3.36: Incorporation at the 5'-end during solid-phase DNA synthesis of phosphoramidite **7** carrying the terminal alkyne group. Attachment of the TEMPO spin label was accomplished post-synthetically by Cu$^+$-catalyzed azide-alkyne cycloaddition (CuAAC).[124–126]

To prevent the exposure of the nitroxide radical to oxidizing conditions during DNA synthesis, its incorporation was planned as post-synthetic modification. Therefore, an alkyne residue (**L^2**) was covalently attached to the 5'-end of the oligonucleotides during solid-phase DNA synthesis. The presence of **L^2** then allowed the attachment of a spin label *via* click chemistry.[127,128] For the incorporation of the alkyne group, literature-known phosphoramidite **7** was synthesized.[124] First, attachment at the 5'-end of an oligonucleotide during solid-phase synthesis was tested with a small strand, oligo **I**. An ESI mass spectrum recorded after purification, proved successful incorporation or the alkyne linker (Section 6.1).

Then the TEMPO-containing artificial nucleoside **9** was synthesized and fully characterized (Section 7.4). Its paramagnetic property was indicated by a signal broadening in the ^{1}H NMR spectrum. The broadening vanished upon addition of a reducing agent such as phenylhydrazine (PhNHNH$_2$) which reduced the nitroxide moiety to the diamagnetic hydroxylamine group (Figure 3.37c). UV-VIS spectroscopy revealed an absorption band at 350–550 nm, which is characteristic for the TEMPO moiety and gives rise to the intense orange color of the nucleoside. Addition of phenylhydrazine caused the disappearance of the band due to reduction of the nitroxide group (Figure 3.37a). By slowly evaporating the solvent of a solution containing nucleoside **9** in methanol and diethyl ether, orange single-crystals were obtained and analyzed with XRD. The solid-state structure proved the radical character of the TEMPO moiety connected to the triazole ring (Figure 3.37b).

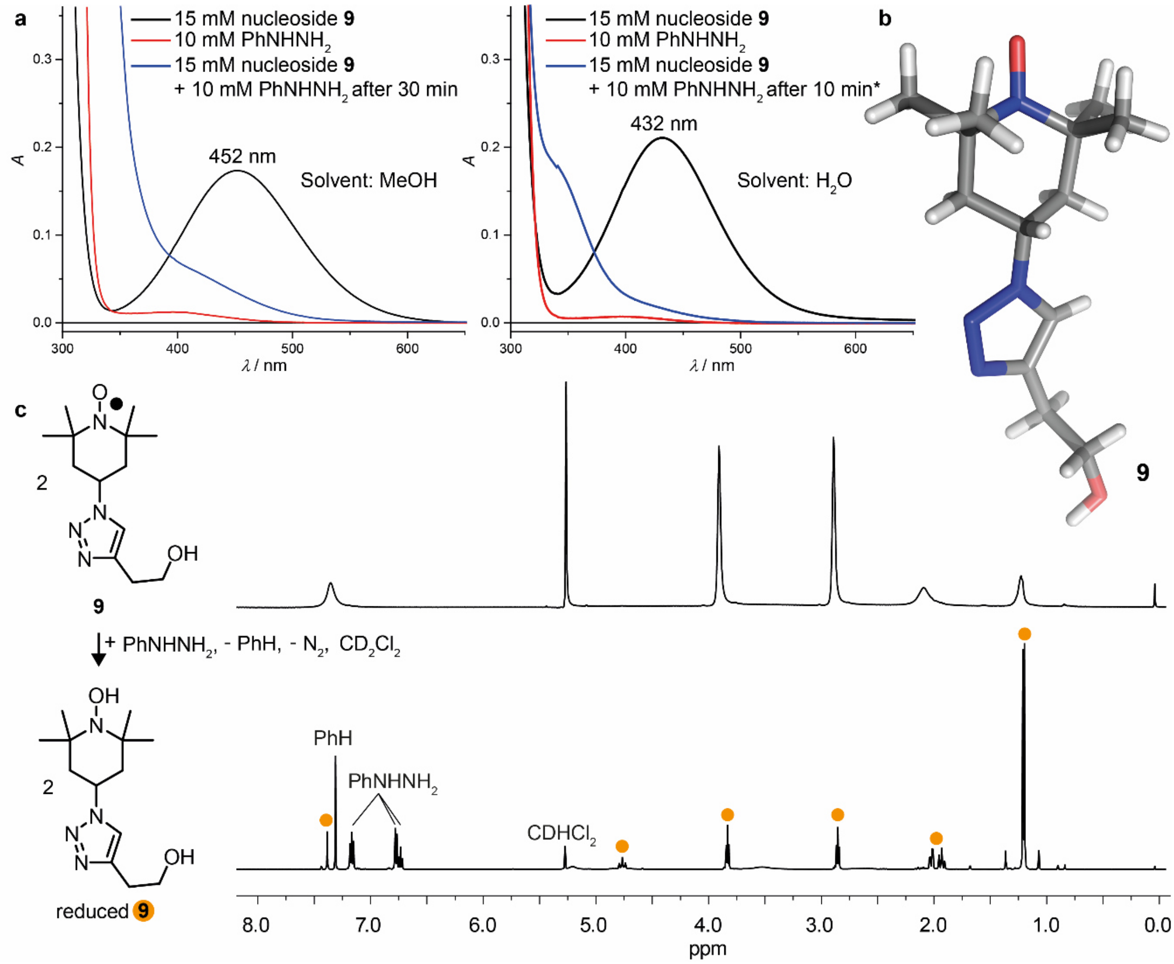

Figure 3.37: (**a**) UV-VIS spectra in methanol (left) and water (right) of nucleoside **9** before and after reduction with $PhNHNH_2$ (*: a formed white precipitate was filtered off). (**b**) Solid-state structure of nucleoside **9** elucidated by XRD. (**c**) ^1H NMR spectrum of nucleoside **9** (in CD_2Cl_2) with signal broadening indicating the paramagnetic property of the molecule. After reduction with phenylhydrazine, sharp signals are visible assigned to the reduced species containing the hydroxylamine group (for full signal assignment see Section 7.4).

Finally, oligo **K** was synthesized containing the alkyne group at the 5'-end. While the oligonucleotide was still bound to the solid support, Cu^+-catalyzed azide-alkyne cycloaddition (CuAAC) with a TEMPO-azide derivative (**8**)[125] allowed attachment of the organic spin label.[124,126] Since spin-labeled oligo **K** was obtained DMT-OFF, the purification method *via* reverse-phase HPLC had to be adapted due to problems with the separation of flawed strands. ESI mass spectrometry proved the attachment of the TEMPO spin label and the integrity of the nitroxide group (Section 6.1).

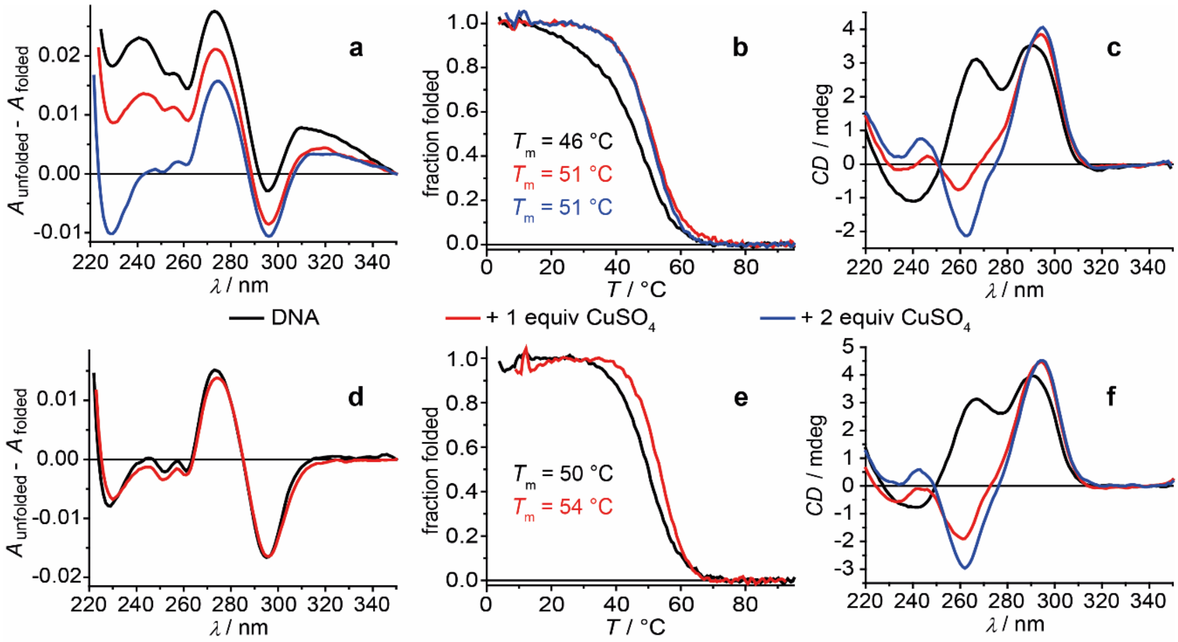

Figure 3.38: (**a**, **d**) UV-based thermal difference spectra, (**b**, **e**) UV-based melting profiles and (**c**, **f**) CD spectra of oligo TEMPO-**K** (**a**–**c**) and oligo **J** (**d**–**f**) in the absence or presence of $CuSO_4$. Sample composition: 1 μM oligonucleotide, 1 or 2 μM $CuSO_4$ (if present), 100 mM KCl, 10 mM lithium cacodylate buffer (pH 7.2).

Samples of TEMPO-**K** with a high K^+ concentration at pH 7.2 showed two pronounced maxima in the CD spectrum at ~265 and ~295 nm indicating a mixture of folded unimolecular G-quadruplexes with different topologies (Figure 3.38c).[7,9] In the presence of Cu^{2+} ions, however, a drastically different pattern in the CD spectrum was observed signifying an antiparallel G-quadruplex topology ([Cu^{2+}@TEMPO-**K**]). Only in this conformation, all four pyridine ligandosides reside on the same side of the G-quadruplex enabling the formation of the $Cu(pyridine)_4$ complex. This metal-induced topology change has been described before in the Clever Lab with the modified strand ttel24-**L**$_4$ (Table 3.7, Figure 3.35a).[95] An antiparallel topology was a requirement for the designated distance measurement between the Cu(pyridine)$_4$ tetrad and the organic spin label as it guarantees both labels to be positioned at opposite sides of the G-quadruplex structure (Figure 3.35b). In addition, thermal difference spectra and UV-based melting profiles including an increase in thermal stabilization in the presence of Cu^{2+} ions supported G-quadruplex as well as Cu(pyridine)$_4$ complex formation. As a control, oligo **J** was synthesized and investigated. The sequence was identical to oligo **K** but lacked the TEMPO nucleoside at the 5'-end. Very similar CD and UV data indicated formation of nearly identical G-quadruplex structures. This result showed that the TEMPO nucleoside (including the triazole ring that could potentially act as a ligand) at the 5'-end neither affected the G-quadruplex folding nor the Cu^{2+} binding.

3.4.2 Distance Measurements Between Cu^{2+}-Based and Organic Spin Labels

G-quadruplex [Cu^{2+}@TEMPO-**K**] containing the Cu(pyridine)$_4$ quartet and the organic spin label at the other side of the structure was further investigated by EPR methods. Figure 3.39a shows a field-swept EPR spectrum. Both the broad Cu^{2+} signal with hyperfine coupling in the parallel region as well as the sharp signal for the nitroxide radical are clearly visible. Preliminary RIDME-based distance measurements were performed at various field positions within the nitroxide EPR line resulting in different distance distributions. The averaged data (Figure 3.39c-f) revealed a broad signal in the distance distribution with a mean distance of $d = 1.73$ nm and a second peak located at $d = 2.40$ nm. The shorter distance lied in the expected range for the distance between the Cu^{2+} complex and the TEMPO spin label residing at opposite sides of the G-quadruplex separated by three G-tetrads. Here, MD simulations still have to be performed to confirm the match between measured distance and expected G4 topology. A broad signal in the distance distribution was expected, since the TEMPO radical was attached to the phosphate backbone *via* a long and flexible linker which allowed to occupy many conformations leading to different distances to the Cu^{2+} ion. It was not further investigated, to which conformation the larger distance could be assigned.

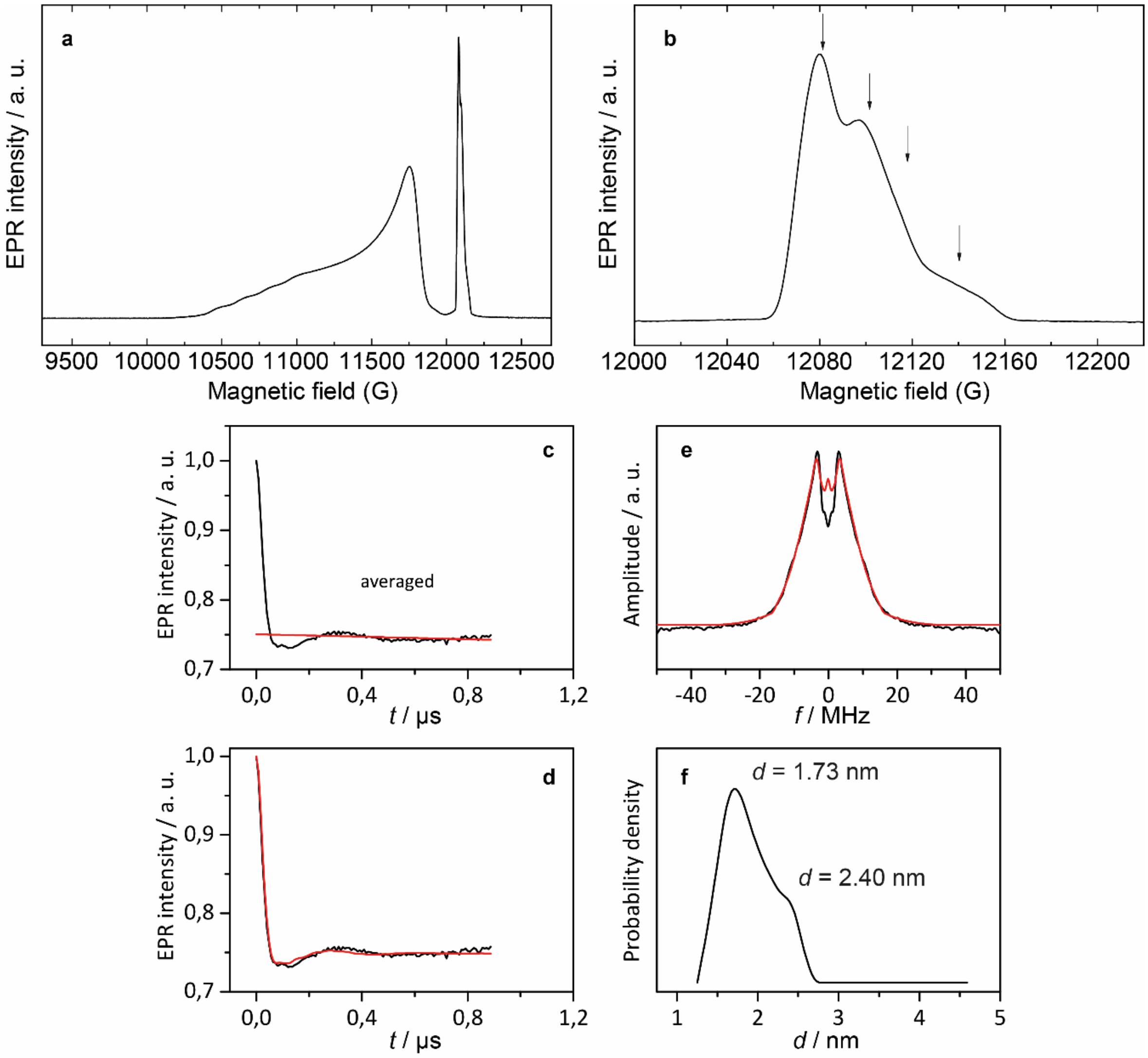

Figure 3.39: Preliminary EPR data for G-quadruplex [Cu^{2+}@TEMPO-**K**]. (**a**, **b**) Field-swept EPR spectrum. (**c**) Average (black) of several primary RIDME traces for different observer positions (indicated in **b**) overlaid with the background fit (red). (**d**) RIDME trace (black) overlaid with best fit (red). (**e**) Resulting dipolar spectrum (black) overlaid with a simulated Pake pattern (red). (**f**) Distance distribution. Sample composition: 150 µM G-quadruplex, 225 µM $CuSO_4$ (1.5 equiv. per G-quadruplex) 50 mM KCl, 5 mM lithium cacodylate buffer (pH 7.2) in a 1:1 (v/v) mixture of water and glycerol.

Due to the consequential low resolution of the distance measurement, the gain in structural information was quite low for this designed G-quadruplex species. Nevertheless, the possibility to measure distances between the Cu^{2+}-based spin label specially designed for G-quadruplexes and an organic spin label commonly used for SDSL of proteins or nucleic acids could successfully be showcased.

3.5 Summary

In this chapter, artificial square-planar Cu(pyridine)$_4$ quartets were incorporated into higher-order DNA G-quadruplex structures and their intrinsic paramagnetic property was exploited for structure elucidation by pulsed dipolar EPR spectroscopy. The spin labels were installed in parallel tetramolecular G-quadruplexes and the formation of π-stacked G-quadruplex dimers was revealed by intermolecular Cu^{2+}-Cu^{2+} distance measurements. Dimers of different spatial dimensions, formed in tail-to-tail or head-to-head stacking mode, were unambiguously distinguished, and obtained distances were in full agreement with MD simulation results.

The covalent attachment of the four pyridine ligands to the four-stranded DNA species resulted in Cu(pyridine)$_4$ complexes tightly fixated in a defined spatial orientation. This rigid arrangement led to unprecedentedly narrow distance distributions, about 5 to 10 times narrower than those obtained for DNA and RNA structures labeled either with nitroxide- or other, less structurally confined Cu^{2+}-based spin labels. In the rigid Cu(pyridine)$_4$ spin label, also the magnetic orbital of the square-planar coordinated Cu^{2+} cation was fixed in a defined spatial orientation causing a deviation of dipolar spectra from a Pake pattern. Therefore, further structural information could be obtained, and a detailed analysis revealed that the z-axes of the two Cu^{2+} spin labels within a dimeric G-quadruplex structure were aligned collinearly. These spatial orientations perfectly fit to the expected dimeric structure with two rigid coplanar Cu(pyridine)$_4$ tetrads and a tight π-stacking interface between the two monomers.

Furthermore, the intercalation of drug-like G-quadruplex-binding ligands, such as PIPER, telomestatin and untethered G-tetrads, into tail-to-tail oriented G-quadruplex dimers resulted in 2:1 sandwich complexes and was detected by an increase of the measured Cu^{2+}-Cu^{2+} distances. Previously unknown binding modes were discovered with the approach. The time-dependent monomer shuffling after mixing of homodimers with different lengths was monitored resulting in the formation of the corresponding heterodimer. This example represented a complex mixture of three different species featuring very similar structural properties, for which structure elucidation is usually challenging (e.g. by NMR spectroscopy). On the other hand, spin-labeled homo- and heterodimers showed different Cu^{2+}-Cu^{2+} distances. Hence, DEER measurements served as an easy readout to detect the different species.

In a different model system, $Cu(pyridine)_4$ spin labels were installed in two unimolecular G-quadruplexes, which were bridged by a duplex fragment. The higher order DNA structure was confirmed with UV and CD spectroscopy, native ESI mass spectrometry and nondenaturing gel electrophoresis. PDEPR spectroscopy yielded the expected Cu^{2+}-Cu^{2+} distance in agreement with an MD simulation result. Since spin labels for structure elucidation in biomolecules are often based on organic radicals, both the $Cu(pyridine)_4$ spin label and an organic TEMPO label was incorporated into a G-quadruplex structure and the distance between the two different spin labels was measured.

The studies described in this chapter showcased the $Cu(pyridine)_4$ tetrad as an extremely rigid spin label designed for G-quadruplex structures with versatile range of possible applications. In future research, the spin label will be exploited for structure elucidation of higher-order DNA structures and protein-DNA adducts with biological or nanotechnological relevance. Examples include the interactions between G-quadruplexes and drug-like binders or the higher-order architecture of telomeric regions.

3.6 References

[1] L. M. Stratmann, Y. Kutin, M. Kasanmascheff, G. H. Clever, *Angew. Chem. Int. Ed.* **2021**, *60*, 4939–4947.

[2] J. D. Watson, F. H. C. Crick, *Nature* **1953**, *171*, 737–738.

[3] J. D. Watson, F. H. C. Crick, *Nature* **1953**, *171*, 964–967.

[4] A. Micsonai, F. Wien, L. Kernya, Y.-H. Lee, Y. Goto, M. Réfrégiers, J. Kardos, *Proc. Natl. Acad. Sci. U. S. A.* **2015**, *112*, E3095–E3103.

[5] N. J. Greenfield, *Nat. Protoc.* **2006**, *1*, 2876–2890.

[6] J. Kypr, I. Kejnovská, D. Renciuk, M. Vorlícková, *Nucleic Acids Res.* **2009**, *37*, 1713–1725.

[7] M. Vorlíčková, I. Kejnovská, J. Sagi, D. Renčiuk, K. Bednářová, J. Motlová, J. Kypr, *Methods* **2012**, *57*, 64–75.

[8] M. Vorlíčková, I. Kejnovská, K. Bednářová, D. Renčiuk, J. Kypr, *Chirality* **2012**, *24*, 691–698.

[9] R. del Villar-Guerra, J. O. Trent, J. B. Chaires, *Angew. Chem. Int. Ed.* **2018**, *57*, 7171–7175.

[10] D. M. Gray, J.-D. Wen, C. W. Gray, R. Repges, C. Repges, G. Raabe, J. Fleischhauer, *Chirality* **2008**, *20*, 431–440.

[11] A. Randazzo, G. P. Spada, M. W. da Silva, *Top. Curr. Chem.* **2012**, *330*, 67–86.

[12] J. C. Kendrew, G. Bodo, H. M. Dintzis, R. G. Parrish, H. Wyckoff, D. C. Phillips, *Nature* **1958**, *181*, 662–666.

[13] M. F. Perutz, M. G. Rossmann, A. F. Cullis, H. Muirhead, G. Will, A. C. T. North, *Nature* **1960**, *185*, 416–422.

[14] S. Raunser, *Angew. Chem. Int. Ed.* **2017**, *56*, 16450–16452.

[15] H. M. Berman, J. Westbrook, Z. Feng, G. Gilliland, T. N. Bhat, H. Weissig, I. N. Shindyalov, P. E. Bourne, *Nucleic Acids Res.* **2000**, *28*, 235–242.

[16] According to Protein Data Bank, Link: https://www.rcsb.org/

[17] Y. Yan, G. Marriott, *Curr. Opin. Chem. Biol.* **2003**, *7*, 635–640.

[18] B. Hellenkamp, S. Schmid, O. Doroshenko, O. Opanasyuk, R. Kühnemuth, S. R. Adariani, B. Ambrose, M. Aznauryan, A. Barth, V. Birkedal, M. E. Bowen, H. Chen, T. Cordes, T. Eilert, C. Fijen, C. Gebhardt, M. Götz, G. Gouridis, E. Gratton, T. Ha, P. Hao, C. A. Hanke, A. Hartmann, J. Hendrix, L. L. Hildebrandt, V. Hirschfeld, J. Hohlbein, B. Hua, C. G. Hübner, E. Kallis, A. N. Kapanidis, J.-Y. Kim, G. Krainer, D. C. Lamb, N. K. Lee, E. A. Lemke, B. Levesque, M. Levitus, J. J. McCann, N. Naredi-Rainer, D. Nettels, T. Ngo, R. Qiu, N. C. Robb, C. Röcker, H. Sanabria, M. Schlierf, T. Schröder, B. Schuler, H. Seidel, L. Streit, J. Thurn, P. Tinnefeld, S. Tyagi, N. Vandenberk, A. M. Vera, K. R. Weninger, B. Wünsch, I. S. Yanez-Orozco, J. Michaelis, C. A. M. Seidel, T. D. Craggs, T. Hugel, *Nat. Methods* **2018**, *15*, 669–676.

[19] S. Tyagi, F. R. Kramer, *Nat. Biotechnol.* **1996**, *14*, 303–308.

[20] E. S. Andersen, M. Dong, M. M. Nielsen, K. Jahn, R. Subramani, W. Mamdouh, M. M. Golas, B. Sander, H. Stark, C. L. P. Oliveira, J. S. Pedersen, V. Birkedal, F. Besenbacher, K. V. Gothelf, J. Kjems, *Nature* **2009**, *459*, 73–76.

[21] G. Jeschke, *Annu. Rev. Phys. Chem.* **2012**, *63*, 419–446.

[22] *Electron Paramagnetic Resonance - A Practitioner's Toolkit* (Eds.: M. Brustolon, E. Giamello), Wiley, **2009**.

[23] *EPR Spectroscopy - Applications in Chemistry and Biology* (Eds.: M. Drescher, G. Jeschke), Springer, **2012**.

[24] J. A. Weil, J. R. Bolton, *Electron Paramagnetic Resonance: Elementary Theory and Practical Applications,* Vol. 2, Wiley, **2006**.

[25] G. Jeschke, *Lecture Notes Physical Chemistry IV*, ETH Zürich, **2006**.

[26] C. Janiak, H.-J. Meyer, D. Gudat, P. Kurz, *Riedel Moderne Anorganische Chemie*, Vol. 5, De Gruyter Studium, **2018**, pp. 441–457.

[27] P. M. Schossler, *Electron Paramagnetic Resonance Study of the Copper(II) Complexation with Carbonate Ligands in Aqueous Solution and at Calcium Carbonate Surfaces*, Doctoral Thesis, ETH Zürich, **1998**.

[28] J. M. Holland, X. Liu, J. P. Zhao, F. E. Mabbs, C. A. Kilner, M. Thornton-Pett, M. A. Halcrow, *J. Chem. Soc., Dalton Trans.* **2000**, 3316–3324.

[29] H. Sameach, S. Ruthstein, *Isr. J. Chem.* **2019**, *59*, 980–989.

[30] O. Schiemann, T. F. Prisner, *Q. Rev. Biophys.* **2007**, *40*, 1–53.

[31] R. Ward, O. Schiemann in *Structural Information from Spin-Labels and Intrinsic Paramagnetic Centres in the Biosciences* (Eds.: C. R. Timmel, J. R. Harmer), Springer, Berlin, **2014**.

[32] D. Abdullin, O. Schiemann, *ChemPlusChem* **2020**, *85*, 353–372.

[33] M. M. Roessler, E. Salvadori, *Chem. Soc. Rev.* **2018**, *47*, 2534–2553.

[34] I. Krstić, R. Hänsel, O. Romainczyk, J. W. Engels, V. Dötsch, T. F. Prisner, *Angew. Chem. Int. Ed.* **2011**, *50*, 5070–5074.

[35] M. Ji, S. Ruthstein, S. Saxena, *Acc. Chem. Res.* **2013**, *47*, 688–695.

[36] P. Roser, M. J. Schmidt, M. Drescher, D. Summerer, *Org. Biomol. Chem.* **2016**, *14*, 5468–5476.

[37] J. P. Klare, H.-J. Steinhoff, *Photosynth. Res.* **2009**, *102*, 377–390.

[38] J. P. Klare, *Biol. Chem.* **2013**, *394*, 1281–1300.

[39] W. L. Hubbell, C. J. López, C. Altenbach, Z. Yang, *Curr. Opin. Struc. Biol.* **2013**, *23*, 725–733.

[40] T. F. Cunningham, M. R. Putterman, A. Desai, W. S. Horne, S. Saxena, *Angew. Chem. Int. Ed.* **2015**, *54*, 6330–6334.

[41] A. G. Jarvi, X. Bogetti, K. Singewald, S. Ghosh, S. Saxena, *Acc. Chem. Res.* **2021**, *54*, 1481–1491.

[42] J. L. Wort, K. Ackermann, A. Giannoulis, A. J. Stewart, D. G. Norman, B. E. Bode, *Angew. Chem. Int. Ed.* **2019**, *58*, 11681–11685.

[43] A. M. Shafer, T. Kálai, S. Q. B. Liu, K. Hideg, J. C. Voss, *Biochemistry* **2004**, *43*, 8470–8482.

[44] M. R. Fleissner, E. M. Brustad, T. Kálai, C. Altenbach, D. Cascio, F. B. Peters, K. Hideg, S. Peuker, P. G. Schultz, W. L. Hubbell, *Proc. Natl. Acad. Sci. U. S. A.* **2009**, *106*, 21637–21642.

[45] M. J. Schmidt, J. Borbas, M. Drescher, D. Summerer, *J. Am. Chem. Soc.* **2014**, *136*, 1238–1241.

[46] M. J. Schmidt, A. Fedoseev, D. Bücker, J. Borbas, C. Peter, M. Drescher, D. Summerer, *ACS Chem. Biol.* **2015**, *10*, 2764–2771.

[47] S. C. T. Nicklisch, D. Wunnicke, I. V. Borovykh, S. Morbach, J. P. Klare, H.-J. Steinhoff, R. Krämer, *Biochim. Biophys. Acta, Biomembr.* **2012**, *1818*, 359–366.

[48] W. K. Myers, X. Xu, C. Li, J. O. Lagerstedt, M. S. Budamagunta, J. C.

Voss, R. D. Britt, J. B. Ames, *Biochemistry* **2013**, *52*, 5800–5808.

[49] M. C. Puljung, H. A. DeBerg, W. N. Zagotta, S. Stoll, *Proc. Natl. Acad. Sci. U. S. A.* **2014**, *111*, 9816–9821.

[50] B. Joseph, A. Sikora, D. S. Cafiso, *J. Am. Chem. Soc.* **2016**, *138*, 1844–1847.

[51] A. Collauto, H. A. DeBerg, R. Kaufmann, W. N. Zagotta, S. Stoll, D. Goldfarb, *Phys. Chem. Chem. Phys.* **2017**, *19*, 15324–15334.

[52] J. E. Banham, C. R. Timmel, R. J. M. Abbott, S. M. Lea, G. Jeschke, *Angew. Chem. Int. Ed.* **2006**, *45*, 1058–1061.

[53] Y. Yang, S.-N. Chen, F. Yang, X.-Y. Li, A. Feintuch, X.-C. Su, D. Goldfarb, *Proc. Natl. Acad. Sci. U. S. A.* **2020**, *117*, 20566–20575.

[54] D. Abdullin, N. Florin, G. Hagelueken, O. Schiemann, *Angew. Chem. Int. Ed.* **2014**, *54*, 1827–1831.

[55] A. G. Jarvi, T. F. Cunningham, S. Saxena, *Phys. Chem. Chem. Phys.* **2019**, *21*, 10238–10243.

[56] O. Schiemann, N. Piton, J. Plackmeyer, B. E. Bode, T. F. Prisner, J. W. Engels, *Nat. Protoc.* **2007**, *2*, 904–923.

[57] O. Schiemann, P. Cekan, D. Margraf, T. F. Prisner, S. Th. Sigurdsson, *Angew. Chem. Int. Ed.* **2009**, *48*, 3292–3295.

[58] A. Marko, V. Denysenkov, D. Margraf, P. Cekan, O. Schiemann, S. T. Sigurdsson, T. F. Prisner, *J. Am. Chem. Soc.* **2011**, *133*, 13375–13379.

[59] K. Halbmair, J. Seikowski, I. Tkach, C. Höbartner, D. Sezer, M. Bennati, *Chem. Sci.* **2016**, *7*, 3172–3180.

[60] N. Erlenbach, C. Grünewald, B. Krstic, A. Heckel, T. F. Prisner, *RNA* **2018**, *25*, 239–246.

[61] M. Heinz, N. Erlenbach, L. S. Stelzl, G. Thierolf, N. R. Kamble, S. T. Sigurdsson, T. F. Prisner, G. Hummer, *Nucleic Acids Res.* **2019**, *48*, 924–933.

[62] J. S. Hardwick, M. M. Haugland, A. H. El-Sagheer, D. Ptchelkine, F. R. Beierlein, A. N. Lane, T. Brown, J. E. Lovett, E. A. Anderson, *Nucleic Acids Res.* **2020**, *48*, 2830–2840.

[63] S. Ghosh, M. J. Lawless, H. J. Brubaker, K. Singewald, M. R. Kurpiewski, L. Jen-Jacobson, S. Saxena, *Nucleic Acids Res.* **2020**, e49.

[64] S. A. Shelke, S. Th. Sigurdsson, *Eur. J. Org. Chem.* **2012**, *2012*, 2291–2301.

[65] O. Schiemann, N. Piton, Y. Mu, G. Stock, J. W. Engels, T. F. Prisner, *J. Am. Chem. Soc.* **2004**, *126*, 5722–5729.

[66] G. Sicoli, F. Wachowius, M. Bennati, C. Höbartner, *Angew. Chem. Int. Ed.* **2010**, *49*, 6443–6447.

[67] E. S. Babaylova, A. V. Ivanov, A. A. Malygin, M. A. Vorobjeva, A. G. Venyaminova, Y. F. Polienko, I. A. Kirilyuk, O. A. Krumkacheva, M. V. Fedin, G. G. Karpova, E. G. Bagryanskaya, *Org. Biomol. Chem.* **2014**, *12*, 3129–3136.

[68] S. Saha, A. P. Jagtap, S. Th. Sigurdsson, *Chem. Commun.* **2015**, *51*, 13142–13145.

[69] N. Erlenbach, B. Endeward, P. Schöps, D. B. Gophane, S. Th. Sigurdsson, T. F. Prisner, *Phys. Chem. Chem. Phys.* **2016**, *18*, 16196–16201.

[70] M. Kerzhner, D. Abdullin, J. Więcek, H. Matsuoka, G. Hagelueken, O. Schiemann, M. Famulok, *Chem. Eur. J.* **2016**, *22*, 12113–12121.

[71] Q. Cai, A. K. Kusnetzow, W. L. Hubbell, I. S. Haworth, G. P. C. Gacho, N. V. Eps, K. Hideg, E. J. Chambers, P. Z. Qin, *Nucleic Acids Res.* **2006**, *34*, 4722–4730.

[72] A. M. Popova, T. Kálai, K. Hideg, P. Z. Qin, *Biochemistry* **2009**, *48*, 8540–8550.

[73] P. Z. Qin, I. S. Haworth, Q. Cai, A. K. Kusnetzow, G. P. G. Grant, E. A. Price, G. Z. Sowa, A. Popova, B. Herreros, H. He, *Nat. Protoc.* **2007**, *2*, 2354–2365.

[74] M. M. Haugland, A. H. El-Sagheer, R. J. Porter, J. Peña, T. Brown, E. A. Anderson, J. E. Lovett, *J. Am. Chem. Soc.* **2016**, *138*, 9069–9072.

[75] N. Barhate, P. Cekan, A. P. Massey, S. Th. Sigurdsson, *Angew. Chem. Int. Ed.* **2007**, *46*, 2655–2658.

[76] P. Cekan, A. L. Smith, N. Barhate, B. H. Robinson, S. Th. Sigurdsson, *Nucleic Acids Res.* **2008**, *36*, 5946–5954.

[77] L. S. Stelzl, N. Erlenbach, M. Heinz, T. F. Prisner, G. Hummer, *J. Am. Chem. Soc.* **2017**, *139*, 11674–11677.

[78] E. Narr, A. Godt, G. Jeschke, *Angew. Chem. Int. Ed.* **2002**, *41*, 3907–3910.

[79] I. M. C. van Amsterdam, M. Ubbink, G. W. Canters, M. Huber, *Angew. Chem. Int. Ed.* **2003**, *42*, 62–64.

[80] J. S. Becker, S. Saxena, *Chem. Phys. Lett.* **2005**, *414*, 248–252.

[81] B. E. Bode, J. Plackmeyer, T. F. Prisner, O. Schiemann, *J. Phys. Chem.* **2008**, *112*, 5064–5073.

[82] A. M. Bowen, M. W. Jones, J. E. Lovett, T. G. Gaule, M. J. McPherson, J. R. Dilworth, C. R. Timmel, J. R. Harmer, *Phys. Chem. Chem. Phys.* **2016**, *18*, 5981–5994.

[83] F. D. Breitgoff, K. Keller, M. Qi, D. Klose, M. Yulikov, A. Godt, G. Jeschke, *J. Magn. Reson.* **2019**, *308*, 106560.

[84] I. Ritsch, H. Hintz, G. Jeschke, A. Godt, M. Yulikov, *Phys. Chem. Chem. Phys.* **2019**, *21*, 9810–9830.

[85] V. Singh, M. Azarkh, T. E. Exner, J. S. Hartig, M. Drescher, *Angew. Chem. Int. Ed.* **2009**, *48*, 9728–9730.

[86] V. Singh, M. Azarkh, M. Drescher, J. S. Hartig, *Chem. Commun.* **2012**, *48*, 8258–8260.

[87] X. Zhang, C.-X. Xu, R. D. Felice, J. Sponer, B. Islam, P. Stadlbauer, Y. Ding, L. Mao, Z.-W. Mao, P. Z. Qin, *Biochemistry* **2016**, *55*, 360–372.

[88] I. T. Holder, M. Drescher, J. S. Hartig, *Bioorg. Med. Chem.* **2013**, *21*, 6156–6161.

[89] M. Azarkh, V. Singh, O. Okle, D. R. Dietrich, J. S. Hartig, M. Drescher, *ChemPhysChem* **2012**, *13*, 1444–1447.

[90] V. M. Marathias, K. Y. Wang, S. Kumar, T. Q. Pham, S. Swaminathan, P. H. Bolton, *J. Mol. Biol.* **1996**, *260*, 378–394.

[91] M. P. Donohue, V. A. Szalai, *Phys. Chem. Chem. Phys.* **2016**, *18*, 15447–15455.

[92] D. M. Engelhard, A. Meyer, A. Berndhäuser, O. Schiemann, G. H. Clever, *Chem. Commun.* **2018**, *54*, 7455–7458.

[93] Y. Wang, D. J. Patel, *Biochemistry* **1992**, *31*, 8112–8119.

[94] Y. Kato, T. Ohyama, H. Mita, Y. Yamamoto, *J. Am. Chem. Soc.* **2005**, *127*, 9980–9981.

[95] D. M. Engelhard, J. Nowack, G. H. Clever, *Angew. Chem. Int. Ed.* **2017**, *56*, 11640–11644.

[96] D. M. Engelhard, L. M. Stratmann, G. H. Clever, *Chem. Eur. J.* **2018**, *24*, 2117–2125.

[97] D. M. Engelhard, R. Pievo, G. H. Clever, *Angew. Chem. Int. Ed.* **2013**, *52*, 12843–12847.

[98] J. Peisach, W. E. Blumberg, *Arch. Biochem. Biophys.* **1974**, *165*, 691–708.

[99] P. Manikandan, B. Epel, D. Goldfarb, *Inorg. Chem.* **2001**, *40*, 781–787.

[100] C. D. Syme, R. C. Nadal, S. E. J. Rigby, J. H. Viles, *J. Biol. Chem.* **2004**, *279*, 18169–18177.

[101] D. Sen, W. Gilbert, *Biochemistry* **1992**, *31*, 65–70.

[102] C. Creze, B. Rinaldi, R. Haser, P. Bouvet, P. Gouet, *Acta Crystallogr., Sect. D: Biol. Crystallogr.* **2007**, *63*, 682–688.

[103] R. G. Larsen, D. J. Singel, *J. Chem. Phys.* **1993**, *98*, 5134–5146.

[104] O. Y. Fedoroff, M. Salazar, H. Han, V. V. Chemeris, S. M. Kerwin, L. H. Hurley, *Biochemistry* **1998**, *37*, 12367–12374.

[105] C. Sissi, L. Lucatello, A. P. Krapcho, D. J. Maloney, M. B. Boxer, M. V. Camarasa, G. Pezzoni, E. Menta, M. Palumbo, *Bioorgan. Med. Chem.* **2007**, *15*, 555–562.

[106] W. Tuntiwechapikul, T. Taka, M. Béthencourt, L. Makonkawkeyoon, T. R. Lee, *Bioorg. Med. Chem. Lett.* **2006**, *16*, 4120–4126.

[107] S. Allenmark, *Chirality* **2003**, *15*, 409–422.

[108] G. N. Parkinson, F. Cuenca, S. Neidle, *J. Mol. Biol.* **2008**, *381*, 1145–1156.

[109] K. Shin-ya, K. Wierzba, K. Matsuo, T. Ohtani, Y. Yamada, K. Furihata, Y. Hayakawa, H. Seto, *J. Am. Chem. Soc.* **2001**, *123*, 1262–1263.

[110] M.-Y. Kim, H. Vankayalapati, K. Shin-ya, K. Wierzba, L. H. Hurley, *J. Am. Chem. Soc.* **2002**, *124*, 2098–2099.

[111] G. N. Parkinson, M. P. H. Lee, S. Neidle, *Nature* **2002**, *417*, 876–880.

[112] B. Heddi, A. T. Phan, *J. Am. Chem. Soc.* **2011**, *133*, 9824–9833.

[113] D. Renčiuk, I. Kejnovská, P. Školáková, K. Bednářová, J. Motlová, M. Vorlíčková, *Nucleic Acids Res.* **2009**, *37*, 6625–6634.

[114] J. Gros, F. Rosu, S. Amrane, A. D. Cian, V. Gabelica, L. Lacroix, J.-L. Mergny, *Nucleic Acids Res.* **2007**, *35*, 3064–3075.

[115] C. J. Lech, B. Heddi, A. T. Phan, *Nucleic Acids Res.* **2013**, *41*, 2034–2046.

[116] P. M. Punt, G. H. Clever, *Chem. Eur. J.* **2019**, *25*, 13987–13993.

[117] P. M. Punt, M. D. Langenberg, O. Altan, G. H. Clever, *J. Am. Chem. Soc.* **2021**, *143*, 3555–3561.

[118] S. L. B. König, J. L. Huppert, R. K. O. Sigel, A. C. Evans, *Nucleic Acids Res.* **2013**, *41*, 7453–7461.

[119] I. Russo Krauss, V. Spiridonova, A. Pica, V. Napolitano, F. Sica, *Nucleic Acids Res.* **2016**, *44*, 983–991.

[120] I. R. Krauss, S. Ramaswamy, S. Neidle, S. Haider, G. N. Parkinson, *J. Am. Chem. Soc.* **2016**, *138*, 1226–1233.

[121] H.-J. Sullivan, C. Readmond, C. Radicella, V. Persad, T. J. Fasano, C. Wu, *ACS Omega* **2018**, *3*, 14788–14806.

[122] S. Mandal, Y. Kawamoto, Z. Yue, K. Hashiya, Y. Cui, T. Bando, S. Pandey, M. E. Hoque, M. A. Hossain, H. Sugiyama, H. Mao, *Nucleic Acids Res.* **2019**, *47*, 3295–3305.

[123] J. Abi-Ghanem, V. Gabelica, *Phys. Chem. Chem. Phys.* **2014**, *16*, 21204–21218.

[124] W. Wang, K. Chen, D. Qu, W. Chi, W. Xiong, Y. Huang, J. Wen, S. Feng, B. Zhang, *Tetrahedron Lett.* **2012**, *53*, 6747–6750.

[125] C. Tansakul, E. Lilie, E. D. Walter, F. Rivera, A. Wolcott, J. Z. Zhang, G. L. Millhauser, R. Braslau, *J. Phys. Chem. C* **2010**, *114*, 7793–7805.

[126] H. C. Kolb, M. G. Finn, K. B. Sharpless, *Angew. Chem. Int. Ed.* **2001**, *40*, 2004–2021.

[127] A. H. El-Sagheer, T. Brown, *Chem. Soc. Rev.* **2010**, *39*, 1388–1405.

[128] A. H. El-Sagheer, T. Brown in *Chemoselective and Bioorthogonal Ligation Reactions: Concepts and Applications* (Eds.: W. R. Algar, P. E. Dawson, I. L. Medintz), Wiley, **2017**.

4 Protein-Inspired Ligand Functionalities Incorporated into DNA G-Quadruplexes

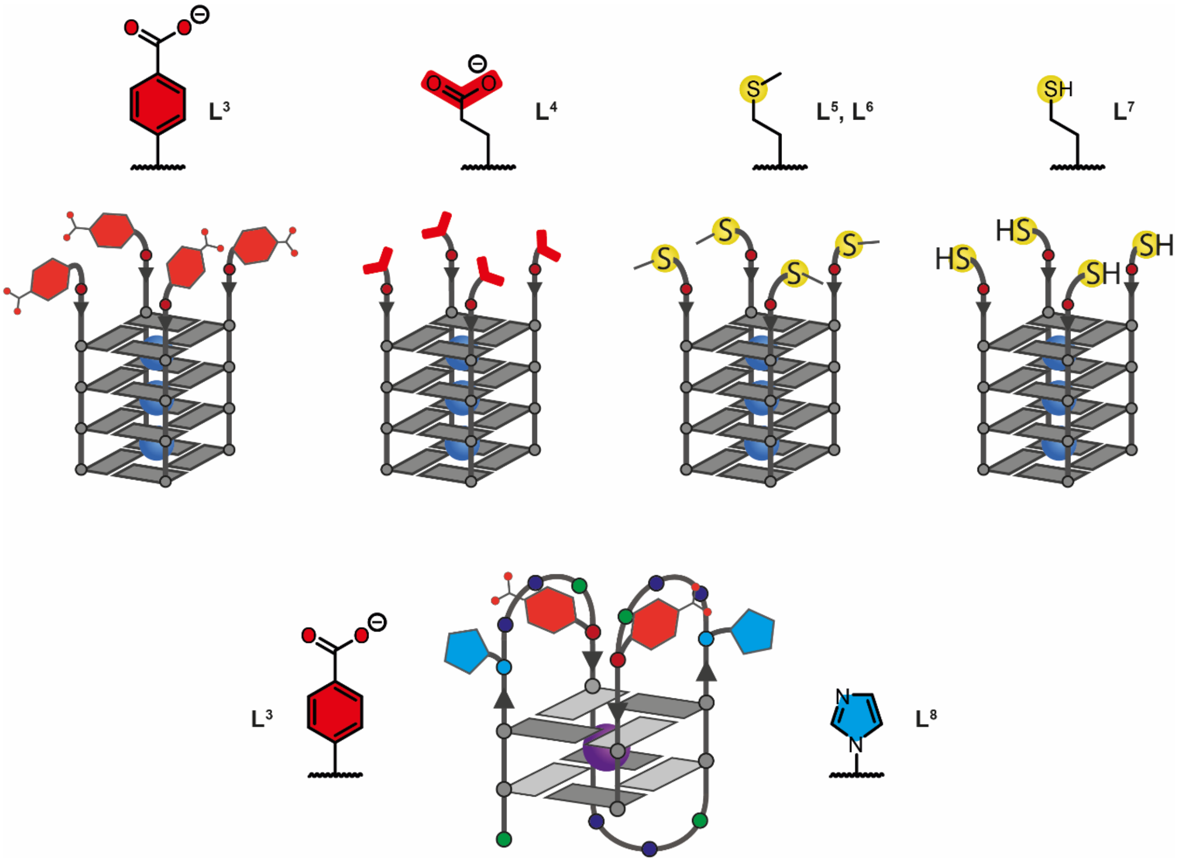

The results presented in this chapter were in part published in

P. M. Punt,$^{+}$ L. M. Stratmann,$^{+}$ S. Sevim, L. Knauer, C. Strohmann, G. H. Clever, ‘Heteroleptic Coordination Environments in Metal-Mediated DNA G-Quadruplexes’, *Front. Chem.* **2020**, *8*, 26.[1] ($^{+}$: these authors have contributed equally to this work)

4.1 Introduction

4.1.1 Metal Complexes in Metallo-Proteins

A detailed look into metallo-proteins discloses a phenomenal plethora of metal complexes. Metals such as iron, copper or zinc can be found in many different coordination environments and are crucial for the function of metallo-proteins. The metal ions are typically involved in fixing the desired protein structure or serve as catalytic centers or redox cofactors. For example, about 50% of all enzymes contain metal cofactors and several metals are therefore essential elements for living organisms.[2]

Interestingly, only around a dozen different metal ions can be frequently found in proteins but they are part of numerous metal complexes comprising a wide range of different fine-tuned properties. It becomes directly clear, that not only the metal ion itself but also its coordination environment determines those complex properties. There are several organic (and inorganic) cofactors that function as ligands. For example, macrocyclic tetradentate tetrapyrrole ligands are found in the heme group, in chlorophyll, or cobalamins. More often, however, ligand functionalities are provided by the amino acid side chains. In the proteinogenic amino acids, several different donor groups can be found, ranging from hard Lewis bases such as carboxylates (glutamate and aspartate) and phenol (tyrosine), borderline Lewis donors like imidazole (histidine) to soft Lewis bases like sulfur-containing ligands (methionine and cysteine). The amide group in the peptide backbone can also function as a donor group.[2]

Metal complexes in metallo-proteins are usually heteroleptic. The choice and number of distinct ligands in combination with the coordination geometry determined by the peptide framework mainly defines the complex properties. In addition, the secondary coordination sphere has an influence by adjusting parameters such as pH, hydrophobicity, or electrostatic potential.[3–5] A marvelous example for the perfect fine-tuning in metallo-proteins becomes apparent when discussing the redox potentials of electron transfer proteins containing three main classes of redox-active metal cofactors. The three major types, namely copper proteins, cytochromes, and proteins with FeS-clusters, cover a wide reduction potential range of about 1.5 V.[6] One of these electron transfer proteins, plastocyanin, contains a $Cu^{+/2+}$ center (Figure 4.1). The characteristic arrangement of two histidine, one cysteine and one methionine ligand is located half way between a tetrahedral (preferred by Cu^{+} ions) and a square-planar (preferred by Cu^{2+} ions) coordination geometry. The special geometry leads to higher energy reactant and product (closer to the transition state) and hence to a decreased activation barrier for the uptake or release of an electron due to a small reorganization energy.[7] This principle is known as the entatic state[8] and makes plastocyanin a very fast and efficient electron shuttle protein.

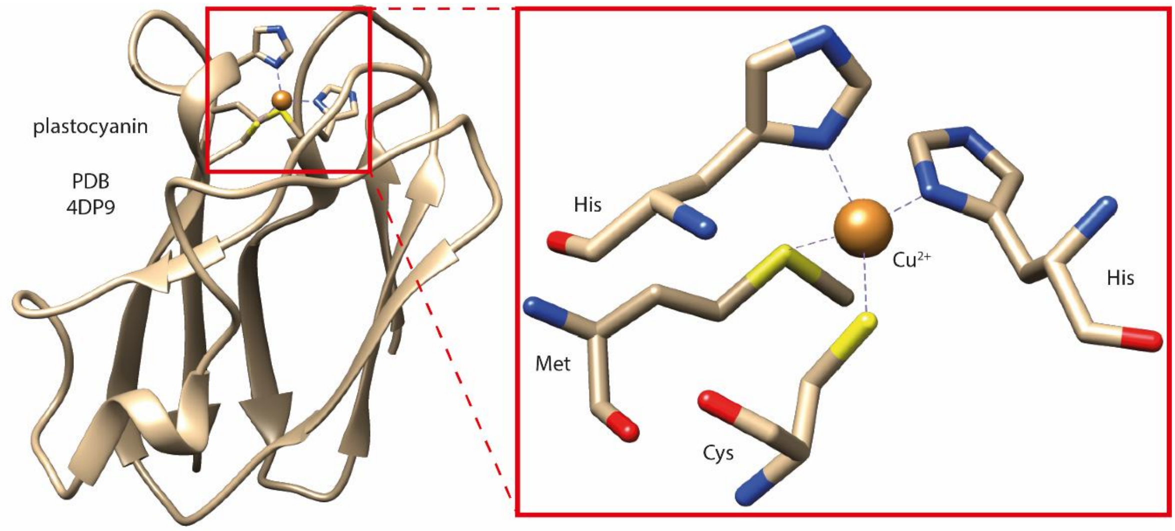

Figure 4.1: XRD structure of poplar plastocyanin in the oxidized state (PDB: 4DP9). The Cu^{2+} ion is coordinated by two histidine, one cysteine and one methionine ligand.[9]

Another fascinating example for fine-balanced coordination environments can be found in hemoglobin, the tetrameric O_2 transport protein. Binding of a first O_2 molecule causes a conformational change in the remaining O_2 binding sites which increases the binding affinity for a second O_2 molecule, which again causes a conformational change, until all four binding sites are occupied. This positive cooperativity due to conformational changes is called allostery.[10]

One goal of bioinorganic chemists is to investigate and understand the role of metal ions in metallo-proteins and to mimic their structure and function in model complexes.[11–14] These models are aimed to function as biotechnological catalysts with simpler structures suited for industrial applications. In the field of protein engineering, scientists try to improve reaction rates of natural enzymes or even to design artificial enzymes for new-to-nature reactions.[15–24] To achieve these goals, several approaches have been developed. One very successful strategy is called directed evolution and was awarded with the Nobel prize in chemistry in 2018 for F. H. Arnold.[25–33] Other concepts use the bottom up approach and design completely new proteins which is a challenging task (*de novo* protein design).[34–37] Another idea is to use DNA instead of peptides as scaffold to bring together ligand functionalities that form active metal complexes. Nucleic acid secondary structures are better predictable and programmable compared to peptides and proteins which might allow easier structural design and can be embedded into larger devices with strategies from DNA nanotechnology (Section 1.3).[38,39]

4.1.2 Ligandosides Incorporated into G-Quadruplexes in the Clever Lab

In the Clever Lab, the concept of incorporating ligand functionalities into DNA secondary structures is pursued to mimic functional metal complexes in metalloproteins. G-quadruplexes serve as a rigid framework and the incorporation of either pyridine- or imidazole-based ligandosides resulted in preorganized coordination environments suitable for transition metal binding (for details, see Section 1.4).[40–46] Thereby, ligandoside incorporation into the loop regions of unimolecular G-quadruplexes allowed a simple, controlled design of tailored ligand arrangements.[41,45]

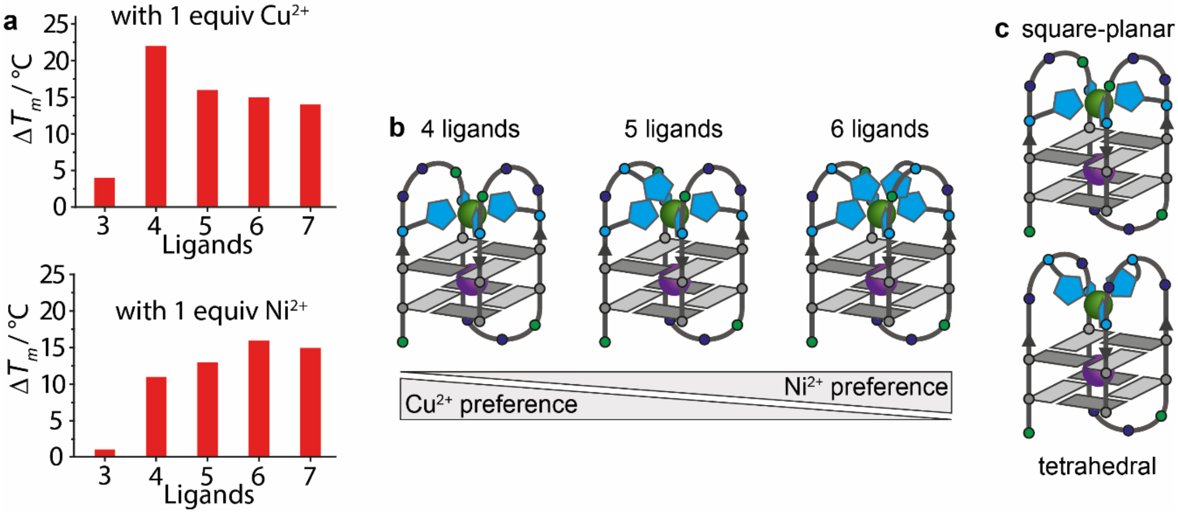

Figure 4.2: (**a**, **b**) Different numbers and (**c**) different positioning of incorporated imidazole ligandosides (light blue) resulted in G-quadruplexes with fine-tuned affinity to Cu^{2+}, Ni^{2+} or Zn^{2+} ions (green).[45]

So far, the modular approach facilitated the fine-tuning of ligand arrangements by two easily adjustable parameters. First, the number of ligandosides was varied leading to a series of distinct coordination environments with varying metal affinity. For example, Cu^{2+} ions which are usually square-planar coordinated showed a higher affinity to G-quadruplexes containing four imidazole ligands. On the other hand, Ni^{2+} ions preferred binding to structures offering six ligands, as judged by their stabilizing effect on the overall secondary structure (Figure 4.2a and b). The second adjustable parameter is the position of the ligands within the G-quadruplex loops which is easily programmable by varying the G-quadruplex-forming DNA sequence. Arrangement of four imidazole ligands in a square-planar or in a tetrahedral manner influenced the affinity to Cu^{2+} and Zn^{2+} ions (Figure 4.2c).

4.1.3 Expansion of Ligand Library

So far, only unsaturated N-heterocyclic ligand functionalities have been reported to be covalently incorporated into G-quadruplexes, either based on pyridine or imidazole donors, resulting in homoleptic metal complexes. With the diversity in metallo-proteins in mind, a further fine-tuning of coordination environments requires further ligand functionalities with different properties. As a simple scale to define those properties, the HSAB concept might be taken into account. Since pyridine and imidazole ligands are halfway between hard and soft Lewis bases, the incorporation of both harder and softer ligands would highly expand the possibilities to bind hard and soft metal ions and to form metal complexes with various properties within G-quadruplexes. Combining different ligand functionalities in unimolecular G-quadruplexes would then allow a further adjustment of coordination environments mimicking heteroleptic motifs found in metallo-proteins.

Inspired by the amino acids aspartate and glutamate, carboxylate ligands were intended to be incorporated as hard Lewis bases into G-quadruplex structures in this thesis. Since the pyridine ligandoside (**L^1**) was already well established,[40–42] a structurally similar benzoate ligandoside (**L^3**) was targeted. While a mononuclear $Cu(pyridine)_4$ complex was found when four pyridine ligandosides were incorporated into G-quadruplexes (Figure 4.3b), for the incorporation of four benzoate ligands, a dinuclear $Cu_2(benzoate)_4$ complex with the known paddle wheel motif was expected to form within a G-quadruplex structure (Figure 4.3d).[47] In addition, it was aimed for an aliphatic carboxylate ligandoside (**L⁴**).

To introduce soft Lewis donors, sulfur-containing ligand functionalities were considered. Thioether (**L⁵**, **L⁶**)) and thiol ligands (**L⁷**) were targeted to mimic the soft donor groups in methionine and cysteine intending to bind soft Lewis acids such as biologically relevant $Fe^{2+/3+}$ and Zn^{2+} ions as well as Hg^{2+}, Cd^{2+} or Ag^{+}.

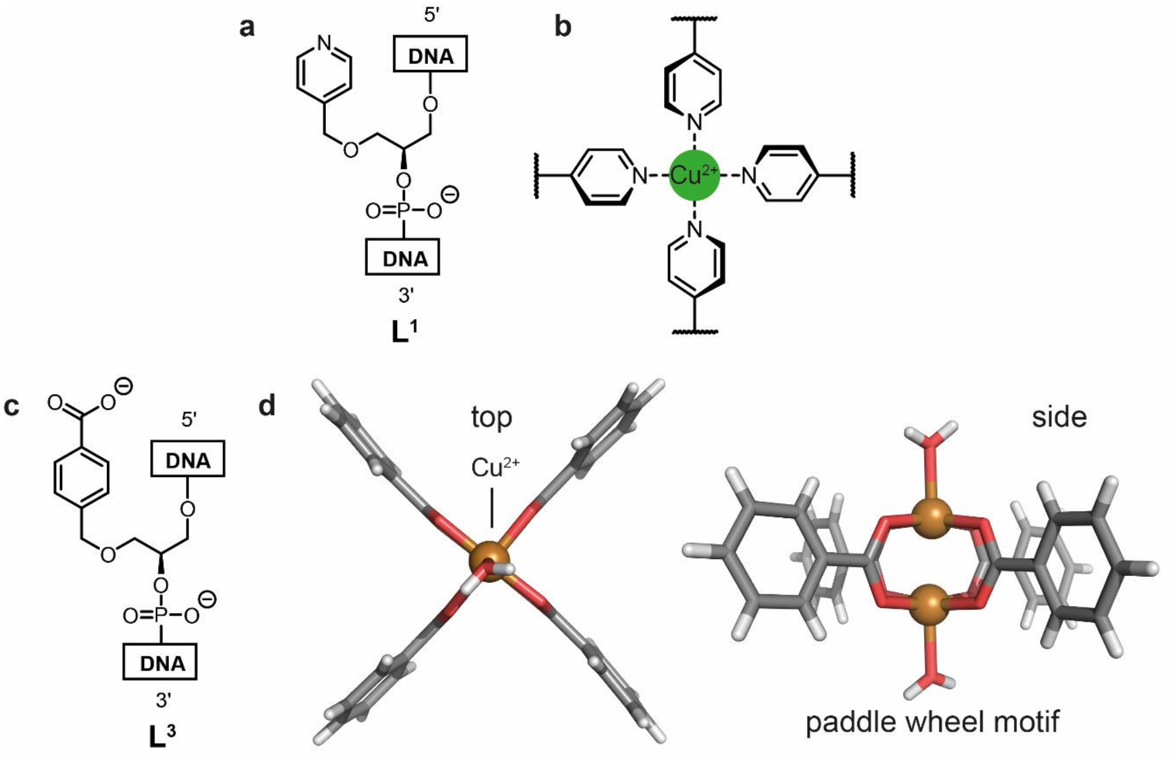

Figure 4.3: (**a**) Chemical structure of pyridine-based ligandoside **L¹** and (**b**) the mononuclear Cu(pyridine)$_4$ tetrad found in modified G-quadruplexes.[40–43,46] (**c**) Chemical structure of benzoate-based ligandoside **L³** and (**d**) the well-known dinuclear Cu$_2$(benzoate)$_4$ complex forming the paddle wheel motif (CCDC: 955889).[47]

4.2 Carboxylate Ligandosides in G-Quadruplexes

4.2.1 Synthesis of a New Benzoate Phosphoramidite

In analogy to the pyridine- and imidazole-based ligandosides developed in the Clever Lab,[41,45] the design of the benzoate ligandoside **L³** was based on an acyclic glycol backbone replacing the canonical deoxyribofuranose ring (Figure 4.4). In earlier works, it has been shown by Meggers *et al.* that oligonucleotides containing this substantial backbone modification termed GNA (glycol nucleic acid) still form typical duplex structures with Watson-Crick base pairing.[48–50] The glycol backbone was chosen in the ligandoside design to simplify the synthesis of the phosphoramidite building block required for automated solid-phase DNA synthesis.

The glycol backbone contains a chiral carbon atom giving rise to two enantiomers of the ligandoside. It was shown before that the chosen configuration of the incorporated ligandoside slightly affects G-quadruplex stability and its metal binding.[41,42,44,45] In this study, however, only one ligandoside enantiomer was incorporated into oligonucleotides. To avoid confusions, it should be noted here that the stereodescriptor (according to CIP rules) for the ligandoside with the same absolute configuration varies if found in the respective phosphoramidite or incorporated into oligonucleotides either at the 5'-end or within the sequence (Figure 4.4).

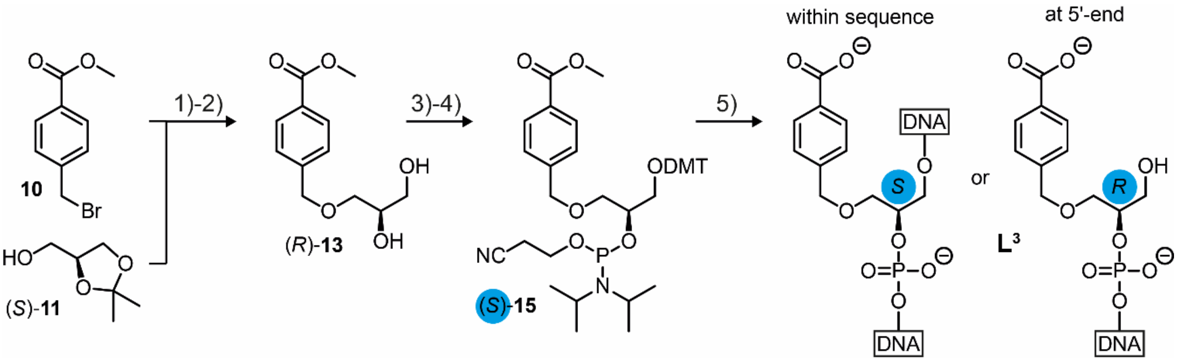

Figure 4.4: Synthetic route to access the phosphoramidite building block (*S*)-**15** required to incorporate benzoate ligandoside **L**^{3} into oligonucleotides by solid-phase DNA synthesis. The stereodescriptor of the ligandoside changes if incorporated within the sequence or at the 5'-end (highlighted in blue). 1) NaH, CH_3CN; 2) CH_3COOH, THF/H_2O; 3) DMT-Cl, DIPEA, DMAP, THF; 4) CEDIP-Cl, DIPEA, CH_2Cl_2; 5) automated solid-phase DNA synthesis and deprotection. For detailed synthetic procedures, see Section 7.5.

The aromatic benzoate functionality was chosen as a first carboxylate ligand since the known synthetic route used for the pyridine ligandoside (**L**^{1}) could be adapted.[41] To avoid undesired side reactions during synthesis, especially during solid-phase DNA synthesis, and to ensure an easy handling (solubility, NMR characterization), the benzoic acid group was protected as methyl ester. The initial nucleophilic attack of deprotonated solketal ((*S*)-**11**) as enantiopure precursor to methyl 4-(bromomethyl)benzoate (**10**) followed by acidic deprotection of the acetal group resulted in the ester-protected benzoate ligandoside (*R*)-**13**. Its structure and absolute configuration were confirmed by single-crystal X-ray diffraction (Figure 4.5a). The primary hydroxyl group was DMT-protected (DMT = dimethoxytrityl) followed by a phosphitylation reaction yielding phosphoramidite building block (*S*)-**15** (for detailed reaction procedures and analytics see Section 7.5). Two low-field signals in the $^{31}P\{^{1}H\}$ NMR spectrum (in $CDCl_3$, Figure 4.5b) proved the expected formation of two diastereomers. Chemical shifts of $\delta = 149.4$ and 149.3 ppm are typical for P(III)-nuclei in phosphoramidites.

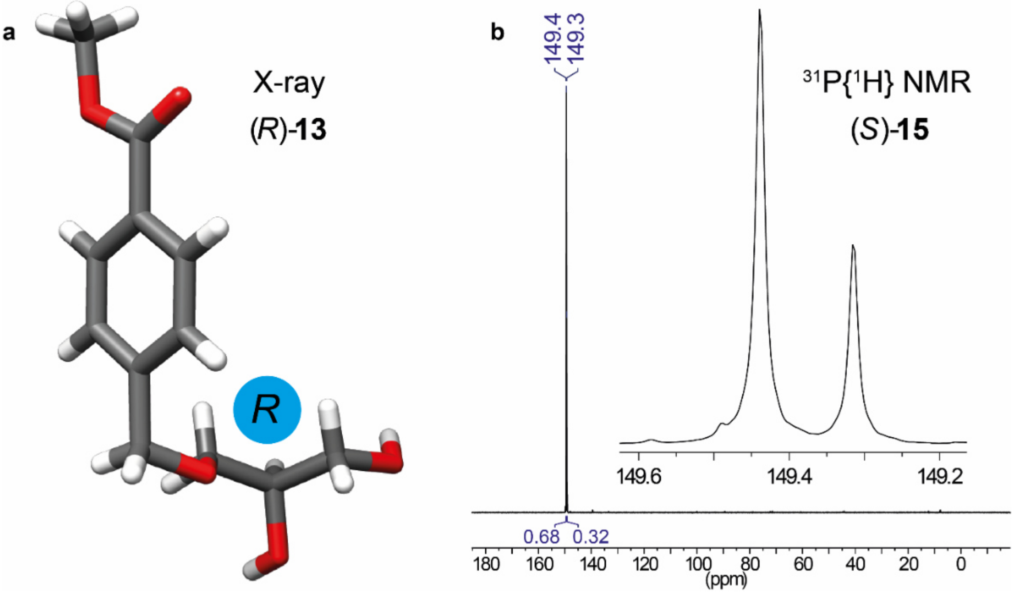

Figure 4.5: (**a**) Molecular structure of ester-protected benzoate nucleoside (*R*)-**13** in the solid state determined with single-crystal X-ray diffraction. The absolute configuration was confirmed. (**b**) $^{31}P\{^{1}H\}$ NMR spectrum (162 MHz, in $CDCl_3$) of phosphoramidite building block (*S*)-**15** shows two product signals indicating the presence of two diastereomers.

Importantly, also the deprotected nucleoside (*R*)-**16** was synthesized *via* basic ester hydrolysis of compound (*R*)-**13**. The UV absorption property of the free nucleoside in water was determined (Figure 7.6), which was later required for UV-based DNA concentration determination of benzoate-modified oligonucleotides (Section 7.9.6).

4.2.2 Benzoate Ligandosides Incorporated into G-Quadruplexes

The phosphoramidite building block (*S*)-**15** was used to incorporate the benzoate ligandoside into oligonucleotides by automated solid-phase DNA synthesis. Care had to be taken with the subsequent cleavage from solid support and deprotection of the modified DNA strands. Standard treatment with concentrated aqueous NH_3 was avoided due to the risk of forming amides instead of carboxylates from the benzoate esters. Instead, cleavage and deprotection were accomplished in 0.4 M NaOH in methanol/water (4:1, v/v) and a subsequent desalting step was implemented prior to semi-preparative reverse-phase HPLC purification (Section 7.9).

Three short guanine-rich oligonucleotides with the benzoate ligandoside $\mathbf{L^3}$ attached at the 5'-end have been synthesized, designed to form tetramolecular G-quadruplexes with varying G-tetrad count (oligos **L**, **M**, **N**: 5'-$\mathbf{L^3}$$G_n$, n = 3,4,5). Successful incorporation and purification were confirmed with MALDI-TOF mass spectrometry and analytical reverse-phase HPLC. Analytical data are exemplarily shown for oligo **L** in Figure 4.6.

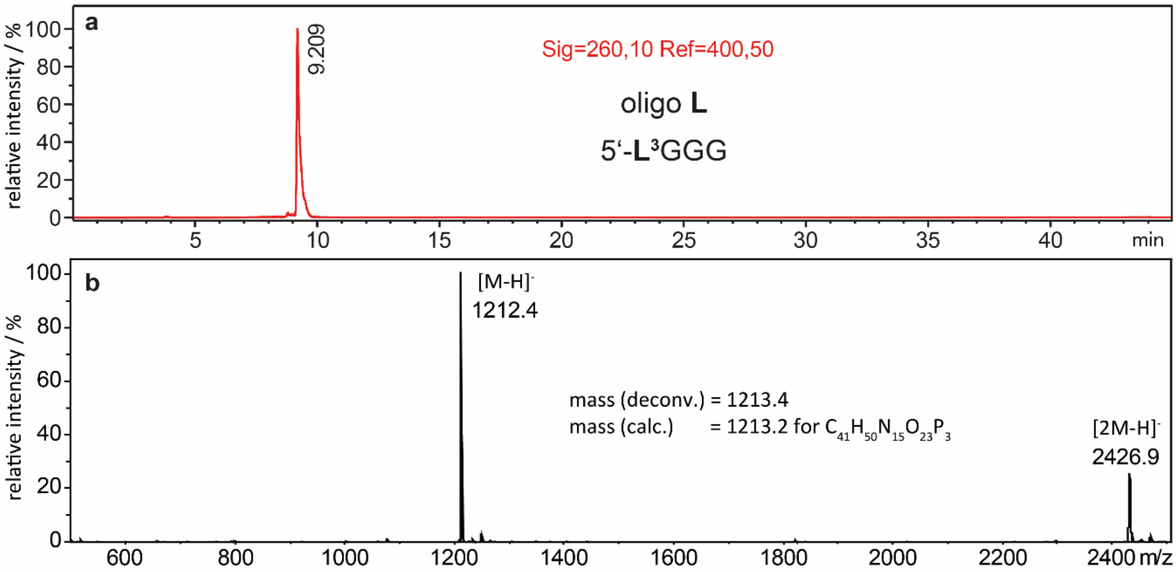

Figure 4.6: (**a**) Analytical reverse-phase HPLC trace and (**b**) MALDI-TOF mass spectrum of oligo **L** after DNA synthesis and purification.

The ability of the benzoate-modified oligos **L**–**N**, respectively, to form G-quadruplex structures ($\mathbf{L}_4$, $\mathbf{M}_4$, and $\mathbf{N}_4$) at high Na^+ concentration and pH 7.2 was examined with UV-based thermal denaturation experiments. No melting

---

oligo **L**: $\mathbf{L^3}$GG G, oligo **M**: $\mathbf{L^3}$GG GG, oligo **N**: $\mathbf{L^3}$GG GGG; ligandoside $\mathbf{L^3}$: benzoate ligand behavior was observed for samples containing oligo **L** (Figure 4.7c and Figure 6.23) in agreement with similar reported cases.[40,44] In Na$^+$-containing solution, tetramolecular G-quadruplexes with three G-tetrads are usually not stable enough to form ($T_{1/2} < 0$ °C). However, samples containing oligos **M** and **N**, respectively, showed sigmoidal melting curves recorded at 295 nm with melting temperatures of $T_{1/2} = 27$ °C and 72 °C, indicating the presence of G-quadruplex species **M**$_4$ and **N**$_4$ (Figure 4.7c). Also, UV-based thermal difference spectra showed a pattern which is typical for G-quadruplexes (Figure 4.7b).

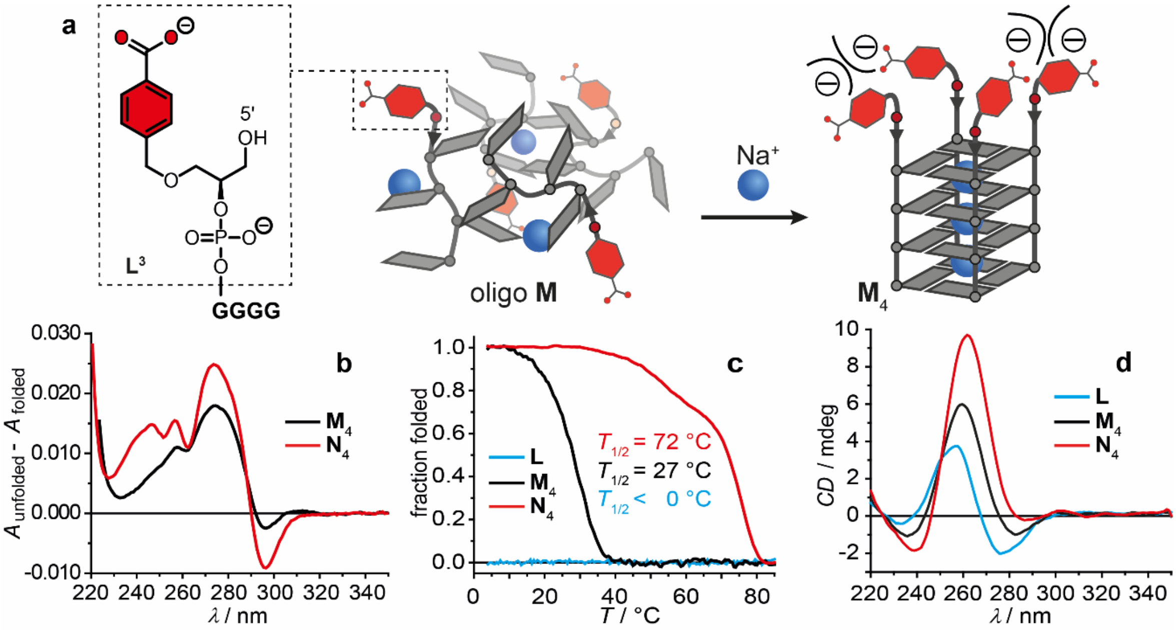

Figure 4.7: (**a**) Self-assembly of benzoate-modified G-quadruplex **M**$_4$. Negatively charged benzoate ligands repel each other. (**b**) UV-based thermal difference spectra, (**c**) UV-based thermal denaturation profiles, and (**d**) CD spectra of the G-quadruplexes **M**$_4$ and **N**$_4$. Oligo **L** does not form a G-quadruplex structure and hence shows no melting behavior and a pattern typical for single-stranded DNA in the CD spectrum. Sample composition: 4 µM oligonucleotide (1 µM G-quadruplex), 100 mM NaCl, 10 mM lithium cacodylate buffer (pH 7.2).

Importantly, the melting temperatures were significantly lower compared to similar tetramolecular G-quadruplexes containing pyridine or imidazole ligandosides at the 5'-end.[42,44,45] The literature-reported pyridine-modified G-quadruplex (5'-**L**^{1}G$_4$)$_4$, for example, differs only in the ligand functionality and shows under very similar conditions a melting temperature of $T_{1/2} = 45$ °C.[42] The tremendous difference in thermal stability ($\Delta T_{1/2} = -18$ °C) can be explained with the negative

---

oligo **L**: **L**^{3}GG G, oligo **M**: **L**^{3}GG GG, oligo **N**: **L**^{3}GG GGG; ligandoside **L**^{3}: benzoate ligand charge of the benzoate ligands at given pH in addition to the negatively charged phosphate groups that repel each other in the folded G-quadruplex structure (Figure 4.7a).

Furthermore, the G-quadruplex formation was investigated with CD spectroscopy. While oligo **L** showed a pattern typical for single-stranded DNA, samples containing oligo **N** gave a pattern with a minimum at ~240 nm and a maximum at ~265 nm, which confirmed the formation of a parallel G-quadruplex topology, typical for tetramolecular G-quadruplexes ($\mathbf{N}_4$, Figure 4.7d). The CD spectrum containing oligo **M** could be interpreted as the sum of the patterns of a parallel G-quadruplex and single-stranded DNA. This result suggested that G-quadruplex formation ($\mathbf{M}_4$) was not complete in this sample. The reason might be a kinetically slower G-quadruplex formation due to the additional negative charges of the benzoate ligands and full annealing could not happen during the applied freeze-thaw protocol (Section 6.9).

The confirmed parallel topology in $\mathbf{M}_4$ and $\mathbf{N}_4$ was a prerequisite for the four benzoate functionalities to reside at the same end of the G-quadruplex structure. It resulted in a prearranged coordination environment, as found before with other ligand functionalities in the Clever Lab.[40,42,44] This chelate environment was subsequently tested for its binding of transition metal ions. As a simple way to detect transition metal binding, the metal salts were added to DNA samples (oligos **L**, **M**, and **N**) prior to the annealing step and UV-based thermal denaturation profiles of the resulting secondary structures were recorded, as it was previously shown that metal complex formation raises the overall stability of the folded G-quadruplex.[42,44] With the characteristic paddle wheel motif of $Cu_2(carboxylate)_4$ complexes in mind (Section 4.1.3), different equivalents of $CuSO_4$ were added. For oligo **L**, still no melting behavior was detected (Figure 6.23). This result was in contrast to previous observations, where addition of Cu^{2+} ions triggered the formation of G-quadruplexes composed of three G-tetrads and pyridine or imidazole ligandosides due to metal complex formation.[40,44]

While TDS spectra confirmed intact G-quadruplex structures $\mathbf{M}_4$ and $\mathbf{N}_4$ in the presence of the Cu^{2+} ions (Section 6.5), however, no increase in thermal G-quadruplex stability expressed in the melting temperature was detected ($\Delta T_{1/2} = \pm 1$ °C, Figure 4.8a and c). Also, Ni^{2+} and Zn^{2+} ions and, considering the

---

oligo **L**: $\mathbf{L}^3$GG G, oligo **M**: $\mathbf{L}^3$GG GG, oligo **N**: $\mathbf{L}^3$GG GGG; ligandoside $\mathbf{L}^3$: benzoate ligand harder character of the benzoate ligand, the lanthanide ions Ce^{3+} and Gd^{3+} as hard Lewis acids were added to G-quadruplex $\mathbf{M}_4$. However, no increase in thermal stability was observed (Figure 4.8b). Also, metal addition at a more basic pH of 9.6 that shifts the equilibrium even further to the deprotonated benzoates making them better Lewis bases, had no effect on the thermal stability (Figure 6.26), indicating that no metal-benzoate complex was formed.

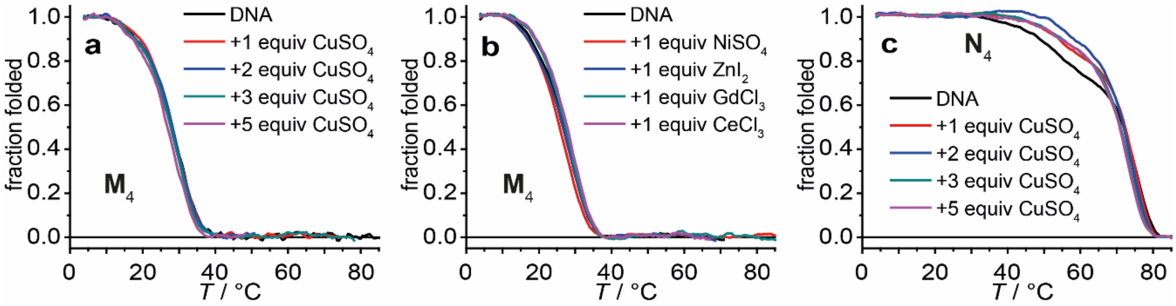

Figure 4.8: UV-based thermal denaturation profiles of benzoate-modified G-quadruplexes $\mathbf{M}_4$ (**a**, **b**) and $\mathbf{N}_4$ (**c**) in the absence and presence of different transition metal salts. Sample composition: 4 µM oligonucleotide (1 µM G-quadruplex), 1, 2, 3, or 5 µM transition metal salt, 100 mM NaCl, 10 mM lithium cacodylate buffer (pH 7.2).

The fact that no transition metal binding of the preorganized benzoate ligandosides at the 5'-end of G-quadruplexes could be observed might be explained with the presence of several other hard ligand functionalities in high concentrations in solution competing with the benzoate ligands. These potential competing ligands are water, cacodylate, chloride, and phosphate groups of the DNA backbone. Moreover, the added transition metal cations (Cu^{2+}, Ni^{2+}, Zn^{2+}, Gd^{3+}, or Ce^{3+}) compete with Na^+ ions as a hard Lewis acid present in a high concentration, which is required for G-quadruplex formation.

4.2.3 Aliphatic Carboxylate Ligandosides Incorporated into G-Quadruplexes

There was considered another idea that the benzoate ligandosides with their large π-systems and short linkers may be too stiff and inflexible to arrange in a square-planar fashion within the G-quadruplex environment, and that this might be a reason for the lack of transition metal complexation. Consequently, an aliphatic carboxylate ligandoside $\mathbf{L}^4$ with a flexible linker was designed. Its simple structure enabled an easy synthesis route but allowed the incorporation only at the 5'-end of oligonucleotides due to the lack of a 5'-OH group.

---

oligo **L**: $\mathbf{L}^3$GG G, oligo **M**: $\mathbf{L}^3$GG GG, oligo **N**: $\mathbf{L}^3$GG GGG; ligandoside $\mathbf{L}^3$: benzoate ligand

The required phosphoramidite was synthesized in two steps (Figure 4.9a) starting with the ring-opening of ε-caprolactone (**17**) by acidic transesterification resulting in the methyl carboxylate with terminal hydroxyl group (**18**). Subsequent phosphitylation reaction yielded phosphoramidite building block **19** which was confirmed by a low-field signal in the $^{31}P\{^1H\}$ NMR spectrum ($\delta = 147.3$ ppm in CD_2Cl_2, Figure 4.9b, for detailed reaction procedures and analytics see Section 7.6).

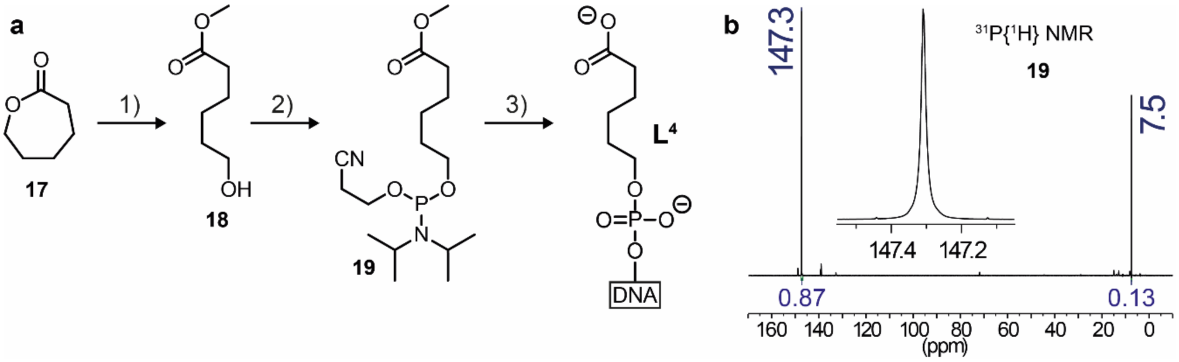

Figure 4.9: (**a**) Synthetic route to access the phosphoramidite building block **19** required to incorporate carboxylate ligandoside **L⁴** into oligonucleotides by solid-phase DNA synthesis. 1) H_2SO_4, CH_3OH; 2) CEDIP-Cl, DIPEA, CH_2Cl_2; 3) automated solid-phase DNA synthesis and deprotection. For detailed synthetic procedures, see Section 7.6. (**b**) $^{31}P\{^1H\}$ NMR spectrum (243 MHz, CD_2Cl_2) of phosphoramidite building block **19**. The high-field signal was assigned to oxidized CEDIP-Cl or oxidized product.

In analogy to the previously described approach, the carboxylate ligandoside was incorporated into G-rich oligonucleotides (oligo **O**: 5’-**L⁴**G₄, oligo **P**: 5’-**L⁴**G₅) and successful purification was confirmed by MALDI-TOF mass spectrometry and analytical reverse-phase HPLC (Section 6.1). The formation of G-quadruplexes **O**₄ and **P**₄ in Na^+-containing solution was confirmed by UV-based thermal denaturation profiles (Figure 4.10). Melting temperatures (**O**₄: $T_{1/2} = 25$ °C, **P**₄: $T_{1/2} = 69$ °C) were slightly lower than observed for benzoate-modified G-quadruplexes **M**₄ and **N**₄ ($\Delta T_{1/2} = -2$ °C and –3 °C, Section 4.2.2). The reason might be additional π-stacking interactions between benzoate functionalities and the 5’-terminal G-quartet as already assumed for pyridine ligandosides in our recent publication.[42] However, upon addition of several transition metal ions including hard Lewis acids such as Fe^{3+}, Gd^{3+}, or Ce^{3+}, no increased thermal stability was obtained ($\Delta T_{1/2} = \pm 1$ °C, Figure 4.10) suggesting no complexation.

---

oligo **O**: **L⁴**GG GG, oligo **P**: **L⁴**GG GGG; ligandoside **L⁴**: aliphatic carboxylate ligand

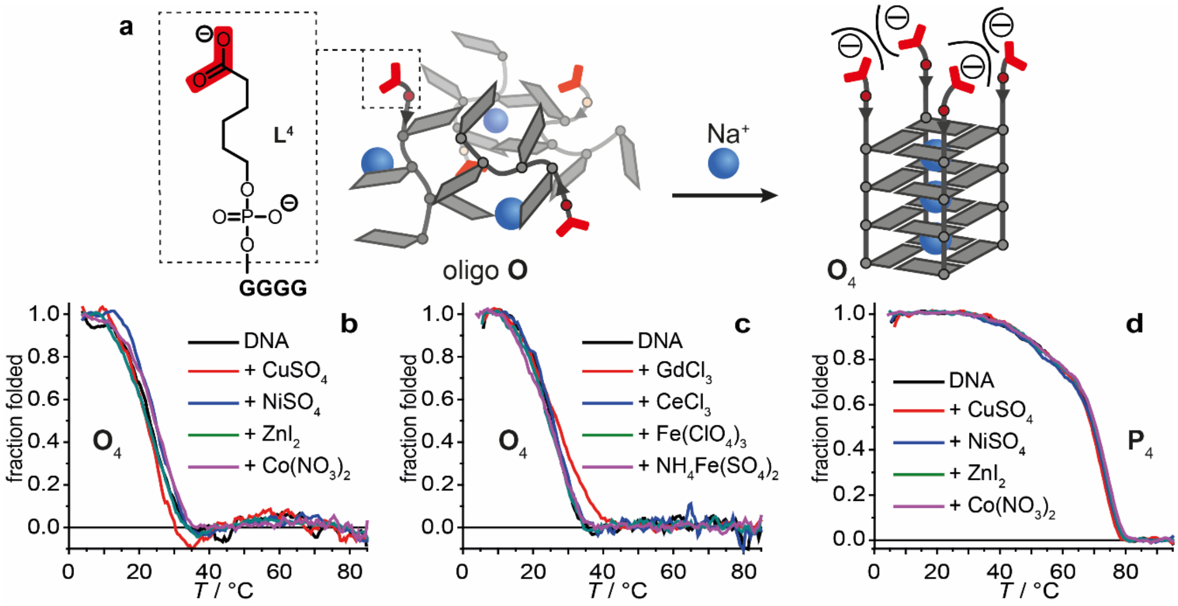

Figure 4.10: (**a**) Self-assembly of carboxylate-modified G-quadruplex **O**$_4$. UV-based thermal denaturation profiles of G-quadruplex **O**$_4$ (**b** and **c**) and G-quadruplex **P**$_4$ (**d**) in absence and presence of different transition metal ions. Sample composition: 4 µM oligonucleotide (1 µM G-quadruplex), 1 µM transition metal salt, 100 mM NaCl, 10 mM lithium cacodylate buffer (pH 7.2).

4.3 Sulfur-Based Ligandosides in G-Quadruplexes

4.3.1 Synthesis of Glycol-Based Thioether Phosphoramidite and Incorporation into Oligonucleotides

In analogy to the hard benzoate ligandoside (Section 4.2.1), the design of soft thioether ligandoside **L**^{5} was based on an acyclic glycol backbone. The phosphoramidite (*S*)-**24** was synthesized in three steps starting with the literature-known DMT-protection of the primary alcohol group in enantiopure glycidol ((*R*)-**20**),[45,49] followed by a ring-opening reaction with an alcoholate anion serving as the nucleophile. Phosphitylation of the resulting secondary alcohol group yielded the phosphoramidite building block (*S*)-**24** which was used in DNA synthesis without further purification (Figure 4.11a, for detailed reaction procedures and analytics see Section 7.7). Two low-field shifted signals in the ^{31}P{^{1}H} NMR spectrum (in CD_2Cl_2) proved the expected formation of two diastereomers (Figure 4.11b). Chemical shifts of $\delta = 149.3$ and 149.1 ppm are typical for P(III)-nuclei in phosphoramidites.

---

oligo **O**: **L**^{4}GG GG, oligo **P**: **L**^{4}GG GGG; ligandoside **L**^{4}: aliphatic carboxylate ligand

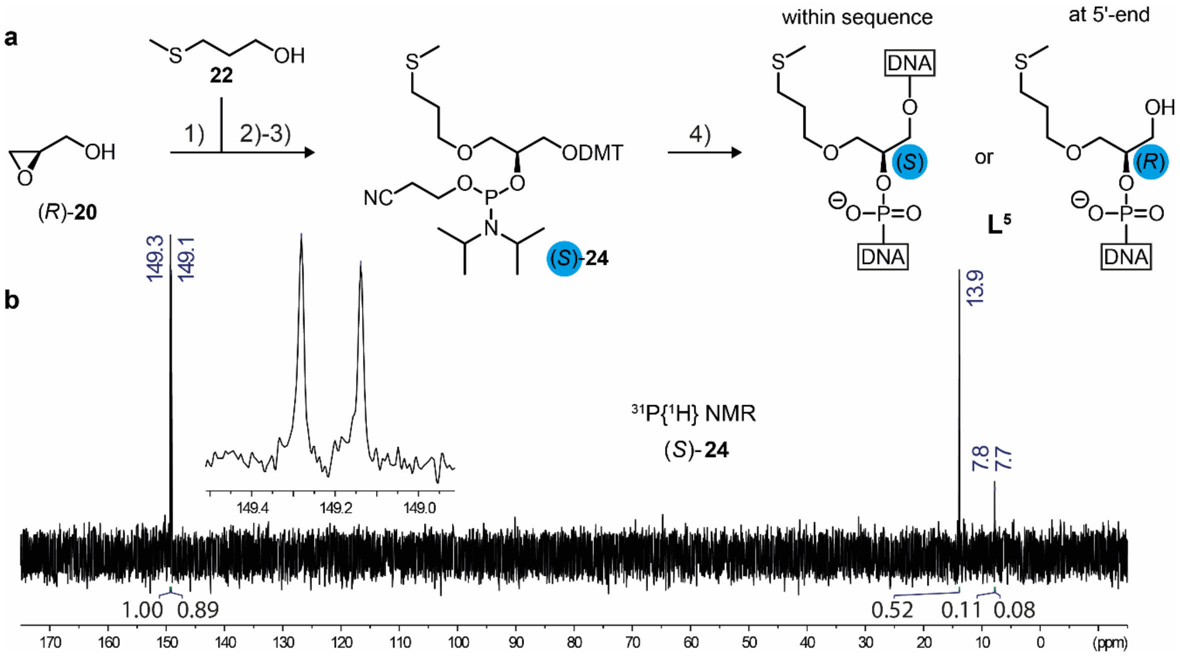

Figure 4.11: (**a**) Synthetic route to access the phosphoramidite building block (*S*)-**24** required to incorporate thioether ligandoside **L⁵** into oligonucleotides by solid-phase DNA synthesis. The stereodescriptor of the ligandoside changes if incorporated within the sequence or at the 5'-end (highlighted in blue). 1) DMT-Cl, Et_3N, CH_2Cl_2; 2) NaH, DMF; 3) CEDIP-Cl, DIPEA, CH_2Cl_2; 4) automated solid-phase DNA synthesis and deprotection. For detailed synthetic procedures, see Section 7.7. (**b**) $^{31}P\{^1H\}$ NMR spectrum (202 MHz, CD_2Cl_2) of phosphoramidite (*S*)-**24** (crude product) showing two signals for two formed diastereomers. In the high-field region, oxidized phosphitylation reagent and oxidized product are detected.

Successful incorporation of thioether ligandoside **L^5** at the 5'-end of two short, guanine-rich oligonucleotides (oligo **Q**: 5'-**L^5**G_4, oligo **R**: 5'-**L^5**G_5) *via* automated solid-phase DNA synthesis and subsequent purification with semi-preparative reverse-phase HPLC (for details see Section 7.9) was confirmed with ESI mass spectrometry and analytical reverse-phase HPLC (Section 6.1).

4.3.2 G-Quadruplex Formation and Addition of Transition Metal Ions

The ability of the thioether-modified oligos **Q** and **R**, respectively, to form tetramolecular G-quadruplexes (**Q**$_4$ and **R**$_4$) at high Na^+ concentration and pH 7.2 was examined with CD spectroscopy. In both cases, the typical CD signature was observed which confirmed the formation of a parallel G-quadruplex structure (Figure 4.12b and Figure 6.47).

---

oligo **Q**: **L^5**GG GG, oligo **R**: **L^5**GG GGG; ligandoside **L^5**: thioether ligand

In addition, UV-based thermal difference spectra and thermal denaturation profiles indicated G-quadruplex formation (Figure 4.12c and d). The denaturation temperature for **Q**$_4$ was observed to be $T_{1/2}$ = 55 °C, which was in the typical range for tetramolecular G-quadruplexes with four G-quartets. The results showed that the thioether modification incorporated at the 5'-end did not strongly effect G-quadruplex formation or its stability.

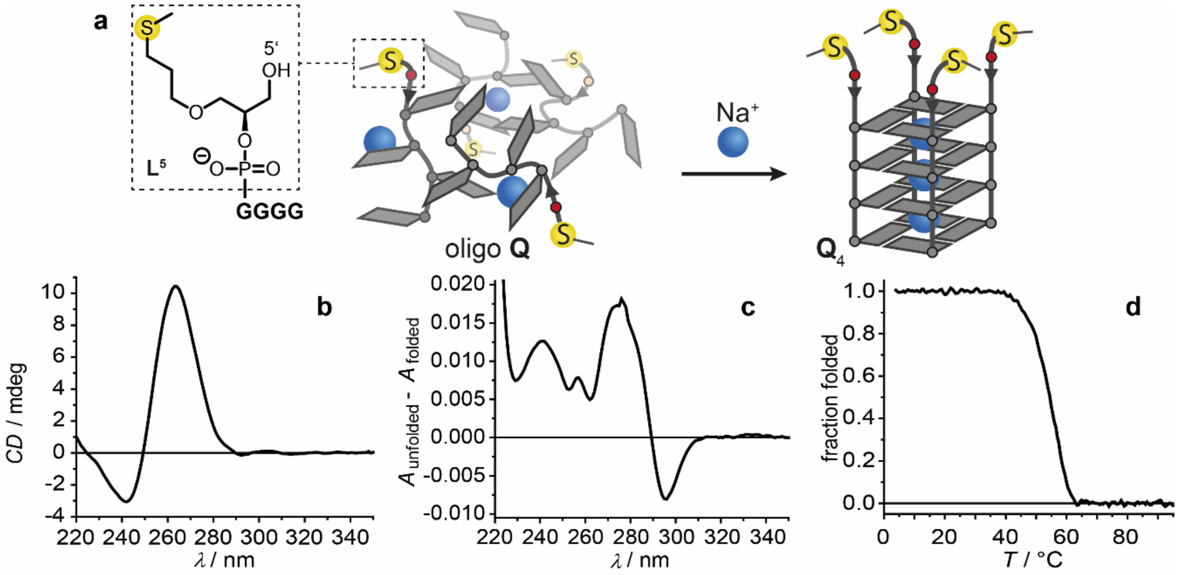

Figure 4.12: (**a**) Self-assembly of thioether-modified G-quadruplex **Q**$_4$. (**b**) CD spectrum, (**c**) UV-based thermal difference spectrum, and (**d**) UV-based thermal denaturation profile of the G-quadruplex. Sample composition: 4 µM oligonucleotide (1 µM G-quadruplex), 100 mM NaCl, 10 mM lithium cacodylate buffer (pH 7.2).

Formation of G-quadruplex **R**$_4$ in K$^+$-containing solution was further confirmed by native ESI mass spectrometry (Figure 4.13). Two observables indicated the presence of the tetramolecular secondary structure in the gas phase. First, instead of the single-stranded oligo **R**, its tetrameric construct was the main detected species. Second, the series of statistically distributed, unspecific adducts with K$^+$ ions started with four K$^+$ ions and not with zero K$^+$ ions as observed for denatured single strands. This observation suggested that four K$^+$ ions are an integral part of the folded species, as expected for a G-quadruplex with five G-tetrads such as **R**$_4$.

---

oligo **Q**: **L**^{5}GG GG, oligo **R**: **L**^{5}GG GGG; ligandoside **L**^{5}: thioether ligand

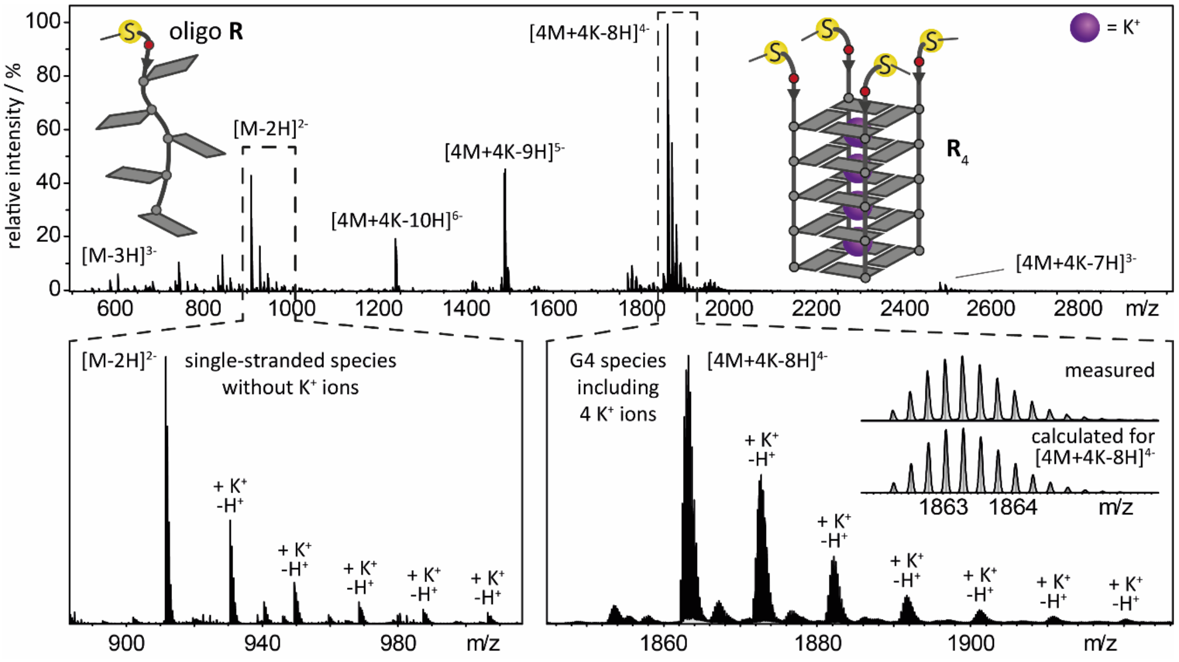

Figure 4.13: Native ESI mass spectrum of G-quadruplex **R**$_4$ in K$^+$-containing solution. The tetrameric main species with the four specifically bound K$^+$ ions confirmed the folded G-quadruplex structure in the gas phase. Sample composition: 50 µM oligo **R**, 500 µM $KClO_4$, 50 mM trimethylammonium acetate buffer (pH 7.0) in a 1:1 (v/v) mixture of water and acetonitrile.

The formation of a parallel G-quadruplex topology, confirmed by CD spectroscopy, was a prerequisite for the four ligand functionalities to reside at the same end of the G-quadruplex structure. It resulted in a prearranged coordination environment, as found before with different ligand functionalities in the Clever Lab.[40,42,44] This chelate environment was subsequently tested for binding of transition metal ions. Therefore, samples containing G-quadruplex **Q**$_4$ and equimolar amounts of different transition metal salts were investigated. In light of the soft character of the thioether ligand, focus was set on softer transition metal ions such as Cd^{2+}, Hg^{2+} and Ag^+, in addition to the medium Lewis acids Cu^{2+} and Zn^{2+}. Also, Au^{3+} ions were added. As a simple assay to detect transition metal binding, UV-based thermal denaturation profiles were recorded, because it was previously shown that metal complex formation raises the overall stability of the folded G-quadruplex.[40,42,44] While CD and TDS spectra confirmed intact G-quadruplex structures (Sections 6.5 and 6.9) the presence of the different transition metal ions resulted, however, in no increase in thermal G-quadruplex stability (Figure 4.14). While the melting curve was not at all effected by the addition of most of the ions,

---

oligo **Q**: **L**^{5}GG GG, oligo **R**: **L**^{5}GG GGG; ligandoside **L**^{5}: thioether ligand the presence of Ag^+ ions slightly decreased the G-quadruplex stability. An excess of Ag^+ or Au^{3+} ions further destabilized the secondary DNA structure. No melting behavior was observed at all upon addition of 1 or 10 equivalents of Pd^{2+} ions (added either as $Pd(NO_3)_2$ or $[Pd(CH_3CN)_4](BF_4)_2$ salt, addition of excess of Pd salt caused a brown precipitation probably due to reduction to metallic Pd) suggesting that no G-quadruplexes were formed at all in Pd^{2+}-containing solution (Figure 6.31).

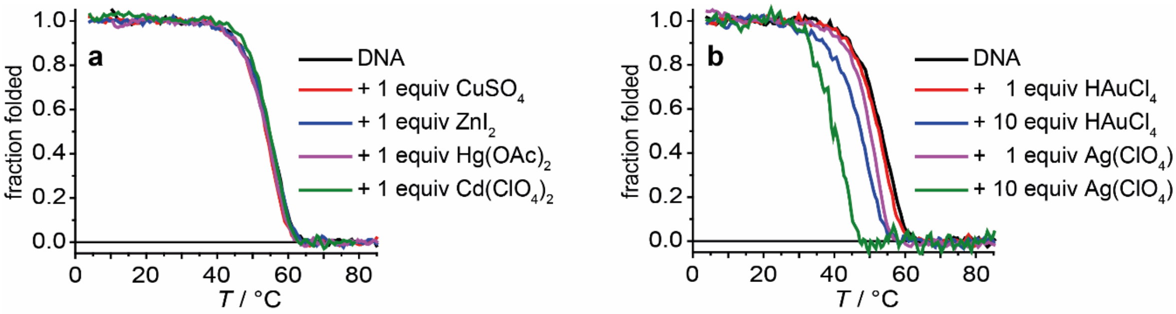

Figure 4.14: UV-based thermal denaturation profiles of thioether-modified G-quadruplex $\mathbf{Q}_4$ in the absence and presence of different transition metal ions. Sample composition: 4 µM oligonucleotide (1 µM G-quadruplex), 1 or 10 µM transition metal salt, 100 mM $NaClO_4$, 10 mM lithium cacodylate buffer (pH 7.2).

In addition to the investigation of metal binding *via* UV-based melting experiments, also native ESI mass spectroscopy should be used to detect potential metal complex formation that does not result in a thermal stabilization of the G-quadruplex structure.

However, the fact that no metal binding was observed is not particularly surprising because thioether ligands are neutral and weak Lewis bases that must compete with other potential ligand functionalities in solution like nucleobases, phosphates, cacodylate, and water. Since in metallo-proteins, methionine is exclusively found in heteroleptic coordination environments, the combination of different ligands within one G-quadruplex will be investigated in future projects to mimic metalloprotein activity such as catalysis or electron transfer.

4.3.3 Synthesis of Threoninol-Based Thioether Phosphoramidite

So far, all ligandosides that can be incorporated internally into G-quadruplex-forming sequences developed by the Clever Lab (pyridine ($\mathbf{L}^1$),[41,42] imidazole

---

oligo **Q**: $\mathbf{L}^5$GG GG, oligo **R**: $\mathbf{L}^5$GG GGG; ligandoside $\mathbf{L}^5$: thioether ligand

(**L**^{8}),[44,45] benzoate (**L**^{3}), and thioether (**L**^{5})) were based on a glycol backbone. Another suited simple backbone is based on threoninol and has been reported in the literature.[51–57] Two advantages might be mentioned for this modification in contrast to the glycol backbone. First, it is structurally closer to the actual deoxyribose found in DNA as it also contains a chain of three carbon atoms to connect two phosphate groups, contrary to the glycol linker that bears a chain of only two carbon atoms (Figure 4.15). Second, the threoninol backbone allows a modular approach to incorporate various functional groups by amide bond formation. It was already reported to be exploited to covalently attach histidine,[57] photo switches,[51,56,58] or fluorophores[53] to DNA. In this way, all amino acids (or better their deamino derivatives) or every functionality covalently attached to a carboxylic acid moiety can be converted into ligandosides.

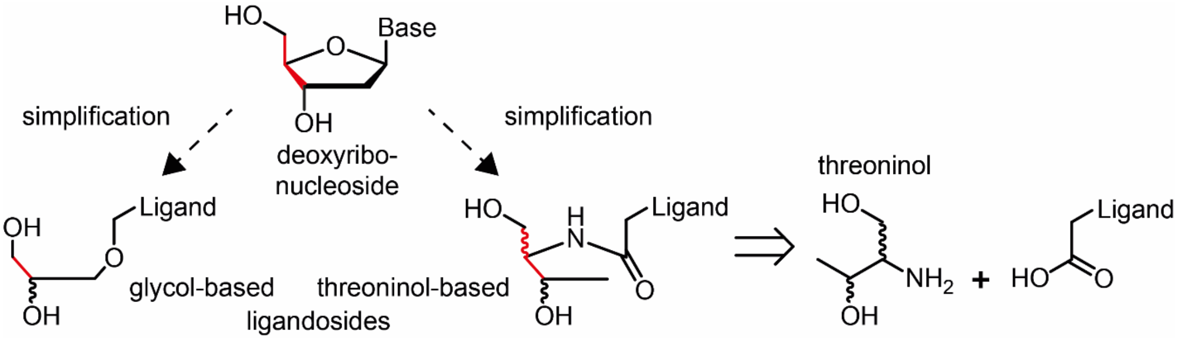

Figure 4.15: Comparison of the canonical deoxyribonucleoside with the simplified glycol- or threoninol-based ligandosides. The latter allows to convert every ligand functionality which is covalently attached to a carboxylic acid group (e.g. amino acids) into a ligandoside.

The thioether ligand functionality has already been introduced into G-quadruplexes as a glycol-based ligandoside **L**^{5} (Section 4.3.1) and was now transferred into phosphoramidite building block (*R*,*R*)-**29** corresponding to a threoninol-based ligandoside **L**^{6}. Therefore, the primary alcohol group of L-threoninol ((*R*,*R*)-**25**) was DMT-protected and the ligand functionality was attached *via* amide bond formation using a carbodiimide for activation of the carboxylic acid. Subsequent phosphitylation reaction yielded phosphoramidite building block (*R*,*R*)-**29** suitable for incorporation into oligonucleotides (Figure 4.17a, for detailed reaction procedures and analytics see Section 7.8). However, its incorporation into oligonucleotides and the investigation of G-quadruplex formation and metal binding were not part of this thesis and will be examined in future studies.

4.3.4 Synthesis of Thiol-Based Phosphoramidite and Incorporation into Oligonucleotides

As a last new ligand functionality, thiol groups were planned to be incorporated into G-quadruplexes. The attachment of thiol moieties into nucleic acids is already a broadly used approach in bioconjugation. They are, for example, attached for immobilizing oligonucleotides on gold surfaces or nanoparticles *via* chemisorption[59–61] or used to covalently bind labels (e.g. fluorescent labels) or proteins to DNA (Figure 4.16a and b).[62] However, commercially available building blocks for the incorporation of thiol groups into DNA *via* solid-phase synthesis can either be only attached at the 5'- or 3'-end of a sequence or contain a very long linker (Figure 4.16c).

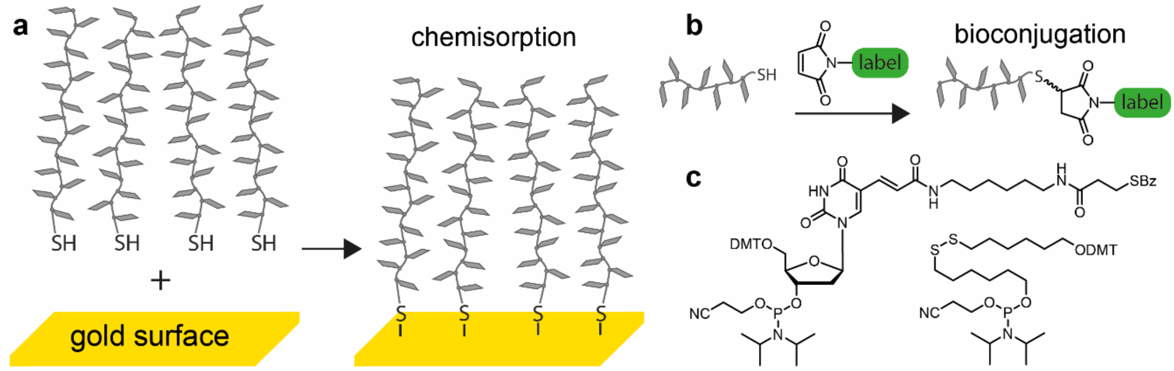

Figure 4.16: (**a**) Schematic immobilization of thiol-modified oligonucleotides on a gold surface *via* chemisorption. (**b**) Attachment of a label to an oligonucleotide by a Michael addition of a thiol group to a maleimide derivative. (**c**) Commercially available building blocks for incorporation of thiol groups into oligonucleotides *via* solid-phase DNA synthesis.

Since the thiol ligandoside was also planned to be incorporated within DNA sequences to build thiol-modified unimolecular G-quadruplexes and since a long linker is not suited to build prearranged ligand environments, a ligandoside **L**^{7} was used that has been reported before.[54] It was based on the threoninol backbone and the respective phosphoramidite building block (*R*,*R*)-**32** was synthesized in analogy to thioether phosphoramidite (*R*,*R*)-**29** (Figure 4.17a). To prevent undesired side reactions during solid-phase DNA synthesis, the thiol residue was protected by benzoylation, in contrast to the literature-reported protection strategy as a disulfide.[54] Two low-field shifted signals in the $^{31}P\{^1H\}$ NMR spectrum (in $CDCl_3$) proved the expected formation of two diastereomers (Figure 4.17b). Chemical shifts of $\delta = 148.0$ and 148.1 ppm are typical for P(III)-nuclei in phosphoramidites.

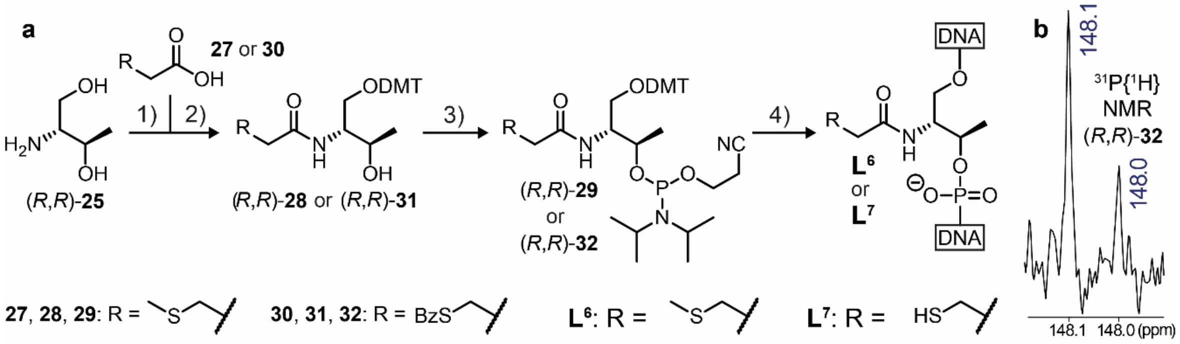

Figure 4.17: (**a**) Synthetic route to access the threoninol-based phosphoramidite building blocks (*R,R*)-**29** and (*R,R*)-**32** required to incorporate thioether ligandoside $\mathbf{L^6}$ or thiol ligandoside $\mathbf{L^7}$ into oligonucleotides during solid-phase DNA synthesis. 1) DMT-Cl, DMAP, pyridine; 2) DMAP, Et_3N, EDC, CH_2Cl_2; 3) CEDIP-Cl, DIPEA, CH_2Cl_2; 4) automated solid-phase DNA synthesis and deprotection. For detailed synthetic procedures, see Section 7.8. (**b**) $^{31}P\{^1H\}$ NMR spectrum (202 MHz, $CDCl_3$) of phosphoramidite (*R,R*)-**32** (crude product) showing two signals for two formed diastereomers.

Using phosphoramidite building block (*R,R*)-**32**, the thiol ligandoside $\mathbf{L^7}$ was, as usual, incorporated into short G-rich oligonucleotides (oligo **S**: 5'-$\mathbf{L^7}G_3$, oligo **T**: 5'-$\mathbf{L^7}G_4$) *via* solid-phase DNA synthesis. Care had to be taken with the subsequent cleavage from solid support and deprotection of the DNA strands. As a known problem applying standard conditions, deprotected thiol groups irreversibly react in a Michael addition with acrylonitrile, a side product from phosphate deprotection (Figure 4.18a and b). Therefore, phosphate groups were deprotected with 10% diethylamine in acetonitrile prior to cleavage from solid support and resulting acrylonitrile was washed out. After that, fast cleavage and deprotection were accomplished with AMA (Section 7.9).

Under the basic conditions, the oxidation of the thiol groups to the respective symmetric disulfides $\mathbf{S^{ox}}$ and $\mathbf{T^{ox}}$ ($G_n\mathbf{L^7}$-S-S-$\mathbf{L^7}G_n$, Figure 4.18c) was highly accelerated and completed within hours. Consequently, two product fractions were

---

oligo **S**: $\mathbf{L^7}$GG G, oligo **T**: $\mathbf{L^7}$GG GG; ligandoside $\mathbf{L^7}$: thiol ligand eluted during purification by semi-preparative reverse-phase HPLC directly after deprotection (gradient had to be adjusted). Keeping the samples overnight under aerobic, basic conditions usually resulted in a single product fraction containing the oxidized species. Purity of the disulfide-bridged oligonucleotides was confirmed by ESI mass spectrometry (Section 6.1).

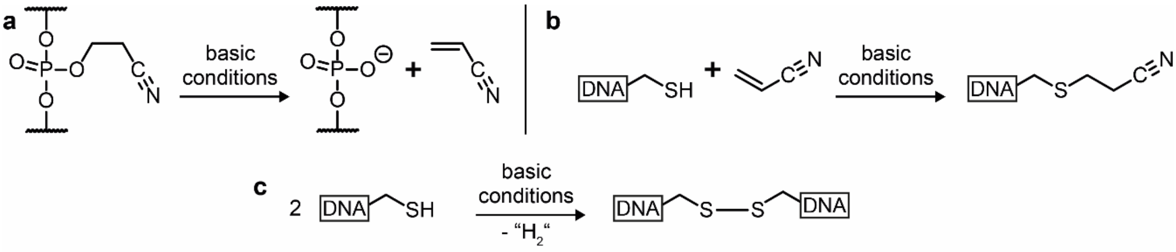

Figure 4.18: (**a**) Phosphate deprotection yields the Michael acceptor acrylonitrile. (**b**) Irreversible Michael addition between thiol group and acrylonitrile. (**c**) Oxidation of the thiol groups which is fast under basic conditions results in symmetric disulfides.

4.3.5 Formation of G-Quadruplexes with Disulfide-Bridges in Loop Regions

The disulfide-bridged oligonucleotides **S**^{ox} and **T**^{ox} were subsequently tested for their ability to fold into G-quadruplex structures. DNA strands containing two G-tracts connected by a loop region usually form bimolecular G-quadruplexes that adopt antiparallel topologies (Figure 4.19).[63] They can also assemble into parallelly oriented G-wires (Section 1.2.1) depending on factors such as DNA and electrolyte concentration or temperature.[64–67]

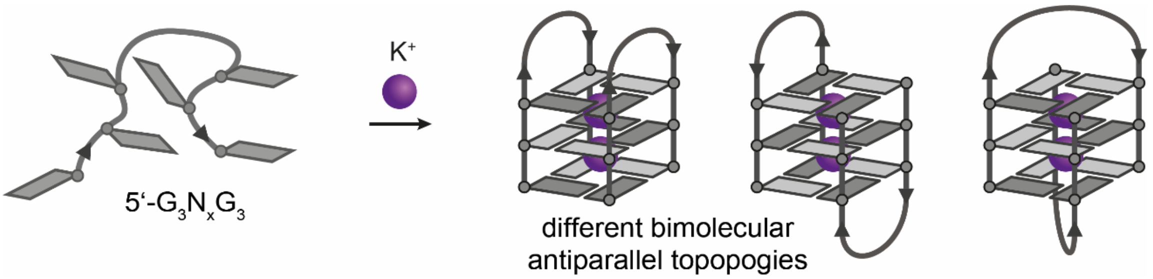

Figure 4.19: Oligonucleotides with two G-tracts separated by a loop region often fold into bimolecular antiparallel G-quadruplexes. The three shown topologies are examples for possible folding arrangements. Dark and light gray tiles indicate guanosines with *syn* or *anti* conformation.

---

oligo **S**: **L**^{7}GG G, oligo **T**: **L**^{7}GG GG; ligandoside **L**^{7}: thiol ligand

In oligos $\mathbf{S}^{\mathbf{ox}}$ and $\mathbf{T}^{\mathbf{ox}}$, on the other hand, the disulfide bridge causes a switch in strand orientation, as it connects the 5'-ends of the G-tracts. Hence, the formation of parallel bimolecular G-quadruplexes was expected. After annealing of $\mathbf{S}^{\mathbf{ox}}$ and $\mathbf{T}^{\mathbf{ox}}$, respectively, in the presence of Na^+ or K^+ ions at pH 7.2, CD spectra were recorded. However, in addition to the typical CD pattern expected for parallel G-quadruplex topologies, a maximum at 290 nm was observed which indicated the presence of heteropolar π-stacking of G-tetrads (Figure 4.20b and e). Heteropolar stacking is not consistent with a clean bimolecular parallel topology and several hypotheses were brought in for explanation: (i) A tetramolecular architecture containing two individual G-tetrad stacks has formed, where the 5'-terminal G-quartets π-stack on top of each other in a heteropolar fashion. (ii) Next to the parallel main topology, one or several antiparallel structures coexisted in solution, which are known to bear heteropolar G-tetrad stacks. (iii) The disulfide loops in a parallel G-quadruplex caused a structural distortion resulting in a flipping of the 5'-terminal G-quartet leading to heteropolar stacking (Figure 4.20a).

To obtain more information about the actual G-quadruplex structures, UV-based melting and reannealing experiments were conducted (Figure 4.20). Thermal difference spectra showed the typical signature for G-quadruplexes. Sigmoidal melting and annealing profiles were revealed both in the presence of Na^+ and K^+ ions for samples containing $\mathbf{S}^{\mathbf{ox}}$ with relatively high melting temperatures of $T_m = 17$ °C (with Na^+) and $T_m = 61$ °C (with K^+). The absence of any hysteresis effect confirmed fast folding kinetics which clearly contradicted hypothesis (i) and suggested bimolecular folding arrangements ($\mathbf{S}^{\mathbf{ox}}{}_2$). A sample with $\mathbf{T}^{\mathbf{ox}}$ in Na^+-containing solution showed a melting behavior with a melting temperature of $T_m = 68$ °C. As expected, no melting process was observed in the presence of K^+ ions, because G-quadruplexes bearing four G-quartets are usually very stable in K^+-containing solution ($T_m > 95$ °C). The clean sigmoidal melting profiles suggest the formation of a single folding topology and was incompatible with hypothesis (ii), where a mixture of species was assumed.

The G-quadruplex species of oligo $\mathbf{T}^{\mathbf{ox}}$ was further investigated by native ESI mass spectrometry (Figure 4.21). Next to a small fraction of single-stranded oligonucleotide, the main species consisted of two $\mathbf{T}^{\mathbf{ox}}$ strands and three specifically bound K^+ ions. This composition ruled out any tetramolecular species

---

oligo **S**: $\mathbf{L}^7$GG G, oligo **T**: $\mathbf{L}^7$GG GG; ligandoside $\mathbf{L}^7$: thiol ligand

(hypothesis (i)) and strongly indicated a bimolecular G-quadruplex (**T**$^{ox}{}_2$) with four G-quartets as the present secondary structure.

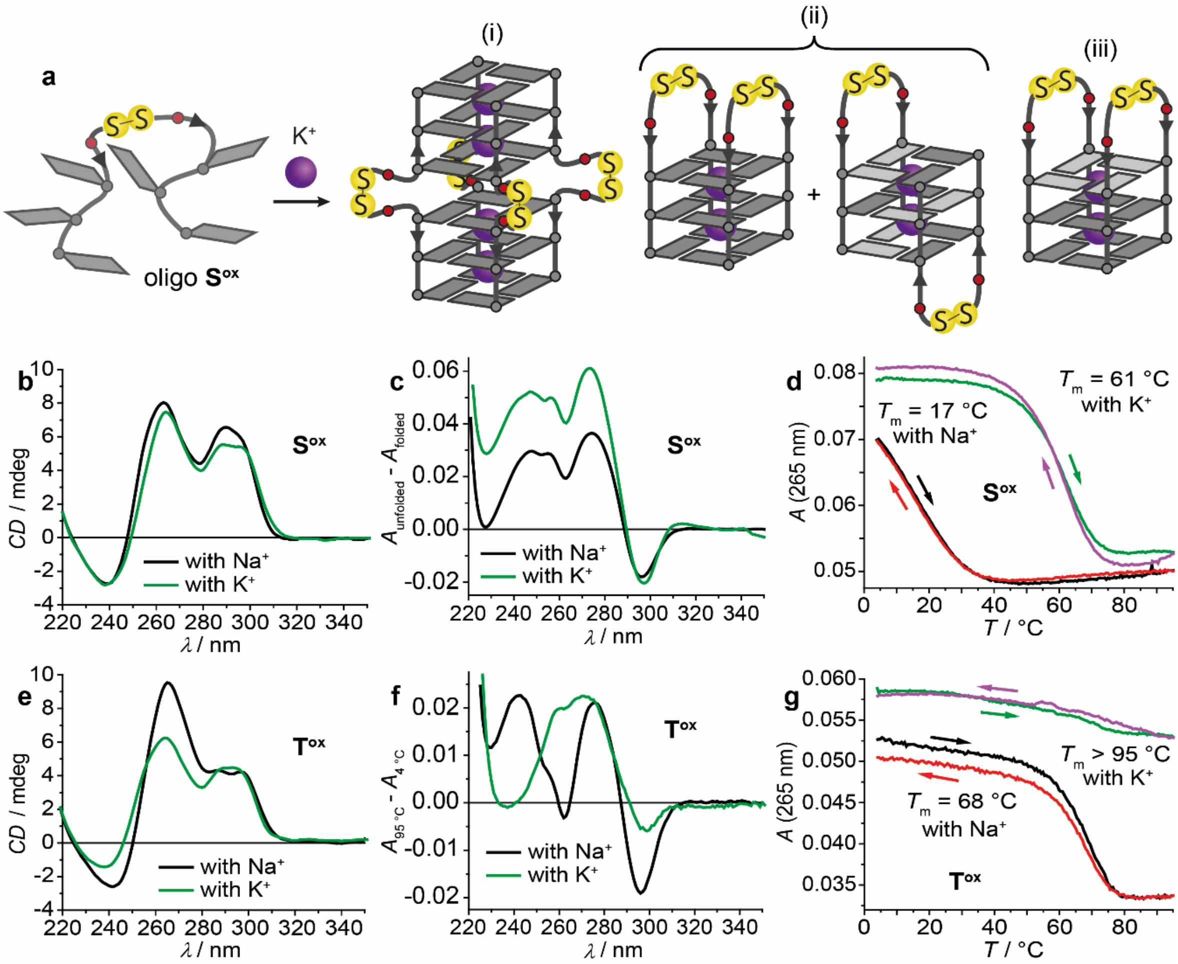

Figure 4.20: (**a**) Possible folded secondary G-quadruplex structures formed by disulfide-bridged oligo **S**^{ox} that might explain the heteropolar G-tetrad stacking suggested by CD spectroscopy. (**b**, **e**) CD spectra, (**c**, **f**) UV-based thermal difference spectra and (**d**, **g**) UV-based thermal melting and annealing profiles of folded G-quadruplex structure **S**$^{ox}{}_2$ (**b**-**d**) and **T**$^{ox}{}_2$ (**e**-**g**) in Na$^+$- or K$^+$-containing solution. Sample composition (**b**-**d**): 4 μM disulfide-bridged oligonucleotide (2 μM G-quadruplex), 100 mM NaCl or KCl, 10 mM lithium cacodylate buffer (pH 7.2). Sample composition (**e**-**g**): 2 μM disulfide-bridged oligonucleotide (1 μM G-quadruplex), 100 mM NaCl or KCl, 50 mM lithium cacodylate buffer (pH 7.2).

Considering all experimental results based on CD and UV spectroscopy and native ESI mass spectrometry, the most likely G-quadruplex structure that disulfide-bridged oligos **S**^{ox} and **T**^{ox} adopted was the bimolecular parallel topology, where the 5'-terminal G-tetrad was flipped due to a structural distortion caused by the disulfide loops (hypothesis (iii)). Terminal G-tetrad flipping is a known

---

oligo **S**: **L**^{7}GG G, oligo **T**: **L**^{7}GG GG; ligandoside **L**^{7}: thiol ligand

phenomenon and has been reported for several G-quadruplex structures induced either by interaction with a G-quadruplex-binding ligand[68] or by nucleoside modification.[69–71] However, more experimental data should be gathered to confirm this assumption. Methods such as ion mobility, native gel electrophoresis and especially NMR spectroscopy might give a more detailed insight. Also, the energetical comparison of different G4 conformations derived from MD simulations might provide additional information.

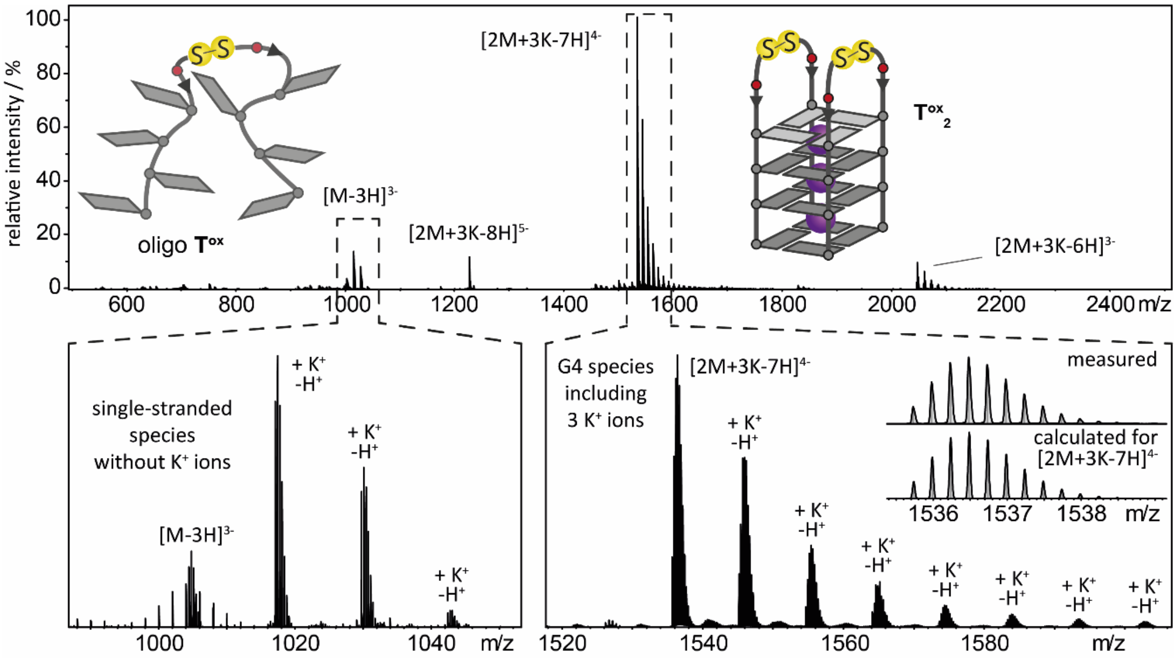

Figure 4.21: Native ESI mass spectrum of G-quadruplex **T**$^{ox}_2$ in K$^+$-containing solution. The dimeric main species with the three specifically bound K$^+$ ions confirmed the folded G-quadruplex structure in the gas phase. Sample composition: 25 µM oligo **T**^{ox}, 500 µM KCl, 50 mM trimethylammonium acetate buffer (pH 7.0) in a 1:1 (v/v) mixture of water and acetonitrile.

4.3.6 Reduction of Disulfide-Bridged Oligonucleotides

The subsequent attempt to reduce the disulfide-bridged oligonucleotides **S**^{ox} and **T**^{ox} was performed in a glove box in an oxygen-free environment to prevent reoxidation. Reducing agents frequently used in biochemistry and molecular biology for disulfide reduction are dithiothreitol (DTT)[72] and tris(2-carboxyethyl)-phosphine (TCEP, Figure 4.22).[73–76] The latter is available immobilized onto an agarose support allowing easy removal of the agent after reduction.

---

oligo **S**: **L**^{7}GG G, oligo **T**: **L**^{7}GG GG; ligandoside **L**^{7}: thiol ligand

The reduction of a 1 mM oligonucleotide stock solution (concentration referred to the fully reduced oligonucleotides) was performed in 100 mM DTT at room temperature for several hours. The reducing agent was subsequently removed by gel filtration (Section 7.9.5). The dilution caused by the purification method was about a factor of 10. Full reduction was confirmed by ESI mass spectrometry (shown as an example for oligo **S** in Figure 4.23a and b) and the absence of reducing agent was verified with UV spectroscopy. In addition, the concentration of thiol groups in the sample was determined with a colorimetric assay using Ellman's reagent (5,5'-dithio-bis-(2-nitrobenzoic acid), Figure 4.23c).[77–79] The good match between the oligonucleotide concentration obtained by absorption measurement at 260 nm and the colorimetrically determined thiol concentration (e.g. for oligo **S**: measured oligonucleotide concentration: 87 µM, determined thiol concentration: 82 µM) supported both the complete reduction of all disulfides and the entire removal of DTT.

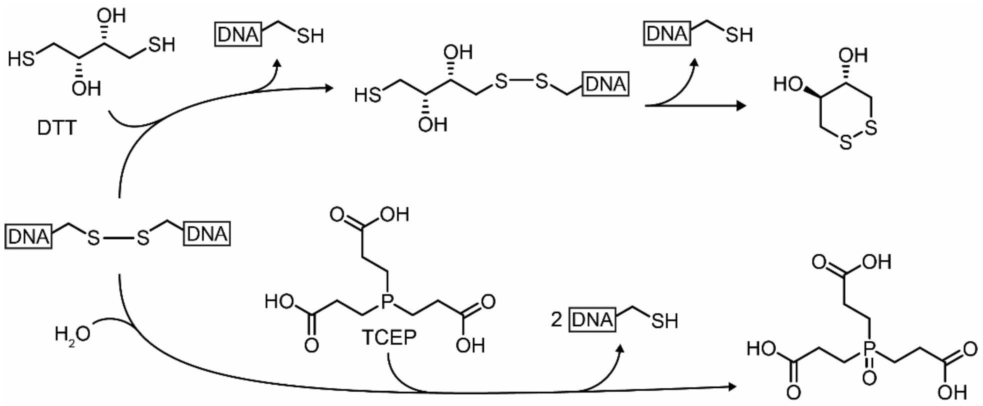

Figure 4.22: Typical reducing agents DTT and TCEP used in biochemistry for the reduction of disulfides.

In the reduced form, the thiol-modified oligonucleotides are suitable for the investigation of tetramolecular G-quadruplex formation and subsequent transition metal complexation of thiol-based preorganized coordination environments. However, these studies were not part of this thesis and will be examined in future work in the Clever Lab.

---

oligo **S**: $\mathbf{L}^7$GG G, oligo **T**: $\mathbf{L}^7$GG GG; ligandoside $\mathbf{L}^7$: thiol ligand

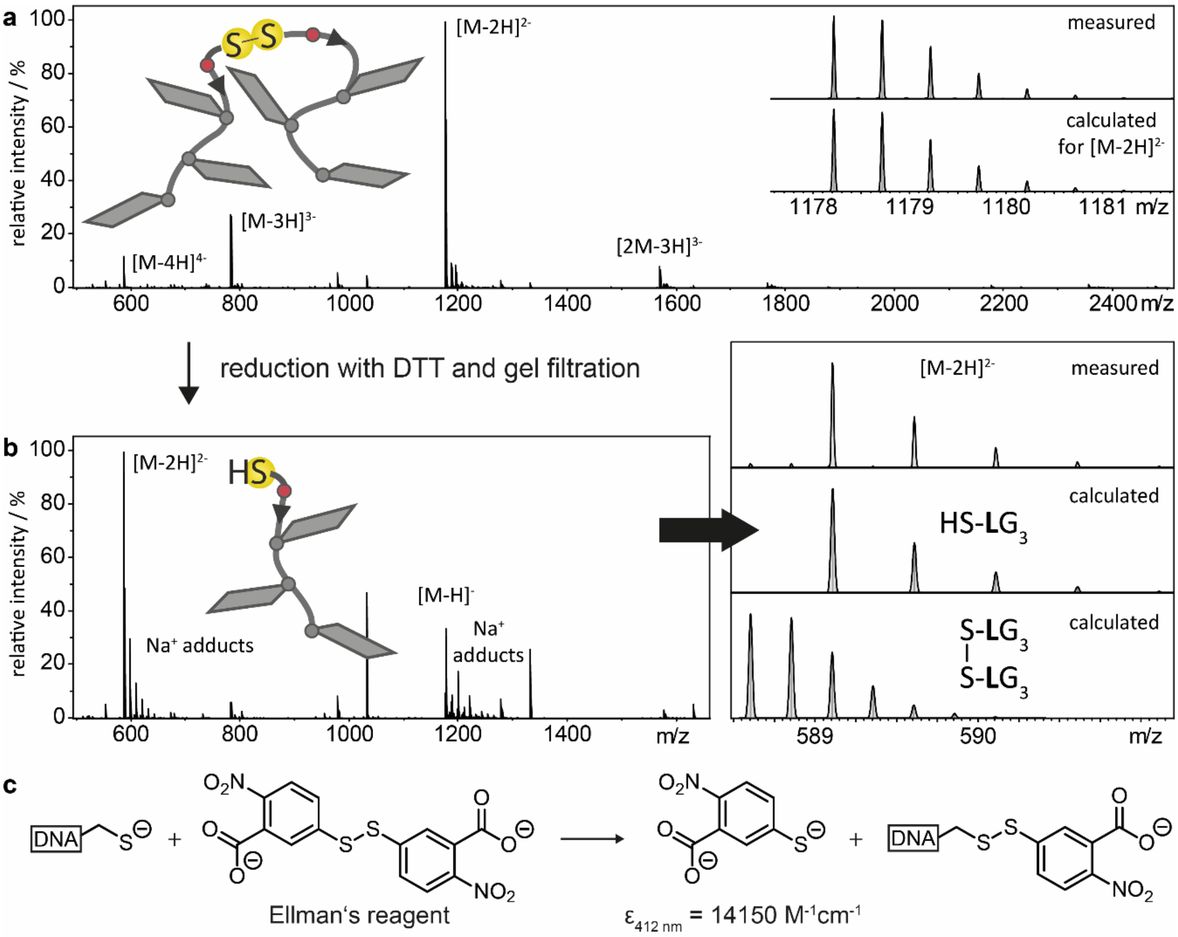

Figure 4.23: ESI mass spectra of oligo **S** (**a**) in the oxidized symmetric disulfide form ($\mathbf{S}^{\mathrm{ox}}$) or (**b**) in the reduced form containing the thiol group. (**c**) Selective colorimetric assay with Ellman's reagent for the concentration determination of thiol groups.[77–79]

4.4 Heteroleptic Coordination Environments in Unimolecular G-Quadruplexes

It should be mentioned here that the following results discussed in this section have been achieved together with Dr. Philip Punt in a collaboration with equal contributions. Consequently, the findings are also part of Dr. Punt's dissertation and were additionally recently published in a chemical journal.[1]

In recent work in the Clever Lab, the concept of ligandoside incorporation into the loop regions of unimolecular G-quadruplexes allowed a simple, controlled design of tailored coordination environments for transition metal complexation.[41,45] While the G-quadruplex stem served as a rigid platform, the modular approach facilitated the fine-tuning of ligand arrangements by varying the number and position of

---

oligo **S**: $\mathbf{L}^7$GG G, oligo **T**: $\mathbf{L}^7$GG GG; ligandoside $\mathbf{L}^7$: thiol ligand

ligandosides programmed in the DNA sequence during solid-phase synthesis. With this strategy, several tailored coordination environments with adjusted metal affinities were achieved (Section 4.1.2).

So far, only one type of ligandoside, based on pyridine[41] or imidazole[45] donors, was reported to be incorporated into a unimolecular G-quadruplex structure leading to homoleptic metal complexes. However, in the last sections, a variety of bioinspired donor groups with properties ranging from hard (carboxylates) to soft Lewis acid character (thioether and thiol) were transferred into ligandosides and incorporated into tetramolecular G-quadruplexes. The modular approach allows to combine all these ligandosides resulting in heteroleptic coordination environments in unimolecular G-quadruplexes. This advancement will help further tuning of ligand arrangements for tailored transition metal complex properties.

Inspiring examples for highly tailored coordination environments resulting in specific transition metal complex properties with numerous functions can be found in metallo-proteins (Section 4.1.1). A ligand combination frequently found in metallo-proteins comprises histidines and carboxylates (i.e. glutamate or aspartate). Examples are urease which contains a dinuclear Ni^{2+} complex[80] or the 2-His-1-carboxylate facial triad found in mononuclear non-heme iron enzymes or in Zn^{2+}-containing proteins.[81–83] Inspired by this ligand combination, our goal was to incorporate two distinct ligand functionalities into G-quadruplexes. The benzoate ligandoside $\mathbf{L^3}$ served as a glutamate/aspartate mimic, while an already literature-reported imidazole ligandoside $\mathbf{L^8}$ was used as a histidine analog.[44,45] For synthetic reasons, the linker to the imidazole ring in $\mathbf{L^8}$ was not bound to a carbon atom as found in histidine, but was bound to a nitrogen atom (Figure 4.25a).

4.4.1 Heteroleptic Environments in G-Quadruplexes with Four Ligandosides

First, we incorporated in total four ligandosides into the known htel22-$\mathbf{L}_4$b sequence (Figure 4.24a) with different possible ratios of the two ligandoside types (htel$\mathbf{L^3}_{4-n}\mathbf{L^8}_n$, n = 0–4, Table 4.1). Important to mention is that exclusively (*S*)-configured ligandosides were incorporated. It was shown before that the chosen configuration of the incorporated ligandoside only slightly affects G-quadruplex stability and its metal binding.[41,45] Also, only one out of several possible sequence isomers for each ligand ratio was investigated to work with a

---

ligandoside $\mathbf{L^1}$: pyridine ligand, ligandoside $\mathbf{L^3}$: benzoate ligand, ligandoside $\mathbf{L^8}$: imidazole ligand manageable number of oligonucleotides (5 out of 256 possibilities). Purity of the oligonucleotides was confirmed by ESI mass spectrometry and analytical reverse-phase HPLC (Section 6.1).

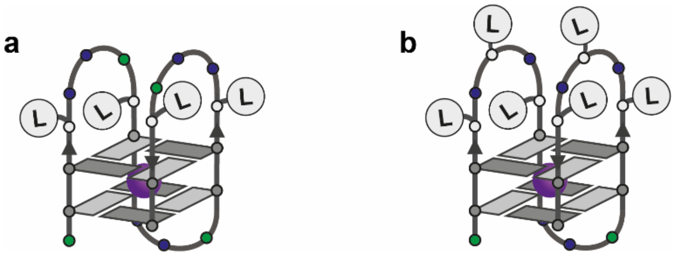

Figure 4.24: Schematic representation of ligandoside positions in unimolecular G-quadruplexes containing (**a**) four ligandosides (htel$\mathbf{L}^{3}_{4\text{-n}}\mathbf{L}^{8}_{\text{n}}$, n = 0–4) or (**b**) six ligandosides (htel$\mathbf{L}^{3}_{6\text{-n}}\mathbf{L}^{8}_{\text{n}}$, n = 2–4, 6).

The formation of unimolecular G-quadruplexes for all oligonucleotides (htel$\mathbf{L}^{3}_{4\text{-n}}\mathbf{L}^{8}_{\text{n}}$, n = 0–4) at pH 7.2 in the presence of K^+ ions was investigated with UV-based thermal denaturation studies. All sequences revealed a sigmoidal melting profile and characteristic TDS pattern proving their ability to form G-quadruplex structures (Figure 4.25 and Section 6.6).

Interestingly, the stability of the folded secondary structures strongly depended on the ratio of the incorporated ligandosides (Table 4.2). While G-quadruplex htel$\mathbf{L}^{3}_{4}$ containing four benzoate ligands ($\mathbf{L}^{3}$) showed a low melting temperature of T_m = 12 °C, successive replacement to the benzoate ligands with imidazole ligands ($\mathbf{L}^{8}$) led to G-quadruplexes with increasing thermal stability. Finally, G-quadruplex htel$\mathbf{L}^{8}_{4}$ containing four imidazole ligands ($\mathbf{L}^{8}$) showed a melting temperature of T_m = 33 °C.[45] The linear correlation between number of benzoate/imidazole ligands and the obtained melting temperature is illustrated in Figure 4.25e. This observation might be explained with the negative charge of the benzoate ligand at given pH, which leads to additional Coulomb repulsion between the ligands and the phosphate backbone in the folded structure and results in a decreased overall stability. The low stability of carboxylate-containing secondary structures was already described for tetramolecular G-quadruplexes in Section 4.2.

---

ligandoside $\mathbf{L}^{3}$: benzoate ligand, ligandoside $\mathbf{L}^{8}$: imidazole ligand

Table 4.1: Sequences of modified oligonucleotides containing different ligandosides ($\mathbf{L}^3$ and $\mathbf{L}^8$) to obtain heteroleptic coordination environments in unimolecular G-quadruplexes.

Name	Sequence (5’ → 3’)	Ratio (Benzoate:Imidazole)
htel22-$\mathbf{L}_4$b[a]	AGG $\mathbf{L}^1$TT A$\mathbf{L}^1$G GTT AGG $\mathbf{L}^1$TT A$\mathbf{L}^1$G G	-
htel$\mathbf{L}^3_4$	AGG $\mathbf{L}^3$TT A$\mathbf{L}^3$G GTT AGG $\mathbf{L}^3$TT A$\mathbf{L}^3$G G	4:0
htel$\mathbf{L}^3_3\mathbf{L}^8$	AGG $\mathbf{L}^8$TT A$\mathbf{L}^3$G GTT AGG $\mathbf{L}^3$TT A$\mathbf{L}^3$G G	3:1
htel$\mathbf{L}^3_2\mathbf{L}^8_2$	AGG $\mathbf{L}^8$TT A$\mathbf{L}^3$G GTT AGG $\mathbf{L}^8$TT A$\mathbf{L}^3$G G	2:2
htel$\mathbf{L}^3_1\mathbf{L}^8_3$	AGG $\mathbf{L}^8$TT A$\mathbf{L}^8$G GTT AGG $\mathbf{L}^8$TT A$\mathbf{L}^3$G G	1:3
htel$\mathbf{L}^8_4$A[b]	AGG $\mathbf{L}^8$TT A$\mathbf{L}^8$G GTT AGG $\mathbf{L}^8$TT A$\mathbf{L}^8$G G	0:4
htel$\mathbf{L}^8_4$B	AGG $\mathbf{L}^8$TT T$\mathbf{L}^8$G GTT AGG $\mathbf{L}^8$TT T$\mathbf{L}^8$G G	0:4
htel$\mathbf{L}^8_6$[b]	AGG $\mathbf{L}^8$T$\mathbf{L}^8$ T$\mathbf{L}^8$G GTT AGG $\mathbf{L}^8$T$\mathbf{L}^8$ T$\mathbf{L}^8$G G	0:6
htel$\mathbf{L}^3_4\mathbf{L}^8_2$	AGG $\mathbf{L}^3$T$\mathbf{L}^8$ T$\mathbf{L}^3$G GTT AGG $\mathbf{L}^3$T$\mathbf{L}^8$ T$\mathbf{L}^3$G G	4:2
htel$\mathbf{L}^3_3\mathbf{L}^8_3$	AGG $\mathbf{L}^3$T$\mathbf{L}^8$ T$\mathbf{L}^8$G GTT AGG $\mathbf{L}^3$T$\mathbf{L}^3$ T$\mathbf{L}^8$G G	3:3
htel$\mathbf{L}^3_2\mathbf{L}^8_4$	AGG $\mathbf{L}^8$T$\mathbf{L}^3$ T$\mathbf{L}^8$G GTT AGG $\mathbf{L}^8$T$\mathbf{L}^3$ T$\mathbf{L}^8$G G	2:4

[a] The sequence has previously been used in the Clever Lab[41] and is shown for comparison. [b] These oligonucleotides and related G-quadruplexes have already been published[45] and were therefore not investigated in this study, but data were compared.

The formation of unimolecular G-quadruplexes for all oligonucleotides (htel$\mathbf{L}^3_{4\text{-}n}\mathbf{L}^8_n$, n = 0–4) was further investigated with CD spectroscopy. As expected, CD signatures indicating antiparallel G-quadruplex topologies were exclusively observed (Figure 4.25d). In the antiparallel structures, all four incorporated ligand functionalities reside at the same side of the secondary structure forming a preorganized coordination environment.

Next, the binding of different transition metal cations was investigated. For htel$\mathbf{L}^3_4$ and htel$\mathbf{L}^3_3\mathbf{L}^8$, thermal denaturation experiments showed no signs for interaction (ΔT_m = 0 °C) with the examined transition metal cations (Co^{2+}, Ni^{2+}, Cu^{2+}, Zn^{2+} and VO^{2+}). This changed for htel$\mathbf{L}^3_2\mathbf{L}^8_2$ and htel$\mathbf{L}^3\mathbf{L}^8_3$ that revealed a weak stabilization after addition of one equivalent of Cu^{2+} (ΔT_m = +1 °C and +4 °C, respectively).

---

ligandoside $\mathbf{L}^1$: pyridine ligand, ligandoside $\mathbf{L}^3$: benzoate ligand, ligandoside $\mathbf{L}^8$: imidazole ligand

These stabilization effects, however, were small compared to all-imidazole G-quadruplex htel$\mathbf{L}^{8}_{4}$A (ΔT_m = +23 °C, Table 4.2).[45] Addition of more Cu^{2+} equivalents resulted in no further stabilization consistent with a specific binding of Cu^{2+} ions. CD spectroscopy further confirmed retention of the antiparallel topology after Cu^{2+}-binding (Section 6.10).

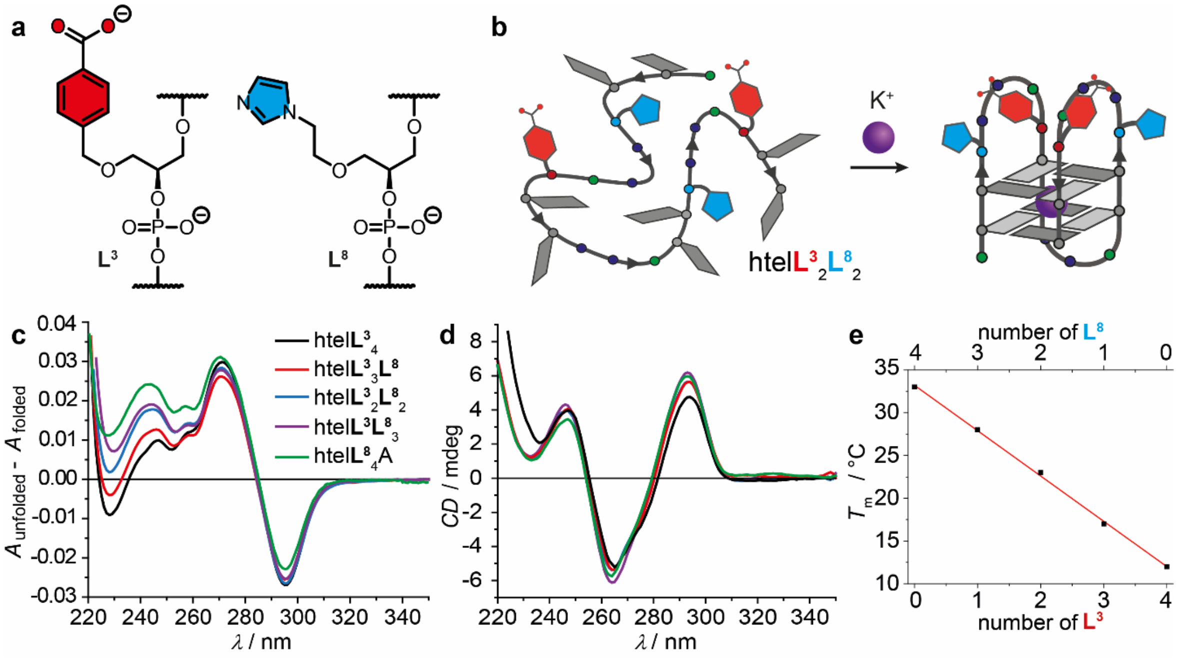

Figure 4.25: (**a**) Chemical structures of ligandosides $\mathbf{L}^3$ and $\mathbf{L}^8$ bearing the benzoate and imidazole functionality, respectively. (**b**) Folding of modified unimolecular G-quadruplex htel$\mathbf{L}^{3}_{2}\mathbf{L}^{8}_{2}$ containing a combination of the two different ligandosides. (**c**) UV-based thermal difference spectra and (**d**) CD spectra of G-quadruplexes htel$\mathbf{L}^{3}_{4-n}\mathbf{L}^{8}_{n}$ (n = 0–4). (**e**) Linear correlation between number of benzoate/imidazole ligands and the obtained melting temperature. For actual melting curves, see Section 6.6. Sample composition: 1.88 µM oligonucleotide, 100 mM KCl, 10 mM lithium cacodylate buffer (pH 7.2).

The described finding raised the question whether the benzoate ligands were at all involved in binding of the Cu^{2+} ions or if coordination was solely accomplished by the imidazole ligands. While this question is in general difficult to answer experimentally, clearer evidence for the role of the benzoate ligands was obtained with G-quadruplexes containing six ligandosides that are discussed in the next section.

---

ligandoside $\mathbf{L}^3$: benzoate ligand, ligandoside $\mathbf{L}^8$: imidazole ligand

Table 4.2: Overview of thermal denaturation temperatures and thermal stabilization upon addition of different transition metal ions for ligand-modified unimolecular G-quadruplexes with four incorporated ligandosides.[a]

Name	T_m / °C (ΔT_m / °C)					Ratio
	-	$Co(NO_3)_2$	$NiSO_4$	$CuSO_4$	ZnI_2	(Benzoate:Imidazole)
htel$\mathbf{L^3}_4$	12	12 (0)	12 (0)	12 (0)	12 (0)	4:0
htel$\mathbf{L^3}_3\mathbf{L^8}$	17	17 (0)	17 (0)	17 (0)	17 (0)	3:1
htel$\mathbf{L^3}_2\mathbf{L^8}_2$	23	23 (0)	23 (0)	24 (+1)	23 (0)	2:2
htel$\mathbf{L^3}_1\mathbf{L^8}_3$	28	28 (0)	28 (0)	32 (+4)	28 (0)	1:3
htel$\mathbf{L^8}_4$A[b]	33	35 (+2)	45 (+12)	56 (+23)	36 (+3)	0:4

[a] Sample composition: 1.88 µM oligonucleotide, 100 mM KCl, 10 mM lithium cacodylate buffer (pH 7.2) and (if present) 1.88 µM $Co(NO_3)_2$, $NiSO_4$, $CuSO_4$ or ZnI_2. [b] Data were taken from published studies for comparison.[45]

4.4.2 Heteroleptic Environments in G-Quadruplexes with Six Ligandosides

Jahn-Teller-distorted Cu^{2+} ions usually favor the coordination of four strongly associated ligands in a square-planar geometry with two additional ligands loosely bound in axial positions. The results reported in the previous sections suggested that at least two imidazole ligandosides are required to complex Cu^{2+} ions within a G-quadruplex structure. Based on this finding, a new series of G-quadruplex-forming sequences was designed containing in total six ligandosides (htel$\mathbf{L^3}_{6\text{-}n}\mathbf{L^8}_n$, n = 2–4, Table 4.1). They were based on the reported G-quadruplex htel$\mathbf{L^8}_6$ where the two additional ligandosides were positioned in two lateral loop regions (Figure 4.24b).[45] The correlation between number of benzoate/imidazole ligands and melting temperature in the absence of transition metal ions was again obtained (although in this case, no linear correlation was found) and the exclusive formation of antiparallel G-quadruplex topologies was confirmed by CD spectroscopy both in absence and presence of transition metals (Section 6.10).

Comparing thermal stabilization upon Cu^{2+} addition for G-quadruplexes htel$\mathbf{L^3}_4\mathbf{L^8}_2$ (ΔT_m = +6 °C) and htel$\mathbf{L^3}_2\mathbf{L^8}_2$ (ΔT_m = +1 °C), an involvement of the additional benzoate ligands in metal binding in htel$\mathbf{L^3}_4\mathbf{L^8}_2$ seemed likely. However, the absolute thermal stabilities of both Cu^{2+}-coordinating G-quadruplexes were nearly identical (T_m = 23 °C and 24 °C). The data suggested that the benzoate ligands

---

ligandoside $\mathbf{L^3}$: benzoate ligand, ligandoside $\mathbf{L^8}$: imidazole ligand were not involved in metal coordination, but the destabilizing effect of negatively charged benzoates in the absence of transition metal ions was compensated upon binding of the dicationic Cu^{2+} ions.

Table 4.3: Overview of thermal denaturation temperatures and thermal stabilization upon addition of different transition metal ions for ligand-modified unimolecular G-quadruplexes with six incorporated ligandosides.[a]

Name	T_m / °C (ΔT_m / °C)					Ratio
	-	$Co(NO_3)_2$	$NiSO_4$	$CuSO_4$	ZnI_2	(Benzoate:Imidazole)
htel$\mathbf{L}^{8}_{4}$B	40	40 (0)	46 (+6)	60 (+20)	40 (0)	0:4
htel$\mathbf{L}^{8}_{6}$[b]	36	44 (+8)	59 (+23)	54 (+18)	44 (+8)	0:6
htel$\mathbf{L}^{3}_{4}\mathbf{L}^{8}_{2}$	17	17 (0)	18 (+1)	23 (+6)	18 (+1)	4:2
htel$\mathbf{L}^{3}_{3}\mathbf{L}^{8}_{3}$	26	25 (-1)	26 (0)	35 (+9)	31 (+5)	3:3
htel$\mathbf{L}^{3}_{2}\mathbf{L}^{8}_{4}$	26	27 (+1)	48 (+22)	60 (+34)	32 (+6)	2:4

[a] Sample composition: 1.88 µM oligonucleotide, 100 mM KCl, 10 mM lithium cacodylate buffer (pH 7.2) and (if present) 1.88 µM $Co(NO_3)_2$, $NiSO_4$, $CuSO_4$ or ZnI_2. [b] Data were taken from published results for comparison.[45]

Further successive replacement of benzoate ligands with imidazole ligands resulted in increasing Cu^{2+}-mediated thermal stabilizations from $\Delta T_m = +9$ °C (htel$\mathbf{L}^{3}_{3}\mathbf{L}^{8}_{3}$) to $\Delta T_m = +34$ °C (htel$\mathbf{L}^{3}_{2}\mathbf{L}^{8}_{4}$, Figure 4.26a and b). The latter extremely high metal-mediated thermal stabilization is unprecedented for ligand-modified unimolecular G-quadruplexes and is significantly larger than found for the reported homoleptic Cu^{2+} complexes in G-quadruplexes htel$\mathbf{L}^{8}_{4}$A ($\Delta T_m = +23$ °C) and htel$\mathbf{L}^{8}_{6}$ ($\Delta T_m = +18$ °C, Table 4.3).

To elucidate whether benzoate ligands were involved in metal complexation in htel$\mathbf{L}^{3}_{2}\mathbf{L}^{8}_{4}$, a control G-quadruplex htel$\mathbf{L}^{8}_{4}$B was investigated, where the two benzoate ligandosides residing in the loops were replaced by thymidines. As expected, the stability in absence of Cu^{2+} ions was significantly higher for htel$\mathbf{L}^{8}_{4}$B ($T_m = 40$ °C) due to the missing destabilizing effect of the negatively charged benzoate groups. However, the stability with a bound Cu^{2+} ion was identical for htel$\mathbf{L}^{8}_{4}$B and htel$\mathbf{L}^{3}_{2}\mathbf{L}^{8}_{4}$ ($T_m = 60$ °C). This result again suggested that the benzoate ligands might not be involved in metal complexation, but that the binding of dicationic Cu^{2+} compensates the destabilizing effect of negatively charged

---

ligandoside $\mathbf{L}^{3}$: benzoate ligand, ligandoside $\mathbf{L}^{8}$: imidazole ligand benzoate ligands within a G-quadruplex. In other words, the incorporation of benzoate ligands greatly enhances the stabilizing effect of Cu^{2+} ions coordinating to G-quadruplexes not by stabilizing the metal-bound species but by destabilizing the transition metal-free G-quadruplex (Figure 4.26d). This finding might be valuable for the tailored design of DNA-based switches, where Cu^{2+} ions can serve as external stimuli. Adjustable stability differences between Cu^{2+}-free and Cu^{2+}-bound states allow to achieve clear and quantitative switching events in variable temperature windows.

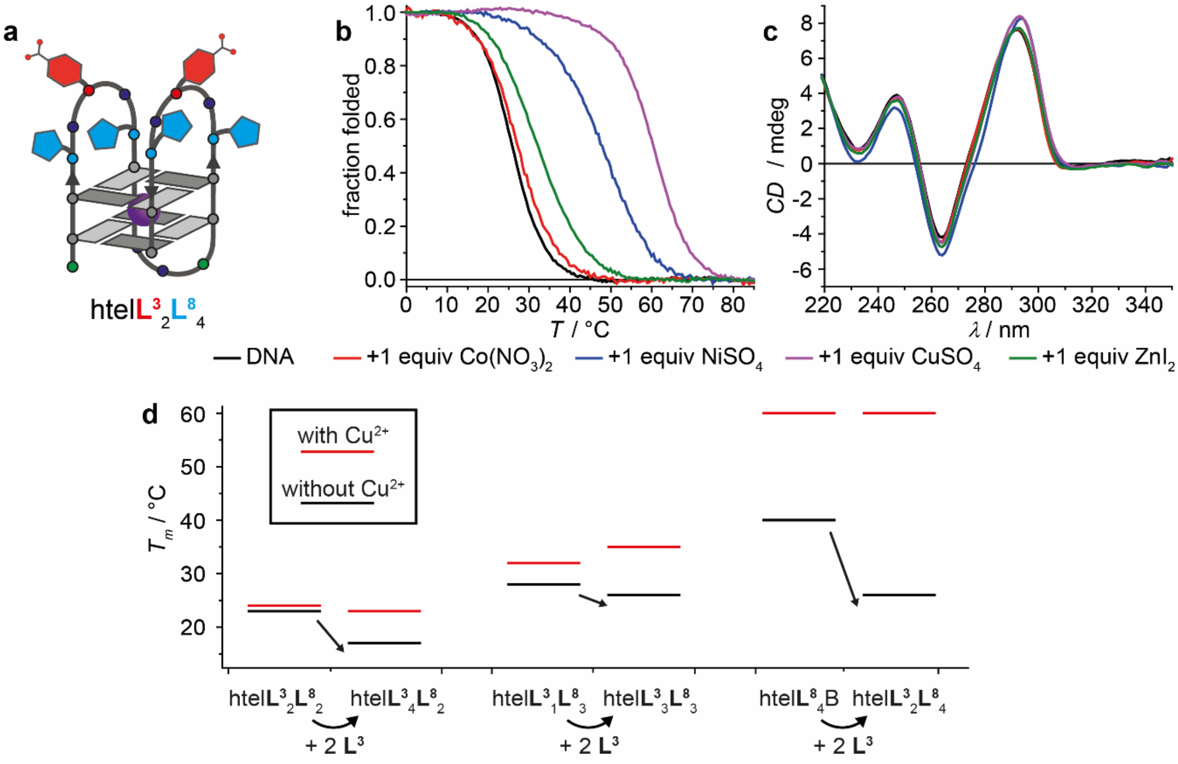

Figure 4.26: (**a**) Schematic representation of G-quadruplex htel$\mathbf{L}^3_2\mathbf{L}^8_4$ containing four imidazole ligands and two benzoate ligands in the loops. (**b**) Melting curves and (**c**) CD spectra of G-quadruplex htel$\mathbf{L}^3_2\mathbf{L}^8_4$ in absence or presence of different transition metal salts. (**d**) Plot of thermal stabilities of different G-quadruplexes in absence or presence of Cu^{2+} ions. An increased number of benzoate ligands leads to no big changes in the stability of the Cu^{2+}-bound species but strongly destabilizes the Cu^{2+}-free species. Sample composition: 1.88 µM oligonucleotide, 100 mM KCl, 10 mM lithium cacodylate buffer (pH 7.2) and (if present) 1.88 µM $Co(NO_3)_2$, $NiSO_4$, $CuSO_4$ or ZnI_2.

In addition to Cu^{2+} ions, also Ni^{2+} and Zn^{2+} ions were coordinated by G-quadruplex htel$\mathbf{L}^3_2\mathbf{L}^8_4$ resulting in high thermal stabilizations (Table 4.3). Cu^{2+} and Ni^{2+} complexes of htel$\mathbf{L}^3_2\mathbf{L}^8_4$ were additionally investigated by native ESI mass

---

ligandoside $\mathbf{L}^3$: benzoate ligand, ligandoside $\mathbf{L}^8$: imidazole ligand

spectrometry (Figure 4.27). One specifically bound K^+ ion (next to a statistical mixture of unspecific K^+ adducts) indicated the folded G-quadruplex structure in the gas phase. Furthermore, one specifically bound Cu^{2+} or Ni^{2+} ion, respectively, confirmed specific transition metal binding in a 1:1 stoichiometry.

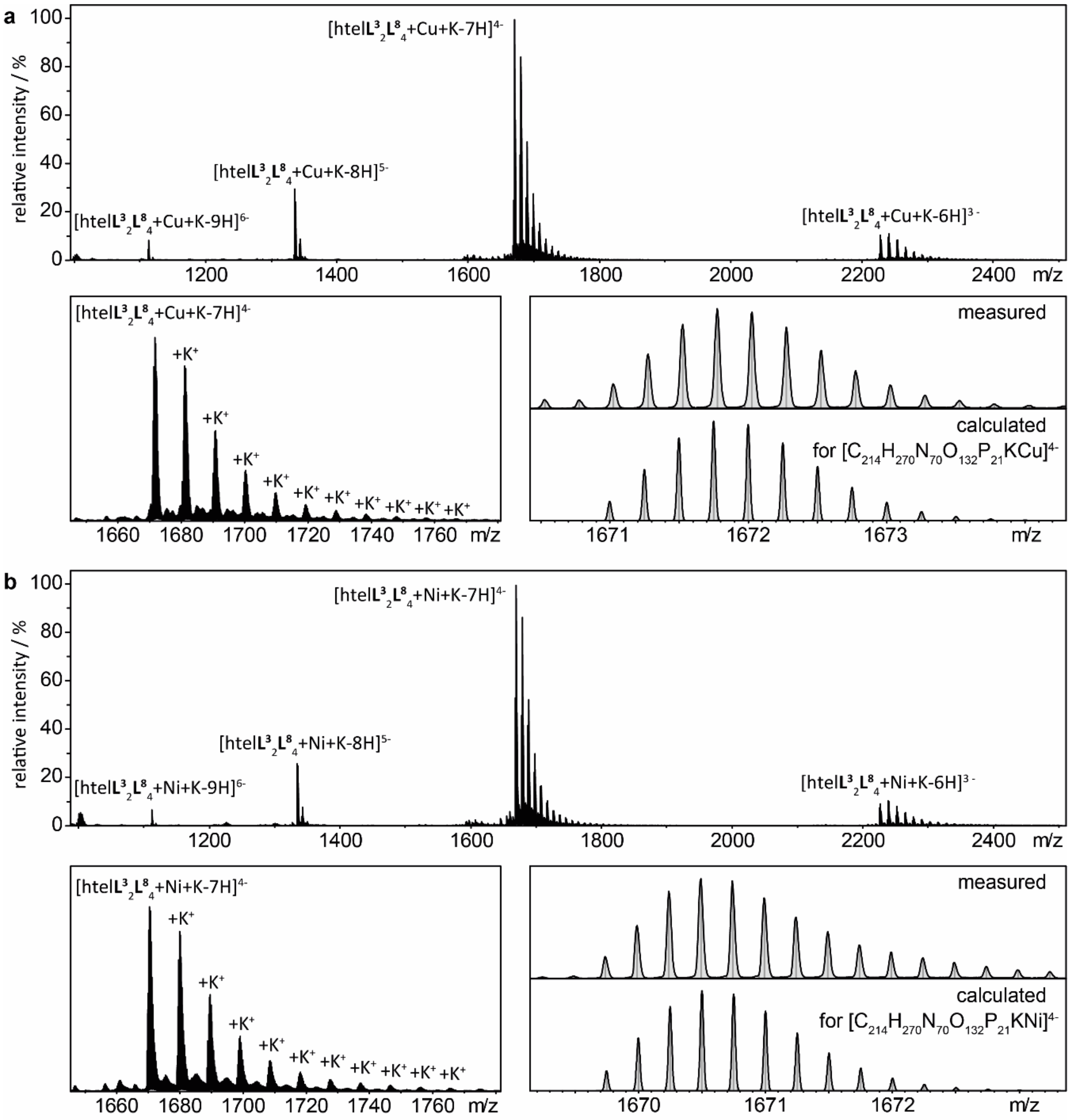

Figure 4.27: Native ESI mass spectra of G-quadruplex htel$\mathbf{L}^3_2\mathbf{L}^8_4$ after addition of (**a**) $CuSO_4$ or (**b**) $NiSO_4$. The main species with one specifically bound K^+ ion and the absence of a peak corresponding to the oligonucleotide without K^+ ion confirmed the G-quadruplex structure in the gas phase. The specific adducts with one Cu^{2+}/Ni^{2+} ion revealed 1:1 stoichiometries. Sample composition: 12.5 µM htel$\mathbf{L}^3_2\mathbf{L}^8_4$, 12.5 µM $CuSO_4$ or $NiSO_4$, 500 µM KCl, 50 mM trimethylammonium acetate buffer (pH 7.0) in a 1:1 (v/v) mixture of water and acetonitrile.

---

ligandoside $\mathbf{L}^3$: benzoate ligand, ligandoside $\mathbf{L}^8$: imidazole ligand

As it remained unclear whether benzoate ligands are involved in transition metal binding, it is refrained from schematically depict metal-binding G-quadruplexes in this section. Nevertheless, these first examples of combining different ligand functionalities in modified G-quadruplexes for obtaining preorganized heteroleptic coordination environments showcased this concept to be suitable for designing ligand arrangements with fine-tuned metal affinities. It paves the way for developing metal complexes with various properties in a DNA environment useful for mimicking enzyme activity and creating artificial DNAyzmes.

4.5 Summary

In this chapter, the design and synthesis of a variety of ligandosides with different donor groups was described. The ligand functionalities ranged from hard Lewis bases (benzoate and aliphatic carboxylate) to soft Lewis donors (thioether and thiol) and were inspired by metal-binding ligands found in metallo-proteins. The new ligandosides were attached at the 5'-end of G-rich oligonucleotides by solid-phase DNA synthesis and the formation of parallel tetramolecular G-quadruplex structures was confirmed by UV and CD spectroscopy as well as native ESI mass spectrometry. Negatively charged carboxylate ligands turned out to strongly destabilize the secondary DNA structures, most probably due to Coulomb repulsion. The resulting prearranged coordination environments in the folded G-quadruplexes were tested for their metal binding ability. A variety of hard and soft metal ions were investigated (VO^{2+}, Ce^{3+}, Gd^{3+}, Fe^{3+}, Co^{2+}, Ni^{2+} Cu^{2+}, Zn^{2+}, Hg^{2+}, Cd^{2+}, Ag^{+}, Au^{3+}, Pd^{2+}). Unfortunately, no increase in thermal stability of the overall secondary structures was detected suggesting that no metal ions were complexated. However, the investigations are not yet completed. Especially the metal binding ability of thiol-modified G-quadruplexes remains to be examined.

To showcase that the modular approach of incorporating ligandosides into unimolecular G-quadruplexes is suitable for the formation of tailored ligand environments resulting in metal complexes with tunable properties, two different ligand functionalities were incorporated in one DNA structure to achieve heteroleptic ligand arrangements. Inspired by a combination of histidine and carboxylate ligands frequently found in metallo-proteins, a series of G-quadruplex-forming sequences containing both benzoate- and imidazole-based ligandosides were synthesized. Their ratio and the overall number of ligands were varied. Formation of antiparallel unimolecular G-quadruplexes and metal ion complexation in the preorganized coordination environment was investigated again by CD and UV spectroscopy and native ESI mass spectrometry. Addition of transition metal ions such as Cu^{2+}, Ni^{2+} or Zn^{2+} resulted in the formation of 1:1 metal complexes embedded in the G-quadruplex structures. The variation of the numbers of benzoate and imidazole ligands resulted in G-quadruplexes with different metal binding affinities, although an involvement of the benzoate ligands in metal coordination remained unclear. The destabilizing effect of negatively charged benzoate ligands on the overall G-quadruplex stability was compensated by binding of dicationic Cu^{2+} ions leading to an unprecedentedly high thermal stabilization (ΔT_m = +34 °C for a G-quadruplex containing two benzoate ligands and four imidazole ligands) that has not been observed for ligand-modified unimolecular G-quadruplexes. The strong metal-triggered stabilizing effect might be valuable for the design of DNA-based switches. This first example of combining different ligand functionalities in modified G-quadruplex structures paves the way for the tailored design of heteroleptic metal complexes and opens possibilities in mimicking active metal complexes found in metallo-proteins in a DNA-based environment.

4.6 References

[1] P. M. Punt, L. M. Stratmann, S. Sevim, L. Knauer, C. Strohmann, G. H. Clever, *Front. Chem.* **2020**, *8*, 26.

[2] W. Kaim, B. Schwederski, *Bioanorganische Chemie*, Vol. 4, Vieweg+Teubner, **2005**.

[3] S. I. Mann, T. Heinisch, T. R. Ward, A. S. Borovik, *Chem. Commun.* **2018**, *54*, 4413–4416.

[4] S. A. Cook, A. S. Borovik, *Acc. Chem. Res.* **2015**, *48*, 2407–2414.

[5] R. L. Shook, A. S. Borovik, *Inorg. Chem.* **2010**, *49*, 3646–3660.

[6] P. Hosseinzadeh, Y. Lu, *Biochim. Biophys. Acta, Bioenerg.* **2016**, *1857*, 557–581.

[7] K. Sato, T. Kohzuma, C. Dennison, *J. Am. Chem. Soc.* **2003**, *125*, 2101–2112.

[8] P. Comba, *Coord. Chem. Rev.* **2000**, *200*, 217–245.

[9] G. S. Kachalova, A. C. Shosheva, G. P. Bourenkov, A. A. Donchev, M. I. Dimitrov, H. D. Bartunik, *J. Inorg. Biochem.* **2012**, *115*, 174–181.

[10] Y. Yuan, M. F. Tam, V. Simplaceanu, C. Ho, *Chem. Rev.* **2015**, *115*, 1702–1724.

[11] A. P. S. Samuel, D. T. Co, C. L. Stern, M. R. Wasielewski, *J. Am. Chem. Soc.* **2010**, *132*, 8813–8815.

[12] J. S. Kanady, E. Y. Tsui, M. W. Day, T. Agapie, *Science* **2011**, *333*, 733–736.

[13] J. S. Anderson, J. Rittle, J. C. Peters, *Nature* **2013**, *501*, 84–87.

[14] B. Dicke, A. Hoffmann, J. Stanek, M. S. Rampp, B. Grimm-Lebsanft, F. Biebl, D. Rukser, B. Maerz, D. Göries, M. Naumova, M. Biednov, G. Neuber, A. Wetzel, S. M. Hofmann, P. Roedig, A. Meents, J. Bielecki, J. Andreasson, K. R. Beyerlein, H. N. Chapman, C. Bressler, W. Zinth, M. Rübhausen, S. Herres-Pawlis, *Nat. Chem.* **2018**, *10*, 355–362.

[15] Y. Lu, N. Yeung, N. Sieracki, N. M. Marshall, *Nature* **2009**, *460*, 855–862.

[16] W. Ghattas, V. Dubosclard, A. Wick, A. Bendelac, R. Guillot, R. Ricoux, J.-P. Mahy, *J. Am. Chem. Soc.* **2018**, *140*, 8756–8762.

[17] P. Srivastava, H. Yang, K. Ellis-Guardiola, J. C. Lewis, *Nat. Commun.* **2015**, *6*, 7789.

[18] J. Zhao, D. G. Bachmann, M. Lenz, D. G. Gillingham, T. R. Ward, *Catal. Sci. Technol.* **2018**, *8*, 2294–2298.

[19] L. A. Churchfield, F. A. Tezcan, *Acc. Chem. Res.* **2019**, *52*, 345–355.

[20] W. J. Song, F. A. Tezcan, *Science* **2014**, *346*, 1525–1528.

[21] L. Villarino, K. E. Splan, E. Reddem, L. Alonso-Cotchico, C. G. de Souza, A. Lledós, J. Maréchal, A. W. H. Thunnissen, G. Roelfes, *Angew. Chem. Int. Ed.* **2018**, *57*, 7785–7789.

[22] H. M. Key, P. Dydio, D. S. Clark, J. F. Hartwig, *Nature* **2016**, *534*, 534–537.

[23] H. J. Davis, T. R. Ward, *ACS Central Sci.* **2019**, *5*, 1120–1136.

[24] I. Drienovská, G. Roelfes, *Nat. Catal.* **2020**, *3*, 193–202.

[25] P. S. Coelho, E. M. Brustad, A. Kannan, F. H. Arnold, *Science* **2013**, *339*, 307–310.

[26] M. Jeschek, R. Reuter, T. Heinisch, C. Trindler, J. Klehr, S. Panke, T. R. Ward, *Nature* **2016**, *537*, 661–665.

[27] S. B. J. Kan, R. D. Lewis, K. Chen, F. H. Arnold, *Science* **2016**, *354*, 1048–1051.

[28] S. B. J. Kan, X. Huang, Y. Gumulya, K. Chen, F. H. Arnold, *Nature* **2017**, *552*, 132–136.

[29] S. C. Hammer, G. Kubik, E. Watkins, S. Huang, H. Minges, F. H. Arnold, *Science* **2017**, *358*, 215–218.

[30] F. H. Arnold, *Angew. Chem. Int. Ed.* **2018**, *57*, 4143–4148.

[31] K. Chen, X. Huang, S. B. J. Kan, R. K. Zhang, F. H. Arnold, *Science* **2018**, *360*, 71–75.

[32] O. F. Brandenberg, K. Chen, F. H. Arnold, *J. Am. Chem. Soc.* **2019**, *141*, 8989–8995.

[33] K. Chen, F. H. Arnold, *Nat. Catal.* **2020**, *3*, 203–213.

[34] G. A. Khoury, J. Smadbeck, C. A. Kieslich, C. A. Floudas, *Trends Biotechnol.* **2014**, *32*, 99–109.

[35] P.-S. Huang, S. E. Boyken, D. Baker, *Nature* **2016**, *537*, 320–327.

[36] B. Koepnick, J. Flatten, T. Husain, A. Ford, D.-A. Silva, M. J. Bick, A. Bauer, G. Liu, Y. Ishida, A. Boykov, R. D. Estep, S. Kleinfelter, T. Nørgård-Solano, L. Wei, F. Players, G. T. Montelione, F. DiMaio, Z. Popović, F. Khatib, S. Cooper, D. Baker, *Nature* **2019**, *570*, 390–394.

[37] B. Basanta, M. J. Bick, A. K. Bera, C. Norn, C. M. Chow, L. P. Carter, I. Goreshnik, F. Dimaio, D. Baker, *Proc. Natl. Acad. Sci. U. S. A.* **2020**, *117*, 22135–22145.

[38] K. Schlosser, Y. Li, *Chem. Biol.* **2009**, *16*, 311–322.

[39] C. E. McGhee, R. J. Lake, Y. Lu in *Artificial Metalloenzymes and MetalloDNAzymes in Catalysis: From Design to Applications* (Eds.: M. Diéguez, J.-E. Bäckvall, O. Pàmies), Wiley-VCH, **2018**.

[40] D. M. Engelhard, R. Pievo, G. H. Clever, *Angew. Chem. Int. Ed.* **2013**, *52*, 12843–12847.

[41] D. M. Engelhard, J. Nowack, G. H. Clever, *Angew. Chem. Int. Ed.* **2017**, *56*, 11640–11644.

[42] D. M. Engelhard, L. M. Stratmann, G. H. Clever, *Chem. Eur. J.* **2018**, *24*, 2117–2125.

[43] D. M. Engelhard, A. Meyer, A. Berndhäuser, O. Schiemann, G. H. Clever, *Chem. Commun.* **2018**, *54*, 7455–7458.

[44] P. M. Punt, G. H. Clever, *Chem. Sci.* **2019**, *10*, 2513–2518.

[45] P. M. Punt, G. H. Clever, *Chem. Eur. J.* **2019**, *25*, 13987–13993.

[46] L. M. Stratmann, Y. Kutin, M. Kasanmascheff, G. H. Clever, *Angew. Chem. Int. Ed.* **2021**, *60*, 4939–4947.

[47] F. Katzsch, A. S. Münch, F. O. R. L. Mertens, E. Weber, *J. Mol. Struct.* **2014**, *1064*, 122–129.

[48] L. Zhang, A. Peritz, E. Meggers, *J. Am. Chem. Soc.* **2005**, *127*, 4174–4175.

[49] L. Zhang, A. E. Peritz, P. J. Carroll, E. Meggers, *Synthesis* **2006**, *2006*, 645–653.

[50] M. K. Schlegel, L.-O. Essen, E. Meggers, *J. Am. Chem. Soc.* **2008**, *130*, 8158–8159.

[51] X. Liang, N. Takenaka, H. Nishioka, H. Asanuma, *Chem. Asian J.* **2008**, *3*, 553–560.

[52] H. Asanuma, T. Toda, K. Murayama, X. Liang, H. Kashida, *J. Am. Chem. Soc.* **2010**, *132*, 14702–14703.

[53] H. Kashida, K. Sekiguchi, X. Liang, H. Asanuma, *J. Am. Chem. Soc.* **2010**, *132*, 6223–6230.

[54] S. Pérez-Rentero, S. Grijalvo, R. Ferreira, R. Eritja, *Molecules* **2012**, *17*, 10026–10045.

[55] K. Murayama, Y. Tanaka, T. Toda, H. Kashida, H. Asanuma, *Chem. Eur. J.* **2013**, *19*, 14151–14158.

[56] H. Asanuma, T. Ishikawa, Y. Yamano, K. Murayama, X. Liang, *ChemPhotoChem* **2019**, *3*, 418–424.

[57] S. Park, H. Matsui, K. Fukumoto, J. H. Yum, H. Sugiyama, *RSC Adv.* **2020**, *10*, 9717–9722.

[58] H. Asanuma, X. Liang, H. Nishioka, D. Matsunaga, M. Liu, M. Komiyama, *Nat. Protoc.* **2007**, *2*, 203–212.

[59] T. M. Herne, M. J. Tarlov, *J. Am. Chem. Soc.* **1997**, *119*, 8916–8920.

[60] A. B. Steel, T. M. Herne, M. J. Tarlov, *Anal. Chem.* **1998**, *70*, 4670–4677.

[61] D. Y. Petrovykh, H. Kimura-Suda, L. J. Whitman, M. J. Tarlov, *J. Am. Chem. Soc.* **2003**, *125*, 5219–5226.

[62] M. H. Stenzel, *ACS Macro Lett.* **2013**, *2*, 14–18.

[63] S. Burge, G. N. Parkinson, P. Hazel, A. K. Todd, S. Neidle, *Nucleic Acids Res.* **2006**, *34*, 5402–5415.

[64] T. C. Marsh, E. Henderson, *Biochemistry* **1994**, *33*, 10718–10724.

[65] T. C. Marsh, J. Vesenka, E. Henderson, *Nucleic Acids Res.* **1995**, *23*, 696–700.

[66] K. Bose, C. J. Lech, B. Heddi, A. T. Phan, *Nat. Commun.* **2018**, *9*, 1959.

[67] D. Miyoshi, H. Karimata, Z.-M. Wang, K. Koumoto, N. Sugimoto, *J. Am. Chem. Soc.* **2007**, *129*, 5919–5925.

[68] G. R. Clark, P. D. Pytel, C. J. Squire, *Nucleic Acids Res.* **2012**, *40*, 5731–5738.

[69] P. L. T. Tran, A. Virgilio, V. Esposito, G. Citarella, J.-L. Mergny, A. Galeone, *Biochimie* **2011**, *93*, 399–408.

[70] J. Dickerhoff, K. Weisz, *Angew. Chem. Int. Ed.* **2015**, *54*, 5588–5591.

[71] B. Karg, L. Haase, A. Funke, J. Dickerhoff, K. Weisz, *Biochemistry* **2016**, *55*, 6949–6955.

[72] W. W. Cleland, *Biochemistry* **1964**, *3*, 480–482.

[73] U. Th. Rüegg, J. Rudinger, *Methods Enzymol.* **1977**, *47*, 111–116.

[74] T. L. Kirley, *Anal. Biochem.* **1989**, *180*, 231–236.

[75] M. E. Levison, A. S. Josephson, D. M. Kirschenbaum, *Experientia* **1969**, *25*, 126–127.

[76] J. C. Han, G. Y. Han, *Anal. Biochem.* **1994**, *220*, 5–10.

[77] G. L. Ellman, *Arch. Biochem. Biophys.* **1959**, *82*, 70–77.

[78] P. W. Riddles, R. L. Blakeley, B. Zerner, *Anal. Biochem.* **1979**, *94*, 75–81.

[79] P. W. Riddles, R. L. Blakeley, B. Zerner, *Methods Enzymol.* **1983**, *91*, 49–60.

[80] L. Mazzei, F. Musiani, S. Ciurli, *J. Biol. Inorg. Chem.* **2020**, *25*, 829–845.

[81] E. L. Hegg, L. Q. Jr, *Eur. J. Biochem.* **1997**, *250*, 625–629.

[82] S. J. Friese, B. E. Kucera, L. Que,, W. B. Tolman, *Inorg. Chem.* **2006**, *45*, 8003–8005.

[83] P. C. A. Bruijnincx, G. van Koten, R. J. M. K. Gebbink, *Chem. Soc. Rev.* **2008**, *37*, 2716–2744.

5 Outlook

EPR-based methods for intermolecular distance measurements between Cu(pyridine)$_4$ spin labels, specially designed for incorporation into G-quadruplex structures, provide extremely narrow distance distributions. As shown in the first part of this thesis (Chapter 3), the tool has the potential to answer important questions on the structure of higher-order DNA architectures. The formation of higher-order adducts by the multitude of unimolecular G-quadruplexes formed in the telomeric region at the end of chromosomes in combination with their non-covalent interactions with drug-like G-quadruplex binders is a hot topic of research with importance for structural and chemical biology and medicinal chemistry. However, the structure elucidation with methods such as NMR spectroscopy or single-crystal X-ray diffraction has so far been unsuccessful due to dynamic and flexibility of the DNA architectures. Therefore, future projects should focus on the incorporation on the Cu^{2+}-based spin labels in long structural model systems for G-quadruplex-forming telomeric overhangs. A careful spatial installation of the Cu^{2+} complexes would allow to detect the proposed higher-order structures (e.g. the beads-on-a-string motif or consecutive π-stacking of parallel G-quadruplexes, Figure 5.1b) under different environmental conditions such as molecular crowding to mimic cell-like environments. So far, Cu(pyridine)$_4$ quartets have not been successfully incorporated into parallel unimolecular G-quadruplexes, which is a prerequisite for the investigation of telomeric higher-order structures and should be addressed first (Figure 5.1a).

Another promising aspect of the EPR-based measurements of Cu^{2+}-labeled G-quadruplexes is the extraction of additional geometric parameters, as demonstrated for G-quadruplex dimers. Since complex DNA constructs with duplex-bridged unimolecular G-quadruplexes and the distance measurements between the Cu(pyridine)$_4$ quartets residing in the four-stranded segments have been established in this thesis, the relative orientation of the capping G-quadruplexes might also be determined. This strategy will allow to detect bending or kinking of the bridging duplex fragment which is often the result of protein binding (e.g. TATA box-binding protein or Trp repressor protein). In addition, other external stimuli such as transition metal ions, DNA binder (e.g. cisplatin) or DNA damage induce special conformational changes of duplex DNA.

Therefore, the introduced EPR-based method allows the time-dependent monitoring of these conformational changes by both detecting changes in the Cu^{2+}-Cu^{2+} distance and in the relative orientation of the capping G-quadruplexes (Figure 5.2).

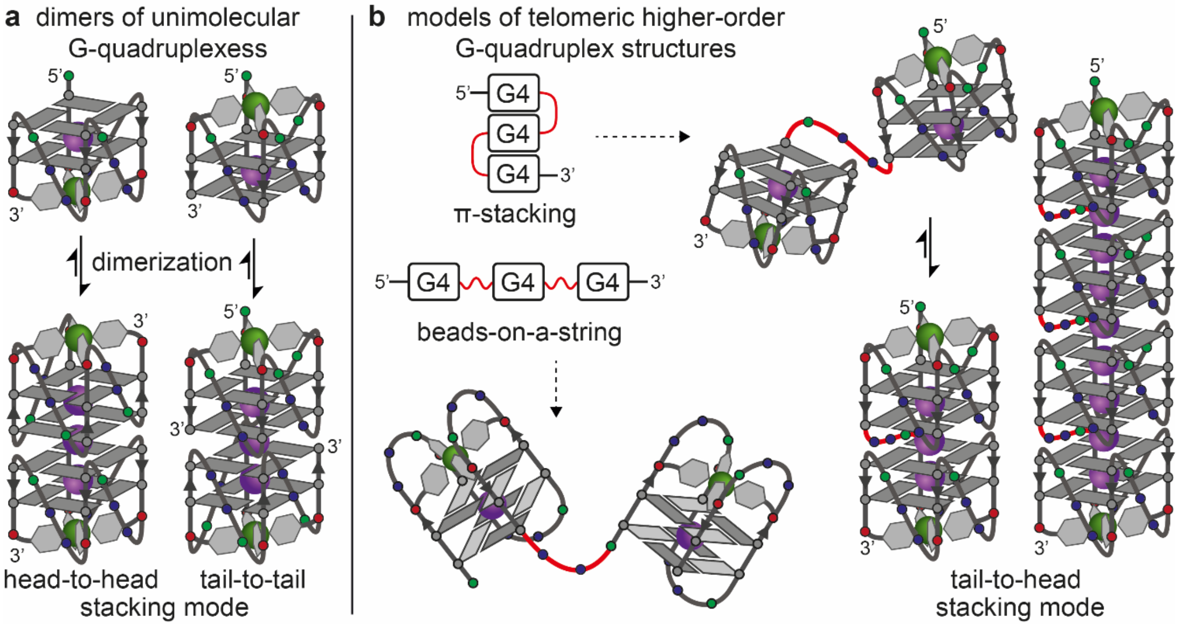

Figure 5.1: (**a**) Site-directed spin labeling of parallel unimolecular G-quadruplexes for the detection of corresponding head-to-head or tail-to-tail stacked dimeric species. (**b**) Model systems of telomeric higher-order G-quadruplex structures discussed in the literature and specific spin labeling for their detection under different environmental conditions.

Further promising fields to investigate using the Cu(pyridine)$_4$ quartets inserted into G-quadruplexes in combination with the EPR-based methods are (i) DNA-protein interactions by direct intermolecular distance measurements between spin-labeled proteins and G-quadruplexes, (ii) additional studies on G-quadruplex-binding ligands that intrinsically carry a spin label (e.g. metal porphyrins or metal salphens), or (iii) the formation of long G-tetrad arrays formed at lower pH by GMP that can be capped and detected with spin-labeled tetramolecular G-quadruplexes and might be interesting as supramolecular DNA-based materials.

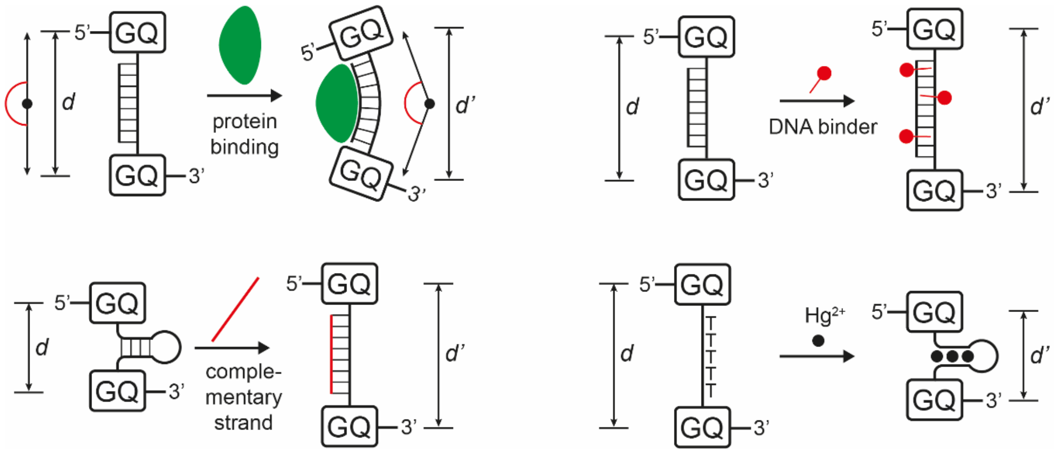

Figure 5.2: Examples for DNA structures capped with spin-labeled G-quadruplexes (GQ). Different external stimuli induce conformational changes which will be detected with pulsed dipolar EPR methods resulting in a different Cu^{2+}-Cu^{2+} distance and/or a different relative orientation of the spin labels with respect to each other.

In the second part of the thesis, a variety of new ligandosides with different donor groups was incorporated into G-quadruplex structures (Chapter 4). Inspired by ligands frequently found in metallo-proteins, carboxylates, thioethers and thiols were introduced in addition to the already established pyridine and imidazole functionalities. The variation of kind, number and positioning of the ligandosides within a sequence forming unimolecular G-quadruplexes results in distinct heteroleptic coordination environments. The modular approach allows to design tailored coordination spheres for transition metal complexes with fine-tuned properties.

In future studies, this approach should be exploited to mimic functional groups found in metallo-proteins with potential application in asymmetric catalysis, hydrogen production and more. A promising idea is to mimic plastocyanin, a small electron transfer protein with a $Cu^{+/2+}$ center coordinated by two histidine, one cysteine and one methionine ligand (Figure 4.1). Incorporation of these four donors into a G-quadruplex structure can be achieved in a tetrahedral or a square-planar fashion which will have a great influence on the redox potential of the resulting copper complex embedded in the DNA structure.

Highly interesting are also thiol-modified G-quadruplexes as they might be suitable anchors to install iron-sulfur clusters into DNA structures which opens further possibilities of electron transport and redox chemistry in DNA-based devices (Figure 5.3). With the goal of generating a new family of DNA-based redox modules for applications important in green chemistry, e.g. hydrogen production or enantioselective synthesis, a cooperation with the group of Prof. Dr. Thomas Happe, expert in semiartificial biocatalysts, was initiated.

Additionally, the option to oxidize thiol modifications to disulfide functions could serve as strategy to stabilize (higher-order) G-quadruplex structures as it is well-known in the protein world. The reversibility of the disulfide formation (dynamic covalent chemistry) can be used as trigger to switch between different G-quadruplex topologies.

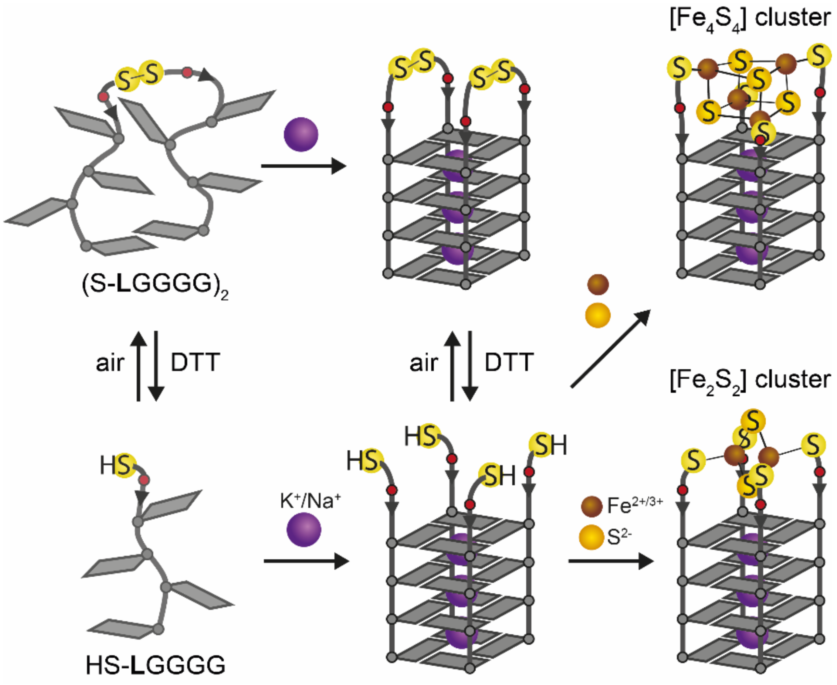

Figure 5.3: Thiol groups in modified G-quadruplexes can be used to reversibly form stabilizing disulfide bridges and might serve as anchors to install iron-sulfur clusters into the DNA structures.

All in all, the concept of covalently incorporating transition metal complexes in DNA G-quadruplex structures bears tremendous potential to answer biologically relevant questions and to contribute functionality in the field of DNA nanotechnology.

6 Methods, Analytical Procedures and Additional Data

In this chapter, analytical procedures are described in detail which have been used for the characterization of DNA samples throughout this thesis. Analytical data that have not been explicitly shown in the results sections (Chapters 3 and 4) can be found here.

6.1 Analytics of Oligonucleotides

6.1.1 Analytical RP-HPLC

To check the purity of the synthesized and purified oligonucleotides, samples (10 µL) with DNA concentrations of around 500 µM in 20 mM TMAA pH 7 or TEAA pH 7.0 were prepared and analytical RP-HPLC was performed on an *Agilent Technologies 1260 Infinity II* system equipped with an autosampler, column oven, DAD detector and a *Macherey-Nagel EC 250/4.6 NUCLEODUR 100-5 C18ec* column (oven temperature: 60 °C, flow rate: 0.75 mL/min, solvent A: 50 mM TEAA pH 7.0, solvent B: 70:30 MeCN/50 mM TEAA pH 7.0). The RP-HPLC traces including the used solvent gradient are shown below. Purity is given in percent relative to the trace total peak areas.

Oligo A (5'-TT**L**^{1} GGG (95%))

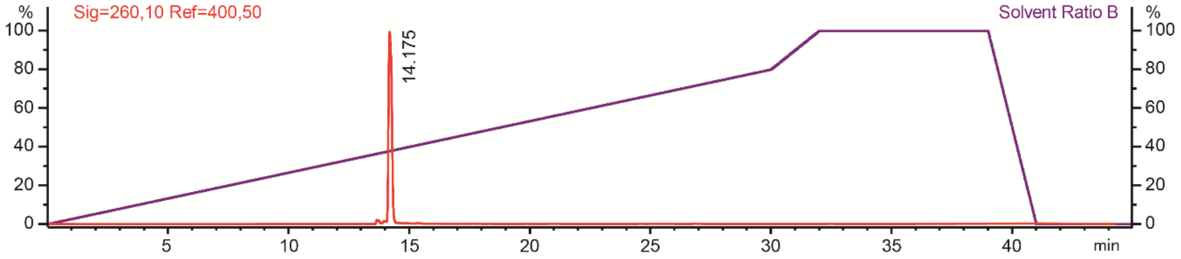

Oligo B (5'-T**L**^{1}G GGG (96%))

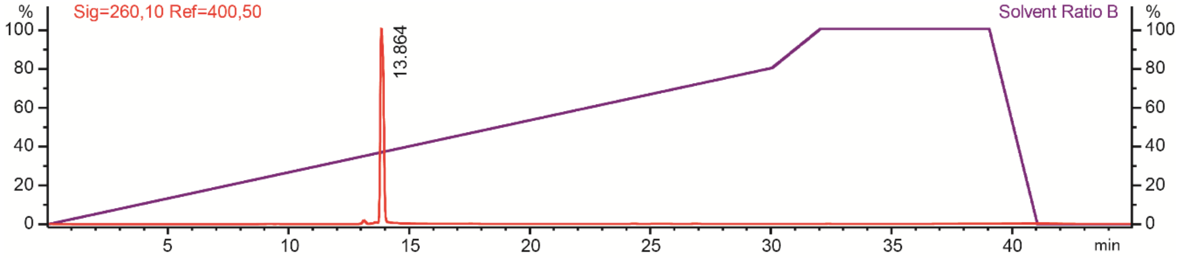

Oligo C (5’-TT**L**^{1} GGG T (91%))

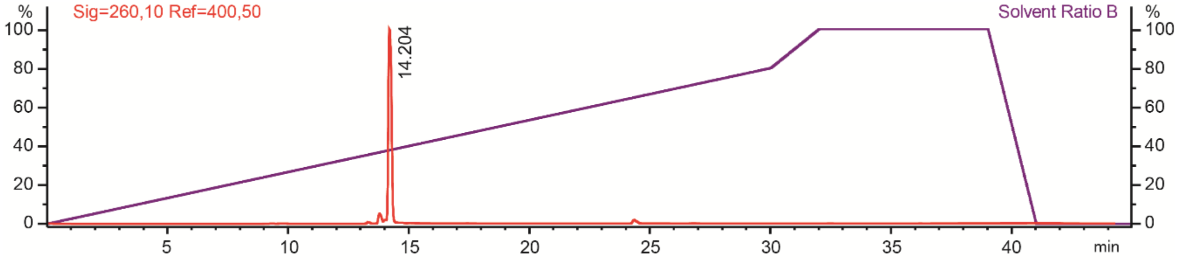

Oligo D (5’-GGG **L**^{1}TT (95%))

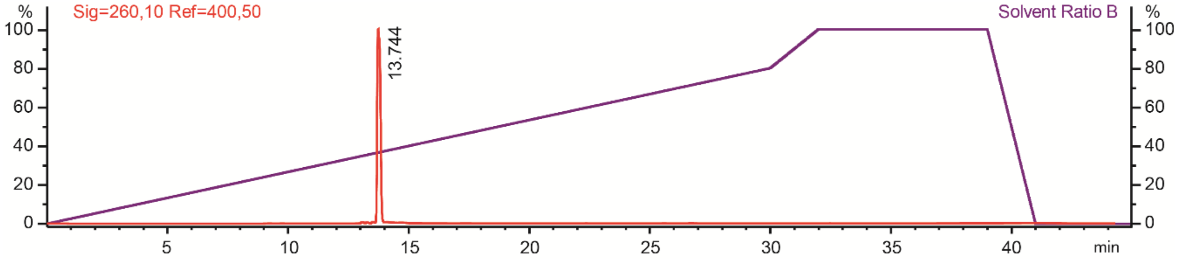

Oligo E (5’-GGG G**L**^{1}T (92%))

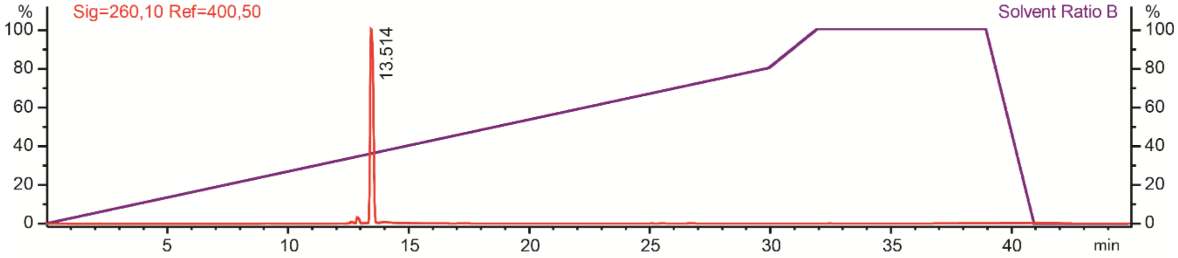

Oligo F (5’-TGG G**L**^{1}T T (93%))

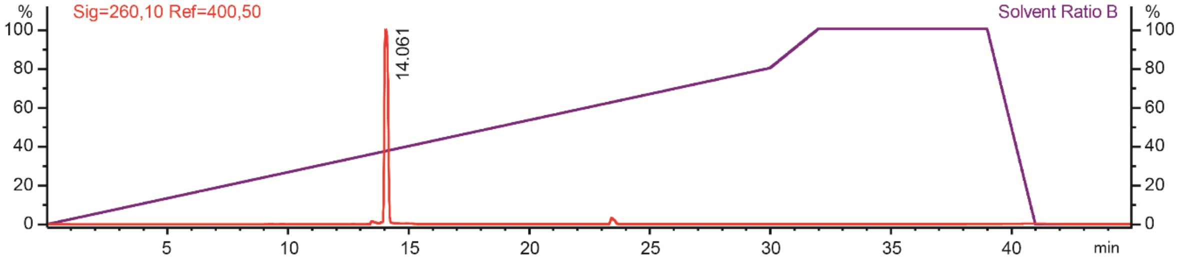

Oligo G (5’-A GG**L**^{1} TTA **L**^{1}GG TTA GG**L**^{1} TTA **L**^{1}GG ATA CAG CTT AT (94%))

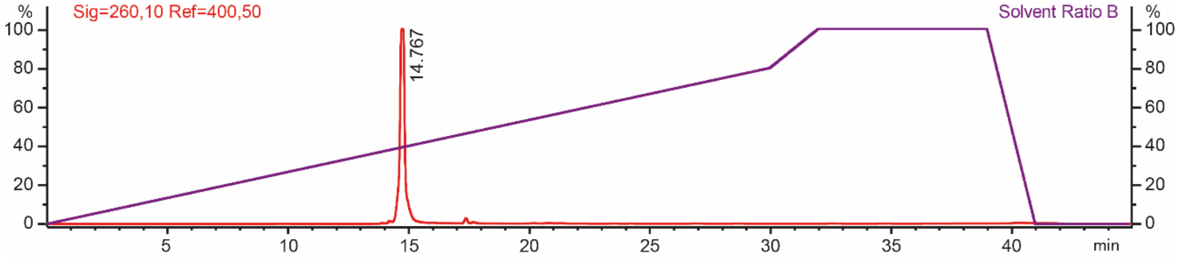

Oligo H (5’-AGG **L**^{1}TTA **L**^{1}GG TTA GG**L**^{1} TTA **L**^{1}GG AAT AAG CTG TA (96%))

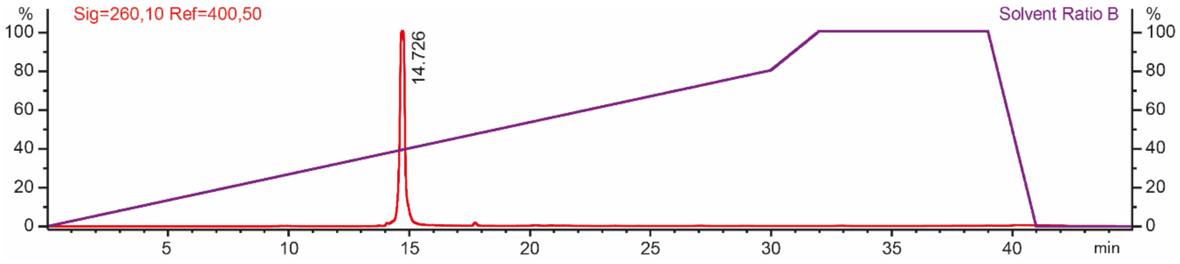

Oligo I (5’-**L**^{2}GG GG (90%))

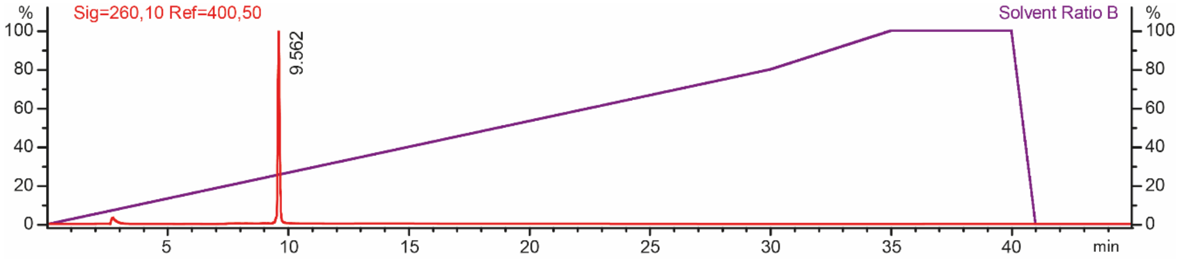

Oligo J (5’-GGG **L**^{1}TT **L**^{1}GG GTT GGG **L**^{1}TT **L**^{1}GG G (91%))

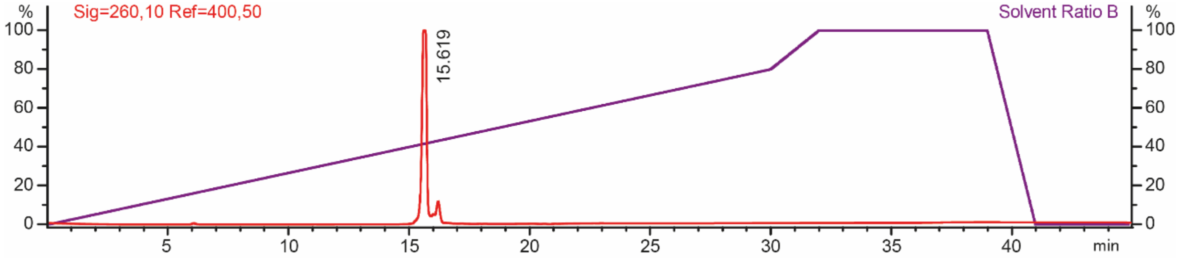

Oligo K (5’- TEMPO-**L**^{2} GGG **L**^{1}TT **L**^{1}GG GTT GGG **L**^{1}TT **L**^{1}GG G (90%))

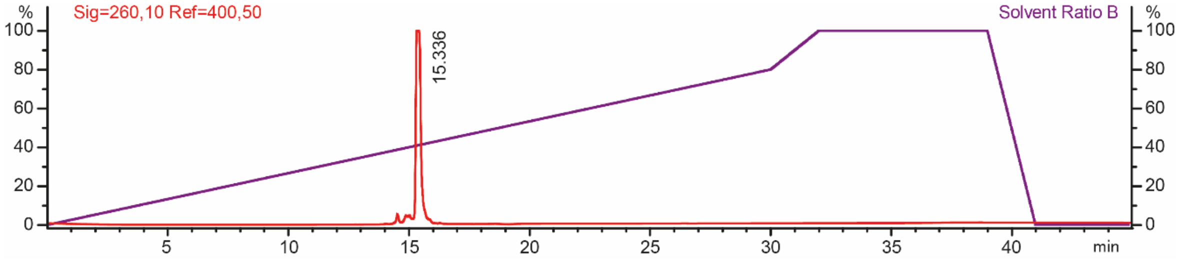

Oligo L (5’-**L**^{3}GG G (96%))

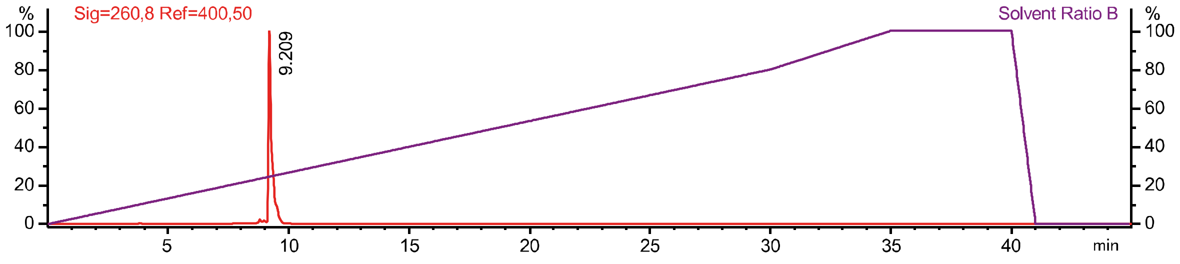

Oligo M (5’-**L**^{3}GG GG (93%))

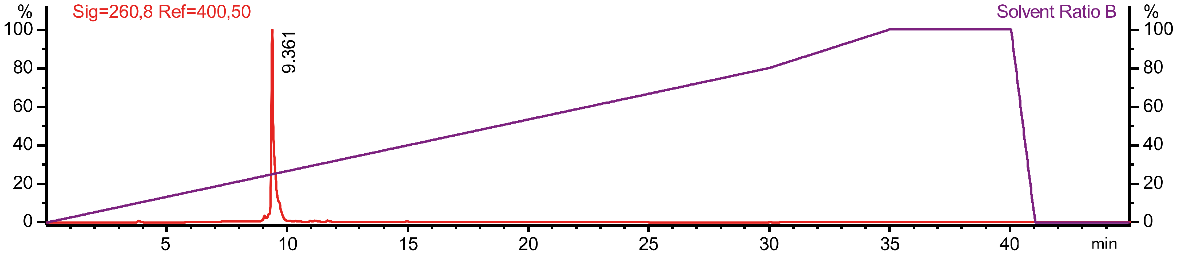

Oligo N (5’-**L**^{3}GG GGG (94%))

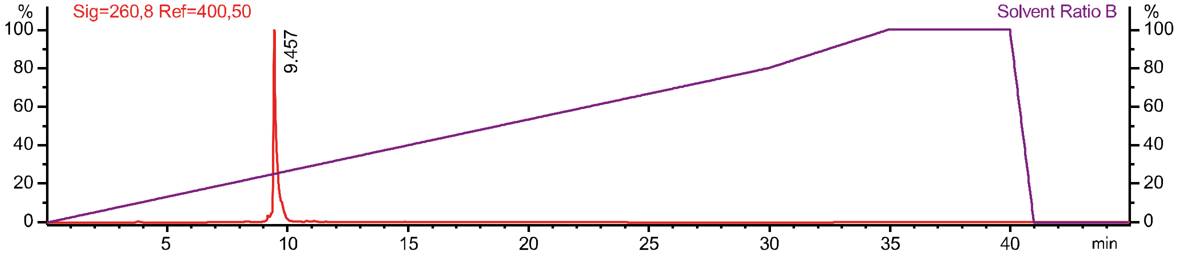

Oligo O (5’-**L**^{4}GG GG (78%))

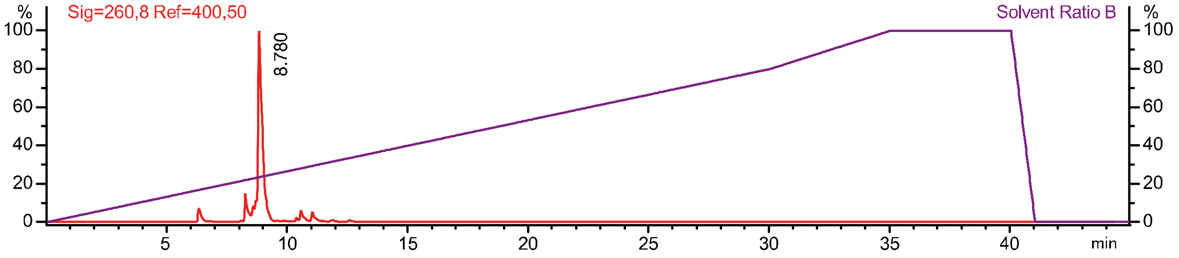

Oligo P (5’-**L**^{4}GG GGG (80%))

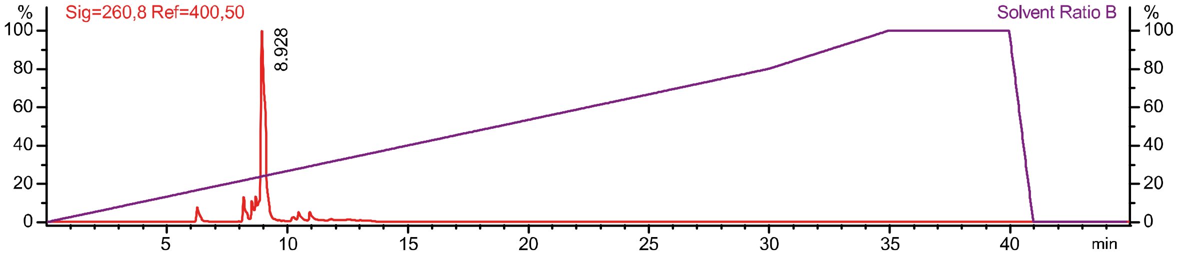

Oligo Q (5’-**L**^{5}GG GG (98%))

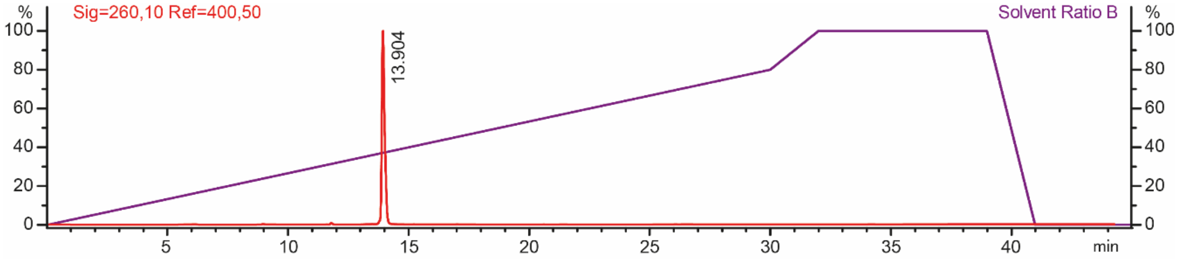

Oligo R (5'-**L**^{5}GG GGG (97%))

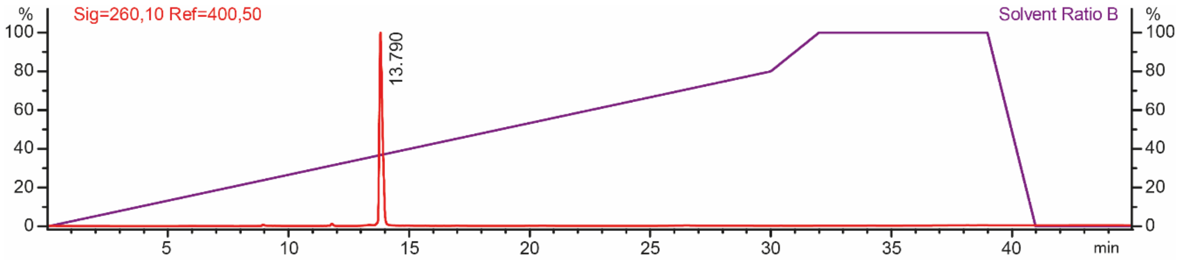

htel**L**$^3{}_4$ (5'-AGG **L**^{3}TT A**L**^{3}G GTT AGG **L**^{3}TT A**L**^{3}G G (86%))

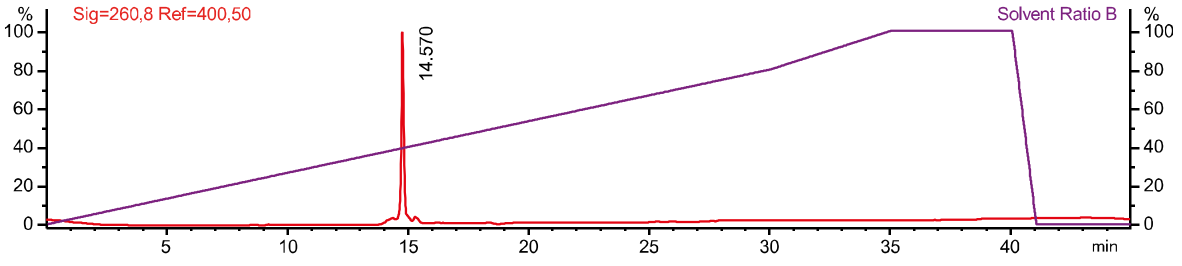

htel**L**$^3{}_3$**L**^{8} (5'-AGG **L**^{8}TT A**L**^{3}G GTT AGG **L**^{3}TT A**L**^{3}G G (91%))

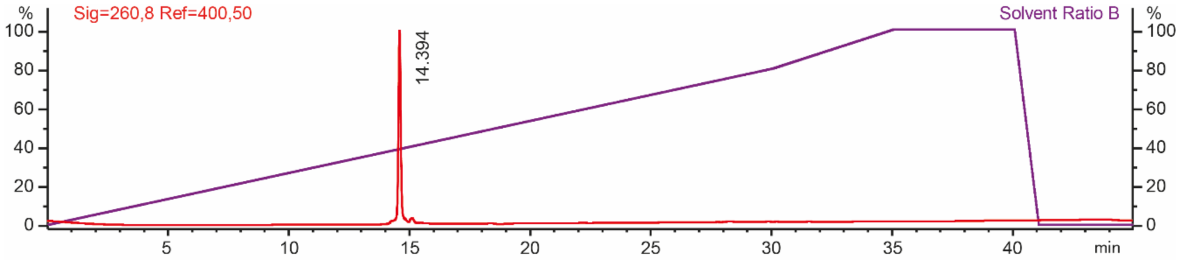

htel**L**$^3{}_2$**L**$^8{}_2$ (5'-AGG **L**^{8}TT A**L**^{3}G GTT AGG **L**^{8}TT A**L**^{3}G G (88%))

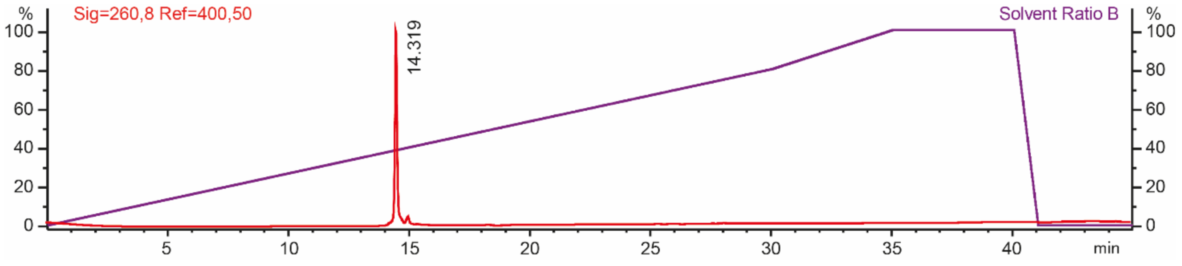

htel**L**^{3}**L**$^8{}_3$ (5'-AGG **L**^{8}TT A**L**^{8}G GTT AGG **L**^{8}TT A**L**^{3}G G (92%))

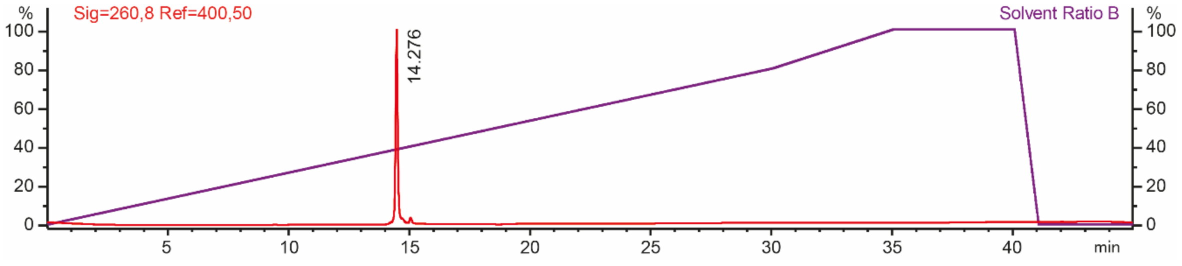

htel**L^3**$_4$**L^8**$_2$ (5’-AGG **L^3**T**L^8** T**L^3**G GTT AGG **L^3**T**L^8** T**L^3**G G (80%))

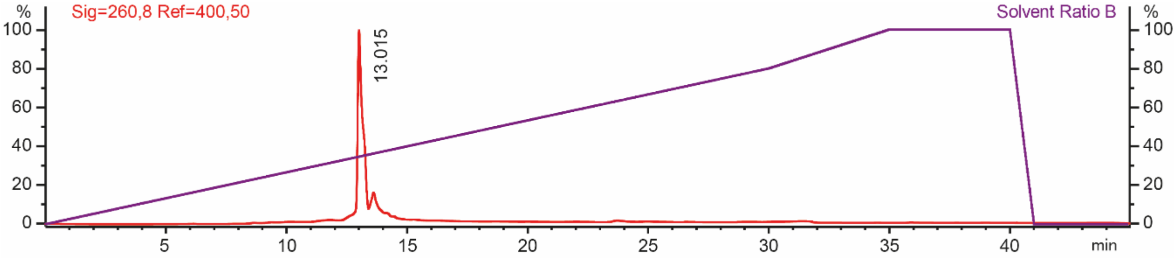

htel**L^3**$_3$**L^8**$_3$ (5’-AGG **L^3**T**L^8** T**L^8**G GTT AGG **L^3**T**L^3** T**L^8**G G (89%))

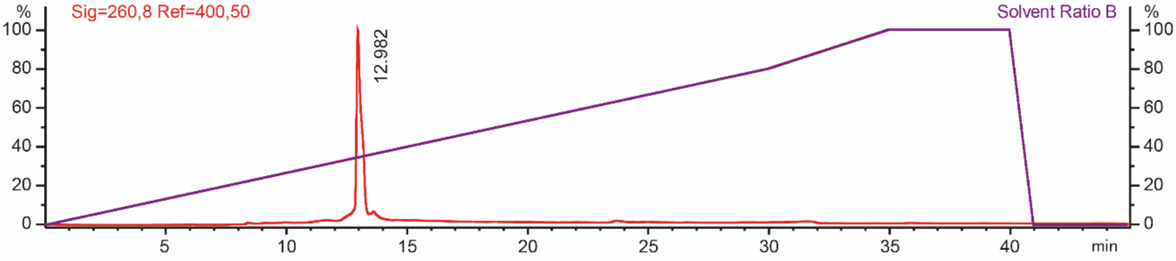

htel**L^3**$_2$**L^8**$_4$ (5’-AGG **L^8**T**L^3** T**L^8**G GTT AGG **L^8**T**L^3** T**L^8**G G (80%))

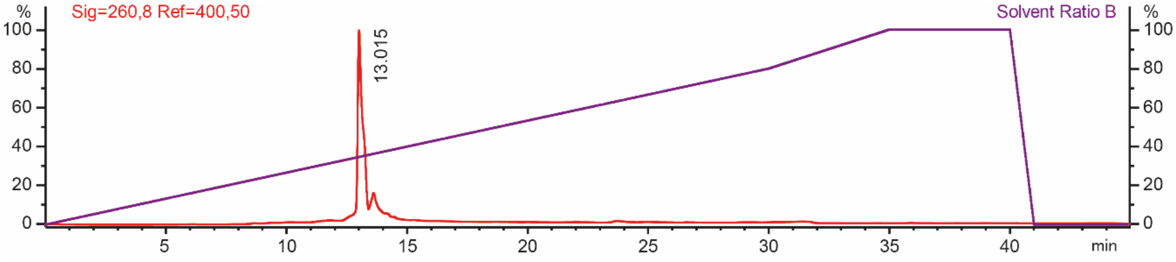

6.1.2 Mass Spectrometry

Oligonucleotide samples were further analyzed either by MALDI or ESI mass spectrometry.

MADLI-TOF mass spectrometry was performed on a *Bruker ultrafleXtreme* MALDI-MS system (negative mode) using a 3-HPA-based matrix. Mass spectra are shown below.

Oligo L (5’-**L^3**GG G)

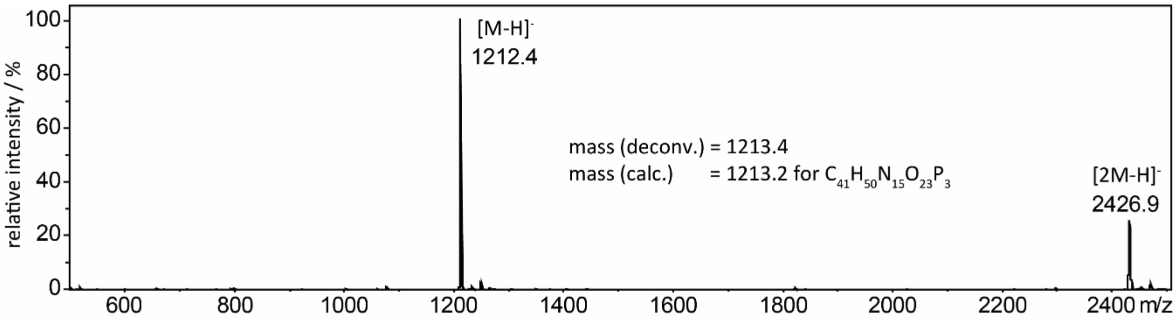

Oligo M (5’-**L**^{3}GG GG)

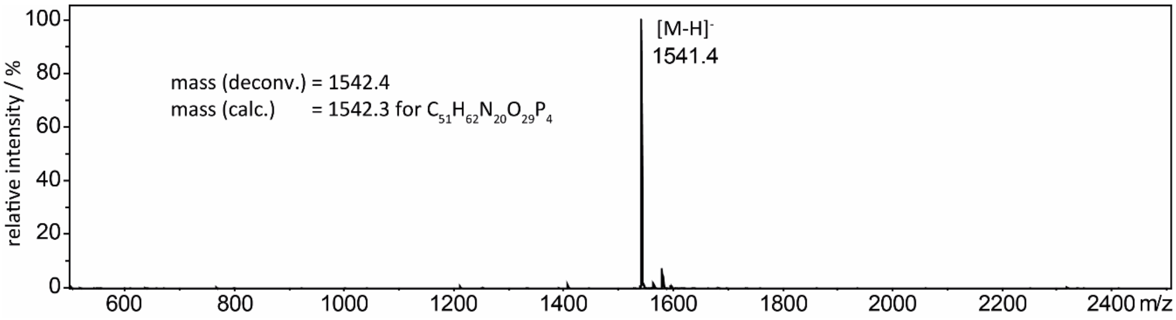

Oligo N (5’-**L**^{3}GG GGG)

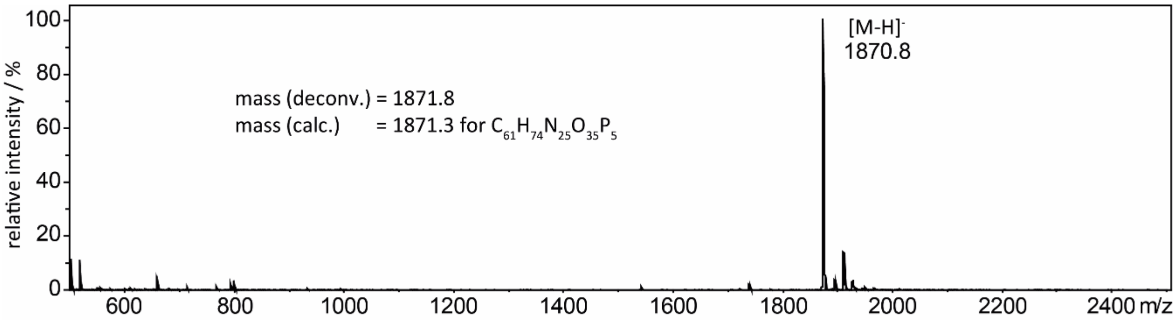

Oligo O (5’-**L**^{4}GG GG)

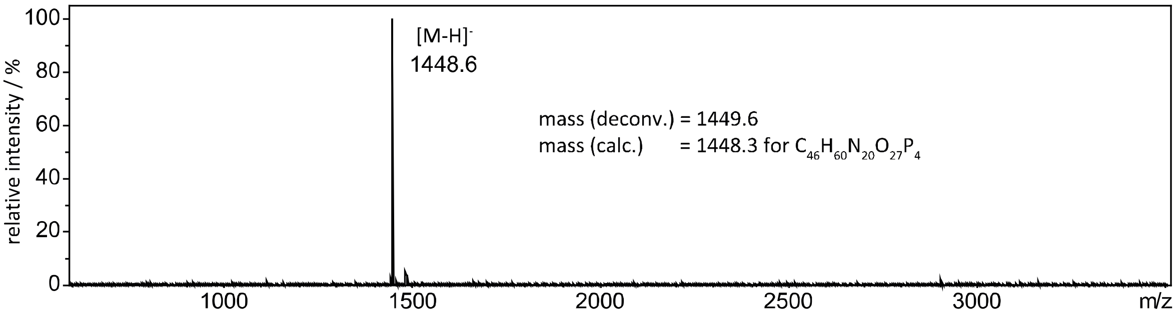

Oligo P (5’-**L**^{4}GG GGG)

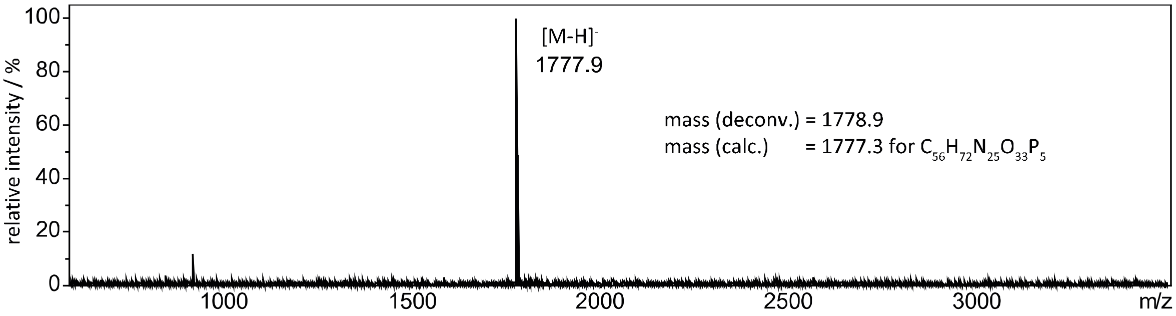

ESI mass spectrometry was performed on *Bruker ESI-timsTOF* and *Compact* mass spectrometers (negative mode). For calibration of the TOF device, *Agilent ESI-Low Concentration Tuning Mix* was used. Samples (5 µL) with DNA concentrations of 150 - 300 µM in 15 mM TMAA pH 7.0 or TEAA pH 7.0 were prepared. Automatic injection of the samples was achieved with the autosampler of an *Agilent Technologies 1260 Infinity* system (flow rate: 0.3 mL/min, solvent: MeCN/H_2O 1:1, v/v). The ESI mass spectra are shown below.

Oligo A (5'-TT**L**^{1} GGG)

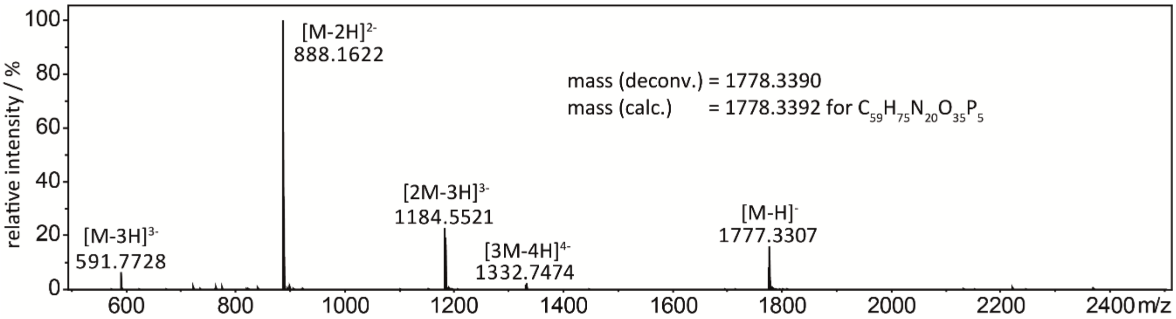

Oligo B (5'-T**L**^{1}G GGG)

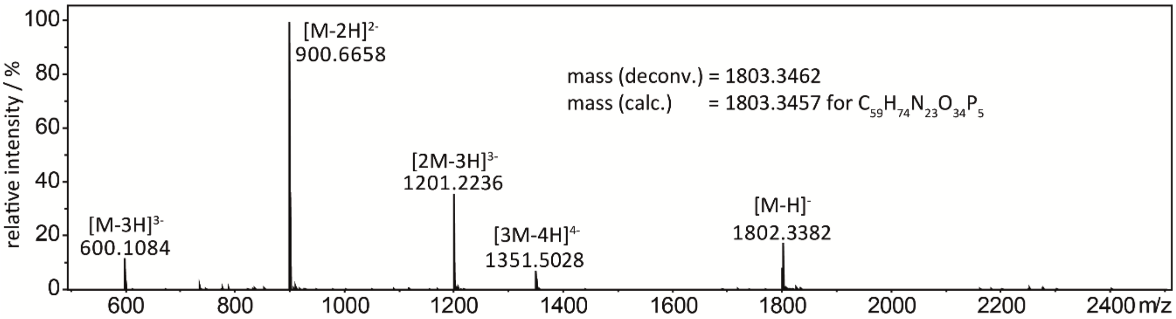

Oligo C (5'-TT**L**^{1} GGG T)

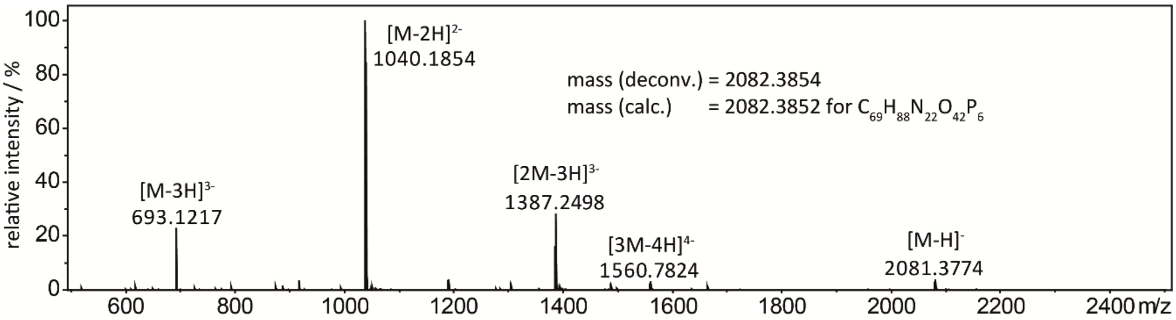

Oligo D (5’-GGG **L**^{1}TT)

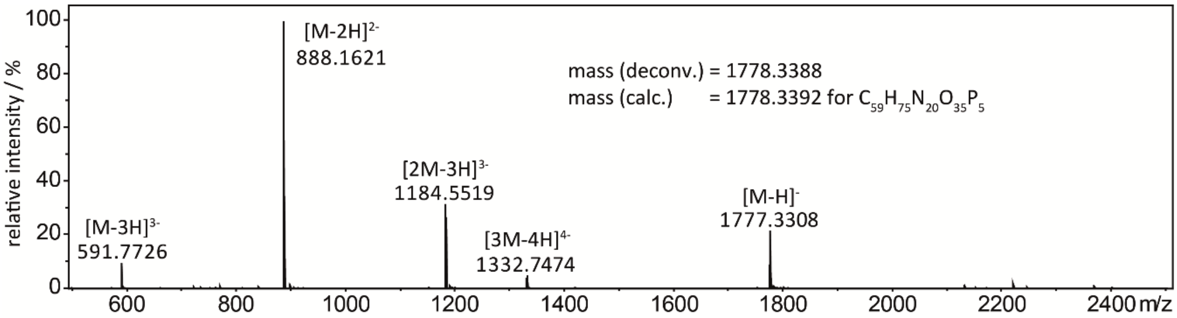

Oligo E (5’-GGG G**L**^{1}T)

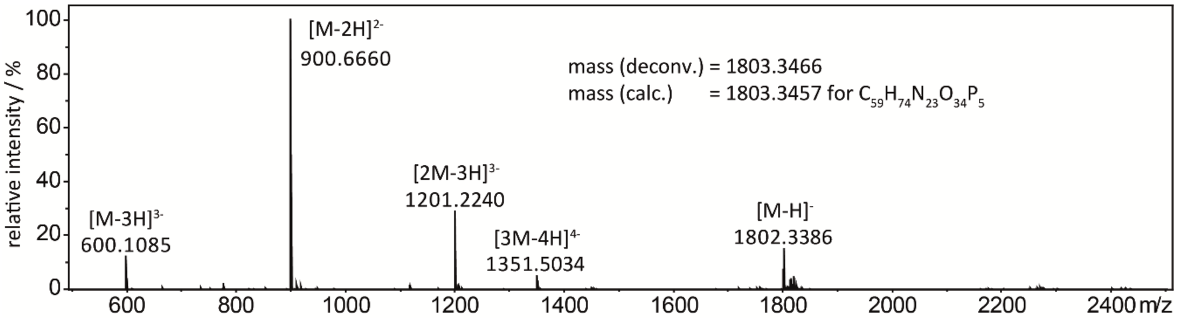

Oligo F (5’-TGG G**L**^{1}T T)

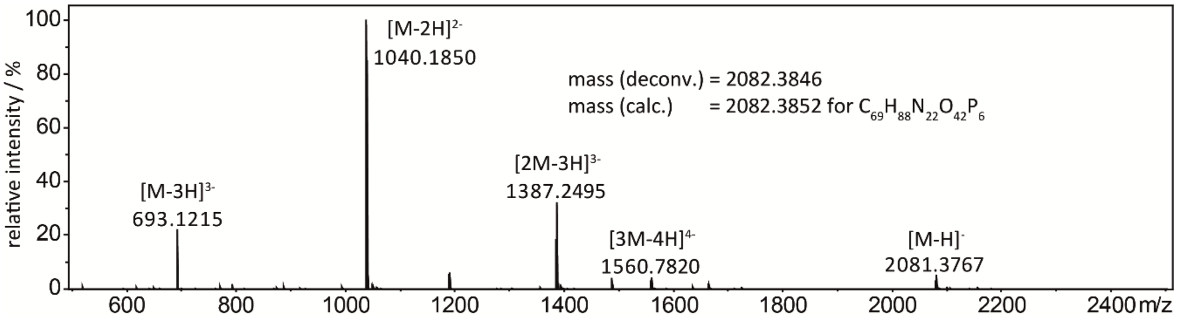

Oligo G (5’-A GG**L**^{1} TTA **L**^{1}GG TTA GG**L**^{1} TTA **L**^{1}GG ATA CAG CTT AT)

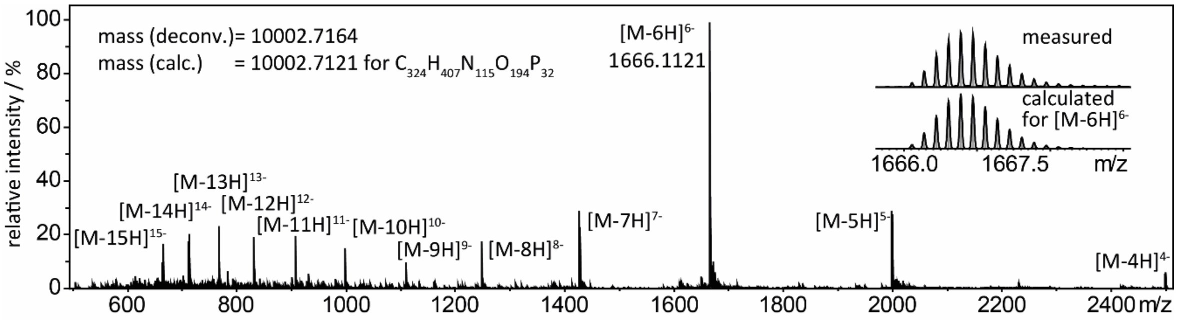

Oligo H (5'-A GG**L**^{1} TTA **L**^{1}GG TTA GG**L**^{1} TTA **L**^{1}GG AAT AAG CTG TA)

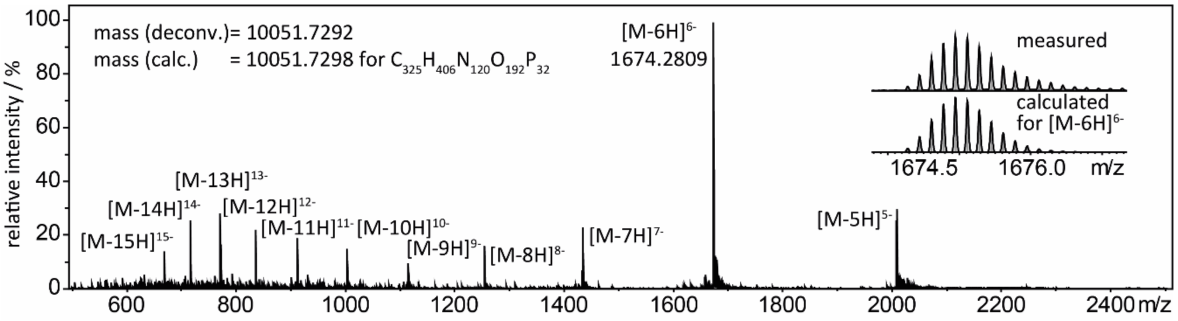

Oligo I (5'-**L**^{2}GG GG)

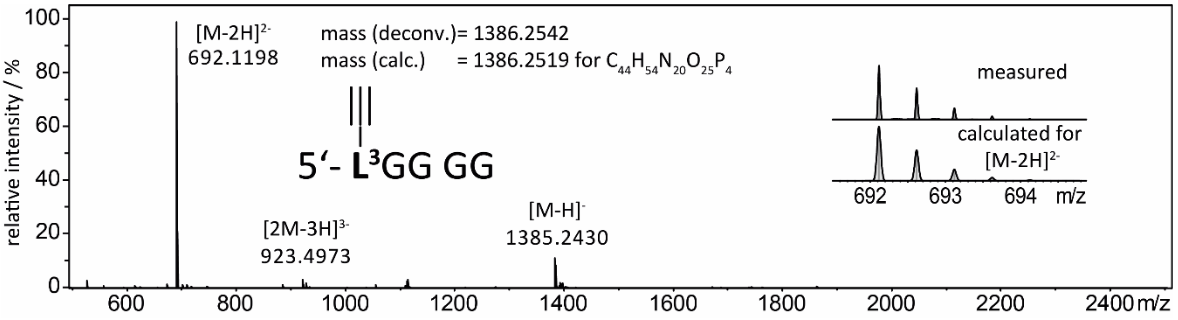

Oligo J (5'-GGG **L**^{1}TT **L**^{1}GG GTT GGG **L**^{1}TT **L**^{1}GG G), measured in pure water

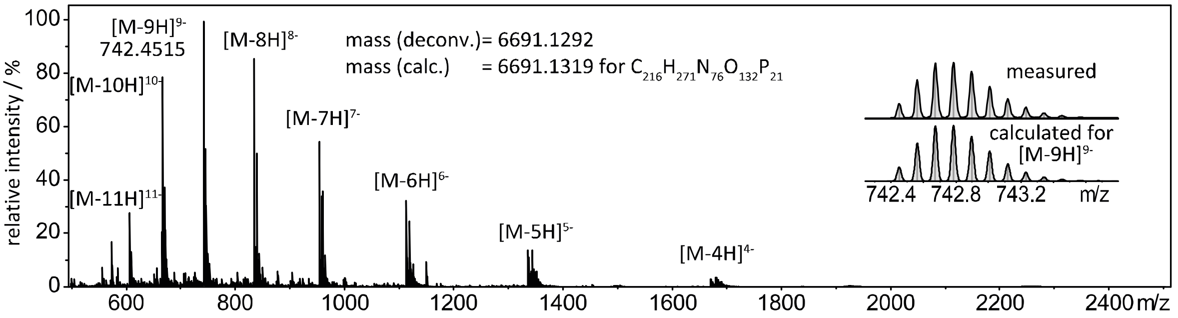

Oligo K (5'-TEMPO-**L**^{2} GGG **L**^{1}TT **L**^{1}GG GTT GGG **L**^{1} TT**L**^{1} GGG)

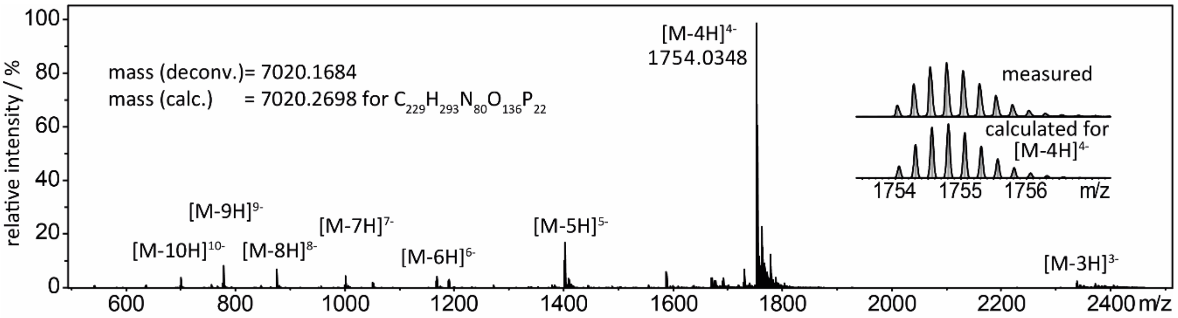

Oligo Q (5'-**L**^{5}GG GG)

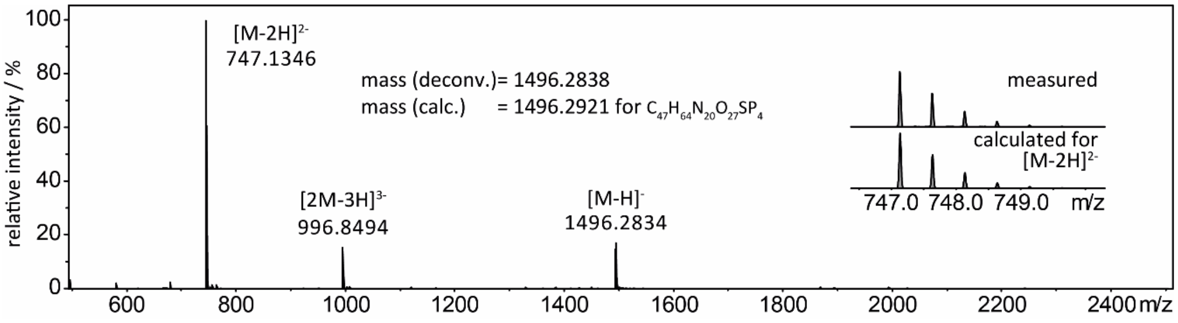

Oligo R (5'-**L**^{5}GG GGG)

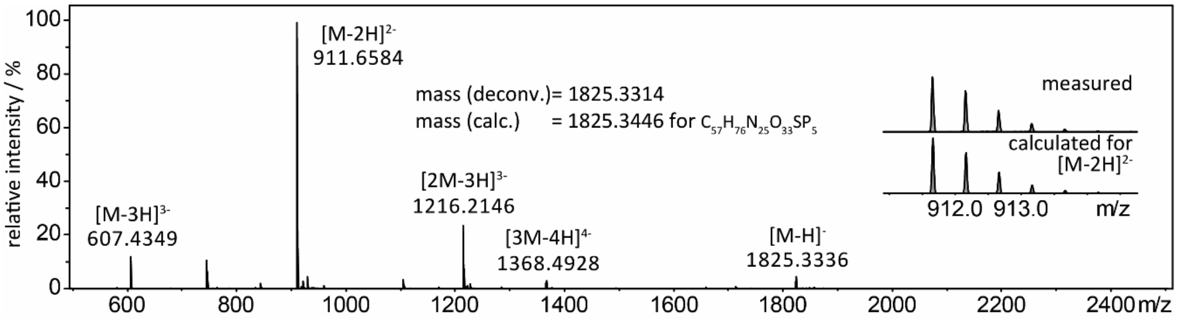

Oligo S^{ox} (5'-**L**^{7}GG G), in the oxidized symmetric disulfide form

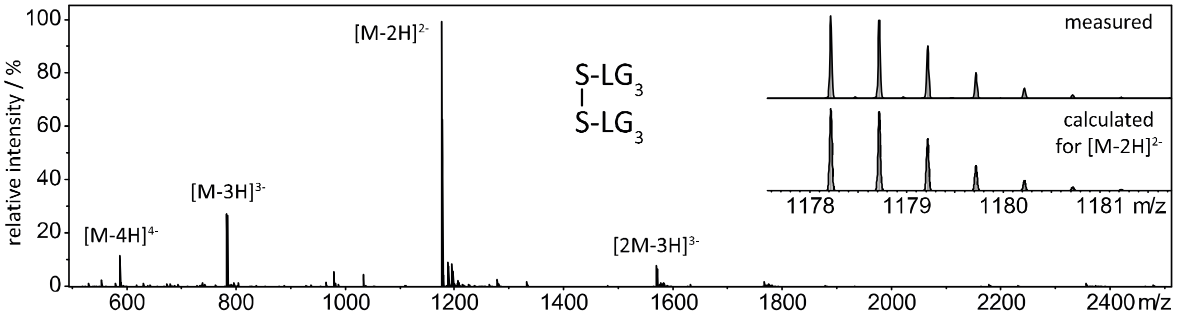

Oligo S (5'-**L**^{7}GG G), in the reduced thiol form, 20 mM DTT is in the sample

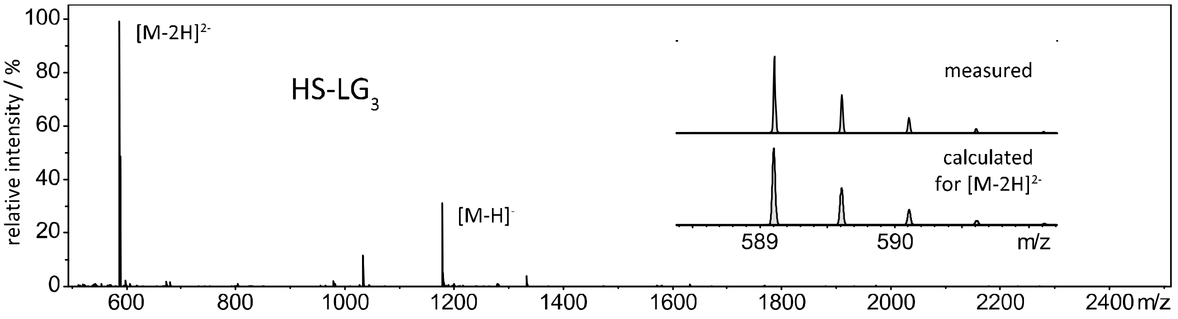

Oligo T^{ox} (5’-**L^{7}**GG GG), in the oxidized symmetric disulfide form

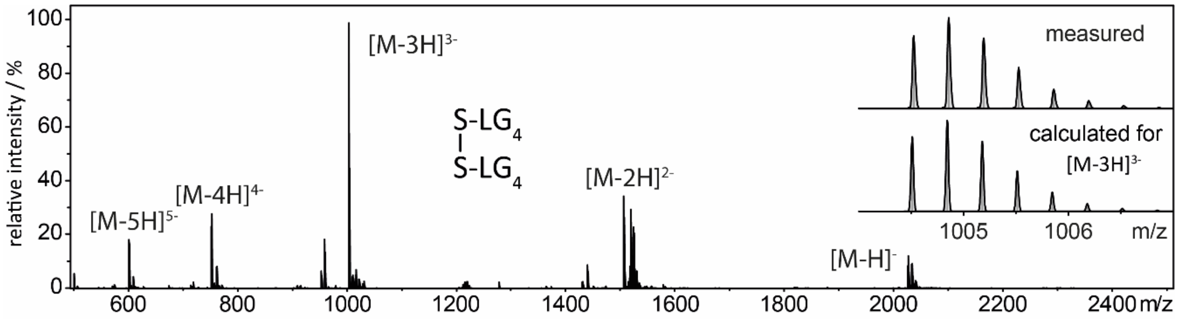

Oligo T (5’-**L^{7}**GG GG), in the reduced thiol form, 20 mM DTT is in the sample

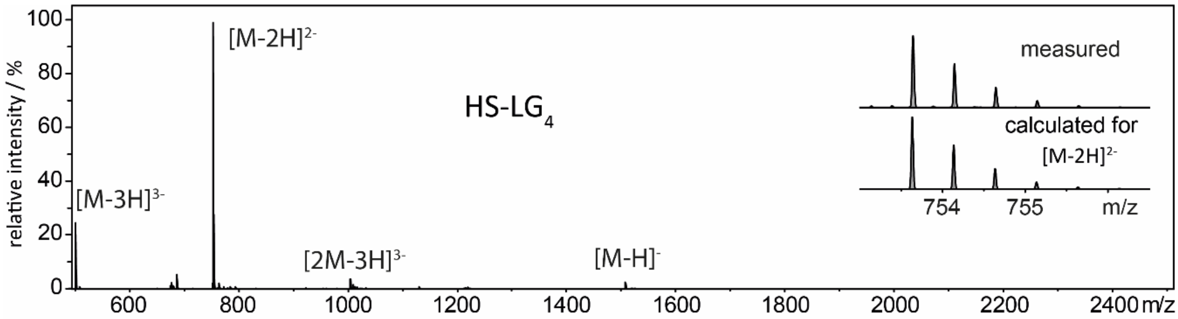

htel**L^{3}**$_{4}$ (5’-AGG **L^{3}**TT A**L^{3}**G GTT AGG **L^{3}**TT A**L^{3}**G G)

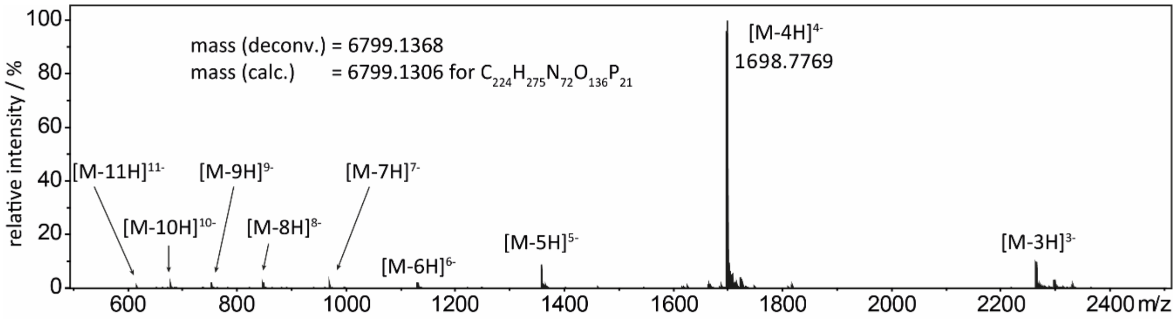

htel**L^{3}**$_{3}$**L^{8}** (5’-AGG **L^{8}**TT A**L^{3}**G GTT AGG **L^{3}**TT A**L^{3}**G G)

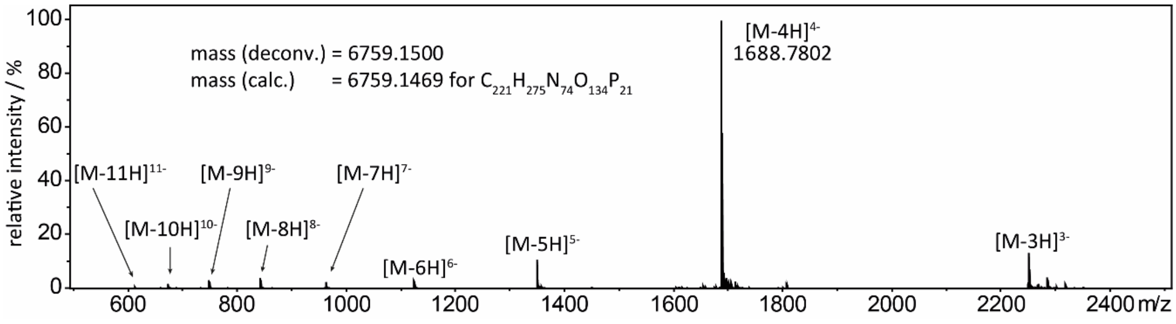

htel$\mathbf{L}^3_2\mathbf{L}^8_2$ (5'-AGG $\mathbf{L}^8$TT A$\mathbf{L}^3$G GTT AGG $\mathbf{L}^8$TT A$\mathbf{L}^3$G G)

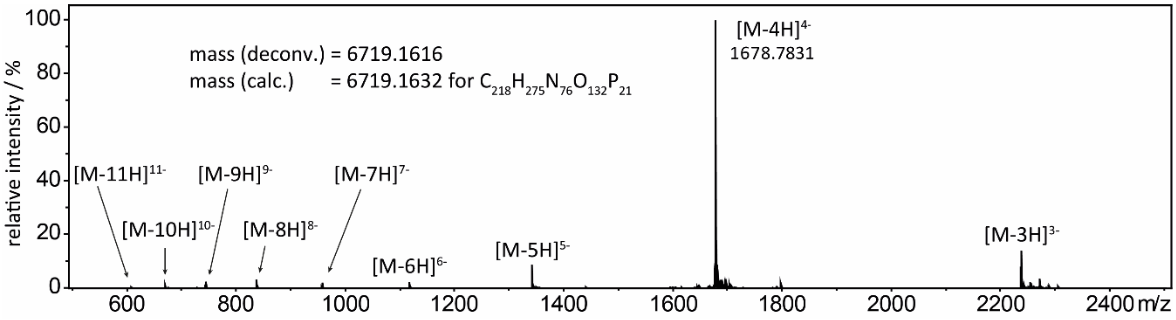

htel$\mathbf{L}^3\mathbf{L}^8_3$ (5'-AGG $\mathbf{L}^8$TT A$\mathbf{L}^8$G GTT AGG $\mathbf{L}^8$TT A$\mathbf{L}^3$G G)

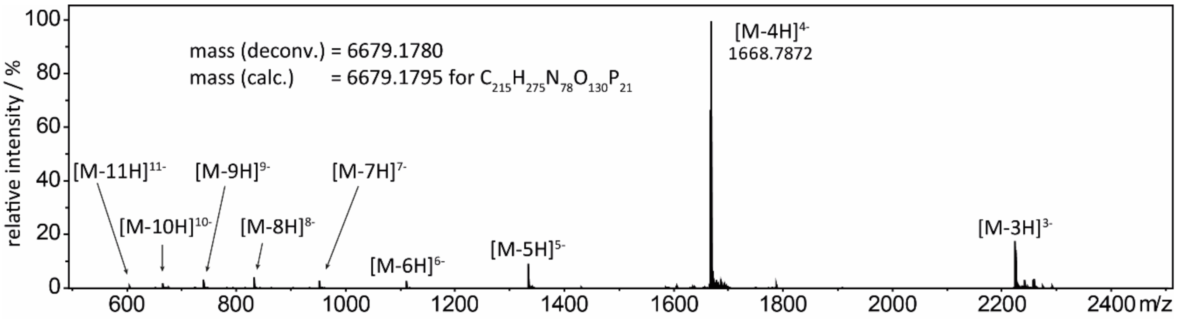

htel$\mathbf{L}^3_4\mathbf{L}^8_2$ (5'-AGG $\mathbf{L}^3$T$\mathbf{L}^8$ T$\mathbf{L}^3$G GTT AGG $\mathbf{L}^3$T$\mathbf{L}^8$ T$\mathbf{L}^3$G G)

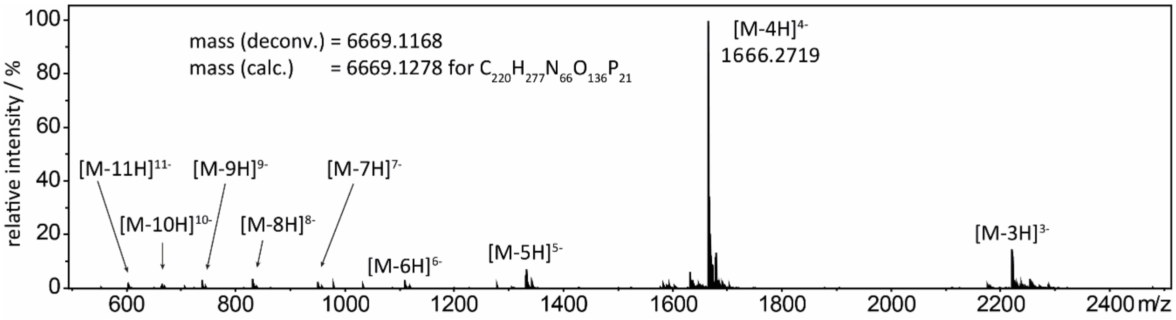

htel$\mathbf{L}^3_3\mathbf{L}^8_3$ (5'-AGG $\mathbf{L}^3$T$\mathbf{L}^8$ T$\mathbf{L}^8$G GTT AGG $\mathbf{L}^3$T$\mathbf{L}^3$ T$\mathbf{L}^8$G G)

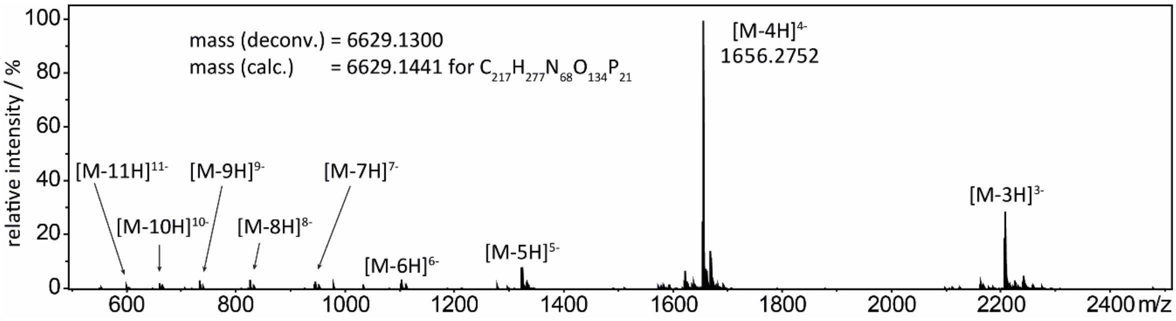

htel$\mathbf{L}^{3}{}_{2}\mathbf{L}^{8}{}_{4}$ (5'-AGG $\mathbf{L}^{8}$T$\mathbf{L}^{3}$ T$\mathbf{L}^{8}$G GTT AGG $\mathbf{L}^{8}$T$\mathbf{L}^{3}$ T$\mathbf{L}^{8}$G G)

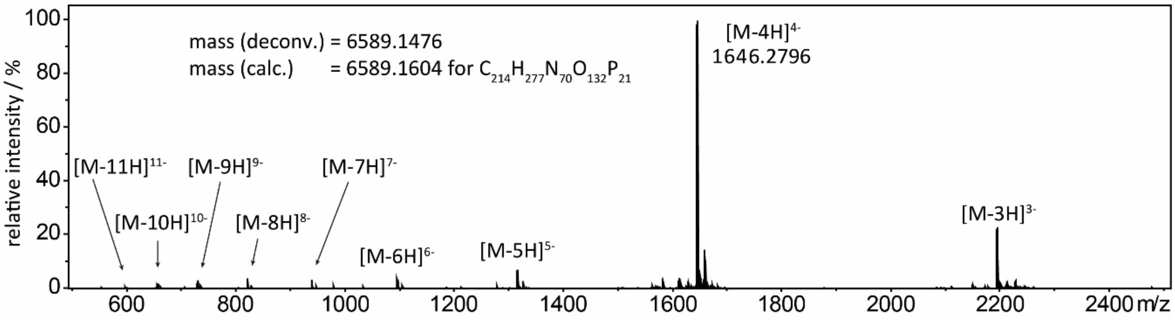

htel$\mathbf{L}^{8}{}_{4}$B (5'- AGG $\mathbf{L}^{8}$TT T$\mathbf{L}^{8}$G GTT AGG $\mathbf{L}^{8}$TT T$\mathbf{L}^{8}$G G)

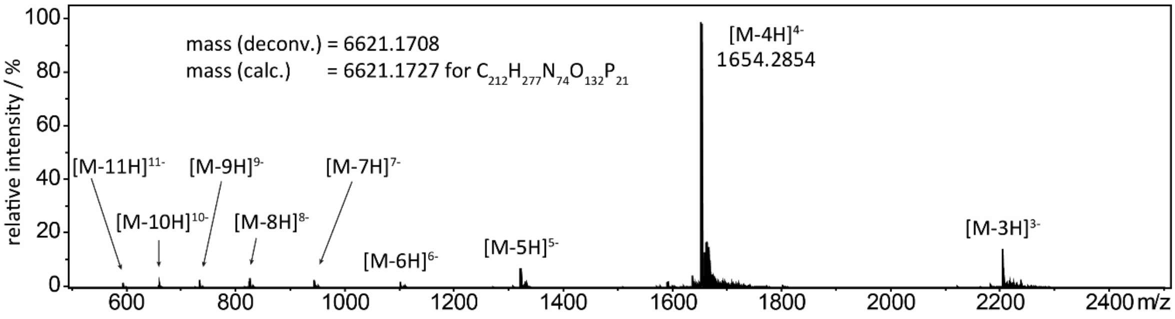

The purity of the oligonucleotides was also regularly checked after longer storage with mass spectrometry. Therefore, stock solutions were desalted if needed with *Millipore Ziptips 0.6 µL C_{18}*.

6.2 UV-VIS-Based Thermal Denaturation Studies of G-Quadruplexes X_4 (X = A–F)

6.2.1 Sample Preparation

G-quadruplex samples contained 16 µM single-stranded DNA (4 µM tetramolecular G-quadruplex DNA), 100 mM KCl or NaCl, 10 mM lithium cacodylate buffer pH 7.2, and, if present, 4 µM $CuSO_4$ or/and 2 µM PIPER. All samples were prepared with ultrapure water (type I, 18.2 MΩ cm), obtained with a *VWR Puranity TU 3 UV*.

Samples were heated to 85 °C for 10 min, slowly cooled to 4 °C with a cooling rate of 0.5 °C/min and then left at this temperature for several hours (typically overnight). To ensure full formation of tetramolecular G-quadruplexes, the samples were frozen at –20 °C for 1 h[1] and thawed again to 4 °C.

6.2.2 Spectrometer and Methods

Both UV-VIS spectra and thermal denaturation profiles (melting curves) were recorded on a *Jasco V-750 UV-Visible Spectrophotometer* equipped with a *PAC-743 6-cell thermostat* for temperature control. The temperature was measured in the measurement cell in a water-filled cuvette. Quartz glass cuvettes (*Hellma Analytics114-QS*, 1 cm path length) were used. In order to avoid condensation of water on the cuvette surfaces or cell windows at low temperatures, a constant flow of air was pumped through the measurement cell. Evaporation of water at high temperatures and resulting changes in the absorption behavior were minimized by a thin layer of silicon oil placed onto the sample and by tightly stoppering the cuvette.

UV-VIS spectra were recorded from 700 to 220 nm with a scan rate of 200 nm/min both before (4 °C) and after thermal denaturation (95 °C). The data interval was set to 1 nm, bandwidth to 2.0 nm and the response time to 0.96 sec. All UV-VIS spectra were background corrected (cuvette, buffer, and electrolyte) and zeroed using the absorption at 700 nm. To obtain the thermal difference spectra (TDS), the spectrum before denaturation (at 4 °C) was subtracted from the one after denaturation (at 95 °C). A negative band (hypochromic shift) at 295±2 nm and positive bands at 243±2 nm and 273±2 nm (hyperchromic shift) indicated G-quadruplex formation.[2]

For the thermal denaturation profiles (melting curves), absorption of the samples at 295 nm was recorded in a 0.5 °C interval with a temperature gradient set to 0.5 °C/min, which corresponds to ~0.174 °C/min including the measurement time. Data points were recorded from 4 °C to 95 °C. Melting curves were background corrected using the absorption at 700 nm and converted to the fraction folded values by linear fitting of the low and high temperature baselines.[3] Thermal denaturation temperatures were then determined by extracting the respective value at the point where 50% of the fraction was denatured.

6.2.3 UV-VIS Spectra, Thermal Difference Spectra and Denaturation Profiles

Oligo A (5’-TT**L**^{1} GGG) in KCl

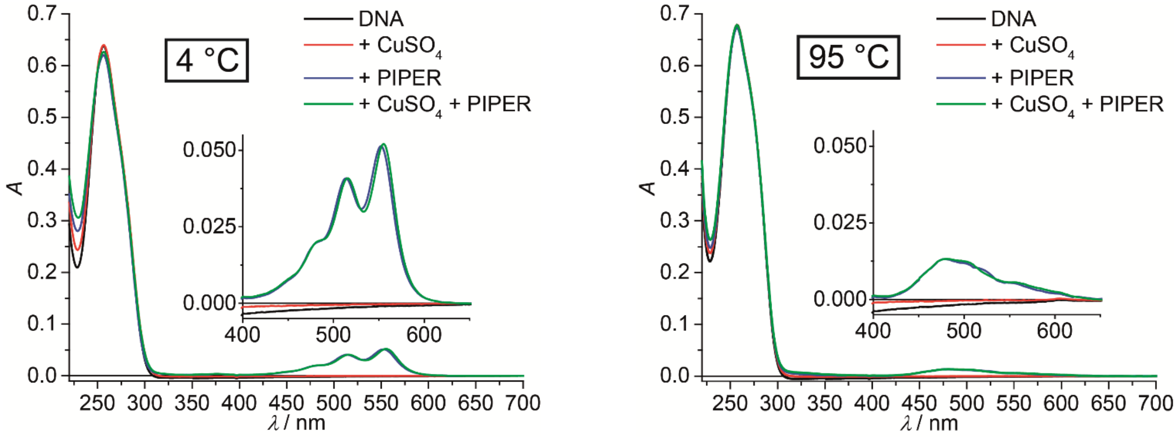

Figure 6.1: UV-VIS spectra of folded (4 °C, left) and unfolded (95 °C, right) G-quadruplex (TT**L**^{1} GGG)$_4$ in absence or presence of 1 equiv. of $CuSO_4$ or/and 0.5 equiv. of PIPER.

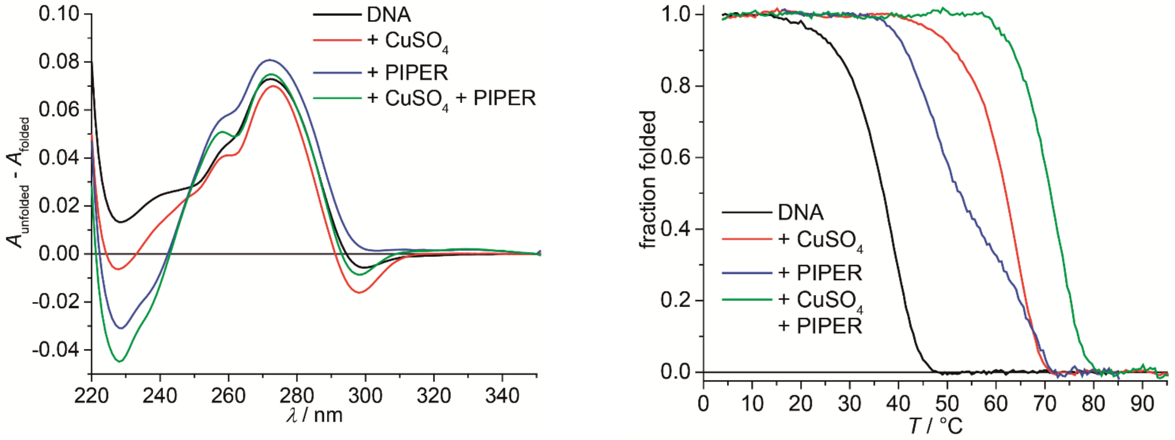

Figure 6.2: Thermal difference spectra (left) and thermal denaturation profiles (right) of G-quadruplex (TT**L**^{1} GGG)$_4$ in absence or presence of 1 equiv. of $CuSO_4$ or/and 0.5 equiv. of PIPER.

Oligo B (5’-T**L**^{1}G GGG) in KCl

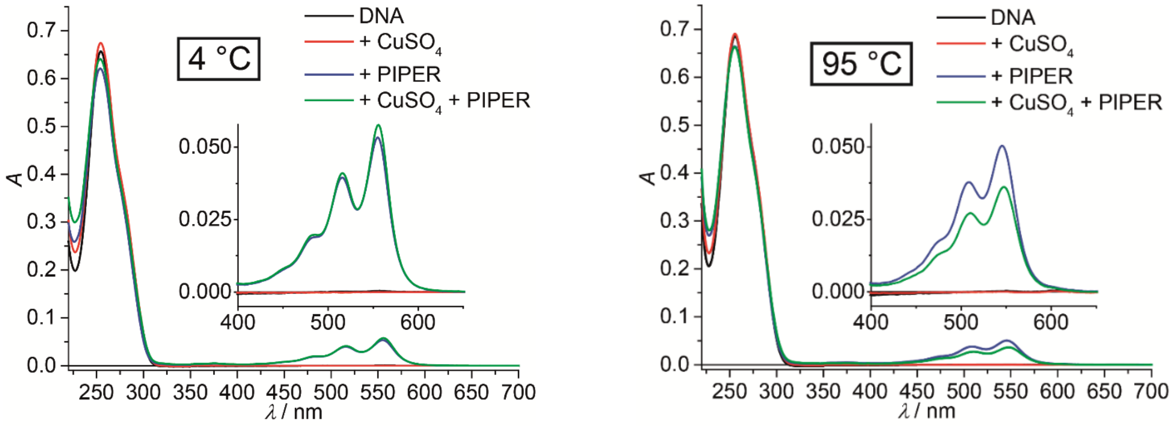

Figure 6.3: UV-VIS spectra of folded G-quadruplex (T**L**^{1}G GGG)$_4$ at 4 °C (left) and at 95 °C (right) in KCl-containing solution in absence or presence of 1 equiv. of $CuSO_4$ or/and 0.5 equiv. of PIPER. The thermal denaturation temperatures are >95 °C.

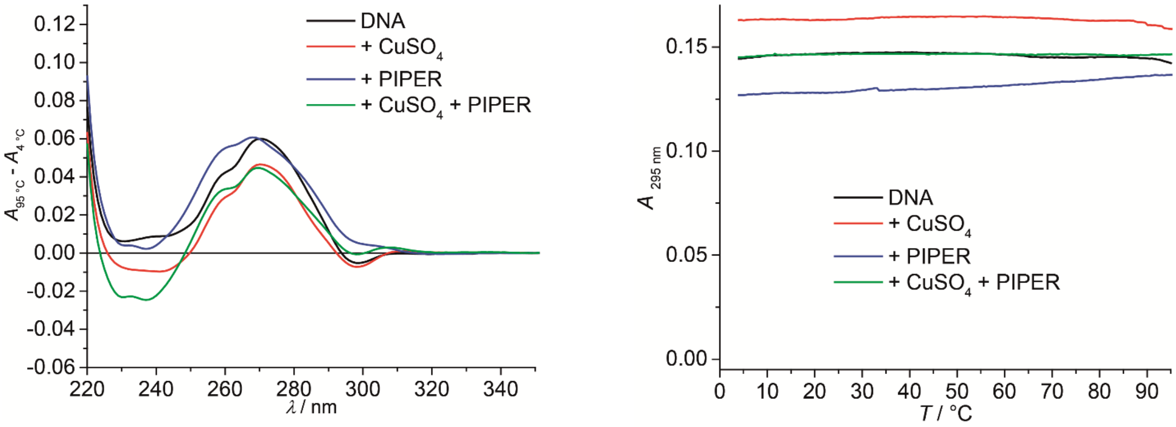

Figure 6.4: Thermal difference spectra (left) and temperature-dependent absorption at 295 nm (right) of G-quadruplex (T**L**^{1}G GGG)$_4$ in KCl-containing solution in absence or presence of 1 equiv. of $CuSO_4$ or/and 0.5 equiv. of PIPER. The thermal denaturation temperatures are >95 °C.

Oligo B (5'-T**L**^{1}G GGG) in NaCl

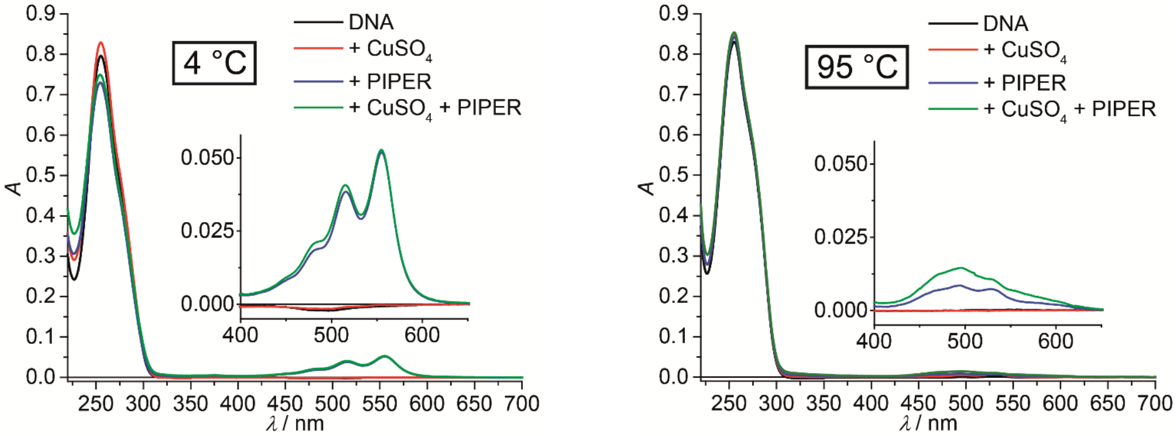

Figure 6.5: UV-VIS spectra of folded (4 °C, left) and unfolded (95 °C, right) G-quadruplex (T**L**^{1}G GGG)$_4$ in NaCl-containing solution in absence or presence of 1 equiv. of $CuSO_4$ or/and 0.5 equiv. of PIPER.

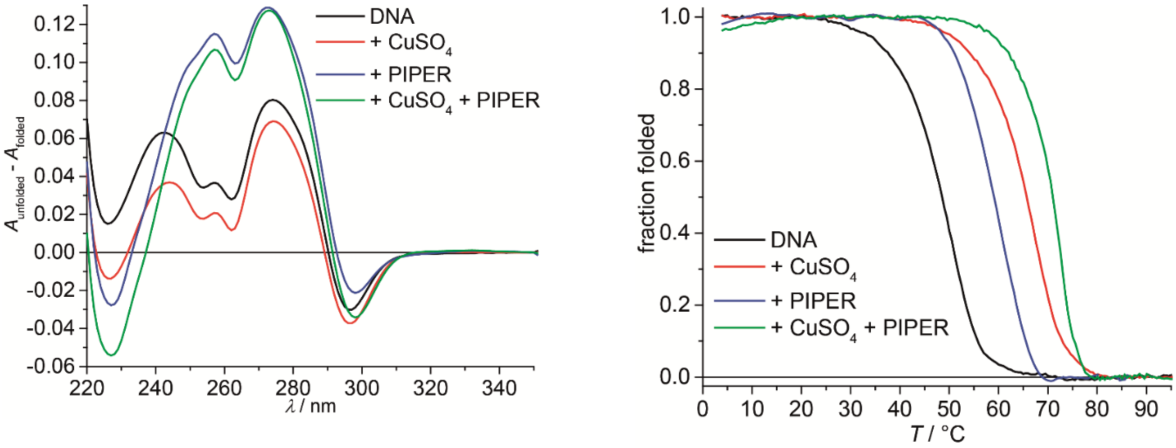

Figure 6.6: Thermal difference spectra (left) and thermal denaturation profiles (right) of G-quadruplex (T**L**^{1}G GGG)$_4$ in NaCl-containing solution in absence or presence of 1 equiv. of $CuSO_4$ or/and 0.5 equiv. of PIPER.

Figure 6.7: Samples of G-quadruplex (5'-T**L**^{1}G GGG)$_4$ in KCl- (left) or NaCl- (right) containing solution after heating to 95 °C and cooling to room temperature. G-quadruplex (T**L**^{1}G GGG)$_4$ does not denature in presence of KCl and keeps PIPER in solution (red colored solutions, left). On the contrary, G-quadruplex (T**L**^{1}G GGG)$_4$ denatures at 95 °C in presence of NaCl and, hence, PIPER precipitates (red precipitate, right).

Oligo C (5'-TT**L**^{1} GGG T) in KCl

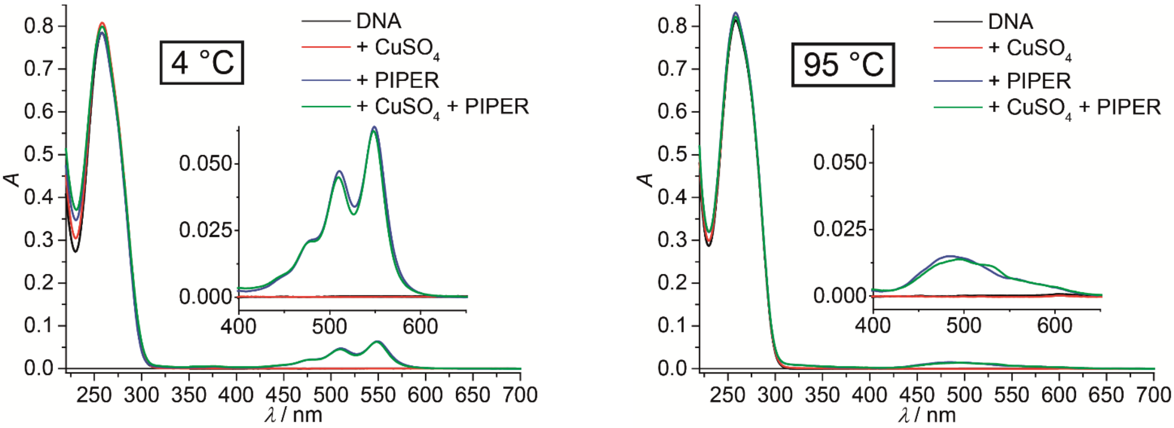

Figure 6.8: UV-VIS spectra of folded (4 °C, left) and unfolded (95 °C, right) G-quadruplex (TT**L**^{1} GGG T)$_4$ in absence or presence of 1 equiv. of CuSO$_4$ or/and 0.5 equiv. of PIPER.

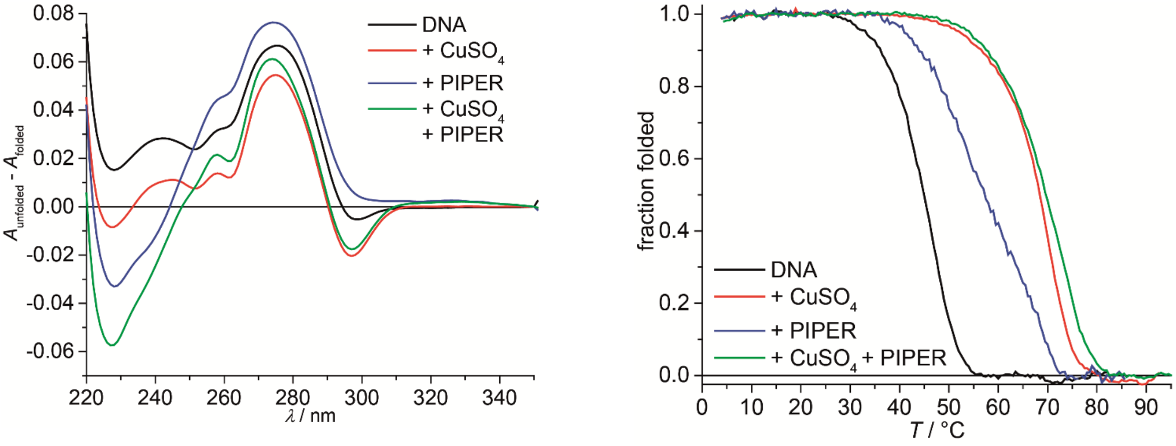

Figure 6.9: Thermal difference spectra (left) and thermal denaturation profiles (right) of G-quadruplex (TT**L**^{1} GGG T)$_4$ in absence or presence of 1 equiv. of CuSO$_4$ or/and 0.5 equiv. of PIPER.

Oligo D (5'-GGG **L**^{1}TT) in KCl

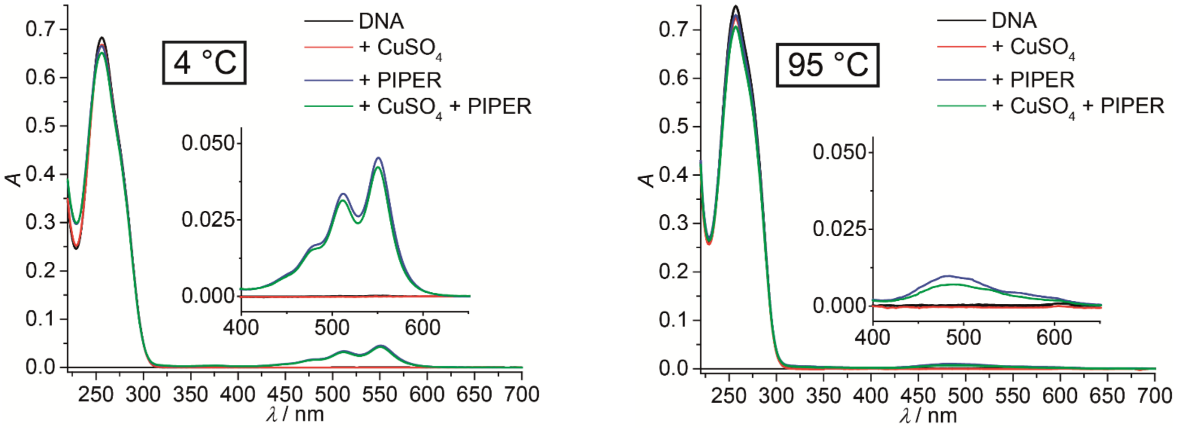

Figure 6.10: UV-VIS spectra of folded (4 °C, left) and unfolded (95 °C, right) G-quadruplex (GGG **L**^{1}TT)$_4$ in absence or presence of 1 equiv. of $CuSO_4$ or/and 0.5 equiv. of PIPER.

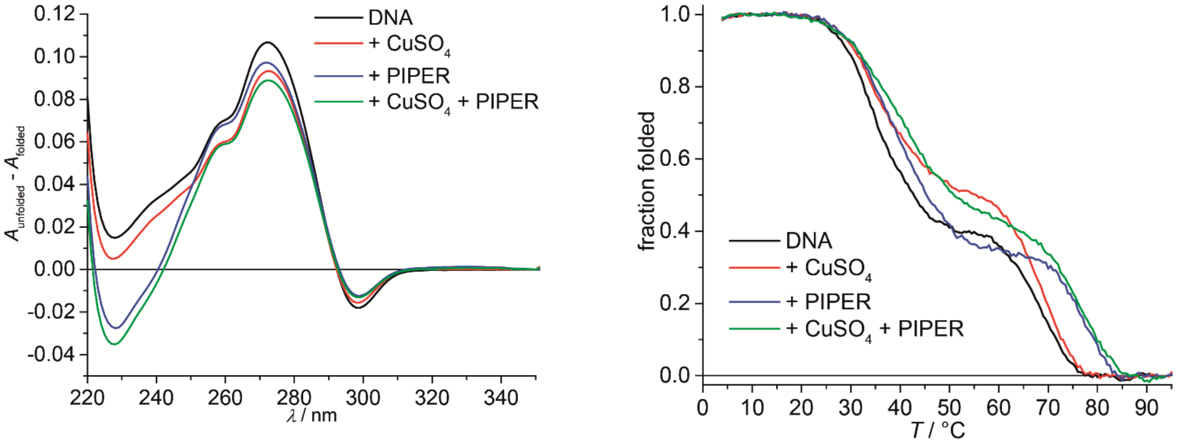

Figure 6.11: Thermal difference spectra (left) and thermal denaturation profiles (right) of G-quadruplex (GGG **L**^{1}TT)$_4$ in absence or presence of 1 equiv. of $CuSO_4$ or/and 0.5 equiv. of PIPER.

Oligo E (5'-GGG G**L**^{1}T) in KCl

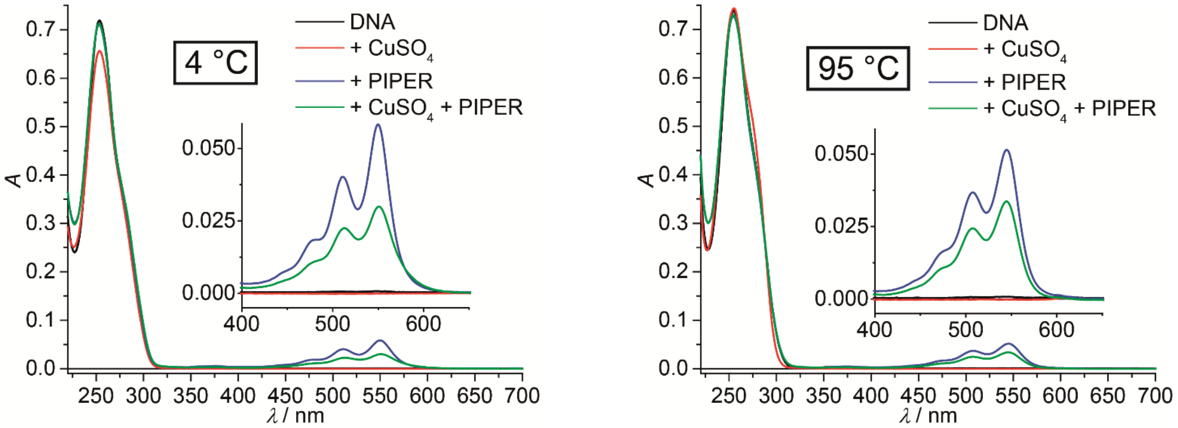

Figure 6.12: UV-VIS spectra of folded G-quadruplex (GGG G**L**^{1}T)$_4$ at 4 °C (left) and at 95 °C (right) in KCl-containing solution in absence or presence of 1 equiv. of $CuSO_4$ or/and 0.5 equiv. of PIPER. The thermal denaturation temperature is >95 °C.

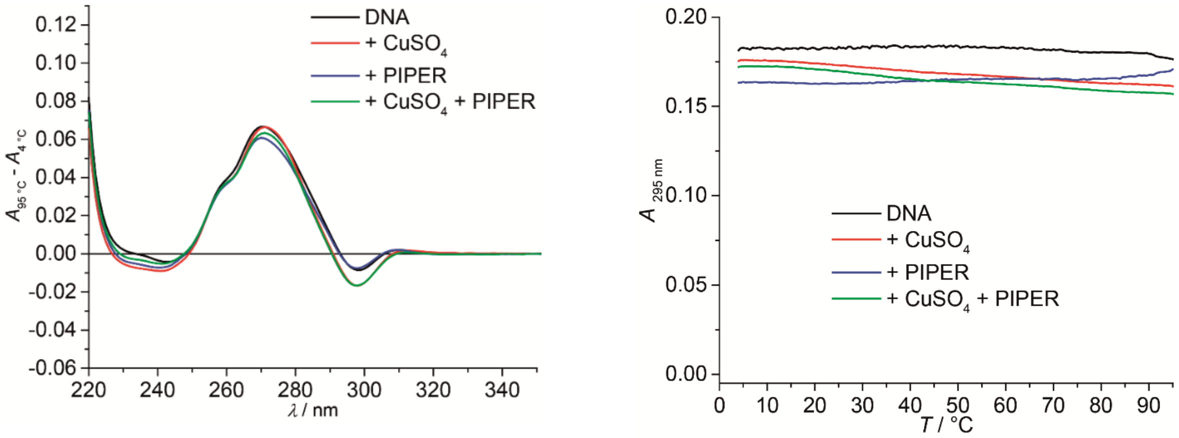

Figure 6.13: Thermal difference spectra (left) and temperature-dependent absorption at 295 nm (right) of G-quadruplex (GGG G**L**^{1}T)$_4$ in KCl-containing solution in absence or presence of 1 equiv. of $CuSO_4$ or/and 0.5 equiv. of PIPER. The thermal denaturation temperature is >95 °C.

Oligo E (5'- GGG G**L**^{1}T) in NaCl

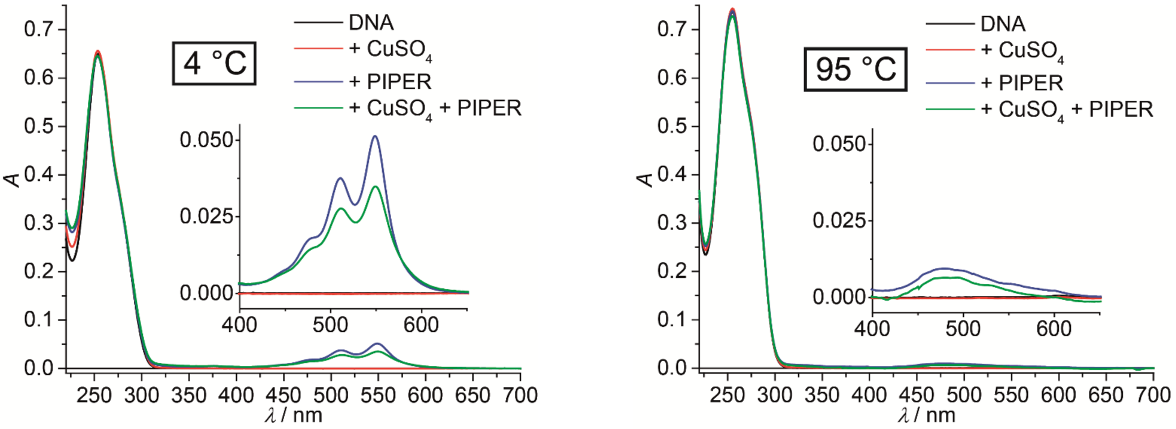

Figure 6.14: UV-VIS spectra of folded (4 °C, left) and unfolded (95 °C, right) G-quadruplex (GGG G**L**^{1}T)$_4$ in NaCl-containing solution in absence or presence of 1 equiv. of $CuSO_4$ or/and 0.5 equiv. of PIPER.

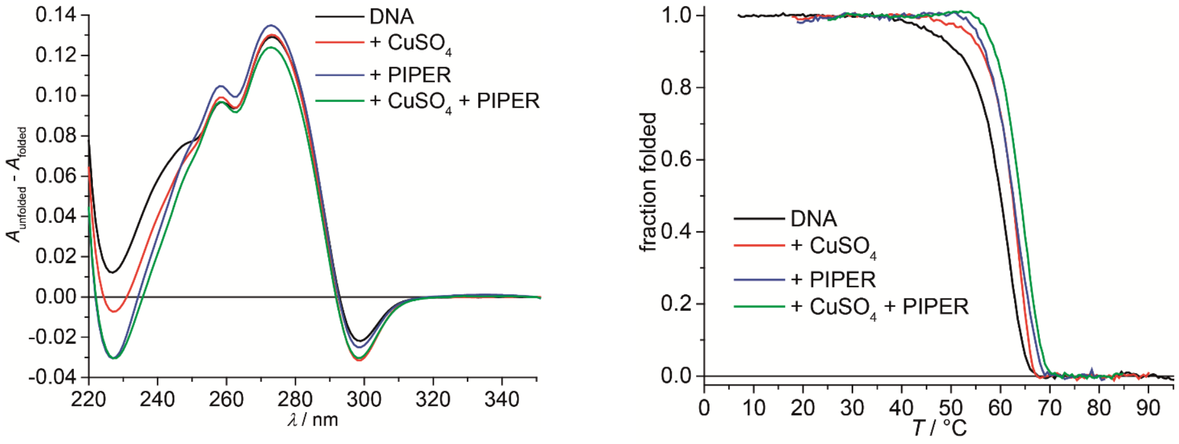

Figure 6.15: Thermal difference spectra (left) and thermal denaturation profiles (right) of G-quadruplex (GGG G**L**^{1}T)$_4$ in NaCl-containing solution in absence or presence of 1 equiv. of $CuSO_4$ or/and 0.5 equiv. of PIPER.

Oligo F (5’-TGG G$\mathbf{L}^1$T T) in KCl

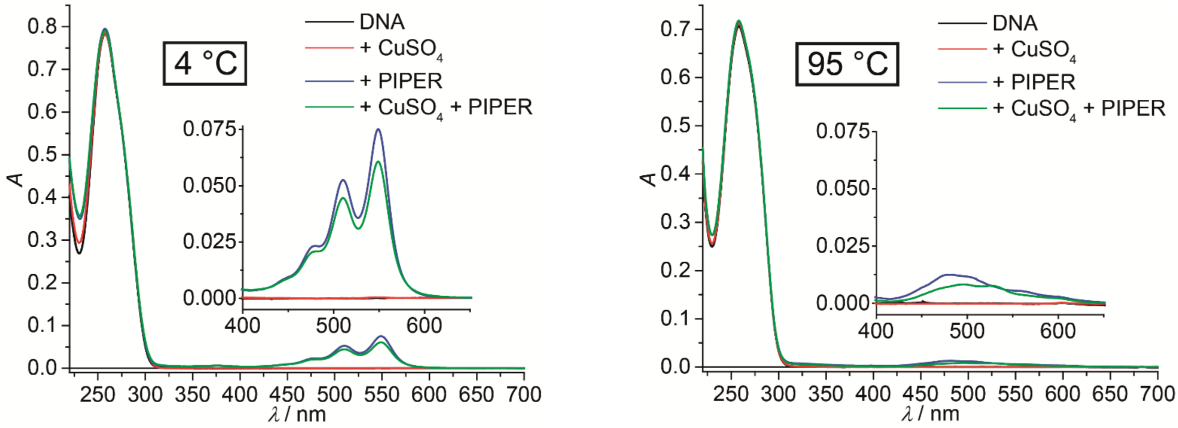

Figure 6.16: UV-VIS spectra of folded (4 °C, left) and unfolded (95 °C, right) G-quadruplex (TGG G$\mathbf{L}^1$T T)$_4$ in absence or presence of 1 equiv. of $CuSO_4$ or/and 0.5 equiv. of PIPER.

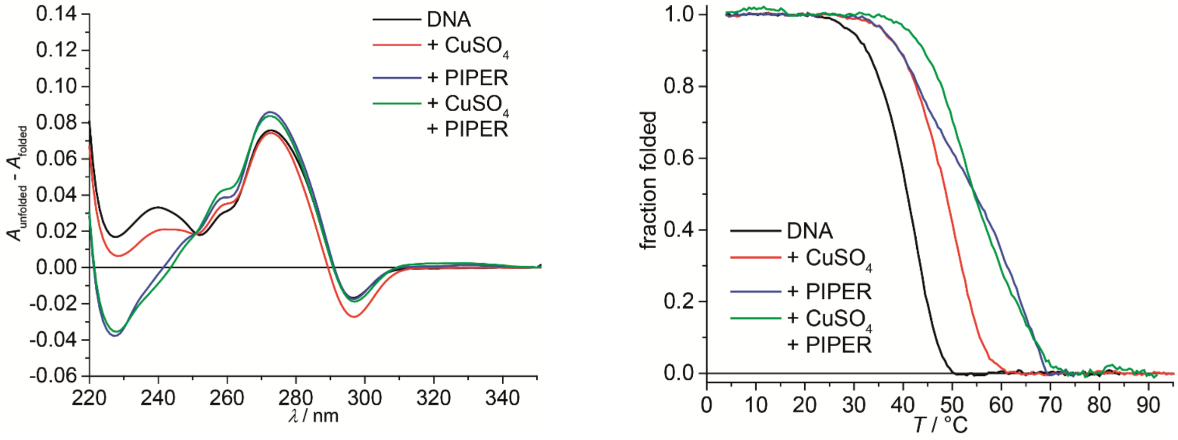

Figure 6.17: Thermal difference spectra (left) and thermal denaturation profiles (right) of G-quadruplex (TGG G$\mathbf{L}^1$T T)$_4$ in absence or presence of 1 equiv. of $CuSO_4$ or/and 0.5 equiv. of PIPER.

6.3 UV-Based Thermal Denaturation Studies of DNA Species Composed of Oligos G and H

6.3.1 Sample Preparation

DNA samples contained 1.5 µM oligo **G** and/or 1.5 µM oligo **H**, 100 mM KCl (explicitly stated, if not present), 10 mM lithium cacodylate buffer pH 7.2 and, if present, 1.5 µM or 3 µM $CuSO_4$ (1 equiv. per oligonucleotide).

Samples were heated to 85 °C for 10 min, slowly cooled to 4 °C with a cooling rate of 0.5 °C/min and then left at this temperature for several hours (typically overnight).

6.3.2 Spectrometer and Methods

Both UV spectra and thermal denaturation profiles (melting curves) were recorded on a *Jasco V-750 UV-Visible Spectrophotometer* equipped as described in Section 6.2.2.

UV spectra were recorded from 350 to 220 nm with a scan rate of 200 nm/min both before (0 °C) and after thermal denaturation (60 °C). The data interval was set to 1 nm, bandwidth to 2.0 nm and the response time to 0.96 sec.

To obtain thermal difference spectra (TDS), the spectrum before denaturation (at 0 °C) was subtracted from the one after denaturation (at 60 °C) and zeroed using the absorption at 350 nm. A negative band (hypochromic shift) at 295±2 nm and positive bands at 243±2 nm and 273±2 nm (hyperchromic shift) indicated G-quadruplex formation.[2]

For the thermal denaturation and reannealing profiles, absorption of the samples was recorded in a 0.5 °C interval with a temperature gradient set to 0.5 °C/min, which corresponds to ~0.174 °C/min including the measurement time. Absorption at 260 nm was recorded to monitor melting of double-stranded fragments, while absorption at 295 nm showed denaturation of G-quadruplex structures. Data points were recorded from 0 °C to 85 °C and back to 0 °C. Melting curves were background corrected using the absorption at 350 nm and normalized. Melting temperatures were determined by extracting the minimum of the first derivative which corresponds to the inflection point of the melting curve.

6.3.3 Melting and Reannealing Profiles and Thermal Difference Spectra

Oligos G + H

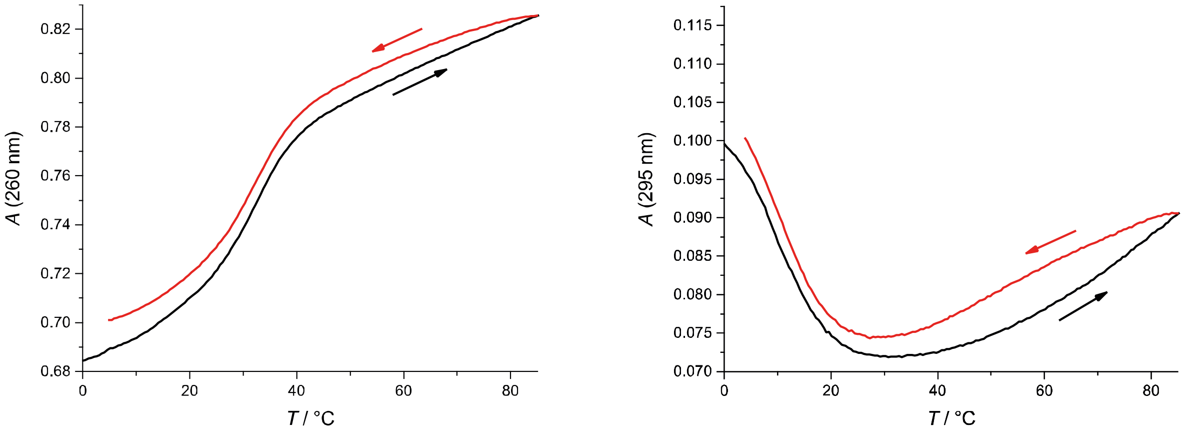

Figure 6.18: Raw thermal denaturation and reannealing profiles of duplex-bridged G-quadruplexes **GH** recorded at 260 nm (left) and at 295 nm (right) in the absence of Cu^{2+} ions.

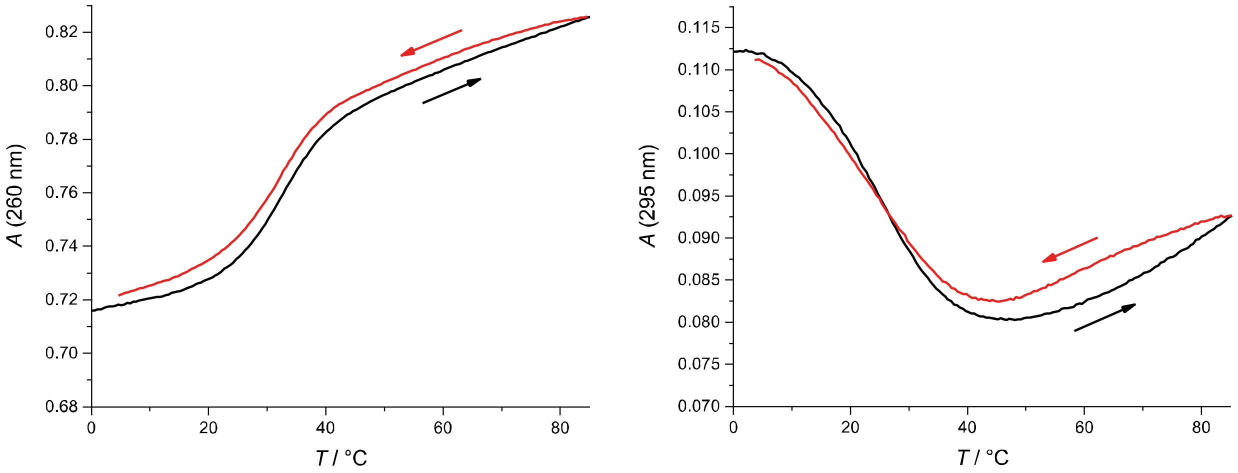

Figure 6.19: Raw thermal denaturation and reannealing profiles of duplex-bridged G-quadruplexes [2Cu²⁺@**GH**] recorded at 260 nm (left) and at 295 nm (right) in the presence of Cu²⁺ ions.

Oligo G

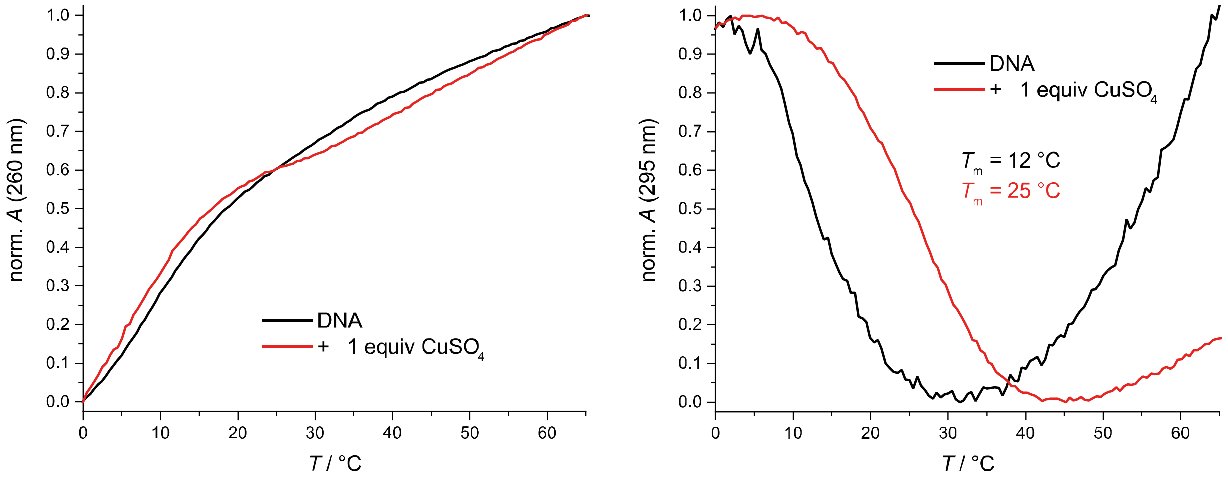

Figure 6.20: Normalized thermal denaturation profiles of oligo **G** recorded at 260 nm (left) and at 295 nm (right) in the absence or presence of Cu²⁺ ions.

Oligo H

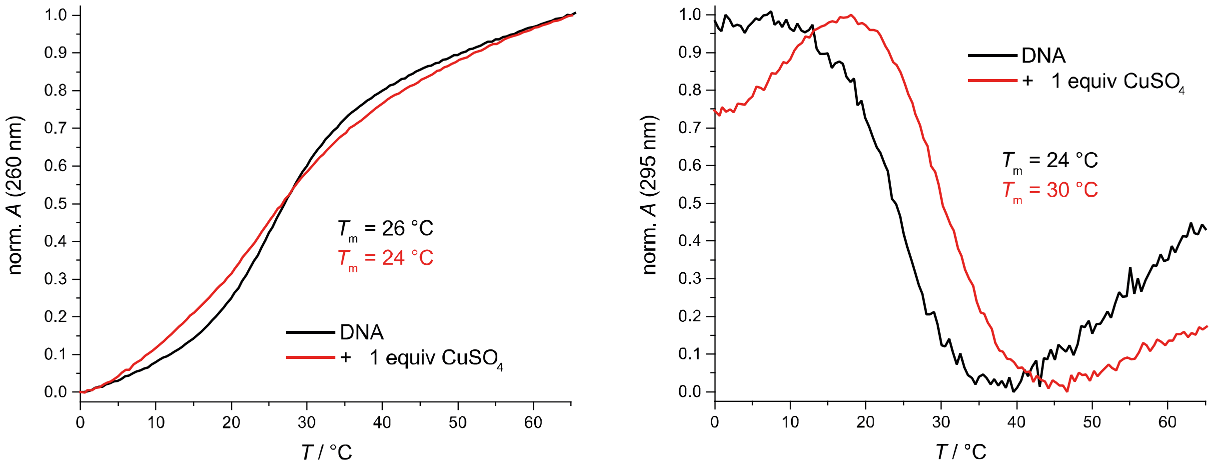

Figure 6.21: Normalized thermal denaturation profiles of oligo **H** recorded at 260 nm (left) and at 295 nm (right) in the absence or presence of Cu²⁺ ions.

Oligo G and oligo H

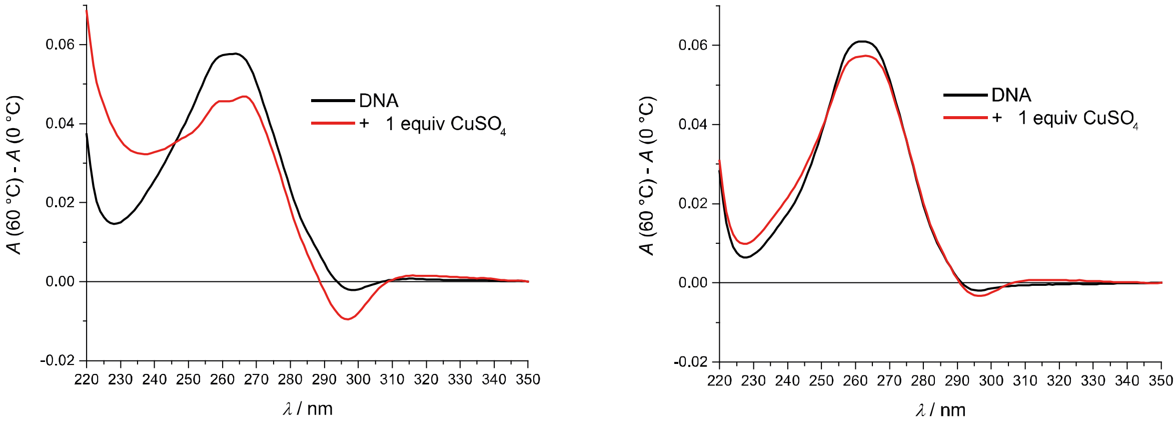

Figure 6.22: Thermal difference spectra of oligo **G** (left) and oligo **H** (right) in the absence or presence of Cu^{2+} ions.

6.4 UV-Based Thermal Denaturation Studies of G-Quadruplexes Formed by Oligos J and TEMPO-K)

6.4.1 Sample Preparation

G-quadruplex samples contained 1 µM single-stranded DNA (1 µM G-quadruplex), 100 mM KCl, 10 mM lithium cacodylate buffer pH 7.2 and, if present, 1 or 2 µM $CuSO_4$. Samples were prepared with ultrapure water (type I, 18.2 MΩ cm), obtained with a *VWR Puranity TU 3 UV*.

Samples were heated to 85 °C for 10 min, slowly cooled to 4 °C with a cooling rate of 0.5 °C/min and then left at this temperature for several hours (typically overnight).

6.4.2 Spectrometer and Methods

Both UV spectra and thermal denaturation profiles (melting curves) were recorded on a *Jasco V-750 UV-Visible Spectrophotometer* equipped as described in Section 6.2.2.

UV spectra were recorded from 350 to 220 nm with a scan rate of 200 nm/min both before (4 °C) and after thermal denaturation (95 °C). The data interval was set to 1 nm, bandwidth to 2.0 nm and the response time to 0.96 sec.

To obtain thermal difference spectra (TDS), the spectrum before denaturation (at 4 °C) was subtracted from the one after denaturation (at 95 °C) and zeroed using the absorption at 350 nm. A negative band (hypochromic shift) at 295±2 nm and positive bands at 243±2 nm and 273±2 nm (hyperchromic shift) indicated G-quadruplex formation.[2]

For the thermal denaturation profiles (and reannealing profiles), absorption of the samples at 295 nm was recorded in a 0.5 °C interval with a temperature gradient set to 0.5 °C/min, which corresponds to ~0.174 °C/min including the measurement time. Data points were recorded from 4 °C to 95 °C. Melting curves were background corrected using the absorption at 350 nm and converted to the fraction folded values by linear fitting of the low and high temperature baselines.[3] Thermal denaturation temperatures were then determined by extracting the respective value at the point where 50% of the fraction was denatured.

6.5 UV-Based Thermal Denaturation Studies of G-Quadruplexes X_4 (X = L–T)

6.5.1 Sample Preparation

Sample compositions for thermal denaturation studies varied for different investigated oligonucleotides and are described below.

For oligos **L**–**R**, G-quadruplex samples contained 4 µM single-stranded DNA (1 µM tetramolecular G-quadruplex), 100 mM NaCl (or 100 mM $Na(ClO_4)$, if indicated), 10 mM lithium cacodylate buffer pH 7.2 (or 10 mM CHES buffer pH 9.6, if indicated) and, if present, 1, 2, 3 or 5 µM $CuSO_4$ or 1 µM $NiSO_4$, ZnI_2, $Co(NO_3)_2$, $GdCl_3$, $CeCl_3$, $Fe(ClO_4)_3$, $NH_4Fe(SO_4)_2$, $Hg(OAc)_2$ or $Cd(ClO_4)_2$, or 1 or 10 µM of $HAuCl_4$, $AgClO_4$, $Pd(ACN)_4(BF_4)_2$ or $Pd(NO_3)_2$.

For oligos $\mathbf{S^{ox}}$ and $\mathbf{T^{ox}}$, G-quadruplex samples contained 4 or 2 µM disulfide-bridged single-stranded DNA (2 or 1 µM bimolecular G-quadruplex), 100 mM NaCl or KCl, and 10 or 50 mM lithium cacodylate buffer pH 7.2.

For all experiments, samples were prepared with ultrapure water (type I, 18.2 MΩ cm), obtained with a *VWR Puranity TU 3 UV*.

Samples were heated to 85 °C for 10 min, slowly cooled to 4 °C with a cooling rate of 0.5 °C/min and then left at this temperature for several hours (typically overnight). To ensure full formation of tetra- or bimolecular G-quadruplexes, the samples were frozen at –20 °C for 1 h[1] and thawed again to 4 °C.

6.5.2 Spectrometer and Methods

Both UV spectra and thermal denaturation profiles (melting curves) were recorded on a *Jasco V-750* or *Jasco V-750 UV-Visible Spectrophotometer* equipped as described in Section 6.2.2.

UV spectra were recorded from 350 to 220 nm with a scan rate of 200 nm/min both before (0 °C or 4 °C) and after thermal denaturation (85 °C or 95 °C). The data interval was set to 1 nm, bandwidth to 2.0 nm and the response time to 0.96 sec.

To obtain thermal difference spectra (TDS), the spectrum before denaturation (at 0 °C or 4 °C) was subtracted from the one after denaturation (at 85 °C or 95 °C) and zeroed using the absorption at 350 nm. A negative band (hypochromic shift) at 295±2 nm and positive bands at 243±2 nm and 273±2 nm (hyperchromic shift) indicated G-quadruplex formation.[2]

For the thermal denaturation profiles (and reannealing profiles), absorption of the samples at 295 nm was recorded in a 0.5 °C interval with a temperature gradient set to 0.5 °C/min, which corresponds to ~0.174 °C/min including the measurement time. Data points were recorded from 4 °C to 85 °C or 95 °C (and back to 4 °C). Melting curves were background corrected using the absorption at 350 nm and converted to the fraction folded values by linear fitting of the low and high temperature baselines.[3] Thermal denaturation temperatures were then determined by extracting the respective value at the point where 50% of the fraction was denatured.

6.5.3 Thermal Difference Spectra and Melting Profiles

Oligo L (5’-**L**^{3}GG G)

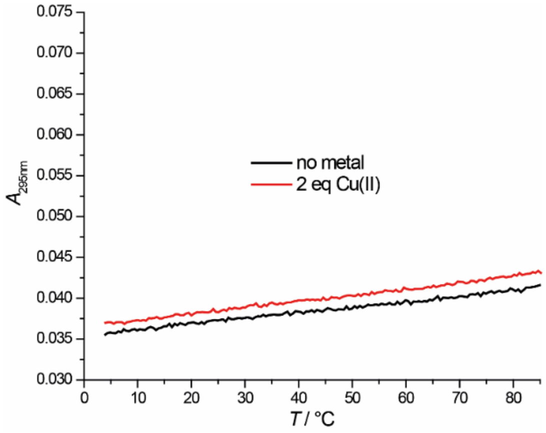

Figure 6.23: Temperature-dependent absorption of oligo **L** at 295 nm. No thermal denaturation is observed in absence or presence of 2 equiv. CuSO$_4$, which suggests no G-quadruplex formation.

Oligo M (5’-**L**^{3}GG GG)

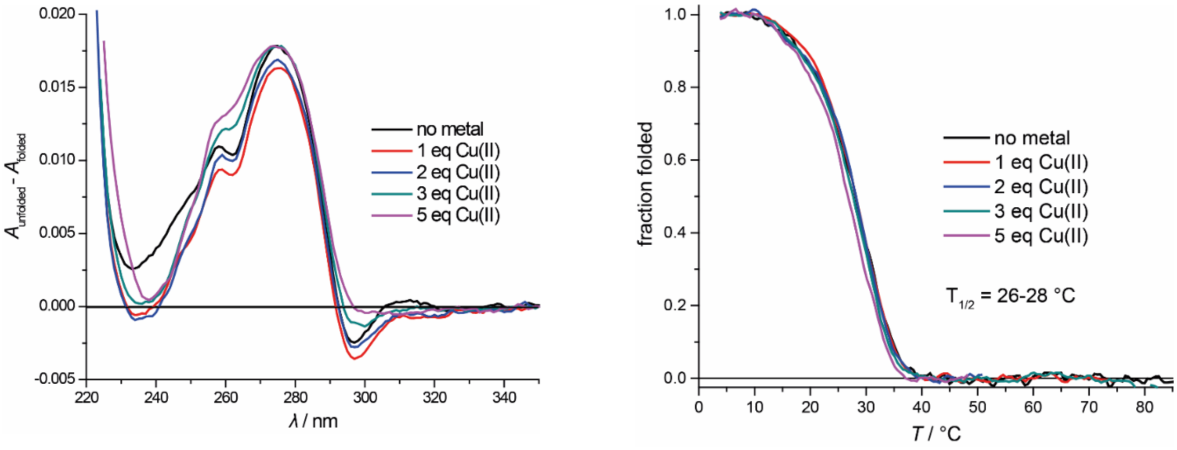

Figure 6.24: Thermal difference spectra (left) and melting profiles (right) of G-quadruplex **M**$_4$ in absence or presence of 1, 2, 3 or 5 equiv. of CuSO$_4$.

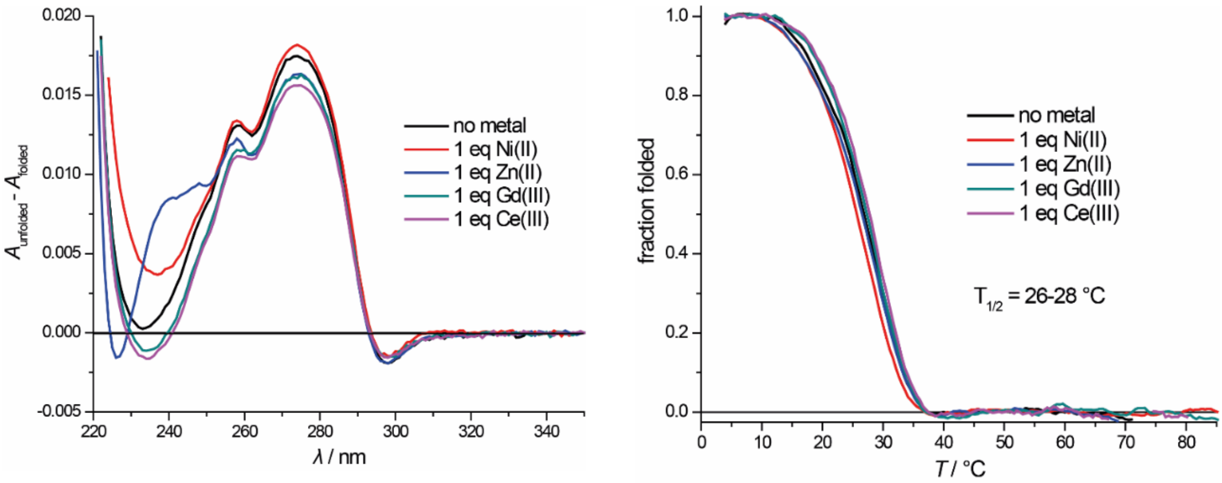

Figure 6.25: Thermal difference spectra (left) and melting profiles (right) of G-quadruplex **M**$_4$ in absence or presence of 1 equiv. of NiSO$_4$, ZnI$_2$, GdCl$_3$ or CeCl$_3$.

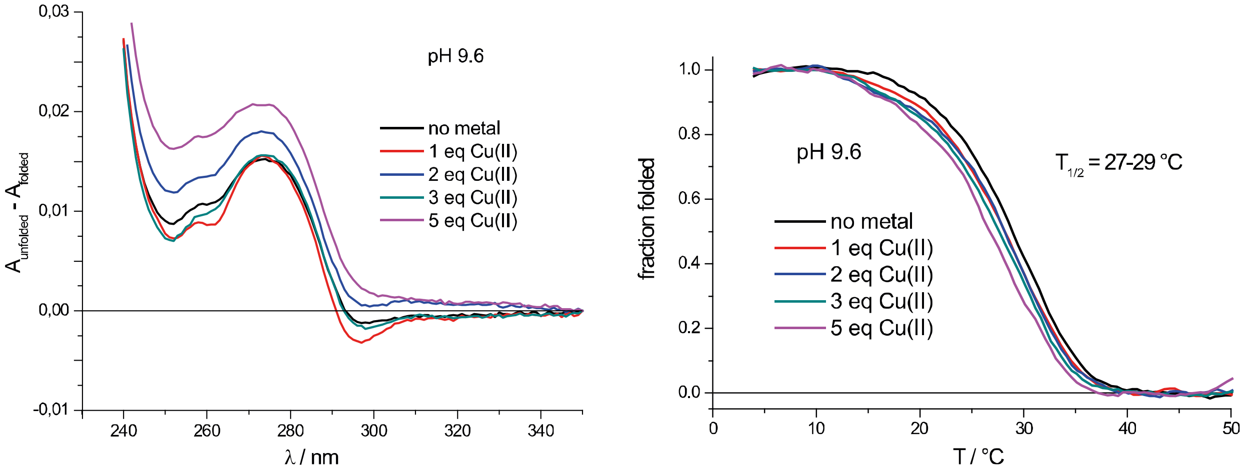

Figure 6.26: Thermal difference spectra (left) and melting profiles (right) of G-quadruplex **M**$_4$ in absence or presence of 1, 2, 3 or 5 equiv. of CuSO$_4$ at pH 9.6.

Oligo N (5'-**L**^{3}GG GGG)

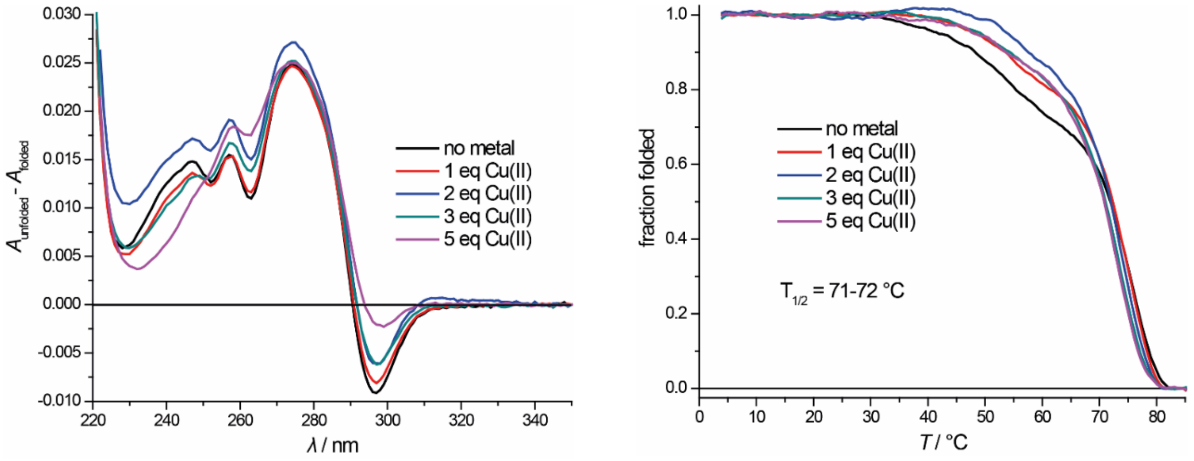

Figure 6.27: Thermal difference spectra (left) and melting profiles (right) of G-quadruplex **N**$_4$ in absence or presence of 1, 2, 3 or 5 equiv. of $CuSO_4$.

Oligo Q (5'-**L**^{5}GG GG)

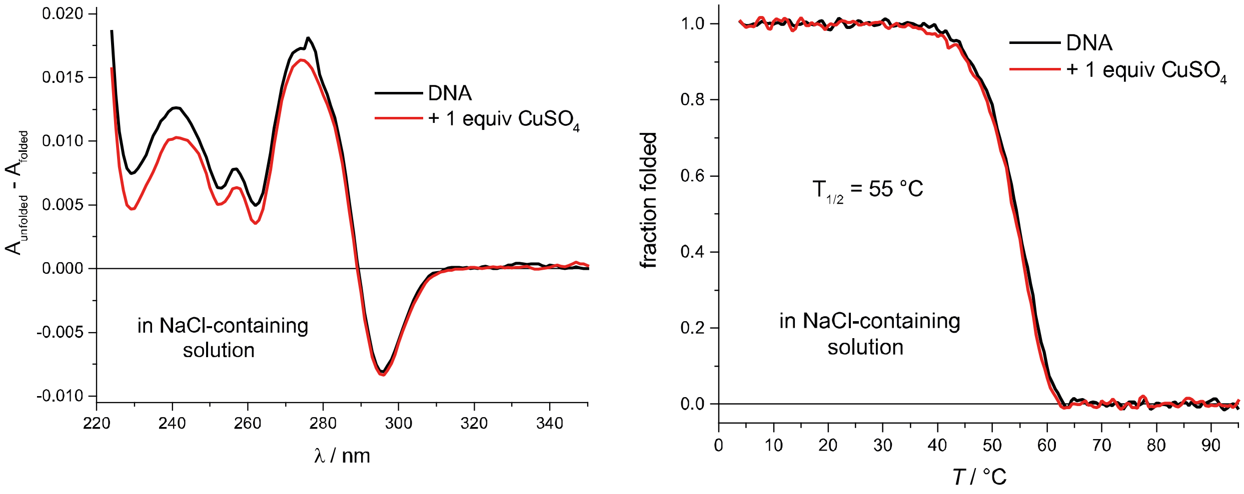

Figure 6.28: Thermal difference spectra (left) and melting profiles (right) of G-quadruplex **Q**$_4$ in absence or presence of 1 equiv. of $CuSO_4$ in NaCl-containing solution.

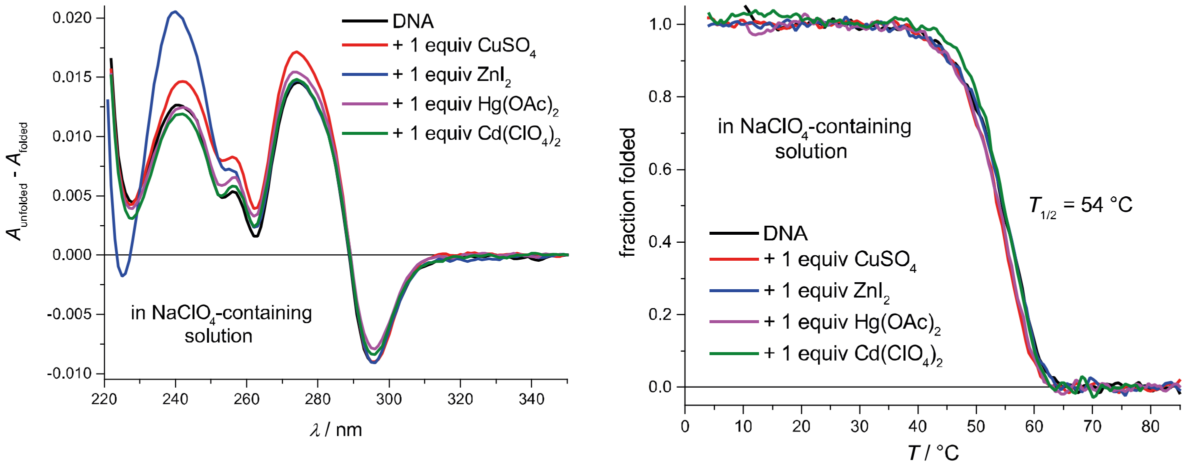

Figure 6.29: Thermal difference spectra (left) and melting profiles (right) of G-quadruplex **Q**$_4$ in absence or presence of 1 equiv. $CuSO_4$, ZnI_2, $Hg(OAc)_2$ or $Cd(ClO_4)_2$ in $NaClO_4$-containing solution.

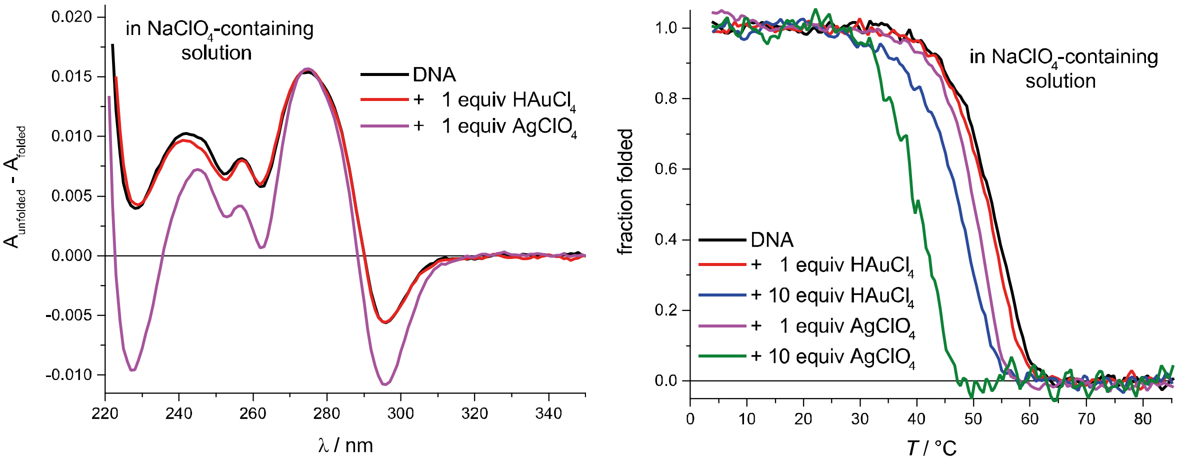

Figure 6.30: Thermal difference spectra (left) and melting profiles (right) of G-quadruplex **Q**4 in absence or presence of 1 or 10 equiv. $HAuCl_4$ or $AgClO_4$ in $NaClO_4$-containing solution.

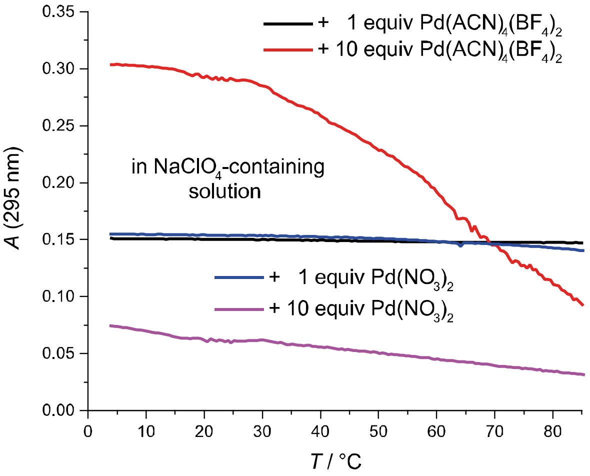

Figure 6.31: Temperature-dependent absorption of oligo **Q** at 295 nm in the presence of 1 or 10 equiv. $Pd(ACN)_4(BF_4)_2$ or $Pd(NO_3)_2$. No thermal denaturation is observed which suggests no G-quadruplex formation. Addition of excess of Pd salt caused a brown precipitation probably due to reduction to metallic Pd.

6.6 UV-Based Thermal Denaturation Studies of Unimolecular G-Quadruplexes htelL$^3_{4\text{-}n}$L^8_n and htelL$^3_{6\text{-}n}$L^8_n

6.6.1 Sample Preparation

G-quadruplex samples contained 1.88 µM single-stranded DNA, 100 mM KCl, 10 mM lithium cacodylate buffer pH 7.2, and, if present, 1.88 µM or 3.75 µM $Co(NO_3)_2$, $NiSO_4$, $CuSO_4$, ZnI_2 or $VOSO_4$. For all experiments, samples were prepared with ultrapure water (type I, 18.2 MΩ cm), obtained with a *VWR Puranity TU 3 UV*.

Samples were heated to 85 °C for 10 min, slowly cooled to 4 °C with a cooling rate of 0.5 °C/min and then left at this temperature for several hours (typically overnight).

6.6.2 Spectrometer and Methods

Both UV spectra and thermal denaturation profiles (melting curves) were recorded on an instrument setup as described in Section 6.5.2. Thermal difference spectra and melting profiles were gathered as described in Section 6.5.2.

Melting curves with $T_m \geq 20$ °C were converted to the fraction folded values by linear fitting of the low and high temperature baselines.[3] Thermal denaturation temperatures were then determined by extracting the respective value at the point where 50% of the fraction was denatured. Baseline fitting in the low temperature range was not possible for melting curves with $T_m < 20$ °C. Consequently, raw data are presented, and the melting temperatures were determined by extracting the minimum of the first derivative which corresponds to the inflection point of the melting curve.

6.6.3 Melting Profiles and Thermal Difference Spectra

htel**L**$^3{}_4$

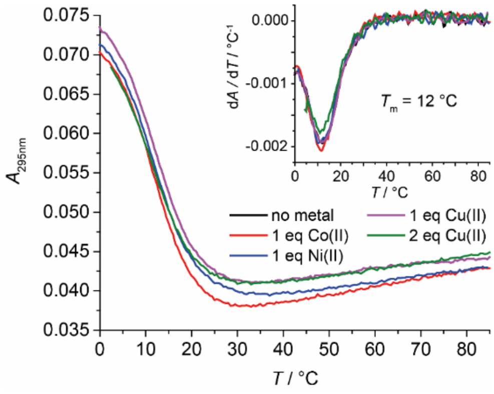

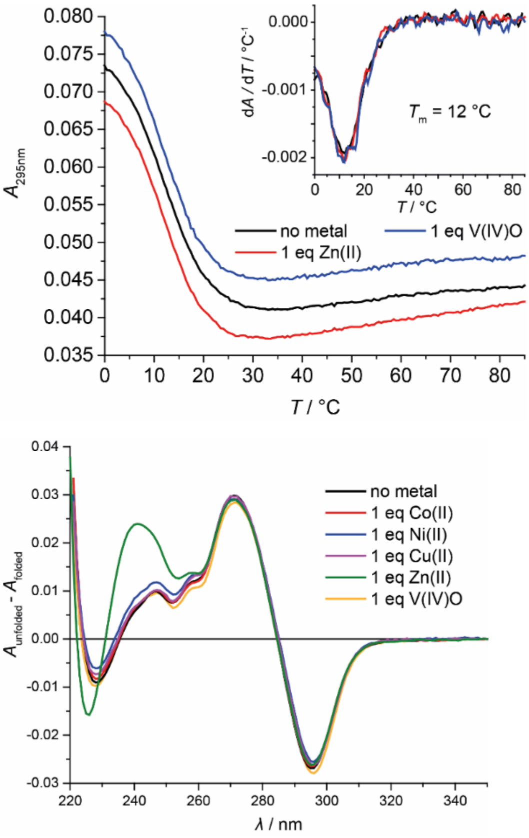

Figure 6.32: Thermal denaturation profiles and thermal difference spectra of G-quadruplex htel**L**$^3{}_4$ in the absence or presence of $Co(NO_3)_2$, $NiSO_4$, $CuSO_4$, ZnI_2 or $VOSO_4$. Melting temperatures were determined by extracting the minimum of the first derivative. No thermal stabilization could be observed after addition of transition metal ions.

htel$\mathbf{L}^3{}_3\mathbf{L}^8$

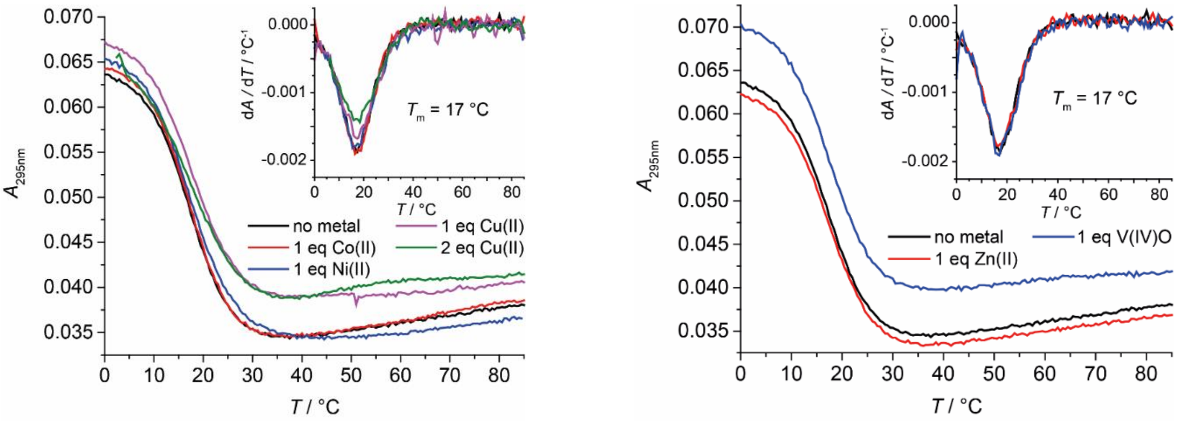

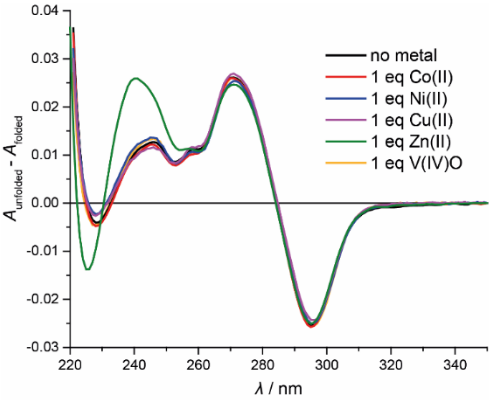

Figure 6.33: Thermal denaturation profiles and thermal difference spectra of G-quadruplex htel$\mathbf{L}^3{}_3\mathbf{L}^8$ in the absence or presence of $Co(NO_3)_2$, $NiSO_4$, $CuSO_4$, ZnI_2 or $VOSO_4$. Melting temperatures were determined by extracting the minimum of the first derivative. No thermal stabilization could be observed after addition of transition metal ions.

htel$\mathbf{L}^3{}_2\mathbf{L}^8{}_2$

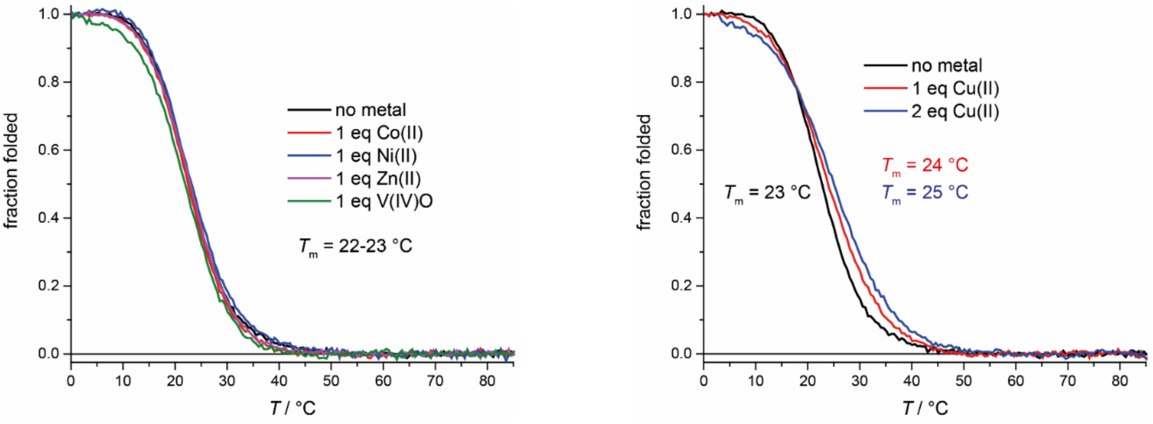

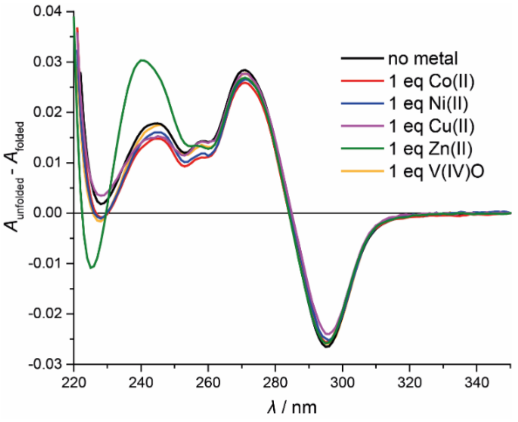

Figure 6.34: Thermal denaturation profiles and thermal difference spectra of G-quadruplex htel$\mathbf{L}^3{}_2\mathbf{L}^8{}_2$ in the absence or presence of $Co(NO_3)_2$, $NiSO_4$, $CuSO_4$, ZnI_2 or $VOSO_4$. A weak thermal stabilization could be observed after addition of Cu^{2+} ions.

htel$\mathbf{L}^3\mathbf{L}^8{}_3$

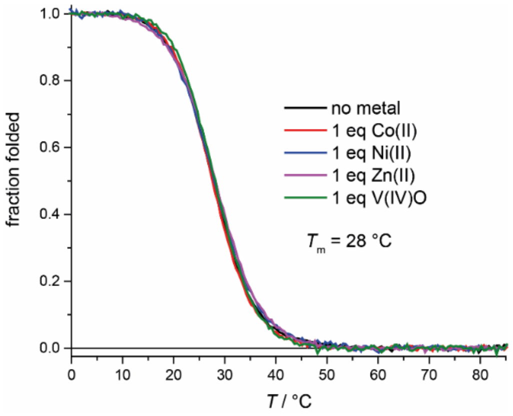

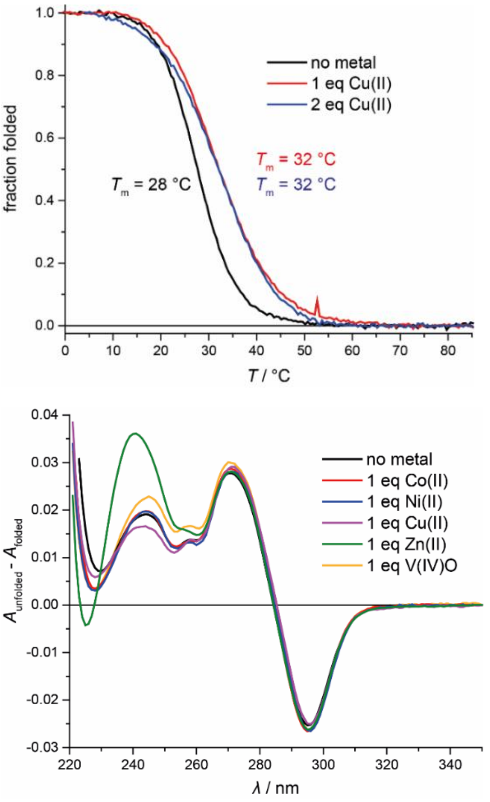

Figure 6.35: Thermal denaturation profiles and thermal difference spectra of G-quadruplex htel$\mathbf{L}^3\mathbf{L}^8{}_3$ in the absence or presence of $Co(NO_3)_2$, $NiSO_4$, $CuSO_4$, ZnI_2 or $VOSO_4$. A weak thermal stabilization could be observed after addition of Cu^{2+} ions.

htel$\mathbf{L}^3{}_4\mathbf{L}^8{}_2$

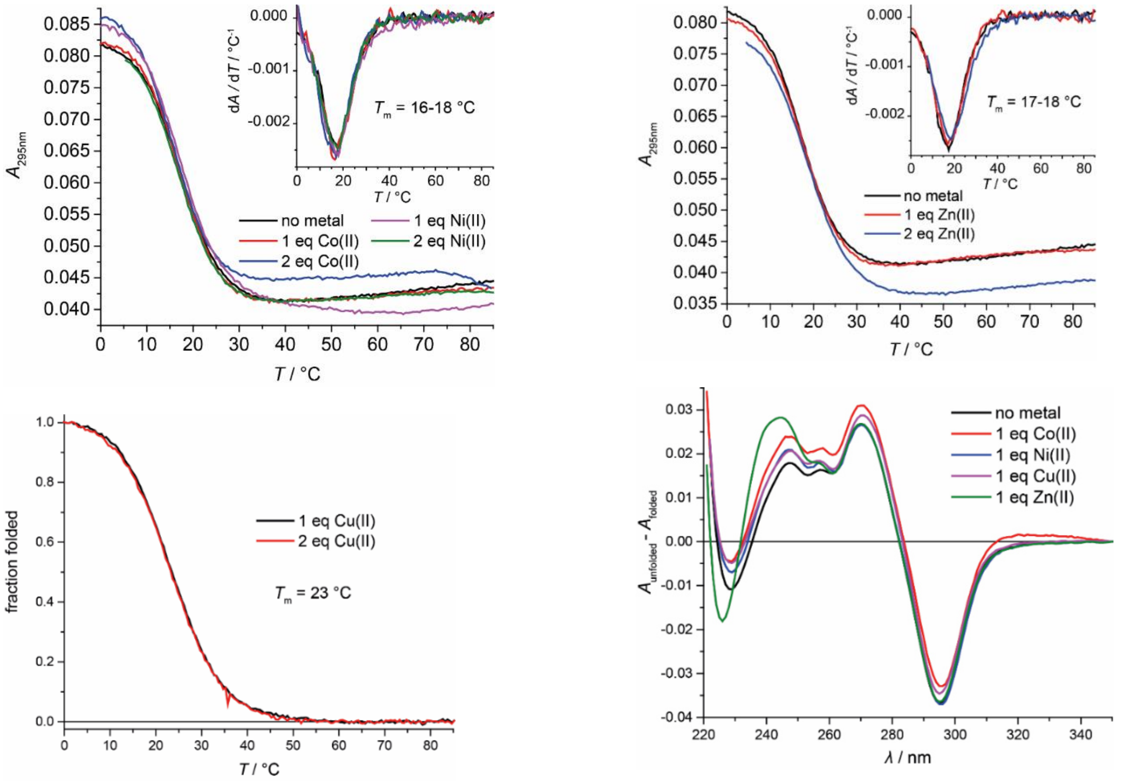

Figure 6.36: Thermal denaturation profiles and thermal difference spectra of G-quadruplex htel$\mathbf{L}^3{}_4\mathbf{L}^8{}_2$ in the absence or presence of $Co(NO_3)_2$, $NiSO_4$, $CuSO_4$ or ZnI_2. Thermal stabilization could be observed after addition of Cu^{2+} ions.

htel$\mathbf{L}^3{}_3\mathbf{L}^8{}_3$

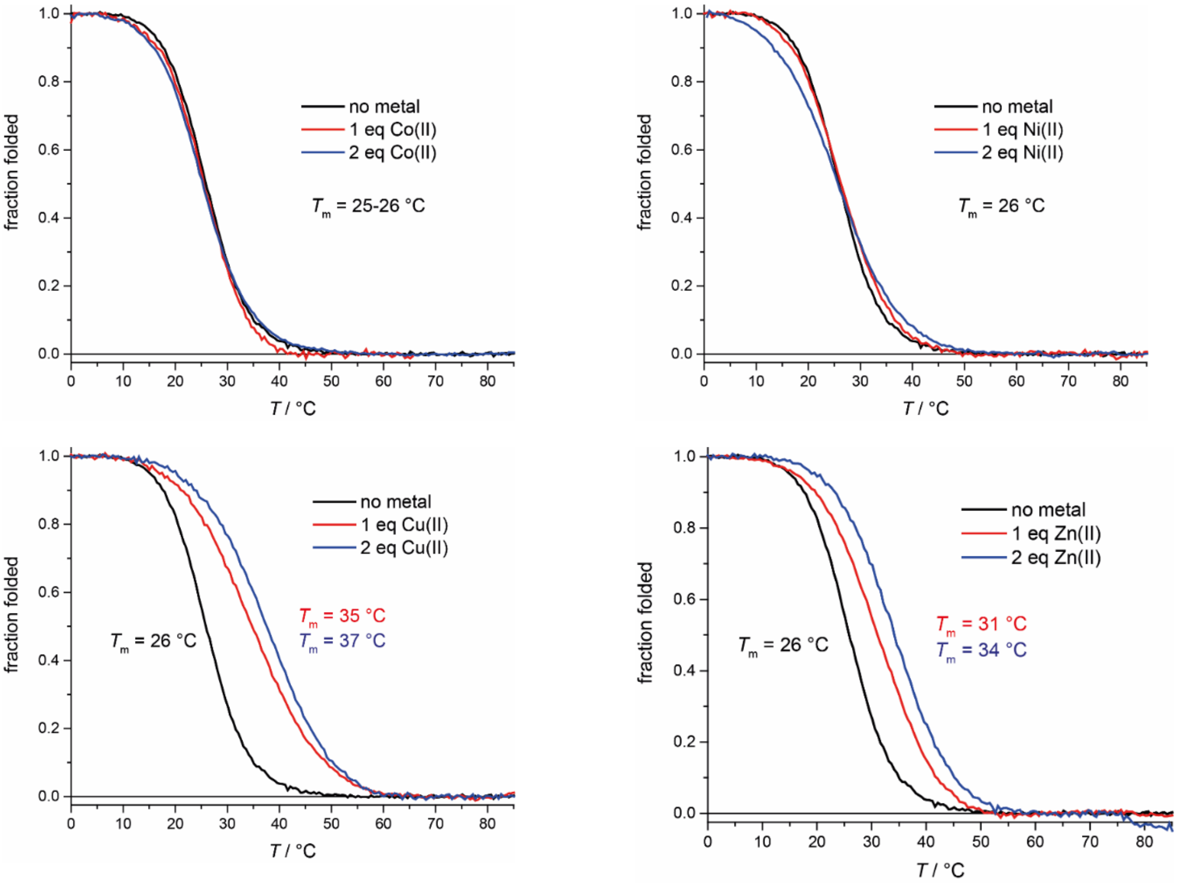

Figure 6.37: Thermal denaturation profiles and thermal difference spectra of G-quadruplex htel$\mathbf{L}^3{}_3\mathbf{L}^8{}_3$ in the absence or presence of $Co(NO_3)_2$, $NiSO_4$, $CuSO_4$ or ZnI_2. Thermal stabilization could be observed after addition of Cu^{2+} and Zn^{2+} ions.

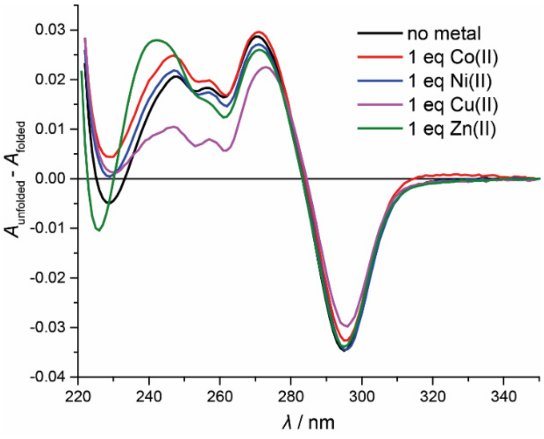

htel$\mathbf{L}^3{}_2\mathbf{L}^8{}_4$

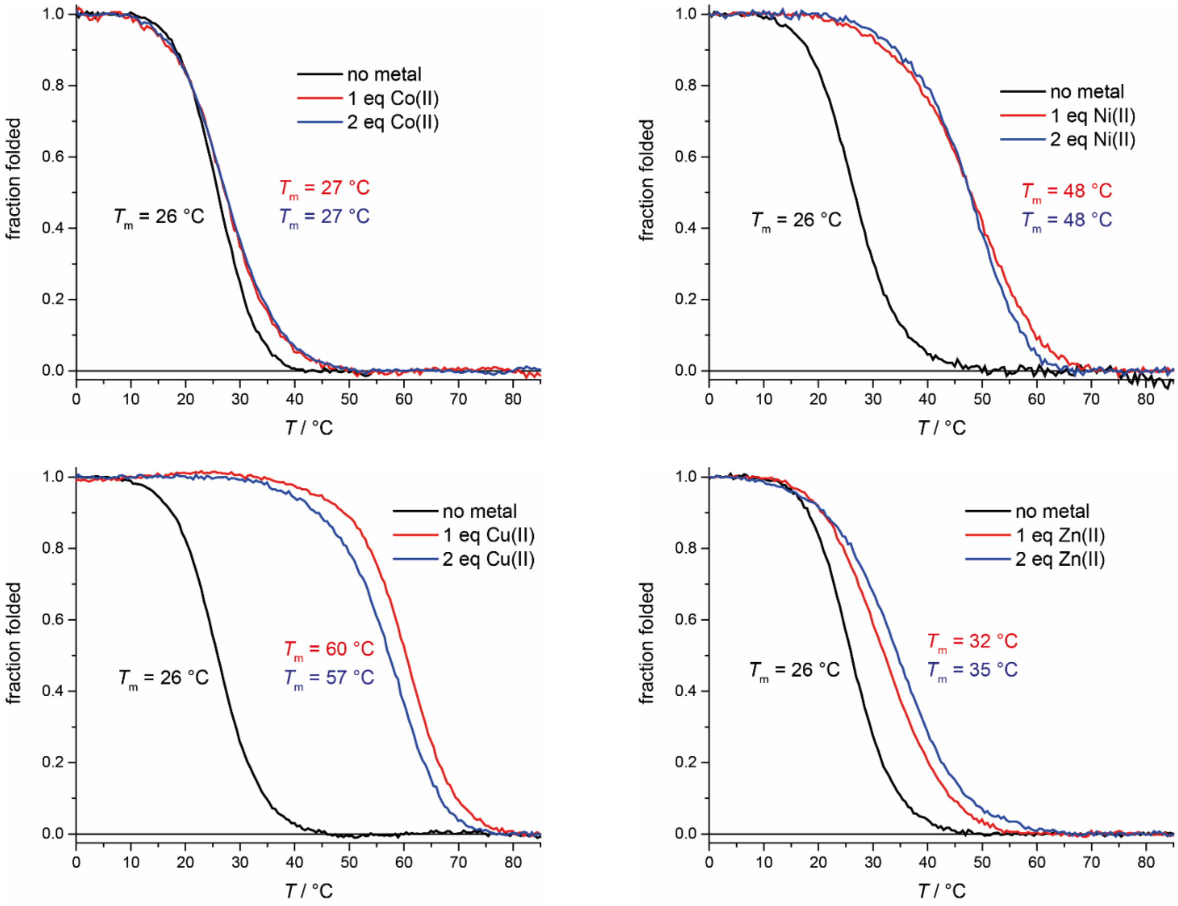

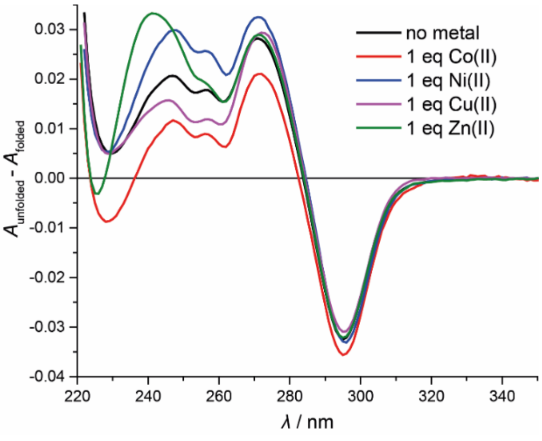

Figure 6.38: Thermal denaturation profiles and thermal difference spectra of G-quadruplex htel$\mathbf{L}^3{}_2\mathbf{L}^8{}_4$ in the absence or presence of $Co(NO_3)_2$, $NiSO_4$, $CuSO_4$ or ZnI_2. Thermal stabilization could be observed after addition of transition metal ions.

htel**L**$^{8}_{4}$B

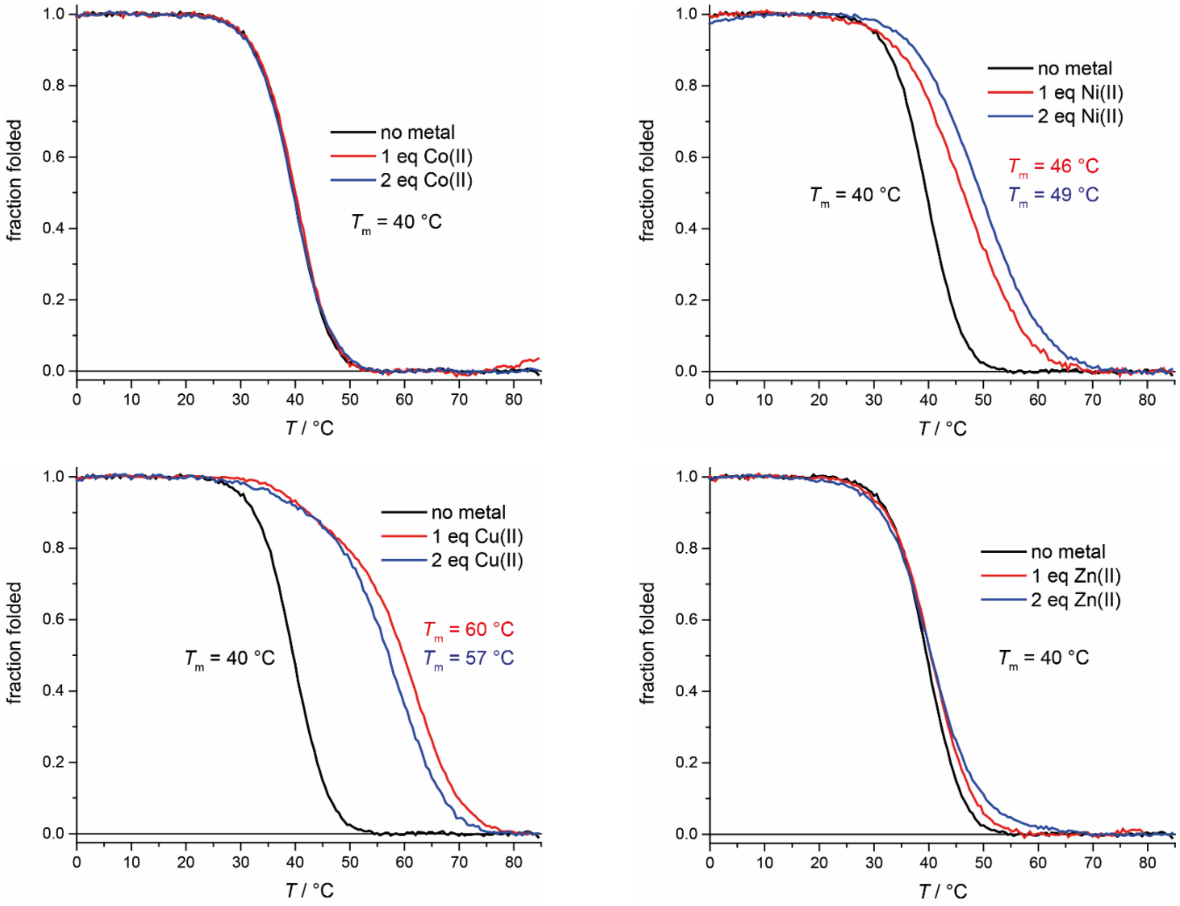

Figure 6.39: Thermal denaturation profiles and thermal difference spectra of G-quadruplex htel**L**$^{8}_{4}$B in the absence or presence of $Co(NO_3)_2$, $NiSO_4$, $CuSO_4$ or ZnI_2. Thermal stabilization could be observed after addition of Cu^{2+} and Ni^{2+} ions.

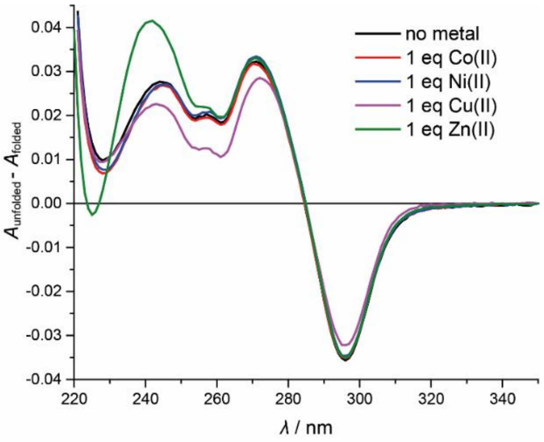

6.7 CD Spectroscopy of G-Quadruplexes X_4 (X = A–F)

6.7.1 Sample Preparation

For standard CD measurements, the samples were prepared in the same way as for the UV-VIS-based thermal denaturation studies (Section 6.2.1). G-quadruplex samples with higher concentration containing 80 µM single-stranded DNA (20 µM G-quadruplex DNA), 100 mM KCl, 10 mM lithium cacodylate buffer pH 7.2, 20 µM $CuSO_4$ and 10 µM PIPER were prepared to detect induced CD.

6.7.2 Spectrometer and Methods

CD spectra were measured on an *Applied Photophysics Chirascan qCD spectropolarimeter* (350–205 nm (or 700–205 nm for the detection of induced CD), 0.5 s time-per-point, step size 1 nm, bandwidth 0.5 nm, 3 repeats) at 4–7 °C. Temperature was controlled using a *Quantum Northwest* temperature control attached to a sample probe. The background was measured in the same cuvette as the sample. To avoid condensation of water onto the cuvette surface or cell window, a constant nitrogen gas flow was maintained. All spectra were averaged, background corrected (cuvette, buffer, and electrolyte), smoothed (Savitzky-Golay, window size 5) and zeroed to the signal at 350 nm.

6.7.3 CD Spectra

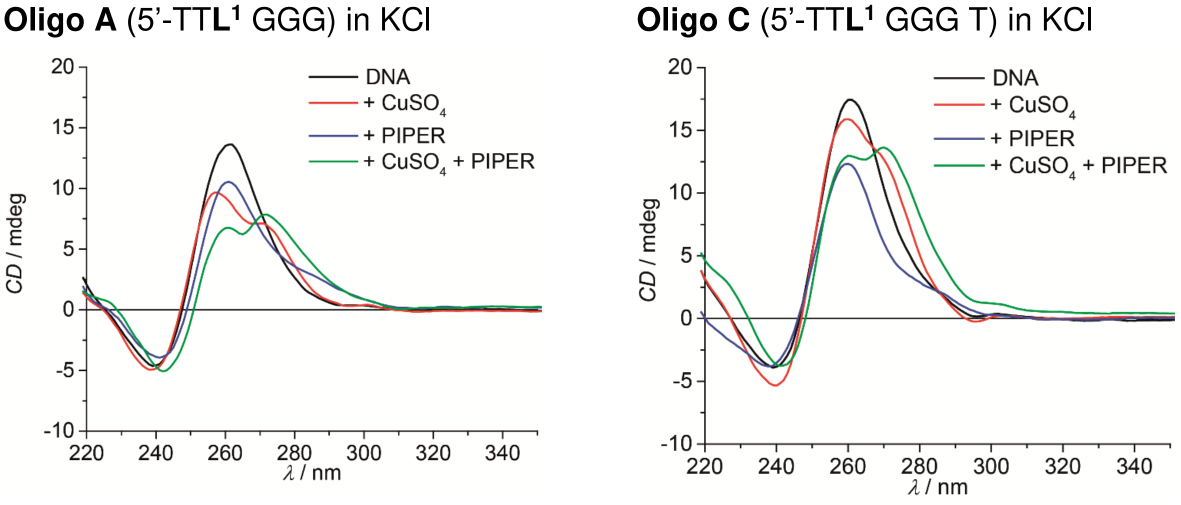

Oligo A (5’-TT**L**^{1} GGG) in KCl

Oligo C (5’-TT**L**^{1} GGG T) in KCl

Figure 6.40: CD spectra of folded G-quadruplex (TT**L**^{1} GGG)$_4$ (left) and (TT**L**^{1} GGG T)$_4$ (right) in absence or presence of 1 equiv. of $CuSO_4$ or/and 0.5 equiv. of PIPER.

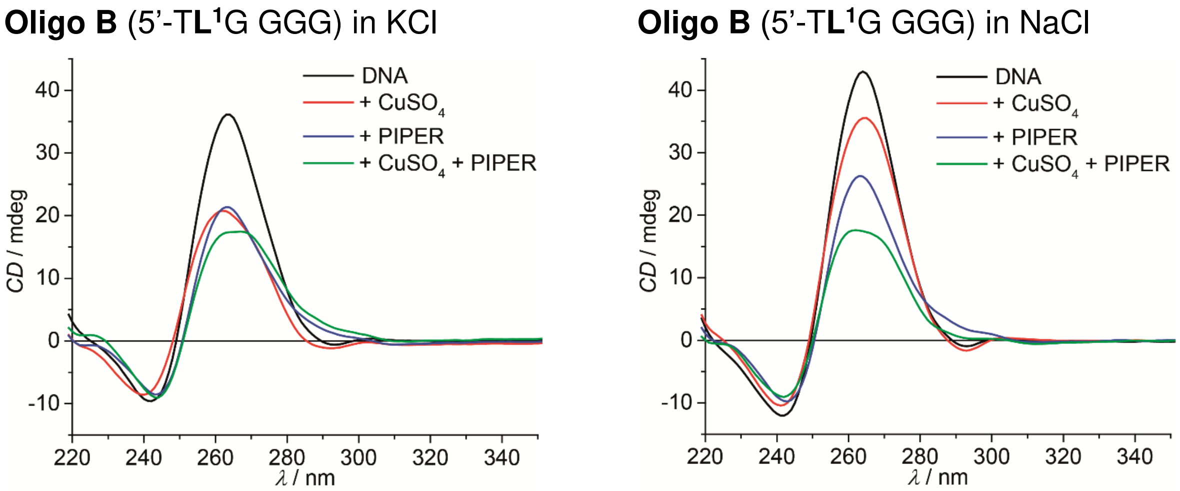

Oligo B (5'-T**L**^{1}G GGG) in KCl

Oligo B (5'-T**L**^{1}G GGG) in NaCl

Figure 6.41: CD spectra of folded G-quadruplex (T**L**^{1}G GGG)$_4$ in KCl- (left) and NaCl- (right) containing solution in absence or presence of 1 equiv. of $CuSO_4$ or/and 0.5 equiv. of PIPER.

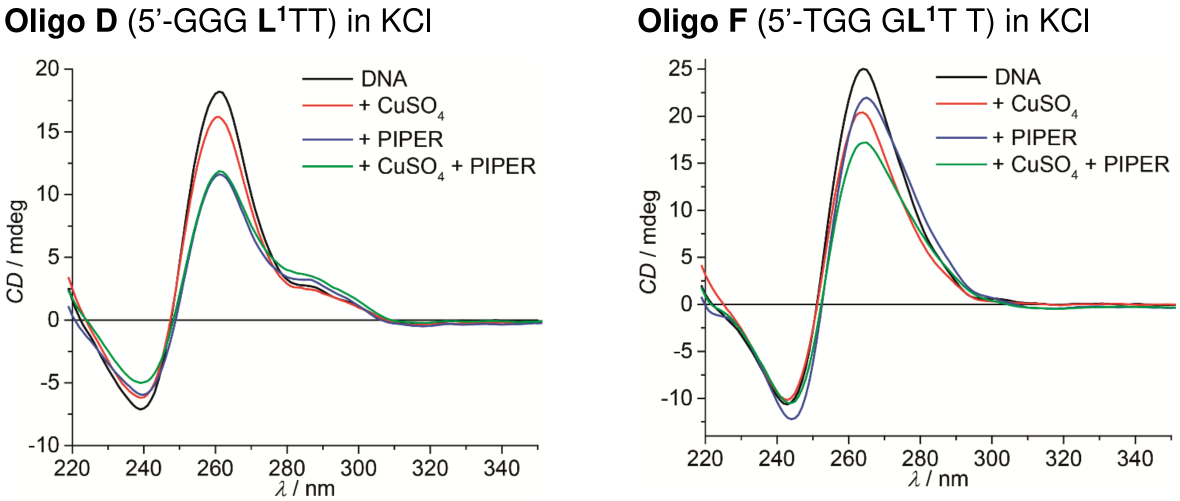

Oligo D (5'-GGG **L**^{1}TT) in KCl

Oligo F (5'-TGG G**L**^{1}T T) in KCl

Figure 6.42: CD spectra of folded G-quadruplex (GGG **L**^{1}TT)$_4$ (left) and (TGG G**L**^{1}T T)$_4$ (right) in absence or presence of 1 equiv. of $CuSO_4$ or/and 0.5 equiv. of PIPER.

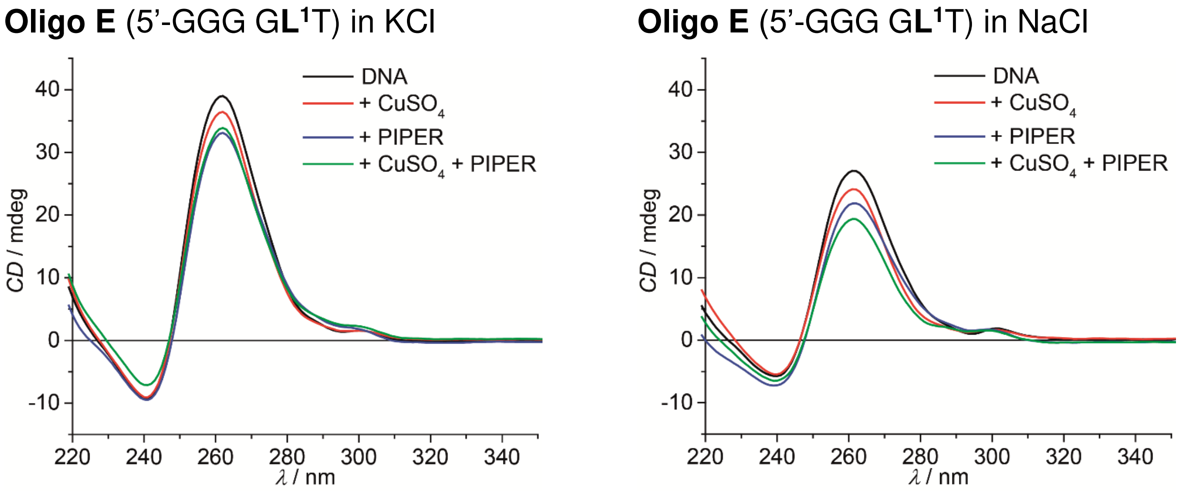

Oligo E (5'-GGG G**L**^{1}T) in KCl

Oligo E (5'-GGG G**L**^{1}T) in NaCl

Figure 6.43: CD spectra of folded G-quadruplex (GGG G**L**^{1}T)$_4$ in KCl- (left) and NaCl- (right) containing solution in absence or presence of 1 equiv. of $CuSO_4$ or/and 0.5 equiv. of PIPER.

6.8 CD Spectroscopy of DNA Species Composed of Oligos G, H, J and TEMPO-K

6.8.1 Sample Preparation, Spectrometer and Method

DNA samples were prepared in the same way as for the UV-based thermal denaturation studies (Sections 6.3.1 and 6.4.1). CD spectra were measured as described in Section 6.7.2, but for some samples, the temperature was varied between 8, 20, and 60 °C.

6.8.2 CD Spectra

Oligo G

Oligo H

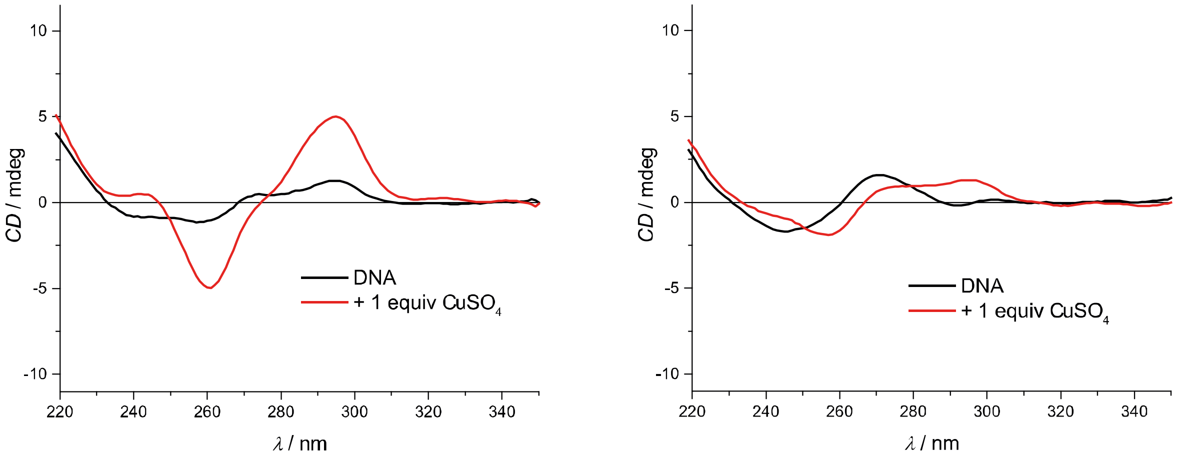

Figure 6.44: CD spectra of oligo **G** (left) and oligo **H** (right) in absence or presence of 1 equiv. of CuSO4.

Oligo G + H

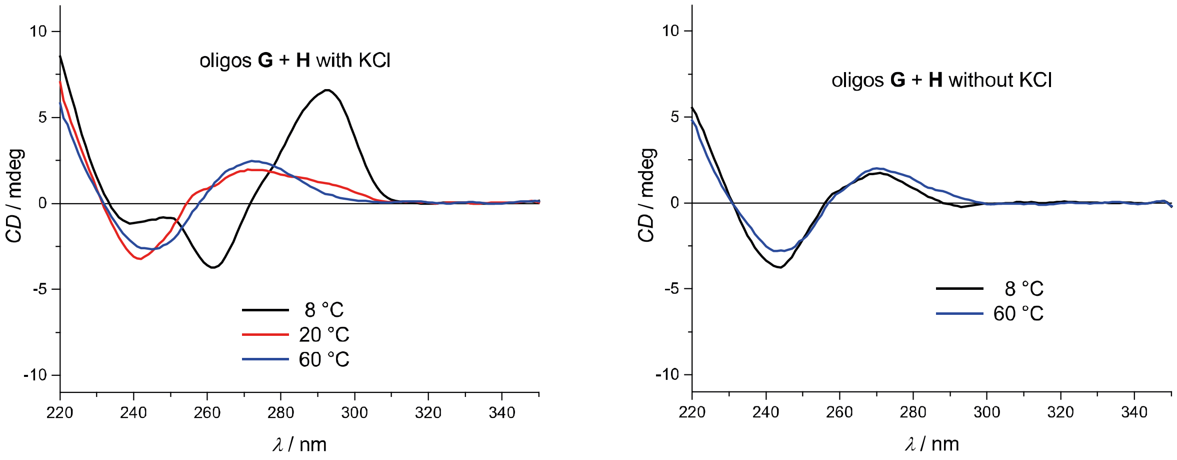

Figure 6.45: CD spectra of a mixture of oligos **G** and **H** at different temperatures in the presence (left) and absence (right) of 100 mM KCl.

6.9 CD Spectroscopy of G-Quadruplexes X_4 (X = L–T)

6.9.1 Sample Preparation, Spectrometer and Method

For CD measurements, the samples were prepared in the same way as for the UV-based thermal denaturation studies (Section 6.5.1). The same instrument setup and equal measurement settings were applied as described in Section 6.7.2.

6.9.2 CD Spectra

Oligo Q (5’-**L**^{5}GG GG)

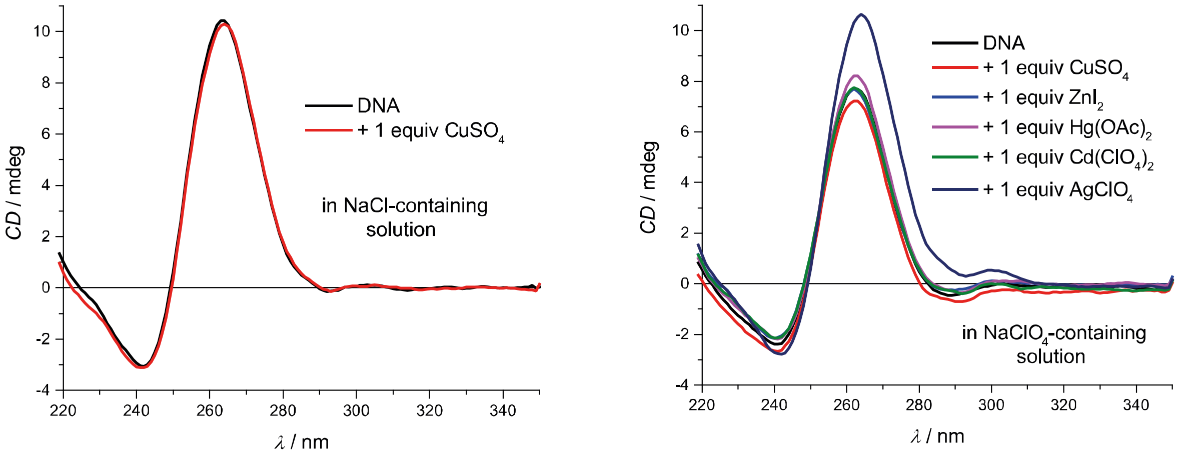

Figure 6.46: CD spectra of folded G-quadruplex **Q₄** in NaCl- (left) or NaClO₄-containing (right) solution in absence or presence of different transition metal ions.

Oligo R (5’-**L**^{5}GG GGG)

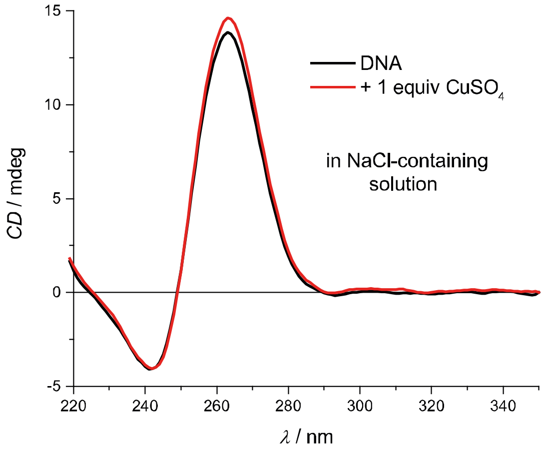

Figure 6.47: CD spectra of folded G-quadruplex **R₄** in NaCl-containing solution in absence or presence of Cu^{2+} ions

6.10 CD Spectroscopy of Unimolecular G-Quadruplexes htel$\mathbf{L^3_{4-n}L^8_n}$ and htel$\mathbf{L^3_{6-n}L^8_n}$

6.10.1 Sample Preparation, Spectrometer and Method

For CD measurements, the samples were prepared in the same way as for the UV-based thermal denaturation studies (Section 6.6.1). The same instrument setup and equal measurement settings were applied as described in Section 6.7.2.

6.10.2 CD Spectra

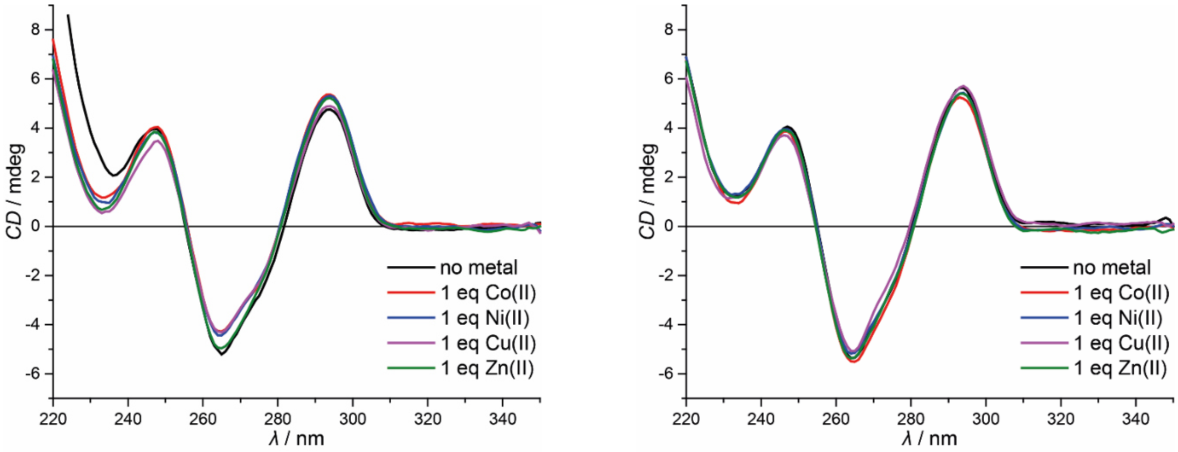
htel$\mathbf{L^3_4}$ htel$\mathbf{L^3_3L^8}$

Figure 6.48: CD spectra of folded G-quadruplex htel$\mathbf{L^3_4}$ (left) and htel$\mathbf{L^3_3L^8}$ (right) in absence or presence of different transition metal ions.

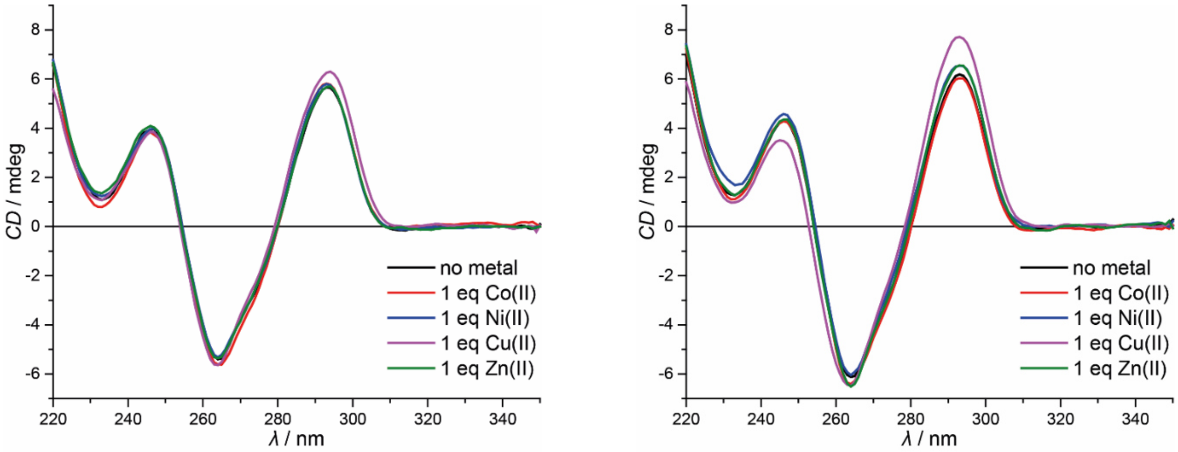
htel$\mathbf{L^3_2L^8_2}$ htel$\mathbf{L^3L^8_3}$

Figure 6.49: CD spectra of folded G-quadruplex htel$\mathbf{L^3_2L^8_2}$ (left) and htel$\mathbf{L^3L^8_3}$ (right) in absence or presence of different transition metal ions.

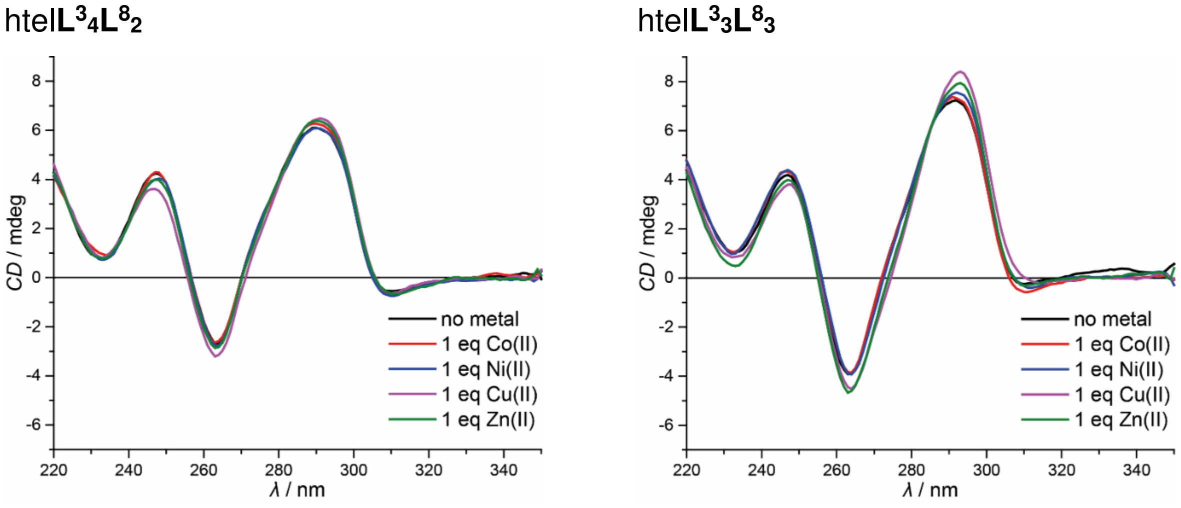

Figure 6.50: CD spectra of folded G-quadruplex htel$\mathbf{L}^3{}_4\mathbf{L}^8{}_2$ (left) and htel$\mathbf{L}^3{}_3\mathbf{L}^8{}_3$ (right) in absence or presence of different transition metal ions.

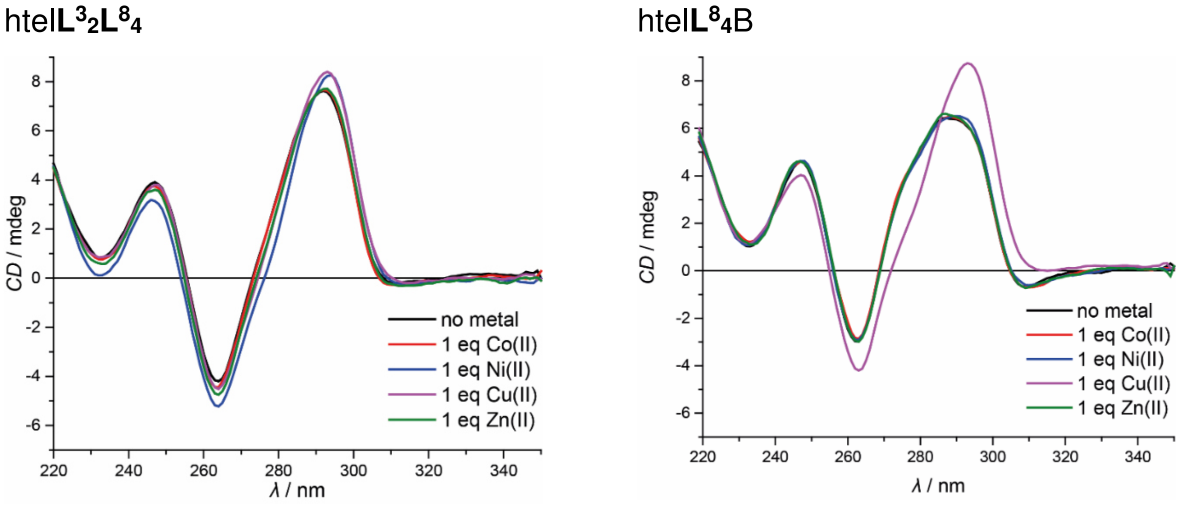

Figure 6.51: CD spectra of folded G-quadruplex htel$\mathbf{L}^3{}_2\mathbf{L}^8{}_4$ (left) and htel$\mathbf{L}^8{}_4$B (right) in absence or presence of different transition metal ions.

6.11 Native ESI Mass Spectrometry

6.11.1 Sample Preparation, Spectrometer and Method

G-quadruplex samples containing 100 µM (for tetramolecular G-quadruplexes), 50 µM (for bimolecular G-quadruplexes) or 25 µM (for unimolecular G-quadruplexes) single-stranded DNA (25 µM each, in case of the samples containing both oligos **G** and **H**), 1 mM KCl or $KClO_4$, 100 mM trimethylammonium acetate buffer pH 7.0, and, if present, 25 or 50 µM $CuSO_4$ or $NiSO_4$ were prepared.

Samples were heated to 85 °C for 10 min, slowly cooled to 4 °C with a cooling rate of 0.5 °C/min and then left at this temperature for several hours (typically overnight). For tetra- and bimolecular G-quadruplexes, the samples were frozen at –20 °C for 1 h[1] and thawed again to 4 °C to ensure full G-quadruplex formation. Prior to measurement, samples were diluted with acetonitrile (1:1, v/v).

Native ESI mass spectrometry was performed on a *Bruker ESI-timsTOF* mass spectrometer (negative mode). For calibration of the TOF device, *Agilent ESI-Low Concentration Tuning Mix* was used. The instrument was calibrated prior to or after each measurement. Ions were generated using the following ionization conditions: capillary voltage: 4500 V; end plate offset voltage: 500 V; nebulizer gas pressure: 0.4/0.6 bar; dry gas flow rate: 6/9 L/min; dry temperature: 303 K.

6.11.2 Indications for Folded G-Quadruplexes in the Gas Phase

The mild ionization conditions applied in native ESI mass spectrometry allow to detect and analyze folded secondary DNA structures in the gas phase. The distinction between folded G-quadruplex and single-stranded oligonucleotide can be mainly achieved by considering two indications. First, in the case of tetra- and bimolecular G-quadruplexes, folded structures give rise to tetrameric or dimeric oligonucleotide adducts, respectively. Signals representing monomeric oligonucleotides are indicative for denatured single-stranded species. Second, the intrinsic property of G-quadruplexes to bear n-1 alkali metal ions residing between n G-quartets is exploited. Usually, a series with varying numbers of unspecifically bound alkali metal ions with statistical distribution is observed for DNA species in the gas phase. However, specifically bound metal ions represent an integral part of the folded G-quadruplex structure. Detection of n-1 specifically bound alkali metal ions are indicative for a folded G-quadruplex with n G-quartets in the gas phase.

6.11.3 Native ESI Mass Spectra

Native mass spectra of oligos **G** and **H** in absence or presence of Cu^{2+} ions are shown below. In the presence of Cu^{2+} ions, G-quadruplexes form. In the absence of Cu^{2+} ions, folded structures are not stable enough and only denatured oligonucleotides can be detected.

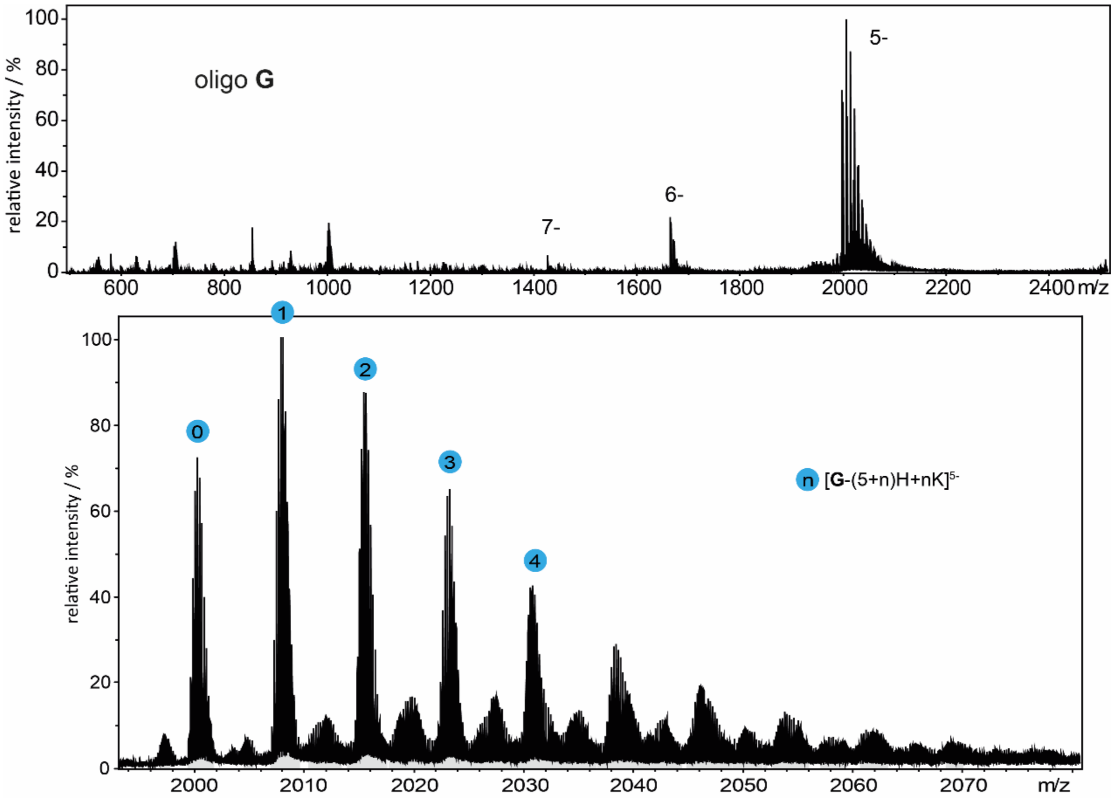

Figure 6.52: Native ESI mass spectrum showing denatured single-stranded oligo **G**.

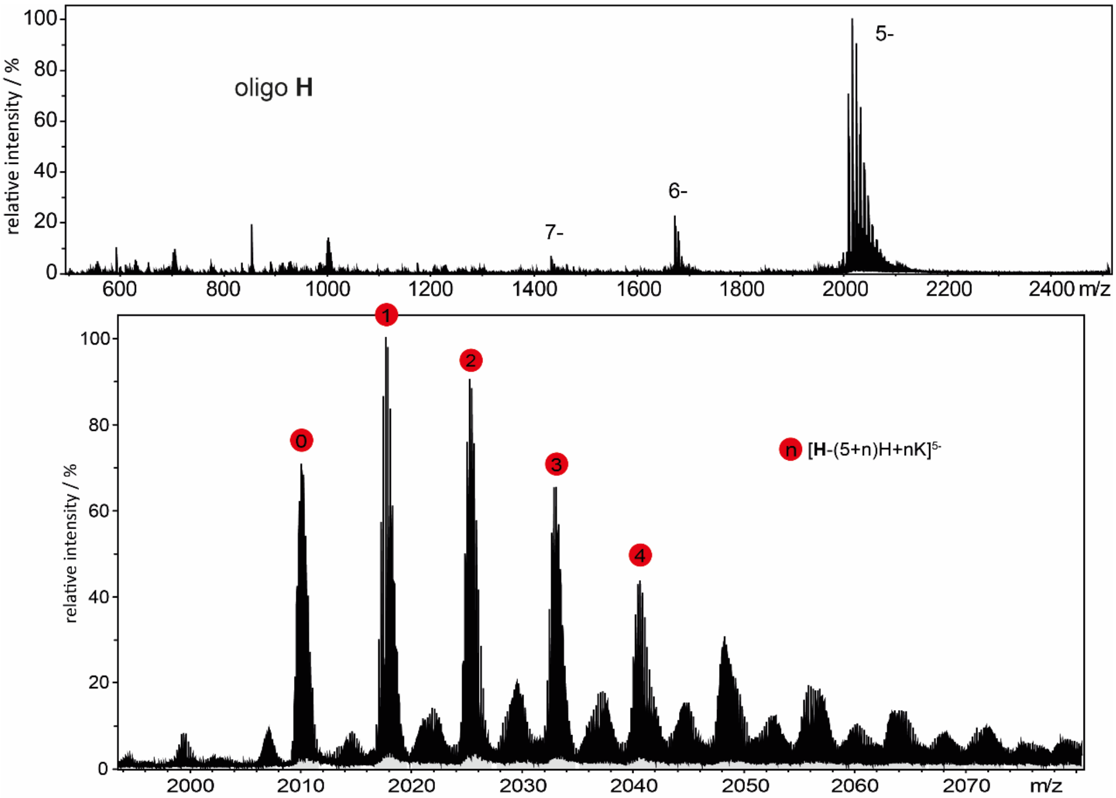

Figure 6.53: Native ESI mass spectrum showing denatured single-stranded oligo **H**.

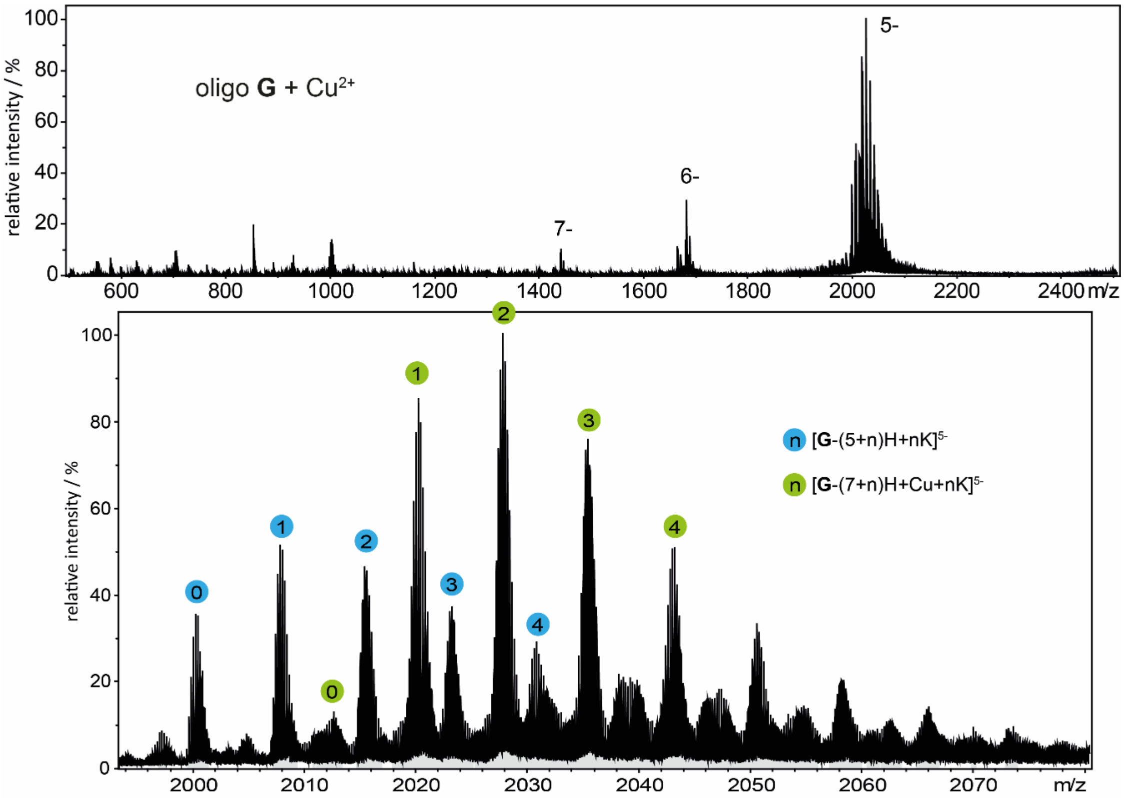

Figure 6.54: Native ESI mass spectrum showing a mixture of denatured single-stranded oligo **G** and folded Cu^{2+}-binding G-quadruplex [Cu^{2+}@**G**].

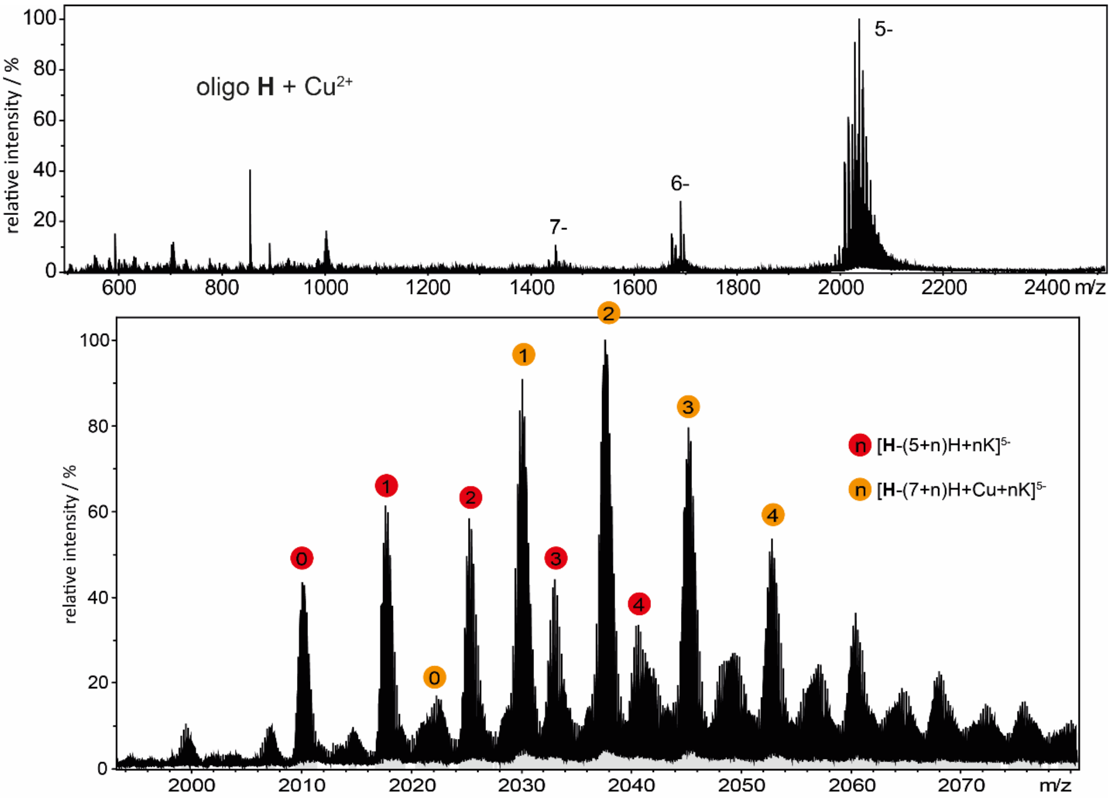

Figure 6.55: Native ESI mass spectrum showing a mixture of denatured single-stranded oligo **H** and folded Cu^{2+}-binding G-quadruplex [Cu^{2+}@**H**].

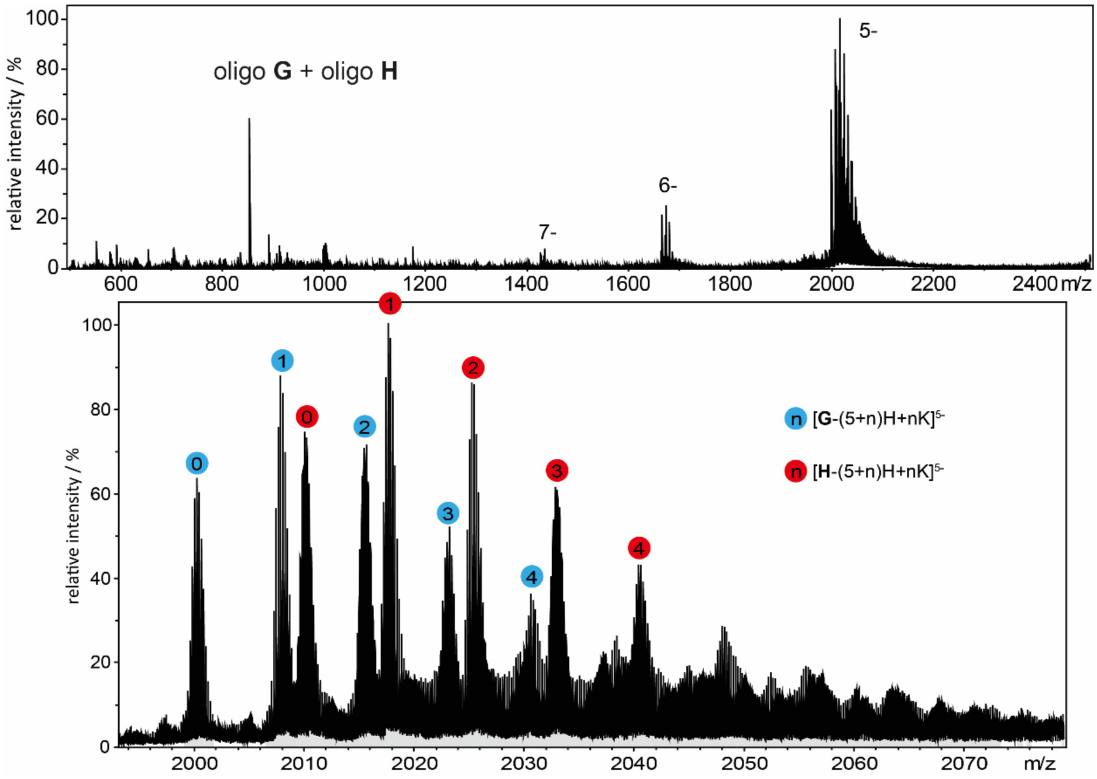

Figure 6.56: Native ESI mass spectrum showing a mixture of denatured single-stranded oligo **G** and oligo **H**.

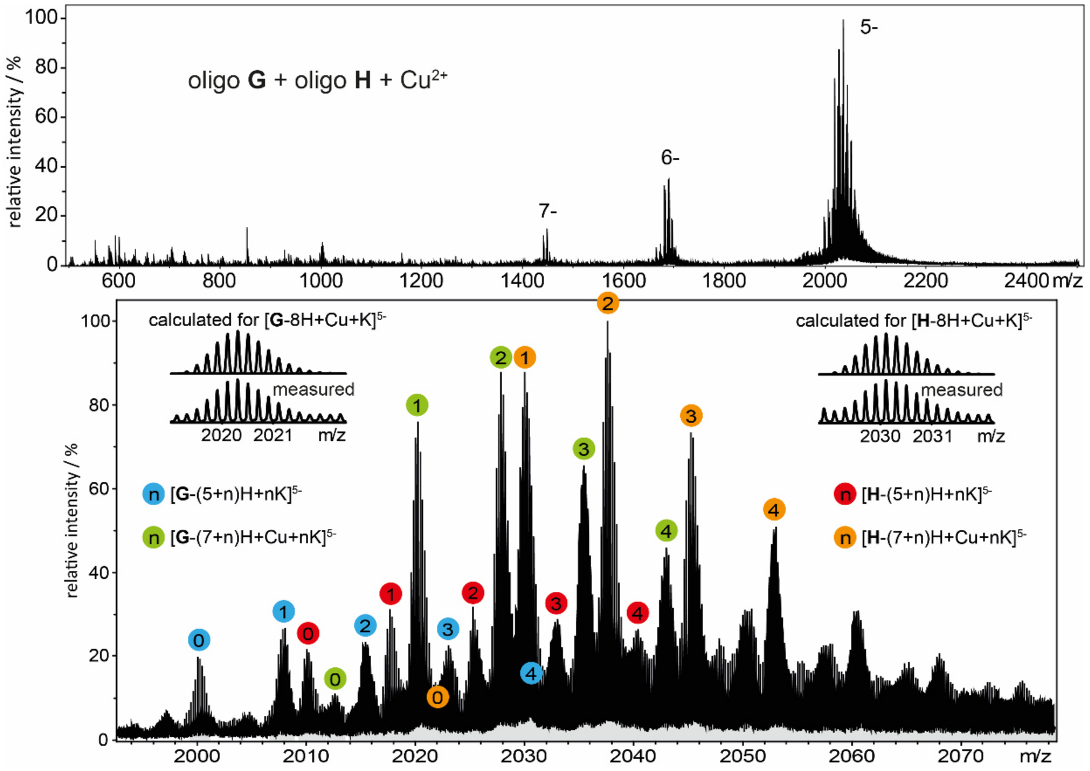

Figure 6.57: Native ESI mass spectrum showing a mixture of folded Cu^{2+}-binding G-quadruplexes [Cu^{2+}@**G**] and [Cu^{2+}@**H**] and denatured oligo **G** and oligo **H**.

6.12 Native Gel Electrophoresis

6.12.1 Sample Preparation

DNA samples contained in total 850 µM single-stranded DNA (either only oligo **G**, only oligo **H**, or oligos **G** and **H** (1:1)), 100 mM KCl, 80 mM lithium cacodylate buffer pH 7.2, and, if present, 850 µM $CuSO_4$. All samples were prepared with ultrapure water (type I, 18.2 MΩ cm), obtained with a *VWR Puranity TU 3 UV*.
Samples were heated to 85 °C for 10 min, slowly cooled to 4 °C with a cooling rate of 0.5 °C/min and then left at this temperature for several hours (typically overnight).

6.12.2 Apparatus and Method

Non-denaturing gel electrophoresis experiments were carried out using a *CBS Dual-Vertical Mini-Gel* system. A tris-borate (90 mM, pH 8.3) running buffer including 100 mM KCl was used and 15% acrylamide gels (29:1 acrylamide:bisacrylamide) were cast in the same buffer with APS and TEMED for initiation of polymerization. Annealed DNA samples were 5:1 diluted with 6x loading buffer (60 mM tris-HCl, pH 7.6, 60% (v/v) glycerol) and gels were loaded with 2.5 µL sample. A commercially available 20 bp DNA ladder (ready-to-use) was used for the reference lanes. Gels were run in constant voltage mode (65 V) at 10 °C for about 140 min. DNA visualization was achieved by silver staining. Therefore, literature-known protocols were followed.[5,6]

6.13 EPR and PDEPR Spectroscopy of Species Containing Oligos A–F

6.13.1 Sample Preparation

Samples for all EPR-based measurements contained 1 mM single-stranded DNA, 50 mM potassium phosphate buffer pH 7.0, 375 µM $CuSO_4$ and, if present, various concentrations of PIPER, telomestatin, guanine, 7-deazaguanine, guanosine or guanosine monophosphate (GMP). For all experiments, ultrapure water (type I, 18.2 MΩ cm) was used, obtained with a *VWR Puranity TU 3 UV*. Telomestatin was added as a 1 mM stock solution in DMSO, guanine and 7-deazaguanine were added as 20 mM stock solutions in 100 mM KOH and guanosine was added as 20 mM suspension in water.

Samples were heated to 85 °C for 10 min, slowly cooled to 4 °C with a cooling rate of 0.5 °C/min and then left at this temperature for several hours (typically overnight). To ensure full formation of G-quadruplexes, the samples were frozen at –20 °C for 1 h[1] and thawed again to 4 °C. The samples were diluted with glycerol (1:1 v/v), mixed, immediately frozen in liquid N_2, and stored in liquid N_2 until measurement.

6.13.2 Spectrometer and Methods

Q-Band pulse EPR measurements were carried out in the temperature range of 19 to 30 K using a *Bruker Elexsys E580* spectrometer equipped with a *Bruker ER 5106QT-2* resonator, *Bruker SpinJet AWG*, *Oxford Instruments CF935* continuous-flow helium cryostat and *Oxford Instruments MercuryiTC* temperature controller. Field-swept EPR spectra were obtained *via* integration of the electron spin echo (ESE) signal. DEER experiments were performed at 19 K with the frequency separation of $Df = f_{\mathrm{pump}} - f_{\mathrm{obs}} = 90$ MHz using an overcoupled resonator, with f_{pump} set to the center of the resonator dip. Throughout the thesis, g_{eff} indicates the observer position. Gaussian pulses were used in order to minimize the pump and observer overlap and suppress the “2+1” artifact.[7] The optimal p-pulse lengths were determined using transient nutation experiments and were typically ~30 ns for the pump pulse and ~80 ns for the detection. The shot repetition time (SRT) was 500 ms. DEER time traces were background-corrected using

DeerAnalysis 2018[8] either assuming an exponential background with dimensionality equal to 3 or by using an empirical polynomial fitting. Dipolar spectra were obtained using DeerAnalysis 2018. Distance distributions were derived from DEER time traces using PeldorFit 2019,[9] with traces' individual contributions to the overall RMSD normalized to their respective modulation depth values.

6.13.3 EPR Spectra of Spin-Labeled Tetramolecular G-quadruplexes

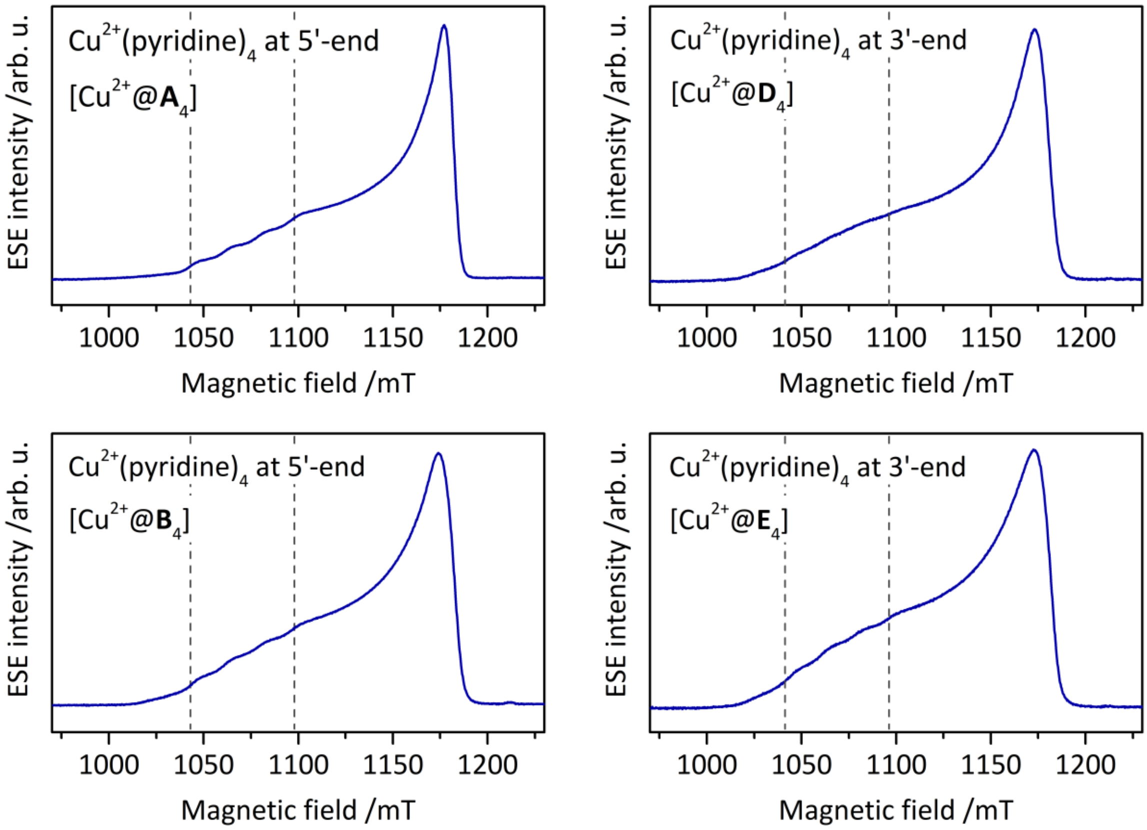

Figure 6.58: Comparison of ESE-detected field-swept EPR spectra of the four G-quadruplex samples, with the Cu^{2+}-based spin label attached at the 5'-end for [Cu^{2+}@**A**$_4$] and [Cu^{2+}@**B**$_4$] and 3'-end for [Cu^{2+}@**D**$_4$] and [Cu^{2+}@**E**$_4$]. Cu^{2+} hyperfine structure in the $g_{\parallel}$ region is less pronounced for samples with the spin label attached at the 3'-end (dashed vertical lines mark the first and fourth lines of the hyperfine structure). Experimental parameters: t_p = 20 ns (rectangular pulses), t = 300 ns, SRT = 1.2 ms, T = 19 K.

6.13.4 Orientation-Selective DEER Data

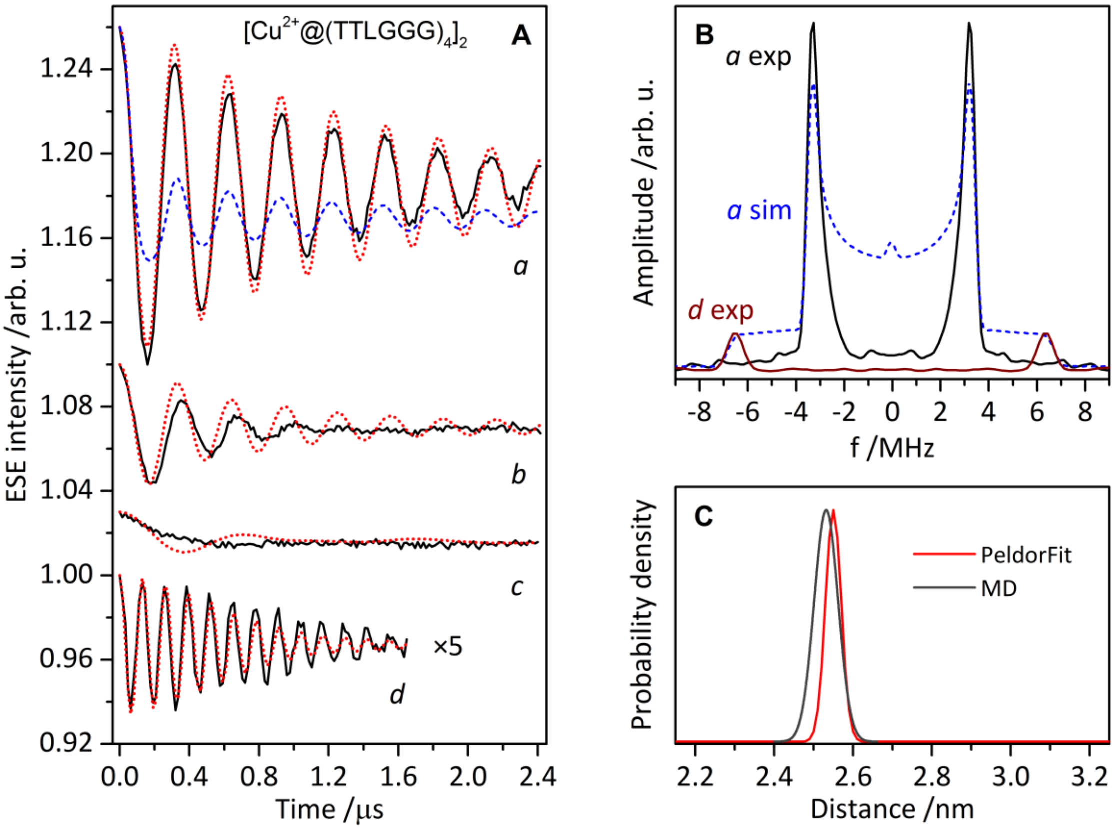

Figure 6.59: (**A**) Background-corrected orientation-selective DEER time traces of [Cu^{2+}@**A**$_4$]$_2$ measured at four field positions (black solid lines) overlaid with the best fit results from PeldorFit (red dotted lines) and DeerAnalysis (blue dashed line). Observer positions are marked with *a*-*d* and correspond to g_{eff} = 2.061, 2.071, 2.121 and 2.315, respectively; Trace *a* corresponds to the $g_\perp$ region and trace *d* to $g_\parallel$. (**B**) Dipolar spectra detected at positions *a* (black solid line) and *d* (frequency axis scaled by $g_\perp^2/g_\parallel^2$, amplitude normalized to the Pake pattern intensity, dark red solid line) overlaid with a Pake pattern simulated by DeerAnalysis based on time trace *a* (blue dashed line); (**C**) Distance distributions obtained from experiment using PeldorFit (red solid line) and from MD simulations (grey solid line).

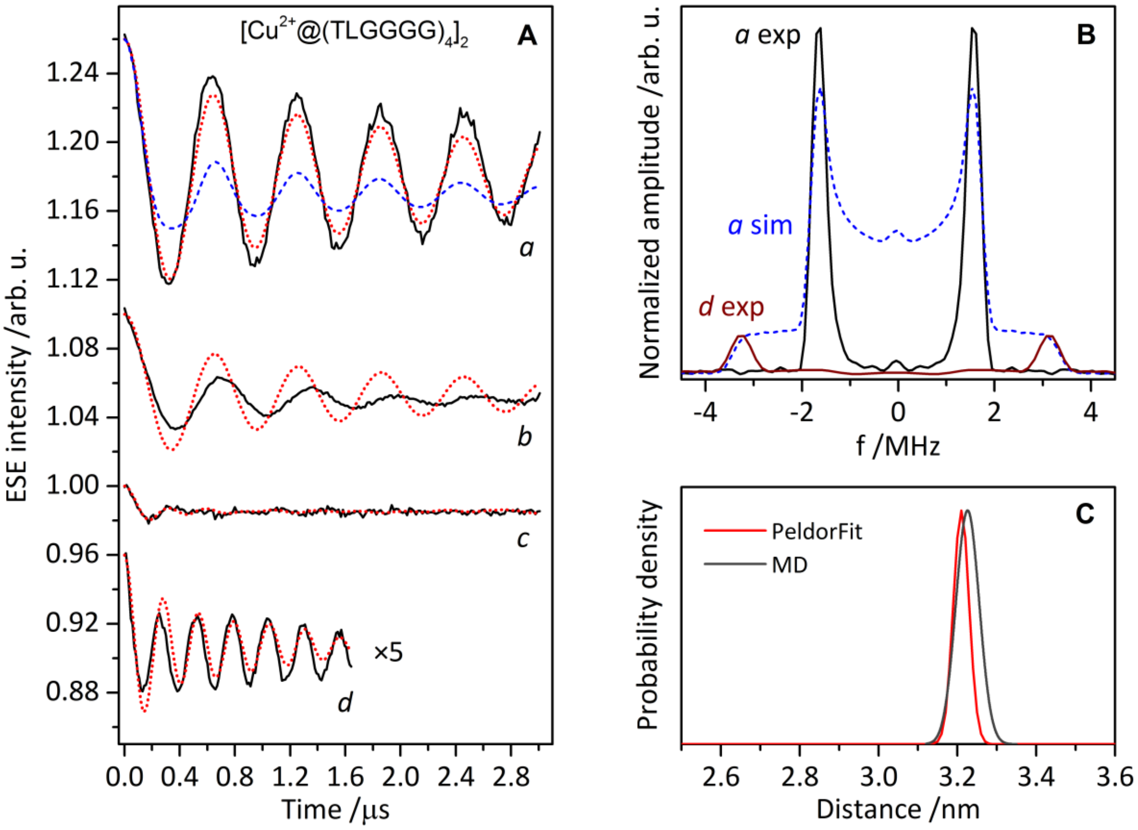

Figure 6.60: (**A**) Background-corrected orientation-selective DEER time traces of $[Cu^{2+}@\mathbf{B}_4]_2$ measured at four field positions (black solid lines) overlaid with the best fit results from PeldorFit (red dotted lines) and DeerAnalysis (blue dashed line). Observer positions are marked with *a*-*d* and correspond to g_{eff} = 2.061, 2.071, 2.225 and 2.315, respectively; Trace *a* corresponds to the $g_\perp$ region and trace *d* to $g_\parallel$. (**B**) Dipolar spectra detected at positions *a* (black solid line) and *d* (frequency axis scaled by $g_\perp^2/g_\parallel^2$, amplitude normalized to the Pake pattern intensity, dark red solid line) overlaid with a Pake pattern simulated by DeerAnalysis based on time trace *a* (blue dashed line); (**C**) Distance distributions obtained from experiment using PeldorFit (red solid line) and from MD simulations (grey solid line).

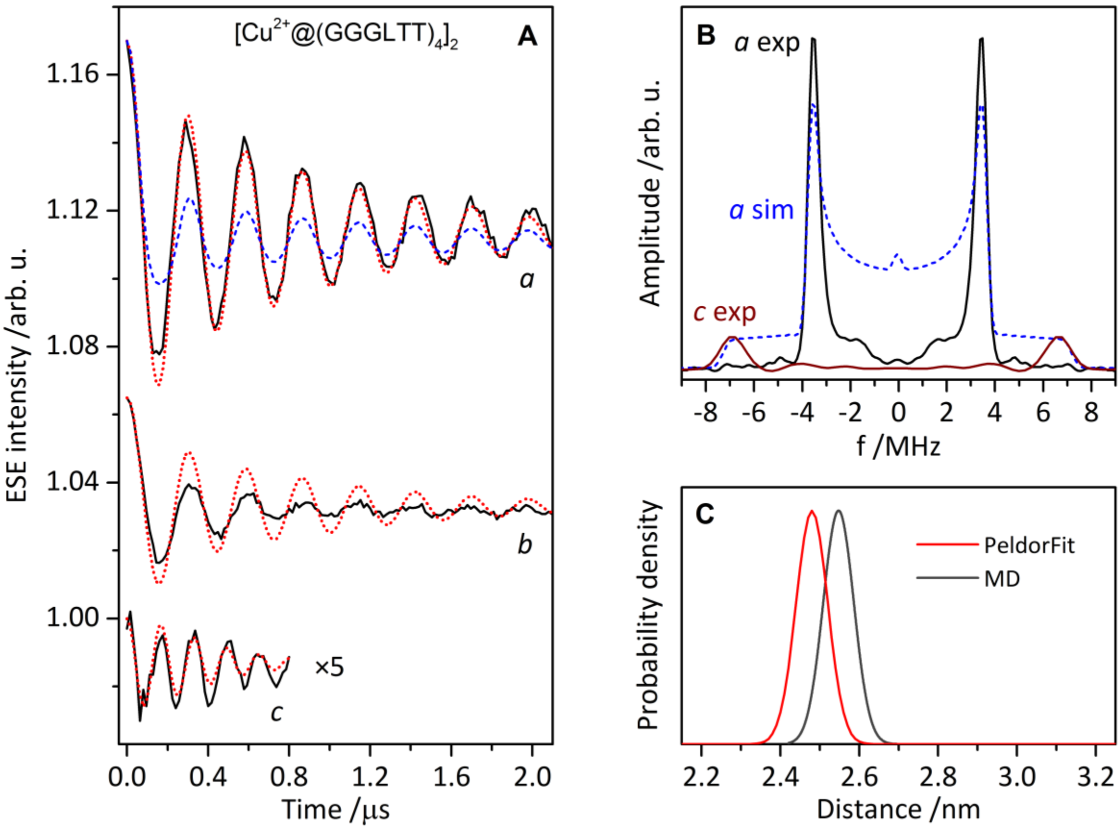

Figure 6.61: (**A**) Background-corrected orientation-selective DEER time traces of $[Cu^{2+}@\mathbf{D}_4]_2$ measured at three field positions (black solid lines) overlaid with the best fit results from PeldorFit (red dotted lines) and DeerAnalysis (blue dashed line). Observer positions are marked with *a*-*c* and correspond to g_{eff} = 2.061, 2.071, and 2.315, respectively; Trace *a* corresponds to the $g_\perp$ region and trace *c* to $g_\parallel$. (**B**) Dipolar spectra detected at positions *a* (black solid line) and *c* (frequency axis scaled by $g_\perp^2/g_\parallel^2$, amplitude normalized to the Pake pattern intensity, dark red solid line) overlaid with a Pake pattern simulated by DeerAnalysis based on time trace *a* (blue dashed line); (**C**) Distance distributions obtained from experiment using PeldorFit (red solid line) and from MD simulations (grey solid line).

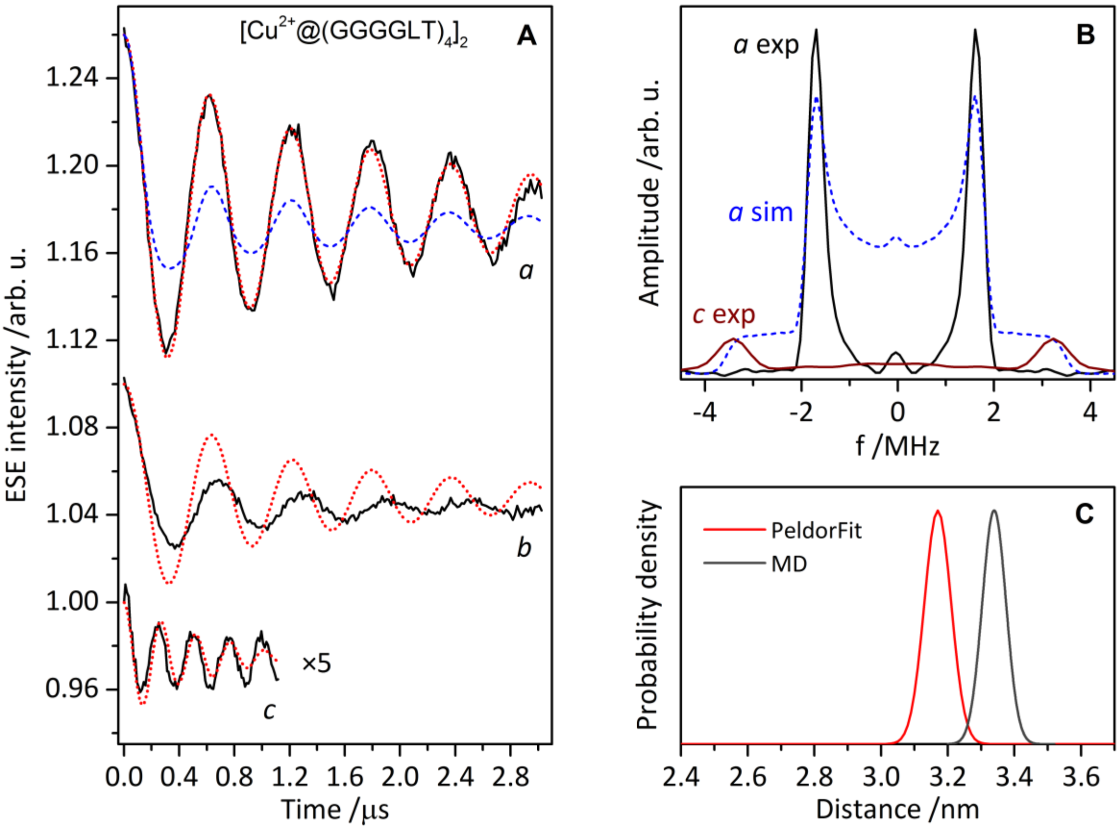

Figure 6.62: (**A**) Background-corrected orientation-selective DEER time traces of [Cu^{2+}@**E**$_4$]$_2$ measured at three field positions (black solid lines) overlaid with the best fit results from PeldorFit (red dotted lines) and DeerAnalysis (blue dashed line). Observer positions are marked with *a*-*c* and correspond to g_{eff} = 2.061, 2.071, and 2.315, respectively; Trace *a* corresponds to the $g_\perp$ region and trace *c* to $g_\parallel$. (**B**) Dipolar spectra detected at positions *a* (black solid line) and *c* (frequency axis scaled by $g_\perp^2/g_\parallel^2$, amplitude normalized to the Pake pattern intensity, dark red solid line) overlaid with a Pake pattern simulated by DeerAnalysis based on time trace *a* (blue dashed line); (**C**) Distance distributions obtained from experiment using PeldorFit (red solid line) and from MD simulations (grey solid line).

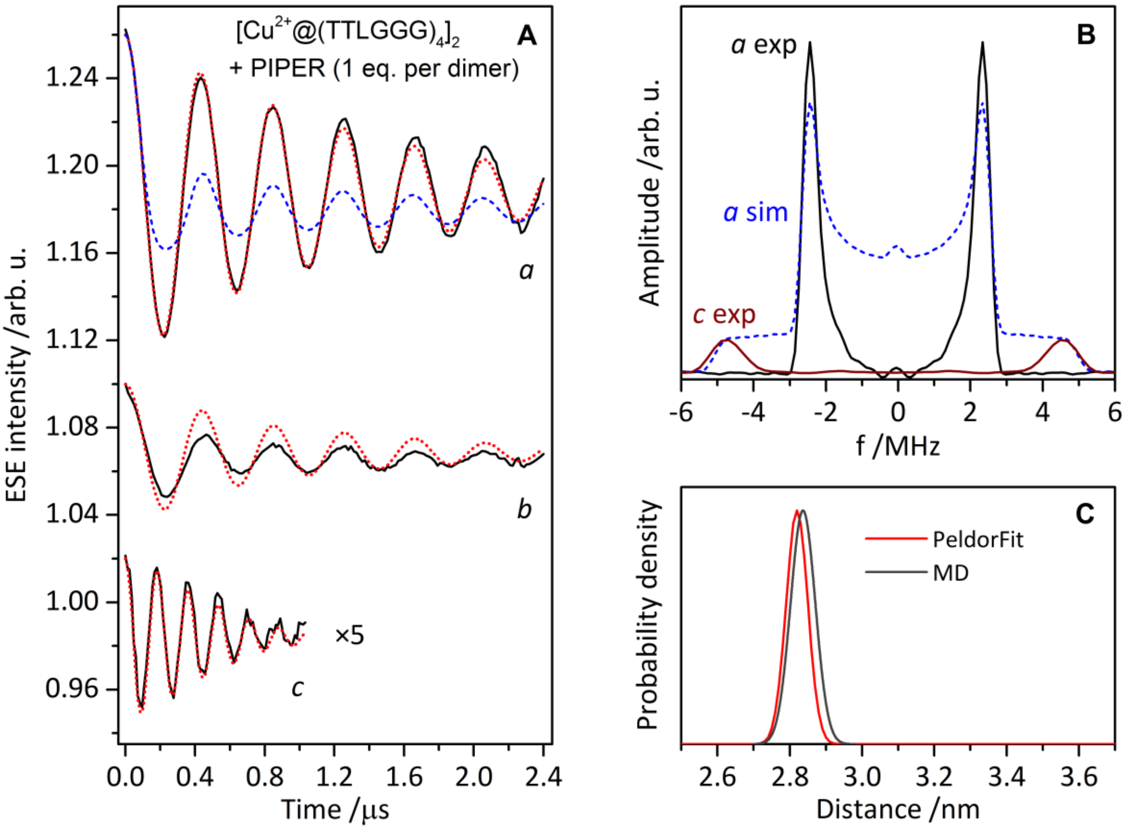

Figure 6.63: (**A**) Background-corrected orientation-selective DEER time traces of [Cu^{2+}@**A**$_4$]$_2$ with PIPER (1 eq. per dimer) measured at three field positions (black solid lines) overlaid with the best fit results from PeldorFit (red dotted lines) and DeerAnalysis (blue dashed line). Observer positions are marked with *a*-*c* and correspond to $g_{\mathrm{eff}} = 2.061$, 2.071, and 2.315, respectively; Trace *a* corresponds to the $g_\perp$ region and trace *c* to $g_\parallel$. (**B**) Dipolar spectra detected at positions *a* (black solid line) and *c* (frequency axis scaled by $g_\perp^2/g_\parallel^2$, amplitude normalized to the Pake pattern intensity, dark red solid line) overlaid with a Pake pattern simulated by DeerAnalysis based on time trace *a* (blue dashed line); (**C**) Distance distributions obtained from experiment using PeldorFit (red solid line) and from MD simulations (grey solid line).

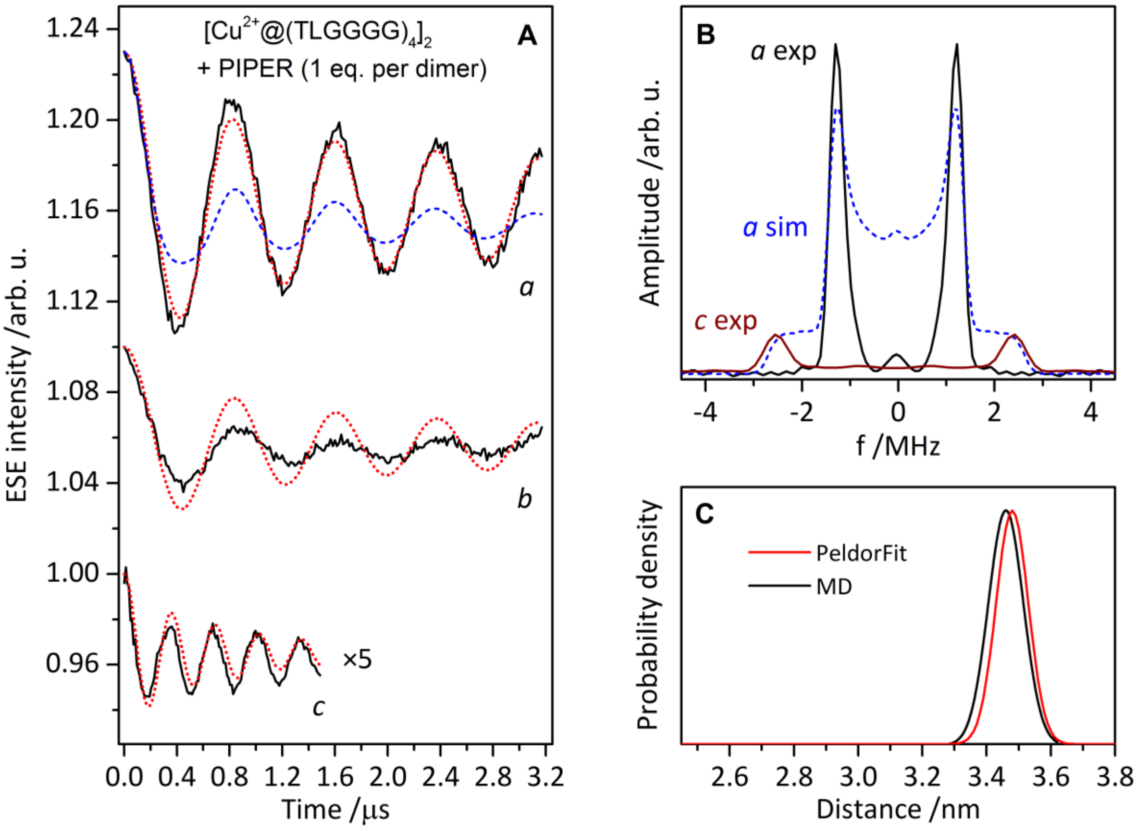

Figure 6.64: (**A**) Background-corrected orientation-selective DEER time traces of $[\mathrm{Cu}^{2+}@\mathbf{B}_4]_2$ with PIPER (1 eq. per dimer) measured at three field positions (black solid lines) overlaid with the best fit results from PeldorFit (red dotted lines) and DeerAnalysis (blue dashed line). Observer positions are marked with *a*-*c* and correspond to $g_{\mathrm{eff}} = 2.061$, 2.071, and 2.315, respectively; Trace *a* corresponds to the $g_{\perp}$ region and trace *c* to $g_{\parallel}$. (**B**) Dipolar spectra detected at positions *a* (black solid line) and *c* (frequency axis scaled by $g_{\perp}^2/g_{\parallel}^2$, amplitude normalized to the Pake pattern intensity, dark red solid line) overlaid with a Pake pattern simulated by DeerAnalysis based on time trace *a* (blue dashed line); (**C**) Distance distributions obtained from experiment using PeldorFit (red solid line) and from MD simulations (grey solid line).

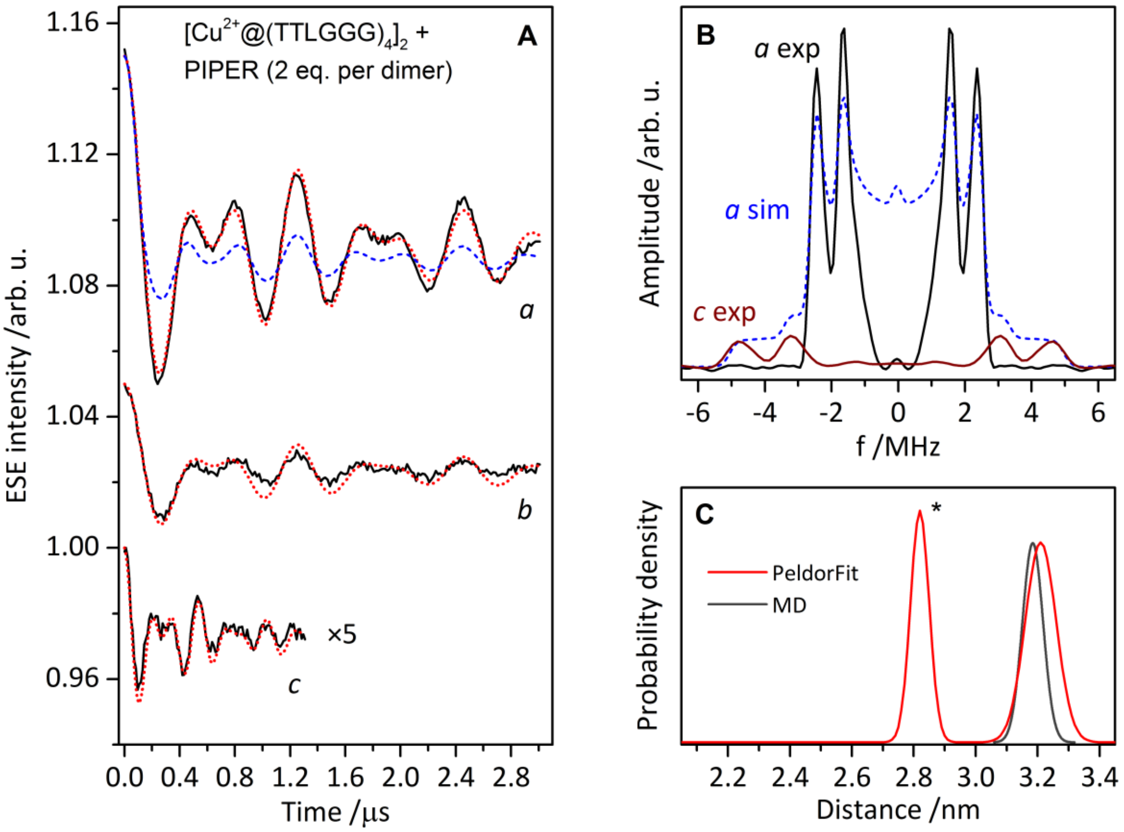

Figure 6.65: (**A**) Background-corrected orientation-selective DEER time traces of [Cu^{2+}@**A**$_4$]$_2$ with PIPER (2 eq. per dimer) measured at three field positions (black solid lines) overlaid with the best fit results from PeldorFit (red dotted lines) and DeerAnalysis (blue dashed line). Observer positions are marked with *a*-*c* and correspond to g_{eff} = 2.061, 2.071, and 2.315, respectively; Trace *a* corresponds to the $g_\perp$ region and trace *c* to $g_\parallel$. (**B**) Dipolar spectra detected at positions *a* (black solid line) and *c* (frequency axis scaled by $g_\perp^2/g_\parallel^2$, amplitude normalized to the Pake pattern intensity, dark red solid line) overlaid with a Pake pattern simulated by DeerAnalysis based on time trace *a* (blue dashed line); (**C**) Distance distributions obtained from experiment using PeldorFit (red solid line) and from MD simulations (grey solid line). The asterisk marks the distance distribution originating from the PIPER@[Cu^{2+}@**A**$_4$]$_2$ dimer subpopulation.

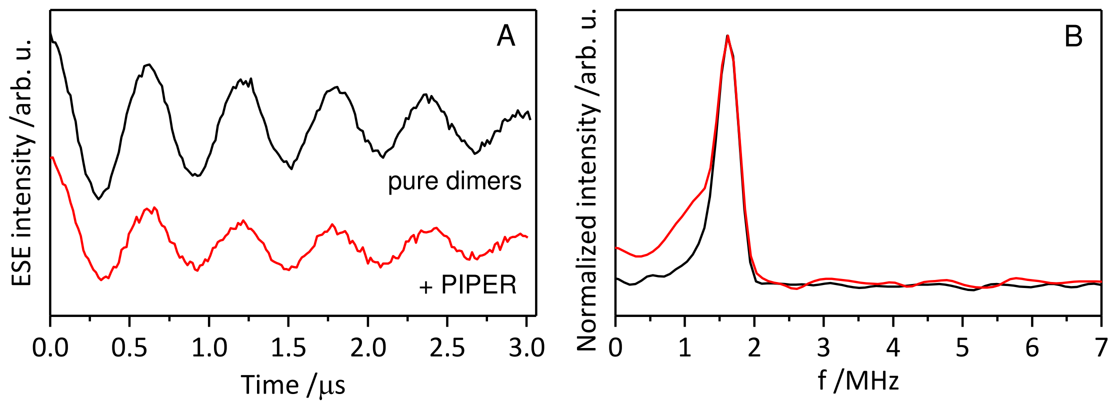

Figure 6.66: (**A**) DEER time traces recorded at $g_{\text{eff}} = 2.061$ for [Cu^{2+}@**E**$_4$] samples without PIPER (black trace) and with 1 eq. of PIPER per dimer (red trace). (**B**) Corresponding dipolar spectra.

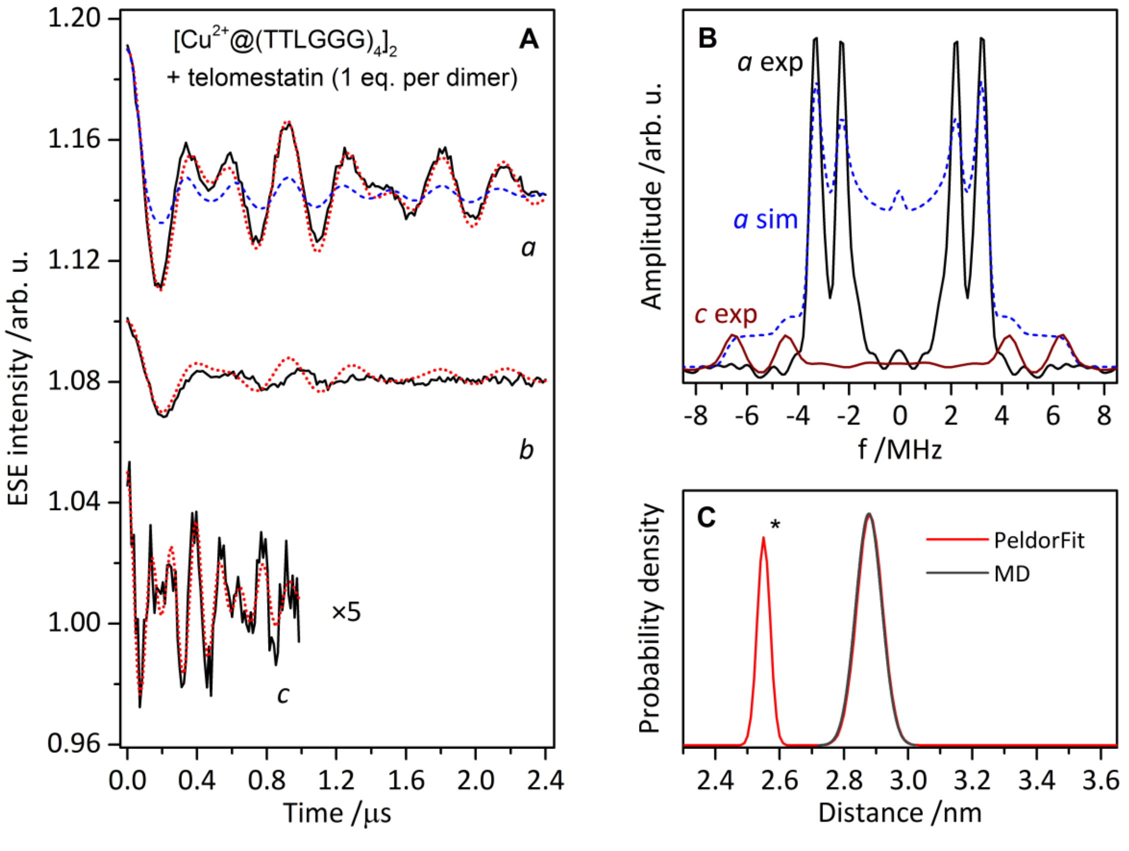

Figure 6.67: (**A**) Background-corrected orientation-selective DEER time traces of [Cu^{2+}@**A**$_4$]$_2$ with telomestatin (1 eq. per dimer) measured at three field positions (black solid lines) overlaid with the best fit results from PeldorFit (red dotted lines) and DeerAnalysis (blue dashed line). Observer positions are marked with *a*-*c* and correspond to $g_{\text{eff}} = 2.061$, 2.071, and 2.315, respectively; Trace *a* corresponds to the $g_{\perp}$ region and trace *c* to $g_{\parallel}$. (**B**) Dipolar spectra detected at positions *a* (black solid line) and *c* (frequency axis scaled by $g_{\perp}^2/g_{\parallel}^2$, amplitude normalized to the Pake pattern intensity, dark red solid line) overlaid with a Pake pattern simulated by DeerAnalysis based on time trace *a* (blue dashed line); (**C**) Distance distributions obtained from experiment using PeldorFit (red solid line) and from MD simulations (grey solid line). The asterisk marks the distance distribution originating from the pure [Cu^{2+}@**A**$_4$]$_2$ dimer subpopulation.

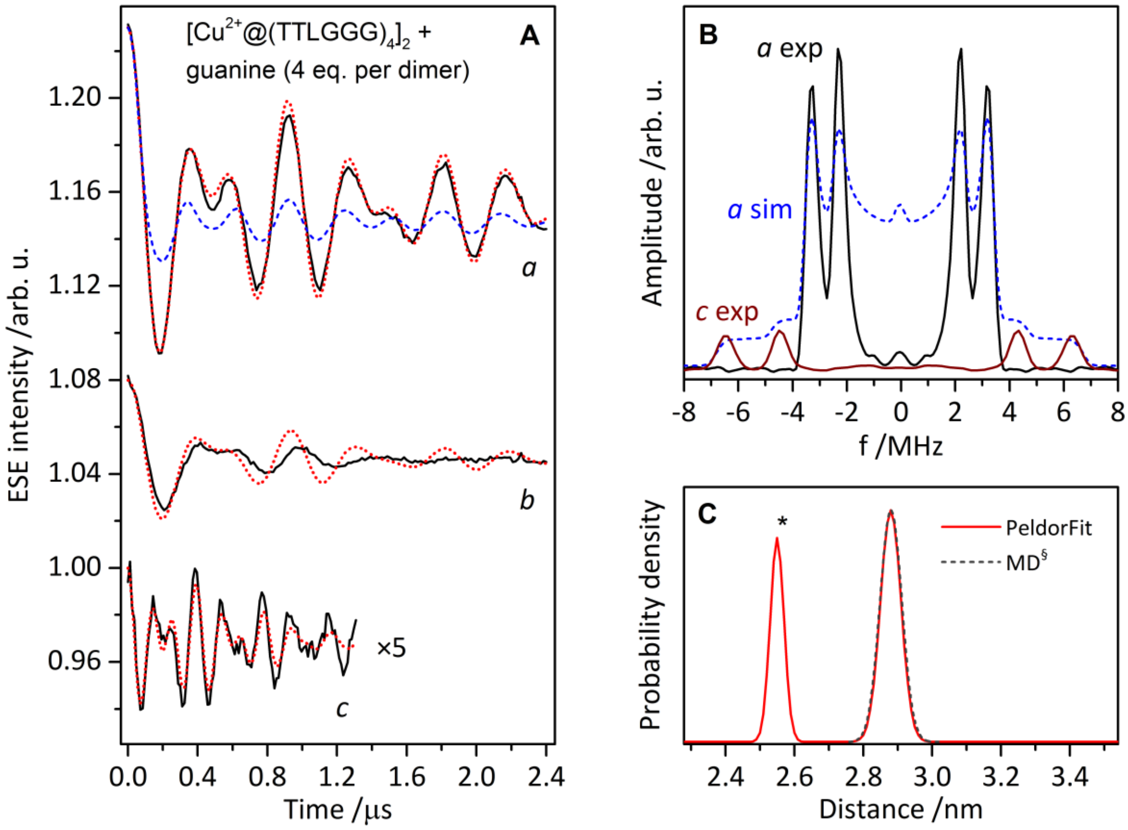

Figure 6.68: (A) Background-corrected orientation-selective DEER time traces of [Cu^{2+}@**A**$_4$]$_2$ with guanine (4 eq. per dimer) measured at three field positions (black solid lines) overlaid with the best fit results from PeldorFit (red dotted lines) and DeerAnalysis (blue dashed line). Observer positions are marked with *a*-*c* and correspond to $g_{\mathrm{eff}} = 2.061$, 2.071, and 2.315, respectively; Trace *a* corresponds to the $g_\perp$ region and trace *c* to $g_\parallel$. (**B**) Dipolar spectra detected at positions *a* (black solid line) and *c* (frequency axis scaled by $g_\perp^2/g_\parallel^2$, amplitude normalized to the Pake pattern intensity, dark red solid line) overlaid with a Pake pattern simulated by DeerAnalysis based on time trace *a* (blue dashed line); (**C**) Distance distributions obtained from experiment using PeldorFit (red solid line) and from MD simulations (grey dashed line). §The MD results are shown for guanosine G-tetrads. The asterisk marks the distance distribution originating from the pure [Cu^{2+}@**A**$_4$]$_2$ dimer subpopulation.

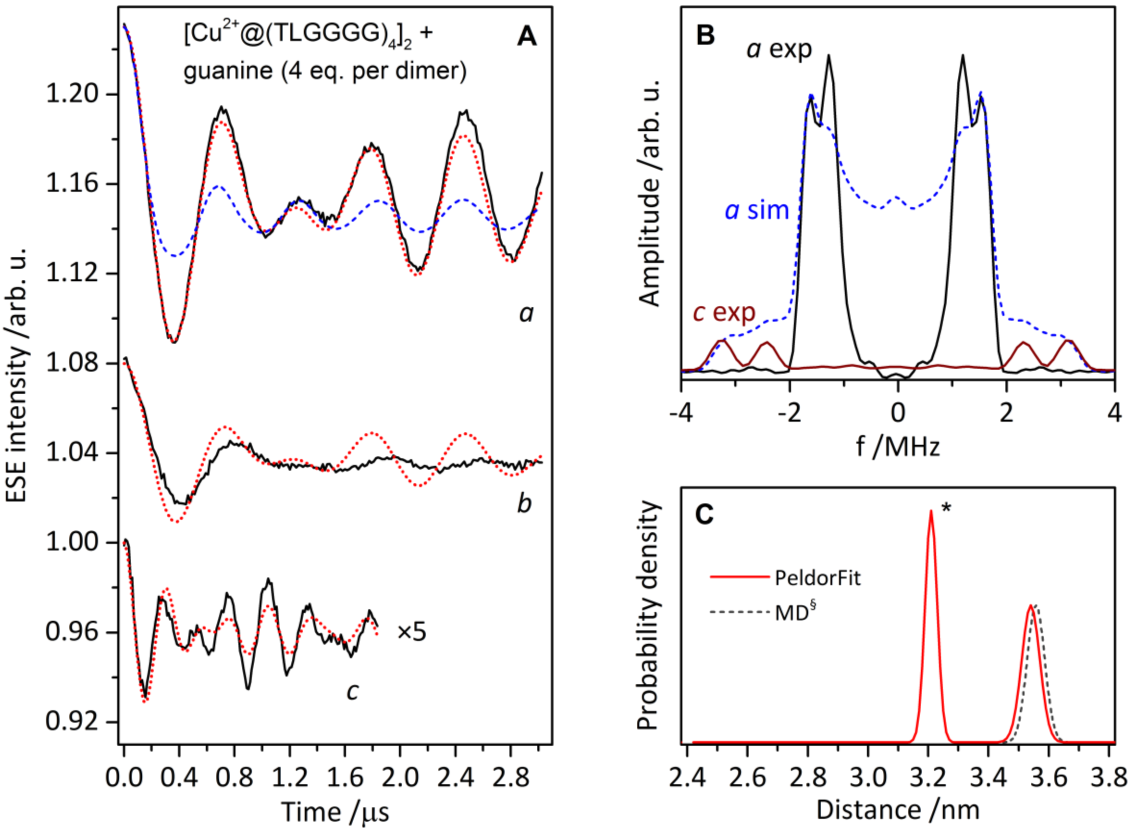

Figure 6.69: (A) Background-corrected orientation-selective DEER time traces of [Cu^{2+}@**B**$_4$]$_2$ with guanine (4 eq. per dimer) measured at three field positions (black solid lines) overlaid with the best fit results from PeldorFit (red dotted lines) and DeerAnalysis (blue dashed line). Observer positions are marked with *a*-*c* and correspond to $g_{\mathrm{eff}} = 2.061$, 2.071, and 2.315, respectively; Trace *a* corresponds to the $g_\perp$ region and trace *c* to $g_\parallel$. (**B**) Dipolar spectra detected at positions *a* (black solid line) and *c* (frequency axis scaled by $g_\perp^2/g_\parallel^2$, amplitude normalized to the Pake pattern intensity, dark red solid line) overlaid with a Pake pattern simulated by DeerAnalysis based on time trace *a* (blue dashed line); (**C**) Distance distributions obtained from experiment using PeldorFit (red solid line) and from MD simulations (grey dashed line). §The MD results are shown for guanosine G-tetrads. The asterisk marks the distance distribution originating from the pure [Cu^{2+}@**B**$_4$]$_2$ dimer subpopulation.

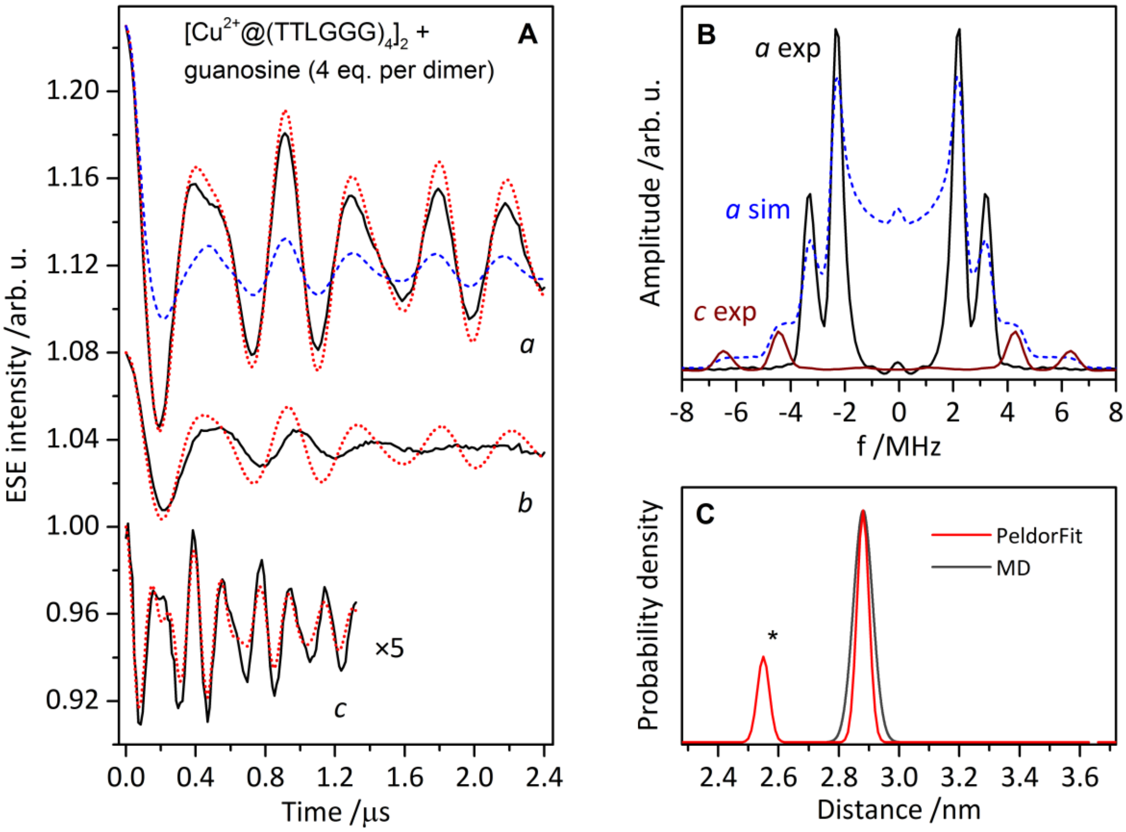

Figure 6.70: **(A)** Background-corrected orientation-selective DEER time traces of $[Cu^{2+}@\mathbf{A}_4]_2$ with guanosine (4 eq. per dimer) measured at three field positions (black solid lines) overlaid with the best fit results from PeldorFit (red dotted lines) and DeerAnalysis (blue dashed line). Observer positions are marked with *a*-*c* and correspond to g_{eff} = 2.061, 2.071, and 2.315, respectively; Trace *a* corresponds to the $g_\perp$ region and trace *c* to $g_\parallel$. (**B**) Dipolar spectra detected at positions *a* (black solid line) and *c* (frequency axis scaled by $g_\perp^2/g_\parallel^2$, amplitude normalized to the Pake pattern intensity, dark red solid line) overlaid with a Pake pattern simulated by DeerAnalysis based on time trace *a* (blue dashed line); (**C**) Distance distributions obtained from experiment using PeldorFit (red solid line) and from MD simulations (grey solid line). The asterisk marks the distance distribution originating from the pure $[Cu^{2+}@\mathbf{A}_4]_2$ dimer subpopulation.

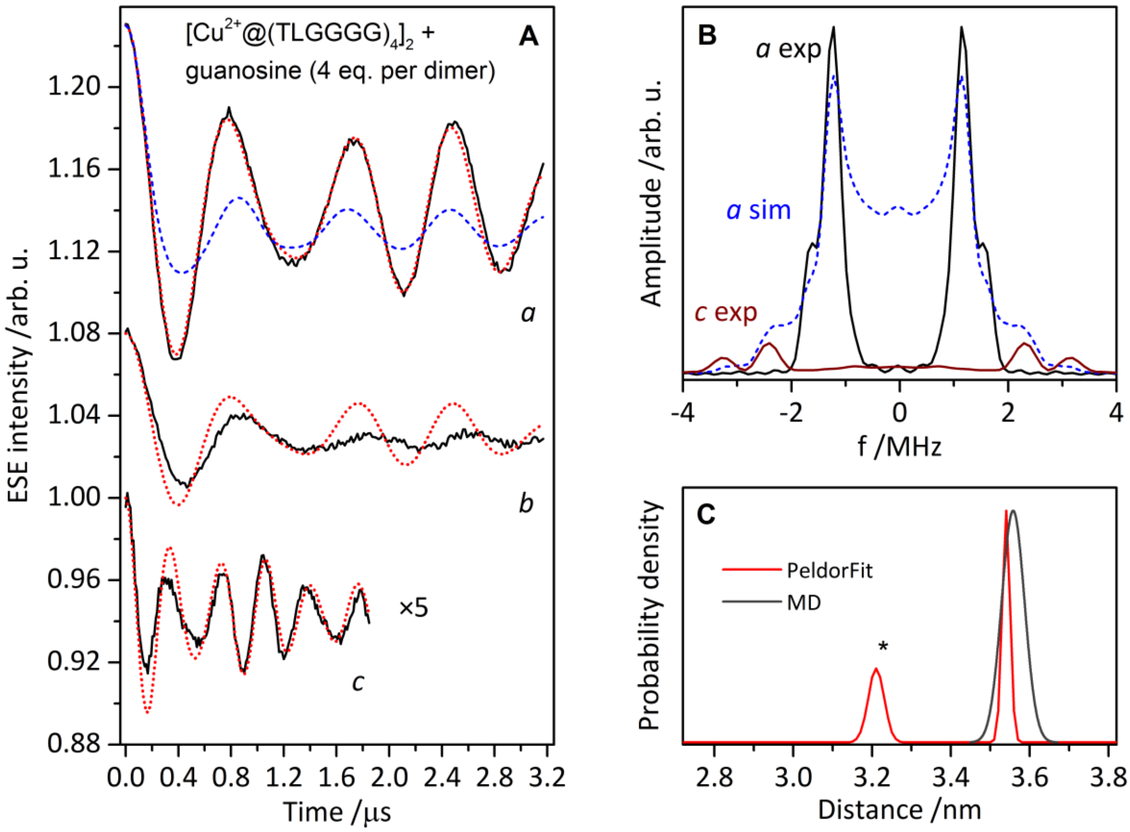

Figure 6.71: (A) Background-corrected orientation-selective DEER time traces of [Cu^{2+}@**B**$_4$]$_2$ with guanosine (4 eq. per dimer) measured at three field positions (black solid lines) overlaid with the best fit results from PeldorFit (red dotted lines) and DeerAnalysis (blue dashed line). Observer positions are marked with *a*-*c* and correspond to g_{eff} = 2.061, 2.071, and 2.315, respectively; Trace *a* corresponds to the $g_\perp$ region and trace *c* to $g_\parallel$. (**B**) Dipolar spectra detected at positions *a* (black solid line) and *c* (frequency axis scaled by $g_\perp^2/g_\parallel^2$, amplitude approximately normalized to the Pake pattern intensity, dark red solid line) overlaid with a Pake pattern simulated by DeerAnalysis based on time trace *a* (blue dashed line); (**C**) Distance distributions obtained from experiment using PeldorFit (red solid line) and from MD simulations (grey solid line). The asterisk marks the distance distribution originating from the pure [Cu^{2+}@**B**$_4$]$_2$ dimer subpopulation.

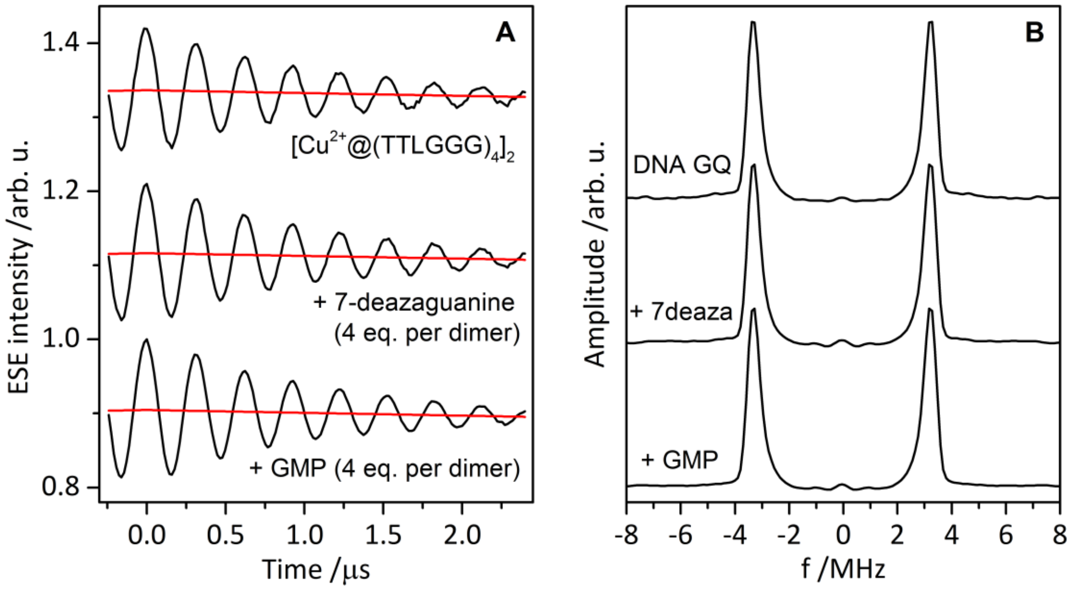

Figure 6.72: (A) Primary DEER traces (black) overlaid with the background fits (red) at the observer position $g_{eff'} = 2.061$ for the pure [Cu^{2+}@**A**$_4$]$_2$ dimers (top trace) and with the addition of 7-deazaguanine (middle trace) and guanosine monophosphate (GMP, bottom trace). (**B**) Comparison of the corresponding dipolar spectra demonstrates that 7-deazaguanine and GMP did not intercalate into the 3’-3’stacked dimers.

6.14 PDEPR Spectroscopy of Species Containing Oligos G–H

6.14.1 Sample Preparation

Samples (40 µL) containing 250 µM oligo **G**, 250 µM oligo **H**, 750 µM $CuSO_4$, 5 mM $MgCl_2$, and 50 mM potassium phosphate buffer pH 7.0 were prepared. Ultrapure water (type **I**, 18.2 MΩ cm) was used, obtained with a *VWR Puranity TU 3 UV*.

The samples were lyophilized and redissolved in 40 µL D_2O. The solutions were heated to 85 °C for 10 min, slowly cooled to 4 °C with a cooling rate of 0.5 °C/min and then left at this temperature for several hours (typically overnight). The samples were diluted with glycerol-d_8 (1:1 v/v), mixed, immediately frozen in liquid N_2, and stored in liquid N_2 until measurement.

6.14.2 Spectrometer and Methods

Q-Band pulse EPR measurements were carried out using a *Bruker Elexsys E580* spectrometer equipped with a *Bruker ER 5106QT-2* resonator, *Bruker SpinJet AWG*, *Oxford Instruments CF935* continuous-flow helium cryostat and *Oxford Instruments MercuryiTC* temperature controller. Field-swept EPR spectra were obtained *via* integration of the electron spin echo (ESE) signal. DEER experiments were performed at 19 K with the frequency separation of $\Delta f = f_{\text{pump}} - f_{\text{obs}} = 90$ MHz using an overcoupled resonator, with f_{pump} set to the center of the resonator dip. Throughout the thesis, g_{eff} indicates the observer position. Gaussian pulses were used in order to minimize the pump and observer overlap and suppress the “2+1” artifact.[7] The optimal π-pulse lengths were determined using transient nutation experiments and were typically ~30 ns for the pump pulse and ~80 ns for the detection. The shot repetition time (SRT) was 500 ms. DEER time traces were background-corrected using DeerAnalysis 2018[8] assuming an exponential background with dimensionality equal to 3. Dipolar spectra and distance distributions were derived from DEER time traces using DeerAnalysis 2018.

6.15 Molecular Dynamics (MD) Simulations of Higher-Order G-quadruplex Structures

MD simulations were carried out as previously described[10,11] using the Gromacs 2019.2 program,[12–14] the AMBER force field ff99bsc1[15,16] for nucleic acid parts and the General Amber Force Field (GAFF)[17] for the PIPER cation and the telomestatin molecule.

6.15.1 Generation of Missing Parameters

Force field parameters and RESP charges for the artificial nucleotide **L^1** and its Cu^{2+} complex were generated in earlier studies[10] and used without changes.

To obtain RESP charges[18] for the PIPER cation and telomestatin, the ESP were calculated at Hartree-Fock level with a 6-31G* basis set and RESP charges were obtained by a two-stages fitting procedure using Antechamber in the AmberTools19 package.[19] Also GAFF atom types were determined using Antechamber. Topology files for Gromacs were obtained using the LEaP program in the AmberTools19 package and the ACPYPE program.[20]

6.15.2 Generation of Initial Structures of G-Quadruplex Dimers and Sandwich Complexes

First, initial structures for the G-quadruplex monomers ($[Cu^{2+}@\mathbf{A}_4]$, $[Cu^{2+}@\mathbf{B}_4]$, $[Cu^{2+}@\mathbf{D}_4]$ and $[Cu^{2+}@\mathbf{E}_4]$) were constructed by using the solid-state structure of the G-quadruplex dimer $[(TG_4T)_4]_2$ (PDB entry 2O4F).[21] All manipulations were carried out in UCSF Chimera.[22] Na^+ ions were replaced by K^+ ions. The second monomer, water molecules, redundant ions and redundant nucleotides were deleted, the geometry-optimized Cu^{2+}-complex was inserted manually and missing nucleotides were duplicated and also inserted manually.

In a next step, initial structures for G-quadruplex dimers were generated. Therefore, the monomeric structures were duplicated and arranged to tail-to-tail ($[Cu^{2+}@\mathbf{A}_4]_2$, $[Cu^{2+}@\mathbf{B}_4]_2$) or head-to-head dimers ($[Cu^{2+}@\mathbf{D}_4]_2$ and $[Cu^{2+}@\mathbf{E}_4]_2$), respectively. G-tetrad stacking distances at the interface of the stacked G-quadruplexes were set in the same range as G-tetrad stacking distances within the G-quartet core. The relative rotation angles at the interfaces were set to a ‘6-ring’ stacking mode for tail-to-tail dimers and to a ‘5/6-ring’ stacking mode for head-to-head dimers, respectively.[23] A K^+ ion was placed between the stacking G-tetrads at the interface, which was found in a dimeric solid-state structure of an unmodified tetramolecular G-quadruplex.[21]

To generate initial structures with a free guanosine quartet intercalating between the two monomers of a dimer, one deoxyguanosine tetrad was cut out from the above-mentioned solid-state structure of a G-quadruplex[21] and the 2'-OH groups were added manually. The free guanosine tetrad was then inserted manually between the two monomers of a dimer. The π-stacking distances were set in the same range as the ones within the G-tetrad cores. Relative rotation angles at the interfaces between G-quadruplexes and free guanosine tetrads were set according to a '6-ring' stacking mode for heteropolar stacking and to a 'partial 5/6-ring' stacking mode for homopolar stacking, respectively.[23] One K^+ ion was placed into every stacking interspace.

To generate initial structures with PIPER or telomestatin, respectively, intercalating between the two monomers of a dimer, the geometry optimized intercalators were inserted manually between the two monomers. The π-stacking distances were set in the same range as the ones within the G-tetrad cores. For telomestatin as the intercalator, one K^+ ion was placed into every stacking interspace between telomestatin and the quadruplex monomers.[24] No K^+ ions were placed into the stacking interspaces between PIPER and the quadruplex monomers.[25] For PIPER as the intercalator, the piperidine side chains were pointing into the grooves of the G-quadruplexes. To create a starting structure for complex 2PIPER@[Cu^{2+}@**A**$_4$]$_2$, the two PIPER molecules were aligned in an orthogonal way to each other.[25]

6.15.3 Generation of Initial Structures of Duplex-Bridged G-Quadruplexes

First, an NMR solution structure of a chair-type G-quadruplex based on a human telomeric sequence variant (PDB entry 5YEY, model 2)[26] was modified in UCSF Chimera.[22] The unnatural thymidine was substituted by an adenosine and one adenosine was added at the 5'-end to obtain the htel22 sequence. Second, the G-tetrad pointing away from the 3'- and 5'-ends was manually substituted by the geometry-optimized Cu(pyridine)$_4$ tetrad and a K^+ ion was placed in between the remaining two G-quartets. The G-quadruplex structures were then duplicated.

Third, the duplex segment including the spacer nucleotides was modeled using the nucleotide model kit in *Wavefunction Spartan'18*[27] and the G-quadruplex parts and the duplex segment were connected manually and orientated with typical π-stacking distances between the G-quartets, the spacer nucleobase and the base pairs in the duplex.

6.15.4 MD Simulation Procedure

The respective models obtained above were put in a periodic rhombic dodecahedron box (cutoff 1.5 nm) and energy minimized 2000 steps of steepest descent (600 kJ/mol nm tolerance) in vacuum. PME and van-der-Waals cutoff of 1.3 nm were used. The system was solvated with TIP3P water molecules and the negative charge of the system was neutralized with the corresponding amount of randomly positioned K^+ ions. An additional 100 mmol/L KCl was added to simulate the ionic strength of the experiments.

The system was then energy minimized in two steps, first 500 steps of steepest descent (500 kJ/mol nm tolerance) and then 3000 steps of conjugate gradient minimization (300 kJ/mol nm tolerance). The non-bonded Lennard-Jones cutoff was set to 1.3 nm, the non-bonded pair list updated every 50 steps. For the coulombic interactions, Particle-mesh Ewald summation (PME) was used.[28] Next, the system was equilibrated with positional constraints on the model's heavy-atoms 100 ps in a first round (NVT ensemble, constraints 1000 kJ/mol $Å^2$, time step 2 fs; Temperature coupling modified Berendsen, 298 K); second round 100 ps with additional pressure coupling (isotropic, Berendsen, 1 bar, time constant for coupling 0.1 ps, compressibility $4.5\ 10^{-5}$) and a third round 100 ps but with lower constraints (100 kJ/mol $Å^2$, Nose-Hoover temperature coupling, 2 ps coupling, Parinello-Rahman isotroic pressure coupling, 2 ps coupling time). The equilibration phase was finished with 200 ps of an unconstraint DNA MD run (coupling times increased to 4 ps). A 50 ns MD production run was then performed. Coordinates were written every 10 ps, resulting in 5001 frames per trajectory. Trajectories were centered, aligned and fitted to the first frame using the built-in Gromacs tools and then analyzed and visualized with UCSF Chimera.[22] For comparison of the simulated Cu^{2+}-Cu^{2+} distance distributions with the experimentally derived ones, the Cu^{2+}-Cu^{2+} distances were extracted from each frame and the 5001 distance values were used to plot a distribution curve with the Origin software (type of distribution curve: normal).

6.15.5 MD-Derived Structures, Cu^{2+}–Cu^{2+} Distances and RMSD Trajectories

The average Cu^{2+}-Cu^{2+} distances and standard deviations were calculated based on the distances of the complete trajectories extracted with Chimera. The depicted structures are representatives of the MD trajectories. For the RMSD plots, the first frame of the trajectory was used as the reference.

Figure 6.73: MD-derived structural model of the G-quadruplex dimer $[Cu^{2+}@\mathbf{A}_4]_2$ (top view and side view), the Cu^{2+}-Cu^{2+} distance throughout the full MD simulation and the corresponding RMSD plots.

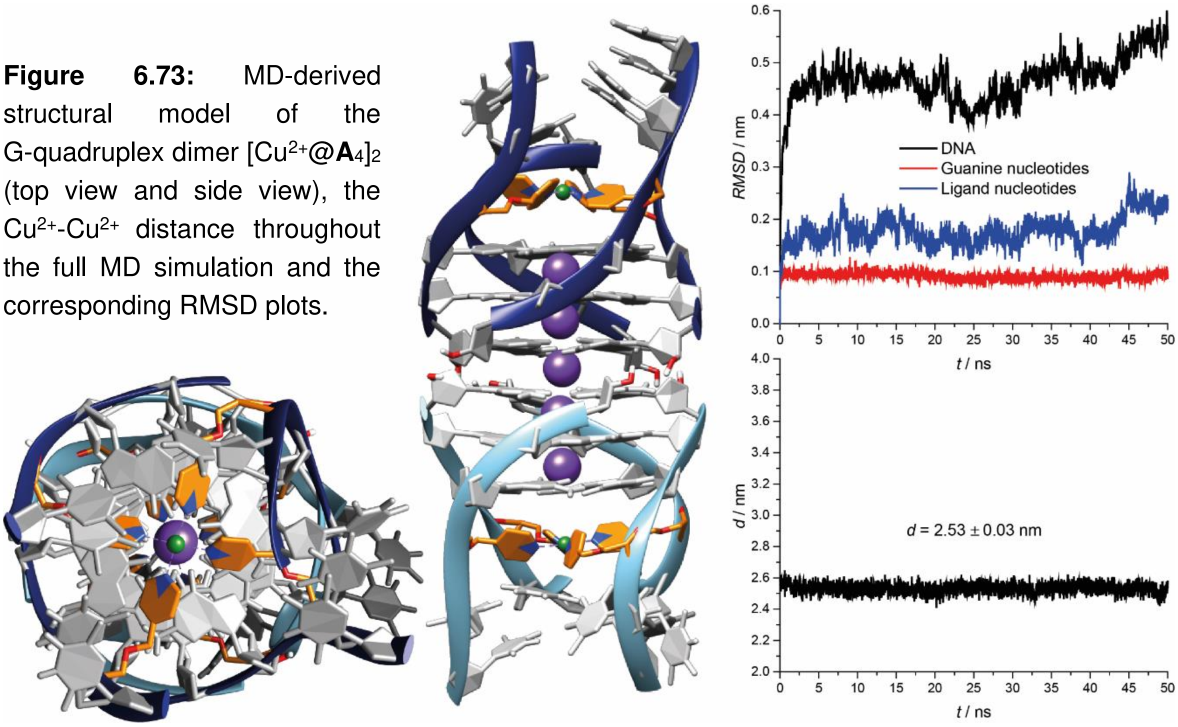

Figure 6.74: MD-derived structural model of the G-quadruplex dimer $[Cu^{2+}@\mathbf{B}_4]_2$ (top view and side view), the Cu^{2+}-Cu^{2+} distance throughout the full MD simulation and the corresponding RMSD plots.

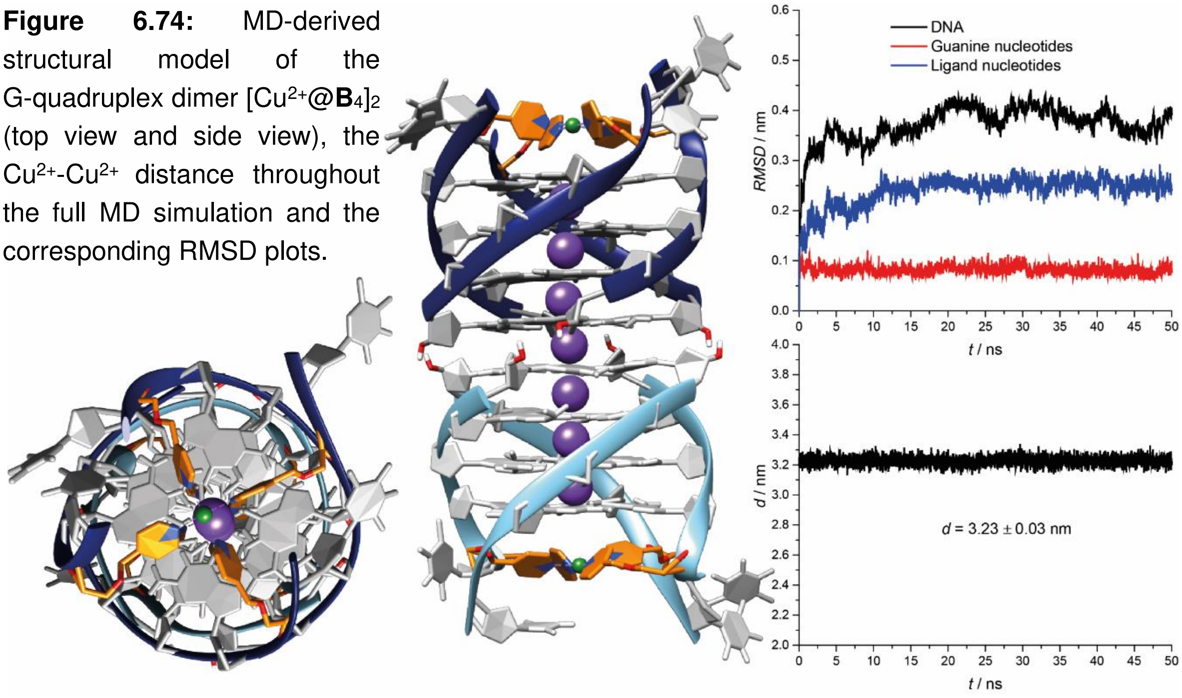

Figure 6.75: MD-derived structural model of the G-quadruplex dimer [Cu^{2+}@**D**$_4$]$_2$ (top view and side view), the Cu^{2+}-Cu^{2+} distance throughout the full MD simulation and the corresponding RMSD plots.

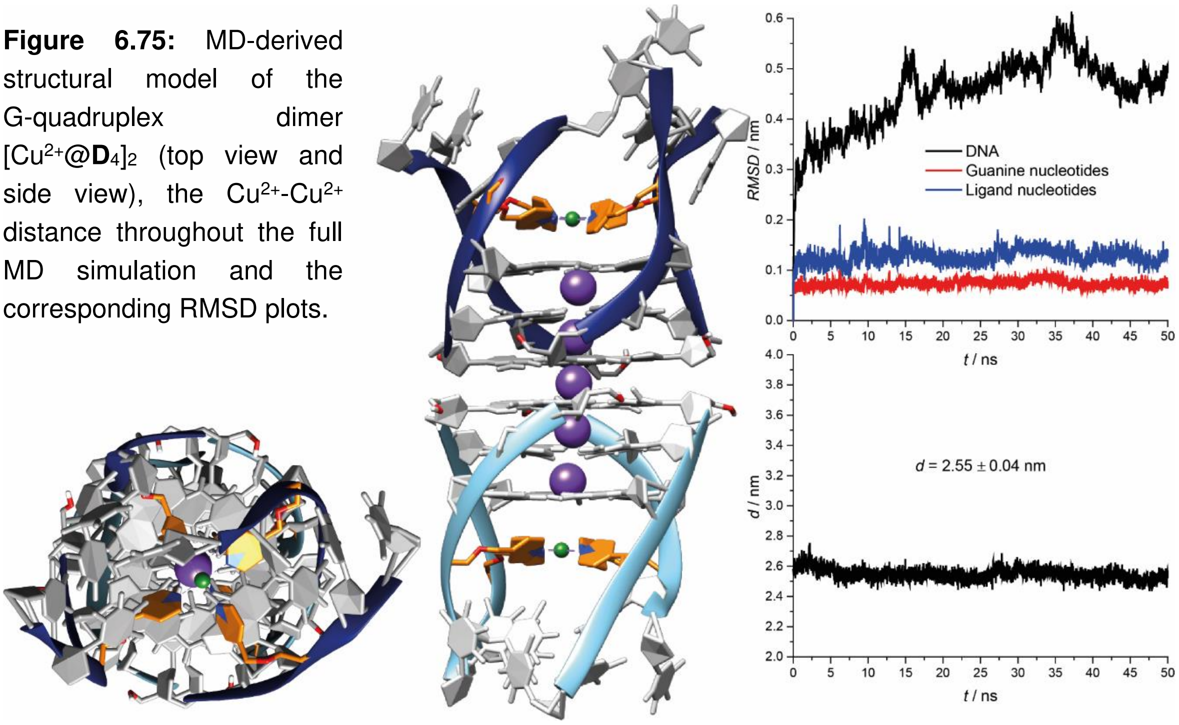

Figure 6.76: MD-derived structural model of the G-quadruplex dimer [Cu^{2+}@**E**$_4$]$_2$ (top view and side view), the Cu^{2+}-Cu^{2+} distance throughout the full MD simulation and the corresponding RMSD plots.

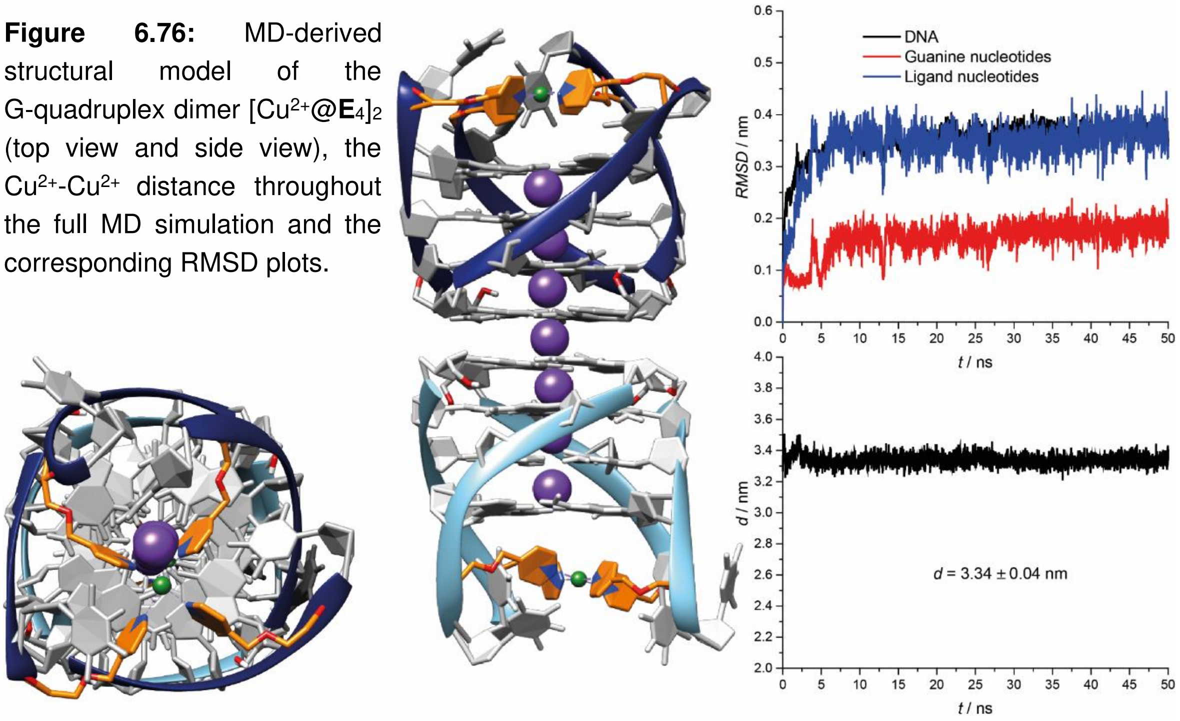

Figure 6.77: MD-derived structural model of the sandwich-type complex guoanosine$_4$@[Cu^{2+}@**A**$_4$]$_2$ (top view and side view, the free guanosine tetrad is shown in green), the Cu^{2+}-Cu^{2+} distance throughout the full MD simulation and the corresponding RMSD plots.

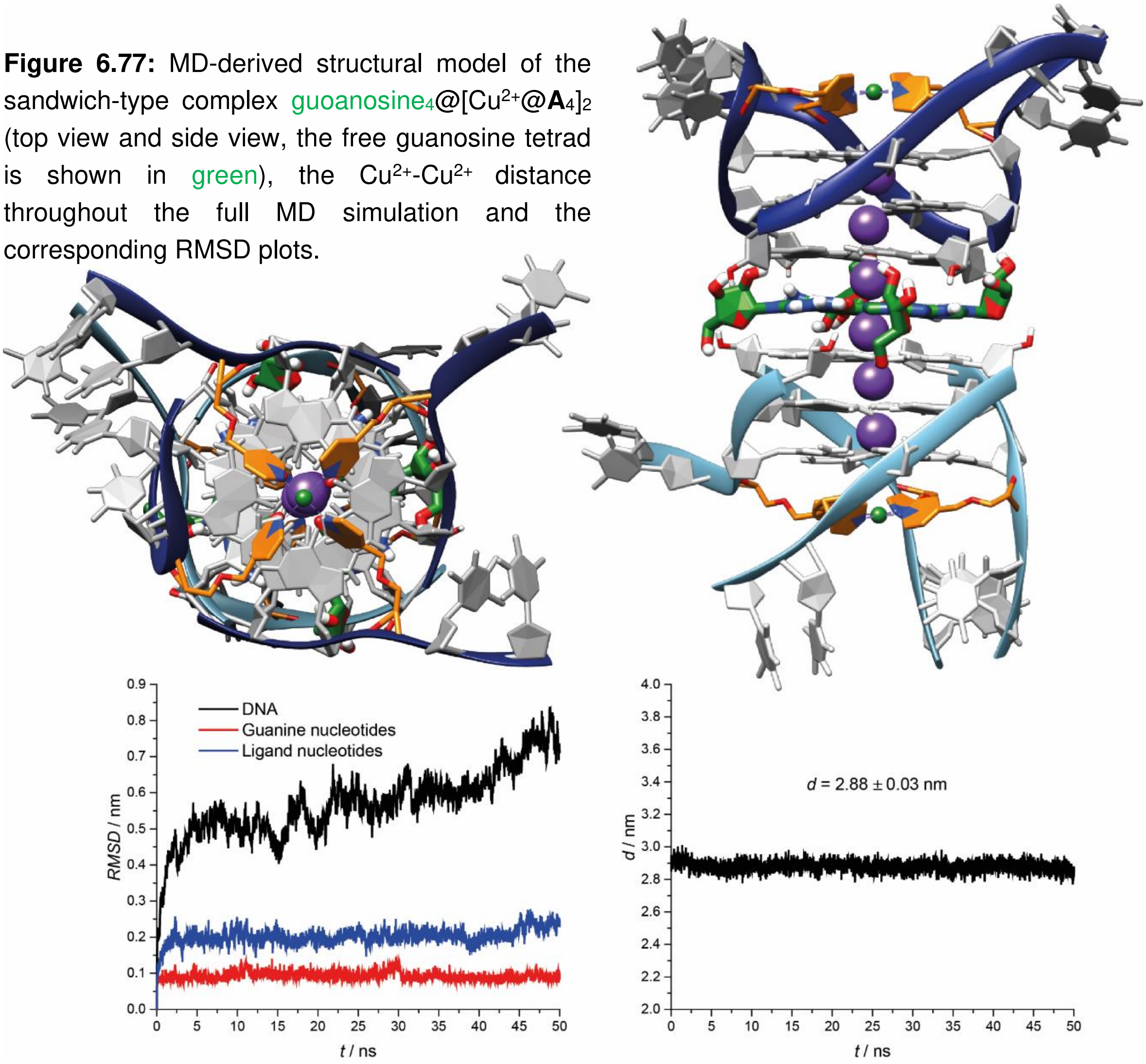

Figure 6.78: MD-derived structural model of the sandwich-type complex guoanosine$_4$@[Cu^{2+}@**B**$_4$]$_2$ (top view and side view, the free guanosine tetrad is shown in green), the Cu^{2+}-Cu^{2+} distance throughout the full MD simulation and the corresponding RMSD plots.

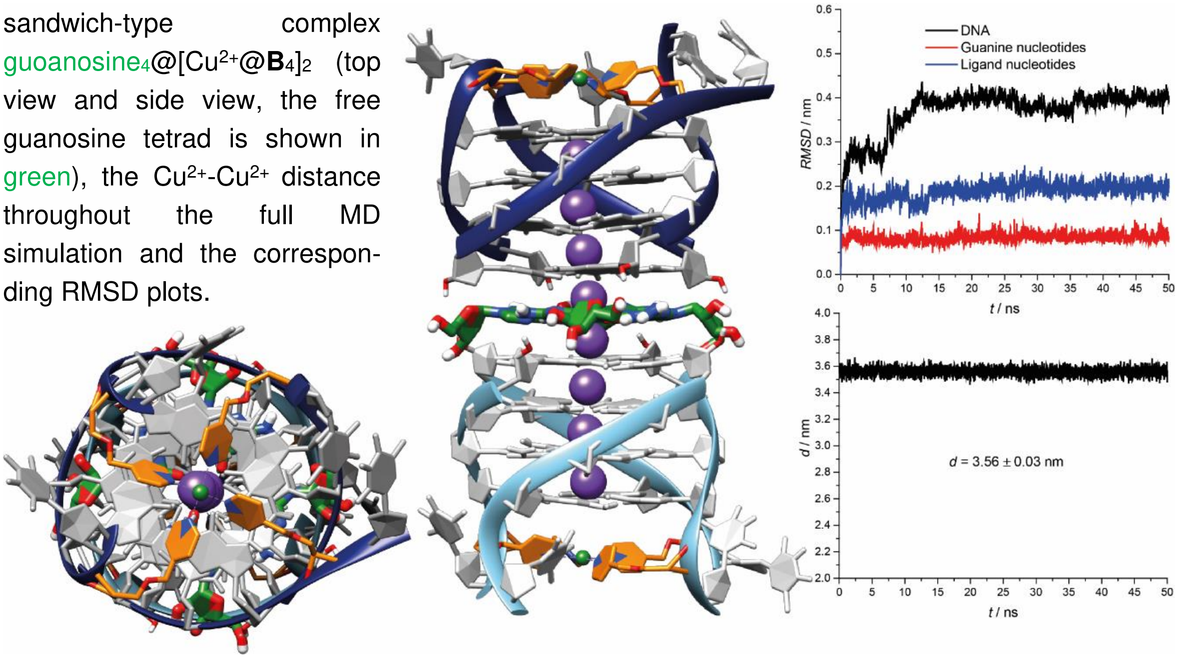

Figure 6.79: MD-derived structural model of the sandwich-type complex PIPER@[Cu^{2+}@**A**$_4$]$_2$ (top and side view, PIPER is shown in red), the Cu^{2+}-Cu^{2+} distance throughout the full MD simulation and the respective RMSD plots.

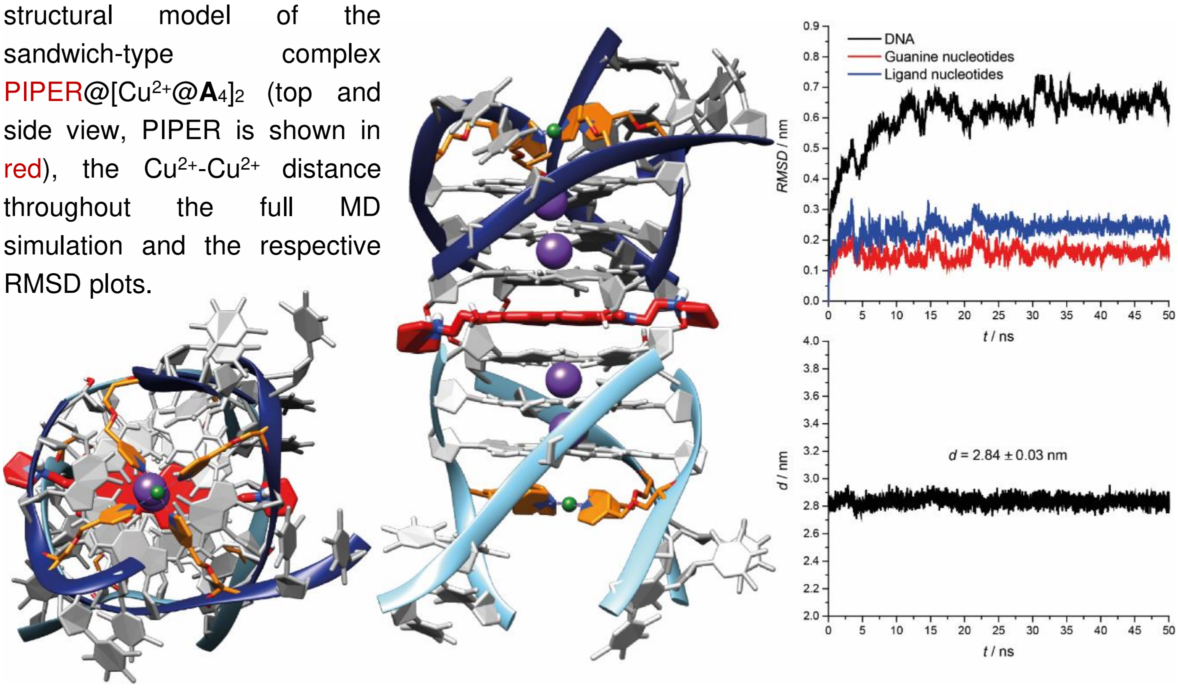

Figure 6.80: MD-derived structural model of the sandwich-type complex PIPER@[Cu^{2+}@**B**$_4$]$_2$ (top and side view, PIPER is shown in red), the Cu^{2+}-Cu^{2+} distance throughout the full MD simulation and the respective RMSD plots.

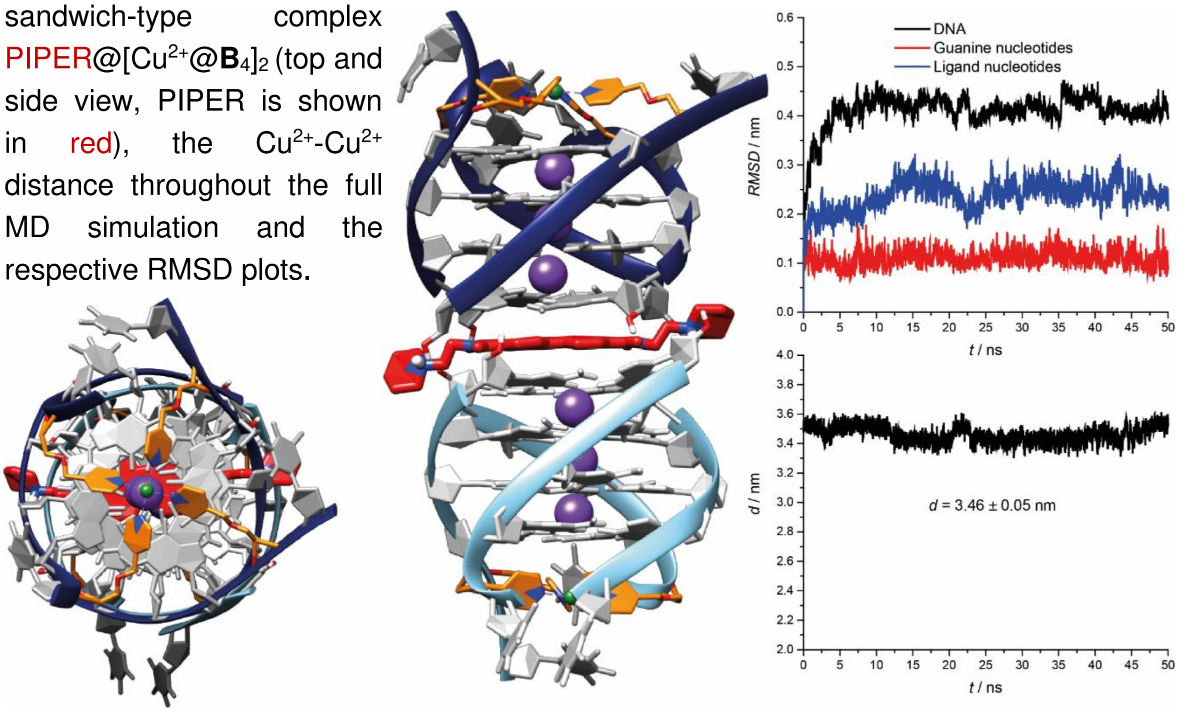

Figure 6.81: MD-derived structural model of the sandwich-type complex telomestatin@[Cu^{2+}@**A**$_4$]$_2$ (top and side view, telomestatin is shown in black), the Cu^{2+}-Cu^{2+} distance throughout the full MD simulation and the respective RMSD plots.

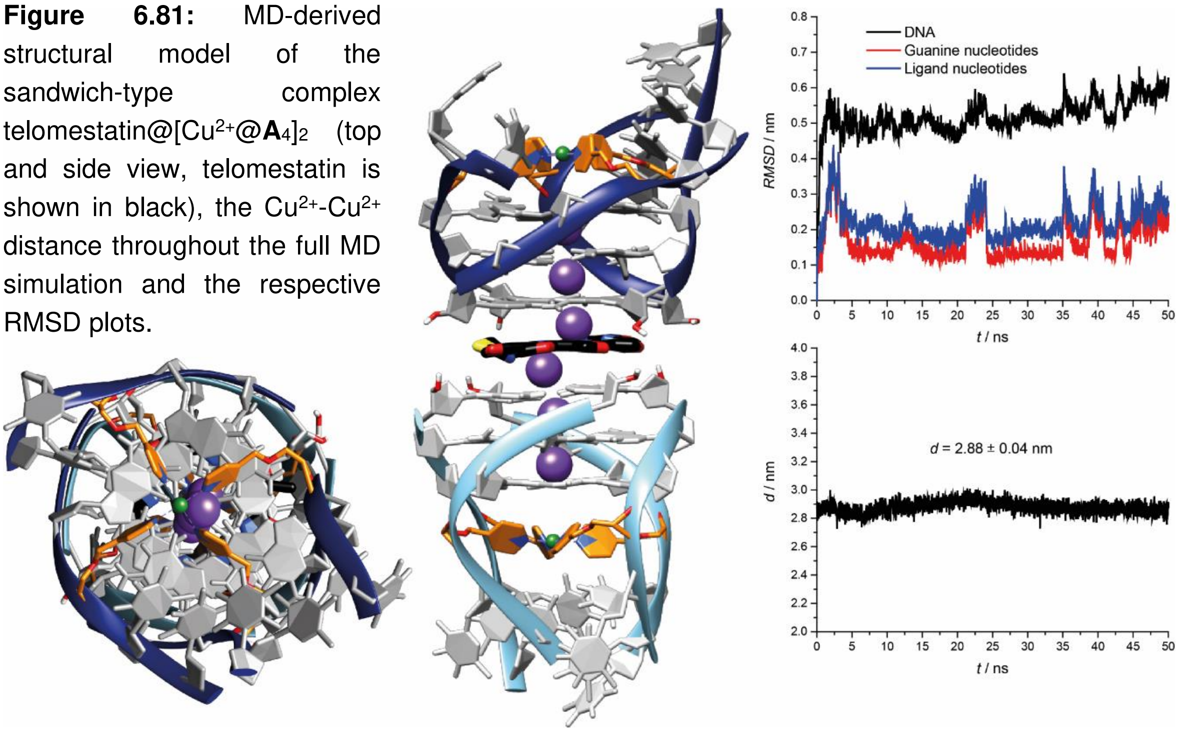

Figure 6.82: MD-derived structural model of the sandwich-type complex 2PIPER@[Cu^{2+}@**A**$_4$]$_2$ (top and side view, PIPER is shown in red), the Cu^{2+}-Cu^{2+} distance throughout the full MD simulation and the respective RMSD plots. Also, the two intercalating PIPER molecules are shown from different perspectives to highlight their relative orientation with respect to each other (relative rotation angle of about 40–60° throughout the MD run).

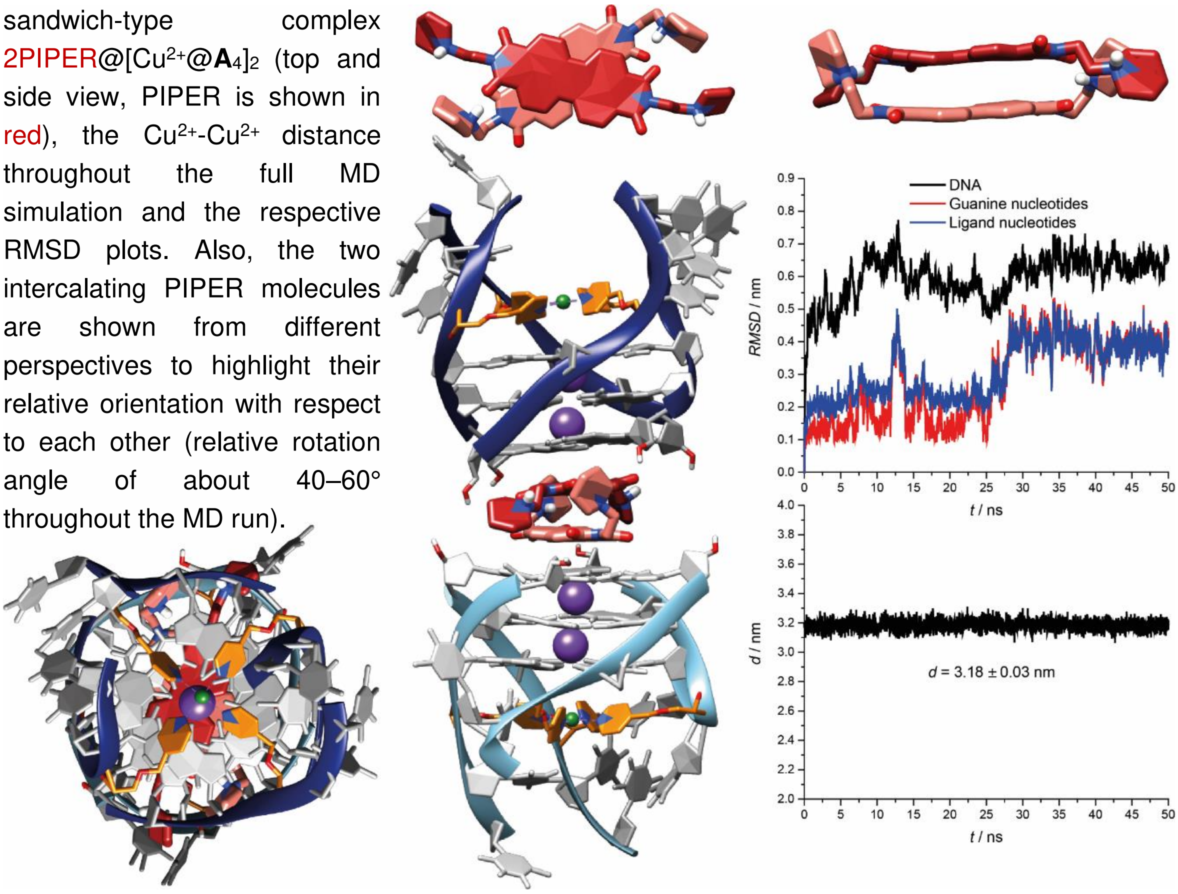

Figure 6.83: MD-derived structural model of the G-quadruplex heterodimer $[\mathrm{Cu}^{2+}@\mathbf{A}_4][\mathrm{Cu}^{2+}@\mathbf{B}_4]$ (top view and side view), the Cu^{2+}-Cu^{2+} distance throughout the full MD simulation and the corresponding RMSD plots.

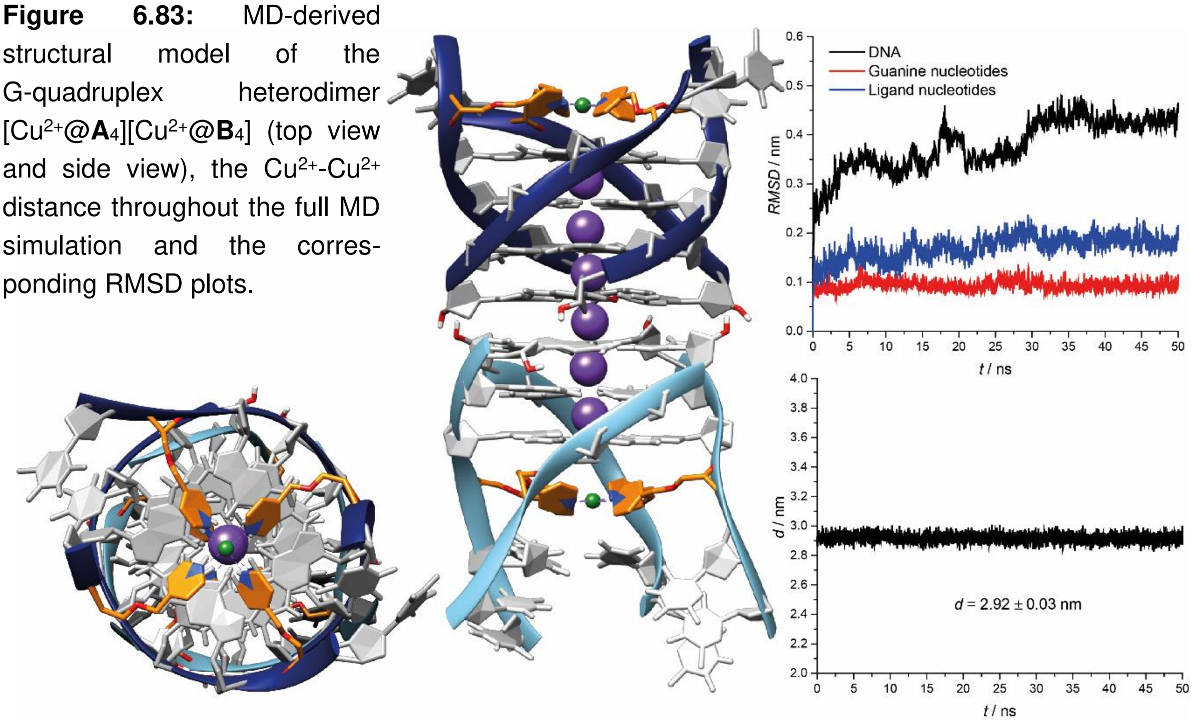

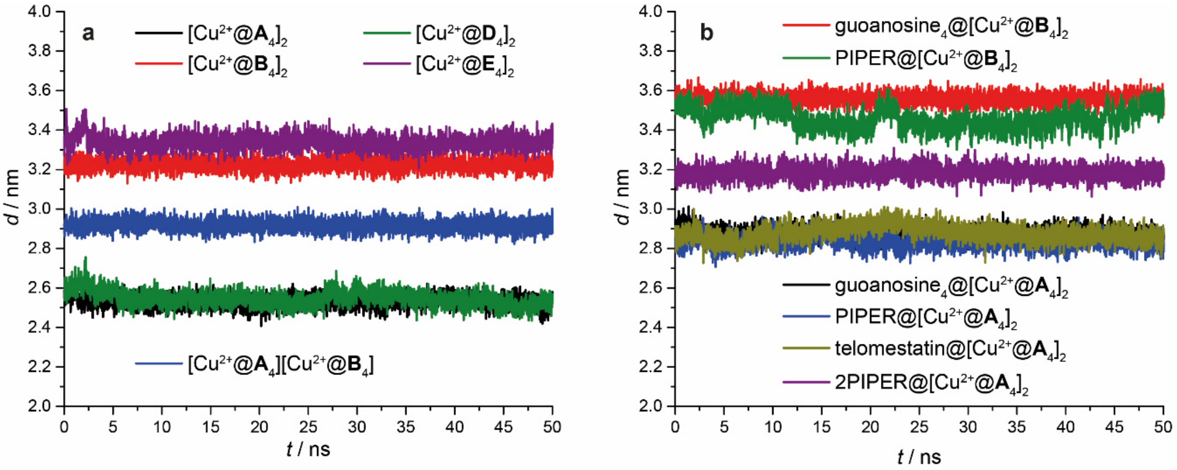

Figure 6.84: Comparison of the Cu^{2+}-Cu^{2+} distances of different (**a**) G-quadruplex dimers and (**b**) related sandwich complexes derived from MD simulations.

6.16 References

[1] Q. Zhai, M. Deng, L. Xu, X. Zhang, X. Zhou, *Bioorg. Med. Chem. Lett.* **2012**, *22*, 1142–1145.

[2] J.-L. Mergny, J. Li, L. Lacroix, S. Amrane, J. B. Chaires, *Nucleic Acids Res.* **2005**, *33*, e138–e138.

[3] J.-L. Mergny, L. Lacroix, *Curr. Protoc. Nucleic Acid Chem.* **2009**, *Chapter 17*, 17.1.1-17.1.15.

[4] S. Allenmark, *Chirality* **2003**, *15*, 409–422.

[5] M. Chevallet, S. Luche, T. Rabilloud, *Nat. Protoc.* **2006**, *1*, 1852–1858.

[6] B. J. Bassam, P. M. Gresshoff, *Nat. Protoc.* **2007**, *2*, 2649–2654.

[7] M. Teucher, E. Bordignon, *J. Magn. Reason.* **2018**, *296*, 103–111.

[8] G. Jeschke, V. Chechik, P. Ionita, A. Godt, H. Zimmermann, J. Banham, C. R. Timmel, D. Hilger, H. Jung, *Appl. Magn. Reson.* **2006**, *30*, 473–498.

[9] D. Abdullin, G. Hagelueken, R. I. Hunter, G. M. Smith, O. Schiemann, *Mol. Phys.* **2014**, *113*, 544–560.

[10] D. M. Engelhard, J. Nowack, G. H. Clever, *Angew. Chem. Int. Ed.* **2017**, *56*, 11640–11644.

[11] D. M. Engelhard, L. M. Stratmann, G. H. Clever, *Chem. Eur. J.* **2018**, *24*, 2117–2125.

[12] S. Pronk, S. Páll, R. Schulz, P. Larsson, P. Bjelkmar, R. Apostolov, M. R. Shirts, J. C. Smith, P. M. Kasson, D. van der Spoel, B. Hess, E. Lindahl, *Bioinformatics* **2013**, *29*, 845–54.

[13] B. Hess, H. Bekker, H. J. C. Berendsen, J. G. E. M. Fraaije, *J. Comput. Chem.* **1997**, *18*, 1463–1472.

[14] D. V. D. Spoel, E. Lindahl, B. Hess, G. Groenhof, A. E. Mark, H. J. C. Berendsen, *J. Comput. Chem.* **2005**, *26*, 1701–1718.

[15] A. Pérez, I. Marchán, D. Svozil, J. Sponer, T. E. Cheatham, C. A. Laughton, M. Orozco, *Biophys. J.* **2007**, *92*, 3817–3829.

[16] I. Ivani, P. D. Dans, A. Noy, A. Pérez, I. Faustino, A. Hospital, J. Walther, P. Andrio, R. Goñi, A. Balaceanu, G. Portella, F. Battistini, J. L. Gelpí, C. González, M. Vendruscolo, C. A. Laughton, S. A. Harris, D. A. Case, M. Orozco, *Nat. Methods* **2016**, *13*, 55–58.

[17] J. Wang, R. M. Wolf, J. W. Caldwell, P. A. Kollman, D. A. Case, *J. Comput. Chem.* **2004**, *25*, 1157–1174.

[18] C. I. Bayly, P. Cieplak, W. Cornell, P. A. Kollman, *J. Phys. Chem.* **1993**, *97*, 10269–10280.

[19] J. Wang, W. Wang, P. A. Kollman, D. A. Case, *J. Mol. Graphics Modell.* **2006**, *25*, 247–260.

[20] A. W. S. da Silva, W. F. Vranken, *BMC Res. Notes* **2012**, *5*, 367.

[21] C. Creze, B. Rinaldi, R. Haser, P. Bouvet, P. Gouet, *Acta Crystallogr., Sect. D: Biol. Crystallogr.* **2007**, *63*, 682–688.

[22] E. F. Pettersen, T. D. Goddard, C. C. Huang, G. S. Couch, D. M. Greenblatt, E. C. Meng, T. E. Ferrin, *J. Comput. Chem.* **2004**, *25*, 1605–1612.

[23] C. J. Lech, B. Heddi, A. T. Phan, *Nucleic Acids Res.* **2013**, *41*, 2034–2046.

[24] F. Rosu, V. Gabelica, N. Smargiasso, G. Mazzucchelli, K. Shin-Ya, E. D. Pauw, *J. Nucleic Acids* **2010**, *2010*, 121259.

[25] G. N. Parkinson, F. Cuenca, S. Neidle, *J. Mol. Biol.* **2008**, *381*, 1145–1156.

[26] C. Liu, B. Zhou, Y. Geng, D. Y. Tam, R. Feng, H. Miao, N. Xu, X. Shi, Y. You, Y. Hong, B. Z. Tang, P. K. Lo, V. Kuryavyi, G. Zhu, *Chem. Sci.* **2018**, *10*, 218–226.

[27] *Spartan`18 Parallel Suite, Wavefunction, Inc., Irvine.*

[28] U. Essmann, L. Perera, M. L. Berkowitz, T. Darden, H. Lee, L. G. Pedersen, *J. Chem. Phys.* **1995**, *103*, 8577–8593.

7 Synthetic Procedures

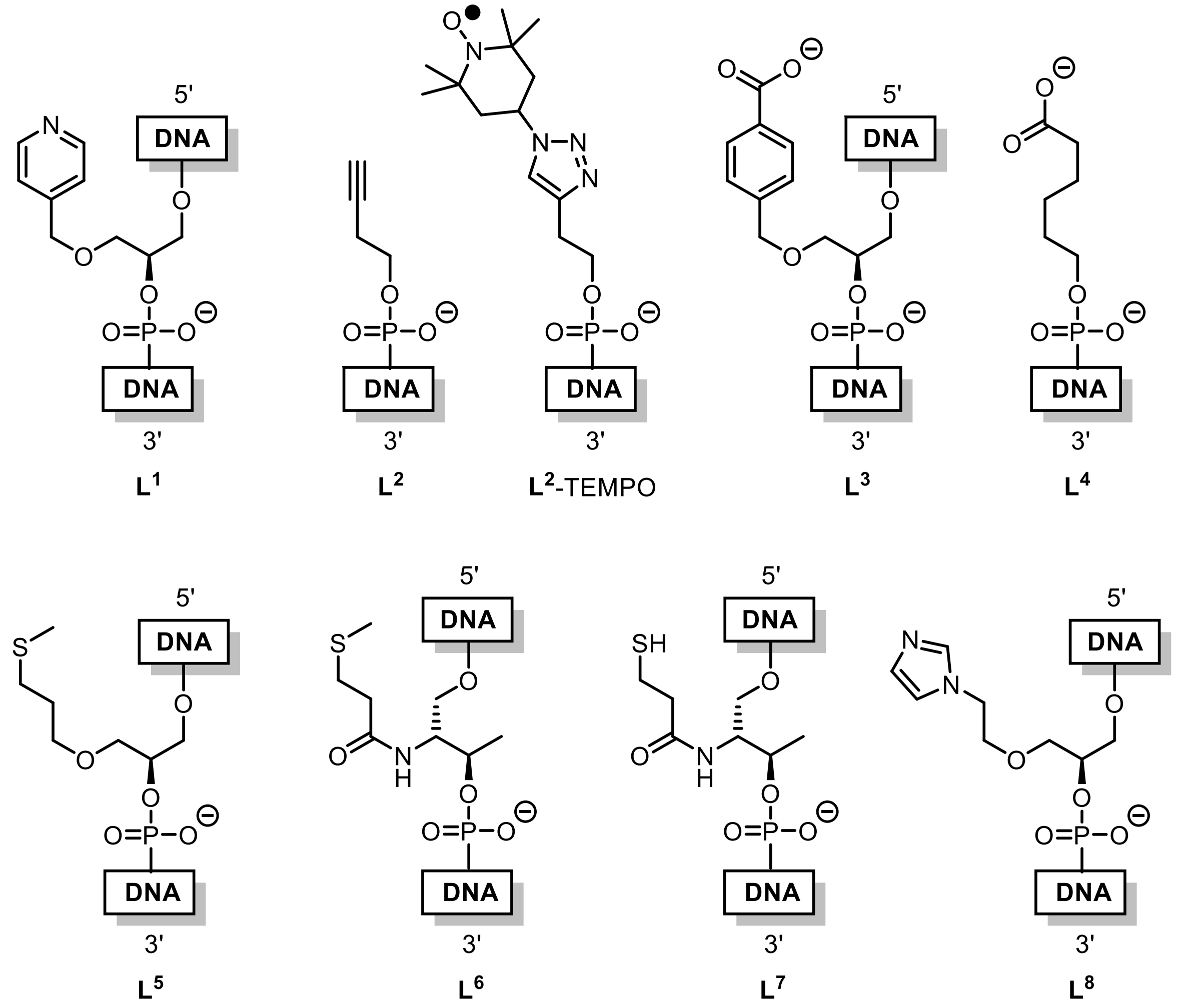

Figure 7.1: Overview of all artificial nucleotides incorporated into oligonucleotides by solid-phase DNA synthesis in this thesis (**L**^{6} was not incorporated so far, but the required phosphoramidite building block was synthesized). Among them are ligandosides with different ligand functionalities such as N-heterocyclic donors (**L**^{1} and **L**^{8}),[1–6] carboxylates (**L**^{3} and **L**^{4}),[4] thioethers (**L**^{5} and **L**^{6}), and thiols (**L**^{7}).[7] In addition, **L**^{2} contains an alkyne moiety[8] for subsequent attachment of further functional groups like spin labels (**L**^{2}-TEMPO). All modifications can be incorporated within DNA sequences, except for **L**^{2} (and **L**^{2}-TEMPO) and **L**^{4} which lack the required 5'-OH group and can only be attached to the 5'-end of a sequence. Two different simplified backbones were used to replace the deoxyribofuranose ring either based on glycol (**L**^{1}, **L**^{3}, **L**^{5}, and **L**^{8}) or on threoninol (**L**^{6} and **L**^{7}).

7.1 General Remarks

Chemicals and standard solvents were purchased from *Sigma Aldrich*, *Acros Organics*, *Carl Roth*, *TCI Europe*, *ABCR* or other suppliers and used as received. If necessary, reactions were carried out under an inert nitrogen atmosphere in a *GS-systems* glovebox or using standard Schlenk techniques. Dry solvents were purified and dried over absorbent-filled columns on a *GS-Systems* solvent purification system or purchased over molecular sieves from *Acros Organics*.

Microwave irradiation-assisted reactions (MW) were performed in a *CEM Discovery SP* microwave reactor. Reactions were monitored with thin layer chromatography (TLC), using silica coated aluminum plates (*Merck*, silica 60, fluorescence indicator F254, thickness 0.25 mm). For column chromatography, silica (*Merck*, silica 60, 0.02–0.063 mesh ASTM) was used as the stationary phase. Flash chromatography was performed on a *Biotage Isolera One* fraction collector with *Biotage SNAP Ultra* columns.

NMR spectra were recorded on a *Bruker AV 400 Avance III HD NanoBay*, *Bruker AV 500 Avance NEO*, *AV 600 Avance III HD* or *AV 700 Avance III HD* spectrometer. Chemical shifts δ are given in ppm. For ^{1}H and ^{13}C NMR spectra, chemical shifts were calibrated to the solvent lock signal. ^{31}P NMR chemical shifts are given relative to 85% H_3PO_4 (external reference). Signal multiplicities are composed of the following abbreviations: s (singlet), d (doublet), t (triplet), q (quartet), m (multiplett).

Mass spectrometry was performed on a *Bruker ESI-timsTOF* mass spectrometer. For calibration of the TOF device, *Agilent ESI-Low Concentration Tuning Mix* was used. Melting points were determined on a *Stuart SMP30* melting point apparatus. Elemental analyses were performed on an *Elementar vario MICRO cube*. IR spectra were recorded on a *PerkinElmer Spectrum Two* FT-IR spectrometer with $LiTaO_3$ MIR detector and an optical system with KBr windows. UV-VIS spectra were recorded on a *Jasco V-750* spectrometer.

7.2 Syntheses of Literature-Known Phosphoramidites

The syntheses and characterization of phosphoramidite building blocks (*S*)-**1** and (*S*)-**2**, which were required to incorporate the artificial ligandosides **L^1** and **L^8** into oligonucleotides by DNA solid-phase synthesis, were published earlier by our lab.[1,5] Their synthesis in this work followed the literature-known procedures.

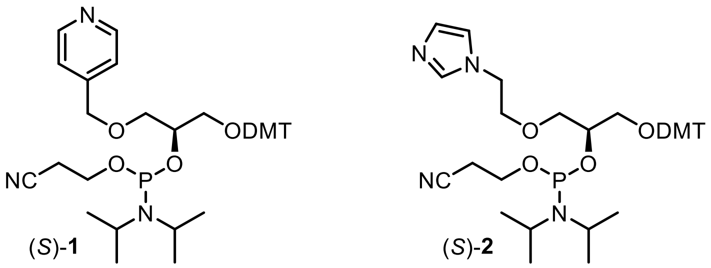

Figure 7.2: Literature-known phosphoramidite building blocks (*S*)-**1** and (*S*)-**2**,[1,5] which were required to incorporate the artificial ligandosides **L**^{1} and **L**^{8} into oligonucleotides.

7.3 Synthesis of the G-Quadruplex-Binding Ligand PIPER

The G-quadruplex-binding ligand **PIPER** was synthesized and purified using modified published procedures.[9,10]

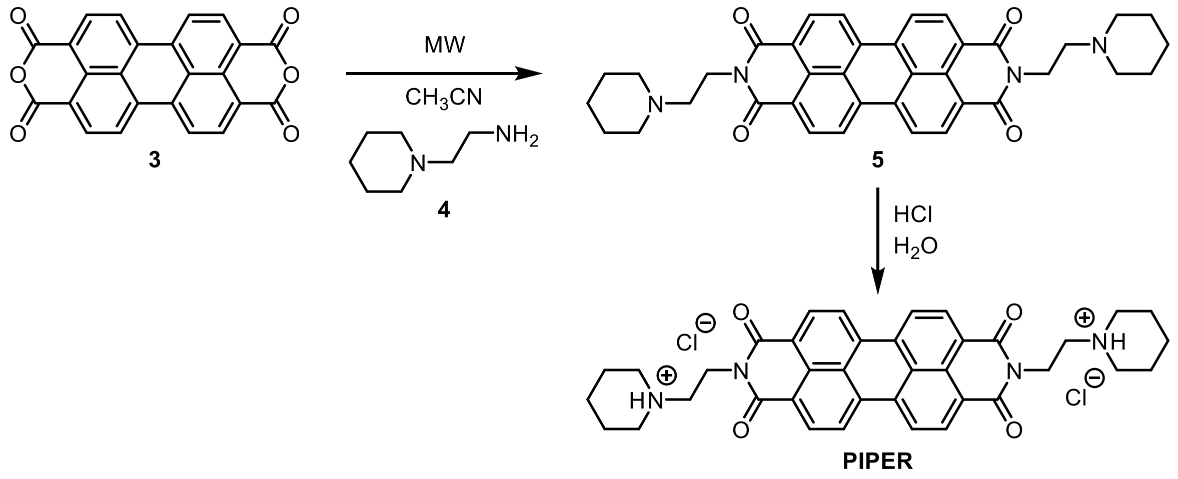

Scheme 7.1: Synthesis of the dicationic G-quadruplex-binding ligand **PIPER**.

7.3.1 Synthesis of *N,N'*-Bis[2-(1-piperidino)ethyl]-3,4,9,10-perylenetetracarboxylic diimide (5)

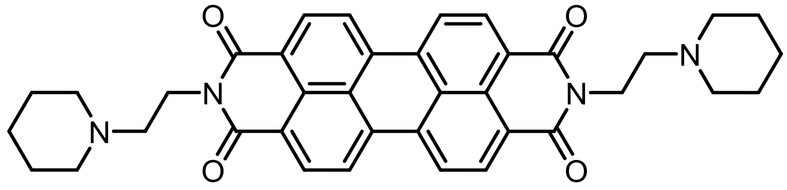

5

A mixture of perylene-3,4,9,10-tetracarboxylic dianhydride (**3**, 1.00 g, 2.55 mmol, 1.0 equiv.) and 1-(2-aminoethyl)-piperidine (**4**, 0.80 mL, 5.61 mmol, 2.2 equiv.) in acetonitrile (10 mL) was stirred and irradiated in a sealed vessel in a microwave reactor (150 watts, 95 °C, 1.5 h). The obtained reaction mixture was extracted with chloroform (300 mL) and the solvent and traces of the primary amine were removed under reduced pressure. Product **5** was obtained as a purple solid (1.31 g, 2.14 mmol, 84%) with a melting point >300 °C.

^{1}H NMR (500 MHz, chloroform-d): δ = 8.66 (d, J = 7.9 Hz, 4H), 8.57 (d, J = 7.9 Hz, 4H), 4.38 (t, J = 7.2 Hz, 4H), 2.70 (t, J = 7.2 Hz, 4H), 2.63 – 2.51 (m, 8H), 1.64 – 1.58 (m, 8H), 1.48 – 1.41 (m, 4H).

HR-ESI MS (positive mode, MeCN/CH_2Cl_2): *m/z* calc. for $C_{38}H_{36}N_4O_4$, 613.2809 $[M+H]^+$; found 613.2802.

7.3.2 Synthesis of *N,N'*-Bis[2-(1-piperidino)ethyl]-3,4,9,10-perylenetetracarboxylic diimide dihydrochloride (PIPER)

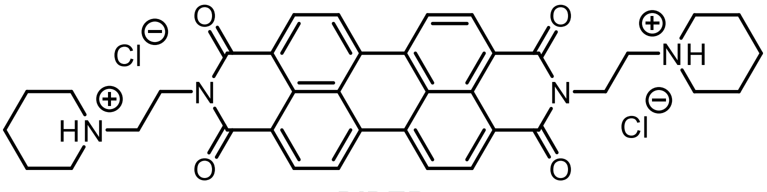

PIPER

Compound **5** (44 mg, 72 µmol, 1 equiv.) was treated with concentrated aqueous hydrochloric acid (2 mL) and triturated with a glass rod until a bright brick red solid formed (~5 min). Water (1 mL) was added and the solid was collected by filtration, washed with diethyl ether (10 mL) and air-dried at 65 °C for 3 days. **PIPER** was obtained as a dark red solid (46 mg, 67 µmol, 93%) with a melting point >300 °C.

^{1}H NMR (500 MHz, deuterium oxide): δ = 7.67 (br s, 4H), 7.32 (br s, 4H), 4.42 (br s, 4H), 3.81 (br s, 4H), 3.48 (br s, 4H), 3.20 (br s, 4H), 2.08 (br s, 4H), 1.92 (br s, 6H), 1.63 (br s, 2H).

HR-ESI MS (positive mode, MeCN/H_2O): *m/z* calc. for $C_{38}H_{38}Cl_2N_4O_4$, 307.1441 $[M-2Cl]^{2+}$, 613.2809 $[M-H-2Cl]^+$, 631.2693 $[2M-H-3Cl]^{2+}$, 649.2576 $[2M-2Cl]^{2+}$, 1225.5546 $[2M-3H-4Cl]^+$, 1261.5313 $[2M-2H-3Cl]^+$; found 307.1455, 613.2821, 631.2692, 649.2570, 1225.5536, 1261.5302.

7.4 Synthesis of Phosphoramidite 7 and Spin-Labeled Nucleoside 9

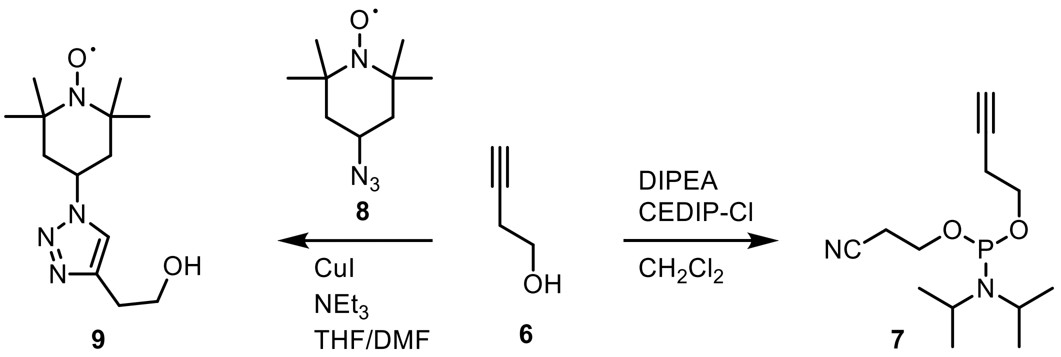

Scheme 7.2. Synthesis of the artificial TEMPO-labeled nucleoside **9** and of phosphoramidite building block **7**[8] which is required to incorporate linker **L**^{2} into oligonucleotides by solid-phase oligonucleotide synthesis.

7.4.1 Synthesis of but-3-yn-1-yl (2-cyanoethyl) diisopropylphosphoramidite (7)

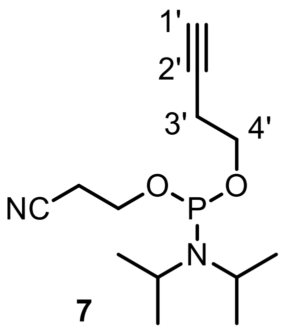

Compound **7** was synthesized using a modified published procedure.[8] To a solution of but-3-yn-1-ol (**6**, 38 µL, 0.500 mmol, 1.0 equiv.) and *N*,*N*-diisopropylethylamine (128 µL, 0.750 mmol, 1.5 equiv.) in dichloromethane (5.5 mL) was added 2-cyanoethyl *N*,*N*-diisopropylchlorophosphoramidite (134 µL, 0.600 mmol, 1.2 equiv.) dropwise and the reaction mixture was stirred for 2 h. The mixture was washed with saturated sodium bicarbonate solution (5 mL) and the aqueous layer was extracted with dichloromethane (1x 5 mL). The combined organic layers were dried over magnesium sulfate and the solvent was removed under reduced pressure. The obtained oil was purified by column chromatography (n-pentane/ethyl acetate, 9:1 + 0.5% triethylamine) to afford product **7** as a colorless oil (57 mg, 0.211 mmol, 42%).

^{1}**H NMR** (400 MHz, chloroform-*d*): δ = 3.92 – 3.52 (m, 6H, 4'-H and $OC\underline{H}_2CH_2CN$ and $N(C\underline{H}(CH_3)_2)_2$), 2.64 (t, J = 6.5 Hz, 2H, $OCH_2C\underline{H}_2CN$), 2.49 (td, J = 6.9 Hz, J = 2.6 Hz, 2H, 3'-H), 1.97 (t, J = 2.6 Hz, 1H, 1'-H), 1.19 (d, J = 2.6 Hz, 6H, $N(CH(C\underline{H}_{a3})_2)_2$), 1.17 (d, J = 2.6 Hz, 6H, $N(CH(C\underline{H}_{b3})_2)_2$).

^{31}P{^{1}H} NMR (162 MHz, Chloroform-*d*): $\delta = 148.1$.

7.4.2 Synthesis of 4-(4-(2-hydroxyethyl)-1H-1,2,3-triazol-1-yl)-2,2,6,6-tetramethylpiperidin-1-oxyl radical (9)

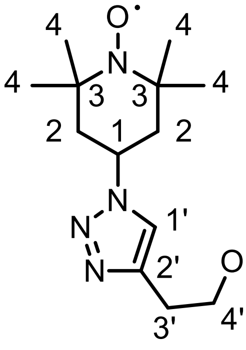

9

To a solution of TEMPO-azide **8** (316 mg, 1.603 mmol, 1.0 equiv., synthesized using a literature procedure)[11] in a mixture of THF and DMF (1:1, v/v) was added but-3-yn-1-ol (**6**, 135 µL, 1.763 mmol, 1.1 equiv.), copper(I) iodide (34 mg, 0.176 mmol, 0.1 equiv.) and triethylamine (25 µL, 0.176 mmol, 0.1 equiv.). The suspension was heated to 35 °C for 2 h. The solvents were removed under reduced pressure and the obtained orange solid was washed with diethyl ether. The solid was suspended in methanol, filtrated and the solvent of the filtrate was removed under reduced pressure. Purification with column chromatography (dichloromethane/methanol, 20:1) and subsequent recrystallization from chloroform yielded product **9** as an orange crystalline solid (151 mg, 0.565 mmol, 35%) with a melting point at 164 °C.

Since the radical character of nitroxide **9** effects a signal broadening in NMR spectra, an excess of phenylhydrazine (PhNHNH$_2$) as a reducing agent was added to the NMR sample prior to measurement to reduce the nitroxide function to a hydroxylamine group.

^{1}H NMR (500 MHz, methylene chloride-d_2 + excess of PhNHNH$_2$): $\delta = 7.44$ (s, 1H, 1’-H), 4.82 (tt, $J = 12.5$ Hz, $J = 4.0$ Hz, 1H, 1-H), 3.88 (t, $J = 6.0$ Hz, 2H, 4’-H), 2.90 (t, $J = 6.0$ Hz, 2H, 3’-H), 2.07 (m, 2H, 2-H$_a$), 1.99 (m, 2H, 2-H$_b$), 1.26 (s, 6H, 4-H$_a$), 1.25 (s, 6H, 4-H$_b$).

^{13}C NMR (126 MHz, methylene chloride-d_2 + excess of PhNHNH$_2$): $\delta = 145.8$ (C2‘), 120.0 (C1‘), 62.2 (C4‘), 59.6 (C3), 53.2 (C1), 45.9 (C2), 32.6 (C4$_a$), 29.3 (C3’), 20.0 (C4$_b$).

HR-ESI MS (positive mode, MeOH): *m/z* calc. for $C_{13}H_{23}N_4O_2$, 268.1894 [M+H]$^+$, 290.1713 [M+Na]$^+$, 557.3534 [2M+Na]$^+$; found 268.1877, 290.1702, 557.3528.

Elemental analysis (%): Calc. for $C_{13}H_{23}N_4O_2$: C 58.4, H 8.7, N 21.0; found: C 58.3, H 8.7, N 20.8.

UV: The extinction coefficient at $\lambda = 260$ nm of the artificial nucleoside **9** in water was determined to $\varepsilon_{260} = 1675$ L mol^{-1} cm^{-1}.

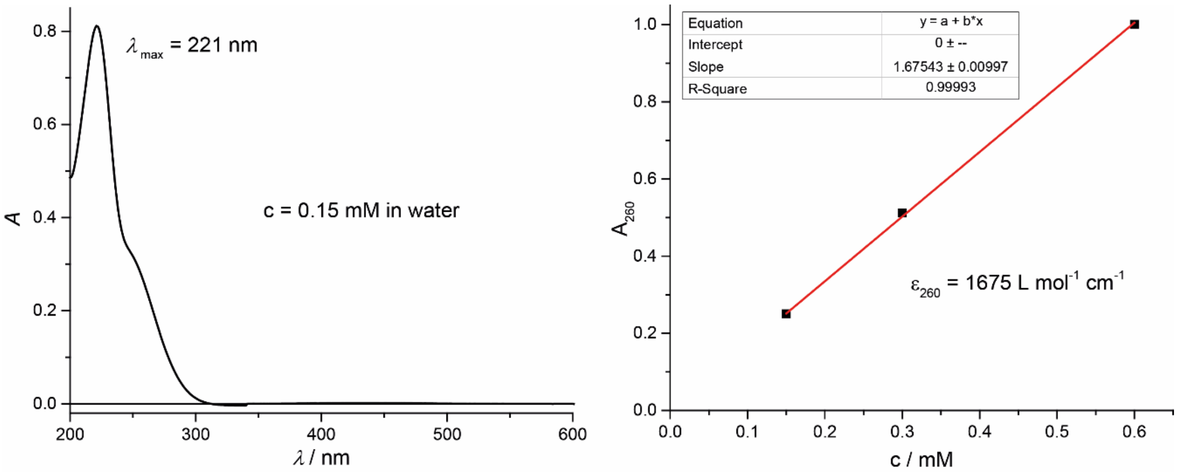

Figure 7.3. Absorption spectrum (left) of **9** (0.15 mM in water) and dilution experiment (right) for the determination of the extinction coefficient ε_{260} of **9**.

7.4.3 Single-Crystal X-ray Diffraction Analysis of 9

Solvent evaporation of a solution of **9** in methanol and ether resulted in orange block-shaped crystals, suitable for single-crystal X-ray diffraction analysis.

Data were collected from a shock-cooled single crystal at 100(2) K on a *Bruker D8 VENTURE* dual wavelength Mo/Cu four-circle diffractometer with a microfocus sealed X-ray tube using mirror optics as monochromator and a *Bruker PHOTON II* detector. The diffractometer was equipped with a low temperature device and used MoK_α radiation ($\lambda = 0.71073$ Å). All data were integrated with *SAINT* and a multi-scan absorption correction using *SADABS-2016/2* was applied. The structure was solved by direct methods using *SHELXT 2014/5*[12] and refined by full-matrix least-squares methods against F^2 by *SHELXL-2014/7*[13]. All non-hydrogen atoms were refined with anisotropic displacement parameters. The hydrogen atoms were refined isotropically on calculated positions using a riding model with their U_{iso} values constrained to 1.5 times the U_{eq} of their pivot atoms for terminal sp^3 carbon atoms and 1.2 times for all other carbon atoms.

Table 7.1: Crystal data and structure refinement of compound **9**.

Compound	**9**
Empirical formula	$C_{13}H_{23}N_4O_2$
Formula weight	267.35
Temperature/K	100(2)
Crystal system	triclinic
Space group	$P\bar{1}$ (2)
a/Å	5.7316(4)
b/Å	8.0045(6)
c/Å	15.8277(12)
α/°	86.198(4)
β/°	86.956(4)
γ/°	74.366(4)
Volume/Å^3	697.28(9)
Z	2
ρ_{calc}g/cm^3	1.273
μ/mm^{-1}	0.088
F(000)	290
Crystal size/mm^3	0.200 × 0.100 × 0.100
Crystal color	orange
Crystal shape	block
Radiation	MoK_α (λ=0.71073 Å)
2Θ range for data collection/°	6.01 to 80.50 (0.55 Å)
Index ranges	$-10 \le h \le 10$, $-14 \le k \le 14$, $-28 \le l \le 28$
Reflections collected	249879
Independent reflections	8779 [R_{int} = 0.0721, R_{sigma} = 0.0187]
Completeness to θ = 25.242°	99.8 %
Data/restraints/parameters	8779/0/241
Goodness-of-fit on F^2	1.140
Final R indexes [I>=2σ (I)]	R_1 = 0.0410, wR_2 = 0.1074
Final R indexes [all data]	R_1 = 0.0480, wR_2 = 0.1126
Largest diff. peak/hole / e Å^{-3}	0.56/-0.30

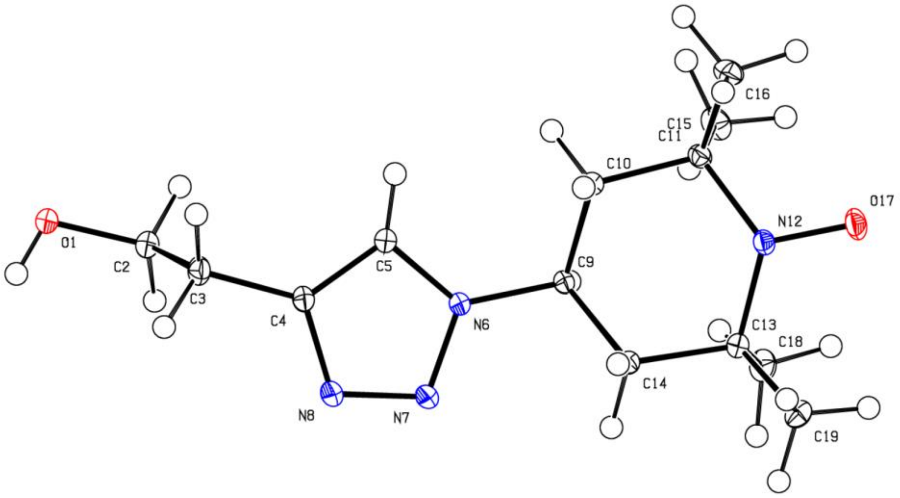

Figure 7.4: Ortep[14] plot and numbering scheme of compound **9**. Displacement ellipsoids are drawn at 50% probability level.

7.5 Synthesis of Nucleoside (*R*)-16 and Phosphoramidite (*S*)-15

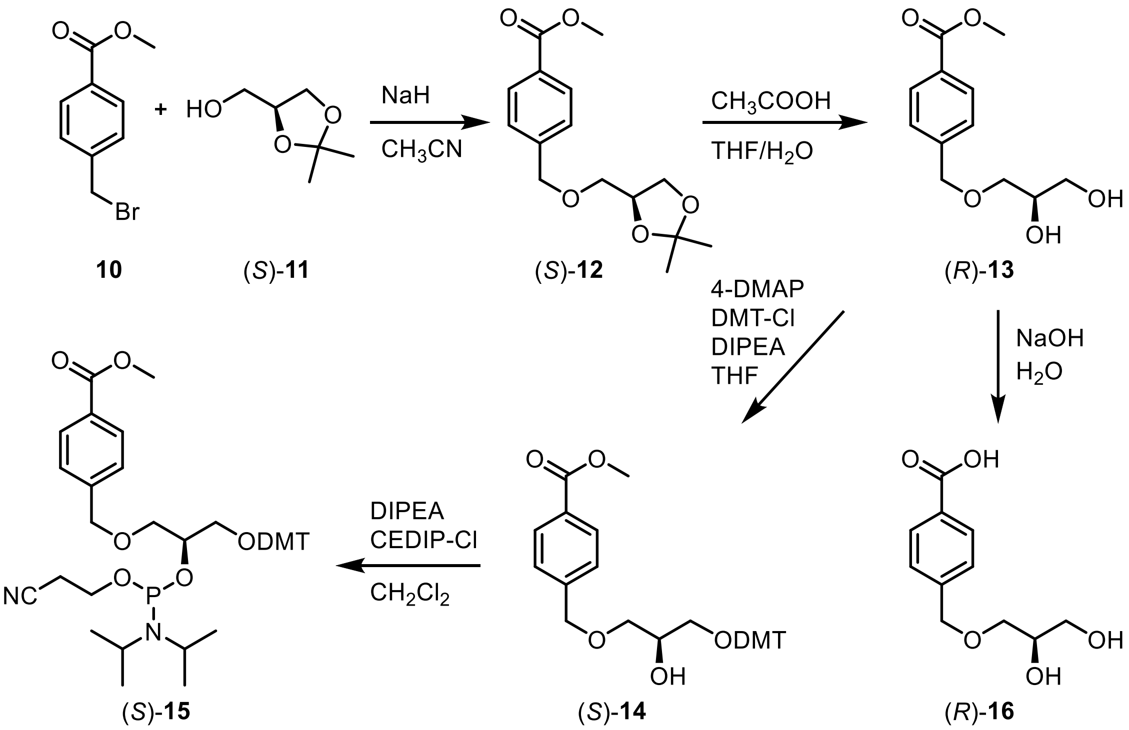

Scheme 7.3. Synthesis of the artificial nucleoside (*R*)-**16** and the corresponding phosphoramidite building block (*S*)-**15**, which is required to incorporate ligandoside **L**^{3} into oligonucleotides by solid-phase oligonucleotide synthesis.

7.5.1 Synthesis of methyl (*S*)-4-(((2,2-dimethyl-1,3-dioxolan-4-yl)methoxy)-methyl)benzoate ((*S*)-12)

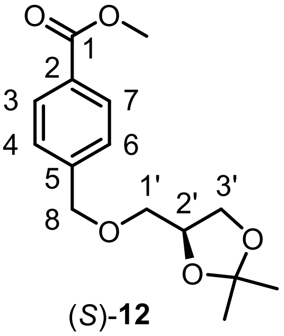

(*S*)-**12**

To a suspension of sodium hydride (60% in mineral oil; 0.36 g, 8.42 mmol, 1.1 equiv.) in acetonitrile (35 mL) was added (*S*)-(2,2-dimethyl-1,3-dioxolan-4-yl)methanol ((*S*)-**11**, 1.00 mL, 8.02 mmol, 1.0 equiv.) dropwise. After 30 min of stirring, the mixture was cooled to 0 °C and methyl 4-(bromomethyl)benzoate (**10**, 1.84 g, 8.02 mmol, 1.0 equiv.) was added. The reaction mixture was allowed to warm up to room temperature and stirred overnight. The solvent was removed under reduced pressure and the obtained solid was suspended in ethyl acetate (50 mL). After filtration, the filtrate was washed with water (50 mL), the aqueous layer was extracted with ethyl acetate (3x 30 mL) and the combined organic layers were dried over magnesium sulfate. The solvent was removed under reduced pressure to afford an oil which was purified by column chromatography (*n*-pentane/ethyl acetate, 5:1) to obtain the product (*S*)-**12** as a colorless oil (1.38 g, 4.93 mmol, 61%).

^{1}H NMR (700 MHz, chloroform-*d*): δ = 7.99 (d, J = 8.4 Hz, 2H, 3-H and 7-H), 7.38 (d, J = 8.5 Hz, 2H, 4-H and 6-H), 4.62 (d, J = 12.9 Hz, 1H, 8-H$_a$), 4.59 (d, J = 12.8 Hz, 1H, 8-H$_b$), 4.32 – 4.27 (m, 1H, 2'-H), 4.05 (dd, J = 8.3 Hz, J = 6.5 Hz, 1H, 3'-H$_a$), 3.89 (s, 3H, $CO_2C\underline{H}_3$), 3.73 (dd, J = 8.3 Hz, J = 6.3 Hz, 1H, 3'-H$_b$), 3.55 (dd, J = 9.9 Hz, J = 5.7 Hz, 1H, 1'-H$_a$), 3.49 (dd, J = 9.9 Hz, J = 5.3 Hz, 1H, 1'-H$_b$), 1.40 (s, 3H, $C(C\underline{H}_3)_2$), 1.35 (s, 3H, $C(C\underline{H}_3)_2$).

^{13}C{^{1}H} NMR (176 MHz, chloroform-*d*): δ = 166.9 (C1), 143.4 (C5), 129.8 (C3 and C7), 129.5 (C2), 127.3 (C4 and C6), 109.6 ($\underline{C}(CH_3)_2$), 74.8 (C2'), 72.9 (C8), 71.5 (C1'), 66.8 (C3'), 52.1 ($CO_2\underline{C}H_3$), 26.8 ($C(\underline{C}H_3)_2$), 25.5 ($C(\underline{C}H_3)_2$).

HR-ESI MS (positive mode, MeCN): *m/z* calc. for $C_{15}H_{20}O_5$, 303.1203 [M+Na]$^+$; found 303.1198.

Elemental analysis (%): Calc. for $C_{15}H_{20}O_5$: C 64.3, H 7.2; found: C 64.0, H 7.3.

7.5.2 Synthesis of methyl (*R*)-4-((2,3-dihydroxypropoxy)methyl)benzoate ((*R*)-13)

A solution of compound (*S*)-**12** (1.05 g, 3.75 mmol, 1.0 equiv.) in a mixture of tetrahydrofuran (26 mL) and 50% aqueous acetic acid (26 mL) was stirred overnight at 60 °C. The solvents were removed under reduced pressure to afford a solid which was purified by column chromatography (dichloromethane/methanol, 10:1) to afford the product (*R*)-**13** as a colorless crystalline material (0.86 g, 3.60 mmol, 96%) with a melting point at 84 °C.

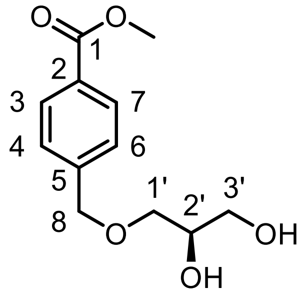

(*R*)-**13**

^{1}H NMR (400 MHz, chloroform-*d*): δ = 8.02 (d, *J* = 8.3 Hz, 2H, 3-H and 7-H), 7.38 (d, *J* = 8.2 Hz, 2H, 4-H and 6-H), 4.60 (s, 2H, 8-H), 3.96 – 3.88 (m, 4H, 2'-H and $CO_2C\underline{H}_3$), 3.72 (dd, *J* = 11.4 Hz, *J* = 3.9 Hz, 1H, 3'-H$_a$), 3.64 (dd, *J* = 11.4 Hz, *J* = 5.6 Hz, 1H, 3'-H$_b$), 3.61 – 3.53 (m, 2H, 1'-H$_a$ and 1'-H$_b$), 2.46 (br s, 2H, 2'-O$\underline{H}$ and 3'-O$\underline{H}$).

^{13}C{^{1}H} NMR (101 MHz, chloroform-*d*): δ = 167.0 (C1), 143.1 (C5), 129.9 (C3 and C7), 129.7 (C2), 127.4 (C4 and C6), 73.1 (C8), 72.2 (C1'), 70.8 (C2'), 64.1 (C3'), 52.3 ($CO_2\underline{C}H_3$).

HR-ESI MS (positive mode, MeCN): *m/z* calc. for $C_{12}H_{16}O_5$, 263.0890 [M+Na]$^+$; found 263.0885.

Elemental analysis (%): Calc. for $C_{12}H_{16}O_5$: C 60.0, H 6.7; found: C 59.9, H 6.7.

IR (ATR): $\tilde{\nu}$ = 3264, 2942, 2864, 1719, 1431, 1415, 1389, 1276, 1207, 1194, 1179, 1103, 1070, 1048, 1025, 1014, 954, 933, 866, 851, 763,712,529 cm^{-1}.

7.5.3 Single-Crystal X-ray Diffraction Analysis of (*R*)-13

Slow solvent evaporation of a solution of (*R*)-**13** in CH_2Cl_2 resulted in colorless needles, suitable for single-crystal X-ray diffraction analysis.

Data collection was conducted on a *Bruker D8 Venture* four-circle diffractometer using a *PHOTON100* CMOS area detector. X-ray radiation was generated by microfocus source *IµS* Mo by *Incoatec* with *HELIOS* mirror optics and a *Bruker* single-hole collimator. For the data collection, the *Bruker APEX 3 Suite* (v.2017.3-0) programs with the integrated programs *SAINT* (integration) and *SADABS* (adsorption correction) were used. Using *Olex*^{2},[15] the structures were solved with the *ShelXT*[12] structure solution program using Intrinsic Phasing and refined with the *XL*[16] refinement package using Least Squares minimization. The absolute configuration was determined *via* anomalous dispersion.

Crystallographic data have been deposited at the CCDC (Cambridge Crystallographic Data Centre). These data can be obtained free of charge from the CCDC, Union Road, Cambridge, CB2 IEZ, UK (Fax: +44-1223-336033; e-mail: deposit@ccdc.cam.ac.uk or www: http://www.ccdc.cam.ac.uk). CCDC deposition number 1961648.

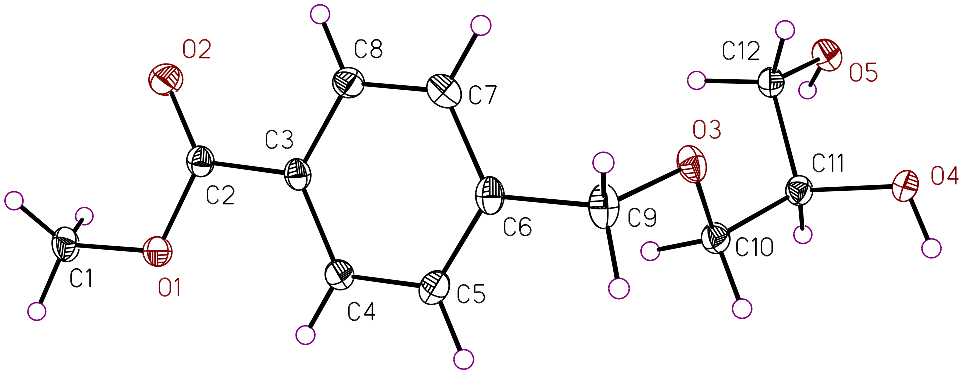

Figure 7.5: Ortep[14] plot and numbering scheme of compound (*R*)-**13**. Displacement ellipsoids are drawn at 50% probability level.

Table 7.2: Crystal data and structure refinement of compound (*R*)-**13**.

Compound	(*R*)-**13**
Empirical formula	$C_{12}H_{16}O_5$
Formula weight	240.25
Temperature/K	100.0
Crystal system	monoclinic
Space group	$P2_1$
a/Å	4.6771(3)
b/Å	5.9336(3)
c/Å	20.7551(12)
α/°	90
β/°	93.4990(10)
γ/°	90
Volume/Å^3	574.92(6)
Z	2
ρ_{calc}g/cm^3	1.388
μ/mm^{-1}	0.908
F(000)	256.0
Crystal size/mm^3	0.495 × 0.407 × 0.296
Radiation	CuKα (λ = 1.54178)
2Θ range for data collection/°	4.266 to 144.992
Index ranges	$-5 \leq h \leq 5$, $-7 \leq k \leq 7$, $-25 \leq l \leq 25$
Reflections collected	10619
Independent reflections	2265 [R_{int} = 0.0214, R_{sigma} = 0.0182]
Data/restraints/parameters	2265/1/158
Goodness-of-fit on F^2	1.064
Final R indexes [I>=2σ (I)]	R_1 = 0.0223, wR_2 = 0.0584
Final R indexes [all data]	R_1 = 0.0224, wR_2 = 0.0592
Largest diff. peak/hole / e Å^{-3}	0.22/-0.13
Flack parameter	0.08(2)

7.5.4 Synthesis of methyl (*S*)-4-((3-(bis(4-methoxyphenyl)(phenyl)methoxy)-2-hydroxypropoxy)methyl)benzoate ((*S*)-14)

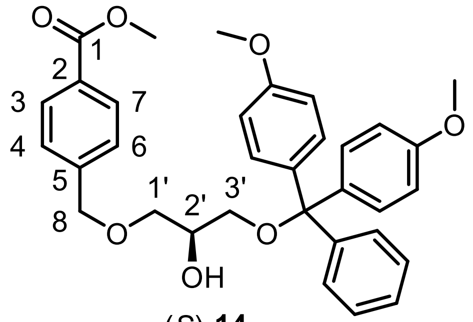

(*S*)-**14**

A solution of compound (*R*)-**13** (1.18 g, 4.93 mmol, 1.0 equiv.) and 4-dimethylaminopyridine (0.04 g, 0.30 mmol, 0.06 equiv.) in tetrahydrofuran (20 mL) was cooled to 0 °C and a solution of 4,4'-dimethoxytrityl chloride (2.01 g, 5.92 mmol, 1.2 equiv.) in tetrahydrofuran (10 mL) was added. After addition of *N*,*N*-diisopropylethylamine (1.68 mL, 9.86 mmol, 2.0 equiv.), the reaction mixture was allowed to warm up to room temperature and stirred overnight. The formed solid was filtered off and washed with ethyl acetate (15 mL). The solvents of the filtrate were removed under reduced pressure and the obtained yellow oil was purified by column chromatography (*n*-pentane/ethyl acetate, 5:1 + 0.5% triethylamine to 2:1 + 0.5% triethylamine) to give product (*S*)-**14** as a yellow oil (1.95 g, 3.59 mmol, 73%).

^{1}H NMR (600 MHz, methylene chloride-d_2): δ = 8.00 – 7.96 (m, 2H, 3-H and 7-H), 7.44 – 7.41 (m, 2H, DMT-$\underline{H}_{ar}$), 7.38 – 7.34 (m, 2H, 4-H and 6-H), 7.32 – 7.26 (m, 6H, DMT-$\underline{H}_{ar}$), 7.24 – 7.20 (m, 1H, DMT-$\underline{H}_{ar}$), 6.85 – 6.80 (m, 4H, DMT-$\underline{H}_{ar}$), 4.57 (s, 2H, 8-H), 3.99 – 3.93 (m, 1H, 2'-H), 3.89 (s, 3H, $CO_2C\underline{H}_3$), 3.77 (s, 6H, DMT-$OC\underline{H}_3$), 3.60 (dd, *J* = 9.6 Hz, *J* = 4.4 Hz, 1H, 1'-H_a), 3.57 (dd, *J* = 9.6 Hz, *J* = 6.0 Hz, 1H, 1'-H_b), 3.18 (d, *J* = 5.4 Hz, 2H, 3'-H), 2.36 (d, *J* = 5.1 Hz, 1H, 2'-O$\underline{H}$).

^{13}C{^{1}H} NMR (151 MHz, methylene chloride-d_2): δ = 167.2 (C1), 159.2 (DMT-C_{ar}), 145.6 (DMT-C_{ar}), 144.2 (C5), 136.5 (DMT-C_{ar}), 130.6 (DMT-C_{ar}), 130.0 (C3 and C7), 130.0 (C2), 128.6 (DMT-C_{ar}), 128.3 (DMT-C_{ar}), 127.7 (C4 and C6), 127.3 (DMT-C_{ar}), 113.6 (DMT-C_{ar}), 86.6 (DMT-$\underline{C}(Ar)_3$), 73.1 (C8), 72.5 (C1'), 70.5 (C2'), 65.0 (C3'), 55.7 (DMT-$O\underline{C}H_3$), 52.5 ($CO_2\underline{C}H_3$).

HR-ESI MS (positive mode, MeCN): *m/z* calc. for $C_{33}H_{34}O_7$, 303.1380 $[DMT]^+$, 565.2197 $[M+Na]^+$, 581.1936 $[M+K]^+$; found 303.1373, 565.2196, 581.1936.

Elemental analysis (%): Calc. for $C_{33}H_{34}O_7$: C 73.1, H 6.3; found: C 73.1, H 6.7.

7.5.5 Synthesis of methyl 4-(((2*S*)-3-(bis(4-methoxyphenyl)(phenyl)methoxy)-2-(((2-cyanoethoxy)(diisopropylamino)phosphaneyl)oxy)propoxy)methyl)benzoate ((*S*)-15)

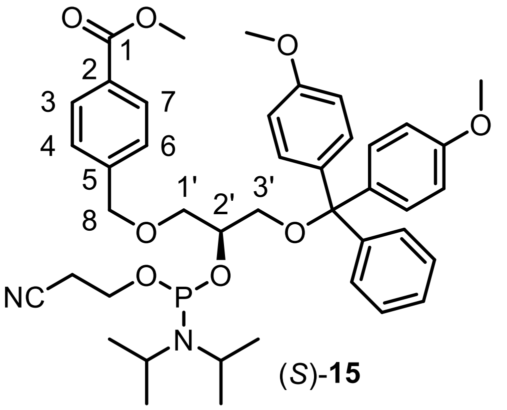

(*S*)-**15**

To a solution of compound (*S*)-**14** (255 mg, 0.470 mmol, 1.0 equiv.) and *N*,*N*-diisopropylethylamine (112 µL, 0.705 mmol, 1.5 equiv.) in dichloromethane (10 mL) was added 2-cyanoethyl *N*,*N*-diisopropylchlorophosphoramidite (126 µL, 0.564 mmol, 1.2 equiv.) dropwise and the reaction mixture was stirred for 2 h at room temperature. The solvent was removed under reduced pressure to afford the crude product (*S*)-**15** as a yellow oil. The compound was used for solid-phase oligonucleotide synthesis without further purification.

^{31}P{^{1}H} NMR (162 MHz, chloroform-*d*): δ = 149.4, 149.3.

HR-ESI MS (positive mode, MeCN): *m/z* calc. for $C_{42}H_{51}N_2O_8P$, 303.1380 [DMT]$^+$, 743.3456 [M+H]$^+$, 844.4660 [M+$C_6H_{15}N$+H]$^+$; found 303.1378, 743.3453, 844.4657.

7.5.6 Synthesis of (*R*)-4-((2,3-dihydroxypropoxy)methyl)benzoic acid ((*R*)-16)

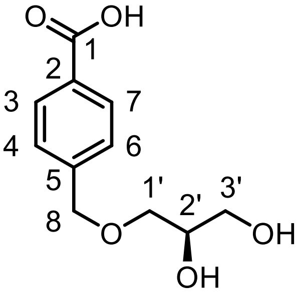

(*R*)-**16**

A solution of compound (*R*)-**13** (60 mg, 0.250 mmol, 1.0 equiv.) in 1 M aqueous sodium hydroxide (5 mL) was stirred at 65 °C for 2.5 h. After neutralization with 1 M aqueous hydrogen chloride, the solvent was removed under reduced pressure and the obtained white solid was purified by column chromatography (dichloromethane/methanol, 10:1 to 5:1) to afford the product (*R*)-**16** as a white solid (51 mg, 0.225 mmol, 90%).

^{1}H NMR (600 MHz, methanol-*d*$_4$): δ = 8.00 (d, *J* = 8.3 Hz, 2H, 3-H and 7-H), 7.47 (d, *J* = 8.2 Hz, 2H, 4-H and 6-H), 4.63 (s, 2H, 8-H), 3.82 (q, *J* = 5.8 Hz, 1H, 2’-H), 3.63 – 3.50 (m, 4H, , 1’-H and , 3’-H).

$^{13}C\{^1H\}$ NMR (151 MHz, methanol-d_4): δ = 170.1 (C1), 144.9 (C5), 131.6 (C2), 130.8 (C3 and C7), 128.3 (C4 and C6), 73.7 (C8), 73.1 (C1'), 72.3 (C2'), 64.5 (C3').

UV: The extinction coefficient at λ = 260 nm of the artificial nucleoside (*R*)-**16** in water was determined to ε_{260} = 1111 L mol^{-1} cm^{-1}.

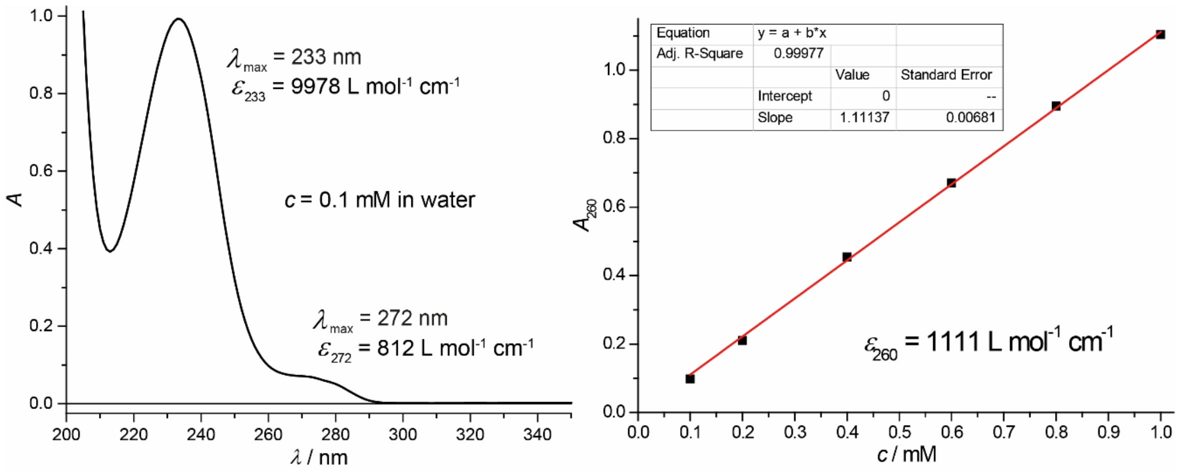

Figure 7.6. Absorption spectrum (left) of (*R*)-**16** (0.1 mM in water) and dilution experiment (right) for the determination of the extinction coefficient ε_{260} of (*R*)-**16**.

7.6 Synthesis of Phosphoramidite 19

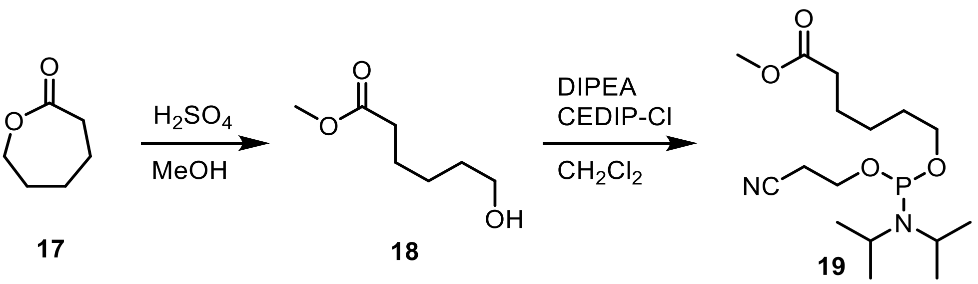

Scheme 7.4. Synthesis of phosphoramidite building block **19**, which is required to incorporate ligandoside **L^4** into oligonucleotides by solid-phase oligonucleotide synthesis.

7.6.1 Synthesis of methyl 6-hydroxyhexanoate (18)

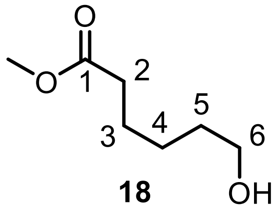

Compound **18** was prepared according to modified literature procedures.[17,18] To a solution of ε-caprolactone (**17**, 1.4 mL, 13.1 mmol, 1.0 equiv.) in methanol (44 mL) was added concentrated sulfuric acid (69 µL, 1.3 mmol, 0.1 equiv.). The reaction mixture was stirred for 4 h at room temperature, the solvent was removed under reduced pressure and water (25 mL) was added. The mixture was neutralized with sodium carbonate and the aqueous phase was extracted with diethyl ether (3x 50 mL). The combined organic phases were washed with saturated aqueous sodium chloride (3x 60 mL), dried over magnesium sulfate and the solvent was removed under reduced pressure. The crude product was purified by column chromatography (dichloromethane/ethyl acetate, 4:1 to 2:1) to afford product **18** as a yellowish oil (419 mg, 2.87 mmol, 22%).

^{1}H NMR (500 MHz, methylene mhloride-*d*$_2$): *δ* = 3.63 (s, 3H, $CO_2C\underline{H}_3$), 3.59 (t, *J* = 6.5 Hz, 2H, 6-H), 2.30 (t, *J* = 7.5 Hz, 2H, 2-H), 1.66 – 1.59 (m, 2H, 3-H), 1.58 – 1.51 (m, 2H, 5-H), 1.44 (br s, 1H, 6-O$\underline{H}$), 1.40 – 1.33 (m, 2H, 4-H).

7.6.2 Synthesis of methyl 6-(((2-cyanoethoxy)(diisopropylamino)phosphanyl)oxy)hexanoate (19)

To a solution of compound **18** (29 mg, 0.200 mmol, 1.0 equiv.) and *N*,*N*-diisopropylethylamine (51 µL, 0.300 mmol, 1.5 equiv.) in dichloromethane (5 mL) was added *N*,*N*-diisopropylchlorophosphoramidite (54 µL, 0.240 mmol, 1.2 equiv.) and the reaction mixture was stirred for 2 h at room temperature. The solution was washed with saturated sodium bicarbonate solution (10 mL), the organic layer was dried over magnesium sulfate and the solvent was removed under reduced pressure. The crude product was either used without further purification in solid-phase oligonucleotide synthesis or purified by column chromatography (dichloromethane/ethyl acetate, 2:1 + 1% triethylamine) to afford product **19** as a colorless oil (54 mg, 0.156 mmol, 78%).

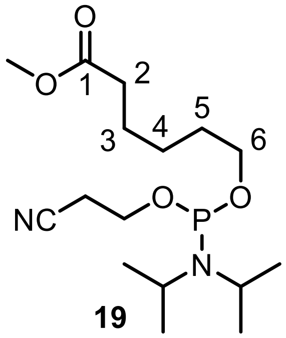

19

^{1}H NMR (600 MHz, methylene chloride-*d*$_2$): *δ* = 3.85 – 3.73 (m, 2H, $OC\underline{H}_2CH_2CN$), 3.67 – 3.56 (m, 7H, $CO_2C\underline{H}_3$ and $C\underline{H}_2(CH_2)_4$ and $N(C\underline{H}(CH_3)_2)_2$), 2.62 (t, *J* = 6.3, 2H, $OCH_2C\underline{H}_2CN$), 2.30 (t, *J* = 7.5 Hz, 2H, $C\underline{H}_2CO_2CH_3$), 1.65 – 1.59 (m, 4H, $CH_2C\underline{H}_2CH_2C\underline{H}_2CH_2$), 1.42 – 1.36 (m, 2H, $(CH_2)_2C\underline{H}_2(CH_2)_2$), 1.18 (d, *J* = 4.9 Hz, 6H, $N(CH(C\underline{H}_{a3})_2)_2$), 1.16 (d, *J* = 4.9 Hz, 6H, $N(CH(C\underline{H}_{b3})_2)_2$).

^{31}P{^{1}H} NMR (243 MHz, methylene mhloride-*d*$_2$): *δ* = 147.3.

7.7 Synthesis of Phosphoramidite (*S*)-24

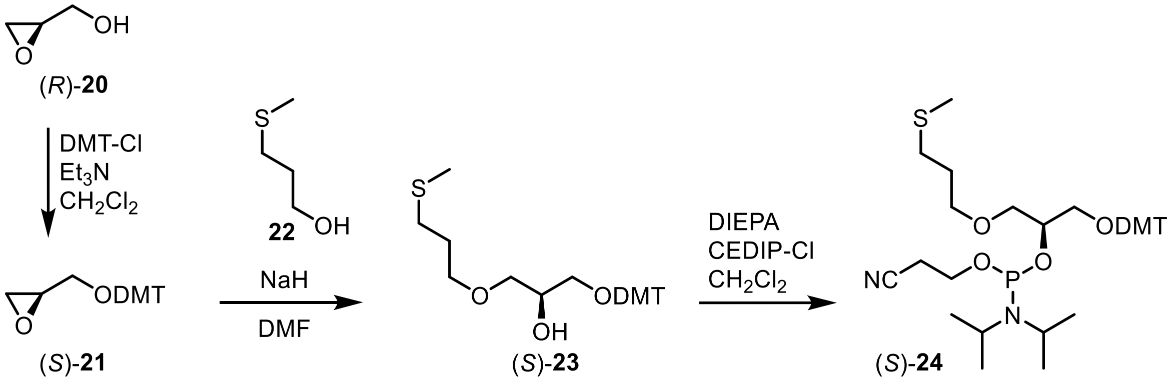

Scheme 7.5. Synthesis of the phosphoramidite building block (*S*)-**24** which is required to incorporate ligandoside $\mathbf{L^5}$ into oligonucleotides by solid-phase oligonucleotide synthesis.

7.7.1 Synthesis of (*R*)-2-((bis(4-methoxyphenyl)(phenyl)methoxy)methyl)oxirane ((*S*)-21)

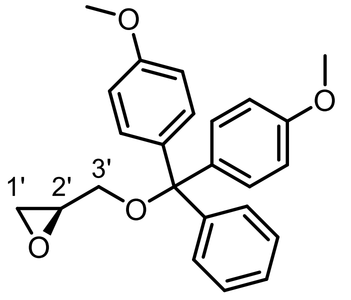

(*S*)-**21**

Compound (*S*)-**21** was prepared according to a modified literature procedure.[19] To a solution of (*R*)-oxiran-2-ylmethanol ((*S*)-**20**, 0.50 mL, 7.49 mmol, 1.1 equiv.) in dichloromethane (17 mL) was added triethylamine (2.70 mL, 19.37 mmol, 2.8 equiv.). After stirring for 5 min, 4,4'-dimethoxytrityl chloride (2.35 g, 6.90 mmol, 1.0 equiv.) was added slowly and the mixture was stirred overnight at room temperature. The reaction mixture was washed with saturated aqueous sodium bicarbonate solution (50 mL) and the aqueous layer was extracted with dichloromethane (3x 30 mL). The combined organic layers were dried over magnesium sulfate and the solvent was removed under reduced pressure to afford a dark red oil. The crude product was purified by column chromatography (n-pentane/ethyl acetate, 9:1 + 0.5% triethylamine) to afford the product (*S*)-**21** as a viscous colorless oil (1.95 g, 5.18 mmol, 75%).

^{1}H NMR (500 MHz, methylene chloride-*d*$_2$): δ = 7.46 – 7.43 (m, 2H, DMT-$\underline{\text{H}}_{\text{ar}}$), 7.34 – 7.27 (m, 6H, DMT-$\underline{\text{H}}_{\text{ar}}$), 7.24 – 7.20 (m, 1H, DMT-$\underline{\text{H}}_{\text{ar}}$), 6.86 – 6.81 (m, 4H, DMT-$\underline{\text{H}}_{\text{ar}}$), 3.78 (s, 6H, DMT-OC$\underline{\text{H}}_3$), 3.31 (dd, *J* = 10.8 Hz, *J* = 2.9 Hz, 1H, 3’-H$_a$), 3.13 – 3.08 (m, 1H, 2’-H), 3.02 (dd, *J* = 10.8, 5.7 Hz, 1H, 3’-H$_b$), 2.73 (dd, *J* = 5.1, 4.2 Hz, 1H, 1’-H$_a$), 2.56 (dd, *J* = 5.1, 2.6 Hz, 1H, 1’-H$_b$).

7.7.2 Synthesis of 1-(bis(4-methoxyphenyl)(phenyl)methoxy)-3-(3-(methylthio)propoxy)propan-2-ol ((*S*)-23)

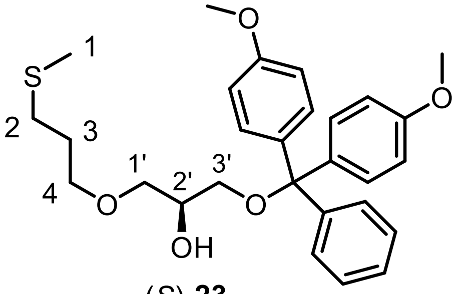

(*S*)-**23**

To a suspension of sodium hydride (60% in mineral oil; 234 mg, 5.84 mmol, 4.4 equiv.) in DMF (10 mL) was added 3-(methylthio)propan-1-ol (**22**, 137 µL, 1.33 mmol, 1.0 equiv.) dropwise. After 30 min of stirring, a solution of (*S*)-**21** (500 mg, 1.33 mmol, 1.0 equiv.) in DMF (10 mL) was added. The reaction mixture was stirred overnight at 60 °C. Half saturated aqueous sodium bicarbonate solution (100 mL) was added and the aqueous layer was extracted with dichloromethane (3x 50 mL). The combined organic layers were dried over magnesium sulfate and the solvent was removed under reduced pressure to afford an oil which was purified by column chromatography (n-pentane/ethyl acetate, 8:1 + 1% triethylamine to 3:1 + 1% triethylamine) to afford the product (*S*)-**23** as a viscous yellowish oil (200 mg, 0.41 mmol, 31%).

^{1}H NMR (500 MHz, methylene chloride-*d*$_2$) *δ* = 7.45 – 7.41 (m, 2H, DMT-$\underline{H}_{ar}$), 7.33 – 7.27 (m, 6H, DMT-$\underline{H}_{ar}$), 7.24 – 7.20 (m, 1H, DMT-$\underline{H}_{ar}$), 6.86 – 6.81 (m, 4H, DMT-$\underline{H}_{ar}$), 3.92 – 3.86 (m, , 1H, 2'-H), 3.78 (s, 6H, DMT-OC$\underline{H}_3$), 3.55 – 3.43 (m, 4H, 4-H and 1'-H), 3.13 (d, *J* = 5.4 Hz, 2H, 3'-H), 2.51 (t, *J* = 7.2 Hz, 2H, 2-H), 2.39 (d, *J* = 4.8 Hz, 1H, 2'-O$\underline{H}$), 2.06 (s, 3H, 1-H), 1.85 – 1.78 (m, 2H, 3-H).

^{13}C{^{1}H} NMR (176 MHz, methylene chloride-*d*$_2$): *δ* = 159.2 (DMT-C$_{ar}$), 145.7 (DMT-C$_{ar}$), 136.6 (DMT-C$_{ar}$), 130.6 (DMT-C$_{ar}$), 128.6 (DMT-C$_{ar}$), 128.3 (DMT-C$_{ar}$), 127.3 (DMT-C$_{ar}$), 113.6 (DMT-C$_{ar}$), 86.6 (DMT-$\underline{C}$(Ar)$_3$), 72.8 (C1'), 70.4 (C2' and C4), 65.2 (C3'), 55.8 (DMT-O$\underline{C}$H$_3$), 31.4 (C2), 29.8 (C3), 15.8 (C1).

HR-ESI MS (positive mode, MeCN): *m/z* calc. for $C_{28}H_{34}O_5S$, 303.1380 [DMT]$^+$, 505.2025 [M+Na]$^+$, 521.1764 [M+K]$^+$, 987.4146 [2M+Na]$^+$, 1003.3885 [2M+K]$^+$; found 303.1376, 505.2021, 521.1761, 987.4142, 1003.3882.

Elemental analysis (%): Calc. for $C_{28}H_{34}O_5S$: C 69.7, H 7.1; found: C 69.4, H 7.2.

7.7.3 Synthesis of 1-(bis(4-methoxyphenyl)(phenyl)methoxy)-3-(3-(methylthio)propoxy)propan-2-yl (2-cyanoethyl) diisopropylphosphoramidite ((*S*)-24)

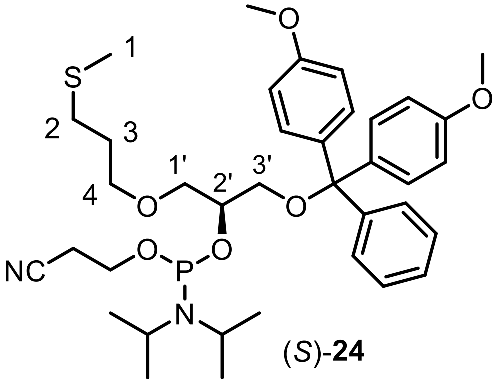

(*S*)-**24**

To a solution of compound (*S*)-**23** (90 mg, 0.186 mmol, 1.0 equiv.) and *N*,*N*-diisopropylethylamine (48 µL, 0.280 mmol, 1.5 equiv.) in dichloromethane (10 mL) was added 2-cyanoethyl *N*,*N*-diisopropylchlorophosphoramidite (53 µL, 0.224 mmol, 1.2 equiv.) dropwise and the reaction mixture was stirred for 2 h at room temperature. The solvent was removed under reduced pressure to afford the crude product (*S*)-**24** as a yellowish oil. The compound was used for solid-phase oligonucleotide synthesis without further purification.

^{31}P{^{1}H} NMR (202 MHz, methylene chloride-*d*$_2$): δ = 149.3, 149.1.

HR-ESI MS (positive mode, MeCN): *m/z* calc. for $C_{37}H_{51}N_2O_6PS$, 303.1380 [DMT]$^+$, 683.3284 [M+H]$^+$, 705.3103 [M+Na]$^+$, 721.2843 [M+K]$^+$; found 303.1374, 683.3278, 705.3097, 721.2848.

7.8 Synthesis of Phosphoramidites (*R,R*)-29 and (*R,R*)-32

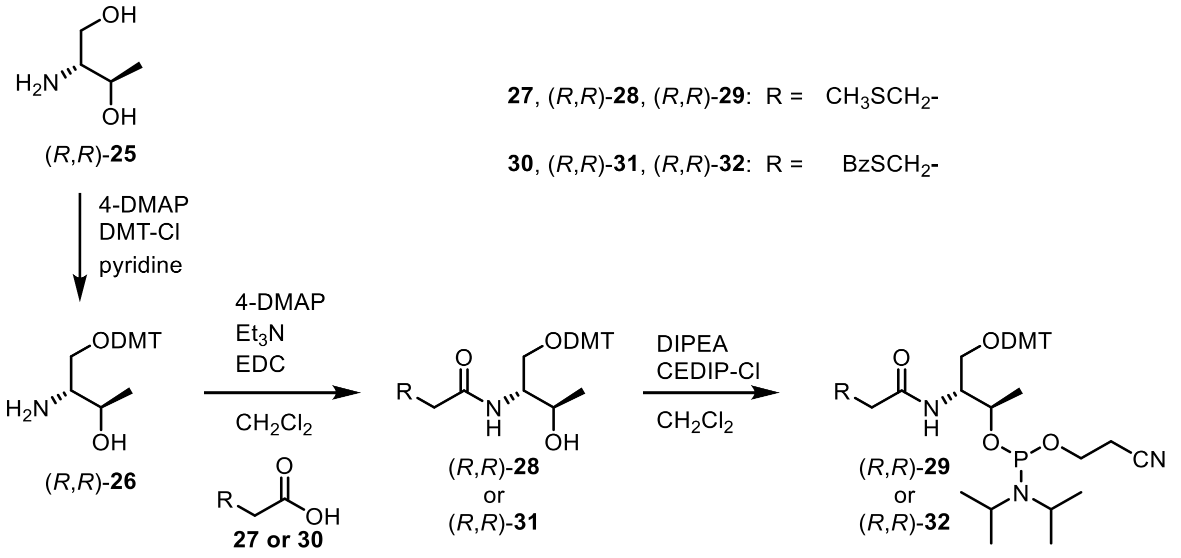

Scheme 7.6. Synthesis of phosphoramidite building blocks (*R*,*R*)-**29** and (*R*,*R*)-**32** which are required to incorporate ligandosides **L**^{6} and **L**^{7} into oligonucleotides by solid-phase oligonucleotide synthesis.

7.8.1 Synthesis of (2*R*,3*R*)-3-amino-4-(bis(4-methoxyphenyl)(phenyl)-methoxy)butan-2-ol ((*R*,*R*)-26)

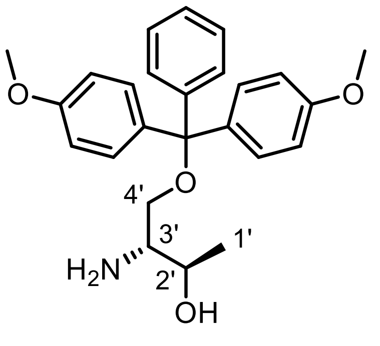

(*R*,*R*)-**26**

To a solution of L-threoninol ((*R*,*R*)-**25**, 1.00 g, 9.51 mmol, 1.0 equiv.) and 4-dimethylaminopyridine (0.58 g, 4.76 mmol, 0.5 equiv.) in pyridine (30 mL) was added 4,4'-dimethoxytrityl chloride (4.83 g, 14.27 mmol, 1.5 equiv.) at 0 °C. The reaction was stirred at room temperature for 4 h and saturated aqueous sodium chloride (100 mL) was added to the reaction solution causing a precipitation. The aqueous phase was extracted with DCM (2x 50 mL) and the combined organic phases were dried over magnesium sulfate. The solvent was removed under reduced pressure and the crude product was purified by flash chromatography (dichloromethane/methanol, 9:1) to yield product (*R*,*R*)-**26** as a foamy solid (2.47 g, 6.07 mmol, 64%).

^{1}H NMR (700 MHz, chloroform-*d*) δ = 8.30 (br s, 2H, 3’-N$\underline{H}_2$), 7.52 – 7.48 (m, 2H, DMT-$\underline{H}_{ar}$), 7.40 – 7.36 (m, 4H, DMT-$\underline{H}_{ar}$), 7.22 – 7.18 (m, 2H, DMT-$\underline{H}_{ar}$), 7.10 – 7.06

(m, 1H, DMT-$\underline{H}_{ar}$), 6.73 – 6.68 (m, 4H, DMT-$\underline{H}_{ar}$), 5.56 (br s, 2’-O$\underline{H}$, 1H), 4.10 (dq, *J* = 12.5, 6.3 Hz, 1H, 2’-H), 3.57 (dd, *J* = 10.6, 2.2 Hz, 1H, 4’-H_a), 3.51 (s, 3H, DMT-OC$\underline{H}_3$), 3.50 (s, 3H, DMT-OC$\underline{H}_3$), 3.35 – 3.28 (m, 1H, 3’-H), 3.15 (dd, *J* = 10.8, 5.2 Hz, 1H, 4’-H_b), 0.86 (d, *J* = 6.2 Hz, 3H, 1’-H).

^{13}C NMR (176 MHz, chloroform-*d*) δ = 158.6 (DMT-C_{ar}), 158.6 (DMT-C_{ar}), 144.2 (DMT-C_{ar}), 135.5 (DMT-C_{ar}), 135.4 (DMT-C_{ar}), 130.2 (DMT-C_{ar}), 130.2 (DMT-C_{ar}), 128.4 (DMT-C_{ar}), 128.2 (DMT-C_{ar}), 127.0 (DMT-C_{ar}), 113.5 (DMT-C_{ar}), 113.5 (DMT-C_{ar}), 87.2 (DMT-$\underline{C}$(Ar)$_3$), 66.1 (C2’), 60.6 (C4’), 58.7 (C3’), 55.2 (DMT-O$\underline{C}H_3$), 55.1 (DMT-O$\underline{C}H_3$), 19.8 (C1’).

HR-ESI MS (positive mode, MeCN): *m/z* calc. for $C_{25}H_{29}NO_4$, 303.1380 [DMT]$^+$, 815.4266 [2M+H]$^+$; found 303.1392, 815.4319.

Elemental analysis (%): Calc. for $C_{25}H_{29}NO_4$ + 2/3(CH_2Cl_2): C 66.4, H 6.6, N 3.0; found: C 66.5, H 6.6, N 3.3.

7.8.2 Synthesis of *S*-(3-(((2*R*,3*R*)-1-(bis(4-methoxyphenyl)(phenyl)methoxy)-3-hydroxybutan-2-yl)amino)-3-oxopropyl) benzothioate ((*R*,*R*)-28)

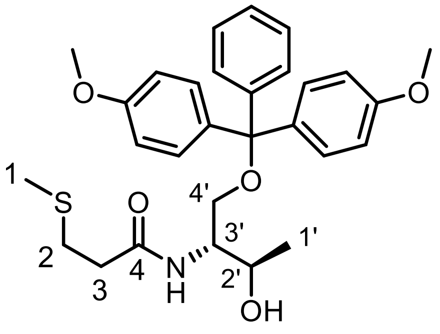

(*R*,*R*)-**28**

To a solution of 4-dimethylaminopyridine (150 mg, 1.23 mmol, 1.0 equiv.), compound (*R*,*R*)-**26** (500 mg, 1.23 mmol, 1.0 equiv.) and triethylamine (170 µL, 1.23 mmol, 1.0 equiv.) in dichloromethane (20 mL) was added 3-(methylthio)propanoic acid (**27**, 127 µL, 1.23 mmol, 1.0 equiv.). After 30 min of stirring at room temperature, N-(3-dimethylaminopropyl)-N′-ethyl carbodiimide hydrochloride (235 mg, 1.23 mmol, 1.0 equiv.) was added and the mixture was stirred at room temperature overnight. The solution was poured into half saturated aqueous sodium bicarbonate solution (60 mL) and the aqueous phase was extracted with dichloromethane (3x 50 mL). The combined organic layers were dried over magnesium sulfate and the solvent was removed under reduced pressure. The crude product was purified by flash chromatography (dichloromethane/methanol, 9:1) to afford product (*R*,*R*)-**28** as a white foamy solid (476 mg, 0.93 mmol, 76%).

^{1}H NMR (500 MHz, methylene chloride-*d*$_2$): δ = 7.44 – 7.42 (m, 2H, DMT-$\underline{H}_{ar}$), 7.33 – 7.30 (m, 6H, DMT-$\underline{H}_{ar}$), 7.26 – 7.22 (m, 1H, DMT-$\underline{H}_{ar}$), 6.89 – 6.83 (m, 4H, DMT-$\underline{H}_{ar}$), 6.26 (d, *J* = 8.8 Hz, 1H, CON$\underline{H}$), 4.09 – 4.05 (m, 1H, 2'-H), 3.96 – 3.89 (m, 1H, 3'-H), 3.79 (s, 6H, DMT-OC$\underline{H}_3$), 3.34 (dd, *J* = 9.5 Hz, *J* = 4.9 Hz, 1H, 4'-H$_a$), 3.23 (dd, *J* = 9.5 Hz, *J* = 4.1 Hz, 2H, 4'-H$_b$), 2.92 (d, *J* = 2.3 Hz, 1H, 2'-O$\underline{H}$), 2.82 – 2.74 (m, 2H, 1-H), 2.50 (t, *J* = 7.0 Hz, 2H, 2-H), 2.12 (s, 3H, 4-H), 1.11 (d, *J* = 6.4 Hz, 3H, 1'-H).

^{13}C NMR (126 MHz, methylene chloride-*d*$_2$): δ = 171.9 (C3), 159.2 (DMT-C$_{ar}$), 145.3 (DMT-C$_{ar}$), 136.2 (DMT-C$_{ar}$), 136.0 (DMT-C$_{ar}$), 130.5 (DMT-C$_{ar}$), 130.4 (DMT-C$_{ar}$), 128.5 (DMT-C$_{ar}$), 128.4 (DMT-C$_{ar}$), 127.4 (DMT-C$_{ar}$), 113.7 (DMT-C$_{ar}$), 87.0 (DMT-O$\underline{C}$(Ar)$_3$), 68.5 (C2'), 65.1 (C4'), 55.7 (DMT-O$\underline{C}$H$_3$), 54.3 (C3'), 36.9 (C2), 30.4 (C1), 20.4 (C1'), 15.9 (C4).

HR-ESI MS (positive mode, MeCN): *m/z* calc. for $C_{29}H_{35}NO_5S$, 303.1380 [DMT]$^+$, 532.2128 [M+Na]$^+$, 548.1868 [M+K]$^+$, 611.3513 [M+$C_6H_{15}N$+H]$^+$, 1041.4364 [2M+Na]$^+$; found 303.1388, 532.2141, 548.1884, 611.3532, 1041.4419.

Elemental analysis (%): Calc. for $C_{29}H_{35}NO_5S$: C 68.3, H 6.9, N 2.8; found: C 68.3, H 6.9, N 2.6.

7.8.3 Synthesis of *S*-(3-(((2*R*,3*R*)-1-(bis(4-methoxyphenyl)(phenyl)methoxy)-3-(((2-cyanoethoxy)(diisopropylamino)phosphanyl)oxy)butan-2-yl)amino)-3-oxopropyl) benzothioate ((*R*,*R*)-29)

To a solution of compound (*R*,*R*)-**28** (30 mg, 0.059 mmol, 1.0 equiv.) and *N*,*N*-diisopropylethylamine (15 µL, 0.088 mmol, 1.5 equiv.) in dichloromethane (3 mL) was added *N*,*N*-diisopropylchlorophosphoramidite (16 µL, 0.071 mmol, 1.2 equiv.). The reaction mixture was stirred for 2 h at room temperature and subsequently the solvent was removed under reduced pressure. The crude product (*R*,*R*)-**29** can be used without further purification in solid-phase oligonucleotide synthesis.

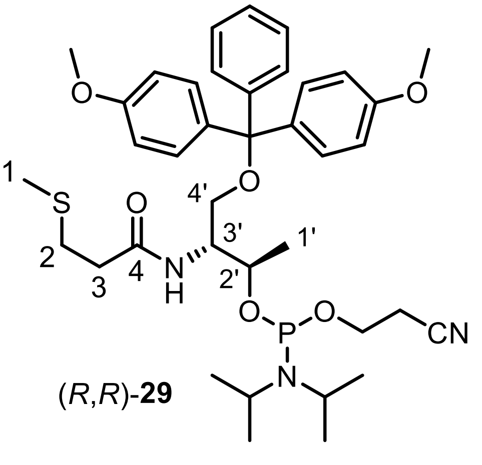

(*R*,*R*)-**29**

^{31}P{^{1}H} NMR (202 MHz, methylene chloride-*d*$_2$): δ = 148.1, 147.9.

HR-ESI MS (positive mode, MeCN/CH_2Cl_2): *m/z* calc. for $C_{38}H_{52}N_3O_6PS$, 728.3493 $[M+H_2O+H]^+$, 811.4592 $[M+C_6H_{15}N+H]^+$, 839.4905 $[M+C_8H_{19}N+H]^+$; found 728.3472, 811.4567, 839.4880.

7.8.4 Synthesis of *S*-(3-(((2*R*,3*R*)-1-(bis(4-methoxyphenyl)(phenyl)methoxy)-3-hydroxybutan-2-yl)amino)-3-oxopropyl) benzothioate ((*R,R*)-31)

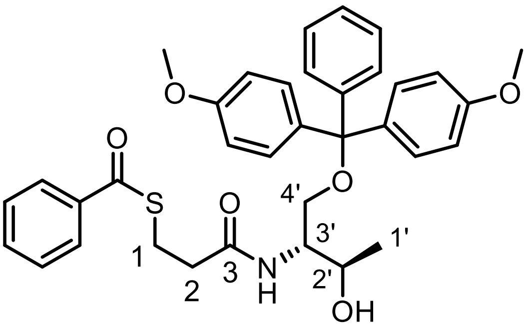

(*R*,*R*)-**31**

To a solution of 4-dimethylaminopyridine (141 mg, 1.15 mmol, 1.0 equiv.), compound (*R*,*R*)-**26** (469 mg, 1.15 mmol, 1.0 equiv.) and triethylamine (160 µL, 1.15 mmol, 1.0 equiv.) in dichloromethane (20 mL) was added 3-(benzoylthio)propanoic acid (**30**, 242 mg, 1.15 mmol, 1.0 equiv., synthesized using a literature procedure).[20] After 30 min of stirring at room temperature, N-(3-dimethylaminopropyl)-N′-ethyl carbodiimide hydrochloride (221 mg, 1.15 mmol, 1.0 equiv.) was added and the mixture was stirred at room temperature overnight. The solution was poured into half saturated aqueous sodium bicarbonate solution (60 mL) and the aqueous phase was extracted with dichloromethane (3x 50 mL). The combined organic layers were dried over magnesium sulfate and the solvent was removed under reduced pressure. The crude product was purified by flash chromatography (dichloromethane/methanol, 9:1) to afford product (*R*,*R*)-**31** as a white foamy solid (549 mg, 0.92 mmol, 80%).

^{1}H NMR (500 MHz, chloroform-*d*): δ = 7.96 – 7.91 (m, 2H, SBz-$\underline{H}_{ar}$), 7.56 (t, J = 7.4 Hz, 1H, SBz-$\underline{H}_{ar}$), 7.44 – 7.40 (m, 2H, SBz-$\underline{H}_{ar}$), 7.39 – 7.35 (m, 2H, DMT-$\underline{H}_{ar}$), 7.30 – 7.24 (m, 6H, DMT-$\underline{H}_{ar}$), 7.19 (t, J = 7.3 Hz, 1H, DMT-$\underline{H}_{ar}$), 6.85 – 6.80 (m, 4H, DMT-$\underline{H}_{ar}$), 6.15 (d, J = 8.8 Hz, 1H, CON$\underline{H}$), 4.07 (q, J = 6.1 Hz, 1H, 2'-H), 3.98 – 3.93 (m, 1H, 3'-H), 3.77 (s, 3H, DMT-OC$\underline{H}_3$), 3.76 (s, 3H, DMT-OC$\underline{H}_3$), 3.43 (dd, J = 9.7 Hz, J = 4.3 Hz, 1H, 4'-H$_a$), 3.36 (td, J = 6.9 Hz, J = 4.0 Hz, 2H, 1-H), 3.29 (dd, J = 9.6 Hz, J = 3.6 Hz, 1H, 4'-H$_b$), 2.93 (s, 1H, 2'-O$\underline{H}$), 2.63 (t, J = 6.9 Hz, 2H, 2-H), 1.12 (d, J = 6.4 Hz, 3H, 1'-H).

^{13}C NMR (126 MHz, chloroform-*d*): *δ* = 192.0 (SBz-$\underline{C}$OS), 171.2 (C3), 158.8 (DMT-C_{ar}), 144.4 (DMT-C_{ar}), 137.0 (SBz-C_{ar}), 135.5 (DMT-C_{ar}), 133.6 (SBz-C_{ar}), 130.1 (DMT-C_{ar}), 128.8 (DMT-C_{ar}), 128.2 (SBz-C_{ar}), 128.1 (DMT-C_{ar}), 127.4 (SBz-C_{ar}), 127.2 (DMT-C_{ar}), 113.5 (DMT-C_{ar}), 87.0 (DMT-O$\underline{C}$(Ar)$_3$), 68.8 (C2'), 65.5 (C4'), 55.4 (DMT-O$\underline{C}H_3$), 53.6 (C3'), 36.7 (C2), 25.0 (C1), 20.0 (C1').

HR-ESI MS (positive mode, MeCN/CH_2Cl_2): *m/z* calc. for $C_{35}H_{37}NO_6S$, 303.1380 [DMT]$^+$, 622.2234 [M+Na]$^+$, 638.1973 [M+K]$^+$, 1221.4575 [2M+Na]$^+$, 1237.4315 [2M+K]$^+$; found 303.1370, 622.2224, 638.1962, 1221.4548, 1237.4300.

Elemental analysis (%): Calc. for $C_{35}H_{37}NO_6S$: C 70.1, H 6.2, N 2.3; found: C 70.0, H 6.2, N 2.3.

7.8.5 Synthesis of *S*-(3-(((2*R*,3*R*)-1-(bis(4-methoxyphenyl)(phenyl)methoxy)-3-(((2-cyanoethoxy)(diisopropylamino)phosphanyl)oxy)butan-2-yl)amino)-3-oxopropyl) benzothioate ((*R*,*R*)-32)

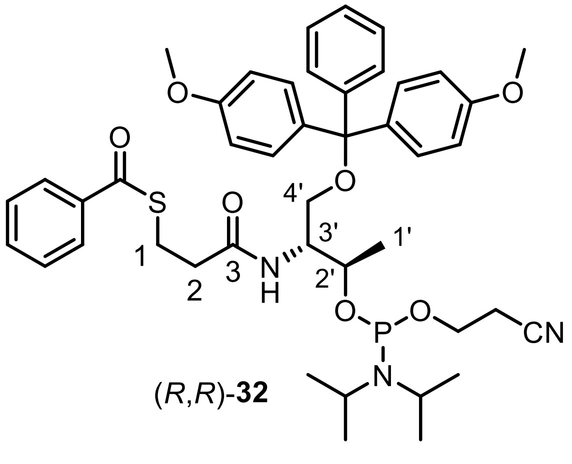

(*R*,*R*)-**32**

To a solution of compound (*R*,*R*)-**31** (225 mg, 0.375 mmol, 1.0 equiv.) and *N*,*N*-diisopropylethylamine (96 µL, 0.563 mmol, 1.5 equiv.) in dichloromethane (7.5 mL) was added *N*,*N*-diisopropylchlorophosphoramidite (101 µL, 0.450 mmol, 1.2 equiv.). The reaction mixture was stirred for 2 h at room temperature and subsequently the solvent was removed under reduced pressure. The crude product (*R*,*R*)-**32** was used without further purification in solid-phase oligonucleotide synthesis.

^{31}P{^{1}H} NMR (202 MHz, chloroform-*d*): *δ* = 148.1, 148.0.

HR-ESI MS (positive mode, MeCN): *m/z* calc. for $C_{44}H_{54}N_3O_7PS$, 303.1380 [DMT]$^+$, 818.3598 [M+H_2O+H]$^+$, 846.3911 [M+C_2H_6O+H]$^+$, 901.4697 [M+$C_6H_{15}N$+H]$^+$, 929.5010 [M+$C_8H_{19}N$+H]$^+$; found 303.1362, 818.3606, 846.3920, 901.4707, 929.5021.

7.9 Oligonucleotide Synthesis and Purification

Table 7.3: List of all modified oligonucleotides synthesized in this thesis.

Name	Sequence (5' → 3')	Name	Sequence (5' → 3')
Oligo **A**	TT$\mathbf{L}^{1}$ GGG	Oligo **B**	T$\mathbf{L}^{1}$G GGG
Oligo **C**	TT$\mathbf{L}^{1}$ GGG T	Oligo **D**	GGG $\mathbf{L}^{1}$TT
Oligo **E**	GGG G$\mathbf{L}^{1}$T	Oligo **F**	TGG G$\mathbf{L}^{1}$T T
Oligo **G**	A GG$\mathbf{L}^{1}$ TTA $\mathbf{L}^{1}$GG TTA GG$\mathbf{L}^{1}$ TTA $\mathbf{L}^{1}$GG ATA CAG CTT AT		
Oligo **H**	A GG$\mathbf{L}^{1}$ TTA $\mathbf{L}^{1}$GG TTA GG$\mathbf{L}^{1}$ TTA $\mathbf{L}^{1}$GG AAT AAG CTG TA		
Oligo **I**	$\mathbf{L}^{2}$GG GG		
Oligo **J**	GGG $\mathbf{L}^{1}$TT $\mathbf{L}^{1}$GG GTT GGG $\mathbf{L}^{1}$TT $\mathbf{L}^{1}$GG G		
Oligo **K**	TEMPO-$\mathbf{L}^{2}$ GGG $\mathbf{L}^{1}$TT $\mathbf{L}^{1}$GG GTT GGG $\mathbf{L}^{1}$TT $\mathbf{L}^{1}$GG G		
Oligo **L**	$\mathbf{L}^{3}$GG G	Oligo **M**	$\mathbf{L}^{3}$GG GG
Oligo **N**	$\mathbf{L}^{3}$GG GGG	Oligo **O**	$\mathbf{L}^{4}$GG GG
Oligo **P**	$\mathbf{L}^{4}$GG GGG	Oligo **Q**	$\mathbf{L}^{5}$GG GG
Oligo **R**	$\mathbf{L}^{5}$GG GGG	Oligo **S**	$\mathbf{L}^{7}$GG G
Oligo **T**	$\mathbf{L}^{7}$GG GG		
htel$\mathbf{L}^{3}_{4}$	AGG $\mathbf{L}^{3}$TT A$\mathbf{L}^{3}$G GTT AGG $\mathbf{L}^{3}$TT A$\mathbf{L}^{3}$G G		
htel$\mathbf{L}^{3}_{3}\mathbf{L}^{8}$	AGG $\mathbf{L}^{8}$TT A$\mathbf{L}^{3}$G GTT AGG $\mathbf{L}^{3}$TT A$\mathbf{L}^{3}$G G		
htel$\mathbf{L}^{3}_{2}\mathbf{L}^{8}_{2}$	AGG $\mathbf{L}^{8}$TT A$\mathbf{L}^{3}$G GTT AGG $\mathbf{L}^{8}$TT A$\mathbf{L}^{3}$G G		
htel$\mathbf{L}^{3}_{1}\mathbf{L}^{8}_{3}$	AGG $\mathbf{L}^{8}$TT A$\mathbf{L}^{8}$G GTT AGG $\mathbf{L}^{8}$TT A$\mathbf{L}^{3}$G G		
htel$\mathbf{L}^{3}_{4}\mathbf{L}^{8}_{2}$	AGG $\mathbf{L}^{3}$T$\mathbf{L}^{8}$ T$\mathbf{L}^{3}$G GTT AGG $\mathbf{L}^{3}$T$\mathbf{L}^{8}$ T$\mathbf{L}^{3}$G G		
htel$\mathbf{L}^{3}_{3}\mathbf{L}^{8}_{3}$	AGG $\mathbf{L}^{3}$T$\mathbf{L}^{8}$ T$\mathbf{L}^{8}$G GTT AGG $\mathbf{L}^{3}$T$\mathbf{L}^{3}$ T$\mathbf{L}^{8}$G G		
htel$\mathbf{L}^{3}_{2}\mathbf{L}^{8}_{4}$	AGG $\mathbf{L}^{8}$T$\mathbf{L}^{3}$ T$\mathbf{L}^{8}$G GTT AGG $\mathbf{L}^{8}$T$\mathbf{L}^{3}$ T$\mathbf{L}^{8}$G G		
htel$\mathbf{L}^{8}_{4}$B	AGG $\mathbf{L}^{8}$TT T$\mathbf{L}^{8}$G GTT AGG $\mathbf{L}^{8}$TT T$\mathbf{L}^{8}$G G		

7.9.1 Solid-Phase Oligonucleotide Synthesis

All oligonucleotides were synthesized on a *K&A Laborgeraete GbR H-8* synthesizer on a 1 µmol scale using the standard phosphoramidite methods on CPG and following previously published procedures for synthesis.[1,3]

Table 7.4: Reagents for DNA synthesis.

Name	Reagent	Composition
DCA	detritylation	3% (v/v) dichloroacetic acid in anhydrous dichloromethane
ACT	activator	0.3 M 5-(benzylthio)-1H-tetrazole in anhydrous acetonitrile
Cap A	capping A	10% (v/v) N-methyl imidazole in anhydrous tetrahydrofuran
Cap B	capping B	2,6-lutidine / acetic anhydride / anhydrous tetrahydrofuran 1:1:8 (v/v/v)
OXI	oxidizer	0.02 M iodine in tetrahydrofuran / pyridine / water 7:2:1 (v/v/v)
ACN		anhydrous acetonitrile

Standard phosphoramidites (DMT-dT-CEP, DMT-dG(*i*Bu)-CEP, DMT-dC(bz)-CEP and DMT-dA(bz)-CEP) were used and cartridges with controlled pore glass (CPG) solid supports (1000 Å, 25-35 µmol/g, DMT-dT-CPG, DMT-dG(*i*Bu)-CPG, DMT-dA(bz)-CPG) were manually packed. Reagent solutions were either self-mixed (Table 7.4) or purchased from Sigma Aldrich (TCA deblock, ETT activator, cap A, cap B, oxidizer). The oligonucleotide synthesis followed the built-in methods of the DNA synthesizer and was slightly modified. First, the cartridges were treated three times with DCA/TCA to deprotect the 5’-OH groups. Second, coupling was achieved by mixing the respective phosphoramidite building block (0.1 M in ACN) with ACT (1:1, v/v). The coupling time was ~0.5 min for standard phosphoramidites and ~3.5 min for modified phosphoramidites. Third, the cartridge was treated with a 1:1 (v/v) mixture of Cap A and Cap B to acetylate unreacted 5’-OH groups, which was followed, by the oxidation with OXI. Here, an additional washing step with ACN was introduced compared to the standard routine. After each individual step of the cycle, the cartridge was washed with ACN followed by a drying step with argon. The described cycle was repeated for every incorporated nucleotide.

7.9.2 Post-Synthetical CuAAC to Attach TEMPO Spin Label (only for Oligo K)

The protocol was adapted from reported procedures.[21] After the solid-phase oligonucleotide synthesis, the obtained CPG (1 µmol scale is equal to 1 equiv.) with the protected oligo **K** attached was suspended in 1 mL of water. In a separate vial, 250 µL of an aqueous 0.1 M $CuSO_4$ solution (25 equiv.) and 250 µL of a 0.2 M TBTA solution (50 equiv.) in DMSO/tBuOH 3:1 (v/v) were mixed and immediately transferred into the oligonucleotide containing suspension. After that, 400 µL or 125 µL of an aqueous 0.1 M sodium ascorbate solution (40 or 12.5 equiv., freshly prepared) and subsequently 2.5 mL of a 0.02 M TEMPO azide (**8**, 50 equiv.) solution in DMSO/tBuOH 3:1 (v/v) were added. After agitation for 2 h at room temperature, the solution was decanted and the CPG with the attached strands was washed with DMSO/tBuOH 3:1 (v/v) (2x 10 mL) and with water (2x 10 mL).

7.9.3 Cleavage from Solid Support and Deprotection of Oligonucleotides

Cleavage of the DNA strands from the solid support and removal of all protection groups (except for the DMT group) was carried out under different conditions, depending on the presence of different incorporated ligand functionalities or modifications.

(i) Strands containing only canonical nucleotides, pyridine (**L^1**), imidazole (**L^8**) or thioether (**L^5**) ligandosides or the alkyne linker with or without TEMPO attached (**L^2** or **L^2**-TEMPO) were treated with concentrated aqueous NH_3 solution (0.5 mL) at 55 °C overnight for cleavage and deprotection. The supernatant solution was then filtered (*VWR Centrifugal filters*), and the solid support was washed with 100 µL H_2O. NH_3 was subsequently removed from the filtrate under reduced pressure using a *H. Saur Laborbedarf S-Concentrator BA-VC-300H* vacuum concentrator and the volume of the solution was reduced to ~300 µL.

(ii) Strands containing carboxylate ligandosides (**L^3** or **L^4**) were treated in 0.5 mL of 0.4 M NaOH in a mixture of methanol and water (4:1, v/v) at 55 °C overnight for cleavage and deprotection. The supernatant solution was filtered, and the solid support was washed with 100 µL H_2O. The filtrate was diluted with water to a volume of 2 mL, methanol was removed under reduced pressure using a vacuum concentrator and the volume of the solution was reduced to ~0.5 mL. 1.5 mL of 0.1 M TEAA buffer pH 7.0 were added, the sample was desalted using *Waters Sep-*

Pak C18 cartridges and the volume was again reduced to ~0.3 mL using the vacuum concentrator.

(iii) Oligonucleotides containing the thiol-based ligandoside (**L**^{7}) were, while still attached to the solid support, first treated with 10% diethylamine in acetonitrile at room temperature for 15 min, washed with acetonitrile (5x 1.5 mL), water (1x 1.5 mL), and with a cold 1:1 (v/v) mixture of concentrated aqueous NH_3 solution and 40% aqueous methylamine solution (AMA, 1x 1.5 mL) and were subsequently treated in 650 µL of AMA at 65 °C for 12 min. The supernatant solution was filtered, and the solid support was washed with 100 µL H_2O. NH_3 and methylamine were removed from the filtrate under reduced pressure using a vacuum concentrator (1 mL of water was added in between) and the volume of the solution was reduced to ~300 µL. The samples were kept under aerobic, basic conditions to ensure full oxidation to the disulfide species.

7.9.4 Purification and Storage of Oligonucleotides

Purification of all oligonucleotides was performed DMT-ON (except for oligonucleotides containing **L**^{2}, TEMPO-**L**^{2} or **L**^{4}) with semipreparative reversed-phase HPLC on an *Agilent Technologies 1260 Infinity II* HPLC system equipped with an autosampler, column oven, DAD detector and a *Macherey-Nagel VP 250/10 NUCLEODUR 100-5 C18ec* column (oven temperature: 60 °C, flow rate: 2.5 mL/min, solvent A: 50 mM TEAA pH 7.0, solvent B: 70:30 MeCN/50 mM TEAA pH 7.0, gradients: (i) from 100% solvent A to 20% solvent A and 80% solvent B in 30 min (standard gradient), (ii) from 100% solvent A to 80% solvent A and 20% solvent B in 60 min (for TEMPO-containing oligonucleotides (DMT-OFF purification)), (iii) from 100% solvent A to 40% solvent A and 60% solvent B in 80 min (for thiol/disulfide-containing oligonucleotides)). To subsequently remove ACN from the sample, the volume of the solution was either reduced to ~300 µL in the vacuum concentrator or the sample was lyophilized using a *Christ Alpha 2-4 LSCbasic* lyophilization device, Then, the sample was diluted/dissolved with 100 mM TEAA pH 7.0 to a volume of 2 mL.

Subsequently, the cleavage of the 5′-OH DMT protecting groups (with 2% TFA) and desalting were accomplished using *Waters Sep-Pak* C18 cartridges. Desalted oligonucleotides were lyophilized and stored either as a solid or as 0.5–2.5 mM stock solutions in pure water or different buffers (100 mM lithium cacodylate pH 7.2, 75 mM potassium phosphate pH 7.0, 50 mM TMAA pH 7.0) at –20 °C.

7.9.5 Reduction of Oligonucleotides Containing Disulfide Bridges

Oligonucleotides containing the thiol-based ligandoside ($\mathbf{L^7}$) were obtained as the oxidized disulfide species. Subsequent reduction was performed in in a *GS-systems* glovebox under oxygen-free conditions. Circa 1 mM oligonucleotide was reduced with 100 mM DTT at room temperature for at least 8 h (100 µL volume). The reducing agent was removed by gel filtration (*PD MiniTrap* columns containing *Sephadex G-10*, cut-off molecular weight: 700 Da).

Quantification of thiol groups in the stock samples was achieved with Ellman's test. Therefore, 4 mg of Ellman's reagent (5,5'-dithio-bis-(2-nitrobenzoic acid)) were dissolved in 1 mL of reaction buffer (0.1 M sodium phosphate pH 8.0, containing 1 mM EDTA). 25 µL of Ellman's reagent solution was mixed with 1.25 mL of reaction buffer and either 125 µL of water were added to obtain the blank sample or 125 µL of reduced oligonucleotide stock solution were added to obtain the probe sample. After mixing and an incubation time of 20 min, absorption was measured at 412 nm. An absorption coefficient of $\varepsilon_{412} = 14150\ \mathrm{M^{-1}cm^{-1}}$ was used to determine the concentration of the resulting dye (2-nitro-5-thiobenzoate) which is equivalent to the initial thiol concentration.

7.9.6 Concentration Determination of DNA Stock Solutions

The concentrations of all oligonucleotide stock solutions were determined *via* the absorbance at 260 nm at 25 °C with a *Thermo Scientific Nanodrop One* instrument and using revised extinction coefficients for the canonical nucleosides[22] and for the artificial nucleosides ($\varepsilon_{260} = 1971\ \mathrm{L\ mol^{-1}\ cm^{-1}}$ for $\mathbf{L^1}$,[1] $1675\ \mathrm{L\ mol^{-1}\ cm^{-1}}$ for $\mathbf{L^2}$-TEMPO (Figure 7.3), $1111\ \mathrm{L\ mol^{-1}\ cm^{-1}}$ for $\mathbf{L^3}$ (Figure 7.6). No significant contribution to the overall absorption at 260 nm was assumed for $\mathbf{L^2}$, $\mathbf{L^4}$, $\mathbf{L^5}$, $\mathbf{L^7}$, and $\mathbf{L^8}$).[5,23]

7.10 References

[1] D. M. Engelhard, J. Nowack, G. H. Clever, *Angew. Chem. Int. Ed.* **2017**, *56*, 11640–11644.

[2] D. M. Engelhard, A. Meyer, A. Berndhäuser, O. Schiemann, G. H. Clever, *Chem. Commun.* **2018**, *54*, 7455–7458.

[3] D. M. Engelhard, L. M. Stratmann, G. H. Clever, *Chem. Eur. J.* **2018**, *24*, 2117–2125.

[4] P. M. Punt, L. M. Stratmann, S. Sevim, L. Knauer, C. Strohmann, G. H. Clever, *Front. Chem.* **2020**, *8*, 26.

[5] P. M. Punt, G. H. Clever, *Chem. Eur. J.* **2019**, *25*, 13987–13993.

[6] P. M. Punt, M. D. Langenberg, O. Altan, G. H. Clever, *J. Am. Chem. Soc.* **2021**, *143*, 3555–3561.

[7] S. Pérez-Rentero, S. Grijalvo, R. Ferreira, R. Eritja, *Molecules* **2012**, *17*, 10026–10045.

[8] W. Wang, K. Chen, D. Qu, W. Chi, W. Xiong, Y. Huang, J. Wen, S. Feng, B. Zhang, *Tetrahedron Lett.* **2012**, *53*, 6747–6750.

[9] O. Y. Fedoroff, M. Salazar, H. Han, V. V. Chemeris, S. M. Kerwin, L. H. Hurley, *Biochemistry* **1998**, *37*, 12367–12374.

[10] C. Sissi, L. Lucatello, A. P. Krapcho, D. J. Maloney, M. B. Boxer, M. V. Camarasa, G. Pezzoni, E. Menta, M. Palumbo, *Bioorgan. Med. Chem.* **2007**, *15*, 555–562.

[11] C. Tansakul, E. Lilie, E. D. Walter, F. Rivera, A. Wolcott, J. Z. Zhang, G. L. Millhauser, R. Braslau, *J. Phys. Chem. C* **2010**, *114*, 7793–7805.

[12] G. M. Sheldrick, *Acta Crystallogr., Sect. Found. Adv.* **2015**, *71*, 3–8.

[13] G. M. Sheldrick, *Acta Crystallogr., Sect. C: Struct. Chem.* **2015**, *71*, 3–8.

[14] L. J. Farrugia, *J. Appl. Crystallogr.* **1997**, *30*, 565–565.

[15] O. V. Dolomanov, L. J. Bourhis, R. J. Gildea, J. A. K. Howard, H. Puschmann, *J. Appl. Crystallogr.* **2009**, *42*, 339–341.

[16] G. M. Sheldrick, *Acta Crystallogr. Sect. Found. Crystallogr.* **2008**, *64*, 112–122.

[17] S. E. Fangour, A. Guy, V. Despres, J.-P. Vidal, J.-C. Rossi, T. Durand, *J. Org. Chem.* **2004**, *69*, 2498–2503.

[18] H. Tsuji, H. Yamamoto, *J. Am. Chem. Soc.* **2016**, *138*, 14218–14221.

[19] O. L. Acevedo, R. S. Andrews, *Tetrahedron Lett.* **1996**, *37*, 3931–3934.

[20] P. Tecilla, V. Jubian, A. D. Hamilton, *Tetrahedron* **1995**, *51*, 435–448.

[21] P. Ding, D. Wunnicke, H. Steinhoff, F. Seela, *Chem. Eur. J.* **2010**, *16*, 14385–14396.

[22] M. J. Cavaluzzi, P. N. Borer, *Nucleic Acids Res.* **2004**, *32*, e13–e13.

[23] P. M. Punt, G. H. Clever, *Chem. Sci.* **2019**, *10*, 2513–2518.

8 Acknowledgments

At first, I would like to thank my PhD supervisor Prof. Guido Clever who allowed me to work in his group in the perfectly equipped labs. I enjoyed working with you motivated by your passion and enthusiasm for science. Thanks for giving me the time I needed to find my way into my PhD research. I also liked very much the humorous half-scientific or non-scientific moments (e.g. the times when you arrived at a Friday afternoon in the DNA office where Philip and me were sitting, you sighed, and said: “Endlich normale Leute!”).

Many thanks go to Prof. Müge Kasanmaschaff for being the co-examiner of this thesis. Further, I am very grateful to Müge and especially Yury for the fruitful interdisciplinary collaboration. Without your effort, both our great paper and half of this thesis would not have been possible at all!

I want to thank all members of the small DNA subgroup of the Clever Lab for working as a team and helping out each other. There is David, who started and developed the whole idea of incorporating metal ions into G-quadruplex structures in the Clever Lab. Julia and Soham were the experienced postdocs helping me a lot when I was starting in the field of DNA chemistry, that was completely new to me at that time. And now there are Hannah and Simon who will carry on our exciting ideas in the lab. I also want to thank my Bachelor students Katharina, Sinem, Rameeya and Viktoria who helped me with my research.

Specifically, I want to thank, of course, Philip who started to work in the Clever Lab together with me and was my office and lab mate since then. It seems that he does not agree with me (have a look in the note of thanks in his thesis :D), but I think we were a great duo supporting each other a lot. I will never forget our awesome conference trips together, with the time in Interlaken sleeping in a tent as my absolute highlight (it is not surprising that Irene was often jealous of you).

I say thank you to the whole Clever Lab! I really enjoyed the international spirit with so many coworkers with different cultures from all over the world (Australia, China, India, Italy, Korea, Japan, Mexico, Switzerland, France and Germany). We had lots of fun together especially at our group trips (e.g. Edersee, Juist, sailing trip). I am very thankful for the amazing trip (my first time out of Europe) with Kristina and Andrè where we visited Lavana’s and Sudhakar’s wedding in India.

Also, I was very proud and honored welcoming you all as “king” in my hometown Illingen at the Schützenfest. I will never forget the moment where Kai and Sudhakar played the symbals in the traditional marching band :D.

Three months after I started my PhD studies, I got to know a new Italian colleague Irene (thanks again to Guido for hiring her!) who now is my wife (feels still strange to write this). We are so different, have both our strengths and weaknesses and it is amazing to realize how well we complement each other in different situations and make each other stronger. You also have a big impact on the success of this thesis <3.

Additionally, I want to thank everyone, who contributed to my research by performing analytic of my samples: The NMR team; Markus Hüffner for elemental analyses; Laura for ESI-MS; Prof. Waldmann and Jens Warmers for access and help with MALDI measurements; Prof. Strohmann, Lena, and Julian for X-ray diffraction.

Ich möchte mich außerdem natürlich bei meinen Eltern und meinen Geschwistern für die bedingungslose Unterstützung bedanken. Meiner Mutter möchte ich besonders dafür danken, dass sie mir respektvolles Diskutieren und den Umgang mit anderen Meinungen und Auffassungen beigebracht hat (und immer noch beibringt). Grazie ai miei nuovi suoceri per la vostra ospitalità. Ho scritto una grande parte di queste tesi nel mio ufficio comodo vicino al caminetto a Fiumicello!

Zum Schluss möchte ich mich bei all meinen Freunden bedanken, die von Chemie keine Ahnung haben und mir glücklicherweise immer wieder zeigen, dass es auch noch andere wichtige Dinge im Leben gibt. Als Ausnahme möchte ich Michael nennen, der als einer der wenigen Personen auch in meinen beiden so unterschiedlichen Welten, Illinger Dorfleben und Promotion in Chemie, zu Hause ist und mir häufiger geholfen hat, als er wahrscheinlich weiß.

Eidesstattliche Versicherung (Affidavit)

Name, Vorname
(Surname, first name)

Matrikel-Nr.
(Enrolment number)

Belehrung:	Official notification:
Wer vorsätzlich gegen eine die Täuschung über Prüfungsleistungen betreffende Regelung einer Hochschulprüfungsordnung verstößt, handelt ordnungswidrig. Die Ordnungswidrigkeit kann mit einer Geldbuße von bis zu 50.000,00 € geahndet werden. Zuständige Verwaltungsbehörde für die Verfolgung und Ahndung von Ordnungswidrigkeiten ist der Kanzler/die Kanzlerin der Technischen Universität Dortmund. Im Falle eines mehrfachen oder sonstigen schwerwiegenden Täuschungsversuches kann der Prüfling zudem exmatrikuliert werden, § 63 Abs. 5 Hochschulgesetz NRW.	Any person who intentionally breaches any regulation of university examination regulations relating to deception in examination performance is acting improperly. This offence can be punished with a fine of up to EUR 50,000.00. The competent administrative authority for the pursuit and prosecution of offences of this type is the chancellor of the TU Dortmund University. In the case of multiple or other serious attempts at deception, the candidate can also be unenrolled, Section 63, paragraph 5 of the Universities Act of North Rhine-Westphalia.
Die Abgabe einer falschen Versicherung an Eides statt ist strafbar.	The submission of a false affidavit is punishable.
Wer vorsätzlich eine falsche Versicherung an Eides statt abgibt, kann mit einer Freiheitsstrafe bis zu drei Jahren oder mit Geldstrafe bestraft werden, § 156 StGB. Die fahrlässige Abgabe einer falschen Versicherung an Eides statt kann mit einer Freiheitsstrafe bis zu einem Jahr oder Geldstrafe bestraft werden, § 161 StGB.	Any person who intentionally submits a false affidavit can be punished with a prison sentence of up to three years or a fine, Section 156 of the Criminal Code. The negligent submission of a false affidavit can be punished with a prison sentence of up to one year or a fine, Section 161 of the Criminal Code.
Die oben stehende Belehrung habe ich zur Kenntnis genommen:	I have taken note of the above official notification.

Ort, Datum
(Place, date)

Unterschrift
(Signature)

Titel der Dissertation:
(Title of the thesis):

Ich versichere hiermit an Eides statt, dass ich die vorliegende Dissertation mit dem Titel selbstständig und ohne unzulässige fremde Hilfe angefertigt habe. Ich habe keine anderen als die angegebenen Quellen und Hilfsmittel benutzt sowie wörtliche und sinngemäße Zitate kenntlich gemacht. Die Arbeit hat in gegenwärtiger oder in einer anderen Fassung weder der TU Dortmund noch einer anderen Hochschule im Zusammenhang mit einer staatlichen oder akademischen Prüfung vorgelegen.	I hereby swear that I have completed the present dissertation independently and without inadmissible external support. I have not used any sources or tools other than those indicated and have identified literal and analogous quotations. The thesis in its current version or another version has not been presented to the TU Dortmund University or another university in connection with a state or academic examination.*

*Please be aware that solely the German version of the affidavit ("Eidesstattliche Versicherung") for the PhD thesis is the official and legally binding version.

Ort, Datum
(Place, date)

Unterschrift
(Signature)